DTIC FILE COPY

Original contains color plates: All DTIC reproductions will be in black and white

MONOGRAPH 90-1

Sea Ice Properties and Processes

Proceedings of the W.F.Weeks Sea Ice Symposium

Stephen F. Ackley and Wilford F. Weeks, Editors

February 1990

AD-A221 723

DTIC
ELECTE
MAY 14 1990
S D
E

DISTRIBUTION STATEMENT A
Approved for public release;
Distribution Unlimited

90 05 14 042

For conversion of SI metric units to U.S./British customary units of measurement consult ASTM Standard E380, Metric Practice Guide, *published by the American Society for Testing and Materials, 1916 Race St., Philadelphia, Pa. 19103.*

Monograph 90-1

U.S. Army Corps of Engineers
Cold Regions Research & Engineering Laboratory

Sea Ice Properties and Processes

Proceedings of the W.F. Weeks Sea Ice Symposium

Stephen F. Ackley and Wilford F. Weeks, Editors

February 1990

Accession For
NTIS GRA&I
DTIC TAB
Unannounced
Justification
By
Distribution/
Availability Codes
Dist | Avail and/or Special
A-1

DTIC COPY INSPECTED 4

"Original contains color plates: All DTIC reproductions will be in black and white"

Approved for public release; distribution is unlimited.

FOREWORD

This proceedings volume results from the San Francisco meeting in December 1988 that we put together in celebration of Willy Weeks' career at CRREL. Someone told me this was a "Festschrift," a word I still can't pronounce or spell, never mind, define. The meeting nicely fit in with what have become regular sea ice sessions at the Fall Meeting of the American Geophysical Union, alternating with similar sessions at the AGU–ASLO Ocean Sciences Meeting in the years when it is held. These meetings, including the Weeks Symposium, have been sponsored by the Snow, Ice and Permafrost Committee of AGU. I'd like to acknowledge Garry Clarke's role in making the Committee "All-Union," rather than having its home in one AGU section (Hydrology), thereby opening the door for sea ice work to be included in its mandate. The rest of the Committee has also been invaluable in supporting the concept that sea ice work should be a regular feature of AGU meetings under their sponsorship.

Willy's retirement from CRREL's Snow and Ice Branch, to become Chief Scientist at the University of Alaska/NASA's Alaskan SAR Facility, marked the occasion to hold this symposium, as well as his being named a Fellow of AGU in 1988. This volume, consisting of 84 papers/abstracts by about 150 authors, is, in my opinion, a fairly astounding but fitting tribute to Willy's endeavors in sea ice research. Consider alone that the number of workers, when Willy began working in this field in the 1950s, was probably of the order of one-tenth the number represented in this volume. That nearly all these people can point to an encounter with Willy, either in person or in the literature, as having contributed to their knowledge or interest in the field, gives some notion of his impact.

I'd like to claim that putting together this volume and organizing the symposium was some superhuman task that would have burned out five ordinary people. That bald-faced lie would make a lot of people upset, so I'd like to thank those people who contributed to the effort, and so made my job relatively carefree and enjoyable. First of all, the support of the Snow, Ice and Permafrost Committee (Jeff Dozier, Chairman), the Meetings Staff of AGU, and Don L. Anderson, AGU President and early colleague of Willy, is gratefully acknowledged. Bill Hibler (Dartmouth College) and G[illegible] Weller (U. of Alaska) hosted the reception held in conjunction with the symposium and contributed moral, technical and economic support along the way. The CRREL publications staff, Ed Wright (editor of this proceedings), Donna Valliere, Steve Bowen, Sandy Smith, Matt Pacillo, Ed Perkins, Cheryl Stiles, etc., have been instrumental in putting together the volume, as well as straightening out Willy's prose and diagrams throughout his career at CRREL. I would also like to express appreciation to the contributors to the volume, who significantly adhered to the deadlines imposed (only the usual three extensions were necessary, primarily to accommodate those well-known malingerers, Weeks and Ackley). The authors are also to be commended for providing papers in relatively completed form, requiring only minimal intervention to finalize them.

Finally, to Willy, I hope this volume provides some small measure of our appreciation of your contributions to the field, of your mentorship of virtually all of us, and, most of all, of your friendship and support. Your ability to see something good in our efforts as we were learning and making our mistakes through the years is a unique characteristic of a great character. Woody Allen once said that some people become immortal through their work but that he'd prefer to become immortal by not dying. That one hasn't been quite worked out yet so you'll have to settle for the lesser option. Cheers.

Steve Ackley

CONTENTS

Page

Foreword ii

Section I. Physical Properties of Sea Ice

A. Structural and Chemical Properties

1. The Internal Structure, Composition and Properties of Brackish Ice from the Bay of Bothnia, *W.F. Weeks, A.J. Gow, P. Kosloff and S. Digby-Argus* 5
2. Snow Cover Effects on Antarctic Sea Ice Thickness, *S.F. Ackley, M.A. Lange and P. Wadhams* 16
3. Development and Physical Properties of Sea Ice in the Weddell Sea, Antarctica, *M.A. Lange* 22
4. Quantification of Sea-Ice Textures Through Automated Digital Image Analysis, *H. Eicken, M.A. Lange and S.F.Ackley* 28
5. The Chemical and Structural Properties of Sea Ice in the Southern Beaufort Sea, *D.A. Meese* 32
6. Nutrient Concentrations in Antarctic Pack Ice During Winter, *D.L. Garrison, A.R. Close and L.I. Gordon* 35
7. Verification Results of the Cox and Weeks Sea Ice Salinity Prediction Model (abstract), *G.F.N. Cox.* 40
8. Heat Transfer to Arctic Sea Ice: Evidence from Dissolved Argon (abstract), *R.M. Moore and W. Spitzer* 41

B. Optical, Electrical, Acoustical and Mechanical Properties

1. Theoretical Estimates of Light Reflection and Transmission by Spatially Inhomogeneous and Temporally Varying Ice Covers, *D.K. Perovich* 45
2. Scattering and Absorption of Light by Sea Ice, *R.G. Buckley and H.J. Trodahl* 49
3. Beam Scattering Measurements in Young Sea Ice, *K.J. Voss, J.S. Schoonmaker and G.D. Gilbert* 53
4. Electrical, Physical and Microwave Properties of Snow-Covered Floating Ice, *C. Garrity* 57
5. Some Observations of Established Snow Cover on Saline Ice and Their Relevance to Microwave Remote Sensing, *A. Lohanick.* 61
6. Acoustical and Morphological Properties of Undeformed Sea Ice: Laboratory and Field Results, *K.C. Jezek, T.K. Stanton, A.J. Gow and M.A. Lange* 67
7. Acoustics of Arctic Ice Floes Modeling, Simulation and Signal Processing, *C.A. Pomalaza-Raez, S.S. Shanan and H.H. Shen* 75
8. Stress Relief in Sea Ice as Related to the Generation of Higher Frequency Noise (abstract), *J.K. Lewis, P.J. Stein and W.W. Denner* 78
9. Comparison of the Compressive Strength of Antarctic Frazil Ice and Columnar Saline Ice Grown in the Laboratory, *J.A. Richter-Menge, S.F. Ackley and M.A. Lange* 79
10. The Variation in the Triaxial Strength of Multiyear Sea Ice With Structure, Salinity and Density (abstract), *P.R. Sammonds and S.A.F. Murrell* 84

C. Biological and Sediment Inclusions in Sea Ice

1. Sea Ice: A Habitat for the Foraminifer *Neogloboquadrina Pachyderma? G. Dieckmann, M. Spindler, M.A. Lange, H. Eicken and S. F. Ackley.* 86
2. Microorganisms Concentrated by Frazil Ice: Evidence from Laboratory Experiments and Field Measurements, *D.L. Garrison, A.R. Close and E. Reimnitz* 92

Page

3. Suspended-Matter Scavenging by Rising Frazil Ice as Observed in Tank Experiments, *E. Reimnitz, E.W. Kempema, W.S. Weber, J.R. Clayton and J.R. Payne* .. 97
4. Wave-Induced Sediment Enrichment in Coastal Ice Cover, *H.T. Shen and N.L. Ackermann* 100
5. Sediment in Eurasian Arctic Sea Ice, *I. Wollenburg, S. Pfirman and M.A. Lange* 102
6. Source, Characteristics and Significance of Sediment Pellets Formed on the Sea Ice of the Arctic Basin, *P.W. Barnes, E.M. Kempema and E. Reimnitz.* 106
7. Sediment Transport by Ice Gouging: Application of Model Experiments to the Arctic Continental Shelf, *P.W. Barnes, R.E. Hunter, A. Lee, E. Reimnitz and W.S. Weber* 109
8. Movements of Fine-Grained Sediment Particles in Freshwater and Seawater-Slush Ice Slurries During Freeze Front Advances, *J.R. Clayton, Jr., J.R. Payne, E.W. Kempema and E. Reimnitz* 111
9. Salt-Water Anchor Ice Formation Observations from the Alaskan Beaufort Sea and Flume Experiments, *E.W. Kempema, E. Reimnitz and P.W. Barnes* 114

Section II. Morphological Processes in Sea Ice: Leads and Pressure Ridges in Sea Ice

1. Lidar Detection of Leads in Arctic Sea Ice, *R.C. Schnell, R.G. Barry, M.W. Miles, E.L Andreas, L.F. Radke, C.A. Brock, M.P. McCormick and J.L. Moorell* 119
2. Review of the Oceanography and Micrometeorology of Arctic Leads and Polynyas, *S.D. Smith* 123
3. Wind-Generated Polynyas off the Coasts of Bering Sea Islands, *T.L. Kozo, L.D. Farmer and J.P. Welsh* 126
4. Recent Measurements of Sea Ice Topography in the Eastern Arctic, *W.B. Krabill, R.N. Swift and W.B. Tucker III* 132
5. Processes Determining the Bottom Topography of Multiyear Arctic Sea Ice, *P. Wadhams and S. Martin* 136
6. A Fractal Description of Ice Keel Small-Scale Roughness, *G.C. Bishop and S.E. Chellis* 141
7. A Small-Scale Under-Ice Morphology Study in the High Arctic, *D.N. Connors, E.R. Levine and R.R. Shell* 145
8. Simulation of the Ice Ridging Process, *M.A. Hopkins and W.D. Hibler III.* 152
9. Periodicities and Keel Spacings in the Under-Ice Draft Distribution, *J. Key and A.S. McLaren.* 156

Section III. Large-Scale Variations in Drift, Extent, Snowmelt and Concentration of Sea Ice

1. Mountain Barrier Effects on Ice Island Drift in a Coastal Ice Zone, *M. Lu and W.M. Sackinger.* 163
2. Analysis of Sea-Ice Drift in a Coastal Ice Zone, *P.A. Smith* 168
3. Variations in Antarctic Sea Ice, *E. Breitenberger and G. Wendler.* 173
4. A Time-Lapse Motion Study of the "Odden" During 1978–87 as Observed With the Nimbus 7 Scanning Multichannel Microwave Radiometer, *P. Gloersen* 177
5. SMMR Observations of the Sea Ice Regime in the Ross Sea 1979–1985, *S. Jacobs and J.C. Comiso* 179
6. Variability of Sea Ice Concentration in the Canada Basin and Associated Atmospheric Forcings: 1979–1984, *J.A. Maslanik and R.G. Barry.* 181
7. Reversals of the Beaufort Gyre Sea Ice Circulation and Effects on Ice Concentration in the Canada Basin, *M.C. Serreze, R.G. Barry and A.S. McLaren* 185

Page
8. Interannual Variability of Ice Melt in Kara/Barents Sea (abstract), *R.C. Crane* 189
9. Quasi-Quinquennial Oscillations in the Arctic Sea Ice Cover (abstract), *V.R. Neralla* 189
10. Arctic Ice Motion from Sequential AVHRR Imagery (abstract), *J. Hawkins, W. J. Emery and C. Fowler* 189
11. Observations of Sea Ice Momentum Budget North of Svalbard and Fram Strait (abstract), *H.C. Hoeber* 189
12. AEDB: Ice, Water-Surface Drifting Buoy Mooring Experiment Through the Southern Transpolar Drift (abstract), *S. Honjo* 190
13. The Drift-Ice Route of the AEDB 4 Aug. 1987 to 15 April 1988 (abstract), *R. Krishfield, S. Honjo and P. Wadhams* 190
14. A Diagnostic Examination of the Synoptic Controls on the Annual Reversal of the Beaufort Sea Gyre (abstract), *E. LeDrew, D. Johnson and M.C. Serreze* 191
15. Model and Satellite-Derived Variations of Multiyear Sea Ice Coverage in the Arctic (abstract), *J.E. Walsh and H.J. Zwally* 191
16. Seasonal and Interannual Variations in Arctic Multiyear Sea Ice Distribution (abstract), *H.J. Zwally and J.E. Walsh* 192
17. Arctic Ice and Concentrations from SSMI and AVHRR (abstract), *M. McElroy and W.J. Emery* 192
18. Snow Melt on Arctic Basin Sea Ice (abstract), *G.R. Scharfen, D.A. Robinson, R.G. Barry and M.C. Serreze* 193
19. Relationships Between Atmospheric Conditions and Passive Microwave Derived Melt/Freeze Periods for Hudson Bay During Spring (abstract), *M.R. Anderson and J.A. Schumacher* 193

Section IV. Satellite and Airborne Remote Sensing

1. NASA Sea Ice Validation Program for the DMSP SSM/I, *D.J. Cavalieri, J. Crawford, B. Holt, D. Eppler, L.D. Farmer, K. Steffen and C. T. Swift* 197
2. NASA SSM/I Data Processing and Archiving of Sea Ice Products, *C.S. Morris* 203
3. Validation of the SSM/I and AES/YORK Algorithms for Sea Ice Parameters, *C.A. Bjerkelund, R.O. Ramseier and I.G. Rubenstein* 206
4. Remote Sensing of Ocean Surface Winds with the Special Sensor Microwave/Imager (SSM/I), *M.A. Goodberlet and C.T. Swift* 209
5. Global Snow Variations Derived from SMMR: Preliminary Results, *A.T.C. Chang and L.S. Chiu* 213
6. Antarctic Ice Sheet Brightness Temperature Variations. *K.C. Jezek, A. Hogan and D.J. Cavalieri.* 217
7. Polar Ice Research Using Passive Microwave Observations (abstract), *H.J. Zwally.* 224
8. Characteristics of Sea Ice During the Arctic Winter Using Multifrequency Aircraft Radar Imagery (abstract), *B. Holt, J. Crawford and F. Carsey* 224
9. Airborne Sea Ice Thickness Sounding, *A. Kovacs and J.S. Holladay* 225
10. On the Relationship Between Ice Thickness and 33.6-GHz Brightness Temperature Observed for First-Season Sea Ice, *D. Eppler, L.D. Farmer and A.W. Lohanick* 229
11. Airborne Passive Microwave Observations of Arctic Sea Ice, *J.C. Comiso, R. Kutz and T. Dod* 233

Section V. Sea Ice and Ice–Ocean Modeling

1. A Cavitating Fluid Sea Ice Model, *G.M. Flato and W.D. Hibler III* 239
2. The Importance of an Interactive Ocean on the Simulation of the Annual Cycle and Interannual Variations of the Ice Cover in the Arctic, *G.H. Fleming* .. 243

Page
3. On Modeling the Baroclinic Adjustment of the Arctic Ocean, *W.D. Hibler III* 247
4. Sensitivity Studies with a Coupled Ice-Ocean Model (abstract), *M.N. Houssais and W.D. Hibler III* 251
5. Full Sea Ice Model Forced With a GCM Atmosphere, *P. Loewe* 251
6 The Warming Effect of Meridional Sea Ice Transport on Climate, *T.S. Ledley* 256
7. Preliminary Testing of a Sea Ice Model for the Greenland Sea, *R.H. Preller, A. Cheng and P.G. Posey* 259
8. Sea Ice Modeling with SMMR and Buoy Data, and a Kalman Filter (abstract), *D.A. Rothrock and D.R. Thomas* 278
9. The Interaction of an Ocean Eddy with a Marginal Ice Zone Ocean Front, *D.C. Smith IV, A.A. Bird and W.P. Budgell* 278
10. Using the Free-Drift Force Balance to Estimate Drag Coefficients and Ice Thickness, *M.G. McPhee* 281
11. Coupling of Ice-Ocean Flow in Polar Seas (abstract), *J. E. Overland and C.H. Pease* 284

Section VI. Polar Oceanography: Field Observations

1. An Attempt to Measure Deep Saline Outflow Through Barrow Canyon, *A.T. Roach and K. Aagaard* 287
2. Oceanic Heat Flux in the Fram Strait Measured By a Drifting Buoy, *D.K. Perovich, W.B. Tucker III and R. Krishfield* 291
3. Mesoscale Ocean Processes in the Marginal Ice Zone (abstract), *O.M. Johannesen, S. Sandven and J.A. Johannessen* 296
4. Vertical Mixing in a Highly Stratified Regime Under Landfast Sea Ice (abstract), *R.G. Ingram, S. Lepage and K. Shirasawa* 297
5. The Freeze Experiment: Oceanographic Conditions During Autumn Freezeup in the Western Arctic (abstract), *C.H. Pease and R.D. Muench* 297
6. Acoustic Doppler Current Measurements from the Arctic Environmental Drifting Buoy (abstract), *A.J. Plueddemann and T.B. Curtin* 298
7. Bering Sea Contributions to the Arctic Ocean (abstract), S. *Salo and K. Aagaard* 298

Author Index 299

Section I:
Physical Properties of Sea Ice

A. Structural and Chemical Properties

The Internal Structure, Composition and Properties of Brackish Ice from the Bay of Bothnia

W.F. WEEKS
Geophysical Institute
University of Alaska
Fairbanks, U.S.A.

A.J. GOW
U.S. Army Cold Regions Research and
Engineering Laboratory
Hanover, New Hampshire, U.S.A.

P KOSLOFF
Finnish Institute of Marine Research,
Helsinki, Finland

S. DIGBY-ARGUS
RADARSAT
Canada Centre for Remote Sensing
Ottawa, Canada

ABSTRACT

Field observations made during the March 1988 BEPERS (Bothnian Experiment in Preparation for ERS-1) remote sensing experiment allow limited characterizations of the temperature, salinity, structure and physical property profiles of the different types of brackish ice that forms in the Bay of Bothnia. During the sampling period, undeformed fast ice thicknesses varied from 40 to 60 cm in the bay to the east of Umeå, Sweden, with somewhat thicker ice occurring in the northernmost, nearly fresh, portions of the bay. Ice salinities were generally less than 1‰ and the ice temperatures were usually higher than –3.5 °C. Although most of the ice examined was simple columnar congelation ice, a variety of c-axis fabrics were observed including random, vertical and horizontal (random and aligned) orientations. There was no obvious pattern to the geographic arrangement of these fabrics. Brine volume profiles are used to estimate representative ice property profiles. Comparisons are made between the properties of ice from the Bay of Bothnia and those of more typical sea ice from the Arctic Ocean at similar ice thicknesses. A variety of structural factors contributing to specific areas of higher radar return in the bay are also discussed.

BEPERS

The Bothnian Experiment in Preparation for ERS-1, better known as BEPERS, is a major component in the Finnish and Swedish preparations for the launch of the first European microwave satellite (ERS-1) in late 1990. The objective of the 1 to 11 March 1988 field program was to produce sea ice remote sensing data, similar to that which will be obtained by ERS-1, together with high quality ground-truth and supporting remote sensing observations. These data are now being utilized in developing algorithms that will process and extract geophysically meaningful information from SAR (synthetic aperture radar) images of sea ice, for evaluating the potential of SAR in operational sea ice mapping and forecasting using numerical models, and in planning future calibration/validation experiments in the Baltic Sea. Also, the BEPERS data set will undoubtedly be valuable in designing future investigations of other brackish ice areas.

The BEPERS program was quite ambitious, involving a complement of scientists from seven countries, three ships and several aircraft, including the Canadian Centre for Remote Sensing Convair 580, which was equipped with a multifrequency SAR system. No attempt will be made here to review the overall BEPERS program. Instead some of the results from the BEPERS ice characterization program will be combined with the results of earlier observational programs to provide a picture of the nature of the ice that forms in the Bay of Bothnia and to compare the properties of this ice with those of more typical sea ice from more representative arctic regions.

PHYSICAL SETTING

The Baltic Sea is characterized by a narrow, shallow (sill depth 18 m) connection with the North Sea and a division into a number of different basins and bays. The northernmost portions of the Baltic are the Sea of Bothnia and finally the Bay of Bothnia, which is separated by a sill of 25 m between the coastal cities of Umeå, Sweden and Vaasa, Finland. The salinity of the Baltic is controlled by a balance between the inflows of saline water from the North Sea and of fresh water from the rivers of the region. As might be expected, the greater the distance from the North Sea proper, the lower the salinity. Figure 1 shows the mean surface salinity in the Baltic during November (Bock 1971) and clearly demonstrates this fact. In the Bay of Bothnia, surface salinities are shown to vary

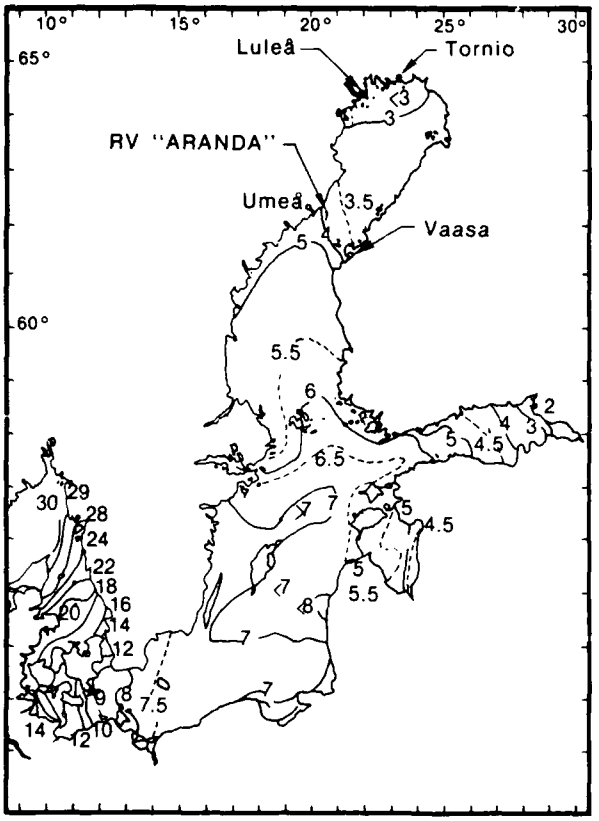

Figure 1. Mean sea surface salinity in the Baltic in November (Bock 1971).

from 4‰ in the south to less than 3‰ in the north. In fact, as will be shown, surface salinities in the northern portions of the Bay are significantly less than 1‰. Maps similar to Figure 1 apparently do not exist for the March time period of the BEPERS program. However, the water salinity values at our sampling sites were in general agreement with the contours shown in Figure 1.

Ice formation starts in the northernmost portions of the Bay of Bothnia in late October, with the ice cover extending southward as air temperatures decrease. During an average year, ice covers the Bay by mid-January and the Sea of Bothnia by mid-February (Thompson and Leppäranta 1987) with the extent of the ice cover varying considerably from year to year. Because there are numerous near-shore islands in some regions of the Bay, fast ice develops early during the ice growth period along many regions of the coast where it is stable for the remainder of the winter (Leppäranta 1981). The fast ice areas are usually in water with depths of less than 5 to 15 m. Further offshore the pack ice is extremely dynamic, drifting in response to winds and currents and forming both complex lead systems and large pressure ridges. Ice floe drifts during storms can be as large as 20 to 30 km/day. The shipping that moves through the Bay during the winter is significantly affected by ice pressure, by ice movements and by pressure ridges.

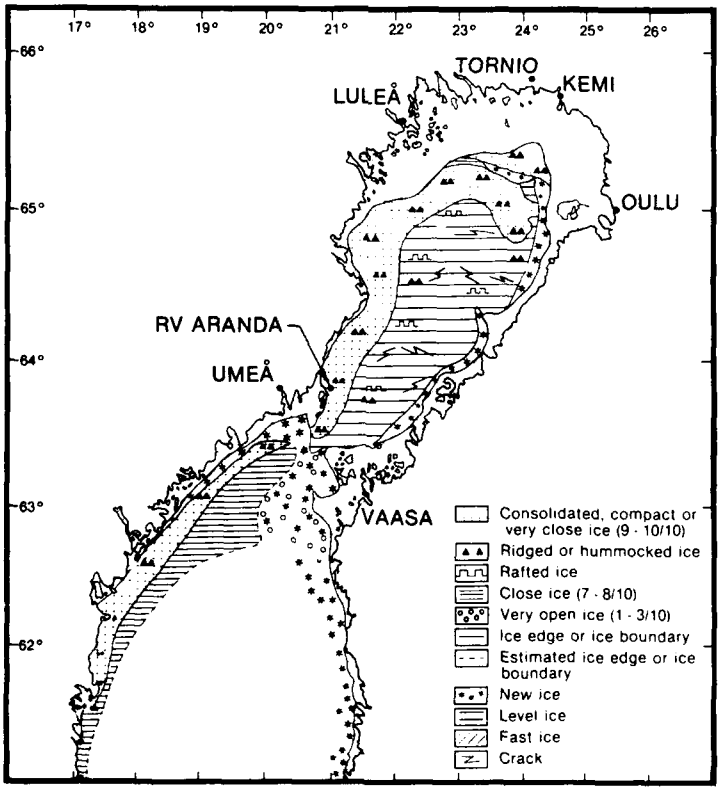

Figure 2. Sea ice conditions at the start of BEPERS-88.

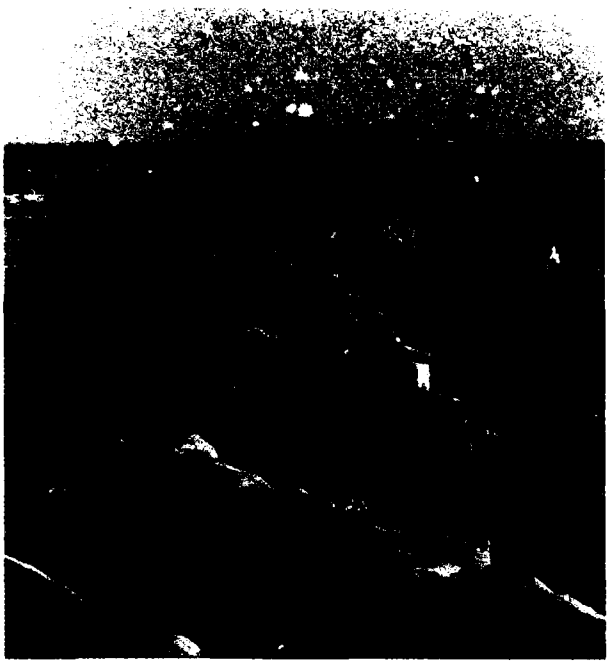

Figure 3. View of the highly deformed pressure ice located near the RV Aranda.

The ice conditions at the start of BEPERS were as shown in Figure 2; conditions that are typical of a light ice year. In fact, the planned deployment positions of the ships involved in the program had to be modified in that the ice edge had been expected to be appreciably further south. As will be seen, the meteorological conditions resulting in a light ice year are also reflected in the low thicknesses and high temperatures of the ice that was available for study.

The Finnish RV *Aranda*, which served as a base for our operations, was emplaced with the assistance of the Swedish icebreaker *Tor* in the fast ice near the edge of the pack near a small island located off the NE corner of the island of Holmön to the east of Umeå, Sweden. Because extremely rough ice conditions made surface travel both difficult and dangerous (see Fig. 3), most sampling was carried out in the near vicinity of the ship. Limited amounts of helicopter time were also available, allowing sampling of the ice in the channel between Holmön and the mainland, as well as of the ice pack nearer the center of the bay (additional sea ice samples were also obtained by field parties on the *Tor*, which operated in the ice pack about 90 km to the NNE of the *Aranda* [Fransson et al. 1989]). Immediately after the completion of the BEPERS-88 field operations, additional fast ice samples were collected in the vicinity of Tornio, Finland, located at the northern end of the bay near the Finnish–Swedish border.

PROCEDURES

Sampling was carried out by removing both cores and blocks from the ice sheets. Immediately upon removal of a sample, ice temperatures were taken at several different levels in the sample by inserting a probe thermometer into a transverse hole that was prepared with a hand drill. Then a portion of the ice was cut into salinity samples, placed in sealed containers, and ultimately melted. The salinities were then determined by measuring the conductivities of the meltwater with a conductivity bridge. It should be noted that in making the transformation from conductivity to salinity, it was assumed that the ratios of the ions in the sample were the same as in standard seawater. As will be seen later, in dealing with samples from the Bay of Bothnia, this procedure may need to be modified in view of recent measurements of the chemical composition of its water, indicating significant differences between its ion ratios and those observed in normal seawater. The brine and gas volumes and densities of the ice were calculated using relations from Cox and Weeks (1983) with the modifications of Leppäranta and Manninen (1988) included to deal with low salinities and near-melting ice temperatures in the range between –2.0 and 0.0°C. Vertical thick sections were then cut from the bulk samples and examined on a light table to determine the ice types present. Vertical and horizontal thin sections were also prepared with a microtome to examine the microstructure of interesting locations in the samples. Finally the c-axis orientations of a number of crystals in selected sections were measured using a Rigsby Stage. Further discussion of these procedures can be found in Weeks and Gow (1978, 1980) and Tucker et al. (1987). It was initially planned to carry out these measurements during the evenings while in the field. However, the near-melting temperatures that were encountered made this impossible (sea ice thin section production at ambient temperatures higher than –5°C is not a practical procedure). Therefore, selected samples were stored in a small freezer on the ship and the thin section studies were carried out in the VTT (Technical Research Center) coldrooms in Espoo, Finland. At the completion of this work, selected thin sections and ice blocks were stored, awaiting shipment to CRREL for detailed microscopic examination of brine layer spacings and details of the grain boundaries. Unfortunately, the freezer failed and these samples were lost.

RESULTS

Because of space limitations, we can only present detailed descriptions of a few of the samples that were studied. Nevertheless, we will attempt to provide the reader with an impression of the nature of the ice from each general region sampled.

Fast ice sites (location of the RV *Aranda*)

Here water salinities ranged from 3.6 to 4.0‰ corresponding to freezing temperatures of –0.19° to –0.22°C. Near-surface ice temperatures varied from –4.6°C at the first site sampled near the ship to higher than –3.0°C at all the other sampling locations. Snow depths generally varied from 5 to 15 cm with the smaller depths corresponding to lower ice surface temperatures. The ice was commonly within 2°C of the melting temperature. Temperature profiles in the ice were approximately linear. Three ice types were commonly observed: fine-grained, presumably randomly oriented; granular ice that forms from either the accumulation of surface slush or frazil crystals; columnar congelation ice that is the result of classic 1-D Stefan growth; and what we have termed *transition*

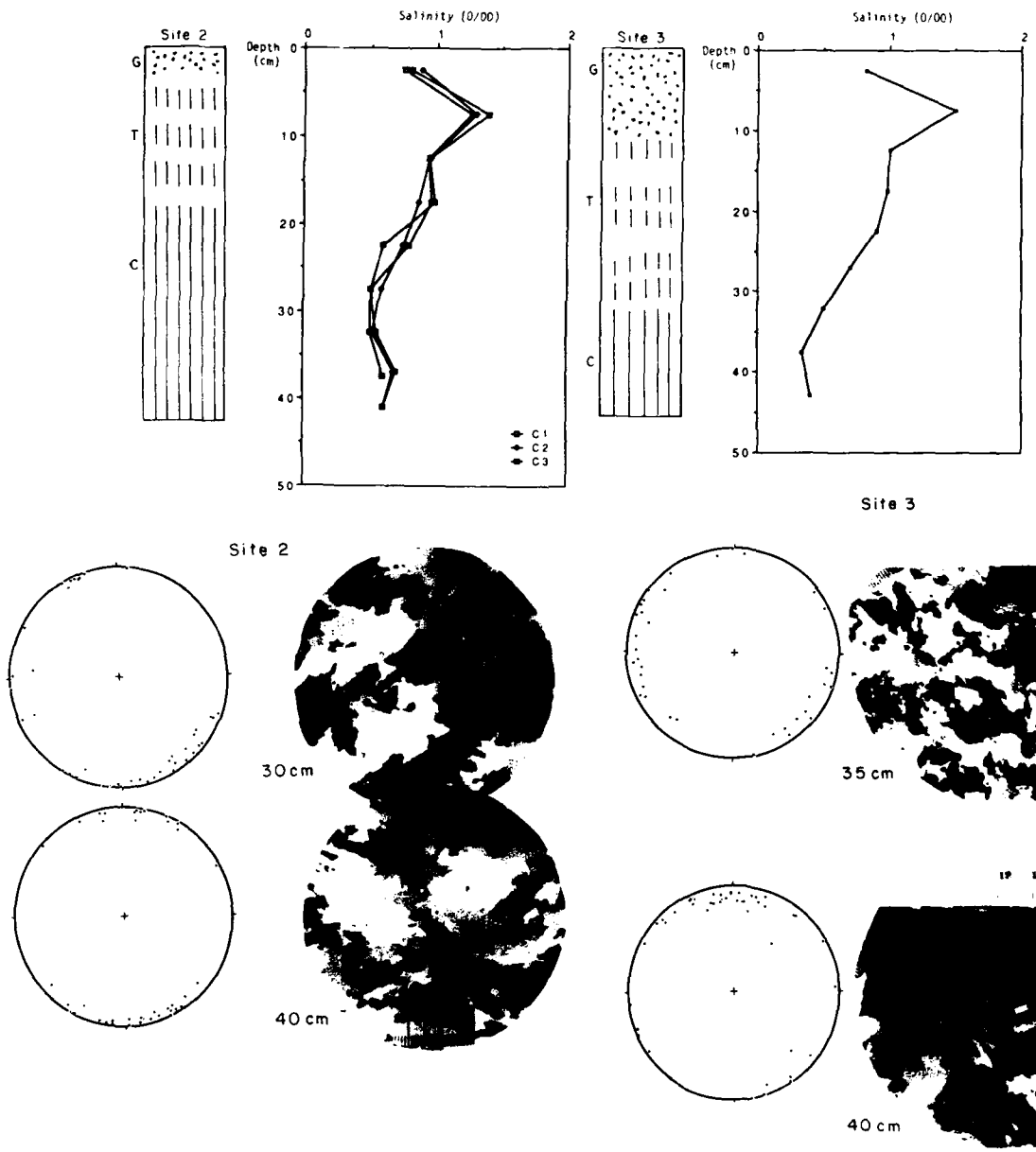

Figure 4. Salinity profiles, thin section photographs, ice structure drawings and fabric diagrams for sampling sites 2 and 3 located in the fast ice in the general vicinity of the RV Aranda *(near Holmöm Island, Sweden). On the drawings, the letters G, T and C indicate granular, transition and columnar ice types.*

ice that appears to be an intermediate state resulting from oscillations between the previously mentioned growth modes. Transition ice commonly shows very irregular horizontal banding, with the crystals in some of the bands exhibiting a slight elongation in the vertical (growth) direction, a feature that presumably indicates the incipient development of a columnar structure. Transition ice is a particularly interesting ice type that has, in the Antarctic, been associated with nearby leads, ice deformation and a rough underice hydrodynamic regime (Eicken and Lange 1989). A similar explanation may well apply in the Bay of Bothnia in that both Omstedt (1985) and Fransson et al. (1989) have found granular and transition ice types to occur frequently within the pack. Figure 4 shows the salinity profiles and drawings indicating the structural ice types for two sampling sites near the *Aranda*. At most sites near this location the sequence was always the same; granular at the top, transition in the middle, and congelation at the bottom. However, there were large variations in the amount of each ice type present. In places, the ice cover was composed of up to 80% granular and/or transition ice. Salinity profiles showed peak values of just over 2‰ and exhibited generally lower salinities (<1‰) with depth. However, in several cores (e.g., site 2), there was also a drop in near-surface salinities.

The orientations of the crystals in the congelation ice were also interesting. At some sites pronounced c-axis alignments within the horizontal plane were observed (Fig. 4, site 2), but at other locations the alignments were, at best, weakly developed. Current thinking attributes c-axis alignments to directional currents at the ice/water interface with the favored alignment direction resulting in c-axes parallel to the mean direction of the current (Weeks and Gow 1978, Stander and Michel 1989). Of the seven fast ice sites studied, four were aligned, two appeared to show some slight degree of non-randomness and one site was random. In all cases the congelation ice showed horizontal c-axis orientations. In comparing these results with similar data from the Arctic Ocean, the Bothnian alignments appeared to be generally weaker (more scatter around the mean axis direction) perhaps implying weaker or more variable currents. Some of the Bothnian fabrics (Fig. 4, site 3; see also Fig. 6, site 6A and 6B) also appeared to be slightly asymmetric, suggesting a directional current in contrast to a reversing tidal current as was characteristic of most of the Alaskan coastal sites studied by Weeks and Gow. It should also be noted that in all the congelation ice there was a clearly developed platy substructure very similar to that observed in sea ice, indicating that a nonplanar interface existed during growth.

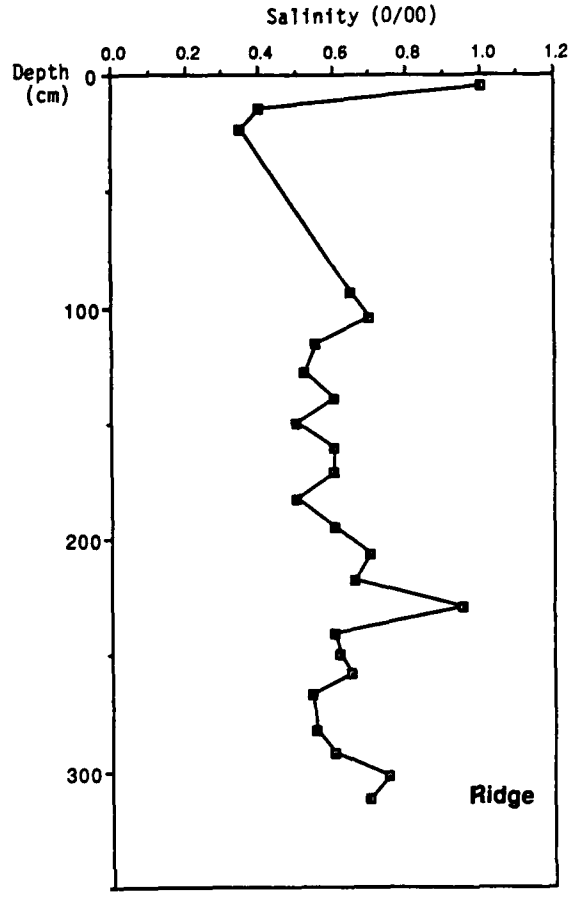

Figure 5. Salinity profile from a small pressure ridge located near the RV Aranda.

It was also possible to core one small pressure ridge (sail height = 1.5 m) located near the *Aranda*. Salinities were in the range of 0.3 to 1.0‰ in the upper portion of the ridge (0 to 1 m) and 0.5 to 0.95‰ at lower levels (Fig. 5). Other than this there was no apparent pattern in the vertical salinity variations. These observations are similar to measurements obtained from ridges in the Arctic (Weeks et al. 1971) except for the generally lower salinity values in the Bay of Bothnia.

Pack ice sites

We were able to sample only three locations in the drifting ice pack to the south and east of the *Aranda*. The areas selected were free of ridging, although there was deformed ice in the general area. Ice from two of these sites showed definite c-axis alignments (Fig. 6). The other site (site 5) showed only a weak alignment but clearly demonstrated the sequence of granular/transition/congelation ice that was common in the fast ice. There is considerable variation in the salinity profiles from site 5 even though the three

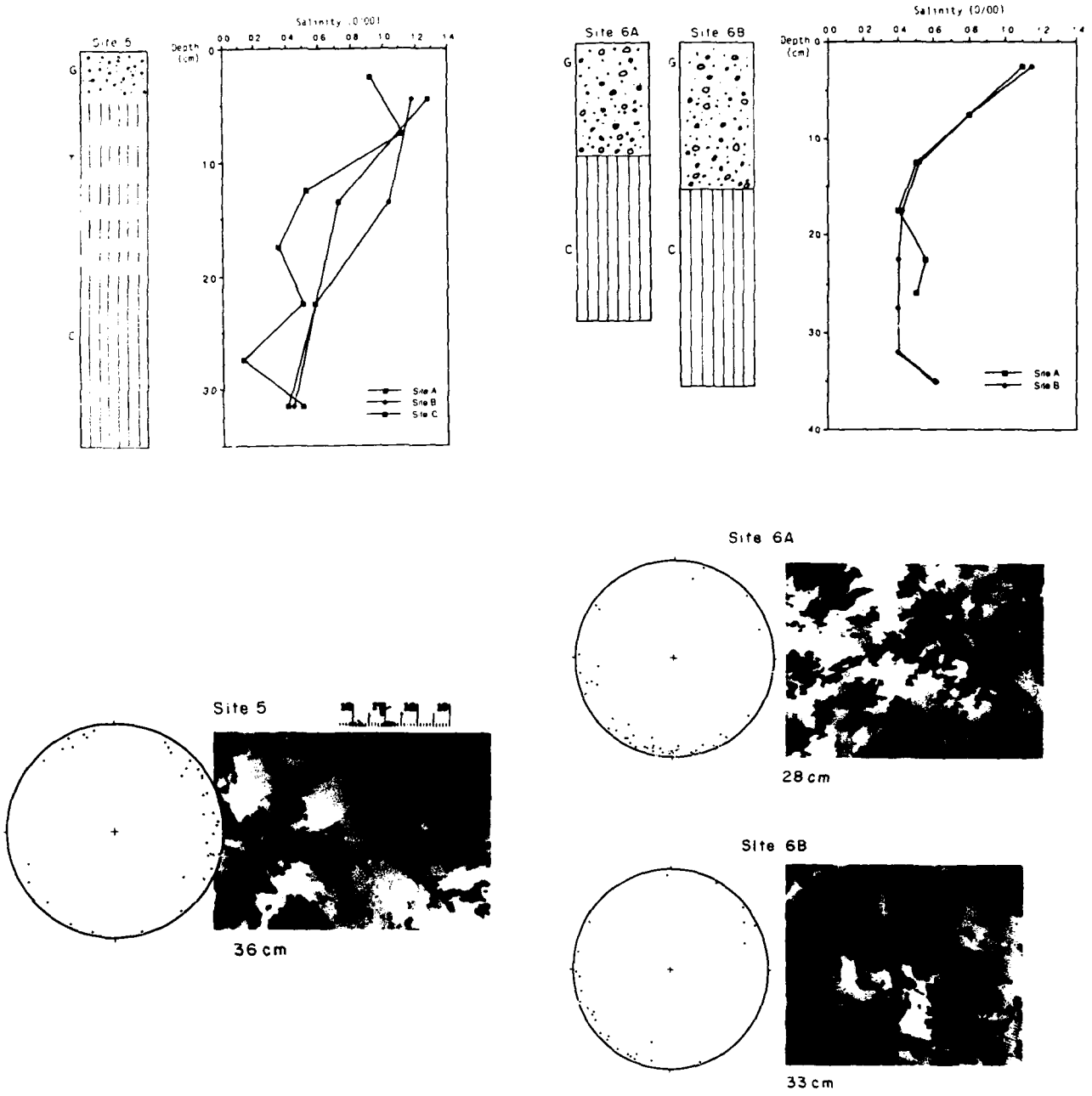

Figure 6. Salinity profiles, thin section photographs, ice structure cartoons and fabric diagrams for ice from sampling sites 5 and 6A and 6B located on pack ice floes that were northeast of Holmön Island, Sweden.

cores were collected within 5 m of each other. The general trend is, however, similar to that observed in the fast ice, salinities above 1‰ in the upper portion of the core and a gradual decrease in salinity values with depth. Pack ice temperatures were –2.2°C or higher.

Low salinity sites near Tornio, Finland

Perhaps the most interesting ice that we examined was obtained after the completion of the formal BEPERS exercise and was collected to the south of the Finnish Coast Guard Station at Röyttä, located south of Tornio on the coast at the Finnish/Swedish border at the north end of the Bay of Bothnia. The reason for sampling here was twofold: to study ice on both sides of the planar/nonplanar ice/water interface transition that should occur at a water salinity of approximately 1‰ (Weeks and Lofgren 1967) and to provide at least limited ground truth for the SAR imagery that had been obtained from this area during the BEPERS flights. Figure 7 shows an isosalinity map of the region based on data collected by Hela during the summer of 1959 (Palosuo 1961). As there were no equivalent under-ice observations of surface salinity, this

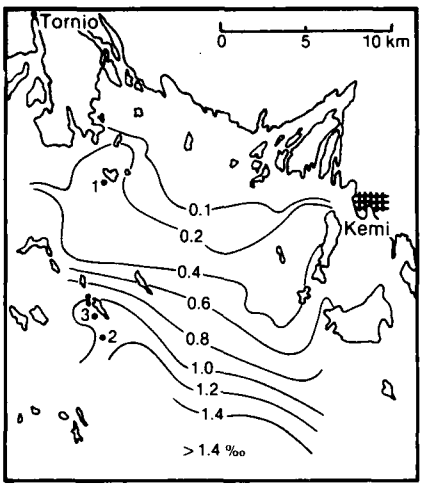

Figure 7. Sea surface salinity map for the northern portion of the Bay of Bothnia, 9-15 June 1959, unpublished data of I. Hela (Palosuo 1961). Sampling sites T1, T2 and T3 are marked.

Figure 8. Generally poor visibility and the featureless nature of the surface of the snow-covered ice at the time it was sampled south of Tornio.

map was used in selecting collection sites. We were also fortunate to have a quick-look SAR image of the area available allowing us to obtain samples from areas of both high and low radar return. Sampling was carried out by snowmobile with navigation provided by members of the Finnish Coast Guard who unerringly positioned us on what initially appeared to be a featureless sea of white (see Fig. 8). It was possible to sample three sites: two with low radar returns (sites T1 and T2) and one with a significantly stronger return (site T3) (see Fig. 6 for site locations). In addition, as the ice cover in this area formed earlier in the winter, the ice here was thicker (68 to 87 cm) and there was also a thicker snow cover (38 to 52 cm) which totally obscured all but the largest surface roughness features.

We found the ice types at the low return sites T1 and T2 to be quite similar; congelation ice from top to bottom. Grain sizes varied from a fraction of a centimeter in the upper portion of the sheet to typically larger than the thin section (8 cm) at locations near the bottom of the ice sheet (Fig. 9). Crystal orientations at 2 cm were random, and at 56 cm the majority of the crystals were c-axis horizontal, although other orientations existed. These features are by themselves not unusual as large grain size increases with depth are common in lake ice. Also the orientations are in agreement with the observations of Gow (1986) that lake ice sheets with random c-axis orientations that result from the seeding of an initial ice skim invariably result in c-axis horizontal fabrics lower in the ice sheet. However, here the ice was completely devoid of gas inclusions and had the general appearance of a plate of glass. This is, in our experience, very unusual as the great majority of the lake ice sheets contain appreciable amounts of gas, resulting in numerous, readily visible inclusions often occurring in layers

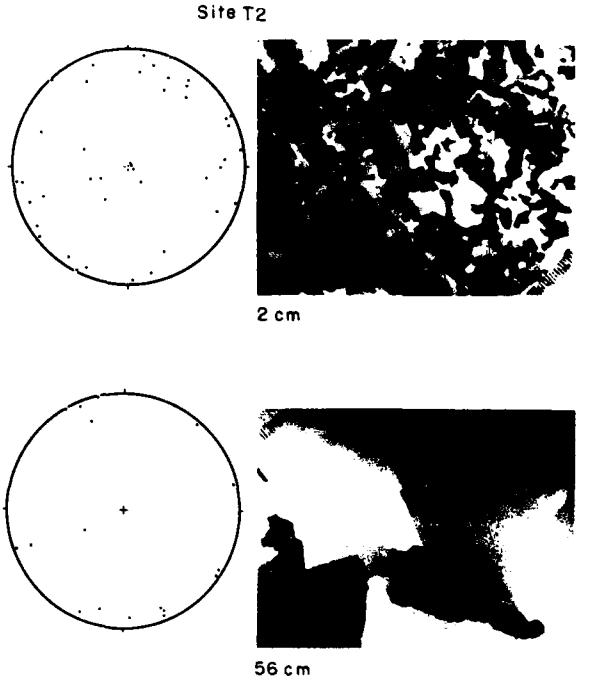

Figure 9. Thin section photographs and fabric diagrams for fast ice sampling site T2 south of Tornio, Finland.

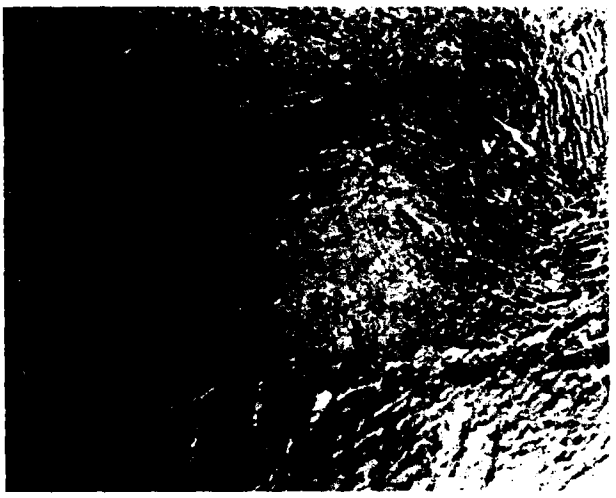

Figure 10. Photograph of the substructure visible on the ice/water interface at site T2 near Tornio, Finland.

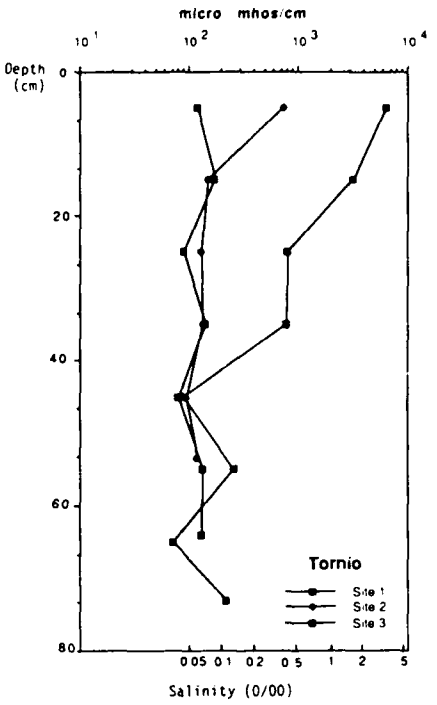

Figure 11. Salinity profiles from the three Tornio sites showing both the conductivity in mmhos/cm and the calculated equivalent salinity (‰) assuming that the ion ratios in the ice are the same as in standard seawater.

(see, for example, Gow and Langston 1977). At present we can only speculate concerning the reasons for this lack of included gas. Perhaps it is the combined result of a chemically reducing aqueous environment in the river water that originates in extensive peat-bog regions and also receives the effluvium of large wood pulp plants and washes from a steel factory, coupled with poor reaeration caused by the impermeable presence of a void-free ice cover.

There was no obvious substructure related to less brine pocket formation visible within this ice. Even so, a substructure, which to the unaided eye could have been mistaken for substructures observed in normal sea ice, could be seen on the ice/water interface of blocks removed from the ice sheet (Fig. 10). Because of the later loss of these samples, we were unable to examine these features with a microscope. There would appear to be three possibilities for the occurrence of the substructure: 1) it is indeed a "low salinity" version of the classical sea ice substructure resulting from a nonplanar growth interface, 2) we could be seeing Forel striations (the surface manifestations of Tyndall figures [Ragle 1963]), or 3) it could represent thermal or solution etching of the basal plane structure within individual ice crystals. Because the water salinities beneath the ice (ca. 0.03‰) were far lower than those (ca. 1.0‰) that have been observed to be necessary to cause a nonplanar interface to form and the water temperature at site T2 was observed to be +0.4°C, clearly possibility 2 or 3 would be favored.

Figure 11 shows the salinity profiles of the three Tornio sites as calculated from the conductivity of the meltwater. Sites T1 and T2 have salinities that are consistently below 0.1‰, with the exception of the upper sample from site T2 whose salinity is just below 0.4‰. The ice above 40 cm at site T3 was surprisingly saline, reaching a maximum value in the uppermost layer of more than 3‰. This unusual salinity profile was probably produced by saline near-surface water, which results from mixing and upwelling caused by offshore winds, gradually being replaced by a lower and lower salinity surface water, as a stable, low-density layer of river water developed beneath the fast ice cover.

There are several reasons for the differences in the strength of the radar returns as observed at Tornio between sites T1 and T2 (low returns) and site T3 (high return). As mentioned, because of the continuous, deep snow cover, all sites initially appeared to be identical when viewed from above. However, removal of the snow showed that both of the low return sites (T1, T2) had flat, smooth upper surfaces. This, when coupled with their flat, smooth ice/water interfaces and a complete lack of cylindrical gas inclusions that are known to act as forward scatterers in studies of arctic lakes (Weeks et al. 1978), results in a strong bistatic radar return but in no return to the receiver at

Figure 12. The irregular upper surface of the ice sheet at site T3 as revealed after removing the hard-packed snow cover.

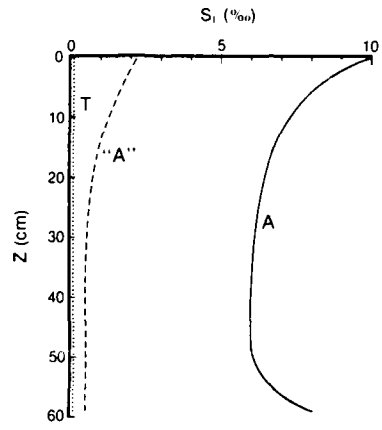

Figure 13. Salinity profiles assumed to be representative of 60-cm-thick ice near Tornio (T), near the RV Aranda *("A") and in the Arctic (A).*

the transmitter site. The ice at site T3, on the other hand, possessed a very rough, blocky upper surface that should result in significant, nondirectional surface scattering (see Fig. 12). Also the ice at T3 contained a large number of spherical gas inclusions that would serve as volume scatterers. All these factors would tend to return an enhanced signal to the receiver site over that observed at sites T1 and T2.

ICE PROPERTIES

Here we examine the attenuation coefficient, the tensile strength and the elastic modulus profiles that would be expected for ice near the *Aranda* site and at Tornio. These values are then compared with profiles expected from more typical arctic sea ice. First-year sea ice properties are commonly estimated by developing correlations between the particular property values of interest and the volume of liquid brine present in the ice. The variation in the attenuation coefficient (κ) as a function of brine volume (V_b) is based on the experimental measurements at 10 GHz (X-band) obtained by Hallikainen et al. (1988) on the 1987 BEPERS Pilot Study in the Gulf of Bothnia. The tensile strength (σ_t) and elastic modulus (E_{eff}) correlations are based on studies by Dykins (1970) and Vaudrey (1977). The appropriate equations are as follows:

$$\kappa\,(\mathrm{dB/m}) = 4.821 + 6.0893\,V_b - 0.02468\,V_b^2 + 3.24158\times10^{-5}V_b^3$$

$$\sigma_t(\mathrm{MPa}) = 0.816\left[1-\sqrt{\frac{V_b}{140.4}}\right]$$

$$E_{eff}\,(\mathrm{GPa}) = 5.31\left[1-\sqrt{\frac{V_b}{148.3}}\right]$$

where brine volume (V_b) is expressed in ‰.

The three salinity profiles that were used are shown in Figure 13 (T = Tornio, "A" = *Aranda* and A = Arctic). The Bothnian salinity and temperature profiles are "synthetic" with values selected to give a representative picture of the cores obtained from the different sampling areas (e.g., the Tornio area is represented by a profile in which the salinity has a constant value of 0.1‰). The arctic salinity values are taken from Cox and Weeks (1988, App. B, profile SG5E-31). The ice at all sites is taken to be 60 cm thick. Temperature profiles are assumed to be linear with ice/snow interface temperatures of –1.2° and–1.0°C near the *Aranda* and at Tornio, respectively. A comparable "warm" ice surface temperature for the Arctic was taken to be –2.8°C. This corresponds to placing a 1°C/60-cm temperature gradient across the ice. In considering temperatures more typical of the Arctic, the surface temperature for all three profiles was taken to be –20°C. Figure 14 shows the brine volume profiles corresponding to the different salinity and temperature profiles. In each pair, the profile with the higher brine volume corresponds to the higher ice temperature experienced in the Bay of Bothnia during BEPERS. Figures 15 and 16 show the corresponding κ and σ_t profiles (the E_{eff} profiles are generally similar to the σ_t profiles). Note that in Figure 16 negative strength values are indicated for parts of several profiles. This simply indicates that the strength/brine volume cor-

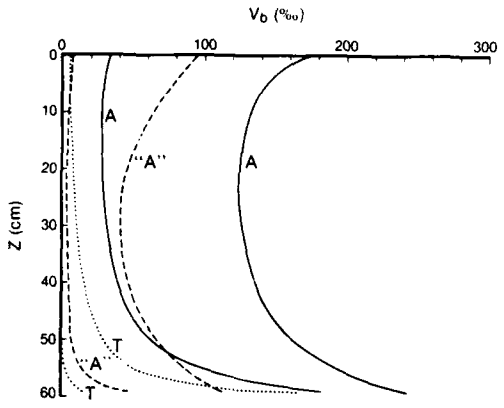

Figure 14. Brine volume profiles corresponding to the salinity profiles shown in Figure 10 and two temperature profiles described in the text (T = Tornio, "A" = Aranda and A = Arctic).

relations used are inadequate to represent the Bothnian data at near-melting temperatures (in the range of large brine volumes). Test sets specific to the Bothnian ice are clearly needed. Figure 17 shows the cumulative one-way loss (dB) for the three different salinity profiles assuming an ice surface temperature of –20 C. In the Arctic profile, a 5-dB loss has occurred at 4 cm; in the *Aranda* profile the same loss occurs at 15 cm and at Tornio at 55 cm.

CONCLUSIONS

One might anticipate that the characteristics of the ice cover in a restricted, economically important water body such as the Bay of Bothnia would be extensively over-studied. This clearly has not been the case. It is hoped that the present paper will help stimulate additional ice studies in this general geographic area.

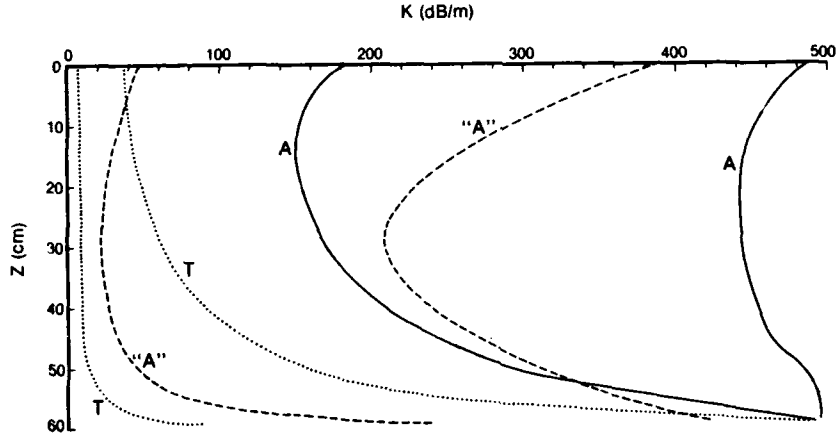

Figure 15. Calculated attenuation profiles corresponding to the brine volume profiles given in Figure 11 and the 10-GHz attenuation measurements of Hallikainen et al. (1988).

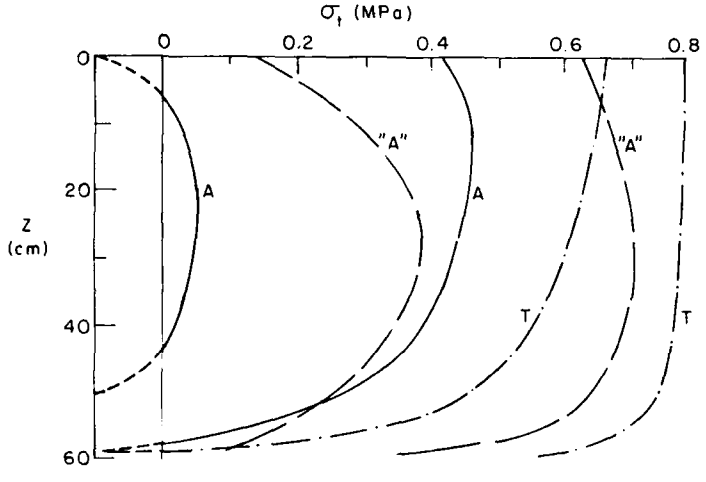

Figure 16. Calculated tensile strength profiles corresponding to the brine volume profiles given in Figure 11 and the tensile strength measurements of Dykins (1970).

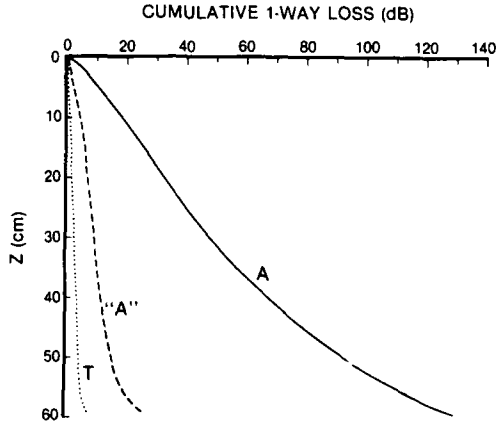

Figure 17. Cumulative one-way loss (dB) at normal incidence corresponding to the brine volume profiles given in Figure 11 assuming an ice surface temperature of –20 C [T = Tornio, "A" = Aranda and A = Arctic].

An improved knowledge of ice growth, structure, composition and properties in the high temperature, low salinity regime would contribute to our knowledge of the geophysics of winter conditions in the Bay of Bothnia, as well as to studies of sea ice in general.

We would like to thank the members of the BEPERS Organizing Committee for permitting us to participate in their experiment. We would also like to thank Matti Leppäranta, Erkki Palosuo and the staffs of the Finnish Institute of Marine Research and VTT and the members of the Finnish Coast Guard for their support of our program. Weeks and Gow's participation was funded by the Oceanic Processes Branch, NASA HQ and by the Office of Naval Research.

LITERATURE CITED

Bock, K.H. (1971) Monatskarten des Salzgehaltes der Ostsee, Dargestellt fur verschiedene Tiefenhorizonte, *Hydrogr. Zeitschrift*, **B**(12), 147 pp.

Cox, G. F. N. and W. F. Weeks(1983) Equations for determining the gas and brine volumes in sea-ice samples, *Journal of Glaciology* , **29**(102): 306–316.

Cox, G. F. N. and W. F. Weeks (1988) Profile properties of undeformed first-year sea ice. USA Cold Regions Research and Engineering Laboratory, CRREL Report 88-13.

Dykins, J. E. (1970) Ice engineering: Tensile properties of sea ice grown in a confined system, Tech. Rept. R689, Naval Civil Engineering Laboratory, Port Hueneme, California, 56 pp.

Eicken, H. and M. Lange (1989) Development and properties of sea ice in the coastal regime of the southern Weddell Sea. *Journal of Geophysical Research*, **94**(C6): 8193–8206..

Fransson, L., L. Stehn, L. Åström, B. Håkansson and A. Omstedt (1989) Variation of ice properties in an area of 1×2 km in the Gulf of Bothnia, March 1988. In *Proceedings, 10th International Conference on Port and Ocean Engineering under Arctic Conditions (POAC '89), 12–16 June, Luleå, Sweden* (K.B.E. Axelsson and L.A. Fransson, Ed.). University of Technology, Luleå, Sweden, vol. 3, 1989: 08.

Gow, A. J. (1986) Orientation textures in ice sheets of quietly frozen lakes, *Journal of Crystal Growth*, **74**: 247–258.

Gow, A. J. and D. Langston(1977) Growth history of lake ice in relation to its stratigraphic, crystalline and mechanical structure. USA Cold Regions Research and Engineering Laboratory, CRREL Report 77-1.

Hallikainen, M. T., M. Toikka and J. Hyyppä (1988) Microwave measurements of ice and snow, BEPERS Pilot Study. Data Report. Styrelsen för Vintersjöfartsforskning/Winter Navigation Research Board Rept. 45: 6983.

Leppäranta, M. (1981) On the structure and mechanics of pack ice in the Bothnian Bay. *Finnish Marine Research*, **248**: 3–86.

Leppäranta, M. and T. Manninen (1988) The brine and gas content of sea ice with attention to low salinities and high temperatures, Finnish Institute of Marine Research Internal Report 1988(2), 14 pp.

Omstedt, A. (1985) An investigation of the crystal structure of sea ice in the Bothnian Bay. SMHI Reports Hydrology and Oceanography, RHO 40.

Palosuo, E. (1961) Crystal structure of brackish and freshwater ice. IASH. No.54, Snow and Ice Commission, Gentbrugge.

Ragle, R. (1963) Formation of lake ice in a temperate climate. USA Cold Regions Research and Engineering Laboratory, Research Report 107.

Stander, E. and B. Michel (1989) The effect of fluid flow on the development of preferred orientations in sea ice: laboratory experiments. *Cold Regions Science and Technology* (in press).

Thompson, T. and M. Leppäranta (1987) BEPERS-88: Experiment plan. Winter Navigation Research Board, Swedish Administration of Shipping and Navigation/Finnish Board of Navigation Research Report No. 46.

Tucker, W. B. III, A.J. Gow and W.F. Weeks (1987) Physical properties of summer sea ice in the Fram Strait. *Journal of Geophysical Research*, **92**(C7): 6787–6803.

Vaudrey, K. D. (1977) Ice engineering—study of related properties of floating sea-ice sheets and summary of elastic and viscoelastic analysis. Naval Civil Engineering Engineering Laboratory, Port Hueneme, California, Report no. TR-860.

Weeks, W. F., A.G. Fountain, M.L. Bryan and C. Elachi (1978) Differences in radar return from ice-covered North Slope lakes, *Journal of Geophysical Research*, **83**(C8): 4069–4073.

Weeks, W. F. and A.J. Gow (1978) Preferred crystal orientations along the margins of the Arctic Ocean. *Journal of Geophysical Research*, **84**(C10): 5105–5121.

Weeks, W. F. and A.J. Gow(1980) Crystal alignments in the fast ice of arctic Alaska. *Journal of Geophysical Research*, **85**(C2): 1137–1146.

Weeks, W. F., A. Kovacs and W.D. Hibler III (1971) Pressure ridge characteristics in the arctic coastal environment. In *Proceedings, 1st International Conference on Port and Ocean Engineering under Arctic Conditions (POAC '71)*. Technical University of Norway, Trondheim, vol. I, p. 152–183.

Weeks, W. F. and G. Lofgren(1967) The effective solute distribution coefficient during the freezing of NaCl solutions. In *Physics of Snow and Ice* (H. Oura, Ed.) Sapporo, Japan: Institute of Low Temperature Science, Hokkaido University, vol. 1, p. 579–597.

Snow Cover Effects on Antarctic Sea Ice Thickness

S.F. ACKLEY
U.S. Army Cold Regions Research and Engineering Laboratory
Hanover, New Hampshire, U.S.A.

M.A. LANGE
Alfred Wegener Institute for Polar and Marine Resarch
Bremerhaven, Federal Republic of Germany

P. WADHAMS
Scott Polar Research Institute
Cambridge, United Kingdom

ABSTRACT

In model simulations of seasonal pack ice growth in both polar regions (e.g., Maykut and Untersteiner 1971, Semtner 1976, Hibler 1979), the snow cover is treated essentially as an insulating layer that inhibits ice growth because of its lower conductivity than pack ice. In the Winter Weddell Sea Project-86, on the cruise of the West German vessel *Polarstern*, we found that several factors negate this behavior predicted by the models. Relatively thin sea ice (40–60 cm) forms initially in Antarctica during the ice edge advance. Surface roughness features act as snow fences and, under the action of relatively high winds (40 knots in frequent storms), the snow cover is shifted around over periods of hours to a few days. Wind-blown snowdrifts build to 1 m or greater thicknesses in a few hours. Snow of this depth can easily depress the existing ice cover surface below sea level, and flooding of the snow cover followed by sub-freezing temperatures leads to a superimposed snow-ice layer on the top surface. The remaining snow cover is redistributed in the next storm within a few days to continue the process. Two sets of measurements showed the general nature of this process. The first, a series of 4000 ice thickness measurements, showed about 17% of the holes drilled had the ice surface at or below sea level at the time of the measurement, sometimes accompanied by slush pools on the surface. Sea ice cores analyzed for oxygen isotopes independently confirmed that the top 10–20 cm of the intact cores was derived from seawater-flooded snow in several cases. We estimate that the snow cover increases mean sea ice thickness in Antarctica by 20–30% (10–20 cm) over model predictions by this flooding-infiltration-refreezing ice growth mechanism. This process also has ramifications for microwave remote sensing of sea ice and biological growth in antarctic sea ice.

INTRODUCTION

Sea ice modeling, in the thermodynamic mode, has usually taken the effect of the snow cover as a reduction in the potential ice thickness. The overriding effect (e.g., Maykut 1986) is caused by the difference in thermal conductivity for snow compared to ice, leading to an insulating effect of the snow cover which reduces the rate of heat withdrawal from the ice. The ice growth rate slows down depending on the thickness and thermal conductivity of the snow cover which to first order is controlled by the snow density. A recent application of that principle was in a modeling study for the Weddell Sea pack ice by Owens and Lemke 1989, whose standard experiments using a 1-D mixed layer-pycnocline model showed the main effect of the snow cover to be a reduction in sea ice thickness and net freezing rate. In turn, the buoyancy flux in the mixed layer is reduced because of the reduction in the freezing rate. It is also clear that the modeled accumulation rate of the snow cover in the winter season will have significant effects on the ice growth rate, depending on the ice thickness when the snowfall occurs. In this paper, we present some results on the properties of the snow and sea ice cover of the Weddell Sea based on data collected during the *Polarstern* cruise in the austral winter of 1986, the Winter Weddell Sea Project, 1986. Based on these data and some calculations showing the potential for snow-load-induced flooding, we infer that the net effect of the snow cover is actually a net increase in the total ice thickness for the Weddell Sea rather than a decrease as predicted by the models.

RESULTS

Snow and ice thicknesses

Figure 1 shows the cruise track of the *Polarstern* in the eastern Weddell Sea during July–September 1986. The symbols show positions where ice cores were made and the closed symbols show where oxygen isotope measurements were taken on the ice cores (these results are discussed later). These locations also coincide with the locations where profiles of ice thickness, snow depth, and ice freeboard were measured. These results are described more completely in Wadhams et al. (1987), where the ice thickness is characterized over the Weddell Sea from the ice edge

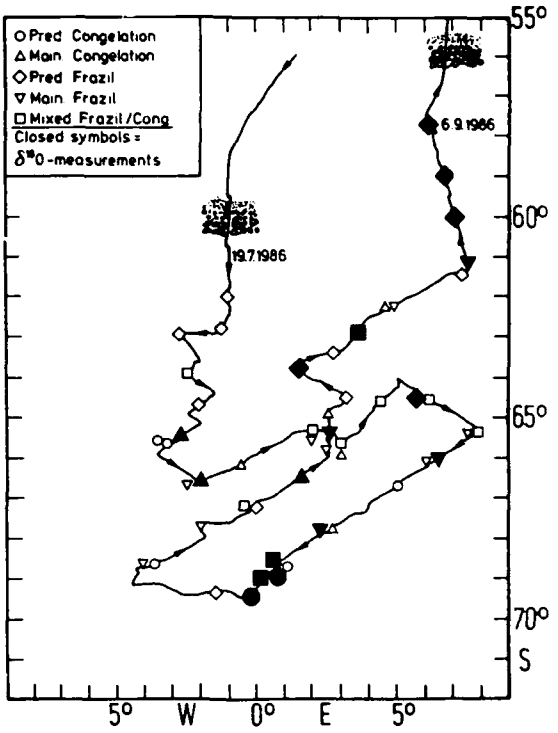

Figure 1. Cruise track of the Winter Weddell Sea Project 1986. Shown are ice station sites (open symbols) and station sites which were selected for isotope analysis (closed, enlarged symbols). The different symbols represent genetic ice classes, which are derived from the textural analysis of sampled cores (Lange et al. 1989).

to near the antarctic continent. Profiles of ice thickness were usually obtained from 50 to 100 holes taken at 1-m intervals, and totaled over 4000 holes for the entire cruise leg. Measurements of snow properties, (depth, density, and temperature profiles), were also taken at these sites. Figure 2 shows the mean ice thickness calculated from these profiles. As shown here, the mean ice thickness usually varied between 40 and 80 cm. Some higher values were found in the extreme southern region. We found that values above 1-m mean thickness were caused by the heavy ridging seen in these locations nearer the antarctic continent. Even there, we found the most frequently observed ice thickness (the mode value in the profiles) was the 40- to 80-cm range seen in the other locations where the mode and mean value nearly coincided. Figure 3 shows the details of one of the individual profiles. The primary ice thickness develops from the pancake ice formation (Lange et al. 1989), with greater thicknesses developing from rafting of the principal thicknesses up to two or three times the primary values. From this figure, we note also the high variability of the snow depth, from a few to over 20 cm over the 100 m of the profile. There are also a significant number of ice surface points that are at or below sea level. A number of similar profiles suggested to us that snow loading could bring the surface profile to below sea level where flooding of the surface could occur through cracks in the ice.

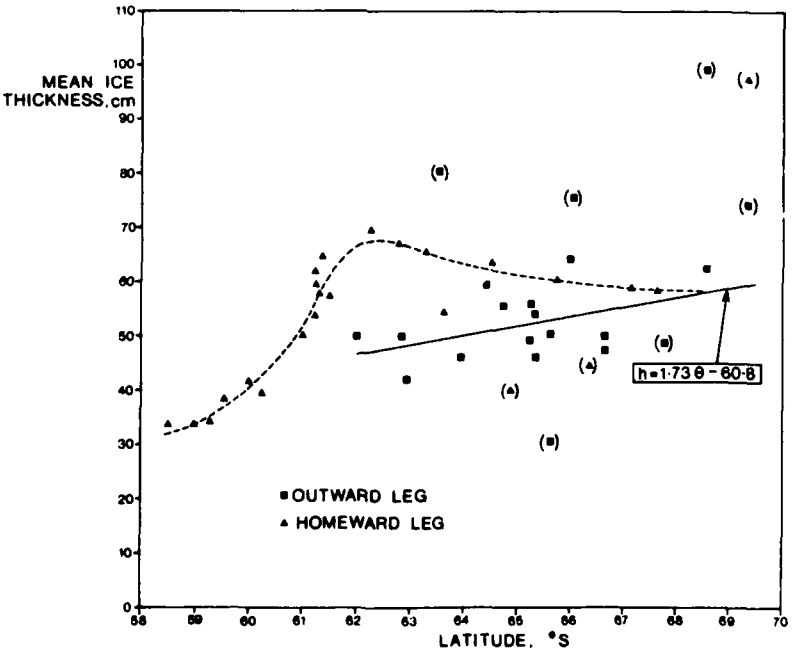

Figure 2. Mean ice thickness vs latitude during the Winter Weddell Sea Project. Squares show the original southbound leg while triangles indicate the northbound leg a few weeks later (Wadhams et al. 1987).

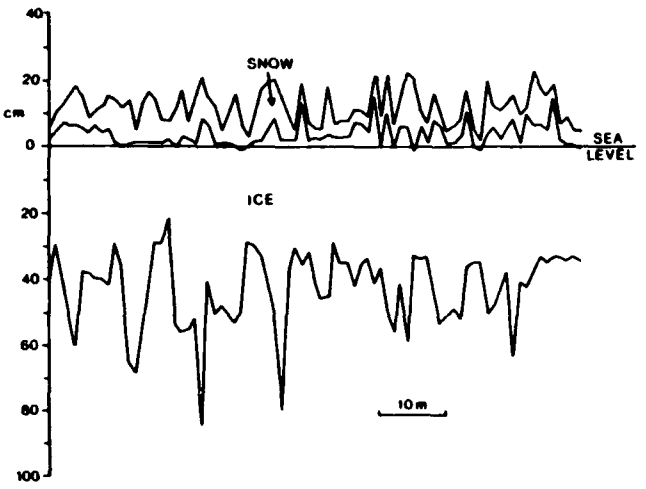

Figure 3. Example profile of snow depths, ice freeboard and ice draft obtained on 23 July 1986.

Table 1. Snow depths and densities on antarctic sea ice.

Latitude	*Snow depth range* (cm)*	*Snow density ($Mg\ m^{-3}$)*
61 26'S	3–24	0.25–0.34 (7 obs)
62 15'S	4–34	0.2
62 46'S	10–19	0.2
62 55'S	3–19	—
63 17'S	—	0.2
63 30'S	9–19	0.2
63 37'S	6–30	0.2
64 26'S	4–24	—
64 29'S	2–24	0.3
64 44'S	3–21	0.3, 0.2, 0.2
64 53'S	3–32	0.4
65 20'S	3–55	0.3, 0.2
65 20'S	1–73	0.3, 0.2
65 35'S	1–45	0.4, 0.3, 0.3
65 36'S	5–23	—
65 46'S	3–10	0.3
66 23'S	3–15	0.4
66 39'S	3–40	—
66 40'S	4–35	0.3, 0.3
67 40'S	10–20	0.3, 0.3
67 65'S	4–65	0.3, 0.3
68 49'S	0–21	0.2, 0.3, 0.3
69 21'S	17–43	0.2, 0.3

*Snow depths were generally taken from two intersecting lines in a "+" pattern at 1-m intervals along each line, totaling about 40 measurements at each location.

Criterion for snow load-induced flooding of sea ice

Based on the hydrostatic balance, we can compute the condition under which a load (snow) on the ice surface can deflect the ice cover sufficiently to allow flooding.

In the following, f, d, and t are the ice freeboard, draft (depth below sea level), and thickness, respectively, s is the snow depth, and ρ is the density of snow (ρ_s), ice (ρ_i) and seawater (ρ_w):

$$\rho_s s + \rho_i(f + d) = \rho_w d.$$

For flooding to occur, $f = 0$ and $d = t$,

$$\rho_s s + \rho_i t = \rho_w t$$

$$\rho_s s = (\rho_w - \rho_i)t$$

$$\rho_w = 1.03\ g/cm^3 \qquad \rho_i = 0.93\ g/cm^3$$

$$\rho_s s = 0.10t$$

$$s/t = 0.10/\rho_s$$

or for

$$\rho_s = 0.2, 0.3, 0.4\ g/cm^3$$

$$s/t = 1/2, 1/3, 1/4$$

where t = 40 to 80 cm, so that s = 10 to 40 cm.

In the examples chosen, for ice thicknesses in the range seen in the Weddell Sea (40 to 80 cm), we find that, depending on the snow density, snow depths in the range of 10 to 40 cm are sufficient to depress the ice sheet to allow flooding.

Evidence for snow load-induced flooding

Table 1 shows the range of snow depths and densities that occurred at the measured sites. From these data we see that the range of snow density assumed in the calculation is of the right order and that each site had some points where sufficient snow depth existed to load the ice surface to below sea level at the measured snow density and ice thickness. Table 1 also indicates that the snow depths at any given location are highly variable over short distances, an indicator that wind effects are instrumental in increasing the variability of the snow depths. In an attempt to assess how often a redistribution of the snow cover might occur, we examined the wind speed records from the ship, which were taken every three hours. Examples of these data are shown for every fourth day of the cruise (the rest of the days were similar) in Table 2.

Table 2. Winter daily wind speeds (kt) (16 July–10 Sept 1986).

Date	*Wind speed range (3-hr observations)*
16 July	1–17
20 July	17–19
24 July	12–22
28 July	12–14
1 Aug	4–21
5 Aug	15–21
9 Aug	14–33
13 Aug	16–22
17 Aug	34–54
21 Aug	18–25
25 Aug	8–15
29 Aug	5–11
2 Sept	18–30
6 Sept	41–51
10 Sept	40–52

(After Rabe 1987).

The threshold speed for blowing snow to occur is about 10 knots. From the data we find that this value of wind speed is exceeded at least once in all days observed and, for about two-thirds of the days, the wind speed was always above 10 knots. The likelihood for the snow cover to be redistributed by high winds was therefore extremely high, as we frequently observed directly.

Evidence that snow loading did produce significant deflection of the ice sheet was shown in the overall statistics for the frequency of the ice surface being at or below sea level (negative freeboard) as shown in Table 3. Here we have divided up the data into latitude bands to examine regional differences.

Table 3. Frequency of drilled holes with negative ice freeboard.

Latitude range (°S)	*Holes drilled*	*Negative freeboard*	*Percent negative*
58–60	360	72	20.0
60–62	894	138	15.4
62–64	660	90	13.6
64–66	1105	166	15.0
66–68	565	104	18.4
68–70	471	135	28.7
Total	4055	705	17.4

Table 3 indicates a higher propensity for negative freeboard in the extreme north and extreme south. This tendency is consistent with some trend toward thinner ice in the north, while the southern regions were subjected to storms with high winds, which along with the increase in ridging noted earlier and possibly an increase in the total amount of snow, produced deep and long snowdrifts during or just prior to the measurement period.

In Wadhams et al. (1987), we also noted that when we grouped all the data for ice freeboard into a probability density function, the most probable ice freeboard values were at the 0- to 4-cm level, which together with existing negative freeboard measurements accounted for over 50% of the ice cover. With these low values for ice freeboard, we suggest that, at any given time, around 20% of the ice cover is potentially or actually being flooded, while an additional 30% can be easily flooded with some shifts in the snow cover. With the frequency of snow transport events (Table 2), there is a high likelihood of flooding occurring over the majority of the ice cover sometime during the winter season.

The following two hypotheses were examined through statistical tests:

1. If the snow depth reduces the heat flux through the ice, then the locations where thick snow cover exists should correlate with thinner ice.

2. If the snow depth causes flooding to occur by loading the ice sheet, then the thick snow should correlate well (high negative value) with low (or negative) ice freeboard.

The correlation coefficients for the first hypothesis (correlating thick snow with thin ice) were found to be 0.124 for all measurements and –0.163 for undeformed ice. The second hypothesis (correlating thick snow with low freeboard) showed a higher correlation coefficient, –0.504 . The snow loading effect on reducing ice freeboard therefore shows a greater frequency of occurrence and is statistically significant, while the reduction in heat flux argument cannot be statistically confirmed from the observations.

Measurement of the snow–ice component in antarctic sea ice

For the cores indicated by the closed symbol locations in Figure 1, oxygen isotope measurements were made as a function of depth in the ice. The oxygen isotope measurement provides a method to determine whether the ice sample under consideration was derived primarily from the freezing of seawater or from some combination of snow and seawater. This is accomplished by measurement of the ratio of heavy (O^{18}) to isotopically light (O^{16}) molecules in the sample

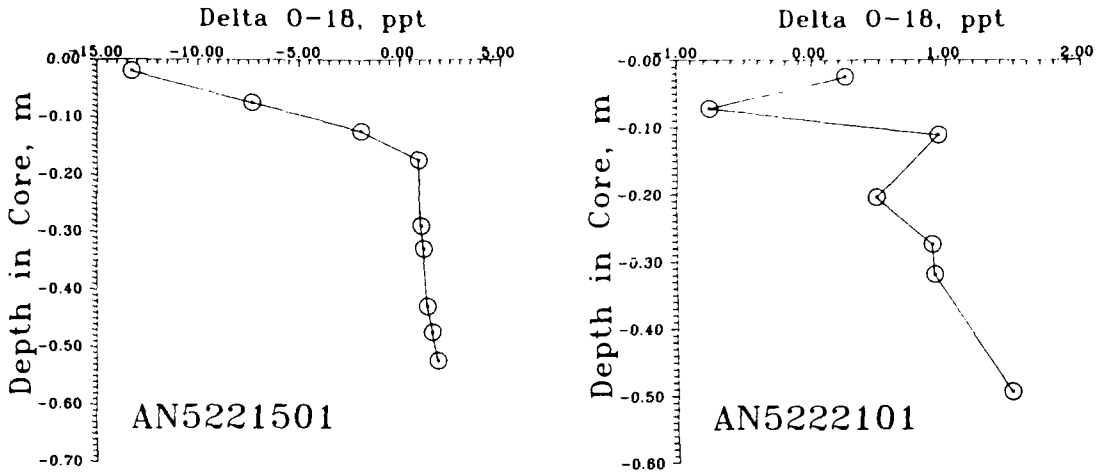

a. High negative values near the surface typical of a core with significant snow ice component.

b. Profile with only one portion dropping below zero in the delta value, indicating little, if any, snow ice contribution.

Figure 4. Delta O^{18} profiles for two cores.

using a mass spectrometer. The ratio is then compared and differenced (ΔO^{18} to O^{16} ratio) with Standard Mean Ocean Water (SMOW). Based on other measurements, the values of this difference for the freezing of seawater should vary between approximately –1‰ and +2‰ in the ratio based on variations in local waters from SMOW and the fractionation caused by freezing which is approximately 2 to 3‰. On the other hand, ice samples derived from snow have large negative values of ΔO^{18} to O^{16} ratio (below –2‰) based on their source derived from evaporation-condensation processes in the atmosphere. Ice delta values below –2‰ therefore have some contribution from atmospherically derived snow, with the magnitude of the negative value depending on the source (temperature) during the snow formation and the percentage of snow in the final sample. Figure 4 shows two examples of core profiles measured at two of the locations shown in Figure 1. Figure 4a indicates, in the top 12 cm, values of the delta isotopic ratio less than –3‰ contrasting with the lower portions of the core which showed values of +1 to +2‰. In this case the top three points are composed of snow ice while the rest of the core contains essentially no atmospherically derived ice; that is, it is composed entirely of frozen seawater. Figure 4b, on the other hand, shows only one point slightly negative so the core contains little to no snow ice. We found that the average value of the snow ice percentage from all the isotope measurements was 7.1 ±5.6%. The values at the high end correspond to 8 cm of snow ice added (Lange et al. in press). The isotope measurements are therefore consistent with the argument that snow ice is being incorporated into the ice cover, with values of the order of that estimated from the thickness data and flooding calculations. These measurements are probably not statistically valid because of the small number of cores relative to the area sampled. On the other hand, we are measuring the percentage of snow ice in the middle of its generation period and can reasonably expect that the process is more advanced nearer the end of the winter period; i.e., we are underestimating the amount of snow ice created in the winter period from these measurements. The present evidence from isotope measurements is consistent with our inferences from the thickness data.

CONCLUSIONS

We find that the variability of snow depths and densities on Weddell Sea pack ice is consistent with reworking of the snow by wind drifting, a feature borne out by direct observation and by wind measurements consistently above the threshold for blowing snow to occur. This process, together with the relatively thin ice cover (40 to 80 cm) observed in the Weddell Sea, can be shown to be sufficient for snow-load-induced flooding of the ice cover to occur. The flooding phenomenon is shown to directly affect 17% of the area of the pack ice, based on measurements of negative freeboards, and potentially affect over 50% of the area because of the near-zero freeboards observed during the thickness measurements. The di-

rect measure of the snow ice component is verified by oxygen isotope analysis in ice cores. This analysis indicates the measured thickness increase due to flooded snow is consistent with estimates of 10 to 20 cm. The statistical correlation of snow depth with ice thickness and ice freeboard indicates the higher likelihood of snow loading vs reduced heat flux through the ice as an observed phenomenon.

The observed increase in mean thickness (Fig. 2) between the inbound and outbound legs of our cruise, together with the lack of supporting textural evidence for ice growth at the bottom of the ice sheet, is consistent with snow-load-induced flooding and we suggest the increase in thickness observed is ascribable to this mechanism.

Some implications of these observations are that modeling simulations for these relatively thin pack ice regions should be adjusted for the possibility that heavy snow (through flooding) thickens the ice cover rather than thinning it. This process has some potential effects on climate simulations since warmer climates with increased precipitation may not lead to significant changes in the amount of ice cover, due to a greater proportion of snow ice forming. This effect has been noted by Gow and Govoni (1983) in studies of the ice covers of New England lakes, where warm wet winters showed little difference from cold dry winters in the thickness of ice formed, but significant differences in the composition of the ice covers, with snow ice dominating the warmer winters.

We also observed both from the ship and from aerial photos that large areas of the ice could be covered by slush pools induced by flooding. The flooded areas of the ice cover would have microwave emissivities closer to that of open water than first-year sea ice (Comiso et al. 1989), leading to significantly different estimates of the open water fraction compared to visible bands available from other satellite sensors.

We expect that the flooding mechanism may have significant effects on the development of sea ice biological communities (Ackley 1986). Flooding brings nutrients and algal seed populations up to higher light levels at the surface rather than the bottom of the ice. This combination can lead to a bloom condition on the top surface of the ice earlier in the spring season than is possible either within the ice or under it.

ACKNOWLEDGMENTS

The authors wish to thank the crew of the *Polarstern* and the Alfred Wegener Institute for the opportunity to participate in this project. We thank Peter Schlosser for the analysis of oxygen isotopes in the cores. We acknowledge support of the U.S. National Science Foundation (SFA), the UK National Environment Research Council (PW) and the Deutsche Forschungsgemeinschaft (MAL) during various phases of this work.

REFERENCES

Ackley, S.F. (1986) Sea-ice pressure ridge microbial communities. *Antarctic Journal of the United States,* **21**(5): 172–174.

Comiso, J., T.C. Grenfell, D.L. Bell, M.A. Lange and S.F.Ackley (1989) Passive microwave in situ observations of winter Weddell Sea ice. *Journal of Geophysical Research.*

Gow, A.J. and J.W. Govoni (1983) Ice growth on Post Pond, 1973–1982. USA Cold Regions Research and Engineering Laboratory, CRREL Report 83-4.

Hibler, W.D. III (1979) A dynamic–thermodynamic sea ice model. *Journal of Physical Oceanography,* **9**: 815–846.

Lange, M.A., S.F. Ackley, P. Wadhams, G.S. Dieckmann and H. Eicken (1989) Development of sea ice in the Weddell Sea. *Annals of Glaciology,* **12**: 92–96.

Lange, M.A., P. Schlosser, S.F. Ackley, P. Wadhams and G.S. Dieckmann (in press) ΔO^{18} to O^{16} Concentrations in sea ice of the Weddell Sea, Antarctica. Submitted to *Journal of Geophysical Research.*

Maykut, G. (1986) The surface heat and mass balance. In *Geophysics of Sea Ice* (N. Untersteiner, Ed). NATO ASI Series, Plenum Press, vol. 146, p.395–463.

Maykut, G. and N. Untersteiner (1971) Some results from a time-dependent, thermodynamic model of sea ice. *Journal of Geophysical Research,* **76**: 1550–1575.

Owens, W.B. and P. Lemke (1989) Sensitivity studies with a sea ice-mixed layer-pycnocline model in the Weddell Sea. Max Planck Institut fur Meteorologie, Report No. 29.

Rabe, W. (1987) Weather and synoptic situation during Winter Weddell Sea Project 1986 (ANT V/2) July 16–Sept 10 1986. Alfred Wegener Institute, Berichte zur Polarforschung, no. 40.

Semtner, A.J. (1976) A model for the thermodynamic growth of sea ice in numerical investigations of climate. *Journal of Physical Oceanography,* **6**: 379–389.

Wadhams, P., M.A. Lange and S.F. Ackley (1987) The ice thickness distribution across the Atlantic sector of the Antarctic Ocean in mid-winter. *Journal of Geophysical Research,* **92**(C13): 14535–14552.

Development and Physical Properties of Sea Ice in the Weddell Sea, Antarctica

M. A. LANGE
Alfred Wegener Institute for
Polar and Marine Research
Bremerhaven, Federal Republic of Germany

ABSTRACT/INTRODUCTION

Sea ice is a major element in the coupled oceanic–atmospheric regime of the polar regions. It strongly alters energy-, mass- and momentum-fluxes between the ocean and atmosphere in a complex, multiply coupled manner. Sea ice also affects global climate because of its important role in the overall albedo of the earth. Its growth and decay influences the heat and salt budget of the ocean over a region far exceeding the polar oceans. Additionally, sea ice provides a unique habitat for a variety of specially adapted organisms, which are of prime importance for the marine ecosystem of the polar oceans.

Despite these facts, investigations into the properties of antarctic sea ice have so far been essentially limited to remote sensing observations and investigations at a few coastal wintering-over stations. This is primarily due to the relative inaccessibility of the closed pack during winter and other logistic difficulties. Only since the advent of modern, ice-going research vessels has it become possible to conduct detailed studies of the sea ice regime of Antarctica and the Arctic throughout the year.

Over the last six years, we have carried out an extensive field/laboratory program with the German research icebreaker, *Polarstern*, addressing the development and physical properties of antarctic sea ice. In the course of five expeditions, we sampled primarily ice of the central, eastern and southeastern parts of the Weddell Sea, both during austral summers and during winter (Fig. 1). In the following we will give a brief account of major achievements of this program, without attempting to completely cover all the aspects of our work, some of which are described in companion papers of this report and some in other publications.

SAMPLING AND ANALYTICAL TECHNIQUES FOR COMBINED PHYSICAL, CHEMICAL AND BIOLOGICAL SEA ICE INVESTIGATIONS

Ambient sea ice properties are coupled in a complex way and are controlled primarily by the tem-

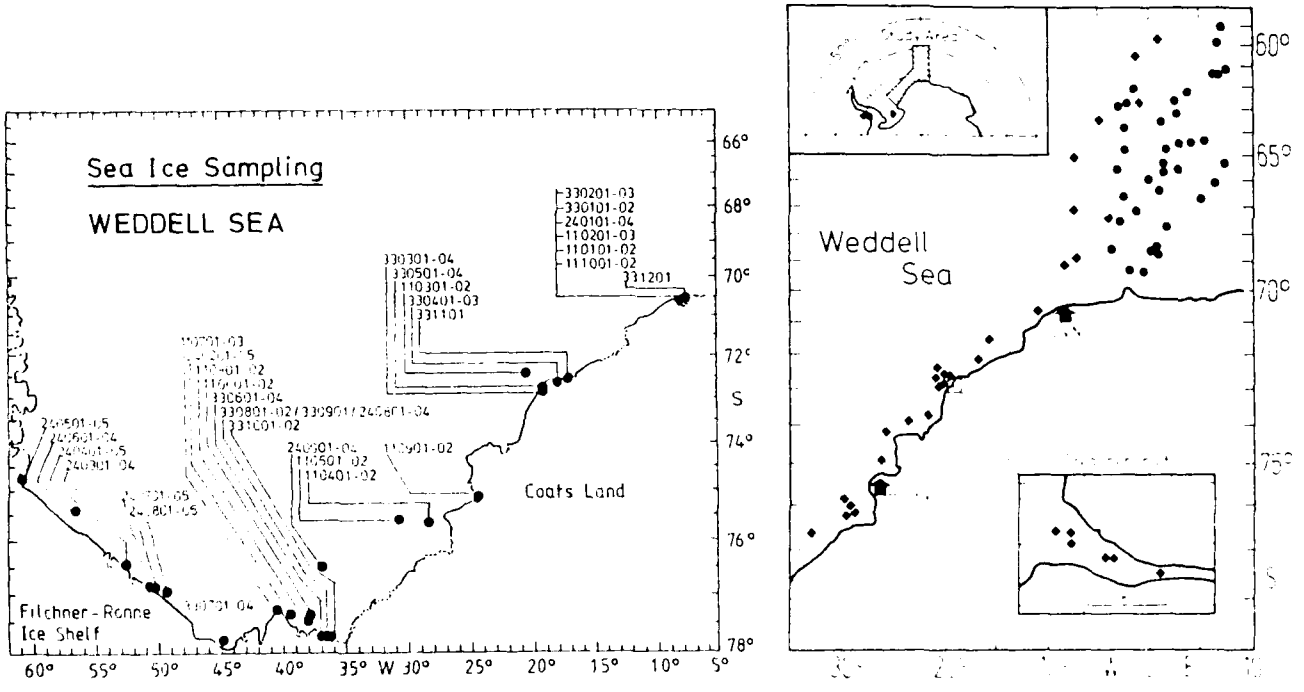

a. Eastern and southern. 1—1982–83, 2—1983–84, 3—1984–85.

b. Central and eastern.

Figure 1. Maps of ice stations for five expeditions in the Weddell Sea (Lange 1988, Lange et al. 1989).

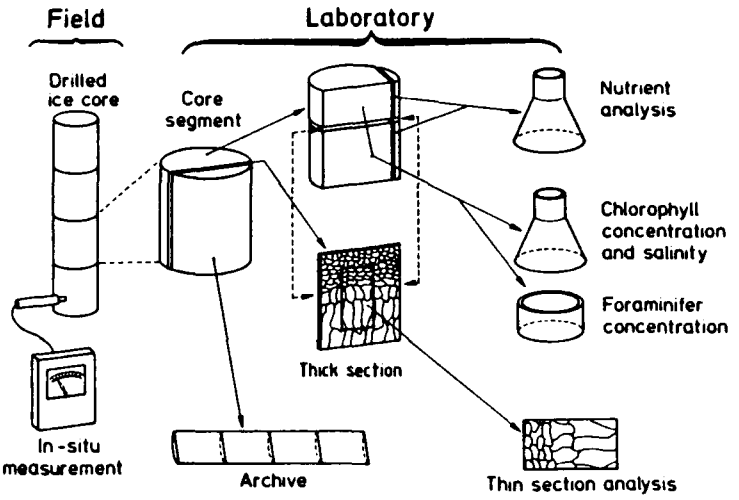

Figure 2. Schematic diagram of essential elements and procedures in our combined physical, chemical and biological sea ice analysis (Clarke and Ackley 1984).

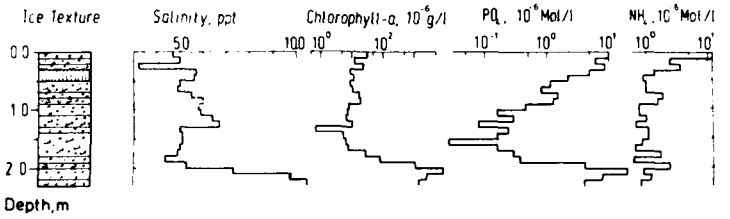

Figure 3. Ice texture, chemical and biological properties of a sea ice core. Note the marked consistent changes in ice properties at textural boundaries. The signatures in the textural cartoon stand for (from top to bottom) polygonal granular, orbicular granular, mixed granular/columnar, columnar and platelet ice, respectively.

perature profile within a floe. A key characteristic, however, that is less affected by temperature, but is well correlated with physical, chemical and biological variables, is the texture of the ice. Sea ice texture is closely related to the formation and subsequent development of the ice under investigation. It thus provides not only a measure of sea ice properties alone, but also records the oceanographical and meteorological conditions that led to its present state.

We have, therefore, chosen ice texture as our prime variable to be studied and have tried to relate other properties to the stratigraphy of individual cores. Our goal lay in the definition of empirical relations between sea ice properties and textural data in order to gain predictive capabilities based on ice texture alone. This has required a standard sampling technique, which we have devised over the last few years.

After retrieving the core (we use primarily 4-in. [10-cm] CRREL augers), in-situ measurements of ice temperatures and light attenuation in and below the borehole are performed (occasionally, we also measure thermal conductivities in the field (Lange 1985). In a ship-based cold laboratory, continuous thick sections over the entire length of a core are cut and inspected. The resulting stratigraphy then provides the basis for subsequent chemical and biological investigations (Fig. 2; Clarke and Ackley 1984).

It is only through this technique that consistent changes in ice properties are to be seen (Fig. 3). They mainly reflect the development of the ice and are therefore best understood in the context of the origin and subsequent evolution of the sea ice sheet. Arbitrarily spaced sampling, in contrast, will mask small scale changes in ice properties, which are caused by alterations in growth conditions.

TEXTURAL CLASSIFICATION OF SEA ICE

Ice texture, i.e., the spatial arrangement of pore space and crystal matrix and their respective geometries, partly reflects the mode of ice formation and partly recrystallization and changes in the air- to brine-filled pore space that arise as a consequence of subsequent development of an ice sheet (as well as sample preparation). As such, texture alone does *not* suffice to characterize the evolution of a sampled floe. It is only the spatial distribution and the relative amounts of textural units within a core that allow the assessment of its development (see below).

Besides the commonly known ice textures, i.e., *granular ice* (often also called frazil ice) and *columnar ice* (e.g., Weeks and Ackley 1982), we have defined a classification scheme consisting of these and an additional three classes (Table 1). One of these is a combination of the aforementioned classes, i.e., *mixed granular/columnar* ice, which occurs either in rafted and/or ridged floes or in transition zones between granular to columnar textures.

The other two additional classes, *intermediate granular/columnar ice* and *platelet ice* are both found in the southeastern Weddell Sea. They are a consequence of the particular oceanographic conditions of the coastal, near ice-shelf edge regime of the Weddell Sea. *Intermediate granular/columnar ice* (Eicken and Lange 1989) develops in a refreezing polynya under relatively rough under-ice oceanographic conditions. The latter are caused by the relatively strong, wind-induced drift of freezing floes. This causes turbulence at the ice/water interface, which inhibits the orderly growth of columnar crystals that would otherwise develop (Eicken and Lange 1989).

Platelet ice, first described by Paige (1966) for McMurdo Sound represents a consolidated layer of ice platelets underneath an existing ice sheet (Fig. 4). The platelets are probably the result of melting/freezing processes under an ice shelf that occur because of a thermodynamically driven cycle, also called an "ice pump" (Lewis and Perkin 1986). Even though platelet ice sometimes resembles columnar ice, its large, irregularly arranged crystals and an ice fabric not exhibiting any c-axis alignment enable a clear identification (Lange 1988, Eicken and Lange 1989).

Table 1. Textural classification of sea-ice samples (after Eicken and Lange 1989).

Textural class	*Grain size (m)*	*Grain shape*	*Brine inclusions*
1. Granular			
a. Polygonal granular	$< 10^{-2}$	Isometric, planar boundaries meeting at 120°.	Spherical droplets at grain junctions.
b. Orbicular granular	$< 10^{-2}$	Isometric, convex, rounded grain boundaries.	Irregular pockets and droplets between grains
2. Columnar	10^{-2} to $> 10^{-1}$	Elongated.	Parallel layers within grains.
3. Intermediate columnar/granular	10^{-2} to 10^{-1}	Slightly elongated, grains indented and interlocked.	Oblong, strings of isolated pockets.
4. Mixed columnar/granular	$< 10^{-2}$ to $> 10^{-1}$	Domains of granular and columnar texture occurring next to each other.	
5. Platelet	$< 10^{-2}$ to 10^{-1}	Inclusion-free, platy crystals in matrix of granular, mixed or intermediate columnar/granular ice.	Pockets and layers within and between grains.

Figure 4: Vertical thin section of platelet ice, photographed between crossed polarizers. Note the distinct zones of of platelet layers, which represent episodic changes in the deposition of ice platelets of varying sizes.

GENETIC ICE CLASSES

As mentioned above, the development of a sampled floe can be assessed only through the distribution and relative proportioning of textural units in a core. Based on the relative proportions of columnar vs granular ice in a core we have defined four genetic ice classes that characterize the basic processes during ice formation (Table 2). *Frazil ice* is formed primarily through the consolidation of suspended crystals (spheres, platelets, needles) in the upper part of the water column as the first form of sea ice to be seen. Thin skims of ice, a few centimeters thick, will quickly develop, once surface temperatures fall below the freezing point. In the presence of a wind-induced wave field, pancake ice forms instead of a continuous ice cover. Pancakes can grow to thicker units (up to 0.2–0.3 m) of agglomerated grains of up to some tens

Table 2. Genetic classification of sea ice samples (after Eicken and Lange 1989).

Genetic class	*Mode of formation*
1. Frazil	Surface accumulation of small ice crystals formed in the upper part of the water column.
2. Congelation	
a. Tranquil congelation	Congelation of seawater at ice/water interface under stable conditions (hydrodynamically smooth regime) resulting in formation of columnar ice.
b. Disturbed congelation	Congelation of seawater at ice/water interface under unstable conditions (hydrodynamically rough regime) resulting in formation of intermediate columnar/granular ice.
Prefixes (applied to discussion of entire cores as shown in Figure 5):	
A. Predominantly	> 80%
B. Mainly	60–80%
C. Mixed	40–60% with two, 20–40% with three components

"Mainly frazil" core indicates that 60–80% of the cover sampled is of frazil origin.

of centimeters in diameter (Weeks and Ackley 1982; see below).

Once a solid ice cover formed, further growth occurs by congelation of ice crystals from the melt, leading to the development of *tranquil congelation ice*. Interruptions of this growth process due to, e.g., turbulence underneath the ice will result in *disturbed congelation ice* (Eicken and Lange 1989). Ridging or rafting results in floes consisting of approximately equal parts of columnar and granular ice and is therefore called *mixed frazil/congelation ice*.

GEOGRAPHICAL DISTRIBUTION OF GENETIC ICE CLASSES

The spatial distribution of genetic ice classes allows a general characterization of the major growth and decay processes of sea ice on a variety of different scales. Figure 5 gives the distribution of genetic ice classes in the eastern and central part of the Weddell Sea as seen during the first leg of the Winter Weddell Sea Project 1986 (WWSP'86; Lange et al. 1989). North of 64°S, frazil ice clearly dominates the distribution. This is because pancake ice formation is the prime process of the advancing ice edge (see below) and because pancake ice consists entirely of frazil ice. Between 64° and 68°S, congelation ice of refrozen leads contributes significantly to the overall distribution. Since the relatively small size of most leads prohibits the buildup of a sizable wave field in the presence of surface winds, tranquil congelation ice forms beneath a thin layer of frazil ice. South of 68°S, increased

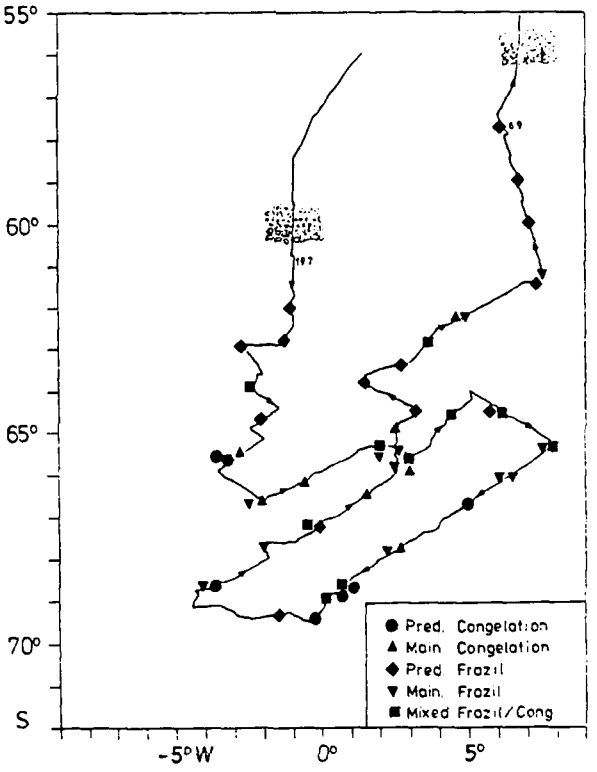

Figure 5. Geographic positions of sampled floes of specific genetic ice class on leg 1 of WWSP'86 (after Lange et al. 1989).

rafting and ridging, caused by the interaction of the Weddell Gyre and the coastal currents, gives rise to a relatively large proportion of mixed frazil/ congelation ice. Frazil and congelation floes are found in about equal proportions.

Thus, even though we can base our analysis on only a limited number of samples (Fig. 1), textural analysis of ice cores and the assignment of genetic ice classes based on this analysis provides a useful tool for unraveling the complex history of sea ice in the Weddell Sea (for further details, see Wadhams et al. 1987, Lange et al. 1989).

MAJOR SEA ICE FORMING PROCESSES IN THE WEDDELL SEA

The sea ice cover in the Antarctic undergoes rapid changes throughout the yearly cycle. While the ice-covered area in the winter months amounts to some 20 million km², melting will reduce the ice coverage to about 4 million km² during summer. Using a mean thickness of 0.5 or 1.5 m north or south of 70°S, respectively and a total ice covered area of 5.3 million km² to be formed during autumn, the ice volume to be produced in the Weddell Sea area amounts to 2820 km³. One of the major questions regarding this rapid change in sea ice volume is the question as to the principal processes of ice production in the Antarctic Ocean.

During the first leg of the WWSP '86, we observed a cycle of events in the region of the advancing ice edge that seems to be the major mode of ice formation in antarctic waters. We call this process the *pancake cycle*. Once surface air temperatures drop below the freezing temperature of the surface water, frazil crystals grow at the advancing ice edge. In the presence of surface-wind-induced wave fields the slushy layer of suspended ice crystals will agglomerate into pancake ice. Pancakes and frazil ice soon cover vast areas of the marginal ice zone and ice formation essentially stops. Persisting winds then lead to rafting of the pancakes and the generation of new open water patches. Here frazil ice will be formed again. Surface winds will lead to waves that penetrate into these open water patches because of the proximity to the open ocean. These will again lead to pancake formation (this is different from the situation within the closed pack, where congelation ice is formed instead). The pancake cycle will continue until either ocean waves cannot penetrate into the pack anymore or until wave energy is not sufficient to lead to rafting of pancakes and new open water areas (Fig. 6; Lange et al. 1986, 1989). Our observations suggest that the

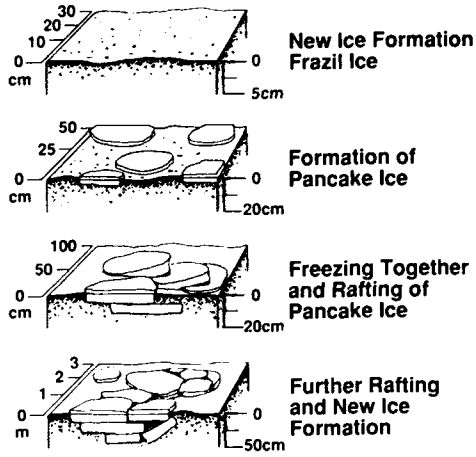

Figure 6. Schematic representation of the pancake cycle *(see text for further details; after Lange et al. 1989).*

latter condition is reached, when the floes have reached a thickness of 0.4–0.6 m (Wadhams et al. 1987).

Aside from the ice edge region, the coastal regions near the ice shelf edge of the Weddell Sea are another major source of sea ice throughout the winter. In these regions, coastal polynyas will form primarily by the action of offshore katabatic winds. This will lead to the northward advection of sea ice, which will become part of the already existing pack. Once a polynya has opened up, heat loss through the atmosphere will result in new ice formation, which quickly covers large fractions of the polynya (Eicken and Lange 1989). Based on satellite imagery, which provides reasonable values on areal extent and refreezing rates for the coastal polynyas, and assumptions for mean ice thicknesses, we have estimated the amount of ice formation in these polynyas. Depending on the values for these principal parameters, our estimated ice growth rates range from a few percent to volumes exceeding the total volume of sea ice in the Weddell Sea. Our observations during the second leg of the WWSP '86, however, suggest values that lead to yearly ice production amounting to 13% of the total ice volume.

ACKNOWLEDGMENTS

Most of the work that is reported here was done in collaboration with a number of dedicated people, whose help I would like to acknowledge. Among those, I would like to thank G. Dieckmann, H. Eicken, M. Scheduikat, P.Mursch and U. Vogel for their contributions in the field and laboratory work. I

thank my colleagues S. Ackley, G. Dieckmann, P. Wadhams and H. Eicken for stimulating discussions. Finally, I would like to thank the crew of the *Polarstern* for their continuous support and help in the field operations.

REFERENCES

Clarke, D.B. and S.F. Ackley (1984) Sea ice structure and biological activity in the antarctic marginal ice zone. *Journal of Geophysical Research*, **89**(2): 2087–2095.

Eicken, H. and M.A. Lange (1989) Development and properties of sea ice in the coastal regime of the southeastern Weddell Sea. *Journal of Geophysical Research*, **94**(C6): 8193–8206.

Lange, M.A. (1985) Measurements of thermal parameters in antarctic snow and firn. *Annals of Glaciology*, **6**: 100–104.

Lange, M.A. (1988) Basic properties of antarctic sea ice as revealed by textural analysis on ice cores. *Annals of Glaciology*, **10**: 95-101

Lange, M.A., S.F. Ackley and G.S. Dieckmann (1986) Development of first-year sea ice in the Weddell Sea (abstract). *Eos*, **67**: 1005.

Lange, M.A., S.F. Ackley, P. Wadhams, G.S. Dieckmann and H. Eicken (1989) Development of sea ice in the Weddell Sea, Antarctica. *Annals of Glaciology*, **12**: 92–96.

Lewis, E. L. and R.G. Perkin (1986) Ice pumps and their rates. *Journal of Geophysical Research*, **91**(C 0): 11,756-11,762.

Paige, R A. (1966) Crystallographic studies of sea ice in McMurdo Sound, Antarctica. U.S. Naval Civil Engineering Laboratory, Port Hueneme, California, Technical Report R494.

Wadhams, P., M.A. Lange and S.F. Ackley (1987) The ice thickness distribution across the Atlantic sector of the Antarctic Ocean in midwinter. *Journal of Geophysical Research*, **92**: 14,535–14,552.

Weeks, W. F. and S.F. Ackley (1982) The growth, structure and properties of sea ice. USA Cold Regions Research and Engineering Laboratory, CRREL Monograph 82-1.

Quantification of Sea-Ice Textures through Automated Digital Image Analysis

H. EICKEN AND M.A. LANGE
Alfred Wegener Institute for Polar
and Marine Research
Bremerhaven, Federal Republic of Germany

S.F. ACKLEY
U.S. Army Cold Regions Research and
Engineering Laboratory
Hanover, New Hampshire, U.S.A.

ABSTRACT/INTRODUCTION

The physical and biological properties of sea ice are governed to a large extent by its texture. The texture of a sea-ice cover, on the other hand, is controlled by the meteorological and oceanographic conditions u: der which growth took place (e.g., Weeks and Ackley 1982). Textural analysis can thus provide insight into the formation and development of sea ice, and at the same time it represents the central link between the evolution and the properties of an ice cover. Studies of sea-ice thin sections have generally relied on subjective, qualitative evaluations of texture. Aside from c-axis distributions determined with a Rigsby stage, textural characteristics such as grain size or shape are usually not evaluated because the procedure is time-consuming (as is determination of c-axis distribution) or even impossible. The complex texture of sea ice—with intertwining grains of diverse shapes, numerous inclusions of brine and gases between and within grains, and sub-grain boundaries—often defies common notions of "grains," "grain size," etc. The introduction of automatic texture analysis might be helpful in overcoming the difficulties outlined above. The method allows quantification of textures, permitting direct comparison between large numbers of samples, which is difficult or impossible to achieve through qualitative examination. Automatic texture analysis also overcomes personal bias inherent in conventional methods by collecting and considering all the information (i.e., all gray values) available for one thin section.

METHODS

Sea-ice thin sections were cut from cores taken in the central Weddell Sea (Lange et al. 1989) to approximately 0.5-mm thickness. Placed on a polarization stage in a glaciological cold lab, the samples were then recorded with a Hamamatsu C2400 video camera at their respective minimum and maximum

Figure 1. Hardware setup.

median gray value and at consistent magnifications to eliminate resolution-dependent effects. The video frames were digitized by a Matrox Pip-1024 image-analysis board installed on a Compaq 386 microcomputer clocked at 20 MHz. Digitized images consisted of a 512×512 pixel array, each pixel with a designated gray value ranging between 0 (black) and 255 (white). The images were then manipulated and analyzed, employing a program developed by Perovich and Hirai (1988) along with a commercially available image-analysis package, by using interactive systems and our own software. A photograph of the configuration is shown in Figure 1.

RESULTS

Figure 2a shows a thin section of columnar ice, photographed between crossed polarizers. The medium-sized grains, denoted by uniform gray values, exhibit parallel alignment of c-axes and a high degree of interlocking. Figure 3a depicts a sample of granular ice, fine-grained with mostly spherical crystals of random orientation. The equal-area sections marked in the photographs were digitized and treated with a low-pass filter (convolution with matrix, setting a pixel to the average of its 3×3 surrounding) to eliminate noise introduced into the frame.

Figures 2b and 3b depict the gray-value histograms obtained from these images. Granular ice shows a broad, stretched-out distribution, because the small size and random orientation of grains lead to a uniform spectrum of gray values. Low gray values are overrepresented because a crystal will turn black in polarized light, independently of the vertical component of its c-axis orientation. Columnar ice results in a much more heterogeneous gray-value distribution, with each larger peak corresponding to a region of uniform orientation (i.e., a grain). For every thin section an infinite number of different gray-value distributions are possible because each grain changes gray value according to its orientation with respect to the polarizers. To normalize digitization and analysis, samples are recorded at their respective maximum and minimum median gray value. The difference between maximum and minimum median is a measure for the degree of alignment within the thin section. For the sample of columnar ice this difference amounts to 83 gray values, and for the granular sample seven gray values, indicating a high and low degree of alignment within the sample, respectively.

Next, the images were convolved with a Laplacian kernel of the form:

−1	−1	−1
−1	8	−1
−1	−1	−1.

Contrary to gray-value histograms this procedure takes into account information regarding the spatial structure of the image by designating high gray val-

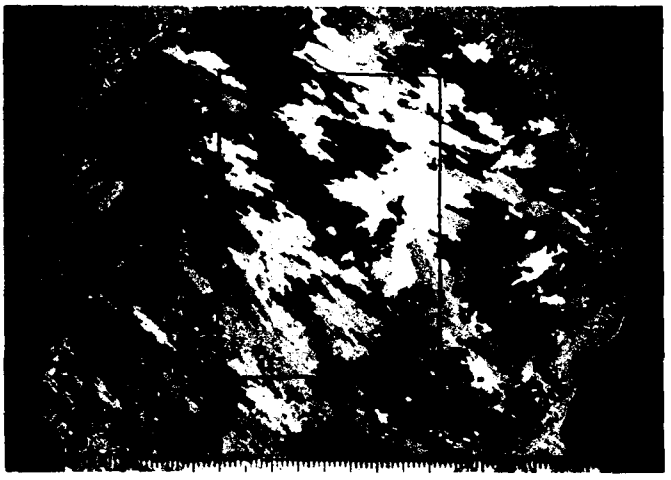

a. Horizontal thin section of columnar ice (photograph taken between crossed polarizers; scale bar in millimeters).

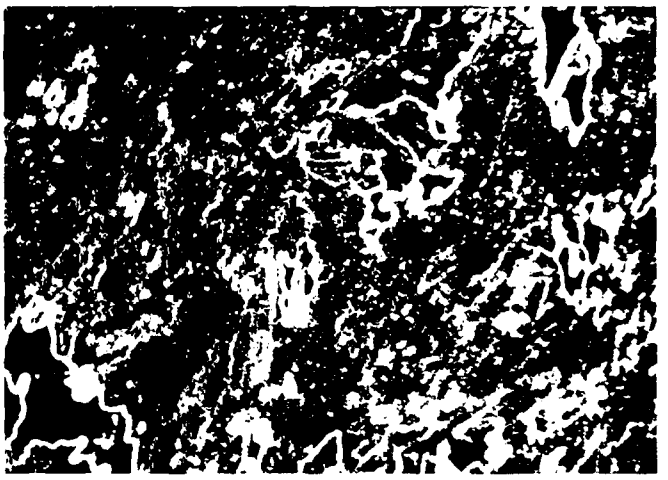

c. Convolution of original image of columnar ice with 3×3 matrix (Laplacian edge detection).

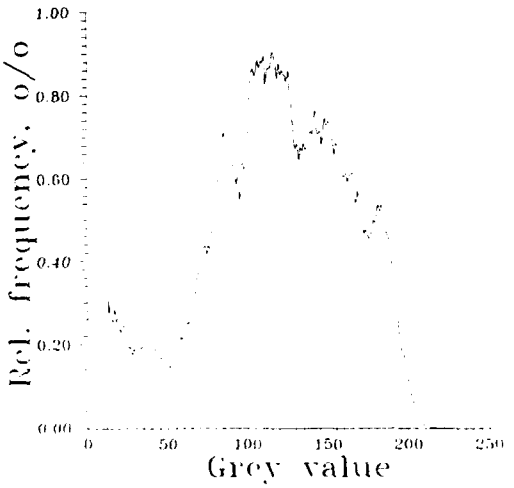

b. Gray value histogram of columnar-ice sample.

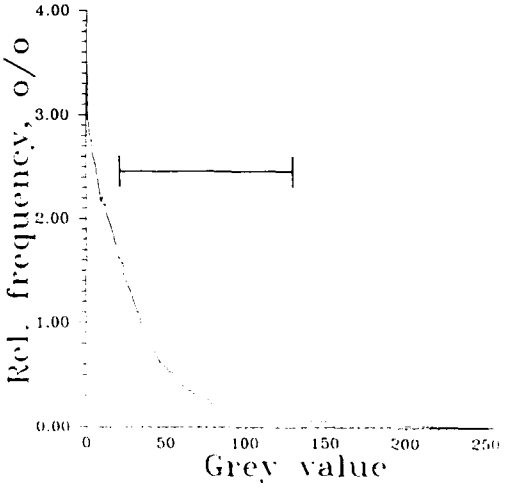

d. Gray value histogram of convolved image of columnar ice. A linear-regression fit to initial part of curve yields gradient of –0.051

Figure 2. Analysis of columnar ice sample.

ues to regions of high contrast and vice versa. Granular ice, consisting of many grains of highly variable orientation, naturally exhibits much higher contrast than columnar ice (Fig. 2c and 3c). For columnar-ice samples contrast is mainly due to high-angle grain boundaries; to a lesser extent it depends on subgrain formation and pore volume.

Gray-value histograms of these Laplacian-convolved images are shown in Figures 2d and 3d. A measure of the amount of contrast within the image is the contrast gradient, i.e., the slope of a linear-regression fit to the curve. As indicated only gray values between 21 and 128 are taken into account, since high and very low gray values are disturbed by noise in the image. The slope of these histograms may serve as a distinction between samples of different texture because it takes into account all information regarding size and orientation of crystals without segmenting the image into "grains." Thus granular ice with small, randomly oriented grains exhibits flat slopes (–0.0039 for Fig. 3d), whereas columnar ice with large grains of parallel alignment shows steep slopes (–0.051 for Fig. 2d). Other textures are distributed in between these extremes. Whereas the absolute values represented here are not too informative, the difference of more than one order of magnitude between the contrast gradients of the two images is important to keep in mind. One of our goals for future

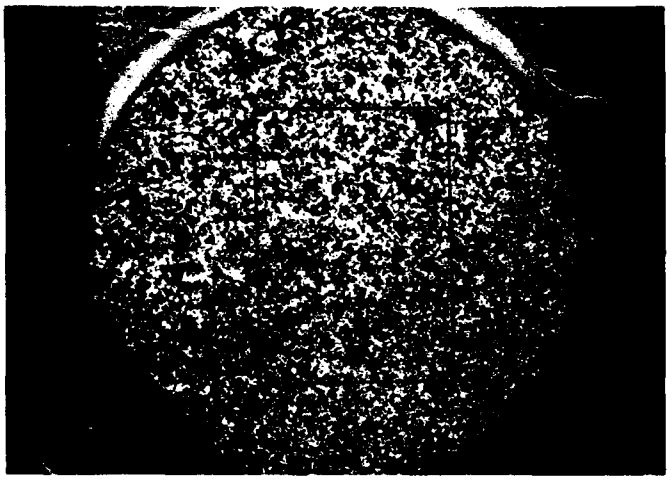

a. Horizontal thin section of granular ice (photograph taken between crossed polarizers; scale bar in millimeters).

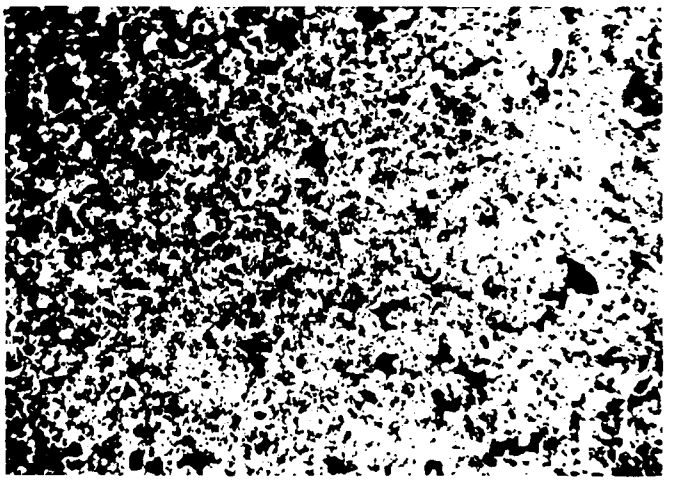

c. Convolution of original image of granular ice with 3×3 matrix (Laplacian edge detection kernel).

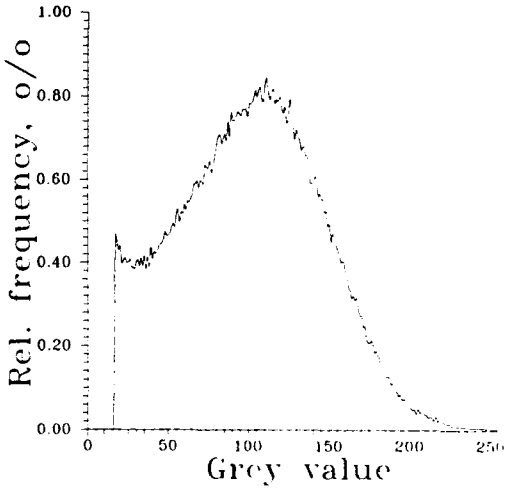

b. Gray value histogram of granular-ice sample.

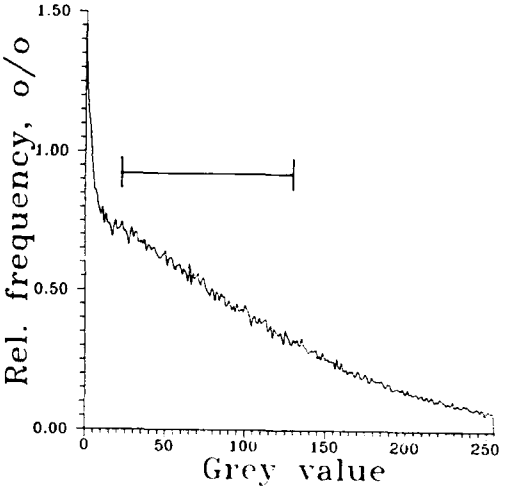

d. Gray value histogram of convolved image of granular ice. Gradient of linear-regression fit –0.0039.

Figure 3. Analysis of granular ice sample.

work lies in the correlation of slope values or ranges with individual textural classes.

The quantification of sea-ice textures outlined above may be extended by the determination of perimeter densities. To these ends images are converted to a binary form, i.e., pixels smaller or equal to a partition value (e.g., the median gray value of an image) are set to 0, all others to 1. The boundary lengths determined on these binary images represent a measure of grain size and shape. Plotting these against the contrast gradient results in a cluster diagram allowing for further classification and distinction between different textures.

CONCLUSIONS

This study demonstrates the feasibility of quantitative texture analysis of sea ice employing microcomputer-based image-processing hardware. The development of a standardized acquisition and evaluation scheme of original thin sections allows consistent and efficient analysis of samples, in addition to eliminating bias involved in manually defining or tracing grains. Regarding integral methods that do not attempt to recognize or distinguish between grains and pores, routines computing the gradients within an image hold more promise than the utilization of

gray-value histograms alone, partly because the latter contain no spatial information.

LITERATURE CITED

Lange, M.A., S.F. Ackley, P. Wadhams, G. Dieckmann and H. Eicken (1989) Development of sea ice in the Weddell Sea, Antarctica. *Annals of Glaciology*, **12**: 92–96.

Perovich, D.K. and A. Hirai (1988) Microcomputer-based image-processing system. *Journal of Glaciology*, **34**(117).

Weeks, W.F. and S.F. Ackley (1982) The growth, structure and properties of sea ice. USA Cold Regions Research and Engineering Laboratory, Monograph 82-1.

The Chemical and Structural Properties of Sea Ice in the Southern Beaufort Sea

D.A. MEESE
U.S. Army Cold Regions Research and Engineering Laboratory
Hanover, New Hampshire, U.S.A.

ABSTRACT/INTRODUCTION

Detailed chemical and structural profiles were determined for 10 first-year and 10 multiyear ice cores collected in the southern Beaufort Sea during April and May 1986 and 1987. Concentrations of Cl, Br and SO_4 were determined with a Dionex ion chromatograph using standard techniques. An eluent of 1.125 mM sodium bicarbonate and 3.5 mM of sodium carbonate was used. Concentrations of Na, Ca, K and Mg were determined by atomic absorption spectrophotometry using standard techniques (Perkin-Elmer 1976). Nutrient analyses (PO_4, SiO_4, NO_3, NO_2 and NH_4) were conducted following the techniques of Glibert and Loder (1977) on the 1986 samples and those of Whitledge et al. (1981) on the 1987 samples. Chlorophyll *a* analyses were conducted using the techniques of Strickland and Parsons (1972). Detailed descriptions of the analysis and blank studies can be found in Meese (1988).

The objectives of the study included determination of what, if any, chemical and/or physical trends exist in sea ice in the Southern Beaufort Sea and to determine the extent of chemical fractionation in the ice.

In order to determine relationships between chemical species and to determine fractionation patterns, linear regressions between all species were calculated. In addition, dilution curves were made for all species and statistical analyses including correlation coefficient matrices and factor analysis were performed. Chemical species were divided into two major categories for data analysis, the major ions (Cl, Br, SO_4, Na, Ca, K and Mg) and nutrients (PO_4, SiO_4, NO_3, NO_2 and NH_4). Additional categories for statistical analyses included all species, all species normalized to Cl, major ions normalized to Cl and nutrients normalized to Cl. These statistics were performed on first-year ice, multiyear ice and all samples.

RESULTS AND DISCUSSION

Major ions

For each core best-fit linear regressions were obtained for each chemical species analyzed vs Cl. In addition, regressions were obtained for Na to SO_4. The purpose of this analysis was to determine which chemical species vary linearly with Cl and which nutrients are linear with each other, in order to determine if factors other than salinity are affecting ice chemistry. The results for the first-year and multiyear ice data are very similar. All regressions are significant at the 99% confidence interval. The R-values for the major ions are all greater than 0.9 indicating strong linearity and a strong dependence on salinity. The R-values for Na and SO_4 are between 0.78 and 0.9. Although these values are statistically significant the lower values indicate that linearity may be weakened by fractionation occurring in the ice.

Dilution curves were produced for the major ions to determine which chemical species are enriched or depleted relative to seawater. Br and Na are fairly linear and do not show any trend toward enrichment or depletion. Ca and SO_4 show the most scatter around the dilution curve. This is not surprising as $CaCO_3$ and Na_2SO_4 are the first salts to precipitate during freezing. As brine drains, changes in the ratio of these species with respect to Cl occur, resulting in vari-

ations in relation to the dilution curve. Mg in the ice is slightly enriched (1–2%), with respect to standard seawater and seawater collected from the sample sites indicating that an enrichment process is occurring and Mg may be precipitating. For Mg enrichment to occur a salt other than Cl must be precipitating with Mg at temperatures higher than -36°C (Assur 1958) suggesting that a revision in Assur's phase diagram may be necessary. K shows a 1–2% depletion from seawater. This is not surprising, however, since the first K salt (KCl) does not form until -36.8°C. K should be more mobile than Cl and show a depletion with respect to seawater (Weeks and Ackley 1982).

Statistical analyses including correlation coefficient matrices and factor analysis show that in most cores significant correlations exist between the major ions. The significant correlations are expected as these are the conservative elements in seawater. This indicates that the ratios of the elements remain fairly constant throughout the ice. Factor analysis revealed that SO_4 and Na fractionation has occurred in many samples, but there is not a distinct overall pattern that exists. All the major ions were then normalized to Cl thereby removing the salinity effect to determine if secondary processes occur in the ice. Normalization showed that while secondary processes do exist, they do not have an impact on the overall ice chemistry.

Nutrients

As with the major ions, best-fit linear regressions were obtained for the nutrients vs Cl and, in addition, NO_3 to the other nutrients and NO_2 to the other nutrients. While R-values for the nutrients were all statistically significant they were all less than 0.78. This indicates that salinity effects are much less dominant and that other processes such as biological activity have affected nutrient concentrations. Nutrients plotted vs each other also show weak linear trends which indicate that the various nutrients are affected by some of the same general processes; however, overall each nutrient behaves differently and is being affected by different processes.

The dilution curves for the nutrients (Fig. 1) all show enrichment with respect to seawater and show considerable scatter around the curve. Alexander (1974) also working in the southern Beaufort Sea found that nitrogen nutrient levels in water drained from sea ice during the spring ice bloom were considerably higher than seawater levels. Nutrient levels in

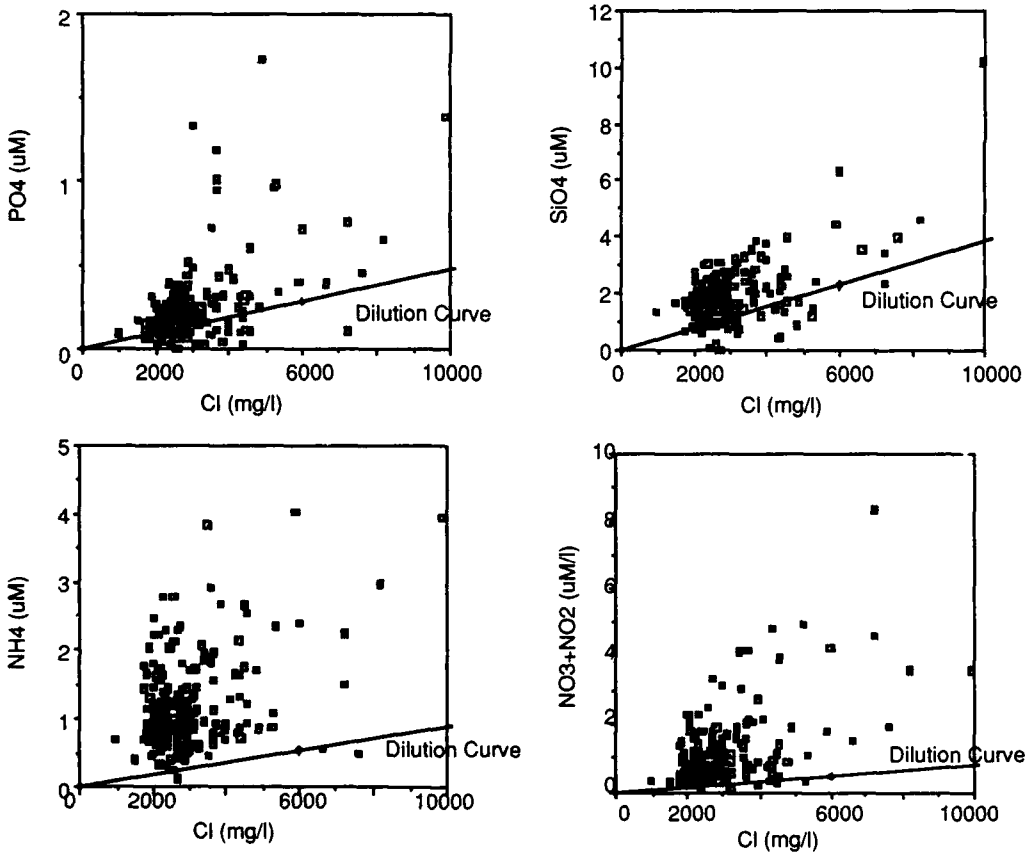

Figure 1. Dilution curves for first-year ice for nutrients: a) PO_4, b) SiO_4, c) NH_4 and d) NO_3+NO_2.

the upper water column typically increase over the winter due to low levels of biological activity and are then readily depleted in the spring. When actual concentrations are considered, nutrients are higher in the surface water than in the ice, with the exception of NH_4 which was usually higher in the bottom 10 cm of ice. This may be due to bacterial recycling (Horner and Schrader 1982).

Redfield ratios of N:P were calculated for the underlying water samples, first-year ice and multiyear ice in order to determine if the N:P ratio is consistent with that normally associated with oceanic organic matter (15:1). The N:P ratio for water collected at the ice/water interface is 4.6, which is significantly lower than the predicted 15. This low ratio may be the result of the substantially decreased biological activity in the water during the winter months. The mean N:P ratio for the first-year ice samples is 18.3. This value is much closer to the expected 15 than that found for the underlying water. This behavior indicates that biological activity is occurring in the ice and is controlling the nutrient ratios. This behavior, also found by Alexander (1974) in the southern Beaufort Sea where inorganic nitrogen was enriched with respect to phosphorus, is probably caused by the high nitrogen concentration of the river waters entering the coastal areas. The N:P ratio for multiyear ice is 7.5 which is lower than the 18.3 found for first-year ice; however, it is higher than that of the underlying surface water (4.6). Because the multiyear ice may have originated in different parts of the Arctic it is difficult to compare values found in the Beaufort Sea with that of the sampled ice. However, Maestrini et al. (1986) also found a decreased ratio in the water in Hudson Bay; this may be a consistent trend throughout the arctic waters in winter. If this is the case, the increased ratio for multiyear ice indicates that biological activity has occurred or is occurring in the ice but that other processes may be affecting the nutrient ratios and concentrations.

Statistical analysis show that no apparent trends exist between major ions and nutrients, indicating that nutrient concentrations are independent of salinity effects and that processes affecting nutrient concentrations may not be consistent throughout the ice pack and may be location specific. In first-year ice fewer correlations exist between the nutrients than the major ions and there is much less consistency between cores. This is a result of processes that can affect nutrient concentrations such as biological activity, brine drainage, bacterial regeneration, nitrification and denitrification. In multiyear ice statistical analysis on nutrients showed that 60–70% of the cores had significant correlations at the 99% confidence interval for NO_3 and NH_4. In addition significant correlations exist in 80% of the cores for NO_3 and NH_4 to PO_4. This indicates biological activity as was also observed in first-year ice. When nutrients in multiyear ice were normalized to Cl, factor analysis showed a strong positive relationship in 70–100% of the cores for PO_4, NO_2 and NH_4. This suggests that in multiyear ice nutrients are not salinity dependent and biological activity may strongly control nutrient concentrations.

CONCLUSIONS

In this study it was found that major ion chemistry is strictly associated with salinity and, although some fractionation does occur, it does not appear to affect the overall ice chemistry. Mg is enriched relative to seawater indicating that a revision in the "sea ice" (Assur 1960) phase diagram may be necessary and K is depleted. Nutrient concentrations appear to be somewhat controlled by salinity, but secondary processes are also important, particularly in multiyear ice.

ACKNOWLEDGMENTS

I would like to especially thank Tony Gow, Terry Tucker, Steve Ackley, Paul Mayewski, Mary Jo Spenser and Ted Loder for the help and support I received while doing this work and for making it all possible.

LITERATURE CITED

Addison, J.R. (1977) Impurity concentrations in sea ice. *Journal of Glaciology*, **18**(78): 117–127.

Alexander, V. (1974) Primary productivity regimes of the nearshore Beaufort Sea, with reference to potential roles of ice biota. In *Coast and Shelf of the Beaufort Sea* (J.C. Reed and J.E. Sater, Ed.), Arctic Institute of North America, Arlington, Virginia, p. 609–632.

Assur, A. (1960) Composition of sea ice and its tensile strength. USA Snow, Ice and Permafrost Research Establishment, Research Report 44. (Available from USACRREL, Hanover, N.H.)

Bennington, K.O. (1963) Some chemical composition studies on Arctic sea ice. In *Ice and Snow* (W.D. Kingery, Ed.), Cambridge, Massachusetts: MIT Press, p. 248–257.

Glibert, P.L. and T.C. Loder (1977) Automated analysis of nutrients in seawater: A manual of techniques.

Woods Hole Oceanographic Institution Technical Report 77-47.
Horner, R. and G.C.Schrader (1982) Relative contributions of ice algae, phytoplankton, and benthic microalgae to primary production in nearshore regions of the Beaufort Sea. *Arctic*, 35:485–503.
Maestrini, S.Y., M. Rochet, L. Legendre and S. Demers. (1986) Nutrient limitation of the bottom-ice microalgal biomass (southeastern Hudson Bay, Canadian Arctic). *Limnological Oceanography*, 31(5):969–982.
Meese, D.A. (1988) The chemical and structural properties of sea ice in the southern Beaufort Sea. Ph.D. dissertation (unpublished), University of New Hampshire.
Strickland, J.D. and T. R. Parsons (1972) A practical handbook of seawater analysis. *Bulletin of Fisheries Resources Board of Canada*, no. 167.
Weeks, W.F. and S.F. Ackley (1982) The growth, structure and properties of sea ice. USA Cold Regions Research and Engineering laboratory, Monograph 82-1.
Whitledge, T.E. S.C. Malloy, C.J. Patten and C.D. Ulrick (1981) Automated nutrient analyses in seawater. Brookhaven National Laboratory Report 5B98.

Nutrient Concentrations in Antarctic Pack Ice During the Austral Winter

D.L. GARRISON AND A.R. CLOSE
Institute of Marine Sciences
University of California
Santa Cruz, California, U.S.A.

L.I. GORDON
College of Oceanography
Oregon State University
Corvallis, Oregon, U.S.A.

ABSTRACT

Nutrient concentrations in sea ice are often measured as a bulk parameter on melted samples. However, for biological studies it is necessary to predict the actual in-situ concentrations within brine inclusions. In previous studies there have been considerable problems in determining the relative importance of physical vs biological effects in controlling nutrient concentrations in ice. During the Antarctic Marine Ecosystem Research in the Ice Edge Zone (AMERIEZ) winter cruise of 1988, we measured salinity, nutrients (nitrate + nitrite, nitrite, silicic acid, phosphate, and ammonia) and other chemical and biological parameters in sea ice.

Salinities in ice ranged from ~0 in some melted core sections to 104‰ in brine from the surface layer in ice. Nutrient concentrations in newly forming ice were close to the levels predicted from seawater nutrient/salinity ratios. In older ice, nitrate, phosphate, and silicate also tended to agree with the seawater nutrient/salinity ratios. Brine samples from the surface layer of ice floes showed considerable variability and were depleted in nutrients relative to values predicted from salinity. Ammonia and nitrite showed a poor relationship with salinity and the levels were markedly elevated in melted ice samples of first and multiyear ice. Nutrient concentrations were uncorrelated with biological parameters such as chlorophyll *a*, POC and PON. The poor relationship between ammonia, nitrite and salinity in bulk samples and the considerable variability in nutrient/salinity ratios in concentrated brine make interpreting nutrient measurements in ice problematic.

INTRODUCTION

Nutrient concentrations have been measured in Antarctic sea ice by several workers (e.g., Bunt and Lee 1970, Oradovskiy 1974, Garrison et al. 1982, Clarke and Ackley 1984, Jennings et al. 1986, Dieckmann et al. 1988, Lange et al. 1988, Grossi 1985). However, it has proved difficult to relate the nutrient levels in ice to those in the water underlying ice floes or to interpret how variations within ice are related to physical or biological processes.

The difficulties of measuring nutrients in ice is partially a sampling problem. At the surface of ice floes, in porous ice and in unconsolidated frazil ice, brine or interstitial water can be separated from ice for nutrient measurements, but the usual procedure is to collect and section ice cores and measure nutrient concentrations as one of the bulk parameters on melted samples (e.g., Clarke and Ackley 1984, Lange et al. 1988). In principle, if nutrient ions remain in the brine fraction and are only affected by brine loss from ice floes, then nutrient: salinity ratios characteristic of the surface waters should be maintained in ice (Fig. 1). Because high concentrations of organisms are also

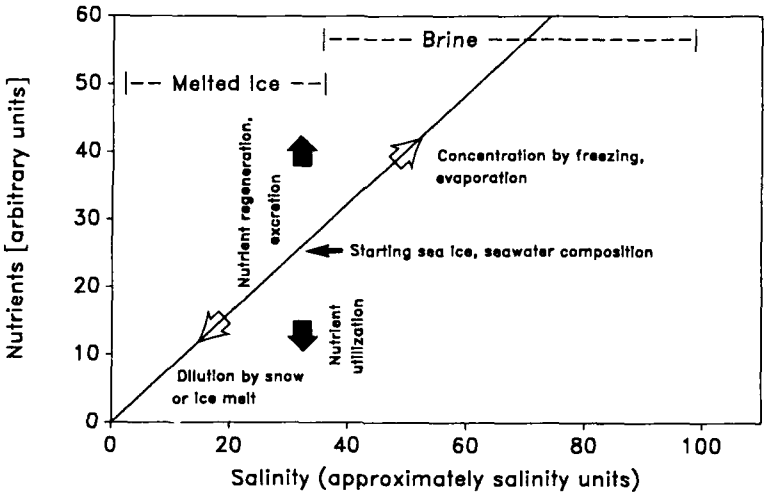

Figure 1. Hypothetical nutrient concentrations to salinity relationships in sea ice. The solid line is the nutrient/salinity dilution relationship determined from surface waters and extrapolated through the origin. The vectors indicate the effects of the respective processes in this concentration-salinity field. We divide the salinity range into ice-melt and brine ranges at the approximate salinity of somewhat diluted, regional surface waters.

found in ice (Garrison et al. 1986), biological uptake or regeneration of nutrients could also change nutrient concentrations within the ice and variations resulting in biological activity should be evident as deviations from the *y*-axis along a hypothetical dilution curve (see Fig. 1). One might expect that deviations from the predicted nutrient: salinity ratios should correlate with biologically relevant variables such as chlorophyll *a*, phaeopigments or particulate carbon. In actual observations, the nutrient/salinity relationships varied with the different nutrient species and have shown agreement, depletion, or concentration relative to a dilution curve with little agreement in the pattern reported by different workers (e.g., Garrison et al 1982, Clarke and Ackley 1984, Jennings et al. 1986). In many cases the nutrient concentrations were uncorrelated with biological variables (e.g., Garrison et al. 1982, Clarke and Ackley 1984). Moreover, Jennings et al. (1986) found that N:P ratios in ice differed from those expected to result from biological uptake or regeneration (i.e., the Redfield ratio of ca. 16:1), and thus they were unable to ascribe any biological significance to the variations in nutrient concentrations within ice samples.

Nutrients are potentially limiting the growth of ice algal populations. This is particularly true in pack ice regions where most of the algal biomass occurs within floes as internal populations (e.g., Ackley et al. 1979, Garrison et al. 1986). The purpose of our study was to determine if nutrient concentrations in ice can be measured and used to interpret biological processes. We report nutrient concentration in antarctic pack ice during the austral winter and discuss problems with interpreting these observations.

MATERIALS AND METHODS

Ice samples were collected from the pack ice region of the Weddell Sea (60–62°S, 40–50°W) during the austral winter (10 June to 2 July 1988) as part of the Antarctic Marine Ecosystem Research in the Ice Edge Zone (AMERIEZ) study. Newly forming pancake ice was collected by bucket and sections of thin ice sheets (nilas) were removed with an ice saw. Ice cores were collected from older, thicker floes using a CRREL ice coring auger. Samples of brine were collected from the surface layer in ice floes by removing a short (~20-cm) core section and allowing brine to accumulate in the void.

Ice samples were allowed to melt approximately 24 hours in the dark. Both brine and melted ice samples were filtered through Gelman GF/F glass–fiber filters. Nutrient samples were run immediately or briefly frozen until they could be analyzed. Nitrate, nitrite, phosphate and silicate were measured using methods adapted from Atlas et al. (1971) and ammonia was analyzed using a modification of Solorzano's (1969) method. The GF/F filters were analyzed for chlorophyll *a* and particulate carbon and nitrogen (Parsons et al. 1984).

Salinity was measured on both brine and melted

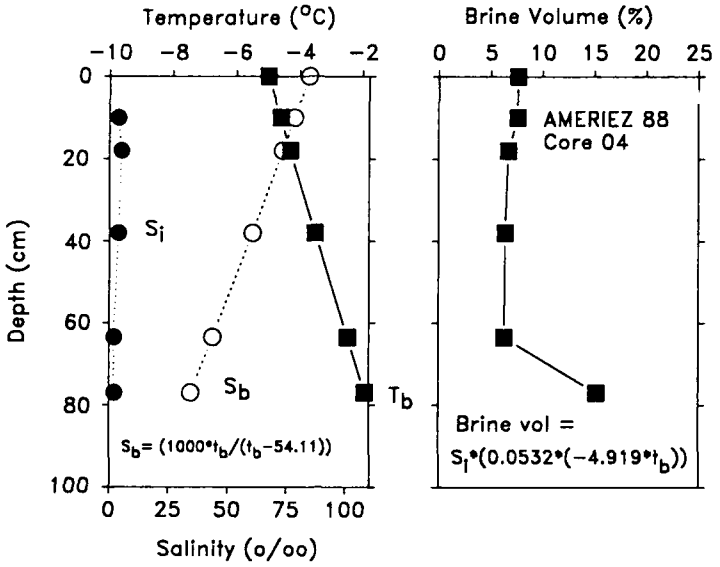

Figure 2. Temperature, salinity and brine volume relationships. T_b *is temperature profile throughout ice.* S_i *is bulk salinity measured on melted sample, and* S_b *is brine salinity calculated from the empirical relationship of Assur (1958). Brine volume was calculated from the formula suggested by Frankenstein and Garner (1967).*

ice samples using either a refractometer (for high salinity brine) or a conductivity salinometer. In-situ temperatures were measured in snow, at the ice surface and in brine. A linear interpolation of temperature from the ice surface to the ice/seawater interface was used to construct a temperature profile. In situ brine volumes and salinities were calculated from empirical relationships (Fig. 2).

RESULTS

Salinity and nutrient measurements in seawater and ice are summarized in Figure 3. Nitrate, phosphate, and silicate concentrations in melted (bulk) samples tended to conform with the predicted dilution curve (Fig. 4). Among surface layer brine samples there was considerable scatter of the data with samples from first and multiyear ice usually showing some apparent depletion. Ammonia and nitrite concentrations were not related to salinity and were enriched in most ice samples relative to the predicted dilution curve (see Fig. 4).

Nitrogen to phosphorus atom ratios (N:P) were calculated both with and without including NH_4^+ as part of the total nitrogen (Fig. 5). Among surface seawater, new ice and brine samples, there was little difference in the N:P ratios (ca. 12–15), which were close to the expected Redfield ratio of 16:1. The higher N:P ratios (>20:1) in melted ice samples were the result of the higher ammonia levels in these samples (Fig. 5). Correlation analysis among nutrient concentrations, nutrient concentrations normalized by salinity, chlorophyll *a*, phaeopigments, POC and PON showed few significant relationships among these variables for any of the ice samples.

DISCUSSION

Concentrations of salinity, nitrate, nitrite, phosphate and silicate were similar to these previously measured by Garrison et al. (1982, unpublished data) and Clarke and Ackley (1984). The close agreement between nutrient concentrations measured in young ice and those predicted from a dilution curve (Fig. 4; also see Figure 1 in Garrison et al. 1982), indicates that nutrients in new ice are primarily controlled by brine loss. For nutrients in older ice, apparent depletion suggests biological uptake but the failure to find significant negative relationships between measures of biomass (chlorophyll *a*, phaeopigments, POC or PON) and nutrient concentrations, makes it difficult to establish this connection. These results may not be particularly surprising, since the winter should be a time of low biological activity in ice, and significant biological activity may have taken place several months prior to our sampling the ice floes.

Because the nutrient: salinity ratios can vary markedly from those in the surrounding water, the poten-

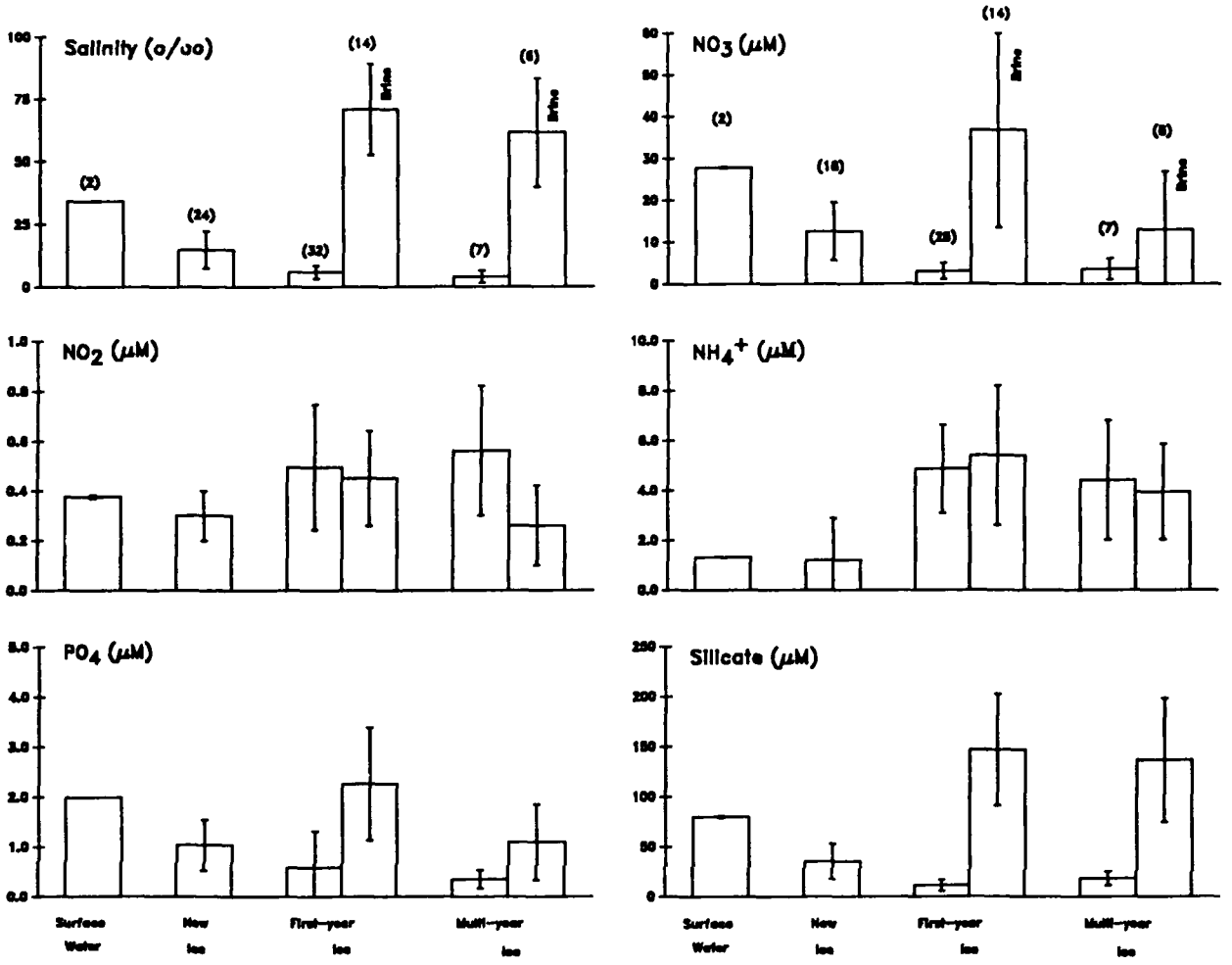

Figure 3. Summary of salinity and nutrient concentrations in sea ice. Mean and standard deviation are shown. N *is the number of samples for each type of ice.*

tial for nutrients to limit production in internal algal assemblages is apparent. The relatively rapid exchange of nutrients that Reeburgh (1984) suggested for the skeletal layer of growing congelation ice or that Bunt and Lee (1970) assumed was characteristic of unconsolidated platelets are apparently not the case for the internal microenvironment of pack ice floes.

Determining the actual in situ nutrient levels in the microenvironment of brine inclusions is problematic. When we normalized bulk-measured nutrients by the calculated brine volumes (see Fig. 2), there was a close agreement at least for nitrate and silicate between the corrected concentrations and those actually measured in brine from first-year ice. However, phosphate values were overestimated by a factor of 2; ammonia and nitrite were also considerably overestimated by using this approach.

The concentration of ammonia in some samples was surprisingly high (see Fig. 3). Similarly high concentrations were reported for arctic ice by Clasby et al. (1976) and in antarctic fast ice by Grossi (1985). Since core sections require ~1 day for melting, there is a potential for nutrient regeneration and/or contamination. However, some brine samples, which were quickly processed, also showed elevated ammonia levels and new ice samples, which were slowly melted, showed low ammonia levels that were not markedly different from those measured in surface waters. In one of the earlier published reports of nutrients in antarctic sea ice, Oradovskiy (1974) noted the high ammonia concentrations in ice and offered the explanation that over time free ammonia is absorbed in the fresh-ice phase from the surrounding brine. Since brine volume occupied about 5% of the ice volume at the time we sampled, any appreciable ammonia associated with ice could have produced the excess ammonia in bulk samples. Since ammonia accumulation in the ice phase would represent a nonbiological concentration, this would also

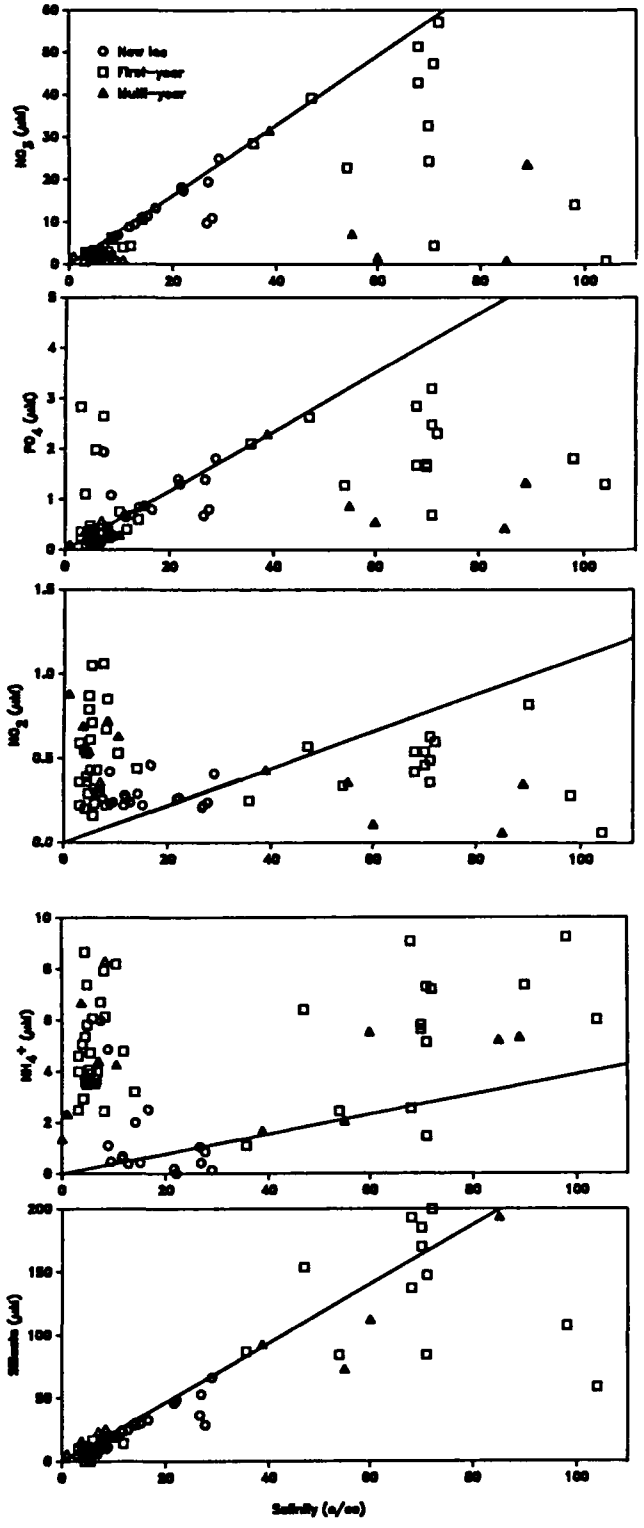

Figure 4. Nutrient concentrations as a function of salinity. The solid line is the nutrient/salinity relationships determined from surface waters. First and multiyear ice samples with salinities >35‰ are surface brine samples.

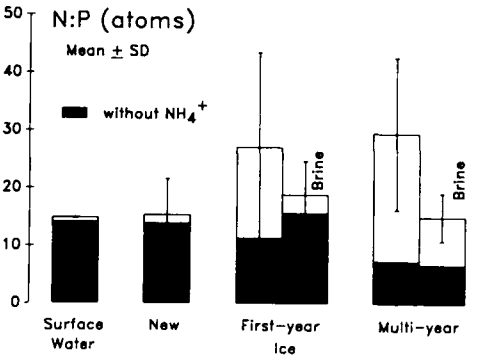

Figure 5. Nitrogen to phosphorus atom ratios (N:P) calculated with and without NH_4^+. Mean and standard deviations are shown for ratios calculated with NH_4^+. Only mean values are shown for ratios calculated without including NH_4^+

account for the anomalously high N:P ratios observed in our samples (see Fig. 5).

ACKNOWLEDGMENTS

This study was supported by National Science Foundation Grants to D. L. Garrison (DPP 84-20184) and to D. M. Nelson and L. I. Gordon (DPP 84-20204).

REFERENCES

Ackley, S.F., K. R. Buck and S. Taguchi (1979) Standing crop of algae in the sea ice of the Weddell Sea region. *Deep-Sea Research*, **26A**: 269–281.

Atlas, E.L., S.W. Hager, L.I. Gordon and P.K . Park (1971) A practical manual for use of the Technicon AutoAnalyzer in seawater nutrient analysis. Department of Oceanography, Oregon State University, Corvallis, Technical Report 215, Ref. 71-22.

Assur, A. (1958) Composition of sea ice and its tensile strength. National Academy of Sciences, National Research Council. Publication 598, p. 106–138.

Bunt, J.S. and C.C. Lee (1970) Seasonal primary production in Antarctic sea ice at McMurdo Sound in 1967. *Journal of Maritime Research*, 28: 304–320.

Clarke, D.B. and S. F. Ackley (1984) Sea ice structure and biological activity in the Antarctic marginal ice zone. *Journal of Geophysical Research*, **89**: 2087–2095.

Clasby, R.C., V. Alexander and R. Horner (1976) Primary productivity of sea- ice algae. In *Assessment of the Marine Environment* (D.W. Hood, Ed.). Fairbanks, Alaska: University of Alaska, Institute of Marine Science, p. 209–304.

Dieckmann, G.S., S. Ackley and J. Jennings (1988) The nutrient status in sea ice of the Weddell Sea: effects of biological activity and sea ice texture (abstract). *Presented at the Fifth Symposium on Antarctic Biology*, Hobart, Tasmania, Australia.
Frankenstein, G. and R. Garner (1967) Equations for determining the brine volume of ice water from –0.5° to –22.9°C. *Journal of Glaciology*, **6**: 943–944.
Garrison, D. L., K.R. Buck, and M. W. Silver (1982) Ice-algal communities in the Weddell Sea, Antarctica. *Antarctic Journal of the U. S.*, **17**: 157–159.
Garrison, D. L., C. W. Sullivan, and S. F. Ackley (1986) Sea ice microbial communities in Antarctica. *BioScience*, **36**: 243–250.
Garrison, D. L. and K. R. Buck (1986) Organism losses during ice melting: a serious bias in sea ice community studies. *Polar Biology*, **6**: 237–239.
Grossi, S. M. (1985) Response of a sea ice microalgal community to a gradient in under ice irradiance. Ph. D. Dissertation (unpublished), University of Southern California, Los Angeles.
Jennings, J.C. Jr., M. A. Lange, and G. S. Dieckmann (1986) Nutrient observations in the Antarctic Seasonal Pack Ice. *EOS*, **67**: 1014–1015.
Lange, M. A. (1988) Basic properties of Antarctic sea ice as revealed by textural analysis of ice cores. *Annals of Glaciology*, **10**: 95–101.
Oradovskiy, S. G. (1974) Investigations of the chemical composition of Antarctic sea ice. *Oceanology*, **14**: 50–54.
Parsons, T. R., Y. Maita and C.M. Lalli (1984) *A Manual of Chemical and Biological Methods for Seawater Analysis*. Oxford: Pergamon Press.
Reeburgh, W. S. (1984) Fluxes associated with brine motion in growing sea ice. *Polar Biology*, **3**: 29–33.
Solorzano, L. (1969) Determination of ammonia in natural waters by the phenolhypochlorite method. *Limnology and Oceanography*, **14**: 799–801.

Verification Results of the Cox and Weeks Sea Ice Salinity Prediction Model

G.F.N. COX
U.S. Army Cold Regions Research and Engineering Laboratory
Hanover, New Hampshire, U.S.A.

ABSTRACT*

Recently Cox and Weeks developed a numerical model to predict the salinity and temperature profiles of a growing first-year sea ice sheet. While the results of the model looked promising, verification runs of the model were performed using the detailed ice salinity, snow, and meteorological data collected by Nakawo and Sinha in Eclipse Sound, Baffin Island, Canada. The first simulation was discouraging. The model was then revised by introducing a new salinization mechanism called "suction" and obtaining a better formulation of the gravity drainage process. Suction is the reverse process of brine expulsion. When the ice is warmed, brine is sucked up from the ice below and the underlying seawater. The gravity drainage equation was improved by performing a multiple regression of laboratory gravity drainage data collected earlier by Cox and Weeks. Once these improvements were made, the resulting salinity profiles were within the experimental scatter of the field data (one part per thousand). Considering the uncertainty in the snow cover properties and thickness, the results are most encouraging.

* Full description of these results is in Cox, G.F.N. and W.F. Weeks (1988) Numerical simulations of the profile properties of undeformed first-year sea ice during the growth season. *Journal of Geophysical Research*, **93**(10): 12,449–12,460.

Heat Transfer to Arctic Sea Ice
Evidence from Dissolved Argon

R.M. MOORE
Department of Oceanography
Dalhousie University
Halifax, Nova Scotia, Canada

W. SPITZER
Chemistry Department
Woods Hole Oceanographic Institution
Woods Hole, Massachusetts, U.S.A.

ABSTRACT

It has recently been suggested (Moore and Wallace, *Journal of Geophysical Research*, **93**: 565, 1988) that the temperature–salinity properties of Arctic Ocean waters in the depth range of about 170 to 450 m are consistent with a simple model in which heat is transferred from the ocean waters into melting sea ice. This model can reproduce the *T-S* relationship observed at a number of widely separated Arctic Ocean locations.

In an attempt to find support for this model in the chemical properties of the waters, attention has been given to the dissolved inert gases. If seawater is cooled by the process of melting ice, the result should be a decrease in the level of gas saturation in the water. In the case where this occurs under a continuous layer of ice, there should be no re-equilibration of the gases in the modified water with the atmosphere. It follows that if the lowering in saturation level can be determined, the amount of cooling can be calculated.

Water samples have been collected from an Arctic Ocean site, 80°58.4'N 112°29'W, and analyzed for dissolved argon. While the surface layer shows a marked supersaturation (about 5%), the extent of supersaturation decreases rapidly with depth, reaching about 1% at 100 m. Undersaturations of 1 to 3% are found between 275 and 700 m. These results are used to estimate the extent to which the Atlantic layer has lost heat by melting ice in the Arctic Ocean.

B. Optical, Electrical, Acoustical and Mechanical Properties

Theoretical Estimates of Light Reflection and Transmission by Spatially Inhomogeneous and Temporally Varying Ice Covers

D.K. PEROVICH
U.S. Army Cold Regions Research and Engineering Laboratory
Hanover, New Hampshire, U.S.A.

ABSTRACT

The reflection, absorption, and transmission of light at visible and near-infrared wavelengths is important for a number of geophysical problems. Light reflection is an important parameter in remote sensing studies, absorption is significant to ice thermodynamics, and transmission strongly influences biological activity in and under the ice. The focus on this paper is on the spectral (wavelength region 400–1000 nm) reflection and transmission of light by spatially inhomogeneous sea ice covers investigated using a two-stream, multilayer radiative transfer model. The model is computationally simple and utilizes available experimental data on the optical properties of sea ice. The ice cover is characterized as a layered medium composed of selections from nine distinct snow and ice types. Two cases are presented illustrating values of spectral albedo, transmittance, and transmitted PAR (photosynthetically active radiation) for a uniform ice cover as it melts and for a spatially inhomogeneous ice cover. The importance of ice thickness and surface conditions on the spectral reflected and transmitted radiation fields is demonstrated.

INTRODUCTION

The reflection, absorption, and transmission of shortwave radiation by a sea ice cover is significant in a variety of geophysical problems. Spectral reflectance is important in the interpretation of imagery from remote sensing instruments that operate at visible and near-infrared wavelengths. Absorption plays a major role in the heat and mass balance of ice covers. The spectral composition of transmitted light strongly affects biological activity.

Understanding radiative transfer in a sea ice cover is considerably complicated by the large temporal and spatial variability in the physical, and therefore the optical, properties of the medium. For example, observations have demonstrated that the optical properties of sea ice depend on brine volume, brine distribution, vapor content, and ice surface conditions. Ice covers can have large spatial variations with bare ice, deep snow drifts, thick pressure ridges and thin young ice all occuring within a few tens of meters. Ice conditions can also change quickly with time, going from snow covered ice to melt ponds in only a few days.

This complexity necessitates the use of theoretical models both to interpret and to extrapolate observational results. Several different models have been formulated to describe radiative transfer in sea ice (Chandrasekhar 1960, Warren 1982, Perovich and Grenfell 1982, Grenfell 1983). These models all have features that both recommend them and limit them for particular applications. Often there are tradeoffs between detailed physics and computational simplicity. The fundamental problem I wish to address is how to calculate light reflection, absorption, and transmission for spatially and/or temporally complex ice covers.

THE MODEL

To address this problem I needed a model that satisfied four criteria. First, the model should be computationally straightforward and fast, and should run easily on a personal computer. Second, it should produce accurate values for spectral albedos and transmittances. (The albedo is the fraction of the incident irradiance that is reflected and the transmittance is the incident fraction that is transmitted.) The model need not compute the angular distribution of radiance. Third, it should utilize the experimental database of optical measurements. Finally, the physical characterization of the ice should be straightforward, requiring only a qualitative depiction, i.e., snow covered ice, blue ice, white ice, and melting ice.

The model developed to satisfy these constraints is a two-stream, multilayer model of radiative transfer at visible and near-infrared wavelengths (Dunkle and Bevans 1956, Grenfell 1979). The model is schematically displayed in Figure 1. The major features of the model are that it a) calculates two streams, an upward and a downward irradiance, b) consists of N distinct, homogeneous layers, c) is continuous at the interfaces between layers, d) applies to the spectral range 400 to 1000 nm, e) assumes that scattering in the medium is isotropic, f) allows specular reflection at the surface of the ice, g) and has no upwelling irradiance from the water column beneath the ice.

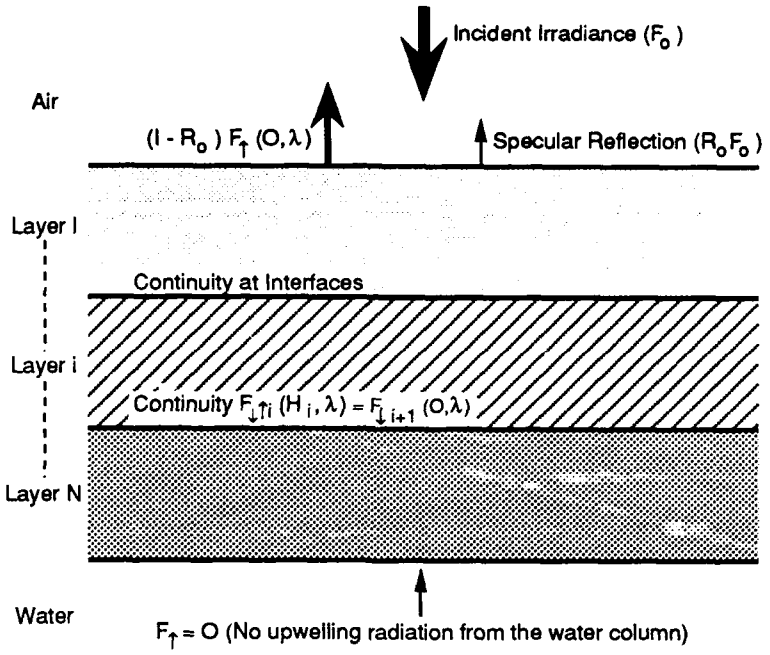

Figure 1. Schematic of two-stream, multilayer model.

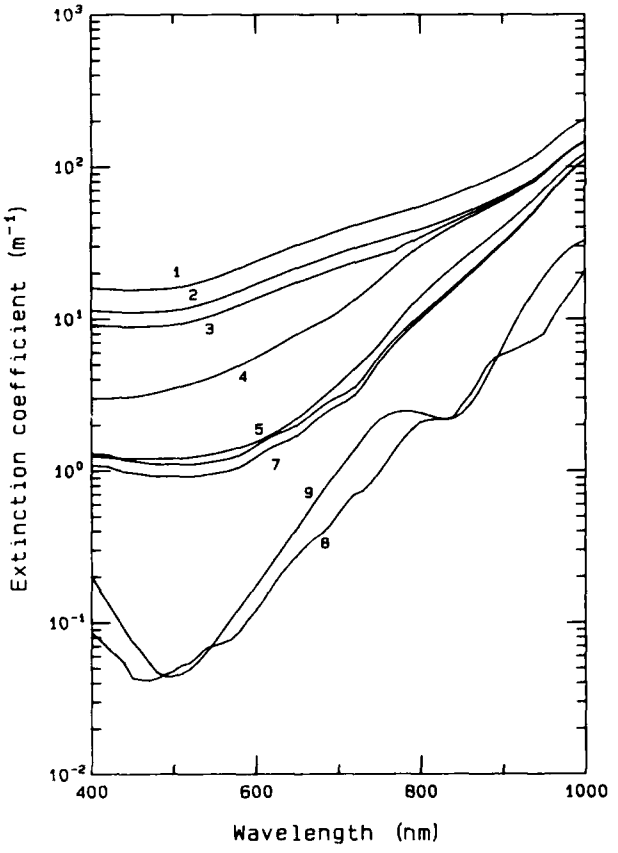

Figure 2. Spectral extinction coefficients for nine medium types used in the model: 1) dry snow, 2) melting snow, 3) ice colder than the eutectic point, 4) surface scattering layer of white ice, 5) interior portion of white ice, 6) cold blue ice, 7) melting blue ice, 8) bubble-free fresh ice, and 9) clear arctic water.

The input parameters for the model are the incident spectral irradiance, the spectral scattering and extinction coefficients for each ice type, and the ice type and thickness for each layer. Currently, nine different ice types can be used for the layers. Experimentally derived extinction coefficients for the nine ice types are presented in Figure 2. Values for ice types 1, 4, 5 and 7 were derived from Grenfell and Maykut (1977), type 3 from Perovich (1979), types 2 and 6 from Grenfell and Perovich (1984), type 8 from Grenfell and Perovich (1981), and type 9 from Grenfell (1979).

RESULTS

To illustrate the utility of this model I would like to apply it to two distinct cases: 1) a deformed ice cover and 2) a uniform ice cover that varies with time.

First consider the case of a cold, deformed, multiyear ice cover with spatially varying snow and ice thicknesses. In Figure 3 the snow depth (top surface) and the ice thickness (bottom surface) are graphed for a 100- × 100-m area.* In this region ice thickness ranged from 1.8 to 6.5 m with a mean of 3.01 m and snow depths from 0 to 0.34 m with a mean of 0.07 m. Using these data as input to the model, spectral albedos and transmittances were calculated for this region. Figure 4 shows the two-dimensional spatial

*W.B. Tucker, U.S. Army Cold Regions Research and Engineering Laboratory, personal communication, 1988.

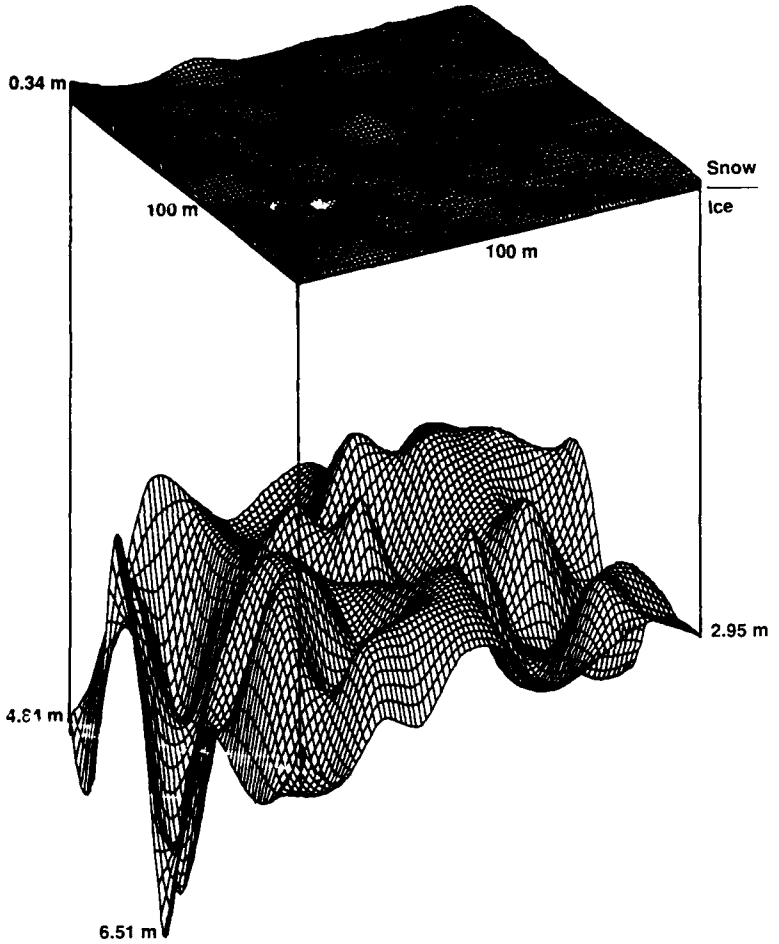

Figure 3. Snow and ice thickness data (W.B. Tucker, CRREL, pers.comm., 1988) measured at 10-m spacings on a 100- × 100-m grid. The top surface represents the snow depth and the bottom surface the ice thickness.

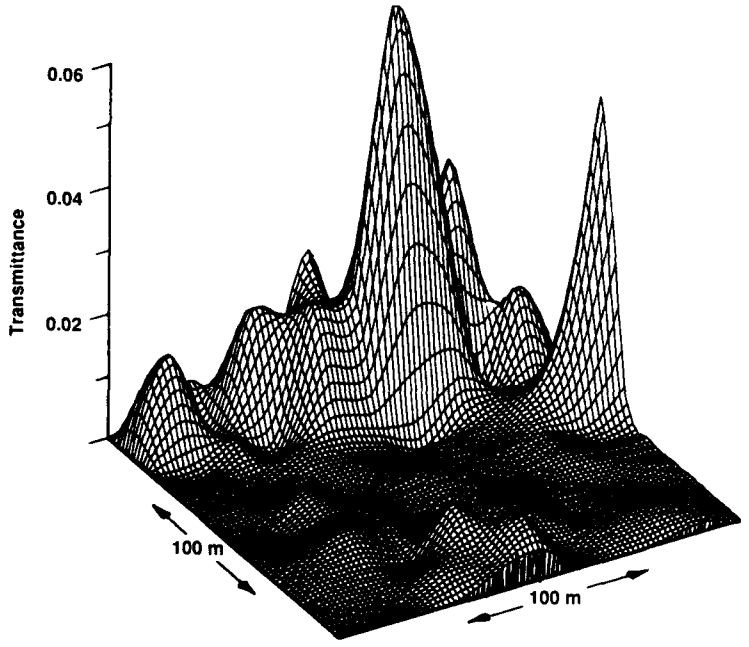

Figure 4. Spatial distribution of transmittance at 470 nm for snow and ice conditions of Figure 3.

distribution of transmitted light at 470 nm. The transmittance spans over five orders of magnitude from 0.88×10^{-6} to 0.63×10^{-1}. Features in Figure 4 do not necessarily correlate with the ice thickness topography. The peaks in transmitted light correspond to areas of bare ice, while minimum values occur where the snow was the deepest. Transmitted light distributions at other wavelengths are similar in shape to Figure 6, but have reduced magnitudes.

Even a spatially uniform ice sheet can be optically complex when it is undergoing temporal changes. From an optical perspective the most dramatic changes occur in the early portion of the melt season as the ice cover evolves from an opaque snow covered medium to translucent bare or ponded ice. On 20 June 1982 Mould Bay fjord was covered by 2.2 m of flat, undeformed, first-year ice overlaid by 0.30 m of cold, dry snow (Perovich 1983). By 10 July all the snow had melted, the ice had thinned to 1.5 m, and the surface was heavily ponded. A question arises regarding how this temporal evolution affected the albedo and transmittance. The input data to the model for this case were daily values of ice type, snow depth, pond depth, ice thickness, incident shortwave irradiance, and cloud conditions.

Spectral albedos from 400 to 1000 nm for 20 June to 10 July are plotted in Figure 5. The initial decrease in albedo occured on 21 June when the snow began to melt. This was followed by a precipitous drop three days later when the snow cover completely disappeared and the ice surface became covered by melt ponds. Thereafter, spectral albedos remained fairly constant with some small variations due to changes in pond depth.

Figure 6 shows spectral and total transmitted PAR (photosynthetically active radiation) for the 20 June to 10 July time period. PAR is proportional to the number of photons available at a particular wavelength. For the first few days a snow cover was present and the amount of transmitted light was negligible. Once the snow melted and ponds formed, PAR values increased sharply, especially at shorter wavelengths. As the ice thinned over the next two weeks there was a general upward trend in trans-

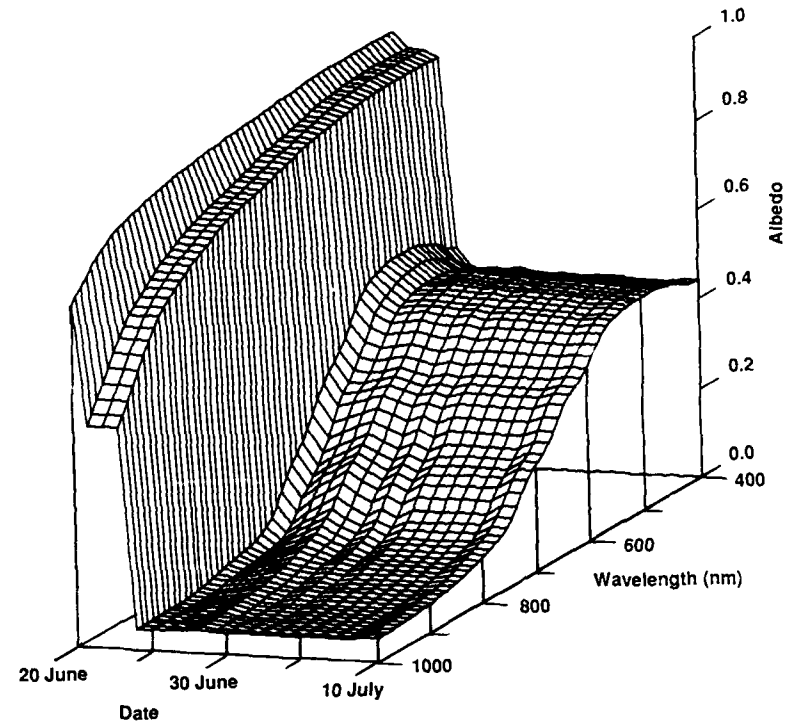

Figure 5. Temporal evolution of spectral albedo for uniform, first-year ice cover.

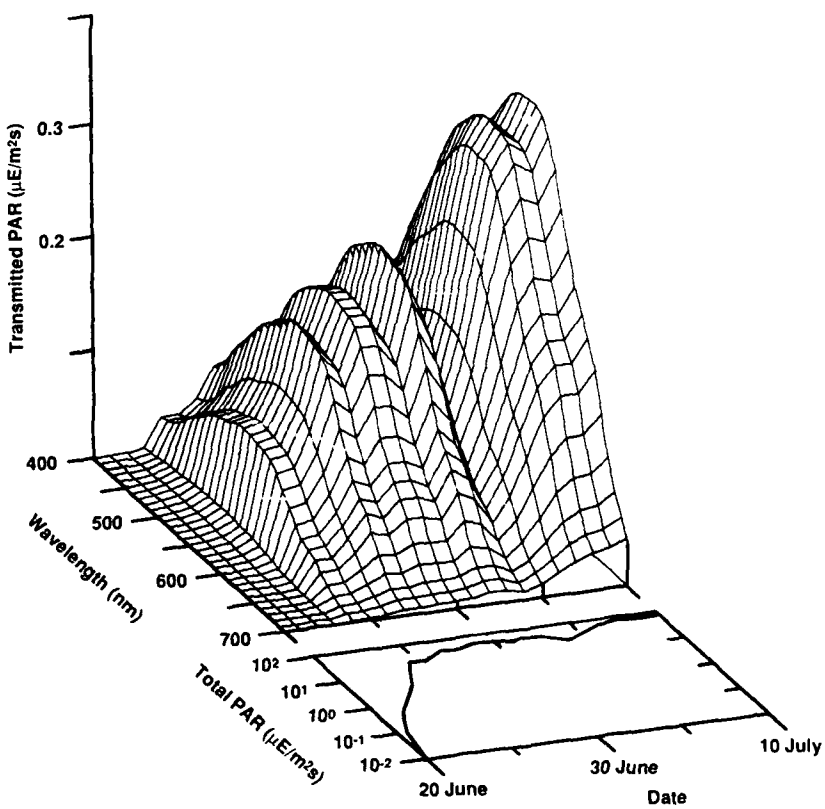

Figure 6. Temporal evolution of spectral and total transmitted PAR for uniform, first-year ice cover.

mitted PAR. The occasional small decrease occurred on cloudy days with small incident solar irradiance. Total PAR (integrated over wavelength from 400 to 700 nm) increased by more than an order of magnitude as the snow began to melt, then sharply by a factor of 100 as the snow cover disappeared and the ice became flooded, and finally by a gradual 10-fold increase as the ice thinned.

SUMMARY

There can be a tremendous amount of spatial and temporal variation in the light reflected and transmitted by a sea ice cover. Because of this, single point optical measurements may be insufficient to characterize albedos and transmittances for regions or time periods. The reflected and transmitted radiation fields can be defined in a detailed and accurate fashion by using this two-stream multilayer model with the easily determined input parameters of ice type, ice thickness, and ice surface conditions.

REFERENCES

Chandrasekhar, S.C. (1960) *Radiative Transfer*. New York: Dover.

Dunkle, R.V. and Bevans, J.T. (1956) An approximate analysis of the solar reflectance and transmittance of a snow cover. *Journal of Meteorology*, **13**(2): 212–16.

Grenfell, T.C. (1979) The effects of ice thickness on the exchange of solar radiation over the polar oceans. *Journal of Glaciology*, **22**(87): 305–320.

Grenfell, T.C. (1983) A theoretical model of the optical properties of sea ice in the visible and near infrared. *Journal of Geophysical Research*, **88**(C11): 9723–9735.

Grenfell, T.C. and G.A. Maykut (1977) The optical properties of ice and snow in the Arctic Basin. *Journal of Glaciology*, **18**: 445–463.

Grenfell, T.C. and D.K. Perovich (1981) Radiation absorption coefficients of polycrystalline ice from 400–1400 nm. *Journal of Geophysical Research*, **86**: 447–7450.

Grenfell, T.C. and D.K. Perovich (1984) Spectral albedos of sea ice and incident solar irradiance in the Southern Beaufort Sea. *Journal of Geophysical Research*, **89**: 3573–3580.

Perovich, D.K. (1979) The optical properties of young sea ice. M.S. Thesis, University of Washington–Seattle (unpublished).

Perovich, D.K. (1983) On the summer decay of a sea ice cover. Ph.D. Dissertation, University of Washington–Seattle (unpublished).

Perovich, D.K. and T.C. Grenfell (1982) A theoretical model of radiative transfer in young sea ice. *Journal of Glaciology*, **28**(99): 341–356.

Warren, S.G. (1982) Optical properties of snow. *Review of Geophysics and Space Physics*, **20**(1): 67–89.

Scattering and Absorption of Light by Sea Ice

R.G. BUCKLEY
Physics and Engineering Laboratory
Department of Scientific and Industrial Research
Lower Hutt, New Zealand

H.J. TRODAHL
Physics Department
Victoria University of Wellington
Wellington, New Zealand

ABSTRACT

The anisotropic and inhomogeneous optical characteristics of antarctic sea ice have been studied by measuring the pattern of radiation emerging from the ice surfaces near a light source placed on the surface. We demonstrate that anisotropic scattering in the bulk of the ice imposes a characteristic angular dependence on the transmitted radiance. The magnitude of the transmitted radiance is found to depend, among other things, on the brine volume of the surface layer and to decrease with the spring warming. It is observed that the ice is particularly transparent during the early spring which coincides with the period of reduced atmospheric ozone. With the resulting high UV radiance this is potentially damaging for life within and under the ice.

INTRODUCTION

The interaction of light with a complex medium such as sea ice is an interesting, although difficult, problem. However, it is a problem of some significance as the interaction is important for energy bal-

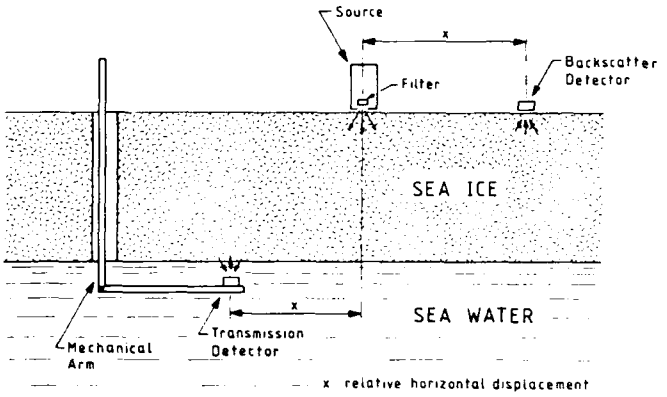

Figure 1. Schematic diagram of the source and detector layout. The radiance is measured as a function of the horizontal source detector separation, ρ.

ances in the southern ocean and for its life forms. In earlier publications (Buckley and Trodahl 1987, Buckley and Trodahl 1987, Trodahl et al. 1987, Trodahl et al., in press) we have demonstrated a simple in-situ experimental technique that allows us to relate the diffusive transport to the known structure of the ice.

Optical measurements were carried out in McMurdo Sound in the antarctic during the spring of 1985 and 1986. The experimental procedure has been published elsewhere (Trodahl et al. 1987) and will only be briefly described. A chopped monochromatic light source is placed on the surface of the sea ice, as illustrated in Figure 1. Wavelength selection is accomplished with narrow band filters. The backscattered radiance is measured with a downward viewing detector placed on the surface of the ice and the transmitted radiance is measured by a detector held under the ice. The experiment entails measuring the radiance as a function of the horizontal separation between the source and the detector.

Because of the complex composition of sea ice, possessing freshwater ice, air, brine and at low tem-

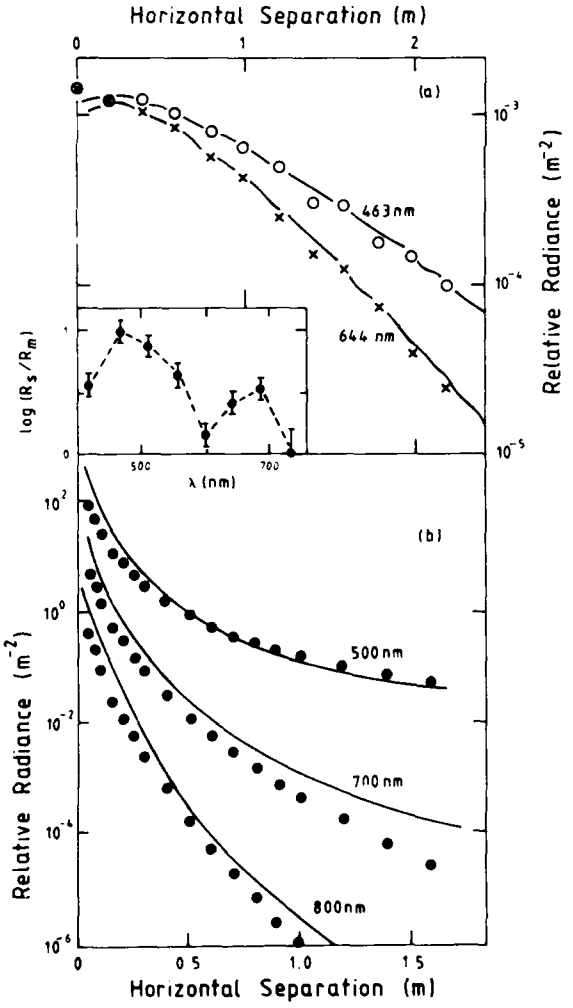

a. Transmitted. (Insert: scaling parameter required to fit the transmitted profile that follows the characteristic absorption of algae.)

b. Backscattered.

Figure 2. Transmitted and backscattered radiance vs source detector separation on 2.1-m sea ice in November 1986. The points represent experimental data and the continuous line results from the model described in the text.

a. Backscattered radiance at 500 nm vs source detector separation. The data were collected on 5 November (•) and 16 November (▲).

b. Brine volume for sea ice collected on the same days as the backscattered radiance displayed in 3a.

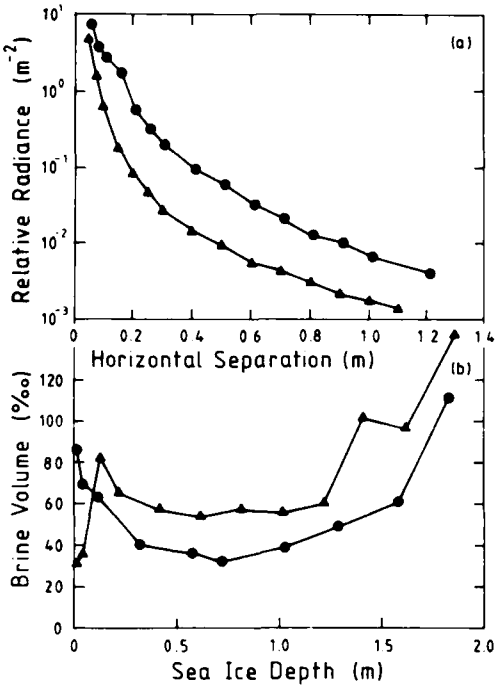

Figure 3. Backscattered radiance and brine volume for sea ice.

peratures precipitated salts (Weeks and Ackley 1982), the optical properties are dominated by the structure (Trodahl et al., in press). Thus, in addition to the optical measurements, the depth dependence of the salinity and temperature of the ice were measured at regular intervals during the course of the optical experiments. These measurements allow for some degree of correlation between the physical properties and the optical properties of the ice.

RESULTS AND DISCUSSION

Typical results of both the backscattering and transmission experiments are displayed in Figure 2. For detailed predictions of these profiles we have relied on Monte Carlo simulations using a variety of scattering models. Published absorption coefficients for ice (Grenfell and Perovich 1981) have been folded into the simulation which predicts the transmitted profile widths. The transmitted profiles are all narrower than predictions by isotropic scattering models and to describe them it is necessary to employ a two-layered model (Trodahl et al., in press) as illustrated in Figure 2. The model consists of an isotropically scattering top layer of 0.2-m thickness with a scattering length of 0.05 m and an anisotropic bulk in which the vertical and horizontal scattering lengths are 0.30 m and 0.18 m, respectively. The modeling predicts that the anisotropic scattering imposes a characteristic angular dependence on the emergent radiance as is observed (Trodahl et al., in press). However, to fit the magnitude a scaling parameter has to be introduced whose wavelength dependence, also shown as an insert in Figure 2, follows the absorption of algae, which were observed to be growing at the base of the ice. Using the same model the fit to the backscattered radiance is less convincing and indicates that the two-layered model with a relatively thin isotropically scattering surface layer is not sufficient. This is not surprising as the backscattered photons, particularly those that appear near the source, travel largely through the top layer of the ice. Structural studies (Weeks and Ackley 1982) clearly indicate that such an isotropic medium is not a good description of the upper part of the ice.

That the backscattering can be related to the brine volume, particularly in the surface layer, is demonstrated in Figure 3. In Figure 3a we show the backscattering at 500 nm from measurements 11 days apart and in Figure 3b the brine volume on the same days. During this period there was an approximately 9°C rise in air temperature that resulted in drainage of brine from about the top 200 mm of the surface with a consequent increase in air volume. Figure 3a shows that at large source-detector separations the curves are near parallel, but as the separation is reduced the curve for the later date rises more rapidly than at the early date. The physical size of the source and detector make it impossible to collect data any closer than 50 mm from the source. This large change in the backscattered radiance at small source-detector sepa-

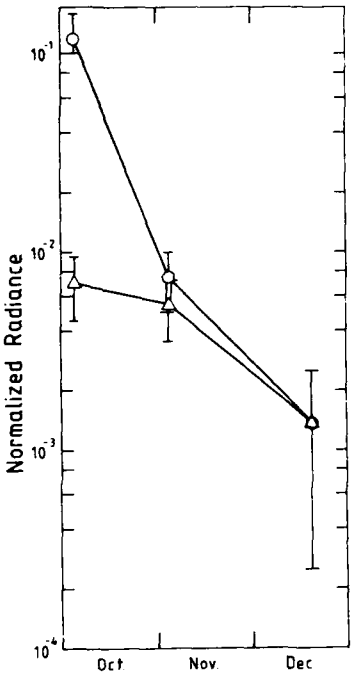

Figure 4. A plot of the temporal development of UV radiance at 305 nm under sea ice normalized to the surface radiance on 21 December (Frederick and Snell 1988). The lower curve (Δ) is for an unperturbed ozone layer, assuming 315 Dobson Units (DU). The upper curve (o) demonstrates the 20-fold increase in UV transmission during the presence of the ozone hole assuming a changing ozone atmosphere, i.e. 110 DU (5 Oct), 250 DU (5 Nov) and 315 DU (21 Dec) (Frederick and Snell 1988). The errors bars on the point for 21 December cover two possible turbidity limits (Trodahl and Buckley, in press) while the others result from variations in sea ice transmission that we have encountered.

rations during a warm spell can be directly related to the decrease in the brine volume at the surface and the consequent increase in backscattering. At large separations the radiance is dominated by photons that have travelled through the relatively unchanged bulk of the ice; thus the profile is unaltered except for its magnitude. The net increase in the backscattered radiance is accompanied by a complementary decrease in the transmitted radiance.

The resulting conclusion is that the ice is more transparent early in the spring, i.e., during October, than later in the season. This period of relatively high transparency coincides with the expected increase in UV surface radiance associated with the reduction in atmospheric ozone. Based on measured values of the transmission it is possible to calculate (Trodahl and Buckley, in press) the expected under-ice UV levels, assuming UV absorptions for sea ice and UV surface radiances (Frederick and Snell 1988). The result of such a calculation is illustrated in Figure 4 where a 20-fold increase in UV levels is predicted for the early spring, associated with the increased transparence of sea ice and the presence of the perturbed atmosphere. This has clear implications for life under the ice (Sayed 1988).

CONCLUSION

We have presented a brief review of a simple in-situ experiment used to probe the optical properties of sea ice. Analysis of the experiments have shown that the interaction of light with sea ice is dominated by scattering in the ice, and the nature of the transmitted radiation field is determined by the anisotropic structure of the ice. It has also been shown that Monte Carlo simulations are a powerful technique for modelling sea ice optical properties. It was shown that the relatively high transparency of sea ice in the spring, before brine drainage occurs, has implications for life in and under the ice.

REFERENCES

Buckley, R.G. and H.J. Trodahl (1987) Scattering and absorption of visible light by sea ice. *Nature*, **1**: 867.

Buckley, R.G. and H.J. Trodahl (1987) Thermally driven changes in the optical properties of sea ice. *Cold Regions Science and Technology*, **14**: 201.

El-Sayed, Sayed Z. (1988) Fragile life under the ozone hole. *Natural History*, **73**.

Frederick, J.E. and H.S. Snell (1988) Ultraviolet radiation levels during the Antarctic spring. *Science*, **241**: 438.

Grenfell, T.C. and D.K. Perovich (1981) Radiation absorption coefficients of polycrystalline ice from 400–1400 nm. *Journal of Geophysical Research*, **86**: 7447.

Trodahl, H.J., R.G. Buckley and J.E. Frederick (1989) Ultraviolet levels under sea ice during the Antarctic spring. *Science*, **245**(4915): 194–195.

Trodahl, H.J., R.G. Buckley and M. Vignaux (1989) Anisotropic light radiance in and under sea ice. *Cold Regions Science and Technology*, **16**(3): 305–308.

Trodahl, H.J., R.G. Buckley and S. Brown (1987) Diffusive transport of light in sea ice. *Applied Optics*, **26**(15): 3005.

Weeks, W.F. and S.F. Ackley (1982) The growth, structure and properties of sea ice. USA Cold Regions Research and Engineering Laboratory, Monograph 82-1.

Beam Scattering Measurements in Young Sea Ice

K.J. VOSS
Institute of Marine Resources, Scripps Institution of Oceanography,UCSD
La Jolla, California, U.S.A.

J.S. SCHOONMAKER AND G.D. GILBERT
Naval Ocean Systems Center
San Diego, California, U.S.A.

ABSTRACT/INTRODUCTION

Past measurements of the light fields and optics of arctic sea ice have largely been concerned with irradiance fields, e.g., the natural light irradiance values, and the albedo and extinction properties of the ice (Perovich et al. 1986). The present work investigates laser beam rather than natural light propagation through young sea ice grown in a tank at the Ice Optics Laboratory (IOL) of the Naval Ocean Systems Center (NOSC). The tank ice is similar to the new sea ice found in a newly opened lead in the Arctic Ocean ice pack where seawater is exposed to much colder air. This paper reports on two laser beam propagation experiments through sea ice grown in a single ice growth sequence at an air temperature of –35°C as the IOL was brought into operation. The measurements were:

1. A beam spread function (BSF) experiment, which measured the spatial spreading of an approximately Gaussian laser beam as it propagated through the ice into the air.

2. A beam scattering experiment, which measured the exiting radiance pattern produced as the laser beam was scattered and refracted into the air after passage through the ice.

IOL FACILITIES

The IOL is located in, and uses the freezing system of, the NOSC Arctic Submarine Laboratory. It consists of three interconnected insulated rooms. The temperature in two rooms can be controlled to ±1° from 25°C to –40°C. One room is maintained at room temperature (approximately 25°C) to house most of the measurement instrumentation. The second room is kept cold and contains a cylindrical seawater tank in which the sea ice is grown. A third, intermediate room houses a similar tank for recirculation. The polyethylene plastic water tanks are 1.1 m in diameter and 1.2 m deep. The coldroom tank has 30 cm of insulation on its side walls and rests on an insulating platform to reduce the heat flow from the sides and bottom of the tank. This tank is plumbed to the recirculation tank. In this manner, water salinity control is maintained while doubling the apparent volume of the water under the ice. Filtered seawater is supplied through a pipeline from the ocean off San Diego.

The same source and source lighting geometry was used for both experiments. The light source, a Spectra Physics 148 air-cooled argon ion laser in the laboratory room, provided blue light (488 nm), which was transmitted into the coldroom and into the tank on multimode optical fiber. A fiber optic beam collimator in the tank produced a 1-cm-diameter beam with approximately 9-mrad divergence. The light exited the collimator in an upward direction and produced an approximately 2-cm-diameter spot on the bottom of the ice.

To monitor ice thickness a simple mechanical "J" shaped gauge was frozen into the ice surface. Ice density and entrapped gas volume were found from ice sampled at three depths. Salinities were measured at six depths. Density, entrapped gas, and salinity values were typical of natural sea ice (Weeks and Ackley 1986).

Vertical and horizontal ice sections were taken to observe the ice crystal and brine cell structures. The ice consisted of vertical columns of crystals with horizontal diameters ranging from less than a millimeter to 0.5 cm. Column length ranged from 1 cm to 7 cm.

THE BEAM SPREAD FUNCTION EXPERIMENT

To define BSF consider an optical propagation path composed of scattering and/or absorbing media and/or optical elements such as lenses, etc. Illuminate the path with a perfectly collimated light beam of no angular divergence, i.e., the radiometric analogue of a delta or impulse function. Energy is scattered as the beam propagates along the path. The irradiance distribution exiting the path represents path-introduced beam spreading. This distribution is defined as the path beam spread function, i.e., the path response to an impulse or pencil beam. Once the BSF is known, the path's response to any arbitrary distribution of input light, G, may be found by convolution of the BSF with G in real space.

The modulation transfer function (MTF) is the

two-dimensional Fourier transform (the Hankel transform for systems with radial symmetry) of the BSF and provides a practical way of obtaining the BSF using a real Gaussian light beam rather than an ideal light pencil. To use the MTF the irradiance spread of the beam is measured before it illuminates the path. The path is then illuminated and the exit irradiance measured. The irradiances are transformed and the quotient of the exiting path irradiance transform divided by the beam transform is the MTF whose inverse transform is the path BSF.

The ice of thickness, z, was illuminated from below by the laser beam. The collector passed over the center of the exit beam and measured the irradiance along a radial line, r, of the circularly symmetric irradiance pattern, $f(r,z)$. An observation sequence started with the measurement of the source pattern projected up through the water, $f(r,0)$, in an ice-free tank and continued as the ice grew from 0 to 18 cm in thickness.

The inherent radial symmetry of the beam pattern simplified BSF data reduction. For a radially symmetric pattern, $f(r,z)$ [or in Cartesian coordinates, $f(x,y,z)$], the two-dimensional Fourier transform $F(u,v)$ of the pattern is related to the Hankel transform, $H(w)$, by the relationship $F(u,v) = 2\pi H(w)$ where $w = (u^2+v^2)^{1/2}$ (Papoulis 1968). The source produced a radially symmetric irradiance, $f(r,z)$ for each ice thickness, z. Starting with the ice-free source irradiance scan, $f(r,0)$, each $f(r,z)$ was transformed using a finite Hankel transform, i.e.,

$$H(w,z) = \int_0^{R_{max}} r f(r,z)\, J_o(rw)\, dr$$

$$\approx \sum_0^{R_{max}} r f(r,z)\, J_o(rw)\, \Delta r.$$

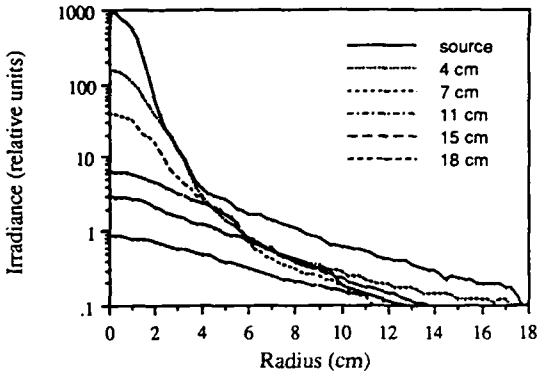

Figure 1. Plot of the irradiances measured for various ice thicknesses in BSF experiment.

The relation $MTF(w,z) = H(w,z)/H(w,0)$ then gave the MTF for each ice thickness [where $H(w,0)$ was the ice free source transform]. The $BSF(r,z)$ for each ice thickness z was then obtained by inverse transforming the computed $MTF(w,z)$.

Figure 1 shows the raw irradiance exiting the ice vs radial distance as seen by the small Lambertian detector. The source irradiance through ice-free water is included. Figure 2 shows the resulting ice BSF normalized to display their shape. Gibbs phenomena oscillations due to the finite width of the calculated MTFs are evident in the BSF wings (Schoonmaker et al. *in prep.*). The spread of the beam with increasing ice thickness, z, was studied by examining the root mean square (RMS) spread at each z [RMS(z)]. RMS(z) was calculated as the second moment of the beam spread function $BSF(r,z)$ at that thickness, i.e.,

$$RMS(z) = \left[\sum_n r_n^2 BSF(r_n z)\right]^{1/2}$$

Figure 3 displays RMS(z) in cm for each ice thickness. As the optical depth of a medium increases and multiple scattering of photons dominate, photon

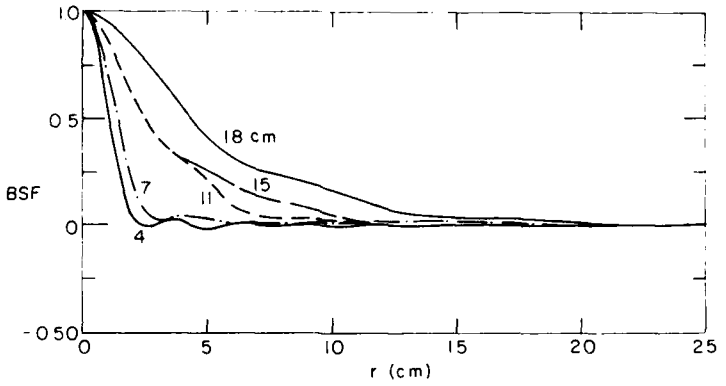

Figure 2. BSF of the ice for different ice thicknesses.

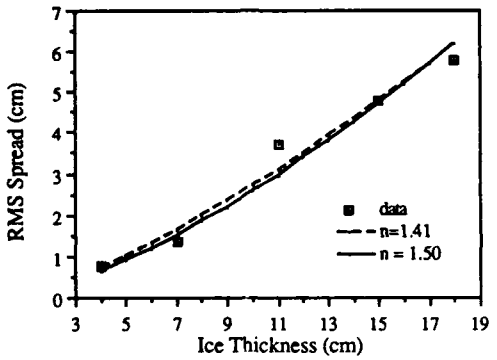

Figure 3. RMS spread vs ice thickness, data points shown as boxes, the two experimental fits are illustrated as lines.

distributions for a Gaussian input beam may be described by Gaussian BSF solutions of the form $BSF(r,z) = B \exp[-r^2/2\sigma^2(z)]$. B is a function of the irradiance level and $\sigma = \sigma(z) = C\, z^{3/2}$ (Arnush 1972) determines the spread with thickness z. RMS(z) was regressed in two ways to fit a power law of the form, $RMS(z) = A\, z^n$. The first regression solved for magnitude A and the exponent n. This regression gave an exponent $n = 1.41$ and an A of 0.105 (correlation coefficient of 0.98). The observed $n = 1.41$ differs from the 1.5 theoretically predicted by 6%. The second regression solved for the single parameter A while setting $n = 1.5$ (correlation coefficient 0.96). Although the 2-parameter fit (n =1.41) gave a smaller mean square residual error than the one parameter fit ($n = 1.5$), it is obvious that the $n = 1.5$ fit is quite good. The data set is too sparse to draw too many conclusions from. Further work will examine if ice grown at different air temperatures spreads light by the 1.5 exponential law.

The central BSF peaks are attenuated with increasing ice growth. An average peak attenuation k_B (Fig. 4) was obtained by a regression fit of the central BSF peaks (correlation coefficient = 0.98, $k_B = 0.405$ cm^{-1}). To summarize our BSF work to this time we have experimentally found a preliminary expression for RMS(z) of a beam passing upward through z cm of new ice grown at –35°C. This expression is

$$RMS(z) = 0.105\, z^{1.41} \text{ cm.}$$

If the BSF is assumed Gaussian it may be approximated by

$$BSF(r,z) = \exp(-k_B z) \exp[-r^2 / 2\, RMS^2(z)]$$

where $k_B = 0.404$ cm^{-1}.

THE BEAM SCATTERING EXPERIMENT

When a slab of ice is illuminated by a submerged light beam the radiance exits the ice with some angular distribution dependent upon the optical properties of the ice. Knowledge of this scattered beam pattern is important in predicting the light received by an airborne radiance sensor some distance from the beam exit point on the ice surface.

The forward scattering beam pattern was measured using a Gershun tube radiometer mounted on a motorized cart traveling on a semicircular goniometer track above the cold room tank. The goniometer track was mounted such that the radiometer was directed at the beam exit point on the ice below at all times.

The normalized radiance distribution data for the angular range from zenith to 55° for the various ice thicknesses are shown in Figure 5. A candidate mathe-

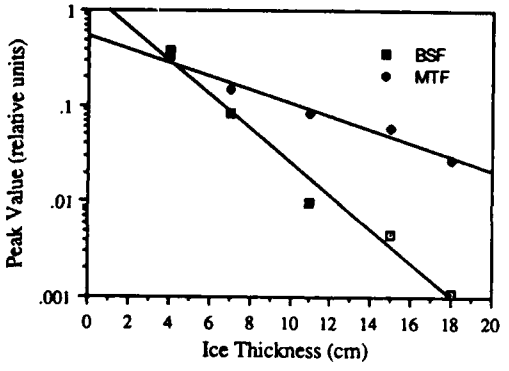

Figure 4. Peak values of MTF and BSF vs ice thickness, lines are empirical fits to the data.

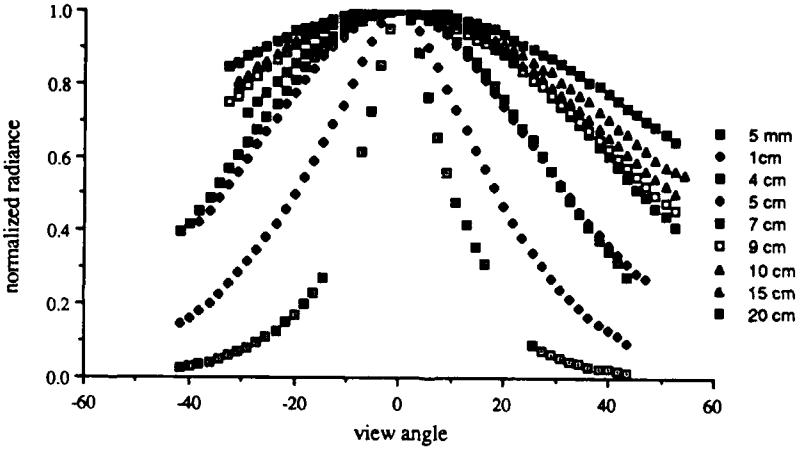

Figure 5. Radiance distributions for the measured ice thicknesses.

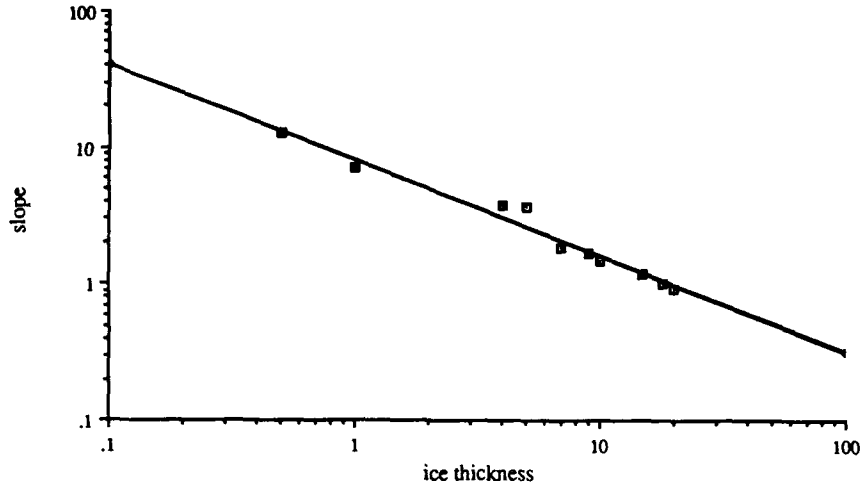

Figure 6. Plot illustrating the exponential coefficient of the cosine function, along with the empirical fit to this function.

matical expression chosen to fit this data was

$$L(\theta,z) = L(0)\cos^{n(z)}(\theta)$$

where θ is the angle from zenith, z is the ice thickness, and $n(z)$ is a function of ice thickness. The $L(\theta,z)$ data for each z were regressed against θ to determine the $n(z)$ for that z. For the entire set of ice thicknesses, z, no correlation coefficient was less than 0.92. The resulting cosine exponent function $n(z)$ was regressed against ice thickness z (correlation coefficient = 0.98, Figure 6). This exponent function is given by

$$n(z) = 8.022\, z^{-0.705} . \qquad (1)$$

The peak value of scattered radiance with ice thickness was described by a regular attenuation function of the form:

$$L(\theta,z) = L(0,0)\exp(-k_L z)$$

where $k_L = 0.2229$ (correlation coefficient of 0.92).

These two empirical expressions allow the radiance field of light emitted from the ice surface when illuminated by an upward projected light beam to be completely described. In summary the angular distribution of radiance L with angle θ and thickness z is

$$L(\theta,z) = L(0,0)\exp(-k_L z)\cos^{n(z)}\theta$$

with $n(z)$ given by expression (eq 1).

SUMMARY AND FUTURE WORK

These results demonstrate that salt ice, which resembles new sea ice observed in the Arctic, may be grown and measured in a laboratory environment. Measurements of underwater through-ice laser-beam spreading and beam pattern have been made for a single sequence of ice grown from 0 to 18 cm in thickness. For this single growth sequence we have described our results in terms of simple functions that may be used for beam transmission and spreading estimation. Further measurements are needed and will be performed to determine the sensitivity of these functions to growth conditions, ice morphology and other physical parameters.

ACKNOWLEDGMENTS

Financial support for this work was provided by the Office of Naval Research under contract N00014-89-J-1043 and N00014-85-C-0730, and the Naval Ocean Systems Center Independent Research Program. We would also like to acknowledge the help of Albert Chapin in data collection, and Lawrence Oblinger and the staff of the Arctic Submarine Laboratory in running the ASL for this experiment.

REFERENCES

Arnush, D. (1972) Underwater light-beam propagation in the small-angle scattering approximation. *Journal of the Optical Society of America*, **6**: 1109–1111.

Papoulis, A. (1968) *Systems and Transforms with Applications in Optics*. New York: McGraw-Hill Inc.
Perovich, D.K., G.A. Maykut and T.C. Grenfell (1986) Optical properties of ice and snow in the polar ocean. I: Observations. In *Ocean Optics VIII, Proceedings of Society of Photo-Optical Instrumentation Engineers*, **637**: 232–241.
Schoonmaker, J.S., K.J.Voss and G.D. Gilbert (In prep.) Laboratory measurements of optical beams in young sea ice. Submitted to *Limnology and Oceanography*.
Weeks, W.F. and S.F.Ackley (1986) *Growth Structure and properties of sea ice*. In Geophysics of Sea Ice (N. Untersteiner, Ed.). New York: Plenum Press, p. 9–164.

Electrical, Physical and Microwave Properties of Snow-Covered Floating Ice

C. GARRITY
Centre for Research in Experimental Space Science
and
Institute for Space and Terrestrial Science
York University, North York, Ontario, Canada

ABSTRACT/INTRODUCTION

Electrical and physical properties of snow over sea ice, low saline ice and freshwater ice were measured in order to further the understanding of snow as a material. Generally, there is a snow layer covering floating ice for all seasons in the Arctic and Antarctic as well as the mid-latitudes of the northern hemisphere. In order to obtain useful information from microwave sensors, the contribution of the snow layer to measurements is important. Snow measurements were obtained from the Gulf of Bothnia in May 1988, in the East Greenland Sea from May to June 1987 and the St. Lawrence River from January to March 1986 and 1988.

During the BEPERS-88 (Bothnia Experiment in Support of ERS-1) experiment, numerous snow measurements were made in fast ice. Measurements were made near the *Tor* icebreaker in an area 2 km long and 1 km wide as well as two areas off the starboard side of the ship to support the SHIPSCAT (scatterometer) measurements. The following snow properties were measured: wetness, permittivity, dielectric loss, depth, structure, temperature and grain size. These were all measured as a function of snow depth.

A shipborne 37-GHz dual-polarized radiometer measured the brightness temperature (T_B) from different ice types and snow conditions as the ship moved through the ice in the East Greenland Sea. A total of 17 ice stations provided an opportunity to measure the snow properties and correlate them to the measured T_B. Since the snow was structured due to freeze–thaw cycles, the T_B was significantly influenced by the snow cover.

The St. Lawrence area is an excellent experimental site for monitoring the changes in T_B due to a variable snow cover on floating ice. There are numerous thaw periods throughout an ice season and often weekly environmental changes.

The snow wetness is measured using a nondestructive method developed by C. Maetzler at the University of Bern, Switzerland (Maetzler 1985). A microwave cavity is placed on the snow surface or filled with snow and the resonance frequency obtained. The Resometer instrument displays this frequency in MHz. From the resonance frequency the permittivity of the snow is determined. Both the snow density and permittivity are used to calculate the percent wetness. The error estimate on the permittivity is 2% and 0.5% on snow wetness (Maetzler 1985).

RESULTS

Correlation coefficients for the snow parameters: wetness, permittivity, grain size, depth and temperature as well as the air temperature indicated which snow parameters were dependent on the other. The only two parameters that showed a good correlation coefficient were the percentage of wetness with permittivity between 800 MHz to 1 GHz. Using 80 measurements obtained during the BEPERS-88 experiment, the correlation coefficient is 0.80.

The surface of the snow is affected by the amount of solar radiation and wind, thus causing a poor correlation of the surface percentage of wetness with permittivity (0.32). The extremely poor correlation coefficient of the snow surface temperature with grain size (0.04) is due to the effect of the changing solar radiation and wind within a day. This is based on the fact that a change in the snow parameters was observed for similar air temperatures (–5°C).

The insulating effect of the snow causes the corre-

lation of the air temperature with the snow temperature to deteriorate as the snow depth increases. For a snow depth of about 10 cm, the correlation coefficient was 0.75, compared to a snow thickness of about 50 cm where the coefficient was 0.32.

Linear regressions were made, resulting in an equation for the permittivity as a function of snow wetness that is comparable to an empirical equation developed by Ambach and Denoth (1980) where the slope is 0.231 and intercept is the permittivity for dry snow. This slope compares well with the slope calculated from the BEPERS-88 measurements of 0.26 and an intercept of 1.52 which is a realistic value for dry snow. The density range for a slope of 0.26 is 0.15–0.3 g/cm^3, whereas a higher density range, 0.3–0.5 g/cm^3 yields a slope of 1.25 and 1.37 for the intercept.

Dielectric mixing models usually use the density to calculate the dielectric constant, which is surprising considering the large variability and poor correlation of measured permittivity with density measurements. However, comparisons of recent models based on the original models of Polder-Van Santen (1946) and Debye (1929) with the snow measurements during BEPERS-88 are good.

The Glen and Paren (1975) model has been reported to be the best for the density range from 0.15–0.3 g/cm^3 whereas for the high density range, 0.3–0.5 g/cm^3, the Bohren and Batten (1982) is preferable (Maetzler 1987). Both models provided a good fit to snow measurements obtained during BEPERS-88 where the snow wetness ranged from 0 to 2%.

Empirical fits of permittivity for dry snow as a function of snow density using Tiuri et al.'s (1984) data, which were based on the above two models (Maetzler 1987) and data of Hallikainen et al. (1986), yielded an even better fit to the recent measurements from BEPERS-88 than the fits to the theoretical models. The measured permittivities were slightly higher than the calculated permittivities using the models and the empirical relationships were within the 2 % measurement error estimate on permittivity.

Comparisons of the measured permittivity for a

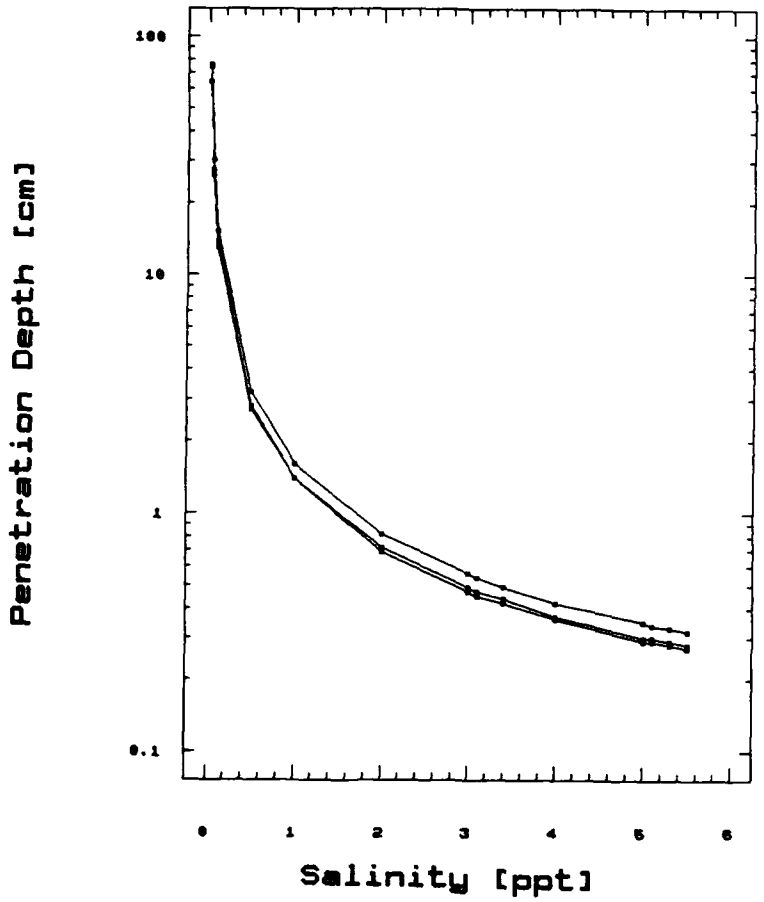

Figure 1. Penetration depth for SSM/I frequencies at an ice temperature of –5 °C.

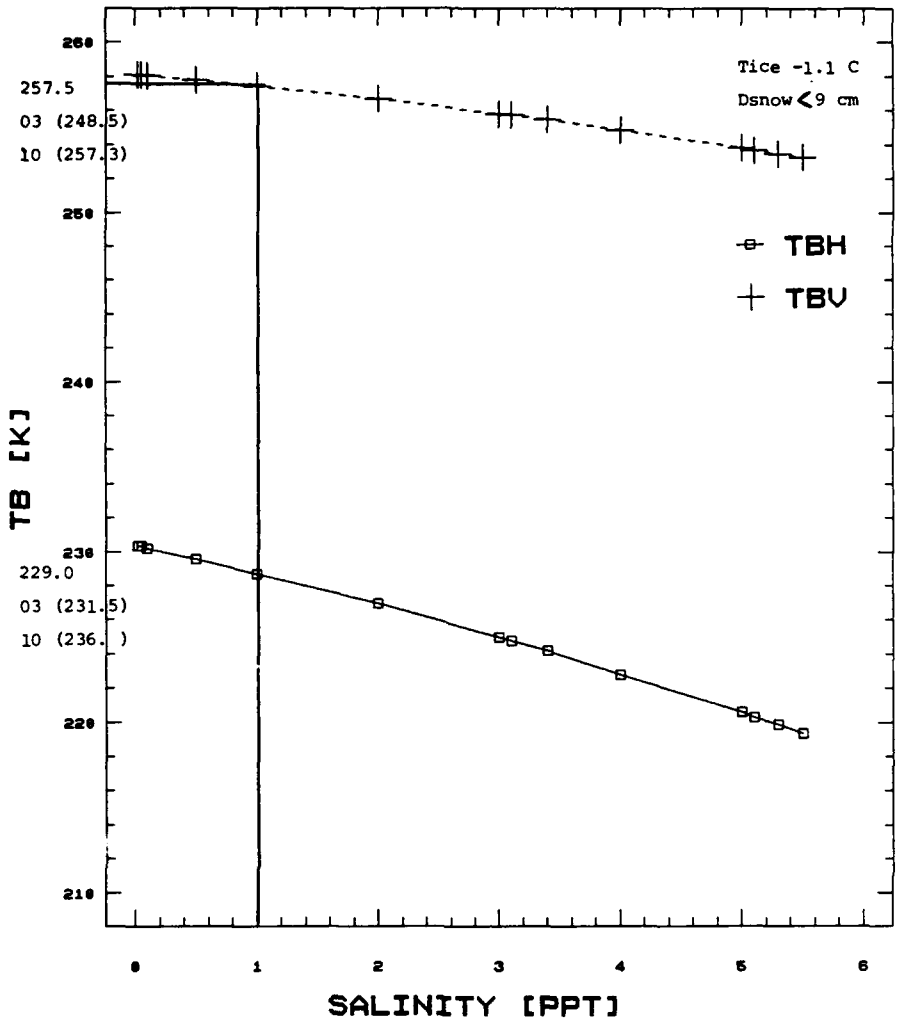

Figure 2. Two percent snow wetness layer over sea ice: T_B *at 53.1° incidence and 37 GHZ, Gulf of Bothnia/BEPERS-88 Experiment.*

2–3% snow wetness with the two phase Polder-Van Santen mixing formula (Ambach and Denoth 1980) and the modified Debye-like model, which was determined from an empirical fit (Hallikainen et al. 1983, 1984, 1986), were good. A comparison was also made to the measured dielectric loss of the wet snow using the modified Debye-like model. The measured value was 0.0014 which is less than the calculated value of 0.0018. The unmodified Debye-like model gave a similar value (0.0019), which is expected in the 2–3% snow wetness range (Ulaby et al. 1986). A comparison of models for the dielectric loss of dry snow could not be made since no dielectric loss measurements for dry snow were made.

The penetration depth (power loss) for low salinity ice was calculated for the SSM/I frequencies (Fig. 1). It is interesting to note that the penetration depth is similar for the following SSM/I frequencies: 19.35 GHz, 37 GHz and 85.5 GHz. Thus, the emission from an ice surface is expected to be similar for these frequencies.

The brightness temperature was calculated for the average snow wetness measured within an SSM/I footprint during the BEPERS experiment. The measured values compare well to those calculated, especially considering the slush and ridge areas associated within a footprint (Fig. 2).

The importance of a snow layer on the microwave signatures from sea ice has been observed in the East Greenland Sea and the St. Lawrence River by the author. Snow stratification had a large influence on passive microwave measurements at 37 GHz during the onset of melt in the spring. Thus, the snow would affect the SSM/I measurements and possibly the SAR and scatterometer measurements collected during the BEPERS-88 experiment.

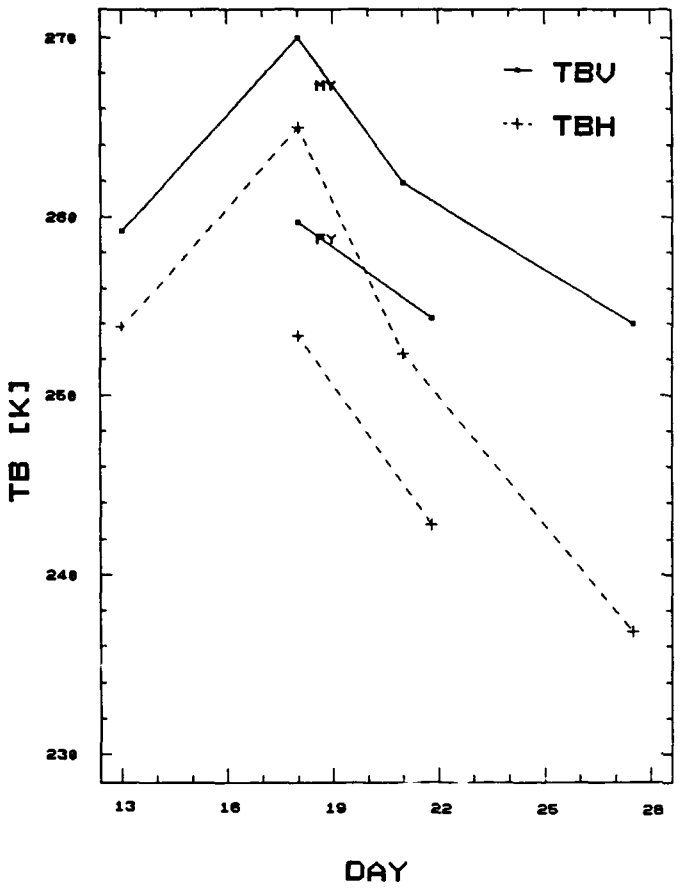

Figure 3. Brightness temperature at 1500–1800: East Greenland Sea, June 1987.

The correlation of snow permittivity with wetness was made for snow on FY and MY ice in the East Greenland Sea mainly in June 1987. The correlation coefficients were good for snow on first-year (FY) ice (0.94) and multiyear (MY) ice (0.95). However, it was interesting that the correlation of the measured brightness temperature (T_B) with snow wetness using a 37-GHz dual polarized radiometer off the research ship, *Polarstern*, was poor. The important parameter affecting the passive signatures was snow stratification rather than snow wetness. By the late spring the snow on FY ice was stratified, causing a decrease in the T_B and increase in polarization. The decrease in FY ice T_B was significant and caused the T_B for MY ice to be greater than the FY T_B (Fig. 3). This is due to the different structure of snow on the two ice types. Passive microwave measurements during the spring period might distinguish FY from MY ice.

The importance of snow stratification has been observed on the St. Lawrence River where the snow will vary tremendously in one season due to changes in the environment and flooding of the ice. The snow cover is a dynamic material affecting the T_B emitted from floating ice.

The snow cover in the fast ice near the icebreaker, *Tor*, was variable in thickness due to the rafted and ridged ice, which caused snow to accumulate in certain areas as a result of wind action. The snow was stratified mainly in areas where the snow accumulations were high. Areas of slush were observed when there was little snow and flooding of the ice. A detailed description of the vertical profiles through the snow covers is contained in two data reports (Garrity and Burns 1988). The analysis of the snow properties is currently being completed (Garrity, in prep.).

A paper summarizing the changes in T_B during the onset of the melt period in the East Greenland Sea is nearing completion (Garrity, in prep.). Reports on the two winter experiments in the St. Lawrence River are available from the Microwave Group, York University, North York, Ontario (Garrity 1987, 1988).

REFERENCES

Ambach, W. and H. Denoth (1980) The dielectric behavior of snow: A study versus liquid water content, National Aeronautics and Space Administration, NASA Conference Publication 2153, Ft. Collins, Colorado.

Bohren, C.F. and L.J. Batten (1982) Radar backscattering of microwaves by spongy ice spheres, *Journal of Atmospheric Sciences*, **39**: 2623–2628.

Debye, P. (1929) *Polar Molecules*. New York: Chemical Catalogue Company.

Garrity, C. (1987) Passive microwave remote sensing using the ground-based radiometer: January to March 1986. Microwave Group, York University, North York, Ontario, Technical Report MWG 87-1.

Garrity, C. (1988) Passive microwave experiment on

the St. Lawrence River in Picton Channel: January–February 1988. Microwave Group, York University, North York, Ontario, Technical Report MWG 88-9.
Garrity, C. (In prep.) Passive microwave signatures from "spring" ice in the East Greenland Sea. In progress.
Garrity, C. (In prep.) Dielectric mixing models for snow: A comparison. In progress.
Garrity, C. and B. Burns (1988) Electrical and physical properties of snow on ice in the Gulf of Bothnia. In progress. Microwave Group, York University, North York, Ontario, Canada, Data Report
Glen, J.W., and J.G. Paren (1975) The electrical properties of snow and ice, Journal of Glaciology, **15**: 15–38.
Hallikainen, M., F.T. Ulaby, and M. Abdelrazik (1983) Modeling of dielectric behaviour of wet snow in the 4- to 18-GHz range. In *1983 IEEE International Geoscience Remote Sensing Symposium (IGARSS '83) Digest*, San Francisco, California, 31 August–2 September.
Hallikainen, M., F.T. Ulaby and M. Abdelrazik (1984) The dielectric behaviour of snow in the 3- to 37-GHz range In *1984 IEEE International Geoscience Remote Sensing Symposium (IGARSS '84) Digest*. Strasbourg, France, 27–30 August, p. 169–176.
Hallikainen, M., F.T. Ulaby and M. Abdelrazik (1986) The dielectric properties of snow in the 3- to 37-GHz Range. In *Microwave Remote Sensing: Active and Passive* (Ulaby et al., 1986). Dedham, Massachusetts: Artech House Inc., vol. III.
Maetzler, C. (1985) *Resometer Manual*. University of Bern, Switzerland.
Maetzler, C. (1987) Applications of the interactions of microwaves with the natural snow cover. *Remote Sensing Reviews*, no. 2, p. 259–392.
Polder, D. and H.J. Van Santen (1946) The effective permittivity and mixture of solids. *Physics*, **XII**(5): 257–271.
Tiuri, M., A.H. Sihvola, E.G. Nyfors and M.T. Hallikainen (1984) The complex dielectric constant of snow at microwave frequencies. *IEEE Journal of Oceanic Engineering*, **OE-9**: 377–382.
Ulaby, F.T., R.K. Moore and A.K. Fung (1986) Microwave Remote Sensing: Active and Passive. Dedham, Massachusetts: Artech House Inc.

Some Observations of Established Snow Cover on Saline Ice and Their Relevance to Microwave Remote Sensing

A.W. LOHANICK
Naval Oceanographic and
Atmospheric Research Laboratory
Polar Oceanography Branch
Hanover, New Hampshire, USA

SUMMARY

Data have been presented showing effects of established ("old") snow covers on multiyear ice, on the brightness temperature at 33.6 GHz. It has been shown that the bottom layer of the snow can be the major contributor to the brightness temperature change due to the snow. It is speculated that this is due to the roughening of the snow/ice interface, over long periods of snow metamorphosis, by the process of wicking of the salt from the ice into the lower layers of the snow. The wicking results in a roughened dielectric surface which in turn increases the transmission coefficient for radiation from the underlying ice.

Other data presented here have shown that snow thickness alone does not seem to determine the change in brightness temperature resulting from a snow cover on saline ice. This does not support a radiative transfer theory with constant, flat dielectric interfaces, but does not rule out effects due to layering in the snow, for example.

OVERVIEW

A debate continues regarding the use of texture vs absolute value to interpret microwave images of saline ice. That is, should one describe multiyear ice as having a backscatter cross section of such-and-such dB, or as having a signature with such-and-such texture?

Passive and active data have limited spatial resolution, and microwave images of saline ice have a character that depends somewhat on antenna pattern. When one looks at an image of, for example, multiyear ice, it is tempting to ascribe the apparent texture of the surface to gradations in the properties of the underlying ice. It is possible, however, that the actual ice surface characteristics vary at a higher spatial frequency than the observed texture, or that variations are not due to the character of the ice itself, but to the overyling snow cover.

Radiometry

Radiometers measure a non-coherent signal, and so spatially and temporally average "automatically." Although radiometers have generally lower spatial resolutions than radars (particularly synthetic aperture radars [SARs]) they allow us to look at an almost arbitrarily small scale and at brightness temperature variations, because they do not suffer from the limitations imposed by "coherent fading" (the way in which a radar measures the strength of its received signal).

If the fine-scale brightness temperatures measured on the surface vary much faster (or slower) spatially then the properties of the underlying ice, as we have found in many cases and will show here, then the spatially integrated numbers measured by either type of sensor may be difficult to model. That is, it may be possible to determine ice type by texture or even absolute calibrations, but to explain the signature requires detailed knowledge of the surface and the resulting spatial variations to be expected.

The snow/ice interface and microwave signature

Martin (1979) listed a number of ways in which snow and saline ice are associated:

1. Snow evolves from salt flowers on the ice surface.
2. Snow falls after salt flowers have developed.
3. Snow mixes with ice as it is forming.
4. Snow depresses the ice until the ice floods.

All of these cases result in a complex highly saline layer at the snow/ice interface. The first attempt at quantifying the effect of this layer on microwave signature was by Lohanick and Grenfell (1986), in which salt transported into the snow from the saline layer is seen as a mechanism that roughens the snow/ice interface, increasing the transmission coefficient in a radiative transfer model. This means that even a "transparent" snow layer can contribute indirectly to microwave signature.

Drinkwater and Crocker (1988) took a preliminary look at the effects of snow cover on the properties of naturally occurring saline ice that affect microwave signatures. Using a dielectric model, they concluded, among other things, that the snow cover could adversely affect the unambiguous identification of young ice types at certain frequencies used in active imagers (SARs, for example), because of the presence of salt in the lower layers of the snow.

One can visualize the snow/ice interface at the top of saline ice as in Figure 1. The case shown is one in which liquid fresh water is in equilibrium with the snow, and there is brine at the ice surface. There is clearly a mechanism for transport of the brine up to the snow. Once all of this freezes, a dielectric interface results that has a roughness that affects microwave signals.

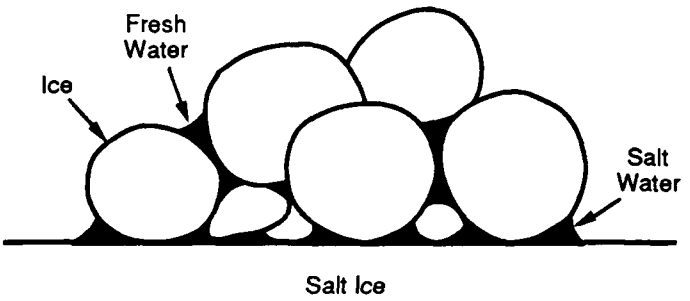

Figure 1. Wicking of salt in a snow layer on saline ice.

The metamorphosis of a layer of snow lasts as long as the snow is in place. Transport processes in a fresh snow layer on any substrate are not yet completely understood (Yen 1988). The presence of brine should further complicate the transport.

OBSERVATIONS

Single-frequency data

When our group began to fly the KRMS airborne imager (then called MICRAD) in 1976, we were told by the people who had already used the sensor that dry snow cover was transparent at 33 GHz, and their conclusion and ours was that we could ignore snow. We have found, however, that it is the snow cover on several types of saline ice that determines the spatial variability and the absolute value of the brightness temperature, and by implication the backscatter. Thus, the snow cover is a contributing factor to any signature, and cannot be ignored.

Some ambiguities caused by a snow layer on saline ice can be removed by using multiple sensor frequencies or a combination of active and passive sensors. It remains to be seen, however, whether the effect of snow is so complex that modeling will prove futile. In such cases, lookup tables must suffice for interpretation.

This discussion includes only passive microwave data at 33.6 GHz, and we will limit ourselves to snow cover found on multiyear ice in the spring (late winter if one uses onset of melt as a test for season change). This snow is typically complex in structure, and can be considered a "worst case" for modeling purposes. All data discussed in this report are taken at an incidence angle (angle measured from nadir) of 45 degrees. The distance from the antenna to the surface, about 1.5 m, is in the far field of the antenna.

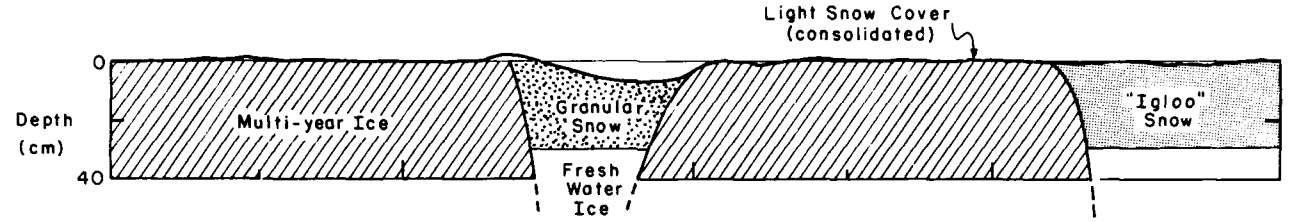

a. Vertical cross section sketch of study area.

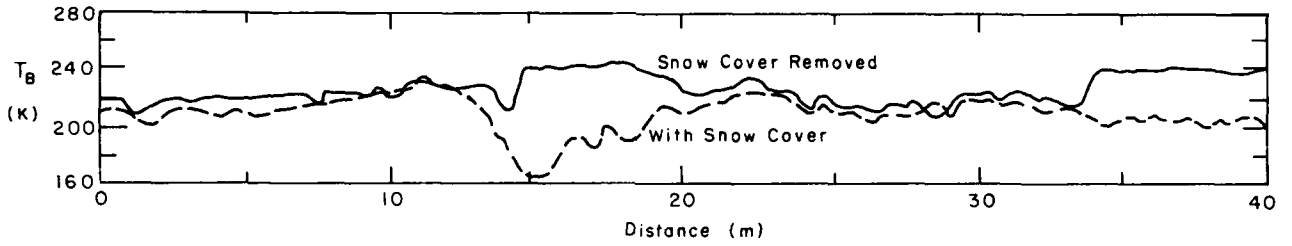

b. Brightness temperatures along track before and after snow removal.

Figure 2. Radiometric study of established snow on multiyear ice.

Field measurements

We first pulled our sled-mounted 33.6-GHz (K_a-band) radiometer around on saline ice in 1979, off Barrow, Alaska. No previous ground-based radiometry on saline ice had recorded brightness temperatures continuously along the surface to look at spatial variations. We discovered that not only did brightness temperature vary from ice type to ice type, but by significant amounts (tens of kelvins) on many single ice types (multiyear ice especially).

We first did a study specifically aimed at linking brightness temperature with snow thickness on multiyear ice near Barrow in 1980 (Lohanick 1982). We chose a 40-m stretch of ice with an undisturbed snow cover, took a brightness temperature profile at vertical polarization (VPOL), removed the snow by shoveling down to bare ice, and repeated the profile. The results are summarized in Figures 2 and 3.

The 40-m track had two frozen melt pond areas covered by snow much deeper than that on the surrounding ice. Furthermore, the snow in one area, I called "granular," consisted of individual loose grains about 2–3 mm in diameter. At the snow/ice interface, grains of this snow were partially embedded in the underlying ice, making the boundary somewhat indistinct. In the second area the snow was more like a solid with 1-mm-diameter air bubbles, and stuck together when shoveled. This snow (which I termed "igloo snow") had a very distinct boundary with the underlying ice, and did not adhere to it. Interestingly, snow in both areas had a measured density of about 0.35 g/cm^3.

It can be seen from Figure 2 that the brightness temperature in areas which had deeper snow cover generally rose when the snow cover was removed. This is consistent with studies of snow on ground (e.g., Ulaby and Stiles 1980). However, four phenomena important to microwave interpretation are suggested.

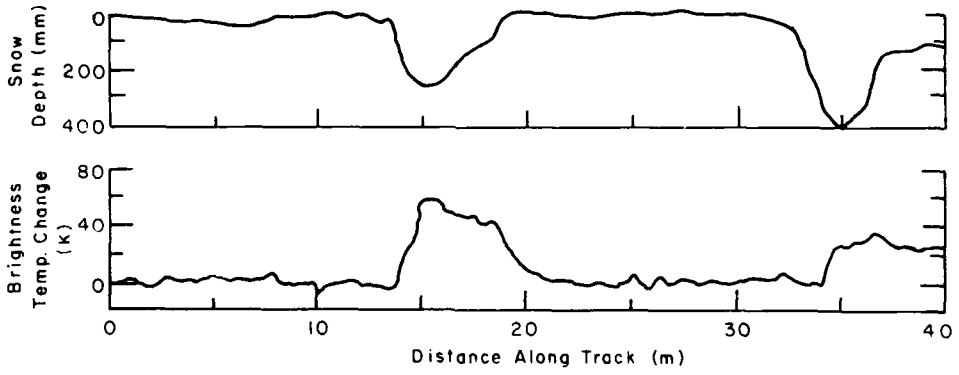

Figure 3. Increase in brightness temperature after removal of snow on multiyear ice.

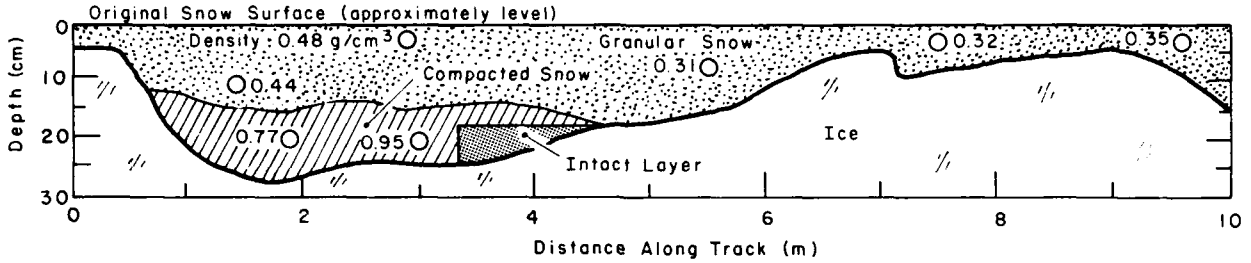

Figure 4. Diagram of vertical section of snow on multiyear ice. Intact layer is discussed in text.

1. Although snow here seems to lower the brightness temperature, changes in brightness temperature do not always correlate well with snow depth (Fig. 3). The increase in brightness temperature (about 60 K) in the first deep snow area (between 10 and 20 m) is twice that in the second deep snow area (between 30 and 40 m), yet the maximum snow depth in the first area is 100 mm less than that in the second. The reason for this discrepancy is not apparent in this data, but is suggested by the difference in snow type between the two areas. For example, the granular snow was probably a stronger scattering medium than the igloo snow, causing a lower brightness temperature when it was in place.

2. The snow cover in this case masks some of the underlying ice types. In the first deep snow area, before snow removal, brightness temperature was generally lower, suggesting some change in surface properties. In this case, it is correct to assume that the underlying ice is different. It is, in fact, a frozen melt pond, consisting of frozen fresh water rather than desalinated ice.

In the second area, before snow removal, the brightness temperature was not noticeably different from that of the surrounding ice. Yet, the underlying ice was another frozen melt pond, and its brightness temperature proved to be the same as that of the first area after the snow was removed from both.

3. Snow cover is associated with changes in brightness temperature as large as 58 K.

4. Some brightness temperature variations are caused by the ice itself, but their cause is often obscure. In the bare ice areas along this course, and over the bare ice which had been cleared of snow, brightness temperature can change by 10 to 20 K over distances which seem to be about the diameter of the spatial resolution of the radiometer antenna (less than one-half meter). In particular, in the area of bare ice between 20 and 30 m aong the track, some of the brightness temperature maxima were located at points at which the ice had no features distinguishable from the surrounding bare ice. That is, the ice appeared to be more uniform spatially than its radiometric signature.

In 1983 we did another (unpublished) snow-depth study at 33.6 GHz on multiyear ice near Barrow. This consisted of a 10-m-long brightness temperature profile, and a profile of about 3 m, both along areas with large variations in snow depth. Both horizontally and vertically polarized (HPOL and VPOL) brightness temperatures were measured. The snow was removed in stages.

Ambient air temperatures for both cases were below –10°C. Since the sky was overcast for much of the time, the temperature of the snow was uniform to 1 or 2 K in the vertical direction.

The data at the 10-m study area are summarized in Figures 4 and 5. Figure 4 shows the detailed descrip-

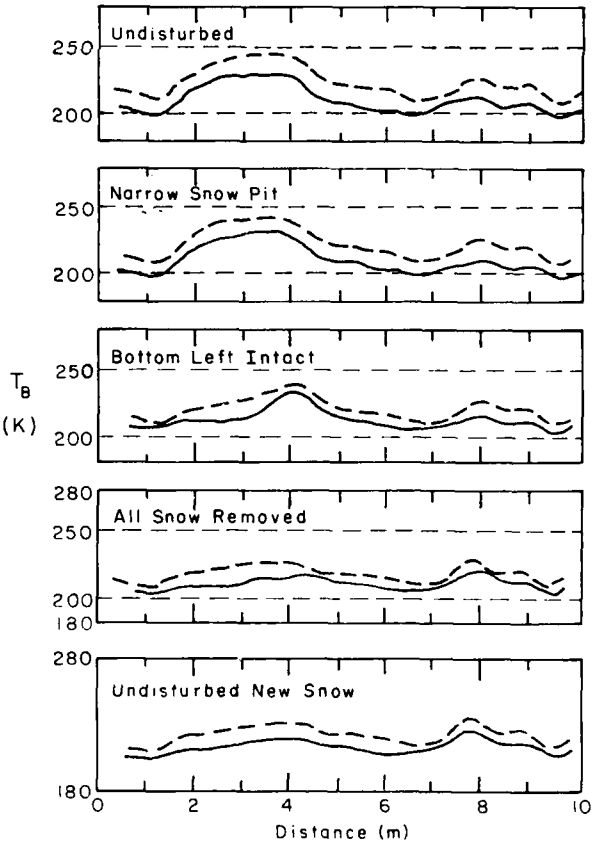

Figure 5. 33.6-GHz brightness temperatures along track during various stages of snow removal.

tion of the undisturbed snow. The surface of the undisturbed snow was quite level, with only a few half-centimeter ripples near the 7-m mark. The deepest snow is about 25 cm deep. The snow structure is somewhat complex, and the main feature of the underlying ice is a "drainage" feature (perhaps with frozen fresh water at the ice surface) near the beginning. This depression was filled by the undisturbed snow. In this study area, in general, deeper snow has a higher brightness temperature, in direct contrast to the case described above for 1980.

Figure 5 shows the brightness temperature profiles measured along the study area:

1. The 33-GHz brightness temperature at both polarizations for the undisturbed snow on ice. The curves are double because of a repeatability measurement to pin down the uncertainties due to sled motion. The repeatability was good to within a few kelvins.

2. Brightness temperature after a narrow snow pit was made to look at snow structure. The pit disturbed the near third of the surface covered by the radiometer antenna pattern, but did not seem to have an effect on the radiometer data.

3. All the snow is removed down to a scraped ice surface, except for the bottom 5 cm of compacted snow in the area in which the T_b maximum occurs. This snow was compacted, had a high density, and adhered to the ice surface, requiring scraping with a shovel to remove it.

4. Small remaining snow wedge removed.

5. Brightness temperature profile after a fresh snowfall over the ice previously cleared. The snow depth varied from 0 to 17 cm, and was deepest in the lowest depression of the ice. Snow temperatures here are about –17°C down to the snow/ice interface. Comparison of data drawn in Figures 5d and 5e shows that the new snow has added only a few kelvins, some of which may be due to errors in the measured along-track position of the sled (registration).

Relevant conclusions to be drawn from the results shown in Figure 5 are as follows:

1. Snow cover does not always reduce the brightness temperature of ice. In a radiative transfer model such as that of Ulaby and Stiles (1980), a snow cover can only lower the brightness temperature of the surface, since the transmission coefficient of the snow/ice interface is taken to be constant. These data do not support such a model. Liquid water in equilibrium with snow at 0°C can raise the brightness temperature (Stiles and Ulaby 1980). However, although we did not make snow liquid water content measurements during this study, all snow temperatures recorded during the period were below –10°C. It should also be noted that the higher brightness temperatures associated with the deeper snow here persisted for the period of about three days during which in-place snow brightness temperatures were recorded.

2. The bottom 5 cm of the snow was the major contributor to the signal change due to snow cover (from Fig. 5c). Removing about 15 cm of snow had very little effect on brightness temperature in this area. The bottom 5-cm layer added about 15 K to the HPOL and VPOL brightness temperatures. This lends strong support to the model proposed by Lohanick and Grenfell (1986), in which a metamorphosed snow layer increases the transmission coefficient of radiation originating in the ice, thus increasing the brightness temperature of the ice.

3. Snow serves to mask the spatial variations in surface properties of the underlying ice. The brightness temperature variations remaining in Figure 5d are due to variations in the surface properties of the remaining ice. Again, as in the 1980 results, we see brightness temperatures changing by 10 to 20 K over distances about the spatial resolution of the radiometer antenna (less than one-half meter). Ice properties were not studied in detail in this case, other than the observation that the surface salinity was below 1 ppt, but a comparison of Figures 5a and 5d shows that the distinct high-brightness-temperature feature caused by the original deep snow area, did not have a distinctive appearance when the snow was removed.

4. Brightness temperature effects caused by snow cover may be time-dependent, and may take entire seasons to change. This is hinted at by the fact that the new snow adds insignificantly to the signature of the ice. This is not a strong argument in this case, since the ice was already highly desalinated when the snow fell. However, a snow layer affects the snow/ice interface by the mechanism of wicking, for example, and we know a snow layer metamorphoses over long time periods.

The 3-m course was on the same multiyear floe, in an area of snow about 35 cm deep over a frozen melt pond (the ice beneath the deep snow was level and smooth). Some wind-swept bare ice next to the deep snow had a low brightness temperature (about 220 K), and the original brightness temperature of the deep snow was only about 10 K higher.

When we removed the snow down to bare ice, the brightness temperature rose considerably (about 30 K). We also removed the snow in steps which coincided with its distinct layers. The vertical structure of this snowpack is shown in Tables 1 and 2.

Figure 6 shows the HPOL brightness temperatures measured for each snow thickness along the 3-m track. An exponential curve of the form derived by

Table 1. Description of snowpack studied for effect of depth.

Step	Distance from surface (cm)	Density (g/cm^3)	Description
Top	0 to 7	0.30	Powder and loose, irregular crystals
Middle	7 to 15	0.55	Adhering larger crystals
Bottom	15 to 23	~0.55	Aggregate smaller crystals
	23 to 28	~0.70	Adhering larger crystals
	28 to 35	0.60	Loose large crystals (2–4 mm diam)

Table 2. Snow structure at study area on multiyear ice, ambient air temperature = –15°C.

Depth above ice (cm)	Snow temp. (°C)	Density (g/cm^3)	
32	–12.2	0.30	Powder
30	–12.5		Larger irregular crystals—increasing hardness*—appears to
28	–12.6		once have been melted or mechanically abraded—no adhesion between crystals
16	–13.1	0.54	Powder (similar to surface—some crystals intact—no melting
24	–13.6		
22	–13.9		Harder, larger crystals
20	–13.7	0.77	Hard, small crystals
18	–13.8		Apparently extensive melting at one time
16	–13.8		Crystals from aggregate clusters (~3–8 crystals) near surface of this layer
14	–13.6	0.56	
12	–13.6		
10	–13.6	0.67	
8	–13.4		
6	–13.3		Hard, large singular crystals (irregular)—similar to layer 22–24
4	–13.2	0.58	
2	–13.1		
	–13.0		Hard, large graupel type crystals
			Ice

* Note: Hard, harder and very hard are relative.

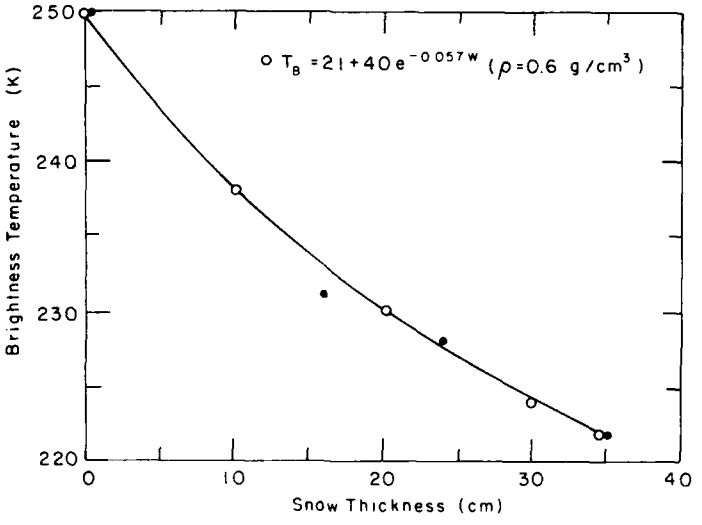

Figure 6. Brightness temperature vs snow thickness on multiyear ice. The theoretical values are based on Ulaby and Stiles (1980).

Ulaby and Stiles (1980) for dry snowpack on soil, is fit using the bare ice brightness temperature (250 K), an assumed asymptotic value for infinite snow depth (210 K), and a snow density about the average (0.6 g/cm^3) of the measured value shown in Tables 1 and 2. The derived constant multiplying the water equivalent (*W*, the snow density times the snow thickness) in the exponent, depends on radiometer incidence angle and the extinction coefficient in the snow. The derived value of 0.057 cm^3/g is quite consistent with values found by Ulaby and Stiles (1980) using a 37-GHz radiometer at an incidence angle of 57 degrees.

Thus, the conclusion to be drawn from the results shown in Figure 6, are that, in some cases, snow cover on ice can be treated as a scattering medium according to a radiative transfer model in which the snow/ice interface is an unchanging boundary.

REFERENCES

Drinkwater, M.R. and G.B. Crocker (1988) Modeling changes in the dielectric properties of young snow-covered sea ice at GHz frequencies. *Journal of Glaciology*, **34**(118): 274–282.

Lohanick, A.W. (1982) Snow thickness and brightness temperature on multiyear ice. Naval Ocean Research and Development Activity, Stennis Space Center, Mississippi, NORDA Technical Note 171.

Lohanick, A.W. and T.C. Grenfell (1986) Variations in brightness temperature over cold first-year sea ice near Tuktoyaktuk, Northwest Territories. *Journal of Geophysical Research*, **91**(C4): 5133–5144.

Martin, S.A. (1979) A field study of brine drainage and oil entrainment in first-year sea ice. *Journal of Glaciology*, **88**: 473–502.

Stiles, W.H. and F.T. Ulaby (1980) The active and passive microwave response to snow parameters. 1. Snow wetness. *Journal of Geophysical Research*, **85**(C2): 1037–1044.

Ulaby, F.T. and W.H. Stiles (1980) The active and passive microwave response to snow parameters. 2. Water equivalent of dry snow. *Journal of Geophysical Research*, **85**(C2): 1045–1049.

Yen, Y.-C. (1988) On the pressure drop through a uniform snow layer. USA Cold Regions Research and Engineering Laboratory, CRREL Report 88-16.

Acoustical and Morphological Properties of Undeformed Sea Ice
Laboratory and Field Results

K.C. JEZEK
U.S. Army Cold Regions Research and Engineering Laboratory
Hanover, New Hampshire, U.S.A.

T.K. STANTON
Woods Hole Oceanographic Institution
Woods Hole, Massachusetts, U.S.A.

A.J. GOW
U.S. Army Cold Regions Research and Engineering Laboratory
Hanover, New Hampshire, U.S.A.

M.A. LANGE
Alfred Wegener Institute for Polar and Marine Research
Bremerhaven, Federal Republic of Germany

ABSTRACT

Sonar echo amplitude data have been collected at carrier frequencies of 188 and 120 kHz from the underside of different sea ice types. Histograms of normal incidence echo amplitudes were formed from over 90 samples of each ice type. Experiments were conducted on saline ice grown in an outdoor pond under relatively controlled conditions at CRREL and on the sea ice cover in the Fram Strait. Analysis shows marked variations (about a factor of 5) in the magnitude of the coherent reflection coefficients as congelation ice at the bottom of an ice sheet evolves from a growing dendritic interface to an ablating, thermally altered interface. Larger differences (about a factor of 10) are observed between growing congelation ice and slush ice, used to simulate frazil. These results indicate that important variations in acoustic regime exist in areas where different ice types are intermingled.

INTRODUCTION

The structure of undeformed sea ice evolves progressively as it cycles from growth to decay (Weeks and Ackley 1982). Initial formation of sea ice may be controlled by mechanical forces inducing the development of fine grained frazil ice in turbulent seas. Small, submillimeter crystals are randomly oriented in a viscous, high salinity matrix. As the ice thickens

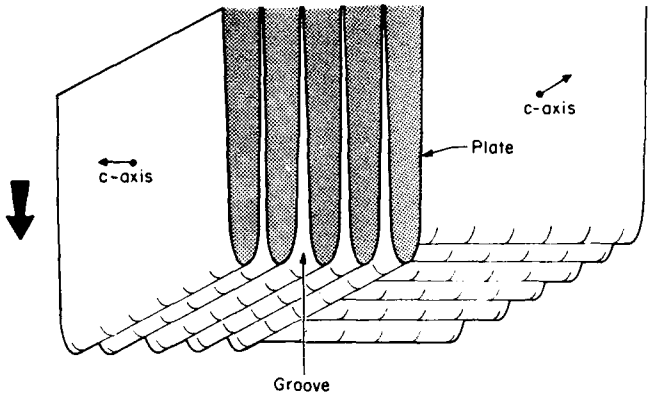

Figure 1. Schematic of interface geometry of two adjacent crystals of sea ice, showing vertical dendrite and groove structure and horizontal c-axis. Brine entrapment is confined to the grooves. The larger arrow on the left indicates the downward direction of growth.

and stabilizes by continued agglomeration of frazil particles or by rafting, thermodynamic growth begins to dominate as is characteristic of more quiescent conditions. In this phase, a vertically elongated structure of columnar ice crystals is developed. The growing interface itself is characterized by the formation of crystals composed of numbers of plate-like dendrites of pure ice that protrude downward into the seawater (Fig. 1). With continued growth, the lateral connections between dendrites eventually pinch off, trapping pockets of brine in the interdendrite grooves. If growth slows or proceeds under very low water salinities, the plate-shaped dendrites may degenerate into cellular structures. In the event of growth under the influence of current flow, it has been observed that the c-axis orientation of different crystals will tend to parallel the direction of the current (Weeks and Gow 1978).

The systematic incorporation of salt into the structure of sea ice causes it to be highly sensitive to changes in temperature. As ice warms, previously isolated brine pockets develop connections, eventually allowing the entrapped brine to drain back into the sea under the force of gravity. Continued warming causes the fragile, anisotropic, dendritic, bottom interface structure to ablate to a smoother surficial and more homogeneous structure.

As sea ice evolves naturally through these different growth textures, so too does it manifest important changes in its high frequency acoustic properties. Variations in the porosity, permeability, and underside roughness of the ice lead to changes in reflected and scattered acoustic energy as well as the degree of attenuation suffered by energy transmitted into the ice. The purpose of this paper is to report results of normal incidence reflection and scattering experiments from sea ice of differing interface morphologies and internal textures encountered under controlled conditions on the saline ice pond at the Cold Regions Research and Engineering Laboratory and on the sea ice cover of the Fram Strait.

BACKGROUND

Reported values of high frequency reflection coefficients from sea ice span the range from 0.10 at 15 degrees angle of incidence for frequencies between 17.9 and 184 kHz (Langleben 1970) to 0.2 at normal incidence at 3.6 MHz for 2 mm of sea ice growing on a block of fresh ice (Bogorodsky et al. 1970). However, little attention was paid to the detailed structure (crystal texture and brine pockets) of the ice under study. Consequently, we conducted an intensive set of acoustical and morphologic measurements on cold, growing congelation ice and published the results in 1986 (Stanton et al. 1986). The reflection coefficient of that ice, which had a well developed dendritic structure, varied from 0.043 at 188 kHz to 0.065 at 120 kHz, much less than previously reported results. On the basis of statistical variations in echo amplitudes for frequencies up to 820 kHz, we were able to show that scattering was dominated by obstacles on the order of 0.5 mm in size—a characteristic dimension of the ice dendrites. This observation stimulated us to perform further research on ice that experienced significant modifications to the dendritic structure.

EXPERIMENTAL APPROACH

All field and laboratory work has been performed in the same manner using the same equipment. A piezoelectric, ceramic transducer with narrow beamwidth (typically about 9 degrees) is mounted on a horizontal arm attached to a vertical shaft. The transducer is deployed below the ice as shown in Figure 2 and the shaft is rotated so as to insonify independent patches of the bottom of the ice at normal incidence. A Hewlett Packard (HP) pulse generator

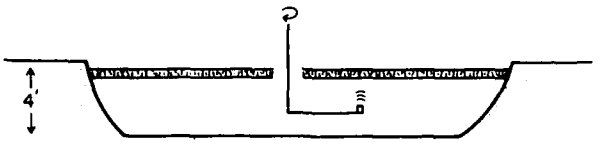

Figure 2. Side view of normal incidence reflection measurement. The echo amplitude is recorded at between 90 and 150 different transducer locations.

8011A produces trigger timing and gate duration (400 μs) for our pings and an HP pulse/function generator 8111A produces tone bursts at the various resonance frequencies of our transducers. A diode "T/R" switch partially isolates the transmitter from the receiver electronics, a bandpass filter and an oscilloscope. The amplitude and travel time of the reflected pulses were manually recorded.

Field measurements were conducted on the sea ice cover of the Fram Strait during May 1988. Investigations were carried out from the research vessel *Polarstern* which was moored to a large floe for the duration of the experiments. The location of the ship was approximately 80°30'N, 3°E; total drift was less than 40 km. The floe was likely a conglomeration of ice fragments of varying age and ranging in thickness from about 1 m to just over 4 m. This seemed typical of most other kilometer-sized or larger floes sampled by helicopter-assisted reconnaissance around the area. Open water concentration in the area was at maximum about 10%; this reduced to nearly 0% when cold air masses advecting in from the east caused thin, congelation ice to form.

Laboratory measurements took place at CRREL. Simulated sea ice was grown in an artificial outdoor pond measuring 12.2 m long by 5.2 m wide by 1.5 m deep and filled with tap water raised to a salinity of 23 to 25‰ by addition of finely granulated sea salt. Evolution of the sea ice sheet was controlled solely by changes in local weather. Proximity to the coldroom complex and associated analysis capabilities greatly facilitated structural and chemical analysis of the ice.

In addition, data were collected on a 30-cm-thick freshwater ice sheet on a small pond 10 miles north of CRREL.

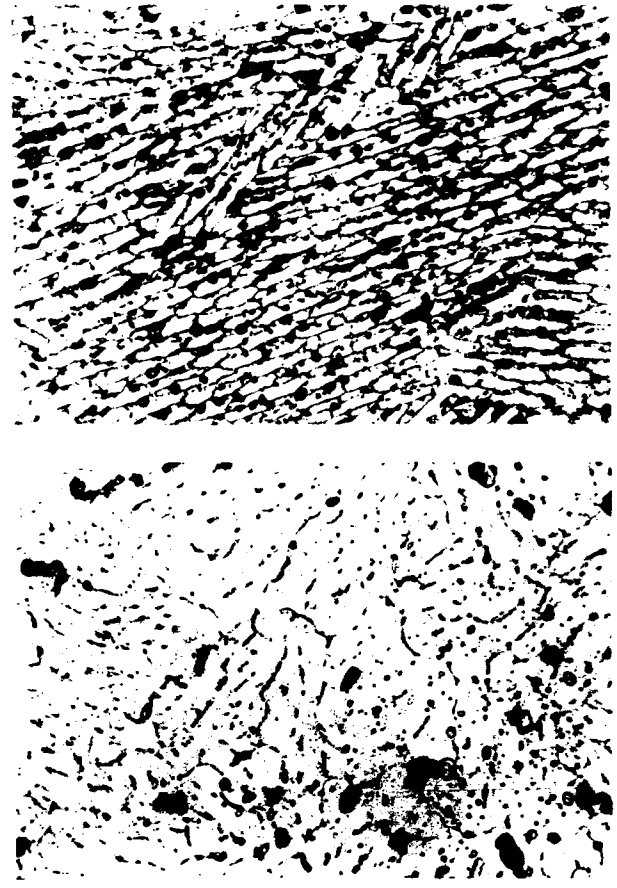

Figure 3. Horizontal thin sections of near-basal ice showing strong dendritic structure (top) and (bottom) ice at about the same depth as (a) but after the total ice thickness had increased to 28 cm and warming had caused desalination and retexturing of the ice.

ICE TEXTURE AND MORPHOLOGY

The principal ice type so far studied has been undeformed congelation ice less than 20 cm thick. This ice thickens by freezing of ice at the tips of pure ice dendrites in contact with seawater. The process of brine incorporation that accompanies this growth produces a vertical gradient in porosity and permeability and accounts, we believe, for the low reflection coefficients and high attenuation we have observed when the ice is cold. An example of structure in a horizontal thin section from near the bottom of growing congelation ice is shown in Figure 3 (top). Figure 3 (bottom) shows congelation ice from approximately the same depth in the same ice sheet after the ice sheet has thickened and has undergone natural warming in place. The distinctive ice plates and brine pocket structure of actively growing ice is obliterated, replaced by a more random assemblage of brine inclusions within crystals now exhibiting substantially rounded grain boundaries. Although the thin section shown in Figure 3b was taken from roughly the midpoint of the ice sheet, the structure it reveals is characteristic of the ice bottom when the ice is ablating (Gow et al. 1987). With the exception of the 0.5-mm dendritic microrelief, the ice/water interface is essentially planar. These changes in structure were also accompanied by significant changes in salinity and profile. The extent of these changes is shown in Figure 4.

Structural features shown in Figure 3 parallel those observed in ice in the Fram Strait experiments. New growth in leads was classified as congelation ice with an obvious dendritic structure at its base. Dendrites were about 0.2 mm in width and the bulk

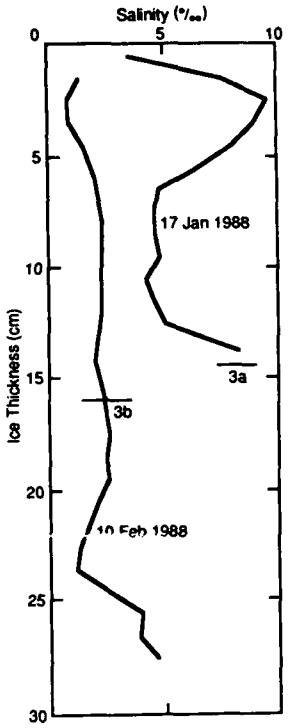

Figure 4. Salinity profiles of ice sheets measured the same day the ice was sampled for structures shown in Figure 3.

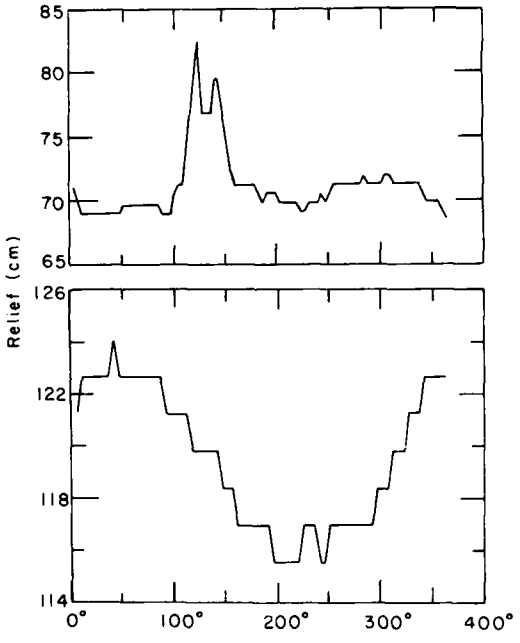

Figure 5. Acoustic profiles of the underside of 1.3 m thick ice in the Fram Strait collected at (a) 188 kHz and (b) 120 kHz at a slightly different location. Horizontal axis is the angular displacement in degrees of the horizontal arm beneath the ice. The 1.2-m length of the arm results in a total angular displacement of 7.3 meters.

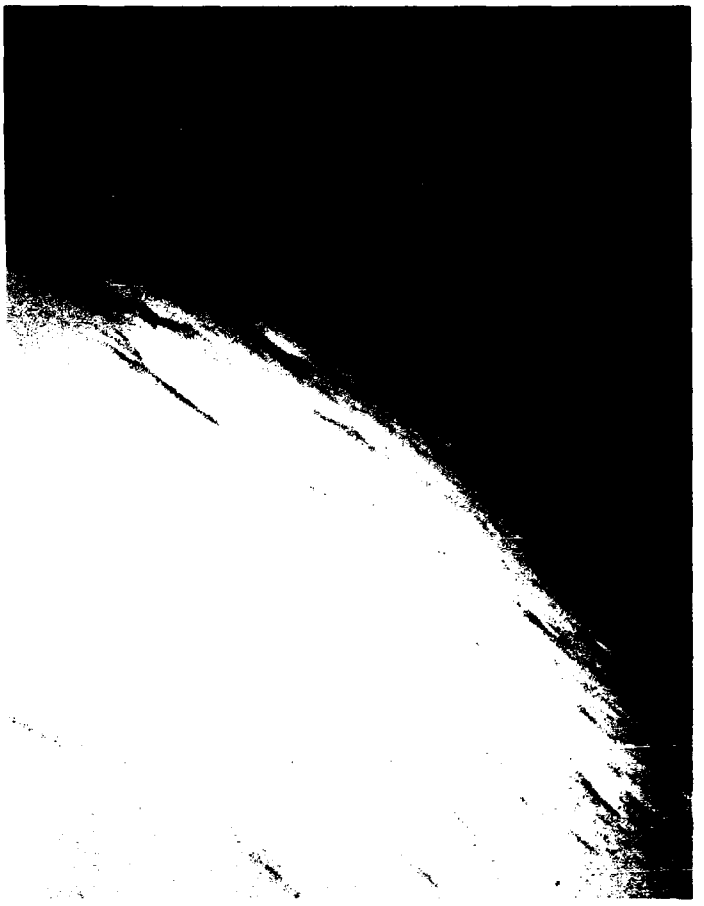

Figure 6. Underwater photograph of the underside of thick ice floes in the Fram Strait showing elongated dimples in underside of the ice.

salinity of 5-cm-thick ice was 10.5 ppt. Except for the early part of the cruise, the underside of ice floes thicker than 1 m appeared more like the thermally altered ice in Figure 3b, presumably because the bottom of the ice was being ablated by warmer surface waters encountered as the ice swept south. This ice appeared under visual inspection to be generally hard, brittle and smooth to the submillimeter scale. Salinities in the lower 10 cm were about 3.5‰. Acoustic travel time measurements (Fig. 5) along with underwater photography (Fig. 6) taken in mid-May revealed the base of the ice to be generally planar with occasional elongated dimples. With a radius arm of 1.2 m, azimuthal rotation of the transducer insonified a circle with a 7.5-m circumference. Ranges to the underside of the ice at the location of the 188 kHz data are shown in Figure 5a. Data from the 120 kHz site are shown in Figure 5b. Only data for which the bottom slopes exceeded 3 degrees were excluded from the acoustic analysis described in the next section.

Figure 7. Horizontal thin section through basal ice growing with a cellular structure.

The cellular structure shown in Figure 7 is of basal ice sampled in March of 1985 after 35 cm of ice had formed in the CRREL saline ice pond. The ice grew under low salinity conditions during a period of cool weather preceded by a brief warming when freshwater runoff flushed through the ice and into the pond. A somewhat similar structure was observed on the bottom of 1.5-m-thick congelation floes in the Fram Strait in early May of 1988 when surface air temperatures were fluctuating between –15° and –10°C. Acoustic travel time measurements at this site showed the range between transducer and ice bottom to vary with a peak to peak amplitude of 4 cm and a period of one revolution of the transducer; this suggests a slight (<1°) slope of the bottom. Given the 9° beamwidth of the transducers, no slope correction was applied to the acoustic data set.

Although we had only limited success growing frazil ice in our outdoor pond, a reasonable simulant was produced when roughly 8–10 cm of snow fell into open water of the CRREL pond and formed a slush cover about 3 cm thick. The snow fell in two stages after which temperatures cooled and congelation growth occurred beneath the consolidated slush. These stages are evident in the vertical thin section shown in Figure 8. The middle zone of fine-grained ice constitutes slush formed during the first snowfall and is overlain by coarser-grained slush derived from the second snowfall. The bottom layer consists of columnar crystals of congelation ice. Acoustic measurements were performed on the slush ice while it still had a viscous consistency and had not consolidated to slush ice.

Acoustic studies of lake ice were made on Post Pond about 10 miles north of CRREL. Measurements were conducted in March 1985 when the ice was 30 cm thick (Fig. 9). The upper 7–8 cm of the ice were opaque and bubble rich. The remain-

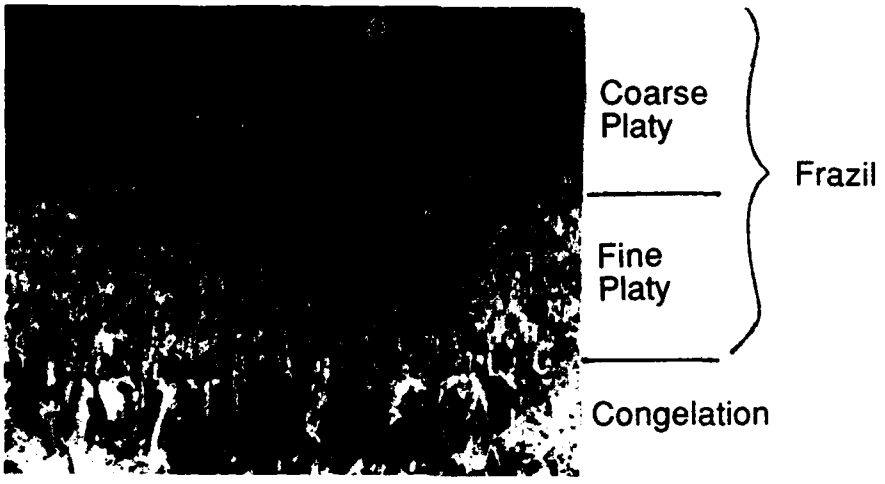

Figure 8. Vertical thin section through slush ice.

Figure 9. Block of lake ice, 30 cm thick, showing elongated crystalline structure that became apparent after several minutes of exposure to warm air temperatures.

der of the ice was substantially transparent save for occasional elongated bubbles. The transparent ice consisted of long columnar crystals with horizontal cross sections on the order of several square centimeters. Acoustic travel time data as well as visual inspection of slabs removed from the pond indicated the bottom surface of the ice was planar.

ACOUSTIC DATA AND ANALYSIS

Data are collected by insonifying the bottom of the ice and recording the echo amplitude. At least 90 samples from independent patches of the ice bottom are compiled into histograms of echo amplitude normalized against the echo strength from a flat, open water surface. The histograms themselves are normalized to unit area to present results as probability density functions (PDF). (Typically 120 to 150 observations of echo amplitude were made during laboratory studies.)

To interpret these data, we use a combination of Eckart scattering theory and Rice statistics described by Stanton (1984). Essentially, we measured the square root of the echo intensity. The mean of the squares of our observations $\langle p^2 \rangle$ is given simply by:

$$\langle p^2 \rangle = \langle p \rangle^2 + \langle s^2 \rangle \quad (1)$$

where $\langle p \rangle^2$ represents the square of the mean echo amplitude (the coherent or specularly reflected signal) and $\langle s^2 \rangle$ represents the mean square of the incoherent or scattered component. When $\langle s^2 \rangle$ is small, that is, the surface is smooth with respect to an acoustic wavelength, then the mean of our observations approaches the coherent reflection coefficient. To determine when this criterion is met, we note that the skewness of the PDFs described by Rice statistics derived for the sum of a constant (coherent vector) plus random noise (incoherent vector), is quantified by a parameter gamma where

$$\gamma = \langle p \rangle^2 / \langle s^2 \rangle \quad (2)$$

When gamma is large, $\langle p \rangle^2$ dominates the sum in equation 1 and the shape of the PDF approaches a narrow Gaussian bell.

Figures 10 and 12 show the individual measured PDFs compiled from observations from the different ice types along with fitted PDFs. In all cases, gamma equals or exceeds 2 so the mean value of our observations approximates a coherent reflection coefficient.

To facilitate comparison of different ice types, the fitted PDFs are displayed in Figures 11 and 13. Looking first at the lake ice data shown in Figure 11, we see the reflection coefficient is 0.4 as predicted for smooth-bottomed freshwater ice on the basis of its bulk density and sound speed. The gamma for this PDF equals 80, demonstrating that the surface is acoustically smooth. As reported by Stanton et al. (1986) the reflection coefficient for young sea ice is almost a factor of 10 less than that of the lake ice. The reflection coefficient for ice with a cellular interface is greater than the reflection coefficient for young ice with a dendritic interface, consistent with the notion that the cellular ice becomes less porous. Curiously, gamma is about 2 for cellular ice as compared to gamma equal to 6 for dendritic ice, suggesting an acoustically rougher surface for the cellular growth. Slush behaves unexpectedly by having an average reflection coefficient approaching that of solid ice. Although the width of the slush PDF is very broad, gamma is about 2.5, slightly higher than that of the cellular ice.

Figure 13 similarly displays results from the field. The mean reflection coefficient from the 5-cm-thick

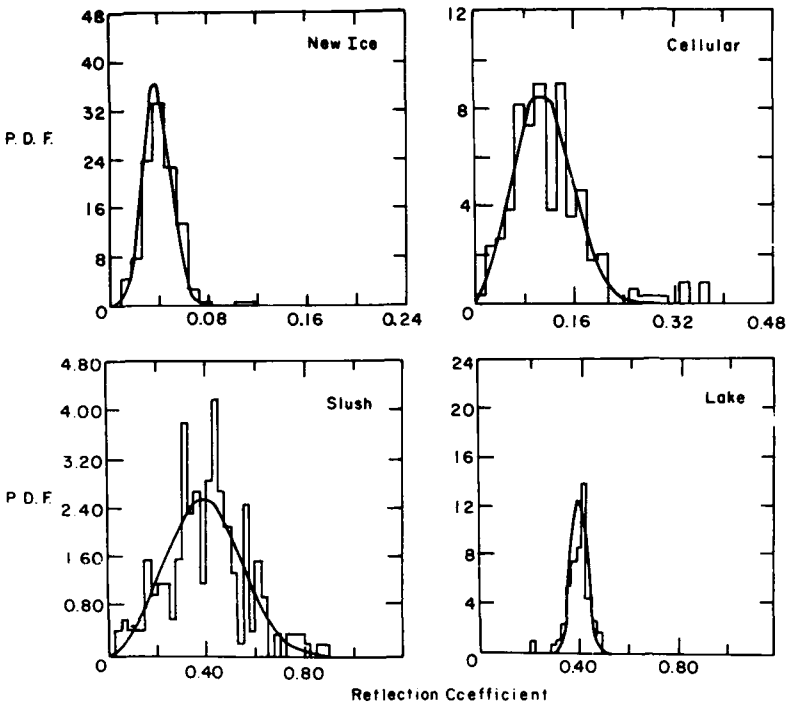

Figure 10. Histograms compiled from normalized echo amplitude data collected on different types of laboratory grown saline ice and lake ice. Carrier frequency is 188 kHz for all data. Measured data are fitted with Rice probability density functions.

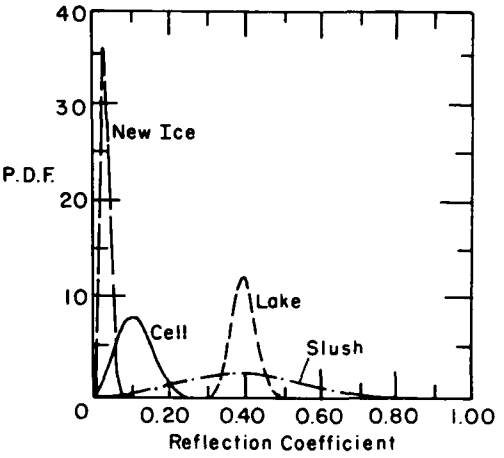

Figure 11. Rice probability density functions from Figure 10 for different laboratory grown ice types and for lake ice.

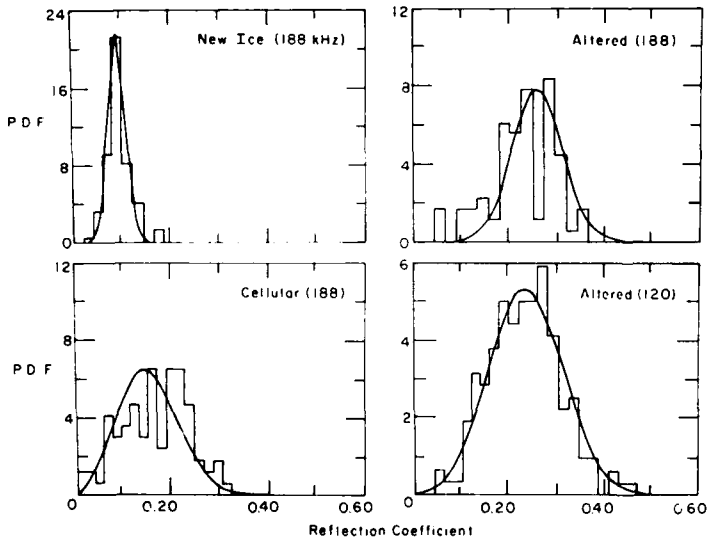

Figure 12. Histograms compiled from normalized echo amplitude data collected on different types of sea ice observed in the Fram Strait. Data were collected at 188 kHz for all samples and at 188 and 120 kHz for the thermally altered ice sample. Measured data are fitted with Rice probability density functions.

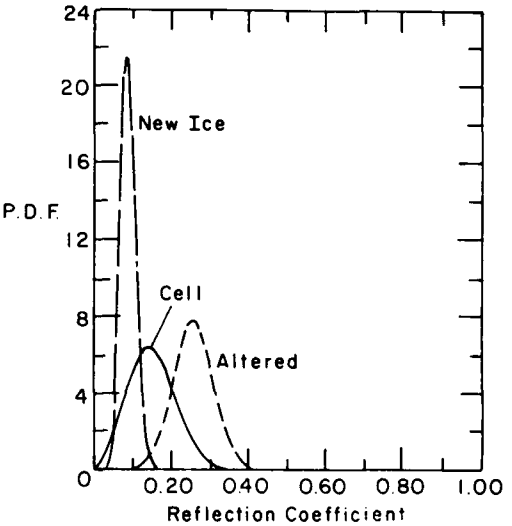

Figure 13. Rice probability density functions from Figure 12 for different types of sea ice observed in the Fram Strait.

lead ice is 0.09 and gamma equals 12. This reflection coefficient is about twice the value reported on 10-cm-thick laboratory grown ice (Fig. 11) but simple modeling indicates that there may be a measurable contribution from the air/ice interface for ice thicknesses less than 5 cm. (For ice thicknesses greater than 5 cm, the total attenuation through the ice is high [Jezek et al. 1987]). Alternatively, the lead ice was probably no longer growing on the day our measurements were taken. As described in the discussion section of this paper, the reflection coefficient of warming dendritic ice could be expected to increase.

The cellular ice measured in early May at the base of a 1.5-m-thick floe in Fram Strait behaves acoustically much the same as the ice measured in the laboratory in both mean and skewness. The thermally altered ice has the highest reflection coefficient, which is again consistent with the loss of brine from the ice and concurrent reduction in its porosity and permeability.

DISCUSSION

Our results show that different ice textures and interface morphologies have markedly different acoustic properties. This is not surprising given the expected differences in porosity, permeability and roughness associated with the development of each ice type and the commensurate effect these factors have on acoustic coupling into the ice and attenuation through the ice. Results similar to ours have been reported by Francois et al. (1988) for congelation ice in the Arctic but over the frequency band 20 to 200 kHz. For cold ice, they found reflection coefficients are about 0.05 across the entire band. We believe this indicates, again, the good coupling associated with the dendritic layer. As the ice warmed, Francois and others reported an increased reflection coefficient at lower frequencies. At 20 kHz, for example, the reflection coefficient increased to 0.225.

We also have observed increases in reflection coefficients for ice formed in the CRREL pond that on visual inspection possessed a dendritic interface. Observations were made over several days on ice about 20 cm thick during a period of cycling warm days (above freezing temperatures) and cold nights (below freezing temperatures). Reflection coefficients ranged as low as 0.07 after a period of low air temperatures to about 0.3 after air temperatures had risen. Although we have not been able to tie these acoustic observations to a quantified change in ice texture or interface morphology, we speculate that warming temperatures erode many of the complicated interconnections between brine pockets formed during the freezing process. Breakdown of the brine pocket structure permits freer flow between the ice plates. While this effect would not increase the coupling into the ice, it might reduce the attenuation suffered by a wave traveling through the ice. Hence, energy could be reflected from stratigraphic discontinuities higher in the ice and ultimately contribute to the total signal strength at the receiver. In fact, horizontal layers of bubbles were observed in core samples taken from that ice sheet and may be the source of additional reflected energy. These observations lead us to suggest that rapid, large-scale changes in the acoustic reflection coefficient occur during the transition period from growth to ablation of the interface.

We offer a second implication of our work based on the observation that several distinctly different ice interface morphologies exist within the same general area of the Fram Strait in May. While the reflection coefficient from the bottoms of large thick floes remained largely unchanged during our visit, the reflection coefficient from bounding leads fluctuated between 0.09 when they were covered with a thin layer of congelation ice to unity when the leads were ice-free.

ACKNOWLEDGMENTS

This work was sponsored by the Office of Naval Research and by the Alfred Wegener Institute for Polar and Marine Research.

REFERENCES

Bogorodsky, V.V., S.A. Smirnov and V.L. Sinitsyn (1970) Simulation of the scattering of underwater sound by sweet ice specimens immersed in artificial sea water. *Tr.* **295**: 174–181.

Francois, R.E., G.R. Garrison and T. Wen (1988) Reflectivity of sea ice (abstract). *Journal of the Acoustic Society of America.*

Gow, A.J., S.A. Arcone and S.G. McGrew (1987) Microwave and structural properties of saline ice. USA Cold Regions Research and Engineering Laboratory, CRREL Report 87-20.

Jezek, K.C., T.K. Stanton and A.J Gow (1987) Attenuation of sound through laboratory grown saline ice (abstract). *Journal of the Acoustical Society of America,* **82**(suppl. 1): 30.

Langleben, M.P. (1970) Reflection of sound at the water/sea ice interface. *Journal of Geophysical Research,* **75**: 5243-5246.

Stanton, T.K. (1984) Sonar estimates of sea floor microroughness. *Journal of the Acoustics Society of America*, **75**: 809-818.

Stanton, T.K., K.C. Jezek and A.J. Gow (1986) Acoustical reflection and scattering from the underside of laboratory-grown sea ice: Measurements and predictions. *Journal of the Acoustical Society of America*, **80**: 1486-1494.

Weeks, W.F. and S.F. Ackley (1982) The growth, structure and properties of sea ice. USA Cold Regions Research and Engineering Laboratory, CRREL Monograph 82-1.

Weeks, W.F. and A.J. Gow (1978) Preferred crystal orientation in the fast ice along the margins of the Arctic Ocean. *Journal of Geophysical Research*, **83**: 5105-5121.

Acoustics of Arctic Ice Floes
Modeling, Simulation, and Signal Processing

C.A. POMALAZA-RAEZ AND S.S. SHANAN
Department of Electrical and
Computer Engineering
Clarkson University,
Potsdam, New York, U.S.A.

H.H. SHEN
Department of Civil and
Environmental Engineering
Clarkson University,
Potsdam, New York, U.S.A.

ABSTRACT

The noise under sea ice, in particular the one produced by ice floes in the Arctic region, is studied by means of a model simulation and the development of signal processing techniques for its measurement and estimation. This noise is due to the interaction among ice floes which produces noise that is non-Gaussian in time and frequency. Based on previous studies, two shapes of the acoustic wave pressure generated by a single event is assumed. The random occurrence of the ice interaction process is modeled as a Poisson sequence of impulses. Different sonar array spectrum estimation techniques (Fourier, autoregressive [R], and minimum variance [MV]) are analyzed for the processing of the resulting acoustic signal. It is found that the minimum variance spectral estimation technique is the overall best for this type of signal for a wide range of the model parameters. The standard periodogram technique used in many previous studies are found to produce significant discrepancies of the actual phenomena.

INTRODUCTION

Under-ice noise in the Arctic is characterized by anomalously high strength levels. This noise signal is hypothetically generated by the interaction of ocean waves, wind, and eddies with ice floes. Such noise is a limiting factor in under sea-ice target detection and estimation problems, making its measurement an interesting area of investigation (Bogorodskii et al. 1969, Greene and Buck 1964, Milne and Ganton 1964). The impulsive character during the ice movement is specific to under-ice noise in the shorefast regions of land floes. Recording of wind-generated noise, and of impulsive noise from ice cracking, were made in Ganton and Milne (1965) with bottom-mounted omnidirectional hydrophones under a variety of meteorological conditions. Windless cooling periods produced pure impulsive non-Gaussian noise, while warming windy periods produced white-Gaussian noise. Recent analyses of the arctic data collected in the spring of 1980 (Dwyer 1983) have shown that the under-ice noise can be at times highly impulsive and non-Gaussian, probably resulting from tensile cracks and rubbing ice masses.

In a theoretical study by Milne (1966), an idealized geometric model is proposed for determining the power spectral density (PSD) of under-ice noise received by omnidirectional hydrophones situated on the bottom. This model (impulsive noise) is constructed on the assumption of a surface distribution of sources having an axisymmetric directivity pattern. It is also assumed that the resultant pressure comprises a superposition of individual pulses of identical shape, but with different amplitudes, periods, and phases. Although the model does not account for bottom-reflected signals and refraction effects, the PSD calculated according to the formulas given in Milne (1966) for under-ice noise generated by exponentially sinusoidal pressure pulses is fairly close to the PSD measured under real conditions during a period of vigorous thermal cracking in the absence of the wind.

The impulsive nature of the arctic noise structure is also evident from the recent data given in Dwyer (1983), in which a higher-than-Gaussian noise kurtosis was obtained. This observation implies a need to carefully evaluate the standard signal processing

techniques, which are designed to have optimal performance for Gaussian type signals.

To the authors' knowledge, there is no previous attempt to examine various spectral estimation algorithms that are different from the traditional Fourier methods for estimating impulsive noise PSD. Consequently, four types of 2-dimensional spectral estimation algorithms are performed (periodogram, correlogram, AR, and MV) to estimate the PSD based on Milne's model. In order to test the performance sensitivity of the estimation algorithm, two types of possible acoustic signals produced by ice interactions are used in the model. Extensive simulating results show that MV and AR processors are the best (in terms of PSD bias and variance) for such types of signal for a wide range of the model parameters.

IMPULSIVE NOISE

Assume that an omnidirectional pressure detector is situated in an isovelocity lossless medium (under ice layer), and all the noise sources are situated within that layer. Assume also, that it is possible for all the acoustic emission events to be observed simultaneously at a unit distance in the vertical direction immediately beneath the location of each event. The pressure pulses from these vantage points should occur randomly with time within the bounds of an elemental annular area, that is, a Poisson distribution function might fit the distribution of these impulses with time with an average occurrence rate, n_0. Also it can be assumed that the individual pulses have identical basic waveforms u, but different amplitudes a, duration τ, and phases ψ. The parameters of pulses incorporate ice floe size, and the physical properties of ice. The shape of the pulses depends on the types of interactions.

It is reasonable to classify the noise sources into two groups: those that form a background noise field (such as wind-induced noise), and those that are sufficiently strong to appear individually and discretely (such as from thermal cracking or ice mass rubbing). The former are very numerous with a resulting high-density Poisson process, whose statistics are asymptotically Gaussian. The latter retain their individual character and remain a Poisson process of low density. Thus one can have a sum of Gauss and Poisson processes:

$$x(t) = g(t) + \sum_i u(a_i, \tau_i, \psi_i, t - t_i) \qquad (1)$$

From Milne (1966), the impulsive noise (Poisson process) PSD, $S(\omega)$, can be written in the following form:

$$S(\omega) = \frac{n_0}{2\pi} E\left[U_i^2(\omega)\right] + \frac{n_0^2}{2\pi} E^2\left[U_i(\omega)\right] \delta(\omega) \qquad (2)$$

where E is the expectation operator, ω is the angular frequency and δ is the Dirac function.

This PSD stochastically characterizes the second order statistics of an impulsive noise. In practice, this PSD is unknown and in many applications must be estimated.

SIMULATION RESULTS

To examine the impulsive noise responses of different spectral estimates, two possible cases of acoustic pulses produced by ice interaction are considered below. These pulses are superimposed with a Gaussian noise such that the resulting Poisson to Gaussian spectral power ratio is 10 dB.

Case I

The acoustic pulses are assumed to be of Gaussian modulated shape (Stephens and Pollock 1971), $u_i(t) = a_i \cos\omega_0 t \exp-(t-m)^2/(2\tau^2)$, with uniformly distributed random amplitude, $a_i = U(-1,1)$, mean, $m = 3\tau$, standard deviation, $\tau = 3$ m/sec, angular frequency, $\omega_0 = 0.2\pi f_s$, and sampling frequency, $f_s = 3300$ Hz, as its parameters. These parameters are chosen based on the data obtained in Ganton and Milne (1965). The resulting PSD of the Poisson part of the noise is given by

$$S_I(\omega) = S_{I1} + S_{I2} \qquad (3)$$

where

$$S_{I1} = \frac{\pi n_0 \tau^2}{2} E\left(a_i^2\right)\left(\exp-\frac{(\omega-\omega_0)^2}{2/\tau^2} + \exp-\frac{(\omega+\omega_0)^2}{2/\tau^2}\right)^2$$

$$S_{I2} = \frac{\pi n_0^2 \tau^2}{2} E^2(a_i)\left(1 + \exp-\frac{(\omega_0^2)}{1/2\tau^2}\right)^2 \delta(\omega-\omega_0).$$

When superimposed with the Gaussian background noise, the corresponding PSD must be obtained numerically.

Case II

The exponentially damped sinusoidal pressure pulses, $u_i(t) = a_i \sin\omega_0 t \exp-(t/\tau_0)$, proposed by Milne (1966) are considered in this case with Rayleigh amplitude distribution, $a_i = (x_i^2 + y_i^2)^{0.5}$, where x_i and y_i are both of Gaussian distribution with zero mean and variance equal to one, and τ_0 equals τ as in case I. The

resulting PSD is given by

$$S_{II}(\omega) = S_{II1} + S_{II2} \qquad (4)$$

where

$$S_{II1} = n_0\tau_0^2 E[a_i^2]\frac{1+\tau_0^2\omega^2}{1+2\tau_0^2(\omega^2+\omega_0^2)+\tau_0^4(\omega^2-\omega_0^2)^2}$$

and

$$S_{II2} = n_0^2\tau_0^2 E^2[a_i]\frac{1+\tau_0^2\omega_0^2}{1+4\tau_0^2+\omega_0^2}\delta(\omega-\omega_0)$$

Again, after superimposed with the Gaussian background noise, the corresponding PSD is obtained numerically.

Sixteen sensors are used in the simulation; at each sensor 50 segments of 256 sample points are produced under assumption of constant sound-speed profile. The statistical average is obtained over these segments. Each spectral estimation method, other than the periodogram, is constructed to estimate the same number of parameters, so that a qualitative comparison would be fair. The exact choices for the model order (AR), lag window (MV) were not made to yield the best results but only to illustrate the typical characteristics of each estimation. Other choices will yield similar although not identical results. The statistical performance of the spectral estimates at different numbers of sampling points are in Figure 1 for the case I pulse, where the PSD bias range is defined to be the difference between the estimation bias margins. The case II pulse gave qualitatively similar results.

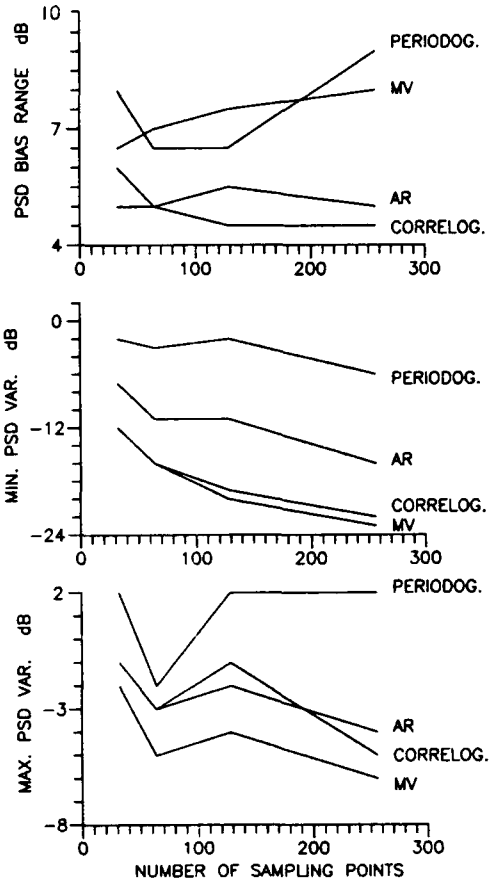

Figure 1. PSD estimator performance at different sampling points of case I.

CONCLUSIONS

An idealized geometrical model, incorporating distributions of ice interaction pulses, has been used to evaluate the statistical properties of 2-D Fourier, LP, and MV PSD estimates. The model is assumed to be the sum of Gaussian and Poisson processes that contributes to wind and ice interaction induced noise generating mechanisms, respectively. PSD bias and variance are used for performance evaluation of different spectral estimates. Through simulation, it is found that: the PSD variance is proportional to the

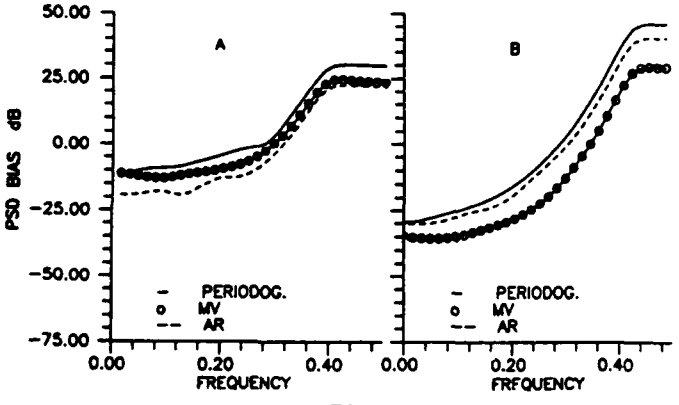

a. Bias.

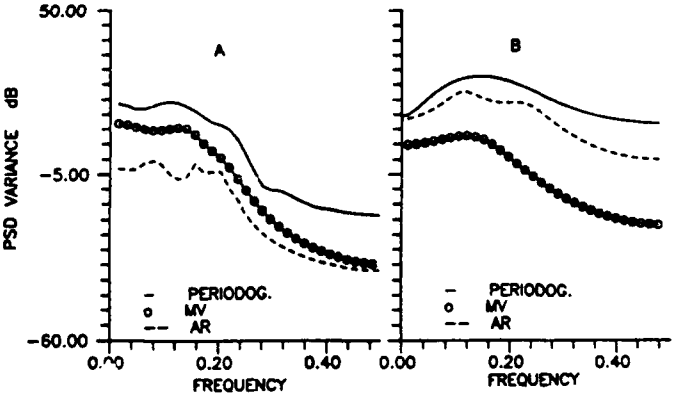

b. Variance.

Figure 2. Variability of PSD with changing the pulse width from 1 (A) to 100 (B) unit time for case I.

PSD estimate for all the used PSD estimates, the periodogram gives the highest range of bias fluctuation, the AR gives the lowest variance range of fluctuation and has the lowest maximum of PSD variance, and the MV has the lowest minimum of PSD variance. Extensive simulations show that there is no change of the statistical performance with the fine change of n_0. For large n_0, it follows directly from the central-limit theorem that the process becomes a Gaussian process, regardless of the specific form that $W(\alpha, \tau, \psi)$ and pulse shape, $u(t)$, may make. The spectral dependence on the pulse width, τ_0, particularly as its multiplicative effect with frequency in the PSD, affects the statistical characteristics of the spectral estimates (AR and MV), such that at wide signal width a switching is occurred in the PSD bias and variance as shown in Figure 2. Thus, identifying this parameter in the field condition seems to have particular importance for deciding the appropriate processing techniques to be used.

ACKNOWLEDGMENT

This study has been supported by USACRREL grant DACA89-88-K-0012.

REFERENCES

Bogorodskii, V.V., V.P. Gavrilo, V.S. Grigor'ev and A.V. Gusev (1969) Sound generation mechanisms in the breaking of ice samples in a liquid. *Journal of Soviet Physics-Acoustics*, **15**(2): 161–164.

Dwyer, R.F. (1983) A technique for improving detection and estimation of signals contaminated by under ice noise. *Journal of the Acoustic Society of America*, **74**(1): 124–130.

Ganton, J.H. and A.R. Milne (1965) Temperature- and wind-dependent ambient noise under midwinter pack ice. *Journal of the Acoustic Society of America*, **38**(3): 406-411.

Greene, C.R. and B.M. Buck (1964) Arctic Ocean ambient noise. *Journal of the Acoustic Society of America*, **36**(8): 1218–1220.

Milne, A.R. (1966) Statistical description of noise under shore-fast ice in winter. *Journal of the Acoustic Society of America*, **39**(6).

Milne, A.R. and J.H. Ganton (1964) Ambient noise under arctic-sea ice. *Journal of the Acoustic Society of America*, **5**(5): 855–863.

Stephens, R.W.B. and A.A. Pollock (1971) Waveforms and frequency spectra of acoustic emissions. *Journal of the Acoustic Society of America*, **50**(3, Part 2),.

Stress Relief in Sea Ice as Related to the Generation of Higher Frequency Noise

J.K. LEWIS
Science Applications International Corporation
College Station, Texas, U.S.A.

P.J. STEIN
Atlantic Applied Research Corporation
Burlington, Massachusetts, U.S.A.

W.W. DENNER
Science Applications International Corporation
Monterey, California, U.S.A.

ABSTRACT

A model is presented for simulating thermally induced stress variations in sea ice. A numerical heat flux model is coupled with a nonlinear Maxwell rheology, thus allowing visoelastic processes. However, the rheology is modified to account for the effect of vertical variations in the horizontal strain rate of the ice. Thus, the effects of other components of the strain rate tensor are considered.

The rheology is seen to be applicable for ice floes > 300 m in diameter and > 1 m in thickness. In such floes, one can expect vertical variations in temperature-induced strain. But these strain variations cannot force the floe to curl up because of gravitational and buoyancy forces. The resulting stress variations are presented for a number of cases, including observed conditions during the spring of 1976.

Simulations show that the nonlinear Maxwell rheology accounts for the fact that maximum under-ice noise levels typically occur 10 to 12 hours after maximum strain rates. For diurnal heating, surpassing the tensile strength of the ice occurs most often in the early morning hours. A 15-cm snow cover will essentially eliminate any of the thermal fracturing.

A surprising finding is that particular heating episodes can cause a considerable amount of fracturing deep within the sea ice (> 1 m). This results from the expansion of the surface layers of the ice due to heating. However, one theory indicates that these episodes of deeper fracturing will produce little under-ice noise. The reason for this is the interference of the acoustic waves within the ice. For fracturing at ~ 0.6 of the ice thickness, the wave patterns reaching the bottom of the ice are exactly 180° out of phase. Thus, the noise intensity in the water column is zero. Model noise events are presented based on this theory.

Comparison of the Compressive Strength of Antarctic Frazil Ice and Laboratory-Grown Columnar Ice

J.A. RICHTER-MENGE AND S.F. ACKLEY
U.S. Army Cold Regions Research and Engineering Laboratory
Hanover, New Hampshire, U.S.A.

M.A. LANGE
Alfred Wegener Institute for Polar and Marine Research
Bremerhaven, Federal Republic of Germany

ABSTRACT

Unconfined, uniaxial compression tests were performed on frazil sea ice samples collected in the Weddell Sea, Antarctica. The tests were done at a constant strain rate of 10^{-3} s^{-1} and at temperatures of –3, –5 and –10°C. Data from the frazil ice tests were compared to results from tests done under the same conditions on transversely isotropic, columnar saline ice. The approximate grain sizes of the frazil and columnar ice were 1 and 10 mm, respectively. The results of this work indicate that the frazil ice generally has a higher strength than columnar ice loaded in the plane of the sheet. Tests done by other researchers on freshwater, equiaxed polycrystalline ice have also shown the compressive strength to vary inversely with grain size according to the Hall–Petch relationship; $\sigma \propto (d)^{-1/2}$. Application of this relationship to the sea ice we tested indicates that the results from these freshwater ice tests at a strain rate of 10^{-3} s^{-1} cannot be directly extended to explain the variation in compressive strength between the frazil and columnar sea ice. We speculate that this may be due to 1) the influence that the increased ductility of sea ice has on the relationship between strength and grain size at 10^{-3} s^{-1}, 2) that another microstructural parameter (e.g., the thickness of the ice between brine inclusions) may be the controlling factor in determining sea ice strength, or 3) that the dominant mechanisms driving deformation vary with each ice type.

INTRODUCTION

The development of models to predict ice-structure interaction for design purposes requires information on the mechanical behavior of ice under complex loading states. Much of this information comes from small-scale laboratory tests designed to gain an understanding of the mechanisms of deformation. The results of these tests must be extended from the micro- to the macro-scale for application in large-scale loading problems. Ideally this extension should be made using ice of similar characteristics. For example, when considering large-scale loading problems that involve Arctic first-year sea ice, laboratory tests done on columnar, saline ice should be applicable. A loading problem in an antarctic scenario, on the other hand, would be likely to involve frazil ice because of the large quantities of this ice type found in this environment (Gow et al. 1987, Lange et al. 1989). While the columnar and frazil saline ice both contain air and brine, the frazil ice is characterized by its granular appearance.

Realistically, much of the work that has been done in the laboratory to determine the failure process of ice on the micro-scale has involved the use of freshwater, equiaxed ice with an extremely low air volume and no brine. This ice differs significantly from both columnar and frazil saline ice. The freshwater ice constitutes a single-phase system, while the saline ice types represent multi-phase systems. Given the lack of data on the failure process in both columnar and frazil saline ice, however, it becomes tempting to base explanations of the failure processes of these ice types on the freshwater, equiaxed ice test results. To date, no work has been done to indicate whether this extension is appropriate. Considering the fundamental difference between the freshwater and saline ice, the extension is not intuitively straightforward.

This work represents an initial effort to investigate the (dis)similarities between the mechanical behavior of saline and freshwater ice types. We present the results of constant-strain-rate compression tests done on frazil and transversely isotropic, columnar saline ice. The results are compared with published results on freshwater, equiaxed ice tests, focusing on the relationship between peak stress and grain size.

ICE PROPERTIES

The frazil ice that we tested was collected in the Weddell Sea, Antarctica. The columnar ice was grown in the laboratory, and it has been shown to accurately model the behavior of unaligned, columnar first-year sea ice found in the Arctic (Richter-Menge 1986, Kuehn 1988). The properties of the frazil and saline, columnar ice are summarized in Table 1. Figures 1 and 2 show the characteristics of the crystal structure of each ice type.

Table 1. Comparison of ice properties. All values represent averages.

	Salinity (ppt)	Density [at −20°C] (g/cm^3)	Grain Size (mm)
Frazil	4.37 ± 1.34	0.904 ± 0.018	1.0
Columnar	3.28 ± 1.10	0.887 ± 0.023	10.0

The most notable difference between these ice types is their crystal structure. As confirmed by thin-section analysis, the frazil ice is granular and equiaxed with the c-axes oriented randomly. The columnar ice is characterized by a long vertical axis, extending in the growth direction of the ice. The c-axes of the columnar ice are oriented in the horizontal plane and are unaligned. As a result of these characteristics, the frazil ice behaves isotropically (independent of direction), while the columnar ice exhibits transverse isotropy (isotropy limited to the horizontal plane). The variation in the structure of the ice is also apparent in the average grain size. The grains in the frazil ice are an order of magnitude smaller than the cross-sectional dimension of the columnar grains. The average salinities and densities of the frazil and columnar ice are comparable. One other significant difference

Figure 1. Typical crystal structure of the frazil ice collected in the Weddell Sea, Antarctica.

a. Vertical thin section (growth direction). *b. Horizontal thin section.*

Figure 2. Typical crystal structure of the columnar, saline ice grown in the laboratory

between the frazil and columnar ice is that the brine inclusions in the frazil ice are intergranular. The brine pockets in the columnar ice, on the other hand, are intragranular.

The ice that was collected for sampling was obtained using 10.2-cm, cylindrical core barrels (Rand and Mellor 1985). The frazil ice samples were cored in the vertical direction, while the columnar ice samples were horizontally cored. We chose to sample the columnar ice in the plane of the ice sheet because, with the ice oriented in this direction, a compressive load applied along the cylindrical axis of the sample will tend to create cracks parallel to the short axis of the ice crystals. We felt that under these loading conditions, the influence of grain size would be similar in the frazil and columnar ice.

TEST PARAMETERS

All of the tests were done at CRREL using a closed-loop, electro-hydraulic testing machine with a load frame capacity of 2.2 MN. The loading actuator used in these tests had a 1.1-MN capacity. The samples were machined to high tolerances, endcapped, and tested according to the methods described in Mellor et al. (1984) and Cole et al. (1985). Displacement measurements up to peak stress were made using transducers mounted directly on the ice. The displacement measurements used for the feedback control and for post-peak data were obtained via an extensometer mounted on the endcaps adjacent to the ice-endcap bond.

The samples were loaded in constant-strain-rate compression along their cylindrical axis. All tests were done at a strain rate of 10^{-3} s^{-1}. The samples were tested at a constant temperature of either –3, –5 or –10°C. A total of 13 tests were completed on frazil ice samples, and 9 tests were done on the columnar ice.

TEST RESULTS

The combined results of the tests are given in Figure 3, a plot of compressive strength or peak stress vs porosity at the test temperature. The porosity of the ice is a combined measurement of the air and brine volume in the ice. It is calculated using the equations derived by Cox and Weeks (1983). Note that for convenience we have combined data from three different test temperatures. We do this assuming that the primary influence of the temperature increase over this range is to increase the sample porosity. For comparison, we have also included results from Sinha's work (1986) on young arctic frazil ice. Sinha's tests were also done under controlled laboratory conditions at strain rate of 10^{-3} s^{-1} and temperature of –10°C.

Figure 3 indicates that there is a comparable decrease in compressive strength with an increase in porosity for both ice types. It also indicates that the strength of the frazil ice is consistently higher at a given porosity. For example, comparative strengths of the frazil and columnar ice at a porosity of 60 ppt are 5.3 and 4.2 MPa, respectively.

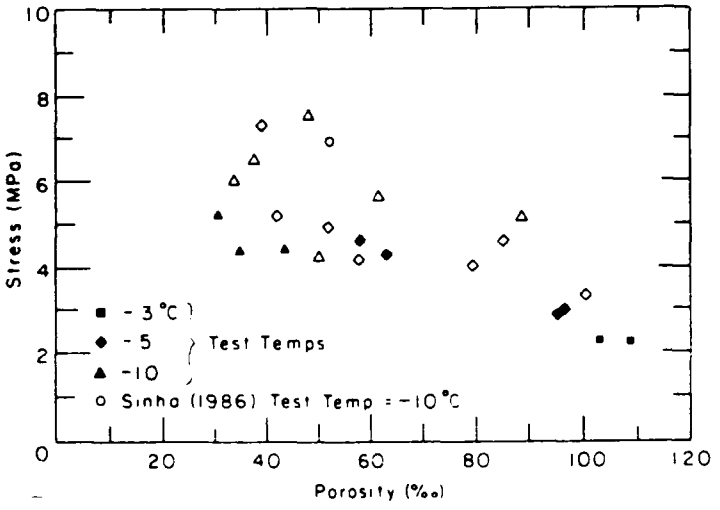

Figure 3. Peak compressive stress vs porosity for saline ice samples. Closed symbols represent columnar ice structure and open symbols indicate frazil ice structure. All samples were tested at a strain rate of 10^{-3} s^{-1}.

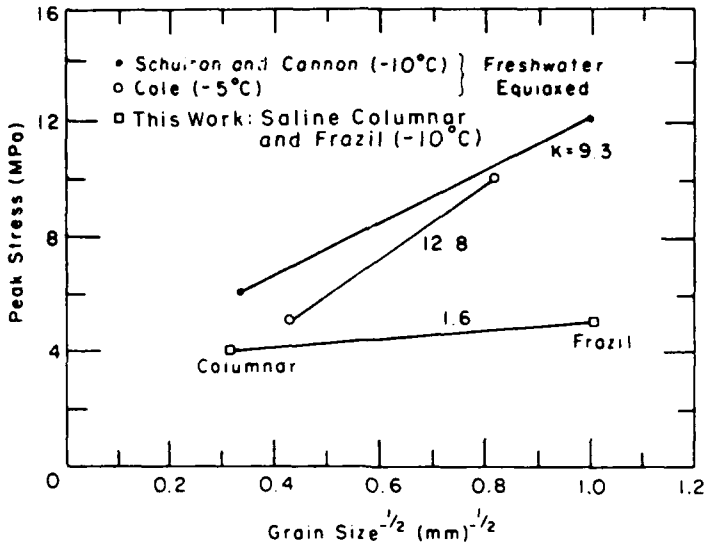

Figure 4. Comparison of the relationship between peak compressive stress and grain size for different ice types tested at a strain rate of 10^{-3} s^{-1}. The analysis is based on the Hall-Petch relationship; $\sigma = kd^{-1/2}$.

DISCUSSION

Our results indicate that grain size may influence the compressive behavior of saline ice. The 1-mm-grain-size frazil ice is consistently stronger than the 10-mm-grain-size columnar ice at comparable porosities. Inverse relationships between grain size and strength have been observed in many materials. This includes freshwater, equiaxed polycrystalline ice with a porosity ≈ 0. This grain size-strength relationship is well described by the Hall-Petch relationship: $s = k(d)^{-1/2}$. Using the Hall-Petch relationship, we have plotted the average peak compressive strength of the frazil and columnar saline ice from our results vs the inverse of the square root of grain size in Figure 4. Included in this plot are results from tests on freshwater, equiaxed ice taken from Cole (1987) and Schulson and Cannon (1984). The data used from these references are from tests done at a strain rate of 10^{-3} s^{-1}. Cole performed his series of tests at a temperature of –5°C, and Schulson and Cannon (1984) performed their tests at –10°C. The slope of the lines that represent the k value in the Hall-Petch relationship are shown above each set of test data.

It is clear from this figure that the relationship between grain size and peak compressive strength at a strain rate of 10^{-3} is much less pronounced for the saline ice. One potential explanation of this difference can be seen in a figure taken from Cole (1987) (Fig. 5). This figure shows that the freshwater ice at a strain rate of 10^{-3} s^{-1} exhibits the greatest variation in strength with a change in grain size. According to Cole (D. Cole, CRREL, pers. comm., 1988), the ductile/brittle character of the ice at this strain rate was dependent on grain size. The finer-grained ice at this strain rate still exhibited some ductile characteristics while the coarser grained ice failed in an explosively brittle manner. At strain rates of 10^{-4} s^{-1} and 10^{-2} s^{-1}, the characteristics of the failure were relatively independent of grain size. The ice behaved in a ductile manner at the lower strain rate and in a brittle manner at the higher strain rate, regardless of grain size. This variation is reflected in the k values (Fig. 5). The values of k at 10^{-4} and 10^{-2} s^{-1} are much less than the value at 10^{-3} s^{-1} that was used in our analysis. If we assume that k = 3.0, based on Cole's results at 10^{-4} and 10^{-3} s^{-1}, the expected increase in strength in the saline ice tests is 2.0 MPa—much closer to the observed variation of 1.1 MPa. Saline ice is intrinsically more plastic than freshwater ice due to the inclusion of brine. The observations made from Cole's work might indicate that, with the more compliant saline ice, the frazil and columnar ice were behaving similarly at the strain rate of 10^{-3} s^{-1}. At a higher strain rate, we might observe a variation in behavior under loading that is more dependent on grain size. We plan to do more testing of both the frazil and the columnar ice over a wider range of strain rates to determine whether this is a reasonable explanation.

A second, and somewhat related, hypothesis which might explain the difference in the results between the freshwater and saline ice test is that different

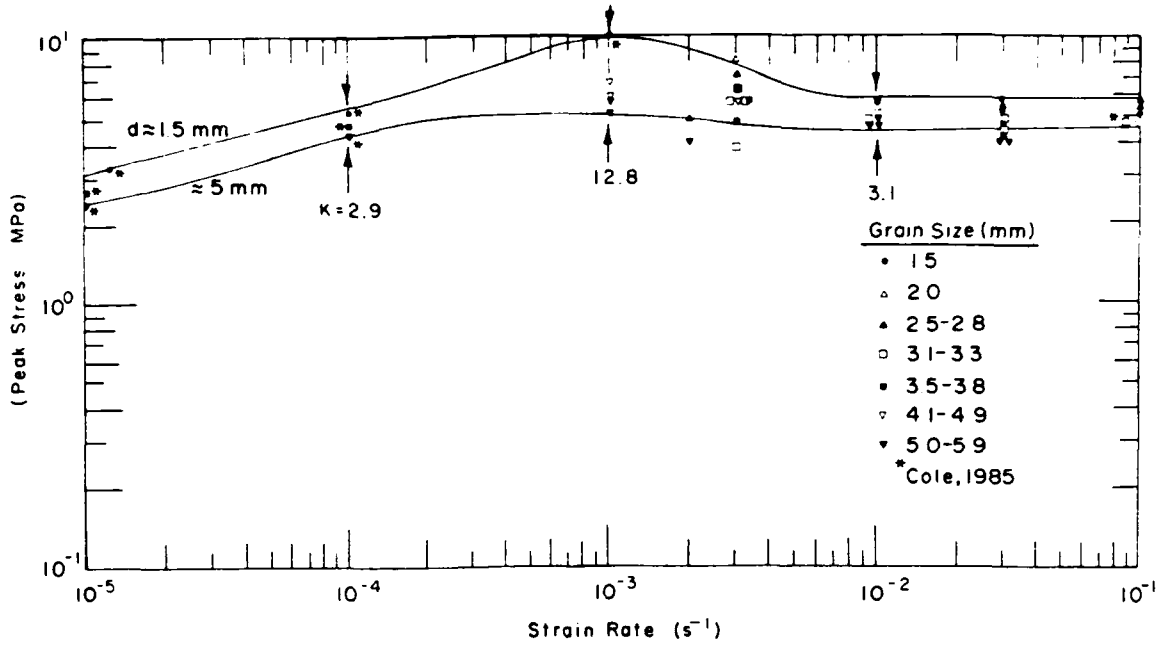

Figure 5. Peak compressive stress vs strain rate for freshwater, equiaxed ice samples tested by Cole (1987). The k value for the Hall-Petch relationship is indicated at strain rates ranging from 10^{-4} to 10^{-2} s^{-1}.

microstructural parameters control the failure processes in the saline ice. Both Cole (1988) and Schulson (1986) suggested that the observed relationship between strength and grain size in freshwater ice is based on the controlling influence that grain size has on the formation of microcracks within the material. Note that the mechanisms that these authors propose as an explanation of the grain size dependency describe several different processes. The explanations put forward seem quite plausible in a single phase system such as freshwater ice, where the individual grains are free of voids and the ice contains no brine. The saline ice, however, is a multiphase system. Within each grain of the columnar ice there is a system of ice platelets and brine pockets. The brine pockets contain either a highly concentrated saline brine solution or, if the brine has drained, air. In the frazil ice, pockets of high brine concentration are found between the individual ice crystals. These networks of brine inclusions may interrupt the progress and influence of cracks and dislocations in the saline ice. They may also significantly alter the internal stress distribution in the loaded ice sample. Hence, we might expect that another microstructural parameter, such as the distance between brine pockets, controls the failure process in saline ice.

One additional and very important factor that cannot be overlooked is that the frazil and columnar ice differ in their fundamental crystal texture, the frazil being equiaxed granular and the columnar consisting of elongated grains. The freshwater tests that we have used for comparison consider the grain size effect in samples of one texture. No work has been done to specifically determine the failure process in either the granular or columnar saline ice. While freshwater ice has been studied extensively as an equiaxed, polycrystalline aggregate, the work done on columnar, freshwater ice is limited (Gold 1970). Gold's work should be extended using current test techniques and equipment.

CONCLUSIONS

Compression tests on saline frazil and columnar ice at a strain rate of 10^{-3} s^{-1} indicate that the finer-grained frazil ice reaches a consistently higher strength than the columnar ice at comparative porosities. An inverse relationship between strength and grain size has also been reported in several studies on freshwater, equiaxed ice. This relationship is much more pronounced, however, in the freshwater ice test results. This difference may be due to the presence of brine in the saline ice and its influence on the deformational processes in this multi-phase system. While we can only speculate as to the specific influence of the brine inclusions until more careful work is done, we can conclude that the results of studies on freshwater ice cannot be directly extended to explain the variation in strength between the columnar and frazil

saline ice. Studies need to be initiated to investigate the failure process in both columnar and frazil saline ice, specifically. Until such work is completed, caution should be taken in developing hypotheses that interpret the behavior of saline ice based on freshwater ice studies.

ACKNOWLEDGMENTS

This is contribution No. 170 of the Alfred Wegener Institute for Polar and Marine Research.

REFERENCES

Cole, D.M. (1988) Crack nucleation in polycrystalline ice, *Cold Regions Science and Technology*, **15**(1988): 79–87.

Cole, D.M. (1987) Strain-rate and grain size effects in ice. *Journal of Glaciology*, **33**(115): 274–280.

Cole, D.M., L.D. Gould and W.D. Burch (1985) A system for mounting end caps on ice specimens. *Journal of Glaciology*, **31**(109): 362–365.

Cox, G.F.N. and W.F. Weeks (1983) Equations for determining the gas and brine volumes in sea ice samples, *Journal of Glaciology*, **29**(2): 306–316.

Gold, L.W. (1970) Process of failure in ice. *Canadian Geotechnical Journal*, **7**(405): 405–413.

Gow, A.J., S.F. Ackley, K.R. Buck and K.M. Golden (1987) Physical and structural characteristics of Weddell Sea pack ice. USA Cold Regions Research and Engineering Laboratory, CRREL Report 87-14.

Kuehn, G.A. (1988) The structure and properties of laboratory-grown saline ice and first-year sea ice, Presented at Dartmouth College, Thayer School of Engineering, June 21 and 22 1988.

Lange, M.A., S.F. Ackley, P. Wadhams, G.S. Dieckmann and H. Eicken (In press) Development of sea ice in the Weddell Sea, Antarctica. *Annals of Glaciology*, **12**: 92–96.

Mellor, M., G.F.N. Cox and H.W. Bosworth (1984) Mechanical properties of multiyear sea ice: Testing techniques. USA Cold Regions Research and Engineering Laboratory, CRREL Report 84-8.

Rand, J. and M. Mellor (1985) Ice-coring augers for shallow depth sampling. USA Cold Regions Research and Engineering Laboratory, CRREL Report 85-21.

Richter-Menge, J.A. (1986) Comparison of the compressive behavior of naturally and laboratory-grown saline ice. In *Proceedings of Second Workshop on Ice Penetration Technology, June 1986, Monterey, California*, p. 331–350.

Schulson, E.M. (1986) The fracture of ice Ih. Presented at the VIIth International Conference on the Physics and Chemistry of Ice, Grenoble, France, September 1–5, 1986.

Schulson, E.M. and N.P. Cannon (1984) The effect of grain size on the compressive strength of ice. In *IAHR '84, Hamburg, West Germany, Proceedings*. International Association for Hydraulic Research, p. 29–38.

Sinha, N.K. (1986) Young arctic frazil sea ice: Field and laboratory strength tests. *Journal of Materials Science*, **21**(5).

The Variation in the Triaxial Strength of Multiyear Sea Ice with Structure, Salinity and Density

P.R. SAMMONDS AND S.A.F. MURRELL
Department of Geological Sciences
University College
London, United Kingdom

Our interest is in the mechanical properties of ice under low temperature triaxial test conditions. We have performed 160 confined constant displacement rate tests on multiyear sea ice under a range of rates up to 10^{-2}/s, temperatures down to –40°C and confining pressures up to 30 MPa, using a 100-mm × 40-mm-diameter test specimen.

The specimens for these tests were taken from sea ice cores, 800-mm × 350-mm-diameter, gathered from a single multiyear sea ice floe, off Buckingham Island in the Canadian Arctic Archipelago, during a British Petroleum expedition. Cores were taken through the thickness of the floe (which was 9 m thick).

The structure, salinity and density of the sea ice were found to vary considerably, which caused a great variation in ice strength. This natural variability of the sea ice is discussed and comparisons are made with published studies on multiyear sea ice.

C. Biological and Sediment Inclusions in Sea Ice

Sea Ice
A habitat for the Foraminifer *Neogloboquadrina pachyderma*?

G. DIECKMANN, M. SPINDLER, M.A. LANGE, S.F. ACKLEY*AND H. EICKEN

Alfred Wegener Institute for Polar and Marine Research
Bremerhaven, Federal Republic of Germany

*U.S. Army Cold Regions Research and Engineering Laboratory
Hanover, New Hampshire, U.S.A.

ABSTRACT/INTRODUCTION

Sea ice of the polar regions is a habitat for a variety of organisms ranging from bacteria, microalgae and protozoans to metazoans such as copepods and small amphipods. Larger animals such ctenophores, krill (*E.superba*), fish and their larvae, as well as penguins and seals frequent the ice/sea interface in order to feed or seek protection (Horner 1985, Garrison et al. 1986, Marschall 1988). Many of the organisms living in the ice grow and reproduce to form what are known as assemblages (Horner et al. 1988), sea ice microbial communities (Sullivan et al. 1985, Garrison et al. 1986) or sympagic communities (Carey 1985). Furthermore, it is very likely that most organisms living in this environment are adapted to and dependent on it for at least part of their life cycle.

The list of organisms comprising the faunal component of sea ice biota is rapidly increasing (Carey 1985), the additions often being new species or genera (Corliss and Snyder 1986, Dahms and Dieckmann 1987,) which in many cases may spend most of their life cycle within the ice.

One organism which has also only recently been found to frequently occur in sea ice of the polar regions is the foraminifer *Neogloboquadrina pachyderma* (Carsola 1953, Lipps and Krebs 1974, Spindler and Dieckmann 1986). Lipps and Krebs (1974) were the first to suggest that the sea ice probably served as a nursery and refuge for juvenile foraminifer which profited from the high algal biomass in the ice. While Spindler and Dieckmann (1986) provide evidence, that *N. pachyderma* were able to survive in sea ice even during winter, they could also only speculate on reasons for the patchy distribution and extent of their occurrence in Antarctic sea ice on both a small and large-scale, and on the mode in which they are incorporated into the ice.

Mechanisms by which microorganisms may be incorporated into sea ice have been postulated by Garrison et al. (1983), Dieckmann et al. (1986) and Ackley et al. (1988). These authors provide different explanations on how planktonic microorganisms may be "harvested" from the water column and included in the ice during its formation.

In this paper we report on a large-scale survey of the Weddell Sea pack ice and water column carried out during the Winter Weddell Sea Project 1986 (WWSP '86) from midwinter to austral spring. We conclude that the incorporation of *N. pachyderma* into sea ice is related to ice formation processes and that their incorporation into the ice is not necessarily accidental but may indicate an overwintering strategy. These observations can have implications for the use of *N. pachyderma* as a marker for water masses since foraminifers growing in the ice may have a different isotopic configuration to those living in the seawater only.

MATERIAL AND METHODS

Data were collected during the (WWSP '86) with RV *Polarstern* on the cruise Leg ANT V/2 from 12 July to 17 September and Leg ANT V/3 from 29 September to 14 December.

The cruise tracks as well as the various types of stations occupied and referred to in the text are shown in Figure 1.

New ice samples (grease ice), consisting of frazil

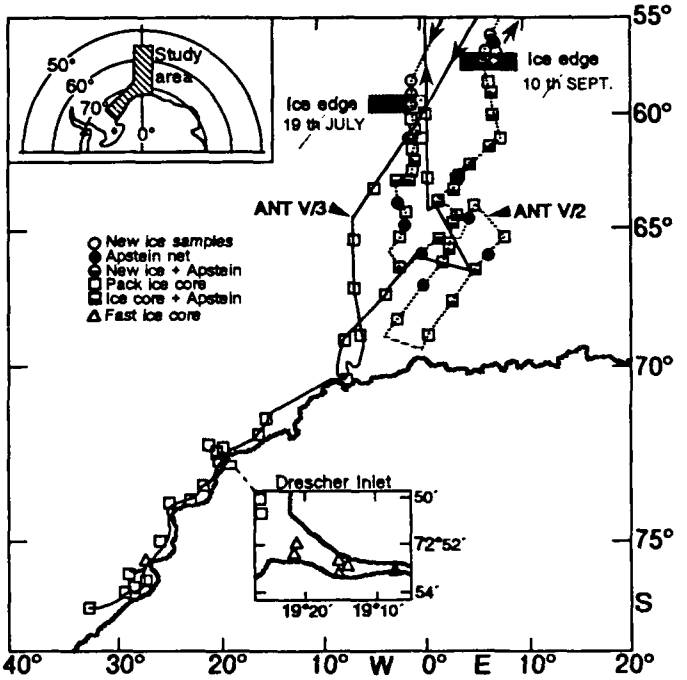

Figure 1. Map of (WWSP '86) study area showing cruise tracks ANT V/2 and ANT V/3 with various station types occupied.

crystals as disaggregated slush in seawater, of approximately 1-liter volume were sampled (skimmed off the sea surface) from the rail of the ship, using a 5-µm mesh dip net. Samples were allowed to melt at 0°C. Foraminifers were picked from the samples, counted and measured under an inverted or dissecting microscope.

Sea ice cores were collected using both 7.5- and 10-cm diameter modified SIPRE and CRREL ice augers. The cores were returned to the ship's cold laboratory in PVC tubes, where one core (10-cm diameter) was subdivided for physical, chemical and biological analyses as described by Lange et al. (1989). After thawing, the biological subsample was analyzed for salinity using a WTW-conductivity meter and for chlorophyll *a* after Evans and O'Reilly (1983). Foraminifers were picked out of the subsample prior to these analyses and counted as described above. In several cases a 7.5-cm-diameter core was cut into 10-cm sections which were melted in 3 to 5 liters of 0.2-µm filtered seawater at 0°C (Spindler and Dieckmann 1986). Foraminifers in these samples were counted after sieving through a 10-µm net.

During ANT V/2 an Apstein-net with a 17-cm mouth opening and 20-µm mesh net was hauled vertically through the water column over a depth of 60 m immediately before or after collection of the sea ice samples (Fig. 1). Samples were preserved in 0.5% buffered formaldehyde and foraminifers analyzed in the same manner as the sea ice samples.

RESULTS AND DISCUSSION

New ice samples were only obtained at the ice edge upon entering the pack ice or on the way out, during Leg ANT V/2 (Table 1). Numbers of *N. pachyderma* (per unit volume) in the new ice exceeded those in the immediately underlying water column of 60-m depth by up to two orders of magnitude. The average number in the water column was 4.5 per liter, while that in all new ice samples was 320 per liter, i.e., higher by a factor of 70.

The size distribution of foraminifers incorporated into newly forming sea ice closely resembles that of the foraminifers collected from the water column. (Fig. 2), indicating that incorporation of the foraminifers was not selective.

Occurrence and distribution of foraminifers in the consolidated pack ice of the northeastern Weddell Sea and underlying water column (ANT V/2) is shown in Figure 3. Numbers of *N. pachyderma* in the pack ice as well as in the water column vary considerably both on a horizontal and vertical scale. As could be expected from the analysis of new ice, the numbers in the pack ice were also much higher, per unit volume, than in the underlying water column. The highest numbers of foraminifers in the water column were found near the ice edge on the outward track. Numbers decreased further into the pack ice with the lowest being encountered near the ice shelf.

Table 1. Foraminiferal numbers in new ice and underlying water column collected at the ice edge during Leg ANT V/2.

Position	*Foraminifer (n/l)*	
Lat. /Long.	*in new ice*	*in water column*
59°S 1°W	15	0.4
59°S 1°W	85	
59°30°S 1°W	450	
60°45°S 1°W	45	
60°45°S 1°W	1075	
60°45°S 1°W	845	
61°S 1°W		0.2
58°58´S 6°42´E		2.6
61°30´S : 6°E	105	12.7
56°40´S 6°35´E	225	
56°29´S 6°41´E		8.4
56°29´S 6°41´E	345	3.2
56°28´S 7°15´E		3.8
57°10´S 7°16´E	170	
56°58´S 7°11´E	150	
Average	320	4.5

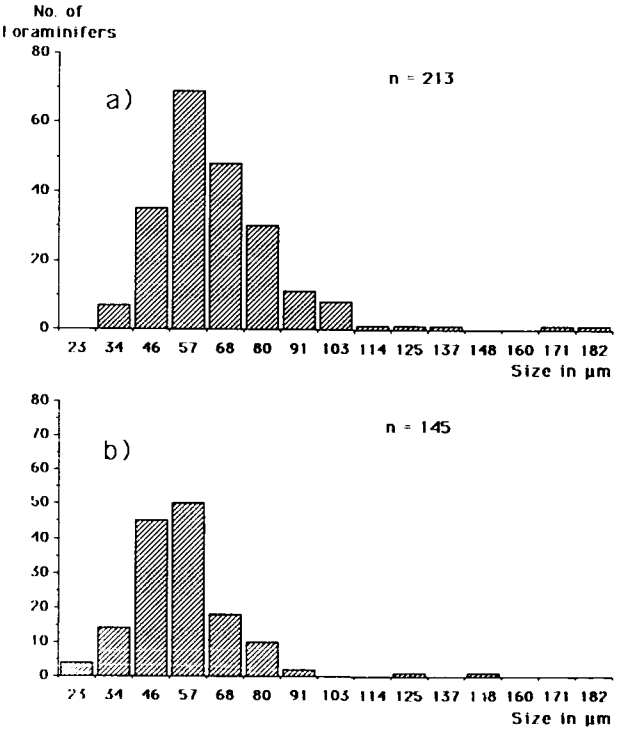

Figure 2. Size frequency distribution of N. pachyderma *in the upper 60 m of the water column (a) and in the overlying new ice (b) at the ice edge during ANT V/2.*

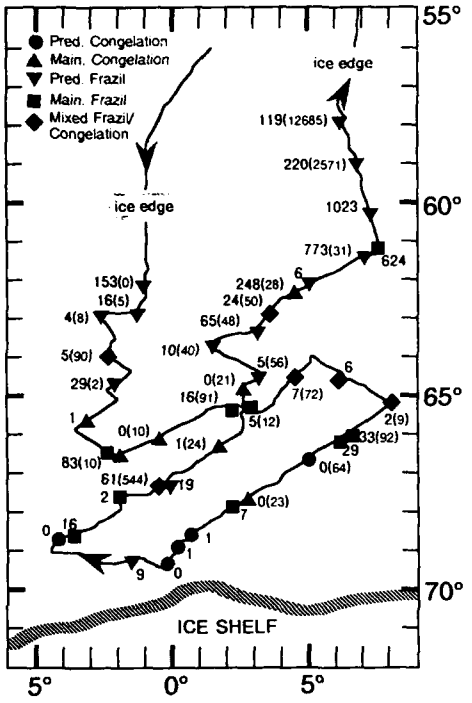

Figure 3. Leg ANT V/2: Numbers of N. pachyderma *per liter of pack ice of different genetic ice classes (bold numbers) and in 60 m of underlying water column (numbers in brackets).*

An accurate quantitative estimate of *N. pachyderma* in the water column throughout the depth in which they occur is difficult to obtain since their size frequency distribution varies with depth. Juveniles tend to frequent the upper layers while large individuals occupy the deeper layers which were not sampled with the Apstein net. Foraminifer numbers integrated over the ice thickness can therefore only be compared with those in the water column to a depth of 60 m (Table 2). *N. pachyderma* were found to occur throughout the pack ice, but were not evenly distributed. In Leg ANT V/2 samples, their numbers ranged from 0 to over 1000 per liter of sea ice (average 87). Integrated over the depth of the ice (average thickness of 85 cm), this amounts to 6.38×10^3 m^{-2} which is almost equivalent to 6.25×10^3 m^{-2}, the average number found in a 60-m water column.

The heterogeneous distribution of *N. pachyderma* in the pack ice is to some extent attributable to various ice formation processes and is thus related to different genetic ice classes. Sea ice formation processes and genetic ice classes encountered in the area investigated are described in detail by Wadhams et al. (1987), Lange et al. (1989) and Eicken and Lange (1989). Essentially the sea ice in the area of investigation can be categorized into three genetic classes which are further differentiated resulting in a total of 5 or 6 subclasses depending on the area where the ice was formed. The genetic ice classes are defined on the basis of various textural ice classes (Table 3).

Distribution of *N. pachyderma* in sea ice cores relative to these differ . ice classes reveals a good rela-

Table 2. Leg ANT V/2: Ice thickness and *N. pachyderma* in pack ice and underlying water column of 60 m.

Station	Core length (m)	Ice core (Forams/core)	Sea ice (Forams/L)	Sea ice (Forams/m^2)	Water (Forams/m^2)
255	0.67	77	14	9890	0
255	0.67	951	173	121190	
255	0.67	1491	271	189700	
259	0.92	115	16	14700	300
263	0.48	15	4	1980	480
268	0.42	18	5	2360	5400
274	—	—	—	—	120
275	0.62	139	29	17700	
280	0.5	2	1	300	
284	0.55	171	40	21800	600
284	0.99	972	125	123000	
286	0.44	0	0	0	600
291	0.43	88	20	11300	5460
293	0.72	32	7	4150	4320
297	0.6	32	6	4110	
303	0.52	8	2	1090	540
307	0.6	142	33	18100	5520
307	4	742	29	94400	
312	0.45	0	0	0	3840
315	0.62	0	0	0	1380
315	4.29	239	7	30400	
317	0.62	5	1	660	
319	0.45	4	1	520	
317	0.4	0	0	0	
317	0.88	252	37	32100	
319	0.54	0	0	0	
322	0.95	68	9	8690	
325	0.31	0	0	0	—
325	0.97	89	16	18030	—
327	1.01	20	2	2660	—
331	0.43	196	61	25000	32640
331	0.94	143	19	18300	—
338	0.47	4	1	550	1440
344	0.6	23	5	3050	720
351	0.41	0	0	0	1260
353	—	—	—	—	3360
354	0.65	28	5	3660	—
363	0.5	41	10	5320	2400
367	1.04	196	65	67700	2880
370	0.4	77	24	9930	3000
375	1.15	2247	248	286000	1680
375	0.24	11	6	1420	—
381	—	—	—	—	1860
381	0.91	6745	773	858000	—
382	0.48	2306	624	293000	—
384	0.51	4098	1023	521000	—
390	0.31	536	220	68300	—
391	—	—	—	—	154260
393	0.35	328	119	41800	—
396	—	—	—	—	761100
400a	—	—	—	—	502380
400b	—	—	—	—	189600
Average	0.85	493	87	63756	62487

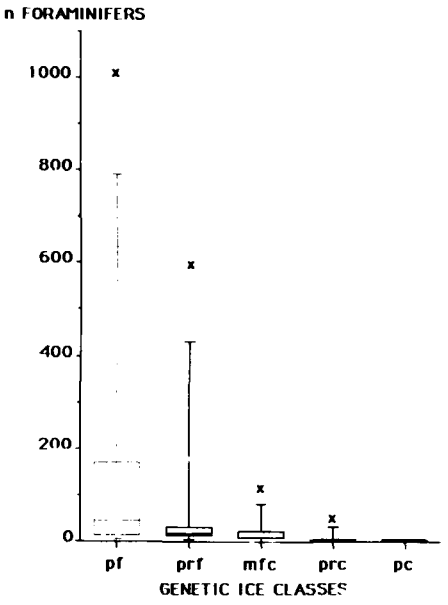

Figure 4. Box plot of N. pachyderma *in pack ice of different genetic ice classes: pf = predominantly frazil, prf = mainly frazil, mfc = mixed frazil columnar, prc = mainly congelation and pc = predominantly congelation ice. x's denote the extreme values; whiskers the main body of the data; outlined central box the middle half of the data between the 25th and 75th percentiles and the horizontal line across the box represents the median.*

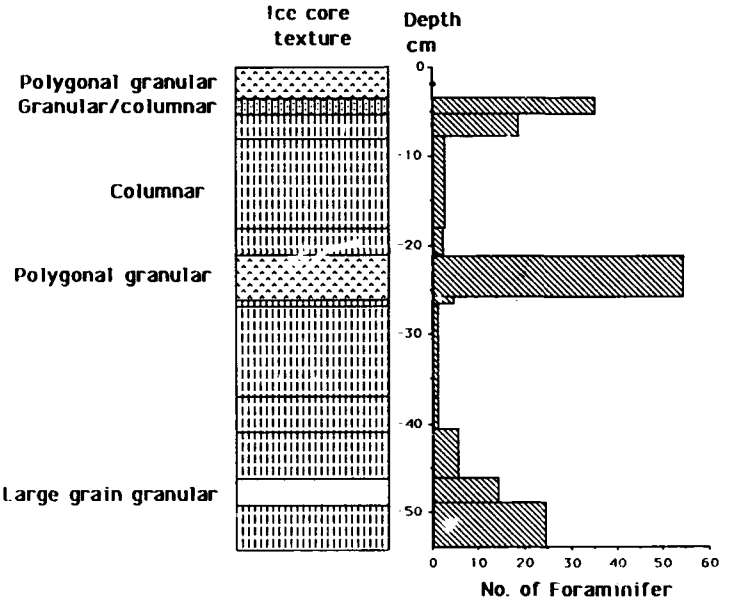

Figure 5. An example of N. pachyderma *distribution in relation to textural ice classes in pack ice core AN52207-1 collected during ANT V/2.*

Table 3. Textural classes by grain characteristics and genetic classes for Antarctic sea ice based on percentage of various textures in the core depth (after Lange et al. 1989).

Textural classes	*Genetic classes*
1. Granular	1. Predominantly frazil
a) polygonal granular	2. Mainly frazil
b) orbicular granular	3. Predominantly congelation
2. Columnar	4. Mainly congelation
3. Intermediate Columnar/granular	5. Mixed frazil/ Congelation
4. Mixed Columnar/granular	
5. Platelet	

tionship between genetic ice class and foraminiferal occurrence as well as abundance (Fig. 4). Despite the large variation in numbers within the various classes, the highest numbers of *N. pachyderma* were clearly encountered in the pure frazil ice class, while mean numbers decrease with an increase in the fraction of congelation ice.

Figure 5 shows a typical example of *N. pachyderma* distribution within an ice core in relation to the ice texture. Highest numbers are again distinctly associated with the granular ice which is of frazil origin.

A comparison of the distribution of foraminifers with that of core chlorophyll *a* in all the cores collected did not show a significant correlation. However, an examination of individual cores did reveal

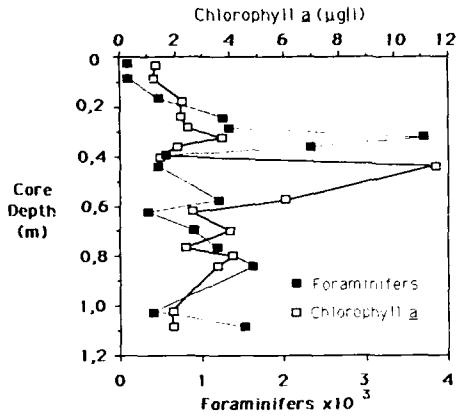

Figure 6. Distribution of chlorophyll a and N. pachyderma *in core AN52245-1 in relation to core depth.*

that the higher foraminiferal numbers were usually associated with elevated chlorophyll levels as shown in the example in Figure 6.

Foraminiferal occurrence in sea ice collected during Leg ANT V/3 showed an essentially similar distribution in relation to ice texture as in sea ice collected during Leg Ant V/2. However, the characteristic ice formation processes at the ice shelf also have additional effects on the distribution and occurrence of *N. pachyderma* in sea ice of this region (Eicken and Lange 1989). Thus we found several ice cores consisting of pure or predominantly frazil ice containing no or very few foraminifers. These were nearly all collected in the vicinity of the the ice shelf in relatively thin ice, i.e., recently formed ice. Since this ice was collected early in spring it is very likely that the water column at this time was still devoid of plankton, meaning that there were no foraminifers there when the ice was formed (Fig. 7).

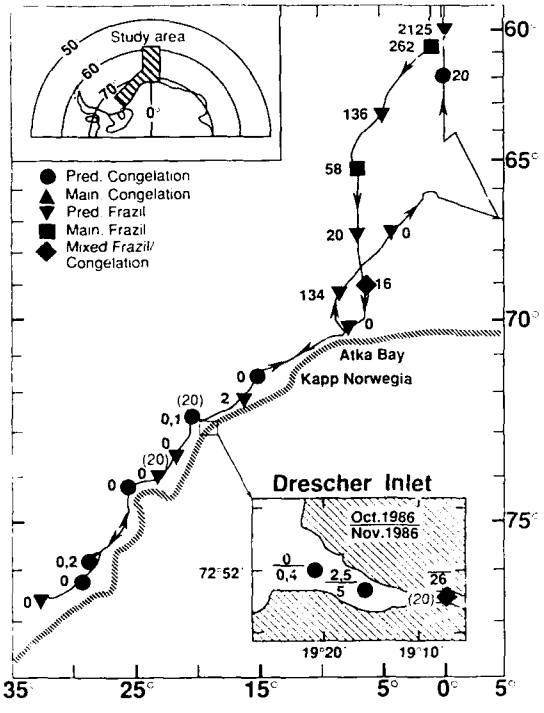

Figure 7. Leg ANT V/3: Numbers of N. pachyderma per liter of pack ice of different genetic ice classes (bold numbers). Numbers in brackets denote proportion of ice platelets as percentage of ice core volume.

The results clearly indicate that *N. pachyderma* are incorporated into newly forming sea ice when it is formed dynamically usually in the presence of waves (frazil textures). The foraminifers can subsequently usually be found in consolidated sea ice which consist substantially of the products of such ice formation processes (Wadhams et al. 1987, Lange et al. 1989). Evidence for mechanisms of incorporation have been proposed by several authors. However, it is still unclear how and out of which range or region in the water column these organisms are "harvested" (Garrison et al., this volume; Shen and Ackerman, this volume). Even in the present case we do not know if the organisms occurred near the surface, i.e., in the neuston, or were in fact distributed evenly throughout the 60-m water column. On the other hand hauls from deeper than 60 m also contained considerable numbers of foraminifers and it is known that *N. pachyderma* is usually associated with high phytoplankton biomass in the water column.

Despite this uncertainty, it is evident that the foraminifers are not able to or in fact do not elude the passage of frazil ice crystals through the water column during ice formation. This means that substantial numbers of *N. pachyderma* are forced to or voluntarily spend at least part of their life cycle in sea ice .

Once incorporated into the ice, the foraminifers are forced to occupy interstitial brine pockets and channels within the ice matrix. The size of these cavities is dependent on ice texture and strongly fluctuating temperatures and salinity (Weeks and Ackley 1982, Maykut 1985). Thus as temperatures in the ice decrease down to below –10°C, salinities may rise to above 150‰ as more and more ice is formed.This means that the actual space or volume of fluid occupied by *N. pachyderma* is a very small fraction of the entire ice volume, meaning that they are even more concentrated per unit volume of fluid in sea ice relative to the water column than when compared to total ice volume.

Sea ice may therefore appear to be a hostile environment. However, it has several advantages when compared with the open water column. Those of

importance with respect to *N. pachyderma* are:

1. The availability of an abundant food source during periods when the water column is devoid of phytoplankton.

2. Protection from many predators which are unable to enter the ice.

3. Conservation of energy as constant buoyancy compensation is not necessary.

Evidence that *N. pachyderma* survive in the ice was provided by Spindler and Dieckmann (1985). They found that many of the foraminifers, which had evidently been incorporated into sea ice at the onset of its formation, were still alive in summer and had increased in size during their migration to the bottom of the ice. Small individuals that had not been successful in evading the extremely harsh conditions which prevail near the ice surface during winter, had succumbed. *N. pachyderma* is the only known foraminifer capable of surviving salinities of up to 82‰ (Hemleben et al. 1988). Sea ice in the Weddell Sea grows mainly dynamically, rather than thermodynamically (Eicken and Lange 1989, Lange et al. 1989). Thus a large fraction of the sea ice accretion or growth takes place in a "pancake cycle," a sequence of processes leading to rapid formation of ice 0.5 to 0.6 m thick (Wadhams et al. 1987). A prerequisite for such a process is that it begins at the advancing ice edge where waves are present and turbulence in the water column is high. This coupled with the fact that biological activity at the advancing ice edge is high (Dieckmann 1987) means a potentially higher source of organisms which can be incorporated into sea ice where it is being formed.

REFERENCES

Ackley, S.F., G. Dieckmann and H. Shen (1988) Algal and foram incorporation into new sea ice. *EOS Transactions, American Geophysical Union*, 68(50): 1736.

Carey, A.G. Jr. (1985) Marine ice fauna: Arctic. In *Sea Ice Biota* (R.A. Horner, Ed.). Boca Raton, Florida: CRC Press, p. 21–83.

Carsola, A.J. (1953) Possible planktonic occurrence of *Globigerina pachyderma* (Ehrenberg). *Journal of Paleontology*, 27: 742–743.

Corliss J.O. and R.A. Snyder (1986) A preliminary description of several new ciliates from the Antarctic, including *Cohnilembus grassei* N.SP. (1). *Protistologica*, **T22**(fasc. 1): 39–46.

Dahms H-U and G. Dieckmann (1987) *Drescheriella glacialis* gen.nov., sp.nov. (Copepoda, Harpacticoida) from Antarctic sea ice. *Polar Biology*, 7: 329–337.

Dieckmann, G., G. Rohardt, H. Hellmer and J. Kipfstuhl (1986) The occurrence of ice platelets at 250 m near the Filchner Ice Shelf and its significance to sea ice biology. *Deep-Sea Research*, **33**: 141–148

Eicken H. and M.A. Lange (1989) Development and properties of sea ice in the coastal regime of the southeastern Weddell Sea. *Journal of Geophysical Research*, **94**(C6): 8193–8206.

Evans and O'Reilly (1983) A handbook for the measurement of chlorophyll *a* in net plankton and nannoplankton. BIOMASS Handbook No. 9. SCAR/SCOR/IABO/ACMRR Group of specialists on Living Resources of the Southern Ocean.

Garrison, D.L., A.R. Close and E. Reimnitz (1989) Microorganisms concentrated by frazil ice. This volume.

Garrison D.L., S.F. Ackley and K.R. Buck (1983a) A physical mechanism for establishing algal populations in frazil ice. *Nature*, **306**: 363–365.

Garrison, D.L., C.W. Sullivan and S.F. Ackley (1986) Sea ice microbial communities in Antarctica. *BioScience*, **36**: 243–250.

Henkben, C.H., M. Spindler and O.R. Anderson (1988) *Modern Planktonic Foraminifera*. New York: Springer Verlag, p. 363.

Horner, R.A. (1985) Ecology of sea ice microalgae. In *Sea Ice Biota* (R.A.Horner, Ed.). Boca Raton, Florida: CRC Press, p. 83-103.

Horner, R.A., E.E. Syversten, D.P. Thomas and C. Lange (1988) Proposed terminology and reporting units for sea ice algal assemblages. *Polar Biology*, **8**: 249–253.

Lange, M., S.F. Ackley, P. Wadhams, G.S. Dieckmann and H. Eicken (1989) Development of sea ice in the Weddell Sea. *Annals of Glaciology*, **12**: 92–96.

Lipps, J.H. and W.N. Krebe (1974) Planktonic foraminifera associated with antarctic sea ice. *Journal of Foraminiferal Research*, **4**: 80–85.

Marschall, H.-P. (1988) The overwintering strategy of antarctic krill under the pack ice of the Weddell Sea. *Polar Biology*, **9**: 129–135.

Shen, H.T. and N.L. Ackerman (1989) Wave-induced sediment enrichment in coastal ice covers. This volume.

Spindler, M. and G. Dieckmann (1986) Distribution and abundance of the planktonic foraminifer *Neogloboquadrina pachyderma* in sea ice of the Weddell Sea (Antarctica). *Polar Biology*, **5**: 185–191.

Sullivan, C.W., A.C. Palmisano, S.T. Kottmeier, S.M. Grossi and R. Moe (1985) The influence of light on growth and development of the sea-ice microbial community of McMurdo Sound. In *Antarctic Nutrient Cycles and Food Webs* (W.R. Siegfried, P.R. Condy and R.M. Laws, Ed.). Berlin–Heidelberg: Springer-Verlag, p. 78–83.

Wadhams, P., M.A. Lange and S.F. Ackley (1987) The ice thickness distribution across the Atlantic sector of the Antarctic Ocean in midwinter. *Journal of Geophysical Research*, 92(C3): 14535–14532.

Weeks, W.F. and S.F. Ackley (1982) The growth structure and properties of sea ice. USA Cold Regions Research and Engineering Laboratory, Monograph 82-1.

Microorganisms Concentrated by Frazil Ice
Evidence from Laboratory Experiments and Field Measurements

D.L. GARRISON AND A.R. CLOSE
Institute of Marine Sciences,
University of California
Santa Cruz, California, U.S.A.

E. REIMNITZ
U.S. Dept. of the Interior Geological Survey
Menlo Park, California, U.S.A.

ABSTRACT

A number of studies have suggested that high concentrations of organisms in sea ice may be the result of harvesting and concentration by frazil ice. In laboratory experiments we were able to show that frazil ice can concentrate organisms from two to four times above levels in the underlying water. The concentrations in nature, however, can be considerably higher. The apparent discrepancy between laboratory results and field observations can be explained by the longer temporal and spatial scale that allows more contact of ice crystals with particles and with one another in the field. It is also likely that small-scale circulation features, such as Langmuir circulation, enhance the ability of frazil ice to concentrate organisms in a natural setting.

INTRODUCTION

A number of studies have reported that organisms ranging from microalgae to foraminifera may be harvested from the water column and concentrated in newly forming sea ice (e.g., Bunt 1968, Bunt and Lee 1970, Lipps and Krebes 1974, Garrison et al. 1983, Spindler and Dieckmann 1986, Ackley et al. 1987, Watanabe and Satoh 1987, Dieckmann et al. 1986a,b,1988, Spindler et al., in press). One mechanism proposed to explain high concentrations of organisms in young ice is that frazil ice crystals form on suspended particles, and the particles encounter and adhere to frazil ice crystals as they form and rise to the sea surface (Ackley 1982, Garrison et al. 1983). Although the process of frazil ice formation has been studied in the laboratory (e.g., see Martin 1981), the question of how organisms are incorporated has received little attention. We have examined the ability of frazil ice to harvest organisms in the laboratory and have related these results to measurements of algal concentration in samples of new and young ice from the antarctic pack ice.

METHODS

Laboratory experiments

Laboratory experiments were designed to determine if frazil ice crystals could harvest and concentrate suspended algal cells. Frazil ice was produced in a Plexiglas column with an aluminum base plate to promote ice formation at the bottom of the column (Fig. 1). Frazil ice crystals that formed at the base of the chamber were able to rise through approximately 1.9 m of seawater before they accumulated at the top of the chamber.

Experimental runs consisted of suspending algal cells in the seawater-filled column, measuring the concentration of chlorophyll *a* before the start of ice formation, allowing frazil ice to form and surface slush ice to accumulate, and then to measure the concentrations of chlorophyll *a* in ice and seawater at the end of the experiment. A stirring motor in the base of the chamber was used to produce and maintain a homogeneous distribution of seawater and suspended particles until ice formation was initiated. An initial chlorophyll sample was collected by siphon from mid-column before the beginning of ice formation. Frazil ice generated at the the base of the column rose to the surface until 500 to 1200 mL of slush ice had accumulated at the surface. The surface slush ice was retained and analyzed for chlorophyll *a* concentration.

After all ice was removed from the chamber, a second sample was drawn from the algal suspension remaining in the chamber. Ice samples were allowed to melt in the dark and both ice and water samples were then filtered on to GF/F glass fiber filters, and chlorophyll *a* was extracted with 90% acetone. Chlorophyll

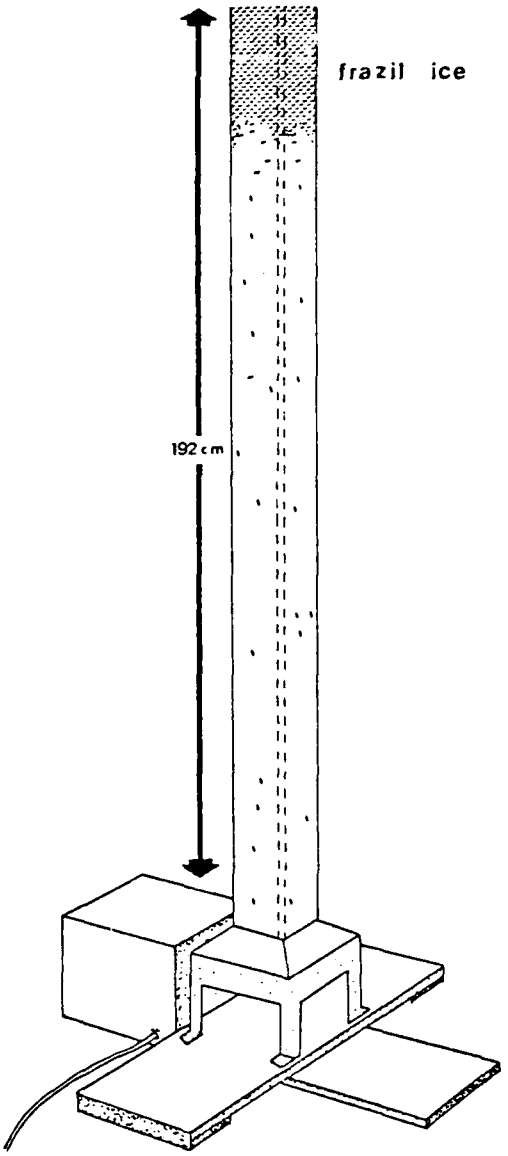

Figure 1. Diagram of frazil-ice-generating chamber (dimensions are 10.8 ×10.95 ×192.5 cm, volume approximately 25 L).

a concentrations were measured by standard fluorometric methods (Parsons et al. 1984). Generally, three replicate samples each of pre-freeze water, post-freeze water and frazil ice were collected and analyzed. There were two variations in our measurements of chlorophyll *a* in frazil ice. In the first three of seven experiments, the total chlorophyll in the surface slush ice was measured. In the latter experiments, the slush was collected and interstitial water allowed to drain in a strainer. Chlorophyll levels were then determined for both the remaining ice and the interstitial or "drain" water. All experiments were conducted in a −20°C coldroom.

The algal cultures used in the experiments were diatoms (primarily *Nitzschia* sp. and *Chaetoceros neogracile*) isolated from antarctic pack ice and maintained in rough cultures at University of California–Santa Cruz. For experimental work, cultures were grown to high densities in 2.7-L flasks. These were transported on ice to the laboratory at the U.S. Geological Survey on the day of the experimental runs, where they were diluted with enough cold, filtered seawater to fill the experimental chamber.

Field samples

We sampled sea ice in several stages of ice formation and growth as part of our field studies in 1980, 1985, 1986, 1987, and 1988. Chlorophyll *a* was measured in both ice and in the water column, and thickness and other characteristics of the ice were also recorded as part of our studies.

RESULTS

In all of our laboratory experiments the concentration of algae in the frazil ice that accumulated at the surface of the ice-generating chamber was higher than in the initial suspension in the water (Fig. 2a–g). In two of the experiments, however, there was considerable variability among the replicate chlorophyll *a* measurements, so that the mean concentrations were not significantly higher (Fig. 2d,g). The concentration factors (chlorophyll *a* in ice/chlorophyll *a* in the underlying water) averaged 1.8 ±0.9 with a maximum of ~4. Although the initial concentrations of chlorophyll *a* in the experiments were higher than those found in natural conditions, there was no indication that concentration factors were related to concentration of initial suspension, the organisms used, the duration of the experimental run, or to the amount of frazil ice formed. The absolute concentrations of chlorophyll *a* retained by ice were a linear function of pre-freeze concentrations normalized by volume of ice formed (Pearson correlation $r = 0.997$, $N = 7$), suggesting that the algal cells harvested were a function of the encounters between ice crystals and cells.

In field samples we have found a considerable amount of variability in chlorophyll *a* among the various types of new and young sea ice (Fig. 3a). Many of these measurements represent concentration factors that agree with the ~2- to 4-fold concentrations we were able to produce in the laboratory experiments (Fig. 3b). However, other samples ranged to over 80 times the concentration of the underlying water column.

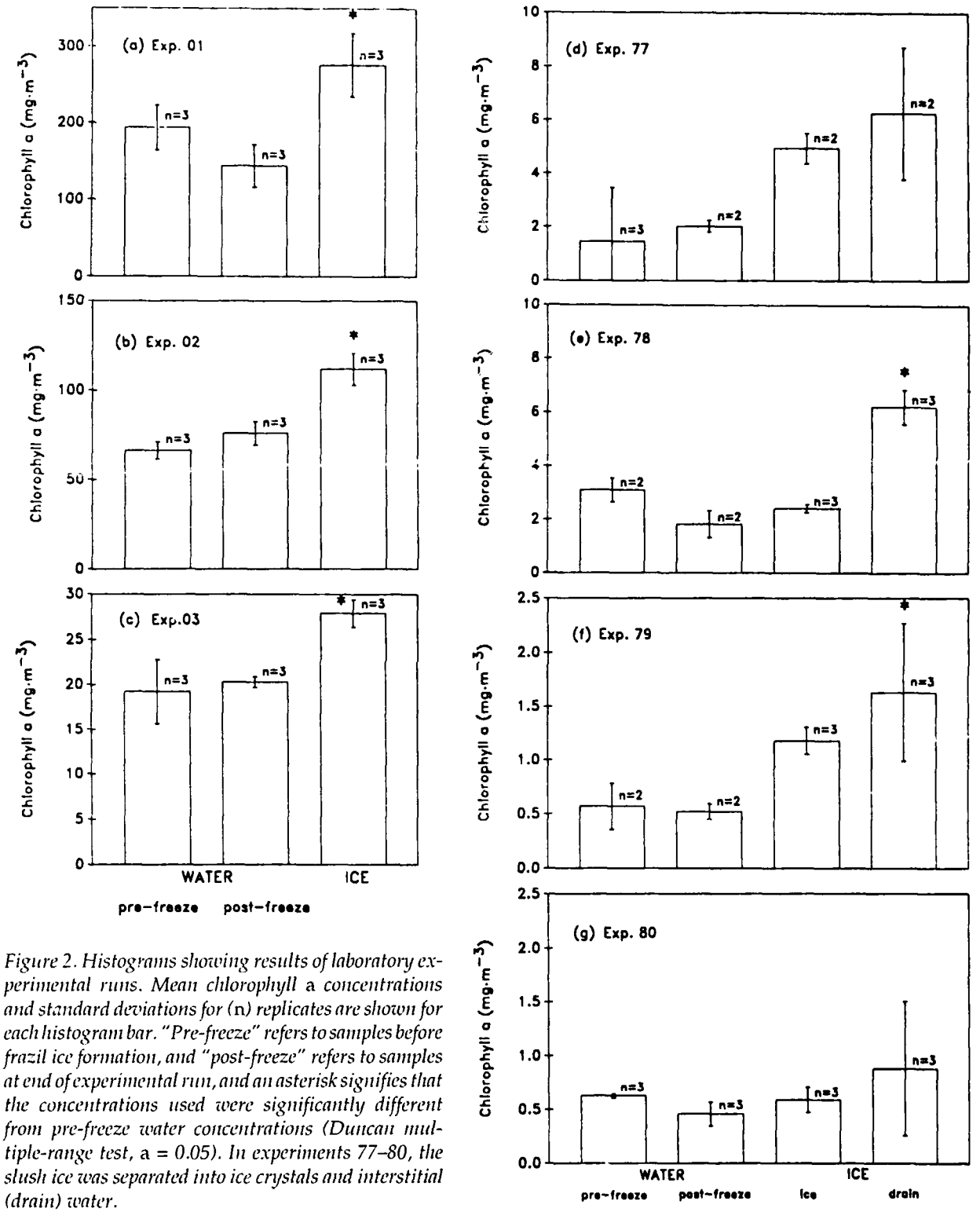

Figure 2. Histograms showing results of laboratory experimental runs. Mean chlorophyll a concentrations and standard deviations for (n) replicates are shown for each histogram bar. "Pre-freeze" refers to samples before frazil ice formation, and "post-freeze" refers to samples at end of experimental run, and an asterisk signifies that the concentrations used were significantly different from pre-freeze water concentrations (Duncan multiple-range test, a = 0.05). In experiments 77–80, the slush ice was separated into ice crystals and interstitial (drain) water.

DISCUSSION

In all of the laboratory experiments frazil ice showed an ability to harvest and concentrate algal cells from the underlying water; thus, the ability for frazil ice to trap algal cells has been adequately demonstrated. The higher chlorophyll *a* concentration in the "drain" water, as compared to that retained by ice crystals, suggests that the mechanism is a simple trapping (or filtration), but nucleation cannot be entirely ruled out as a concentrating factor in these experiments.

The concentration factors of chlorophyll *a* in natural samples were often considerably higher than we were able to produce in the laboratory. The >5 to >10 times higher concentration found in grease ice and very young pancake ice is convincing evidence that physical concentration takes place in nature (Fig. 3; also Garrison et al. 1983). There are, however, differences in ice formation in the field and in the laboratory that account for the apparent discrepancy. In the laboratory, the contact between suspended cells and rising ice crystals is limited to the <2-m path of the rising frazil ice crystals over the few minutes required for them to reach the surface. The depth at which frazil ice forms in the deep-water pack ice regions is not known. Thermohaline convection, which Weeks and Ackley (1982) propose as one mechanism for generating frazil ice at sea, can extend to tens of meters (Foster and Weiss 1988, T. D. Foster, personal communication; also see Dieckmann et al. 1986a). In the field, we have also observed horizontal drift of several meters as frazil ice forms and aggregates at the surface. Moreover, during the duration of the laboratory experiment (usually about 30 minutes), there is limited time for contact between ice crystals so that flocculation, which occurs in nature (see Martin 1981), is less likely. We suspect that both increased encounters between suspended cells and frazil ice crystals and increased filtration (or harvesting) efficiencies of flocculated frazil ice result in higher concentration factors in nature, but it would be impractical to scale up the experimental apparatus to test this directly.

We believe that there are secondary mechanisms that operate in conjunction with frazil ice harvesting to produce the concentrations of organisms found in ice in nature. Langmuir circulation (e.g., Bainbridge 1957, Stavn 1971) is a likely mechanism. Langmuir circulation clearly aggregates frazil ice in converging circulation cells (see Fig. 5 in Martin 1981), and this surface aggregation of frazil ice crystals should act as a filter for suspended organisms transported in these circulation cells. The scale of the Langmuir circulation is sufficient to produce most of the concentration that we observed in nature. For example, we calculated that the concentration factors observed in the field could be explained by harvesting cells from 1- to 2-m depth. In the extreme concentration, the harvesting would still be less than 6 m. Since high concentrations in ice vs low concentrations in the water column are likely to be found after harvesting, this calculation is a conservative estimate of the depth of harvesting.

Ackley et al. (1987) and Shen and Ackermann (1988, 1989) have suggested another mechanism, which requires a wave field propagating through a layer of surface frazil to concentrate suspended material in ice. This model has not been extensively evaluated with experimental evidence or with field observations. Such a mechanism seems unlikely to explain the concentrations of algae in antarctic pack ice that was formed under relatively calm conditions where waves were either not present or where they would be markedly damped (e.g., see Martin 1981, Weeks and Ackley 1982).

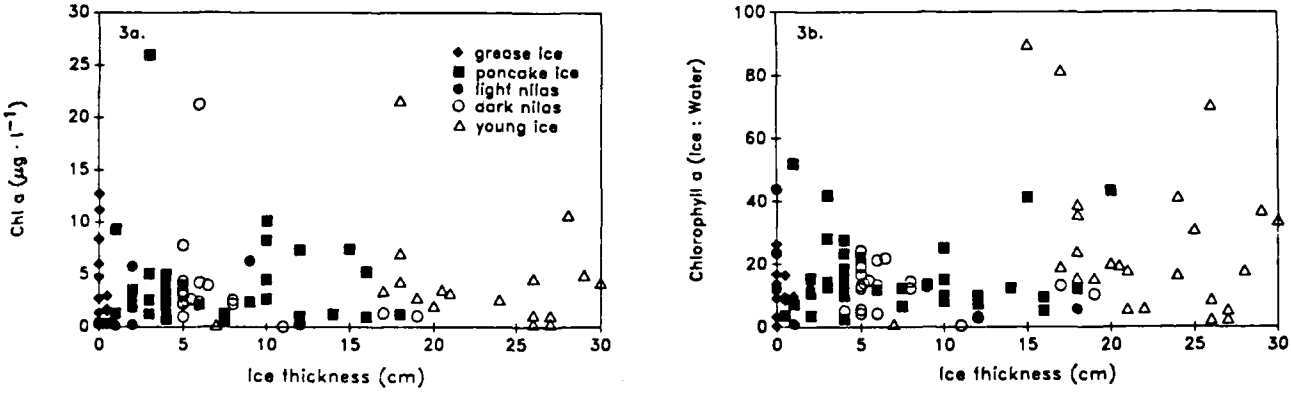

a. Absolute concentrations.

b. Concentration factor expressed as a ratio of chlorophyll a in ice to chlorophyll a in the underlying water.

Figure 3. Chlorophyll a in newly forming and young sea ice as a function of ice type and thickness.

ACKNOWLEDGMENTS

This study was supported by National Science Foundation Grant to D. L. Garrison (DPP 84-20184) and USGS support to E. Reimnitz. We thank Laura Gilman and William Weber for their assistance in running the experiments, and Ed Kempema for developing the experimental apparatus. Discussions with T.D. Foster were helpful in evaluating the physical conditions under which ice forms in nature.

LITERATURE CITED

Ackley, S.F. (1982) Ice scavenging and nucleation: Two mechanisms for incorporation of algae into newly formed sea ice. *Eos*, **63**: 54.

Ackley, S.F., G. Dieckmann and H. Shen (1987) Algal and foram incorporation into new sea ice. *Eos*, **68**: 1736.

Bainbridge, R.(1957) The size, shape and density of marine phytoplankton concentrations. *Biological Review*, **32**: 91–115.

Bunt, J.S. (1968) Microalgae of the antarctic pack-ice zone. In *Symposium on Antarctic Oceanography* (R.I. Currie, Ed.). Scott Polar Research Institute, Cambridge, p. 198–218.

Bunt, J.S. and C.C. Lee (1970) Seasonal primary production in Antarctic sea ice at McMurdo Sound in 1967. *Journal of Marine Research*, **28**: 304–320.

Dieckmann, G.S., G. Rohardt, H. Hellmer and J. Kipfstuhl (1986a) The occurrence of ice platelets at 250-m depth near the Filchner Ice Shelf and its significance for sea ice biology. *Deep-Sea Research*, **33**: 141–148.

Dieckmann, G.S., M.A. Lange and S.F. Ackley (1986b) Sea ice biota and ice formation processes in the Weddell Sea during winter. *EOS*, **67**: 1005.

Dieckmann, G.S., M.A. Lange, M. Spindler and S. Ackley (1988) The foraminifer *Neogloboquadrina pachyderma* in sea ice of the Weddell Sea. *Eos*, **69**: 1262.

Foster, T.D. and R.F. Weiss (1988) Antarctic bottom water formation in the northwestern Weddell Sea. *Antarctic Journal of the U.S.*, **23** (in press).

Garrison, D.L., S.F. Ackley and K.R. Buck (1983) A physical mechanism for establishing algal populations in frazil ice. *Nature*, **306**: 363–365.

Lipps, J.H. and W.N. Krebes (1974) Planktonic foraminifera associated with antarctic sea ice. *Journal of Foraminiferal Research*, **4**: 80–85.

Martin, S. (1981) Frazil ice in rivers and oceans. *Annual Review of Fluid Mechanics*, **13**: 379–397.

Parsons, T.R., Y. Maita and C. Lilli (1984) *A Manual of Chemical and Biological Methods for Seawater Analysis*. Oxford: Pergamon Press.

Shen, H. and N.I. Ackermann (1988) Wave-induced sediment enrichment in ice covers. *Eos*, **69**: 1262.

Shen, H.T. and N. Ackermann (1989) Wave-induced sediment enrichment in coastal ice covers. This volume.

Spindler, M. and G.S. Dieckmann (1986) Distribution and abundance of the planktic Foraminifer *Neogloboquadrina pachyderma* in sea ice of the Weddell Sea (Antarctica). *Polar Biology*, **5**: 185–191.

Spindler, M., G.S. Dieckmann and M.A. Lange (1989) Seasonal and geographic variations in sea ice community structure of the Weddell Sea, Antarctica. *Polar Biology* (in press).

Stavn, R. (1971) The horizontal–vertical distribution hypothesis: Langmuir circulations and *Daphnia* distributions. *Limnology and Oceanography*, **16**: 453–466.

Watanabe, K. and H. Satoh (1987) Seasonal variations of ice algal standing crop near Syowa Station, East Antarctica, in 1983/84. *Bulletin of the Plankton Society of Japan*, **34**: 143–164.

Weeks, W.F. and S.F. Ackley (1982) The growth, structure, and properties of sea ice. USA Cold Regions Research and Engineering Laboratory, CRREL Monograph 82-1.

Suspended-Matter Scavenging by Rising Frazil Ice

E. REIMNITZ, E.W. KEMPEMA, AND W.S. WEBER
U.S. Geological Survey
Menlo Park, California, U.S.A.

J.R. CLAYTON AND J.R. PAYNE
Science Applications International Corporation
San Diego, California, U.S.A.

ABSTRACT/INTRODUCTION

Widespread occurrence of sediment-laden (turbid) sea ice and high concentrations of diatoms and foraminifers in new ice relative to the underlying water have recently been reported from both polar hemispheres (i.e., Barnes et al. 1982, Ackley 1982, Garrison et al. 1983, Dieckman et al. 1986, Reimnitz and Kempema 1987a,b, Thiede 1988, Kempema et al. 1989). Many possible mechanisms of particle entrainment into ice have been postulated (Osterkamp and Gosink 1984); scavenging by rising frazil ice and adhesion of ice onto suspended particles are the most widely accepted. No reliable experimental data on the mechanisms are available. Because of the geological importance of sediment rafting by ice (Reimnitz and Kempema 1987b), we designed and constructed tanks in which frazil crystals produced naturally at the bottom can be monitored rising through nearly 2 m of water column charged with various types of particulate matter, including plankton (Fig. 1). We here report on observations and measurements made in saltwater.

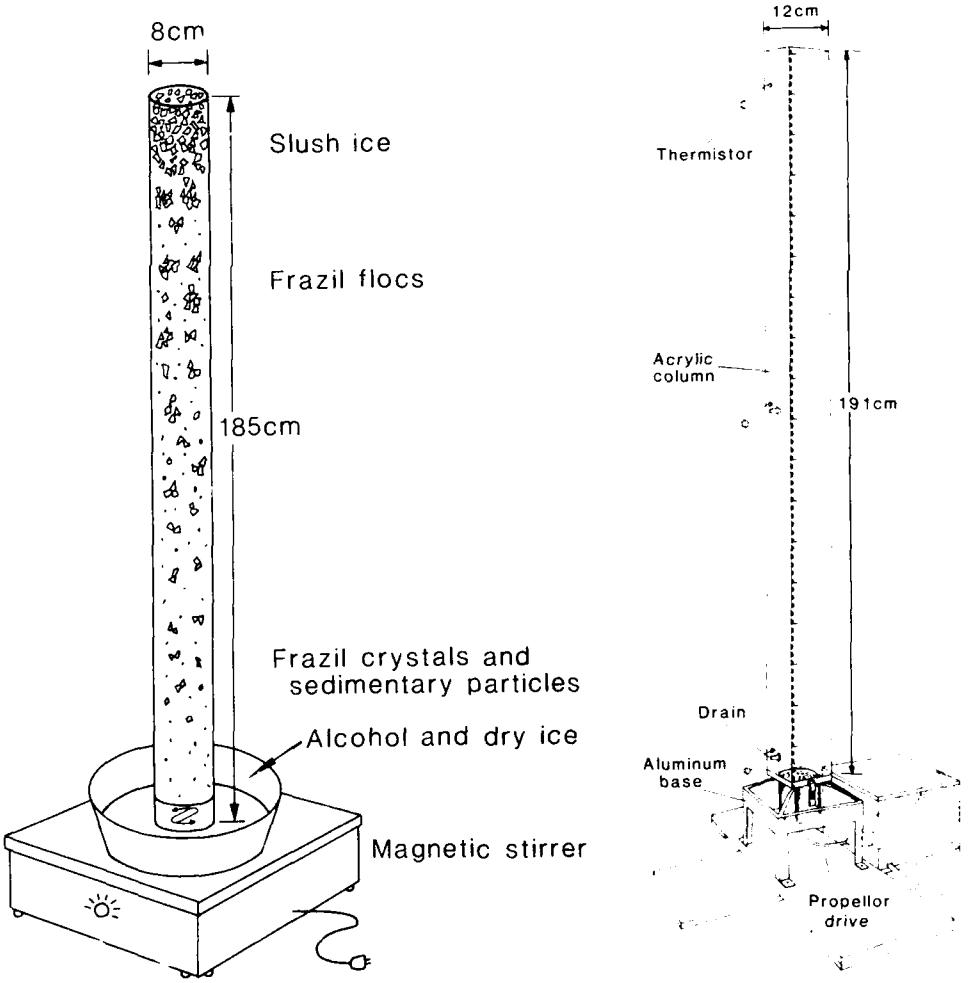

Figure 1. Experimental apparatus used in the study of sediment/frazil interaction: (A) simple version using a plastic core-liner stirred with a magnet, (B) improved, fat-walled version, stirred by an electric drill and paddle, with an aluminum heat exchanger to produce frazil in the base.

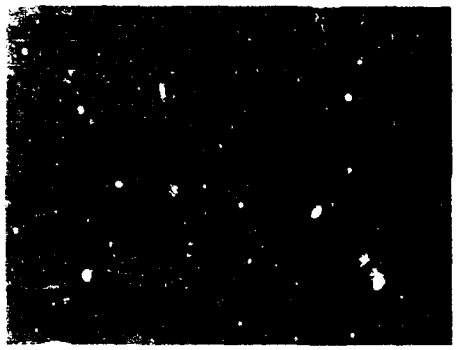

a. Frazil 60 cm above the base.

b. Frazil 120 cm above the base with one 2-cm- diameter floc.

Figure 2. Photographs of frazil ice.

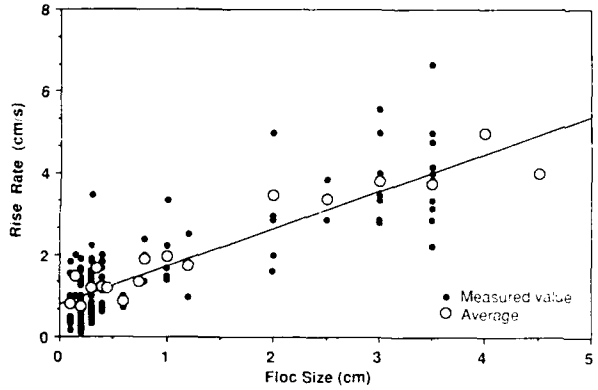

Figure 3. Scatter diagram of frazil floc rise rates as a function of size.

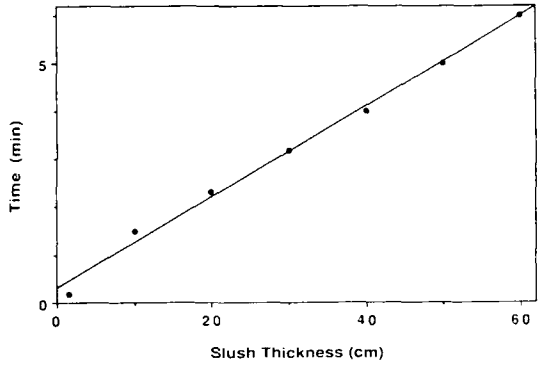

Figure 4. Scatter diagram of surface slush accumulation during one experiment.

RESULTS

Over a distance of 1.5 m, <1-mm-diameter frazil is observed to grow to crystals or flocs several centimeters in diameter (Fig. 2), rising at average rates of 2 to 3 cm/s. Measured rise rates are a function of frazil size (Fig. 3); the scatter in data is a function of local turbulence from flocs and crystals with very different rise rates occurring together and interacting. A typical accretion rate for the surface slush-ice layer containing sediment is 5 cm/min (Fig. 4). Concentrations of particulate matter were obtained by sampling from the tank at about mid-depth, and by skimming the surface slush layer, which, in some cases, was separated into interstitial water and frazil by draining over a sieve.

In 13 out of 17 experiments using various amounts of suspended silt and clay, frazil rising through less than 2 m of saltwater (in <2 min) resulted in increased sediment concentrations in the surface slush layer relative to those in the water column at the conclusion of the experiment (Fig. 5). In the few minutes available, plankton, consisting dominantly of live copepods, is concentrated in frazil to values 10 times higher than in the water (experiment 56). Diatom concentrations (measured as chlorophyll-*a*), were highest in the water that drains from the sieve in which surface slush ice was collected (drain water, experiments 77 through 80). In clear water charged with rapidly settling sand grains or with plankton, rising ice flocs were observed to bump particles upward or to temporarily drag them upward in their turbulent wakes. Particles were also trapped in the crystal skeleton of flocs, where they commonly became locked-in by continuing floc accretion.

In these tests we saw no clear evidence for ice adhesion onto particles. However, frazil effectively scavenges suspended particulate matter from the water in several minutes of travel under conditions which in nature may last for days and for which available suspended sediment theories do not apply. Aggregates called marine snow, similar in size to frazil flocs, accelerate particle settling rates, and are thought responsible for much of the vertical sediment mass

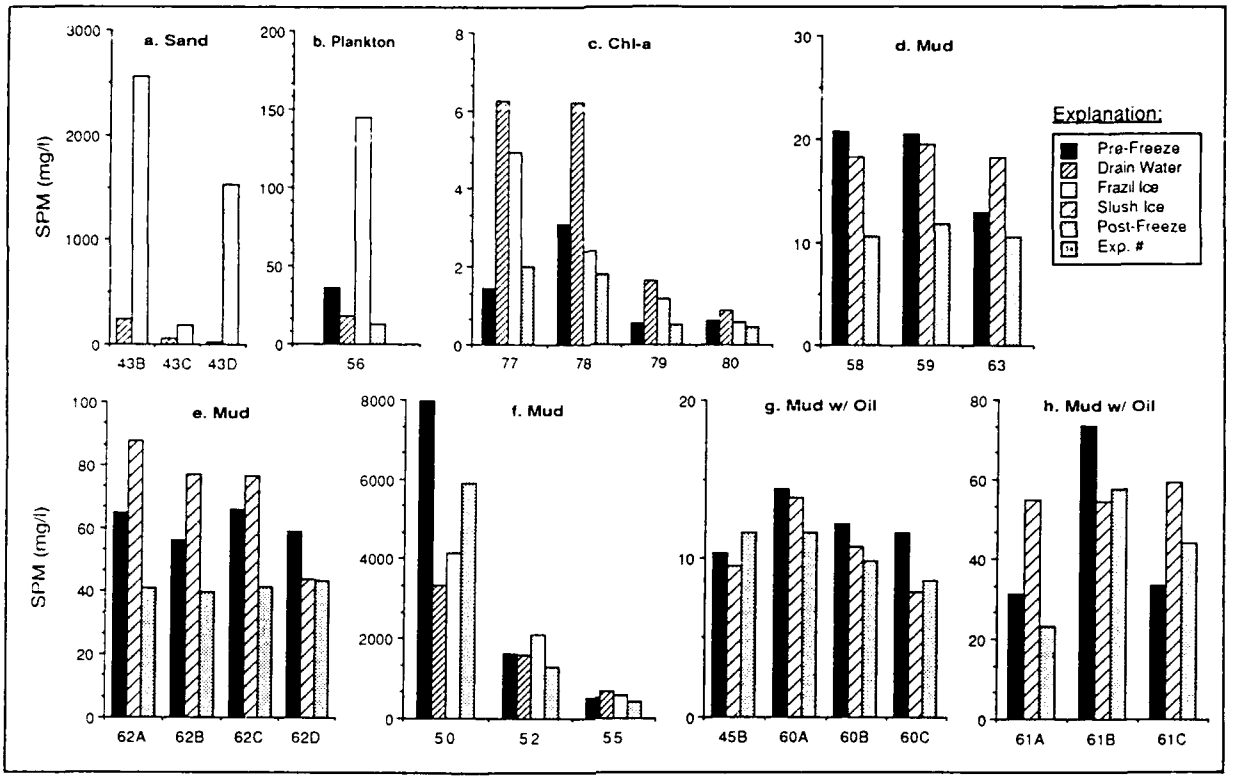

Figure 5. Histograms showing concentrations of suspended particulate matter (SPM) and planktonic organisms in 1) tank at mid-depth before ice formed (pre-freeze), 2) interstitial water from surface slush (drain water), 3) frazil ice after drainage of interstitial water from surface slush (frazil), 4) combined interstitial water and frazil (slush ice), and 5) tank at mid-depth at the conclusion of experiment (post-freeze). Most values are averages for 2–3 subsamples.

flux at some settings in low latitudes (Wells and Shanks 1987). In the presence of positively buoyant frazil, the settling of particulate matter is retarded or reversed, leading to upward sediment flux. The ultimate result is turbid ice, which is capable of rafting sediment over great distances.

ACKNOWLEDGMENTS

The measurements on scavenging of live diatom cultures were obtained through cooperation with A.R. Close and D.L. Garrison (see companion paper in this volume).

REFERENCES

Ackley, S.F. (1982) Ice scavenging and adhesion: two mechanisms for incorporation of algae into newly-forming sea ice. *Eos*, **63**(3): 54.

Barnes, P.W., E. Reimnitz and D. Fox (1982)Ice rafting of fine grained sediment, a sorting and transport mechanism, Beaufort Sea, Alaska. *Journal of Sedimentary Petrology*, **52**(2): 493–502.

Dieckmann, G.S., M.A. Lange and S.F. Ackley (1986) Sea ice biota and ice formation processes in the Weddell Sea during winter. *Eos*, **67**(44): 1005.

Garrison, D.L., S.F. Ackley and K.R. Buck (1983) A physical mechanism for establishing algal populations in frazil ice. *Nature*, **306**: 363–365.

Kempema, E.W., E. Reimnitz and P.W. Barnes (1989) Sea ice sediment entrainment and rafting in the Arctic. *Journal of Sedimentary Petrology*, **59**(2).

Osterkamp, T.E. and J.P. Gosink (1984) Observations and analysis of sediment laden sea ice. In *The Alaska Beaufort Sea: Ecosystem and Environment* (P.W. Barnes, D.M. Schell, and E. Reimnitz, Ed.). San Francisco: Academic Press, p. 73–94.

Reimnitz, E. and E.W. Kempema (1987a) Field observations on slush ice generated during freeze-up in arctic coastal waters. *Marine Geology*, **77**: 219–231.

Reimnitz, E. and E.W. Kempema (1987b) Ice rafting: an indication of glaciation? *Journal of Glaciology*, **654** (117): 254–255.

Thiede, J. (1988) Scientific cruise report of Arctic Ex-

pedition ARKIV/3. Berichte zur Polarforschung, Alfred Wegener Institute for Polar and Marine Research, Bremerhaven, Germany, no. 43.
Wells, J.T. and A.L. Shanks (1987) Observations and geologic significance of marine snow in a shallow-water, partially enclosed marine embayment. *Journal of Geophysical Research*, **92**(C1 2): 13,185–13,190.

Wave-Induced Sediment Enrichment in Coastal Ice Covers

H.T. SHEN AND N.L. ACKERMANN
Department of Civil and
Environmental Engineering
Clarkson University,
Potsdam, New York, U.S.A.

ABSTRACT/INTRODUCTION

In arctic regions, fine-grained sediments have often been observed to accumulate in great quantities within coastal ice covers. The sediment concentrations in these covers are often observed to be several orders of magnitude greater than that in the underlying water column. Field observations have also indicated that the sediment concentration within the ice cover increases downward to an abrupt interface formed by the division between the sediment-laden ice and the still lower layer of sediment-free ice (Barnes et al. 1982, Reimnitz and Kempema 1986). A similar phenomenon of enrichment of algal population in sea ice has been observed (Ackley et al. 1979, Horner 1980). The concentration of sediment in the ice cover can have important biological and geological consequences and can create significant alterations to the thermal and mechanical properties of the ice cover.

The mechanism by which the fine-grained sediments are concentrated within the ice cover is poorly understood. Osterkamp and Gosink (1984) listed nine possible scenarios by which sediment can become entrained in coastal ice covers, and suggested that scavenging (Osterkamp and Gosink 1984), interstitial trapping, and filtering (Naidu 1980) as the most possible mechanisms. Reimnitz and Kempema (1986) ruled out these mechanisms as the cause of sediment enrichment in coastal ice covers. Our laboratory experiments using a turbulence jar also show that no sediment enrichment can be produced by these mechanisms. In these experiments, frazil ice was produced in a tank of water containing fine-grained sediments that were kept in suspension by the turbulent field created by a submerged oscillating grid. Sediment concentrations in the frazil ice accumulations at the surface of the tank were found to be 60 to 70% lower than the concentration in the water column. In this paper, a wave-related sediment enrichment mechanism is proposed. This enrichment process considers that floating slush ice in a wave field is subjected to a wave-induced vertical oscillatory pressure at its base. This oscillatory pressure produces a periodic flow that flushes suspended sediment into and out of the slush ice. With the continuous action of the cyclic flow, and the deposition of sediment on surfaces of ice particles in the slush, the sediment concentration in the ice cover will increase as the freezing of the interstitial water continues.

THEORETICAL ANALYSIS

For a slush ice cover in a progressive wave field, the equation of motion for the ice cover can be expressed as:

$$m\frac{\partial^2\eta}{\partial t^2} = -mg + \delta p + \nu_i \rho_i t_i \left(\frac{\partial^3\eta}{\partial^2 x \partial t}\right) \qquad (1)$$

where t_i = slush layer thickness
η = the vertical displacement of the ice/water interface
m = the time-dependent mass of the saturated ice mixture per unit surface area
ν_i = an effective kinematic viscosity of the slush ice
ρ_i = slush density
g = gravitational acceleration
δp = the excess pressure on the underside of the ice cover.

We will assume that the ice cover surface can be described by a progressive wave with wavelength λ and period T:

$$\eta = A\cos(kx - \omega t) \qquad (2)$$

where A = wave amplitude
k = wave number $2\pi/\lambda$
ω = wave frequency, $2\pi/T$.

The pressure δp under the ice cover can then be expressed as

$$\delta p = mg - m\omega^2\eta + \rho_i \nu_i t_i \omega\, Ak^2 \sin(kx-\omega t). \quad (3)$$

If we assume that the submerged ice thickness can be approximated by an average value, then the flow rate can be derived from Darcy's law. The flow rate q can be expressed as:

$$q = \left(\frac{ad^2 g}{\nu_f}\right)\left(\frac{\omega^2 A}{g}\right)(\cos\theta - \nu_i k^2 \sin\theta) \quad (4)$$

where q = rate of flow into the ice cover per unit area
θ = $kx-\omega t$
ν_i = kinematic viscosity of the sediment water mixture
d = ice particle size
ad^2 = permeability.

Flow into the ice canopy will transport a sediment load q_s. The removal efficiency of the ice cover is related to the residence time of the sediment in the cover and the fall velocity of the sediment, w_s.

Consider that the residence time is proportional to the ratio between the submerged thickness h_i and the sediment transport rate q_s. Then, the following functional relationship can be obtained for the volume of sediment, V_s, deposited in a unit area of the ice cover during a period of t^*:

$$\left(\frac{\nu_f}{w_s d_s}\right)\left(\frac{V_s}{C_s g t^{*2}}\right) = F\left[\frac{A}{gT^2} + C_2\left(\frac{\nu_i}{gT\lambda}\right)\left(\frac{A}{\lambda}\right)\left(\frac{\rho_f}{\rho_i}\right)\right] \quad (5)$$

where C_s = sediment concentration on the underside of the cover
d_s = average pore size in the ice cover
F = an unknown function
C_2 = a constant, both F and C_2 are to be determined experimentally.

PRELIMINARY LABORATORY TESTS

Preliminary tests were performed in a 300-cm-long wave tank with a thick slush cover placed on the surface of the water wave. By injecting a neutrally buoyant dye at the ice/water interface, the movement of water into the ice cover could be observed. In order to study the sediment transport phenomena in a more convenient manner, an oscillatory flow tank (a rigid transparent tank having a rectangular cross section) was used. In its upper portion, the tank is divided into two compartments with a plunger on one side to create an oscillatory flow. During experiments, the tank was filled with sediment on the bottom and slush ice on the surface. With the periodic flow generated by the plunger, the bottom sediment was suspended, and an increasing accumulation of sediment in the slush ice cover was observed. Figures 1–4 are photographs of sediment-enriched ice created in the experiments. The sediment-laden ice samples shown in these figures were obtained by freezing the entire slush-ice and water column in the tank. Figure 1 shows the frozen ice cover enriched with a bottom sediment consisting of a silt having a medium grain size of approximately 0.01 mm. Figure 2 shows a cut sample of silt-laden ice segments from a similar test. A photograph of these ice segments, when rotated, is shown in Figure 3. The ice column in Figure 4 was obtained from tests in which the bottom sediment consisted of a sand having a median grain diameter of 0.3 mm.

Figure 1. Silt-enriched ice cover: Short duration.

Figure 2. Segments of silt-enriched ice cover and portions of underlying frozen water column.

Figure 3. Segments shown in Figure 2 rotated to provide different perspective.

Figure 4. Segment of sand-enriched ice cover and portion of underlying frozen water column.

ACKNOWLEDGMENT

This study is supported by NSF Grant No. DPP-8721901.

REFERENCES

Ackley, S.F., K.R. Buck and S. Taguchi (1979) Standing crop of algae in the sea ice of the Weddell region. *Deep-Sea Research*, **26**: 269–282.

Barnes, P.W., E. Reimnitz and D. Fox (1982) Ice rafting of fine-grained sediment, a sorting and transport mechanism, Beaufort Sea, Alaska. *Journal of Sedimentary Petrology*, **52**(2): 0493–0502.

Horner, R.W. (1980) Plankton. In *Beaufort Sea Winter Watch, Ecological Processes in the Nearshore Environment* (D.M. Schell, Ed.). Fairbanks, Alaska: OSCEAP Arctic Project Office, University of Alaska, Special Bulletin 29.

Naidu, A.S. (1980) An alternative conceptual model for sediment concentration in frazil sea ice of north arctic Alaska. In *Beaufort Sea Winter Watch, Ecological Processes in the Nearshore Environment* (D.M. Schell, Ed.). Fairbanks, Alaska: OSCEAP Arctic Project Office, University of Alaska, Special Bulletin 29.

Osterkamp, T.E. and J.P. Gosink (1984) Observations and analysis of sediment-laden sea ice. In *The Alaska Beaufort Sea: Ecosystems and Environment* (P.W. Barns, D.M. Schell, and E. Reimnitz, Ed.). Orlando: Academic Press, Inc.

Reimnitz, E. and E.W. Kempema (1986) Field observations on slush ice generated during freeze-up in arctic coastal waters. Final Report on Freeze-up Studies, RU 205, Department of the Interior, U.S. Geological Survey Open-File Report 86-515, Menlo Park, California.

Sediment in Eurasian Arctic Sea Ice

I. WOLLENBURG AND S. PFIRMAN
GEOMAR
Research Center for Marine Geoscience
Federal Republic of Germany

M.A. LANGE
Alfred Wegener Institute for Polar and
Marine Research
Federal Republic of Germany

ABSTRACT/INTRODUCTION

In July and August 1987, sea ice investigations were conducted along a transect from northeast of Svalbard to the central Eurasian Arctic Basin (Fig. 1). The expedition proceeded along a transect of stations between 15° and 32°E longitude and from 81°N up to 86°22'N latitude. Because of heavy ice conditions the *Polarstern* turned back at this point and left the Arctic Ocean south through Fram Strait. Surface snow and ice sampling, ice coring and ice observations from the ship and helicopter represent the first large-scale survey of ice texture and sediment content in sea ice from the interior of the Arctic Basin. The main geologic objective of the sea ice program was to determine the contribution of sea-ice-rafted sediments to sedimentation in the Arctic, Norwegian/Greenland and Barents seas.

RESULTS

Although the 1987 investigations represent the first large-scale survey of sediment-laden ice in this region, many researchers have previously observed sediment-laden floes in the Arctic: Clark and Hanson (1983) reported large patches of particle-laden ice; Drewry (1986) noted that in the Nansen Basin north of Svalbard as much as 10% of the ice surface may be affected by accumulations of particulate material. Vinje (1985) observed in the Barents Sea that the areal coverage of "brownish ice" was as high as 20–30% of a given area; also the group of Barnes, Reimnitz and Kempema (pers. comm.) observed particle-laden sea ice during several years of sea ice investigations off eastern Alaska.

The first investigation of sea ice cores for lithogenic components was carried out by Larssen et al. (1987). In 1983 and 1984, Larssen et al. (1987) obtained 13 ice cores along two transects between the ice margin and Greenland, at 79° and 80°N. On our transect into the Eurasian Basin in 1987, 72 cores with a total length of 173 m were drilled at 31 stations. An average of two cores were obtained at each station. The shortest core was 38 cm; the longest one was 455 cm. In addition to sea ice coring, 102 large volume samples of surface snow/ice, mostly from "dirty" ice floes were taken. Observations of the distribution of the "dirty" ice, ridges and meltwater ponds, ratio of first-year to multiyear ice and ice concentration were carried out on 36 helicopter flights. Detailed map-

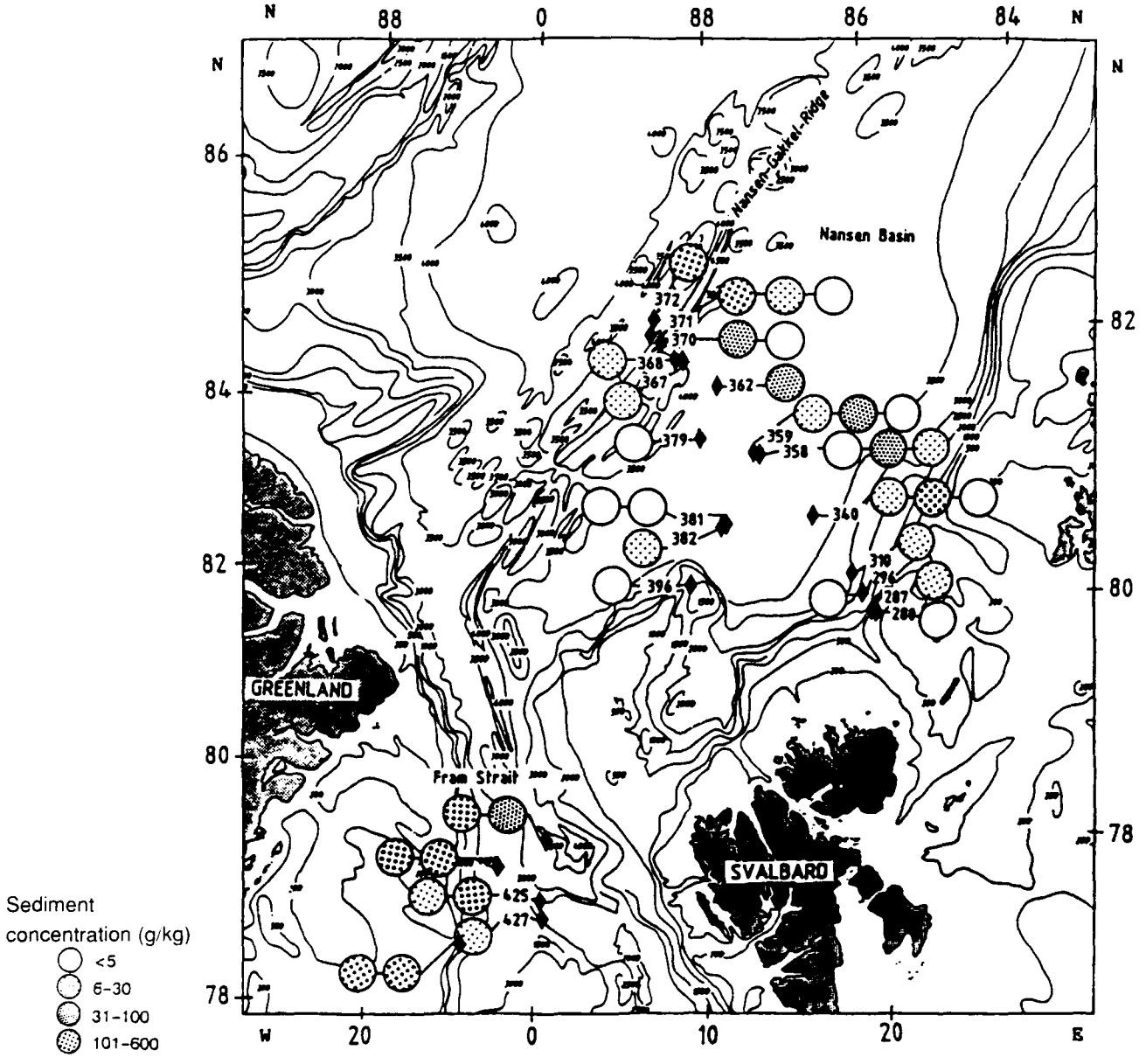

Figure 1. Concentration of sediment (g/cm) in surface sea ice samples obtained during the transect into the Eurasian Basin on the 1987 expedition with R/V Polarstern. *Highest concentrations were found in the area north of 84°N in the vicinity of the Transpolar Drift stream. Variable concentrations occur in Fram Strait, where the ice of the Transpolar Drift stream mixes with younger marginal ice with less sediment content, and old ice from the Beaufort Gyre.*

ping was carried out over an 8-mile grid to characterize the regional distribution of these dirty spots (Fig. 2). Because of the high sediment content observed in the Eurasian Arctic ice, sea ice investigations were continued in July and August 1988 in Fram Strait. Ice coring and surface snow sampling was carried out at 65 locations. Sea ice observations again documented the typical ice characteristics in this region and should aid in identifying "dirty" ice in satellite images. These observations were carried out in order to aid in estimating clastic sediment content and distribution in sea ice. However, such observations must be interpreted with care because 1) surface particle accumulations may contain a large biogenic component, 2) depending on the observation season deposits may be partially or totally masked by snow, and 3) surface observations exclude particle-rich layers occurring below the ice surface.

Two major circulation patterns characterize arctic sea ice drift. In the Amerasian Basin the Beaufort Gyre and the Transpolar Drift stream influence the waters of the Eurasian Basin. The Transpolar Drift

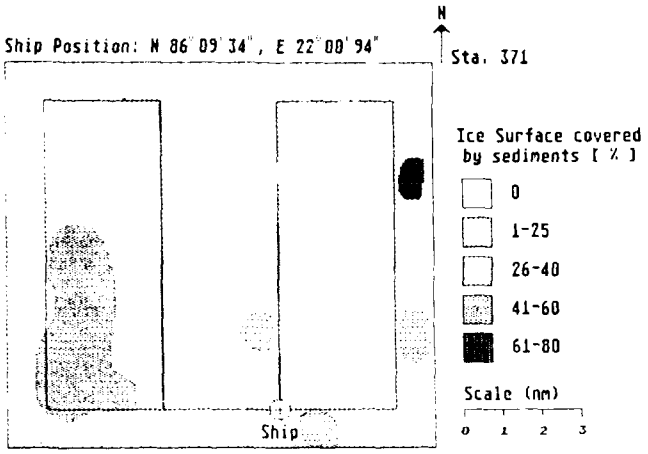

Figure 2. Example of a helicopter survey to map in detail the regional distribution of sediment accumulations on the ice surface. Ice characteristics were reported at 2-nmi intervals with continual notation of special features. 100% means the entire ice surface was covered by material accumulations (from Pfirman et al. 1989b).

stream transports sea ice from the shelf regions in the Kara, Laptev and East Siberian Seas where it is formed, westward over the Arctic Ocean. Drift trajectories of buoys deployed on the ice during our cruise (Pfirman et al. 1989a) showed that much of this ice exits the Arctic Basin through Fram Strait where the East Greenland current transports it further south. During 1987 and 1988 we observed very high sediment accumulations on the ice surface over areal extents greater than 15×15 km^2. Highest concentrations were found in the area north of 84°N in the vicinity of the Transpolar Drift stream. Variable concentrations of sediment-laden floes occur in Fram Strait, where the ice of the main path of the Transpolar Drift stream mixed with younger marginal ice with less sediment content, and old ice from the Beaufort Gyre system (Fig. 1). Particulate accumulations (lithogenic and biogenic) reach concentrations of 560 g sediment/kg sediment-laden snow or ice in the dirty spots. On average the concentrations in the sediment patches on the ice surface are about 70 g/kg.

The sea-ice-rafted material can be described as a silty clay or clayey silt, sometimes as a sandy clayey silt. Sand–silt–clay analyses indicate variability in the silt to clay ratio with about 5% sand-sized material. The maximum grain size is about 300–400 µm in diameter. Only at one location (82°N 32°E) were some angular feldspar grains of 2–3 mm in diameter sampled. The plots of the grain size distribution vs latitude (Fig. 3) show no well-defined variations in the sea ice sediments that could be used to distinguish between different sources. Only in the sand fraction do we find some evidence for higher values in the south.

The silt-sized material was analyzed by a sedigraph and laser particle analyzer. All samples show a negative skewness and the bulk of the material is finer than 16 µm. From these data one can conclude either a stable and similar incorporation mechanism favorable for this size of sediment or the same source area that delivers material in this size distribution.

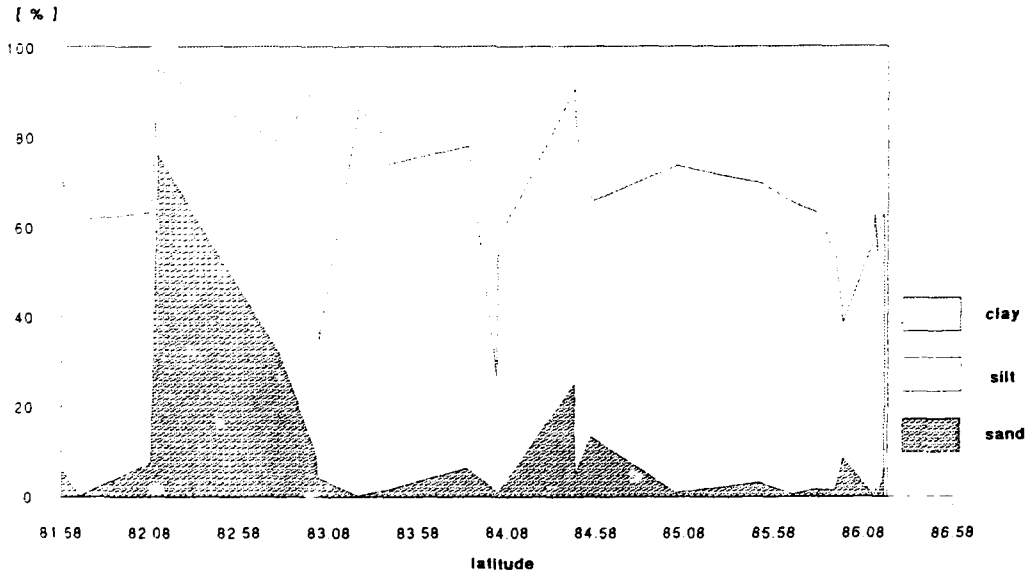

Figure 3. Plot of grain size distribution vs latitude. These data show no well-defined variations in the sea ice sediments between the southern marginal ice and the sea ice in the Transpolar Drift stream. Only in the sand fraction do we find some evidence for higher values in the south.

The coarse fraction (>63 μm) consists mainly of quartz, plagioclase and orthoclase feldspar (up to 98%). Minor components are mica (biotite, muscovite), pyroxene and amphiboles, coal, and siltstone fragments. The bulk of the biogenic material consists of marine benthic diatoms. Minor components are sponge spicules foraminifers, tintinids, pollen, spores and fragments of brown algae (Pfirman et al. 1989a).

Small pockets and holes in the ice surface were observed to contain accumulations of particulate material. They were also observed by Nansen on his famous "Fram" expedition (Nansen 1906) and are well known by many Arctic explorers (e.g., Poser 1933), and are called cryoconites by Nordenskjöld (1870). These holes are mostly filled with meltwater and have a mean depth of about 10–20 cm. The diameters are variable but lie usually at about 10–15 cm. The material at the bottom of these cryoconite holes is frequently aggregated. Especially in the vicinity of our northernmost station (86°22'N) these pellets are widespread, very cohesive and are approximately 1–4 cm long (*Polarstern* Shipboard Scientific Party 1988). First analyses of the silt- and sand-sized material and the biogenic matter show no difference between the cryoconites and the material lying on top of the ice. In many sea floor cores we obtained from the Eurasian Arctic Basin horizons of mud clasts were observed apparently similar to those found in sea ice (Pfirman et al. 1989b). Pellet-rich horizons in Arctic Ocean sediment cores were also discussed by Clark et al. (1980), Minicucci and Clark (1983) and Goldstein (1983), and a glacier origin was suggested for some of these pellets. Future work will include more detailed comparisons of lithogenic and biogenic composition of the mudclasts from the sea floor with the cryoconite material in the ice.

Because much of the ice in the Siberian Branch of the Transpolar Drift stream is thought to have been formed on the Siberian Shelf (Nansen 1897, Koch 1945, Gordienko and Laktionov 1969, Colony and Thorndike 1985, Larssen et al. 1987) it is probable that incorporation of particles occurred during ice growth in this region. Evidence for a shallow water origin was found in the biogenic components of the surface samples from particle-rich areas. Agglutinated and calcareous benthic marine foraminiferas and shallow water mollusks were found in some of the Eurasian Basin and Fram Strait samples. Especially from the occurrence of agglutinated benthic marine foraminifers it appears that sea floor material is included into the ice pack. Both anchor and frazil ice formation (e.g., Barnes and Reimnitz 1974, Barnes et al. 1982, Osterkamp and Gosink 1984, Reimnitz and Kempema 1988, Reimnitz et al. 1987) are known to incorporate sediment resuspended from the sea floor and represent likely processes for sediment incorporation. Larger scale aeolian input may also add a small amount of material during drift through the central Eurasian Basin (Pfirman et al. 1989). Analyses of the crystal structure of the arctic sea ice indicate that high surface sediment concentrations were associated with multiyear ice. Such surface accumulations may form as follows. During transport in the Transpolar Drift (about three years) summer surface melting of the original turbid ice with sediment distributed throughout the ice column (Reimnitz and Kempema 1988) will concentrate the sediment on the ice surface. In wintertime relatively clean ice is added to the bottom of the ice floes.

Future investigations will focus on using the sea ice sediment analyses to determine the contribution of ice-rafted debris to sea floor sediment accumulations. Of particular interest are variations in the flux of sea-ice-rafted sediments over glacial/interglacial cycles.

REFERENCES

Barnes, P.W. and E. Reimnitz (1974) Sedimentary processes on arctic shelves off the northern coast of Alaska. In *The Coast and Shelf of the Beaufort Sea* (J.C. Reed and J.E. Sater, Ed.). Arlington, Virginia: Arctic Institute of North America, p. 439–476.

Barnes, P.W., E. Reimnitz and D. Fox (1982) Ice rafting of fine-grained sediment, a sorting and transport mechanism, Beaufort Sea, Alaska. *Journal of Sedimentology and Petrology*, **52**(2): 493–502.

Clark, D.L. and A. Hanson (1983) Central Arctic Ocean sediment texture: Key to ice transport mechanisms. In *Glacial-Marine Sedimentation* (B.F. Molnia, Ed.). New York: Plenum Press, p. 301–330.

Clark, D.L., R.R. Whitman, K.A. Morgan and S.D. Machay (1980) Stratigraphy and glacial-marine sediments of the Amerasian Basin, central Arctic Ocean. Geological Society of America, Special Paper 181.

Colony, R. and A.S. Thorndike (1985) Sea ice motion as a drunkard's walk. *Journal of Geophysical Research*, **90**(C1): 965–974.

Drewry, D. (1986) *Glacial Geologic Processes*. London: Edward Arnold Ltd.

Goldstein, R.H. (1983) Stratigraphy and sedimentology of ice-rafted and turbidite sediment, Canada Basin, Arctic Ocean. In *Glacial–Marine Sedimentation* (B.F. Molnia, Ed.). New York: Plenum Press, p. 367–400.

Gordienko, P.A. and A.F. Laktionov (1969) Circulation and physics of the Arctic Basin waters. In *Annals*

of the International Geophysical Year, Oceanography. New York: Pergamon, New York 46, p. 94–112.
Koch, L. (1945) The East Greenland Ice. *Meddelelser om Gronland,* **130**(3): 373.
Larssen, B.B., A. Elverhoi, and P. Aagaard (1987) Study of particulate material in sea ice in the Fram Strait—a contribution to paleoclimatic research? *Polar Research,* **5**(3): 313–315.
Minicucci, D.A. and D.L. Clark (1983) A late Cenozoic stratigraphy for glacial–marine sediments of the eastern Alpha Cordillera, central Arctic Ocean. In *Glacial–Marine Sedimentation* (B.F. Molnia, Ed.). New York: Plenum Press, p. 331–365.
Nansen, F. (1897) *Farthest North.* Whitehall Gardens, Great Britain: Archibald Constable and Co.
Nansen, F. (1906) Protozoa on the ice-floes of the North Polar Sea. In *The Norwegian North Polar Expedition 1893–1896* (F. Nansen, Ed.). London: Longmans, Green and Company, *Scientific Results,* **4**(13).
Nordenskjold, A.E. (1870) Redegorelse for en expedition till Gronland ar 1870. *Ofv. af kgl. Vetensk.-Akad. Forh.* 10.
Osterkamp, T.E. and J.P. Gosink (1984) Observations and analyses of sediment-laden ice. In *The Alaskan Beaufort Sea, Ecosystems and Environments* (P.W. Barnes, D.M. Schell and E. Reimnitz, Ed.). Orlando: Academic Press, Inc., p. 73–93.
Pfirman, S., J.-C. Gascard, I. Wollenburg, P. Mudie, and A. Abelmann (1989a) Particle-laden Eurasian Arctic sea ice, July and August 1987. *Polar Research,* **7**.
Pfirman, S., I. Wollenburg, J. Thiede and M.A. Lange (1989b) Lithogenic sediment on arctic pack ice: Potential aeolian flux and contribution to deep sea sediments. In *Proceedings of NATO Advanced Research Workshop: Paleoclimatology and Paleometeorology; Modern and Past Patterns of Global Atmospheric Transport 15–19 November 1987, Oracle, Arizona.*
***Polarstern* Shipboard Scientific Party** (1988) Breakthrough in arctic deep-sea research: The R/V *Polarstern* expedition 1987. *Eos,* **69**(25): 665–678.
Poser, H. (1933) Uber Abschmelzformen auf dem gronlandischen Packeise und Landeise. *Zeitschrift fur Gletscherk,* **21**: 1–20.
Reimnitz, E. and E.W. Kempema (1988) Ice rafting: An indication of glaciation? *Journal of Glaciology,* **34** (117): 254–255.
Reimnitz, E., E.W. Kempema and P.W. Barnes (1987) Anchor ice, seabed freezing, and sediment dynamics in shallow arctic seas. *Journal of Geophysical Research,* **92**(C13): 14671–14678.
Vinje, T. (1985) Drift, composition, morphology and distribution of the sea ice fields in the Barents Sea. Norsk Polarinst. Skr. 179C.

Source, Characteristics, and Significance of Sediment Pellets Formed on the Sea Ice of the Arctic Basin

P. W. BARNES, E. M. KEMPEMA, AND E. REIMNITZ
U.S. Geological Survey
Menlo Park, California, U.S.A.

ABSTRACT/INTRODUCTION

The sediment content of sea ice has received little attention from arctic geoscientists. Nevertheless, fine-grained sediment is often found disseminated through ice floes in all parts of the Arctic Ocean (Barnes et al. 1982, Clark and Hanson 1983, Reimnitz and Kempema 1988, Wollenburg et al., this volume). These homogeneous mixtures of sediment and ice, called turbid ice (Fig. 1), are a significant part of the arctic sediment-transport regime, providing a mechanism for cross-shelf transport and erosion of the continental shelf and coast (Reimnitz et al. 1987, 1988). Milli-

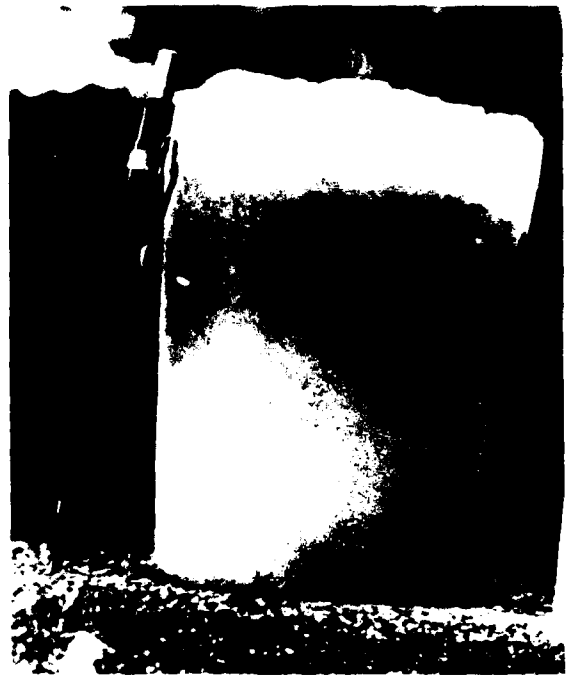

Figure 1. Turbid ice mass frozen from seawater and sediment mixture under turbulent conditions and the presence of frazil ice.

Figure 2. Sea ice samples from the outer edge of the continental shelf off northern Alaska, with individual and agglutinated sediment pellets of silt and clay. Scale in centimeters.

meter-size pellets of agglutinated, inorganic silt and clay are common on the upper surface of turbid ice (Fig. 2; Barnes et al. 1982) and in cores collected from the sea floor of the Arctic Basin (Goldstein 1983). Turbulent freezing storms over eroding shallow arctic continental shelves re-suspend and sort fine-grained sediment, which, along with frazil ice crystals, initiate the formation of turbid ice (Reimnitz et al. 1987), commonly containing sediment concentrations of >1 g/L when melted (Barnes et al. 1982). The decay of turbid ice concentrates sediment on the ice surface as the water escapes. The surface sediments commonly coagulate to form millimeter-size pellets (Fig. 2). The pellets are located in centimeter-size surficial melt pockets (cryoconites in glacial environments) that form because of increased heat adsorption (Fig. 2 and 3). Sediments forming the pellets vary in texture but are typically clay and silt, and they are finer and better sorted than most of the sediments on the shelf, their presumed source (Barnes and Reimnitz 1974). Similar pellets reported from glacial icebergs may be distinguished by a prominent coarse component and are commonly poorly sorted compared with sea-ice pellets (Ovenshine 1970).

RESULTS

Several experiments were performed to ascertain the mechanism for pelletization of turbid ice during decay. Turbid-ice masses made from seawater (Fig. 1) were allowed to decay under varied radiation conditions (heat lamp) in a freezer over a period of sev-

Figure 3. Pitted surface of sea ice off northern Alaska containing sediment pellets. The largest pits with agglomerations of pellets are 15–20 cm in diameter.

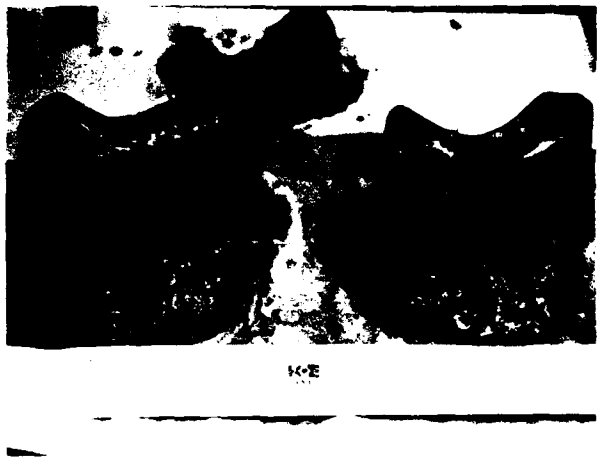

a.

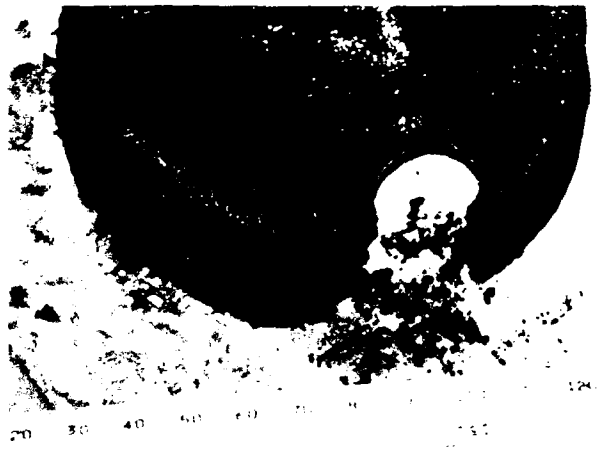

b.

Figure 4. Turbid sea-ice masses (see Fig. 1) after evaporation and melt during freeze–thaw cycling in a freezer with a heat lamp. Note the pitted nature of the surface which faced the lamp (a) and the pellets and other residue after melting (b). Scale is in millimeters.

eral days (Fig. 4). Most of the water from the ablating ice blocks was lost by sublimation rather than runoff. Preliminary results suggest that the pellets form in a sublimating environment where they are consolidated by freeze-thaw cycling (Fig. 4), a condition that is prevalent during the arctic spring and early summer.

Pelletoid layers reported from the Arctic Basin floor (Goldstein 1983) suggest that, when released from the sea ice, they quickly settle to the sea floor without breaking up and may mark areas and times of intensive sea-ice decay. The occurrence of similar pellets in modern and ancient high-latitude sediments could indicate sea-ice rafting from a shallow stormy source area with abundant fine-grained sediments.

REFERENCES

Barnes, P.W. and E. Reimnitz (1974) Sedimentary processes on arctic shelves off the northern coast of Alaska. In *The Coast and Shelf of the Beaufort Sea* (J.C. Reed and J.E. Sater, Ed.). Arlington, Virginia: The Arctic Institute of North America, p. 439–576.

Barnes, P.W., E. Reimnitz and D. Fox (1982) Ice rafting of fine-grained sediment, a sorting and transport mechanism, Beaufort Sea, Alaska. *Journal of Sedimentary Petrology*, **52**(2): 493–502.

Clark, D.L. and A. Hanson (1983) Central Arctic Ocean sediment: A key to ice transport mechanisms. In *Glacial-Marine Sedimentation* (B.F. Molnia, Ed.). New York: Plenum Press, p. 301–330.

Goldstein, R.H. (1983) Stratigraphy and sedimentology of ice-rafted and turbidite sediment, Canada Basin, Arctic ocean. In *Glacial-Marine Sedimentation* (B.F. Molnia, Ed.). New York: Plenum Press, p. 367–400.

Ovenshine, A.T. (1970) Observations of iceberg rafting in Glacier Bay, Alaska, and the identification of ancient ice-rafted deposits. *Geological Society of America Bulletin*, **81**: 891–894.

Reimnitz, E., S.M. Graves and P.W. Barnes (1988) Map showing Beaufort Sea coastal erosion, sediment flux, shoreline evolution, and the erosional shelf profile. U.S. Geological Survey, Miscellaneous Investigation Series, Map I-11 82-G.

Reimnitz, E. and E.W. Kempema (1988) Ice rafting: an indication of glaciation? *Journal of Glaciology*, **34** (117): 254–255.

Reimnitz, E., E.W. Kempema and P.W. Barnes (1987) Anchor ice, seabed freezing, and sediment dynamics in shallow arctic seas. *Journal of Geophysical Research*, **92**: 14,671–14,672.

Sediment Transport by Ice Gouging
Application of Model Experiments to the Arctic Continental Shelf

P.W. BARNES, R.E. HUNTER, A.LEE,
E. REIMNITZ AND W.S. WEBER
U.S. Geological Survey
Menlo Park, California, U.S.A.

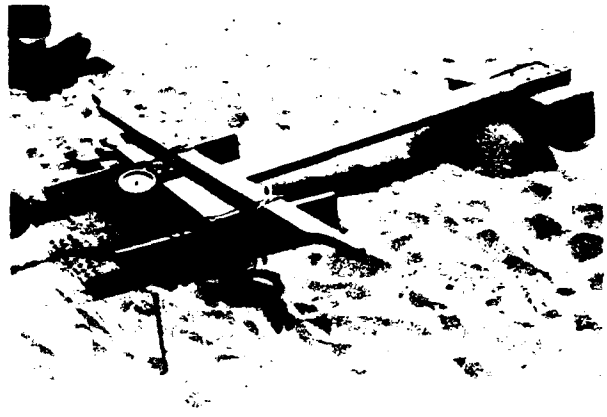

Figure 1. Experimental configuration on dry sand beach. Gouge tool is at the right end of the sled. At the front edge of the sled the surficial wooden pegs and pebbles are arranged on the surface (and in the subsurface, see Fig. 2) in the path of the gouge tool.

ABSTRACT/INTRODUCTION

Linear troughs and berms are the dominant small-scale morphology of the central continental shelf off northern Alaska. This morphology is created by the keels of ice floes gouging the sea floor and displacing sediment in the manner of a bulldozer. The physical character and recurrence rate of ice gouging on the inner shelf are reasonably well documented (Barnes et al. 1984, Barnes and Rearic 1985, Weber et al. 1989); however, the distance and volume of sediment transported by ice gouging (volume transport rate) and thus the effect of ice gouging on shelf erosion are not known. Sixteen experiments that modeled the ice-gouging transport process were conducted in dry, medium-grained beach sand. The purpose of the model experiments was to determine an average grain displacement value to use in estimating sediment transport. The experimental results were extrapolated using available ice-gouge data from the north coast of Alaska to provide a crude estimation of volume transport rates of sediment by ice gouging.

RESULTS

The model experiments used gouging tools, or "keels," consisting of ~130-kg concrete blocks with wooden and concrete plow faces of varying size and shape. The gouging tools were mounted on a sled (Fig. 1) and guided by hand to aid with direction and depth control. Each keel was towed a distance of approximately 3 m at an average speed of 30 cm/s using a stationary winch and pulley. A dynamometer was inserted between the winch and sled to measure the pulling (gouging) force. The resultant gouges (Fig. 2) ranged in width from 8.5 to 75 cm and had depths of up to 12 cm. To simulate the movement of sand grains, 1-cm labeled wooden pegs and pebbles were buried 2.5 cm apart at depths up to 10 cm, normal to the gouge path (Fig. 1 and 3). The positions of the pegs intercepted and displaced by the keel (Fig. 3) were recorded. Some pegs were found to be displaced as much as 5 m along the track of the gouge. Over the range of tool widths used, the average peg displacement correlates well ($r^2 = 0.83$) with gouge incision width (Fig. 4), suggesting that the average grain displacement is 2.3 times the gouge width. Poor correlation between peg displacement and gouge depth resulted partly, we believe, from poor depth control during our experiments.

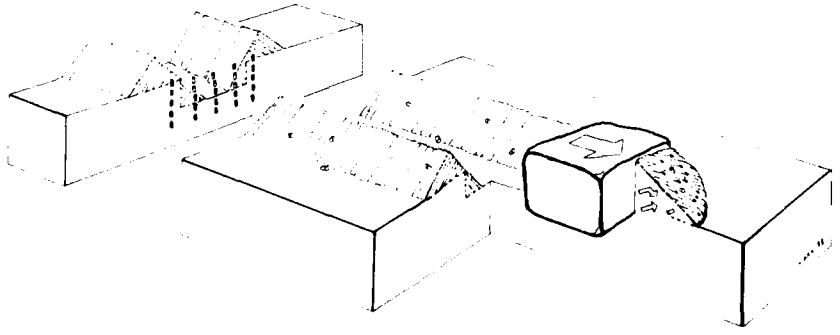

Figure 2. Block diagram of beach experiment showing the placement of the tracer pegs, displaced pegs, and sand movement observed on the push berm.

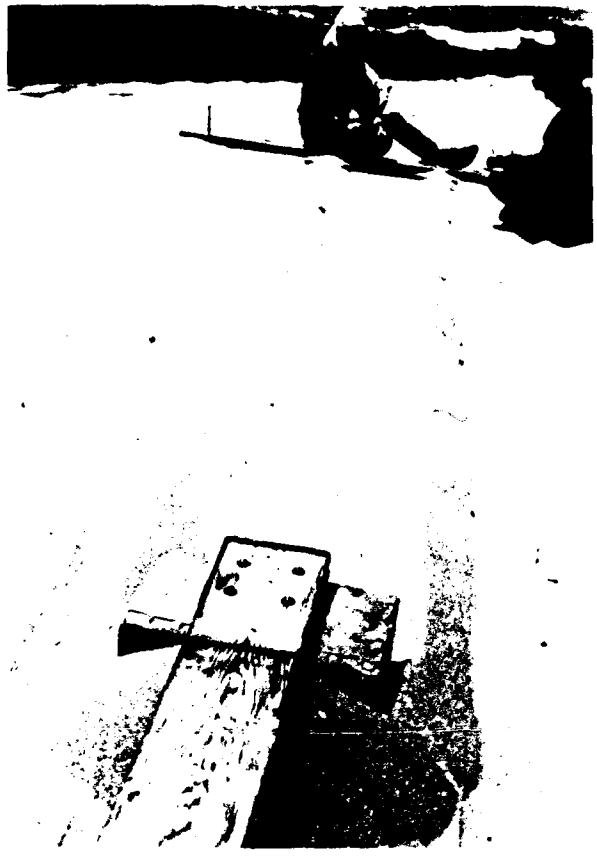

Figure 3. "Gouge" created by towing a "keel" through beach sand showing push berm, flat floor, and flanking berm at angle of repose.

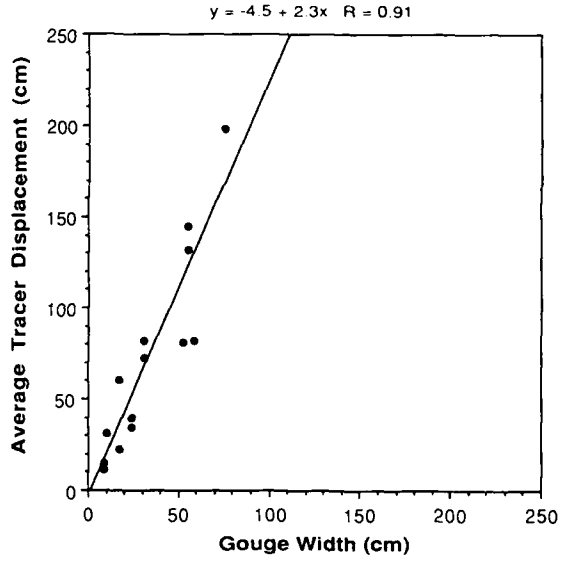

Figure 4. Graph of "gouge" width vs average displacement of wooden peg tracers observed during the beach experiments.

Applying our beach experiment results to estimations of sediment transport by arctic ice gouging requires several significant assumptions, not the least of which is an order of magnitude increase in scale. In addition, we assume that the dry beach sands of the experiment emulate shelf sediment of the arctic marine environment. On areas of the arctic shelf with noncohesive sands the beach experiment may be comparable. However, this assumption is poor for most of the Arctic Shelf, as sediments are known to be highly variable and often composed of cohesive silts and clays (Barnes and Reimnitz 1974). Because of the problems associated with extrapolating the beach experiments to the arctic environment, the following example must be considered speculative and viewed with caution.

Barnes et al. (1984) and Barnes and Rearic (1985) provide data on ice gouge dimensions and rates of recurrence that can be used to estimate the volume and rate of sediment transported by ice bulldozing. The volume transported is estimated from the cross-sectional area of the gouge (simplified as gouge width

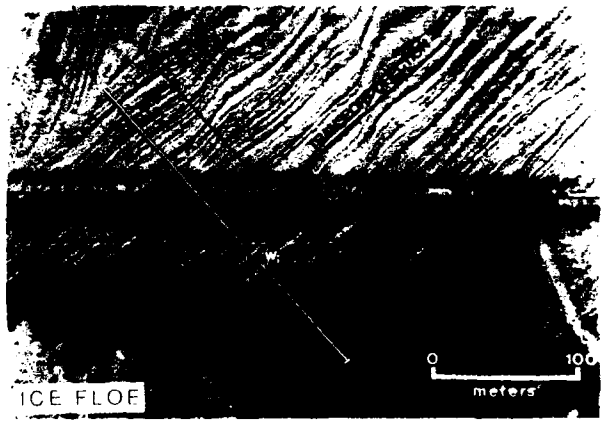

Figure 5. Sonograph of the seabed showing a multiplet ice gouge formed by ice raking the seafloor from upper right to lower left. The multiplet consists of about 56 individual gouges of w_i width.

× gouge depth, $\bar{w}_g$), multiplied by the average grain displacement, D. The rate of sediment transport T is the volume passing a line of unit length (l), oriented transverse to the transport path, in unit time t, or:

$$T = \bar{w}_g D l^{-1} t^{-1}.$$

Annual survey data from the inner shelf of the Beaufort Sea (water depths up to 20 m) show an average of 8.5 new gouges per kilometer of shelf, each gouge having an average width of 3.5 m and an average incision depth of 0.2 m (Rearic 1986). Applying the empirical relationship between width and displacement (D = 2.3$\bar{w}$), as determined from the beach experiments, the Alaskan field data indicate a transport of 48 m^3 km^{-1} per year for the average gouge, tempered by the assumptions discussed above. If we assume that all of the transport is parallel to the coast and occurs to the west (Barnes et al. 1984) then, for an average shelf width of 60 km, the volume transported westward and eroded from the shelf is 2880 m^3 per year.

As transport increases by a power of 2 with increasing gouge width (Fig. 4 and 5), mid-shelf areas (15- to 45-m water depth), where we expect wider gouges and high yearly rates of sea-floor gouging (Barnes et al. 1984), should experience substantially higher transport rates. In the example shown in Figure 5 the single multiplet ice event of 56 gouges is 238 m wide. Excluding the assumed 30% berm widths, and estimating 20-cm gouge depths, we calculate sediment transport of 230 m^3 for this one gouge event.

REFERENCES

Barnes, P.W. and E. Reimnitz (1974) Sedimentary processes on Arctic shelves off the northern coast of Alaska. In *The Coast and Shelf of the Beaufort Sea* (J.C. Reed and J.E. Sater, Ed.). Arlington, Virginia: The Arctic Institute of North America, p. 439–576.

Barnes, P.W., D.M. Rearic and E. Reimnitz (1984)Ice gouge characteristics and processes. In *The Alaskan Beaufort Sea—Ecosystem and Environment* (P.W. Barnes, D.M. Schell and E. Reimnitz, Ed.). New York: Academic Press, New York, p. 159–184.

Barnes, P.W. and D.M. Rearic (1985) Rates of sediment disruption by sea ice as determined from characteristics of dated ice gouges created since 1975 on the inner shelf of the Beaufort Sea, Alaska. U.S. Geological Survey, Open-File Report 85-473.

Rearic, D.M. (1986) Temporal and spatial character of newly formed gouges in eastern Harrison Bay, Alaska, 1977–1982. U.S. Geological Survey, Open-File Report 86-391.

Weber, W.S., P.W. Barnes and E. Reimnitz (1989) Data on the characteristics of dated gouges on the inner shelf of the Beaufort Sea, Alaska: 1977–1985. U.S. Geological Survey, Open-File Report 89-151.

Movements of Fine-grained Sediment Particles in Freshwater- and Seawater-Slush Ice Slurries During Freezing Front Advances

J.R. CLAYTON, JR.,* E. REIMNITZ,† J.R. PAYNE* AND E.W. KEMPEMA†

*Science Applications International Corporation
San Diego, California, U.S.A.
†U.S. Geological Survey
Branch of Pacific Marine Geology
Menlo Park, California, U.S.A.

Broad regions of sea ice at high latitudes are known to contain substantial quantities of fine-grained sediment particles. Such inclusions of sediment can have important implications for not only geological, physical and biological processes but also human commercial activities in regions affected by sea ice. In light of these facts, experiments were performed under reasonably well-controlled laboratory conditions to investigate several aspects of the effects of freezing front advances on the distributions of fine-grained sediment particles in congealing slush ice matrices.

In one experiment, clay-sized particles were homogeneously suspended in fresh water in a cylindrical container. Freezing of the suspension inward from the container walls was initiated until the contents of the container were completely frozen. Horizontal thin sections of the ice plug were then prepared to document the final particle distributions. A photograph of one of the final thin sections is shown in Figure 1. As indicated, particles were "moved" laterally toward the center of the container. Furthermore, differential migration as a function of particle size is also shown to be in evidence. In particular, the concentric rings approximately halfway to the center of the thin section appear to comprise mostly larger particles. In contrast, finer-grained particles "moved" farther and are responsible for the "turbid" appearance at the center of the thin section. Other studies (e.g., Corte 1962, Uhlmann et al. 1964, Gilpin 1980) have shown that particles will move horizontally as

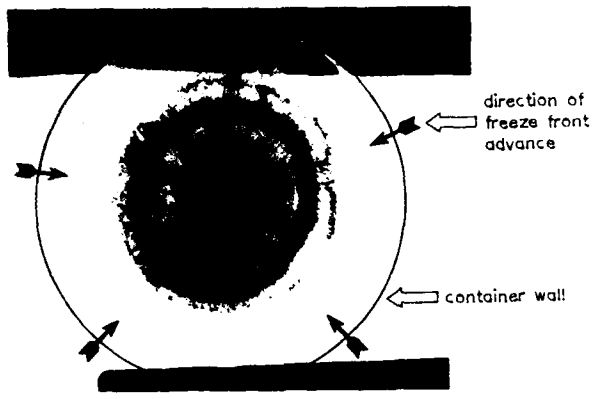

Figure 1. Horizontal thin section of the final solid ice plug removed from the cylindrical vessel that contained an initial homogeneous suspension of clay-sized particles in fresh water.

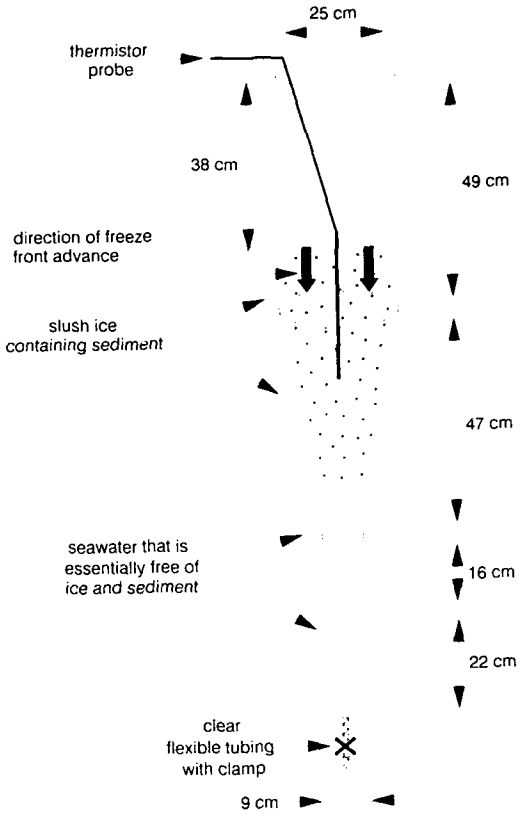

Figure 2. Schematic representation of the modified sedimentation trap used for the sediment "expulsion"/retention experiment.

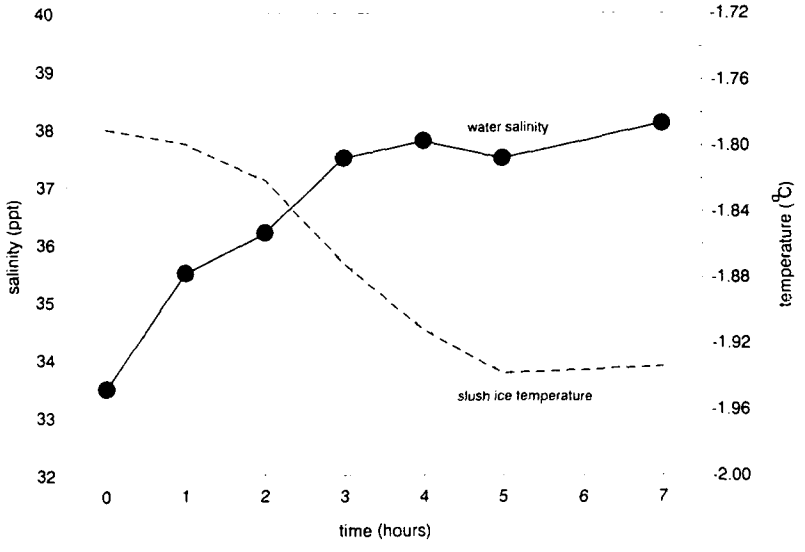

Figure 3. Time-series measurements of temperature (°C) in the slush ice matrix (25-m depth) and salinity (parts per thousand, or ppt) in the underlying water column in the sediment "expulsion"/ retention experiment. No water sample was collected and no temperature measurement was obtained at 6 hr.

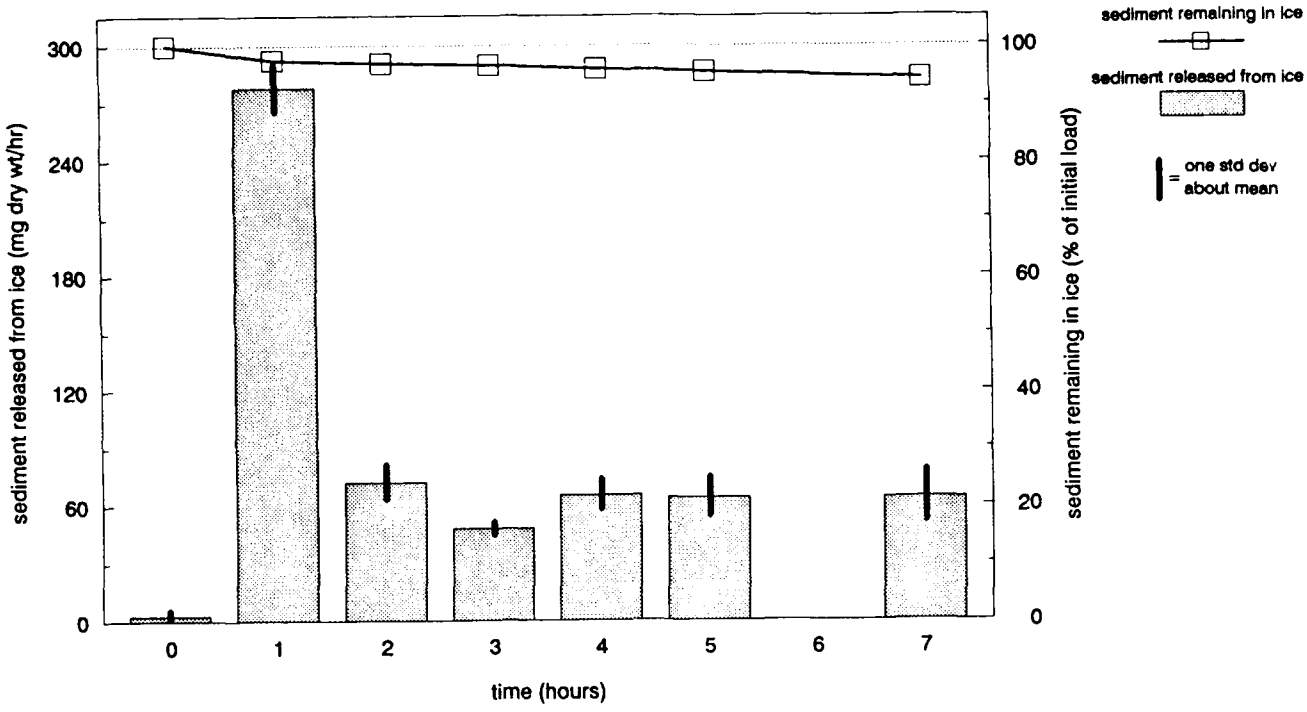

Figure 4. Time-series measurements in the sediment "expulsion"/retention experiment for "settled" sediment loads (mg dry weight/hr) collected from the bottom of the container and the residual sediment load remaining in the slush ice canopy. No water sample was collected at 6 hr.

well as vertically under the influence of advancing freezing fronts, and that the size and shape of a particle will affect the degree to which it moves in a manner consistent with the particle distributions noted in Figure 1.

A second experiment was performed to evaluate releases as well as retention of fine-grained sediment particles from a seawater-slush ice slurry undergoing freezing in a downward direction. A schematic illustration of the experimental setup is shown in Figure 2. Special precautions were taken to ensure that mechanical disturbance of the sediment-laden slush ice layer did not occur and that freezing proceeded only downward from the air/ice interface (i.e., not inward from the container walls). During the course of the experiment, the following variables were monitored as a function of time: 1) temperature in the ice matrix and salinity in the water beneath the ice (Fig. 3) and 2) quantities of sediment released from the ice and the residual sediment load remaining in the ice matrix (Fig. 4). As shown in Figure 4, a purging of at least a portion of the entrained sediment load from the ice layer did occur during the evolving freezing process. However, the majority of the sediment mass still remained in the slush ice layer at the conclusion of the experiment. If the latter results can be extrapolated to real-world situations, the retention of sediment by a congealing slush ice layer would have significant implications to processes related to eventual spatial transport and deposition of ice-rafted sediments. In particular, the rafting of fine-grained sediments by sea ice does appear to play an important role in overall sediment budgets in regions affected by sea ice (e.g., Reimnitz and Kempema 1987, Kempema et al. 1989).

In summary, freeze front advances through sediment-laden layers of slush ice can produce dynamic situations with regard to not only movement but also to "extrusion"/retention of particles by a congealing ice matrix. These processes can in turn have important implications for a variety of natural geological, physical and biological processes as well as human-related activities in arctic marine and nearshore regions.

REFERENCES

Corte, A.E. (1962) Vertical migration of particles in front of a moving freezing plane. *Journal of Geophysical Research*, **67**: 1085–1090.

Gilpin, R.R (1980) Theoretical studies of particle engulfment. *Journal of Colloid and Interface Science*, **74**: 44–63.

Kempema, E.W., E. Reimnitz and P.W. Barnes (1989) Sea ice sediment entrainment and rafting in the Arctic. *Journal of Sedimentary Petrology*, **59** (in press).
Reimnitz, E. and E.W. Kempema (1987) Field observations of slush ice generated during freeze-up in arctic coastal waters. *Marine Geology*, **77**: 219–231.
Uhlmann, D.R., B. Chalmers and K.A. Jackson (1964) Interaction between particles and a solid-liquid interface. *Journal of Applied Physics*, **35**: 2986–2993.

Salt-Water Anchor Ice Formation
Observations from the Alaskan Beaufort Sea and Flume Experiments

E.W. KEMPEMA
School of Oceanography
University of Washington
Seattle, Washington, U.S.A.

E. REIMNITZ AND P.W. BARNES
U.S. Geological Survey
Menlo Park, California, U.S.A.

Diving traverses made immediately after fall freezeup storms in the Alaskan Beaufort Sea near Prudhoe Bay have revealed the presence of anchor ice in shallow water (Reimnitz et al. 1987). Anchor ice has been observed only in the fall, although many dives have been made throughout the winter; this suggests that anchor ice is an ephemeral phenomenon associated with fall storms. The anchor ice seen on the diving traverses consisted of rounded, pillow-shaped masses of ice and ice-bonded sediment, 10 to 40 cm across and 5 to 15 cm high, resting on a rippled sand and gravel bottom (Fig. 1). The anchor ice had a porous outer crust composed of randomly oriented ice crystals up to 1 cm in diameter, with sediment grains trapped in the interstices between ice crystals. Below the fragile outer crust, the pillows were firmer, denser, and had higher sediment concentrations. The anchor-ice pillows were best developed at 3- to 4-m water depth, and occurred singly or in patches up to 4 m across. The strong bond between anchor ice and its substrate exists for only a short time during and after ice formation when the water column is supercooled (Tsang 1982). When this bond is broken, anchor ice can rise to the surface and be incorporated into the ice cover (Dayton et al. 1969). This floating, sediment-laden anchor ice results in patchy distributions of sand, pebbles, shells, and sticks in the seasonal ice cover in the Alaskan Beaufort Sea (Fig. 2). Once coarse sediment is entrained into the ice canopy, it may be transported throughout the Arctic Basin.

Figure 1. Anchor ice in 4-m-deep water on the seaward side of a barrier island in the Alaskan Beaufort Sea. Individual pillows are about 40 cm in diameter and are composed of a sediment-rich, ice bonded core surrounded by a rind of delicate ice crystals and sand.

Figure 2. Masses of sand-laden anchor ice entrained in the seasonal ice cover near Prudhoe Bay, Alaska. The largest anchor-ice masses are 30 cm long.

Figure 3. Anchor ice made when frazil crystals adhered to an ice-bonded sediment block in the race-track flume. This mass is very similar to the anchor-ice pillows seen along diving traverses in the Beaufort Sea (Fig. 1). Scale is 5 cm long.

To gain insight on saltwater anchor ice formation, we performed a series of experiments in a race-track flume. The flume had a channel that was 20 cm wide and deep; the total water volume in the flume was 110 L. The floor of the flume was covered with 2 cm of medium-grained sand, and current speeds were varied between 30 and 70 cm/s. In the flume experiments, anchor ice never formed on non-ice-bonded sediments; however, it formed readily when frazil crystals in suspension adhered to objects suspended in the flow or to artificially ice-bonded sand. Anchor-ice pillows produced in the flume (Fig. 3) were very similar to naturally occurring anchor ice seen in the Alaskan Beaufort Sea. This suggests that naturally occurring saltwater anchor ice grows at least in part by frazil accretion. All the ice features seen in natural settings cannot be duplicated in flume experiments, possibly because supercooling of flume water cannot be maintained for long time periods (Tsang 1982).

Based on the field observations and the flume experiments, we conclude the following:

1. Anchor ice in the Beaufort Sea forms during fall storms when frazil is being produced. At least some anchor ice growth occurs by frazil adhering to the seafloor.

2. Saltwater anchor ice forms only on previously ice-bonded sediment. Two possible methods of substrate ice bonding suggested by the flume experiments are freezing of interstitial water with a salinity of less than the overlying water column or burial of sediment-laden frazil flocs by migrating bed forms (Kempema et al. 1986).

3. Not enough data are available to estimate the contribution that anchor ice makes to the total sediment load on the seasonal ice cover of the Beaufort Sea. However, the release of sediment-laden anchor ice may be the most important mechanism for incorporating sand and coarser material into the ice canopy. Once in the ice canopy, this sediment may be transported to the deep Arctic Basin (Kempema et al. 1989).

REFERENCES

Dayton, P.K., G.A. Robilliard and A.L. DeVries (1969) Anchor ice formation in McMurdo Sound, Antarctica and its biological effects. *Science*, **163**: 273–274.

Kempema, E.W., E. Reimnitz and R.E. Hunter (1986) Flume studies and field observations on the interaction of frazil and anchor ice with sand-sized sediment. U.S. Geological Survey Open-File Report 86-515.

Kempema, E.W., E. Reimnitz and P.W. Barnes (1989) Sea ice sediment entrainment and rafting in the Arctic. *Journal of Sedimentary Petrography*, **59**(2).

Reimnitz, E., E.W. Kempema and P.W. Barnes (1987) Anchor ice, seabed freezing, and sediment dynamics in shallow arctic seas. *Journal of Geophysical Research*, **92**(C13): 14,671–14,678.

Tsang, G. (1982) Frazil and anchor ice: A monograph. Subcommittee on Hydrology of Ice-Covered Rivers, National Research Council, Ottawa, Ontario, Canada.

Section II:

Morphological Processes in Sea Ice

Leads and Pressure Ridges in Sea Ice

Lidar Detection of Leads in Arctic Sea Ice

R.C. SCHNELL, R.G. BARRY AND M.W. MILES
Cooperative Institute for Research in Environmental Sciences (CIRES)
University of Colorado
Boulder, Colorado, U.S.A.

E.L ANDREAS
U.S. Army Cold Regions Research and Engineering Laboratory
Hanover, New Hampshire, U.S.A.

L.F. RADKE AND C.A. BROCK
University of Washington
Seattle, Washington, U.S.A.

M.P. McCORMICK
NASA, Langley Research Center
Hampton, Virginia, U.S.A.

J.L. MOORE
Wyle Corporation
Hampton, Virginia, U.S.A.

ABSTRACT

Remote sensing using an airborne infrared lidar (Uthe et al. 1982) has shown an unexpected capability to detect open leads (linear openings) in arctic sea ice and their associated meteorology in winter. Here we show that vertical profiles of backscattered radiation demonstrate strong returns from hydrometeor plumes originating from leads having a surface water temperature near –1.8°C. Recently refrozen leads are also distinguishable by the lidar backscatter from adjacent thicker, older sea ice. Wide leads release enough energy to create buoyant plumes which penetrate the arctic boundary layer inversion, transporting heat and moisture into the troposphere. These results show that the role of the Arctic as a global heat sink may need to be re-evaluated, and that lead plumes have a significant effect on the radiation budget.

RESULTS

A hydrometeor plume rising from an open lead and a plume streamer from another lead are shown in Figure 1 from an arctic flight by the National Aeronautics and Space Administration (NASA) Electra (Kent et al. 1986), ~83°87'N, 70°W, on 27 January 1984. The rising plume (left side of Fig. 1) has an apparent ice source ~300 km north of Ellesmere Island and reaches an altitude of nearly 4 km. The streamer to the south probably comes from a wide lead off Ellesmere Island, which is not in Figure 1 but was observed on the return flight. This streamer extended downwind (northward) for ~250 km and reached a height of 4 km. The layer of aerosol observed at 3 km (16:37 to about 16:50 GMT) is thought to be arctic haze air pollution. As the backscatter signals in the plumes are strongest near the surface and decrease upward, these features are not consistent with precipitating clouds. Because of these unexpected observations, a further study of the phenomenon was undertaken.

On 15 April 1986, as part of the Arctic Gas and Aerosol Sampling Program (AGASP) (Schnell 1988), a research aircraft operated by the Cloud and Aerosol Research Group of the University of Washington, equipped with cloud-physics instrumentation (Hobbs and Rango 1985) and a 1.06-μm downward-pointing lidar (Radke et al. in press), obtained cloud-microphysical data over open leads near Thule, Greenland. The lead-induced clouds were clearly associated with open-water regions. A transect through the cloud tops showed the presence of ice crystals < 50 μm in diameter, at a temperature of –25°C. The bulk of the condensation below the aircraft had the visual appearance of cloud (stratocumulus) containing liquid water, although the aircraft did not penetrate it. Condensation immediately above the surface of open leads is in the form of water droplets ~10 μm in diameter (Andreas et al. 1981). These may exist as supercooled droplets at temperatures as low as –40°C, depending on the presence of freezing nuclei or ice multiplication mechanisms (Mason 1971).

The lidar system flown on the aircraft was also able to identify newly frozen leads. A flight made on 18 April 1986 off Baffin Island, Canada (Fig. 2), shows both refrozen leads and a hydrometeor plume from an open lead. These lidar data were processed in a backscatter ratio color spectrum designed to highlight ice features. In Figure 2, the surface appears as a sharp boundary near the bottom edge; below the surface is a region of colors fading down the backscatter scale. Large areas with multiple leads and single leads with dimensions greater than the horizontal resolution of the lidar (40 m) lack the gradual color gradient immediately "beneath" the surface. This gradient results because when the laser beam from the lidar strikes the highly reflective snow surface, a strong return pulse saturates the receiver, which takes many nanoseconds to recover, thus producing a false signal below the surface. The less reflective

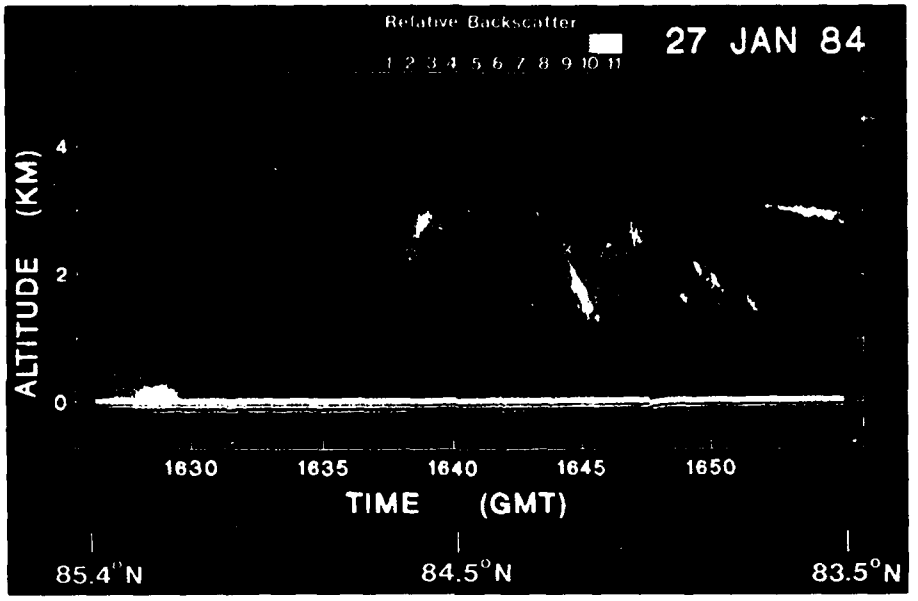

Figure 1. Backscatter signal from a 1.06-μm downward-viewing lidar flown on the NASA Electra north of Ellesmere Island on 27 January 1984. White indicates maximum backscatter signal, decreasing linearly to black, which is indicative of scattering from gas molecules only. Shown are an apparent rising plume of hydrometeors (left) and a plume of aerosol (center and right) that had a surface origin at a nearshore lead 250 km to the south off Alert. The aerosol layer at 3 km is thought to be arctic haze air pollutants.

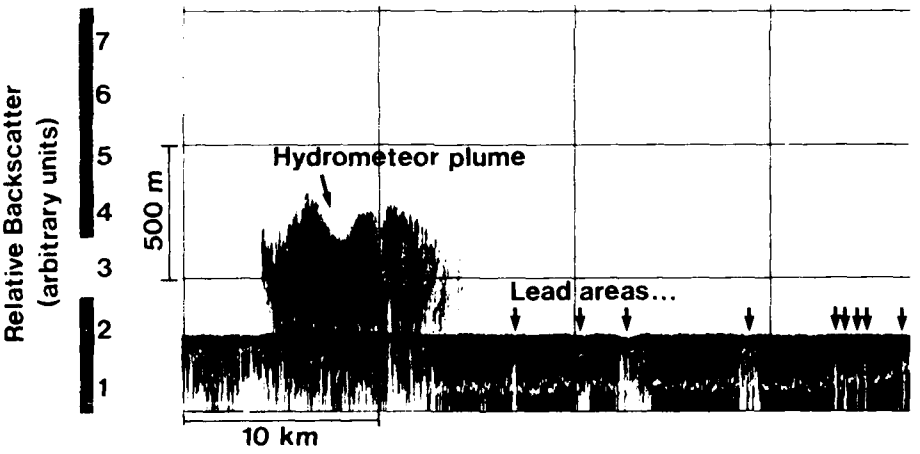

Figure 2. False-color imagery of the relative backscatter signal from the lidar operated on the aircraft. Colors indicate backscattering intensity from the lead-produced hydrometeor plume and the ice surfaces. The signal is corrected and scaled to eliminate returns from gas molecules and aerosol particles. Lower backscatter beneath the ice surface indicates refrozen leads.

surface of open and thinly covered leads produces no such saturation and thus no false signal. The "below surface" signal should be interpreted as a measure of reflectivity, not of ice thickness. The location and presence of the open and refrozen leads was confirmed by photography and visual observations.

DISCUSSION

Leads are of considerable interest to oceanographers and atmospheric scientists. Much of the heat lost from the Arctic in winter is converted into ice in the leads; the resulting salt rejection and brine drain-

age from the ice helps to maintain the Arctic Ocean halocline and may drive secondary circulation patterns. Leads result from ice deformation, primarily under wind forcing, and have typical widths of 10–100 m. Analyses of aircraft photographs, Landsat imagery and submarine sonar data on under-ice draft show that the size distribution of leads in arctic sea ice follows a negative power law such that along a 100-km track we could expect to encounter 30 leads that are 50 m wide but only 3 that are 500 m wide (Wadhams 1981). In winter, in the absence of ice deformation or movement of frazil ice by the wind, leads rapidly refreeze, forming new ice within a few hours (Badgley 1966, Andreas 1980). Although open water and areas of new ice represent only a few per cent of the ice-covered Arctic Ocean in winter, they have a major role in turbulent heat transfer to the atmosphere (Maykut 1982, Makshtas, in press). Refrozen leads with ice 0.2–0.8 m thick may account for more than half of the turbulent energy transfer from the ocean to the atmosphere in winter in the central Arctic (Badgley 1966, Andreas 1980, Maykut 1982, Ledley 1988, Makshtas, in press).

Previous field measurements (Andreas et al. 1979, 1981; Smith et al. 1983; Makshtas, in press) of the turbulent scalar fluxes over leads suggest that the heat and moisture transferred to the atmosphere remains within the atmospheric boundary layer because of the strong low-level temperature inversion which dominates the lower arctic troposphere in winter. Our observations show, however, that highly energetic plumes can penetrate to an altitude of at least 4 km.

The upper-air sounding from Alert, Ellesmere Island, for 12:00 GMT 27 January 1984—five hours before the observations in Figure 1—shows an inversion of 8°C between the surface and a pressure level of 850 mbar with an equivalent potential temperature (θ_e) at 4 km of 0°C. As θ_e is conservative for adiabatic processes, to penetrate the inversion and reach 4 km, a plume originating from a lead must be warmed and moistened at the surface to a θ_e of 0°C. We have developed a simple model to see whether such drastic modification of the surface-level air is possible.

The heat and moisture escaping from leads generally remain within an internal boundary layer (tens to hundreds of meters deep), which grows in height in the along-wind direction (x) approximately as $\delta(x) = 0.22\,x^{0.8}$ (Andreas 1982). Using this idea, Andreas et al. (1979) developed conservation equations for the sensible (H_s) and latent (H_L) heat lost by leads. Andreas and Murphy (1986) recently showed how to estimate these surface-averaged heat fluxes by bulk aerodynamic formulas. Putting these results together, we have derived a prediction equation for the average air temperature in the lowest $\alpha\delta$ of the internal boundary layer ($\alpha = 0.05$),

$$\bar{T} = T_i + \left(\frac{XC_H}{\alpha\delta}\right)(T_s - T_i)$$

where T_i = average upwind air temperature
T_s = water surface temperature
X = fetch (distance travelled by the wind) across the lead
C_H = bulk aerodynamic transfer coefficient for sensible heat (Andreas and Murphy 1986).

A similar equation can be derived for the average water vapor content ($\bar{Q}$) of the layer.

Table 1 shows values of $\bar{T}$, θ_e (including freezing), the condensate concentration C, and the average sensible and latent heat fluxes predicted by this model. We computed C and the number of condensate droplets N by converting all the water vapor $\bar{Q}$ in excess of the saturation limit into droplets of radius 5 μm (Andreas et al. 1981).

According to Table 1, a lead must be ~10 km wide to warm and moisten the air flowing over it to a θ_e of 0°C. Realistically, however, this is the narrowest lead that could produce a plume that reaches 4 km for conditions in the Alert sounding. A plume will not rise adiabatically; through entrainment it will lose heat and moisture to the colder, drier ambient air. Therefore, to reach 4 km, the plume must have a surface θ_e value in excess of 0°C; a more sophisticated plume model, however, is necessary to predict how much in excess of 0°C θ_e should be. Although 10 similar major leads, estimated to be 5–10 km wide, are visible on Defense Meteorological Satellite Program infrared (2.7-km resolution) imagery along the flight path for 27 January 1984, only three produced plumes; the others had evidently recently refrozen.

It is not surprising that such extensive plumes have not been recognized before. They are not necessarily visible to the naked eye. Also, previous research has focused on relatively narrow open-water areas (Badgley 1966, Andreas 1980, Andreas et al. 1979, 1981, Maykut 1982, Ledley 1988, Makshtas, in press). Our calculations suggest that small leads are unable to warm and moisten the air enough to allow for vertical transport through a strong inversion.

CONCLUSIONS

Our observations are significant for three reasons. First, airborne lidar provides a capability for locating

Table 1.Model results.

Fetch (*m*)	$\overline{T}$ (°C)	θ_e (°C)	10^4 C ($kg\,m^{-3}$)	10^9 N (m^{-3})	H_s ($W\,m^{-2}$)	H_L ($W\,m^{-2}$)
50	–23.7	–21.6	8.3	1.6	218	52
100	–22.1	–19.5	9.1	1.7	214	51
500	–17.4	–13.7	10.4	2.0	204	49
1,000	–15.3	–11.0	10.4	2.0	197	48
5,000	–9.1	–3.1	8.2	1.6	182	45
10,000	–7.0	–0.4	6.4	1.2	169	43
20,000	–4.2	3.1	3.2	0.4	160	41

$\overline{T}$ = near-surface air temperature
θ_e = equivalent potential temperature
C = condensate concentration
N = number of condensate droplets, assuming each has a diameter of 10 μm
H_s = surface-averaged fluxes of sensible heat (enthalpy)
H_L = surface-averaged fluxes of latent heat.
Water temperature = –1.8°C;
Upwind air temperature = –35.8°C
10-m wind speed = 2.5 m s^{-1}.
The near-surface absolute humidity is always the saturation value at $\overline{T}$.

narrow leads that are smaller than the resolution of current satellite sensors. Recently refrozen leads are as easily detectable by lidar as the plumes from open leads. This capability is important for operational forecasting and for fuller understanding of ice dynamics. Second, the current view that turbulent fluxes from leads and polynyas affect only the boundary layer needs modifying. If heat and moisture from leads can regularly reach the mid-troposphere, the role of the Arctic as a global heat sink may need re-evaluating, and climate models will require more realistic parameterizations of surface-atmosphere fluxes. Third, our results suggest that lead plumes may affect the radiation budget. Using observed ice-crystal spectra, Curry et al. (1989) calculated a significant heating effect at the surface, due to the downward infrared radiation from the ice crystals. Table 1 shows that even narrow leads produce particle concentrations larger than those assumed by Curry et al. (1989). Thus, plumes will affect the radiation budget in their immediate vicinity and in large areas downwind. Airborne and satellite-borne lidar provide the potential for determining the impact of leads on the energy and moisture fluxes from the polar ocean to the atmosphere. Further research will focus on developing a climatology of lead occurrence (Barry et al. 1989) and of plume frequency and distribution in the Arctic from lidar profiles and satellite data, identifying the phase of the plume moisture with lidar polarization measurements, and on developing parameterizations to relate lidar backscatter to plume moisture content.

ACKNOWLEDGMENTS

This work was supported by the Office of Naval Research, NSF's Division of Polar Programs, and NASA. The lidar used on the University of Washington aircraft was owned and operated by SRI International, Menlo Park, California, under contract to the AGASP project supported by NOAA.

REFERENCES

Andreas, E.L (1980) Estimation of heat and mass fluxes from Arctic leads. *Monthly Weather Review*, **108**: 2057–2063.

Andreas, E.L (1982) Sensible and latent heat fluxes and humidity profiles following a step change in surface moisture. USA Cold Regions Research and Engineering Laboratory, CRREL Report 82-12.

Andreas, E.L and B. Murphy (1986) Bulk transfer coefficients for heat and momentum over leads and polynyas. *Journal of Physical Oceanography*, **16**: 1875–1883.

Andreas, E.L, C.A. Paulson, R.M. Williams, R.W. Lindsay and J.A. Businger (1979) The turbulent heat flux from arctic leads. *Boundary Layer Meteorology*, **17**: 57–91.

Andreas, E.L, R.M. Williams and C.A. Paulson (1981) Observations of condensate profiles over arctic leads with a hot-film anemometer. *Quarterly Journal of the Royal Meteorological Society*, **107**: 437–460.

Badgley, F.I. (1966) Heat budget at the surface of the Arctic Ocean. In *Proceedings of the Symposium on Arctic Heat Budget and Atmospheric Circulation*. Santa Monica: Rand Corporation, p. 267–277.

Barry, R.G., M.W. Miles, R.C. Cianflone, G. Scharfen and R.C. Schnell (1989) Characteristics of Arctic sea ice from remote-sensing data and their relationship to atmospheric processes. *Annals of Glaciology*, 12: 9–15.

Curry, J.A., L.F. Radke, C.A. Brock and E.E. Ebert (1989) Arctic ice cryastal haze. In *Proceedings of Symposium on the Role of Clouds in Air Chemistry and Global Climate*. Boston: American Meteorological Society, p. 114–117.

Hobbs, P.V. and A.L. Rango (1985) Ice particle concentrations in clouds. *Journal of Atmospheric Science*, **42**: 2523–2549.

Kent, G.S., L.R. Poole and M.P. McCormick (1986)

Characteristics of Arctic polar stratosphere clouds as measured by airborne lidar. *Journal of Atmospheric Science*, **43**: 2148–2166.
Ledley, T.S. (1988) A coupled energy balance climate– sea ice model: Impact of sea ice and leads on climate. *Journal of Geophysical Research*, **93**: 15919–15932.
Makshtas, A.P. (In press) *The Heat Budget of Arctic Ice in the Winter* (E.L Andreas, Ed.). Washington, D.C.: Division of Polar Programs, National Science Foundation.
Mason, B.J. (1971) *The Physics of Clouds*. Oxford: Clarendon Press, p. 171–172, 2nd edition.
Maykut, G.A. (1982) Energy exchange over young sea ice in the central Arctic. *Journal of Geophysical Research*, **87**: 7971–7984.
Radke, L.F., C.A. Brock, J.H. Lyons, P.V. Hobbs and R.C. Schnell (In press) Aerosol and lidar measurements of hazes in mid-latitude and polar air masses. *Journal of Atmospheric Chemistry*.
Schnell, R.C. (1988) Arctic air chemistry. *Arctic Research*, **2**: 39–41.
Smith, S.D., R.J. Anderson, G. denHartog, D.R. Topham and R.G. Perkin (1983) An investigation of a polynya in the Canadian Archipelago. 2. Structure of turbulence and sensible heat flux. *Journal of Geophysical Research*, **88**: 2900–2910.
Uthe, E.E., C.M. Morley and N.R. Nielsen (1988) Airborne lidar measurements of smoke plume distribution, vertical transmission, and particle size. *Applied Optometrics*, **21**: 460–463.
Wadhams, P. (1981) Sea ice topography of the Atlantic Ocean in the region 70°W to 25°E. *Philosophical Transactions of the Royal Society, London*, **A302**: 45–85.

Review of the Oceanography and Micrometeorology of Arctic Leads and Polynyas

S.D. SMITH*
Department of Fisheries and Oceans
Bedford Institute of Oceanography
Dartmouth, Nova Scotia, Canada

ABSTRACT/INTRODUCTION

At predictable, recurrent locations throughout the polar regions, there are oceanic areas that remain either partially or totally ice-free under climatological conditions where we would expect the waters to be ice-covered. These are polynyas; they appear in winter, when ice temperatures are well below the freezing point for seawater and they are surrounded by water which is ice-covered. Polynyas are typically rectangular or elliptical and occur quasi-continuously in the same region. They range in size from a few hundred meters to hundreds of kilometers.

Polynyas are of interest for a number of reasons encompassing both physics and biology. Many polynyas, particularily those bordering arctic and antarctic lee coastlines during winter, are sites for active brine formation. This brine may affect the local water density structure and current field, and may also influence larger-scale water masses as it is mixed and advected beyond the polynya region. The relatively regular occurrence of polynyas makes them important as biological habitats, and associated open water can contribute, in spring, to a localized plankton bloom that can "seed" down-current areas. Large mammals use them as feeding grounds, and Inuit people have used polynyas as hunting grounds for the past 4000 years.

OBSERVATIONS

Polynyas can form via two different physical mechanisms. First, ice may form within the regions and be continually removed by winds, currents or both. The heat required to balance loss to the atmosphere and hence to maintain the open water is provided by the latent heat of fusion of the continually forming ice. In the second mechanism, oceanic heat may enter the region in sufficient quantities to locally prevent ice formation. The first mechanism creates "latent heat" polynyas, and the second creates "sensible heat" polynyas. These two mechanisms are not mutually exclusive, and both contribute in many cases to the maintenance of polynyas. As compared to the latent heat polynyas, whose primary oceanographic effect is introduction of brine into the water column, sensible heat polynyas are sites of very large sea-air heat fluxes that remove large quantities of heat from the water.

In certain areas, such as the portion of the Beaufort Sea west of Banks Island, polynyas may gradate into preferred areas for lead formation. Leads are open-

* Visiting Scholar, Department of Atmospheric Sciences, University of Washington–Seattle, Washington.

ings in pack ice which form as a result of local divergences in its drift. They characteristically take the form of long, narrow fissures meters to hundreds of meters wide and kilometers to tens of kilometers long. Leads have no fixed locations, but are more prevalent in areas of thinner ice and in the marginal ice zone. Even in the central polar pack ice during winter leads typically cover at least 1% of the area. Typical ice cover is shown in ice atlases: for Alaskan waters see LaBelle et al. (1983) and for Canadian waters see Markham (1981). Wadhams (1981) reviewed the ice cover of Greenland and the Norwegian Seas. Wadhams et al. (1985) report that the average distance of travel between leads varies from 5 km in the marginal ice zone to as much as 275 km in the central arctic pack ice. Thorndike et al. (1975) have modeled the ice thickness using data from U.S. and Soviet drifting stations in the Beaufort Sea and estimate about 1% of 1- to 10-cm ice cover during the winter months. From a submarine traverse under the North Pole in summer, McLaren (1988) reported 2.6% of open water and new ice (<30 cm).

In the winter pack ice, a newly formed lead can freeze over within less than a day (Bauer and Martin 1983) or can close up without warning in response to converging ice drift. At other times the processes that initially open up a lead can continue to keep it open for weeks. The thin ice of a frozen-over lead remains thinner and weaker than the surrounding pack ice, even though it grows faster. Converging ice drift forces can cause a refrozen lead to fail in compression, piling up ice blocks which freeze together as an ice ridge. The physics of arctic pack ice, leads and polynyas are reviewed by Pritchard (1980) and Untersteiner (1986), and Jacobs (1985) gives an overview of work in the Antarctic. The very substantial contributions of Soviet scientists (e.g., Makshtas 1984) are not covered here.

THE SURFACE HEAT BUDGET

The atmospheric processes associated with polynyas and leads are basically the same. Extreme sea-air temperature differences of 20–40°C are common in winter. Upward sensible and latent heat fluxes depend mainly on air temperature, wind speed and fetch. The sensible heat flux in air is several times larger than the latent heat flux because of the relatively low specific humidity of saturated air in contact with seawater at the freezing point. Radiative transfers may be influenced by fog, which is characteristic of very cold air over a water surface.

The surface heat balance (Badgley 1966, Vowinckel and Orvig 1971) is expressed by

$$H + LE - Q_s(1-A) + Q_L = H_w + L_f F \qquad (1)$$

where H = sensible heat flux in air
H_w = sensible heat fluxes in water
L = latent heat of evaporation
L_f = latent heat of fusion
E = rate of evaporation at the surface (mass per unit area per unit time)
F = rates of freezing at the surface (mass per unit area per unit time)
Q_s = incident solar radiation
A = surface albedo
Q_L = net upward long wave radiation.

Positive values indicate upward heat transport. Terms on the left-hand side represent atmospheric processes, while those on the right-hand side occur in the water. All terms are vastly different for the open water of a lead or polynya than for the surrounding ice and snow surface. Heat exchange at the open water surface of a lead is two orders of magnitude greater than that through surrounding snow-covered pack ice, and so even a small percentage of leads and thin ice can dominate regional heat budgets in winter (Maykut 1978). Release of heat from the ocean is one of the principal reasons why winters in the Arctic are less frigid than those in the Antarctic, even at sea level. In the spring and summer, open water surfaces absorb over 90% of incoming solar radiation while snow-covered ice reflects a similar proportion. Leads then provide centers of initial warming prior to the spring breakup (Hall and Rothrock 1987).

LEAD AND POLYNYA EXPERIMENTS

Several experiments have studied the atmospheric and oceanographic processes in the vicinity of leads and polynyas. The Miyake (1961) experiment established techniques and marked an early application of modern boundary-layer theory. The AIDJEX Lead Experiment of 1974, planned as a multidisciplinary study of arctic leads, was particularly successful in determining turbulent fluxes of sensible heat over natural and artificial leads (Andreas et al. 1979, Andreas and Murphy 1986). However, the structure and extent of oceanic convection beneath leads (Kozo 1983) remains an area of theoretical speculation. Radiative properties of the ice fog, which typically overlies leads and polynyas also remain an area of conjecture. A difficulty is that deployment times of typical experiments was comparable to the lifetime of leads and that the limited deployment radius did not always encompass a suitable lead.

Rather than being continually ice free, the northern Bering Sea polynyas open up during periods of northerly winds and close when winds are southerly. Southerly winds advect existing pack ice into the region, closing the polynyas. Closing may also occur when the surface radiation balance shifts strongly upward (rapid cooling) during periods of clear skies and low wind speeds. Pease (1987) has modeled the size of latent heat polynyas in the Bering Sea using a simplified surface heat budget (eq 1), and has successfully compared predictions of the model with field data. Ou (1988) extended the Pease steady-state model to include time-dependent winds and temperatures and with a finite drift rate for frazil ice.

The North Water is a polynya with a large area of relatively loose pack ice between Canada and Greenland. An international study in 1978–1981 led to a heat budget taking into account the distribution of pack ice and open water (Steffen 1985, 1986). While it is generally held that the North Water is maintained mainly by southward drift of ice, this study concluded that advection of warmer water is also a major factor.

The Dundas polynya experiment (Topham et al. 1983) was successful in determining sensible heat flux and verifying a parameterization scheme (Smith 1981, 1988) which was used to calculate a surface heat budget (den Hartog et al. 1983) for the duration of the experiment. Current and ocean temperature measurements in the strong tidal current regime of the area showed that advection of water up to 2°C above the freezing point was sufficient to maintain the group of polynyas in the area. Smith et al. (1989) will present a more extensive review of the physics of polynyas and leads.

REFERENCES

Andreas, E.L and B. Murphy (1986) Bulk transfer coefficients for heat and momentum over leads and polynyas. *Journal of Physical Oceanography*, **16**: 1875–1883.

Andreas, E.L, C.A. Paulson, R.M. Williams, R.W. Lindsay and J.A. Businger (1977) The turbulent heat flux from Arctic leads. *Boundary-Layer Meteorology*, **17**: 57–91.

Badgley, F.J. (1966) Heat budget at the surface of the Arctic Ocean. In *Proceedings of Symposium on Arctic Heat Budget and Atmospheric Circulation* (J.O. Fletcher, Ed.). Rand Corporation, p. 267–277.

Bauer, J. and S. Martin (1983) A model of grease ice growth in small leads. *Journal of Geophysical Research*, **88**: 2917-2925.

den Hartog, G., S.D. Smith, R.J. Anderson, D.R. Topham and R.G. Perkin (1983) An investigation of a polynya in the Canadian Archipelago: 3. Surface heat flux, *Journal of Geophysical Research*, **88**: 2911–2916.

Hall, R.J. and D.A. Rothrock (1987) Photogrammetric observation of the lateral melt of sea ice floes. *Journal of Geophysical Research*, **92:** 7045–7048.

Jacobs, S.S. (Ed.) (1985) *Oceanology of the Antarctic Continental Shelf.* Antarctic Research Series, American Geophysical Union, 43.

Kozo, T.L. (1983) Initial model results for Arctic mixed layer circulation under a refreezing lead. *Journal of Geophysical Research*, **88**: 2926–2934.

LaBelle, J.C., J.L. Wise, R.P. Voelker, R.H. Schulze and G.M. Wohl (1983) Alaska Marine Ice Atlas. Arctic Information and Data Center, University of Alaska, Fairbanks.

Makshtas, A.P. (1984) Heat balance of arctic ice in winter. *Gidrometeoizdat, Leningrad.* (English trans. to be published by National Science Foundation).

Markham, W.E. (1981) Ice Atlas, Canadian Arctic Waterways. Canadian Atmospheric Environment Service, Hull, Canada.

Maykut, G.A. (1978) Energy exchange over young sea ice in the central Arctic. *Journal of Geophysical Research*, **83**: 3646–3658.

McLaren, A.S. (1988) Analysis of under-ice topography in the Arctic Basin as recorded by the USS *Nautilus* during August 1958. *Arctic*, **41:** 117–126.

Miyake, M. (1961) Transformation of atmospheric boundary layer induced by inhomogeneous surfaces (Growth of internal boundary layer). M. Sc. Thesis, Department of Atmospheric Science, University of Washington, Seattle.

Ou, H.W. (1988) A time-dependent model of a coastal polynya. *Journal of Physical Oceanography*, **18**: 584-590.

Pease, C.H. (1987) The size of wind driven coastal polynyas. *Journal of Geophysical Research*, **92**: 7049–7059.

Pritchard, J.A. (1980) *Sea ice processes and models.* Seattle: University of Washington Press.

Smith, S.D. (1981) Coefficients for sea-surface wind stress and heat exchange. Report Bedford Institute of Oceanography, Dartmouth, Nova Scotia, Canada, BI-R-81-19.

Smith, S.D. (1988) Coefficients for sea surface wind stress, heat flux and wind profiles as a function of wind speed and temperature. *Journal of Geophysical Research*, **93**: 15467–15472.

Smith, S.D., R.D. Muench and C.H. Pease (1989) Polynyas and leads: An overview of physical processes and environment. *Reviews of Geophysics* (submitted).

Steffen, K. (1985b) Warm water cells in the North Water, northern Baffin Bay during winter. *Journal of Geophysical Research*, **90:** 9129–9136.

Steffen, K. (1986) Ice conditions of an arctic polynya: North water in winter. *Journal of Glaciology*, **32**: 383–340.
Thorndike, A.S., D.A. Rothrock, G.A. Maykut and R. Colony (1975) The thickness distribution of sea ice. *Journal of Geophysical Research*, **80**: 4501–4513.
Topham, D.R., R.G. Perkin, S.D. Smith, R.J. Anderson and G. den Hartog (1983) An investigation of a polynya in the Canadian Archipelago: 1. Introduction and oceanography. *Journal of Geophysical Research*, **88**: 2888–2899.
Untersteiner, N., Ed. (1986) *The Geophysics of Sea Ice*. New York: Plenum Press.
Vowinckel, E. and S. Orvig (1971) Synoptic energy budgets at three polar stations. *Journal of Applied Meteorology*, **10**: 387–396.
Wadhams, P. (1981) The ice cover of the Greenland and Norwegian Seas. *Reviews of Geophysics and Space Physics*, **19**: 345–393.
Wadhams, P., A.S. McLaren and R. Weintraub (1985) Ice thickness distribution in Davis Strait in February from submarine sonar profiles. *Journal of Geophysical Research*, **90**: 1069–1077.

Wind-Generated Polynyas off the Coasts of the Bering Sea Islands

T.L. KOZO, L.D. FARMER AND J.P. WELSH
Naval Oceanographic and Atmospheric Research Laboratory
Polar Oceanography Branch
U.S. Army Cold Regions Research and Engineering Laboratory
Hanover, New Hampshire, U.S.A.

ABSTRACT

The relationship of winds derived from mesoscale meteorological networks to polynya sizes and orientations was investigated. Defense Meteorological Satellite Program imagery was merged with atmospheric pressure network data from the Bering Sea for March 1988. During the month, wind systems drove sea ice southward, creating and maintaining polynyas south of St. Lawrence, St. Matthew, and Nunivak Islands. Existing land stations, the deployment of a moored pressure buoy south of the ice edge, and a new automated weather station on St. Matthew Island have allowed the "creation" of meso-networks that surround these lee-shore polynyas. This analysis (rather than synoptic) has shown that polynya lengths and orientations can be simply related to the mesonet computed geostrophic winds. The typical time lag between the onset of a geostrophic wind and the appearance of "windsock" type tracking of the polynyas is 24 hours.

INTRODUCTION

Undercast-free visible band satellite imagery of the ice-covered Bering Sea appearing in scientific literature over the past 15 years points to a very striking phenomenon. Lee shore polynyas are almost always present off the St. Lawrence, St. Matthew, and Nunivak Island south coasts. The relative openness of these polynyas and their resemblance to "windsocks" are unmistakable. Representative studies by Shapiro and Burns (1975), Cavalieri et al. (1983), Paluszkiewicz and Niebauer (1984), Reynolds et al. (1985), and Shapiro et al. (1988) show evidence of these features.

These latent heat polynyas (Smith 1988) open and persist because sea ice is removed as on a wind-driven conveyor belt almost as fast as it forms. Apparently the combination of wind speed, air temperature, and solar radiation in this area does not allow the polynyas to reach maturity (polynya length ceases to increase) within a typical synoptic period of 5 days (Pease 1987). Oceanic processes driven by brine rejection (Kozo 1983) lead to density-induced current flow (Schumacher et al. 1983) beneath the polynyas.

An initial study focusing only on wind effects has been launched to relate mesoscale meteorological network (Kozo et al. 1987) data to polynya orientation and length. The polynya information was taken from Defense Meteorological Satellite Program (DMSP) Imagery obtained in 19 March 88. Existing land weather stations, a moored oceanic weather-buoy below the southern limit of sea ice in the Bering Sea, and an automated weather station on St. Matthew Island have allowed the implementation of polynya-surrounding mesonets (Fig. 1) for the above-mentioned Bering Sea Islands. Previous work (Kozo 1984) has shown that synoptic analyses from the National Meteorological Center (NMC) are often insufficient to reproduce actual wind stresses at specified locations due to mesoscale effects and/or poor resolution. In addition, synoptic charts from the Bering Sea region during the study period did not have the detail necessary for precise predictions of winds at each of the three study islands on moderate to light wind days (see Fig. 2).

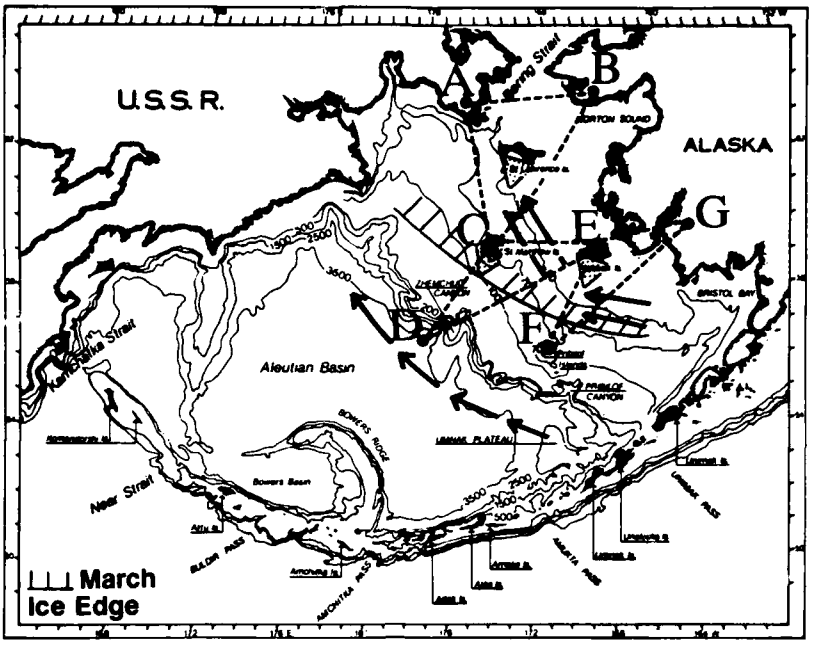

Figure 1. Map of the Bering Sea shelf and basin (from Paluszkiewicsz and Niebauer 1984) showing the ice island polynyas (speckled triangles). The St. Lawrence Island mesonet stations are Provideniya (A), Nome (B), and St. Matthew Island (C). The St. Matthew Island mesonet stations are C, Mekoryuk Airport (E) and Buoy 35 (D). The Nunivak Island mesonet stations are E, St. Paul (F) and Bethel Airport (G). The 50-m, 100-m, and 200-m (shelf break) isobaths define three hydrographic domains. The coastal and slope current locations are shown by bold arrows.

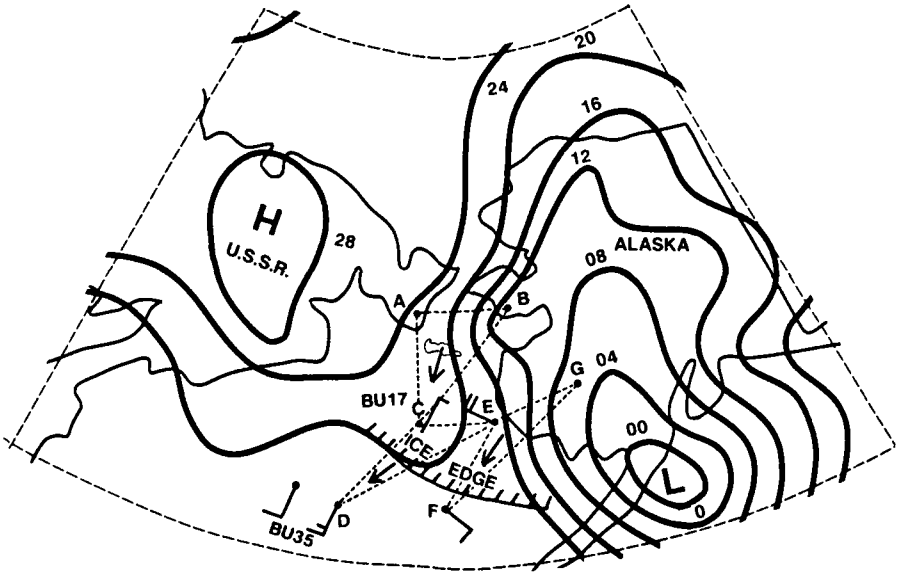

Figure 2. Surface atmosphere pressure chart showing the lack of detail in the area covered by the mesonets (dashed triangles). The arrows show that three different wind stress directions are predicted within nets A-B-C, C-D-E, and E-F-G for 13 March 1988.

STUDY AREA

The eastern Bering Sea has a wide (~500 km), shallow (~170 m at the shelf break) continental shelf (Paluszkiewicz and Niebauer 1984). Just to the east and west of St. Lawrence Island (Fig. 1), the northern flow is strong (0.10–0.15 m/s) but south of St. Lawrence the mean flow is weak (0.02–0.04 m/s) (Schumacher et al. 1983). In fact, the characteristic flow on the shelf is normally slow (≤ 0.02 m/s, Kinder and Schumacher 1981). Three distinct hydrographic domains (Fig. 1) are defined: 1) the coastal domain inshore of 50 m, dominated by buoyancy-driven flow (0.01–0.03 m/s) contains the St. Lawrence Island and Nunivak Island polynyas, 2) the middle domain between 50 m and 100 m (weak flow) that contains the St. Matthew Island polynya, and 3) the outer domain between 100 m and the shelf break (weak flow). Seaward of the shelf break, the Bering slope current (Fig. 1) flows at a speed of approximately 0.1 m/s (Paluszkiewicz and Niebauer 1984). In essence, the available oceanographic data for the lee shore polynyas areas in this study indicate that sea ice drift will be dominated by wind systems.

During March 1988, there was a tendency for low pressure systems to propagate zonally across the southern Bering or northward across the Alaskan side of the Bering Sea. Both situations resulted in driving sea ice southward (Pease et al. 1982) creating and maintaining polynyas off the southern coasts of St. Lawrence, St. Matthew, and Nunivak Islands.

DATA AND ANALYSIS TECHNIQUES

Satellite imagery

The polynya's size and ice motion data for March 1988 came from visible band DMSP satellite imagery. The net 24-hour ice motion was measured directly by tracking an ice edge location south of the study islands. The system resolution (designated LF, light fine) is 0.5 km. Displacements were determined by registration of images relative to adjacent topographic features. The estimated uncertainty is ± 5 km.

Atmospheric pressure, temperature, and geostrophic winds

Sea level barometric pressure and temperature data were taken simultaneously from weather station combinations in the study area (Fig. 1). The three meso-networks used were:

1. Bukhta Provideniya (Russian)—Nome—St. Matthew Island (Buoy 17, automated station designator from the National Climatic Center [NCC]).

2. Buoy 17—Buoy 35, a moored (57°N, 177.7°W), automated meteorological station; NCC collected the data)—Mekoryuk Airport.

3. St. Paul—Mekoryuk Airport—Bethel Airport.

Pressure and temperature data from first-order weather stations, such as Nome, Bethel, and St. Paul, have accuracies better than ±0.25 mb and ±1°C, respectively. Provideniya and the buoys 17 and 35 are part of a global station network transmitting to the National Meteorological Center (NMC). Their accuracies are within the same limits. Mekoryuk Airport data are assumed to be close to the above limits since it has air traffic.

Geostrophic winds are computed from station pressure and temperature data for the above-mentioned network combinations. The solution is best at the geometric center of each network, which was chosen for its proximity to the study polynyas. The atmospheric flow is assumed to be in geostrophic balance. Using the station geometry as shown in Figure 1, pressure can be represented as a function of latitude (y) and longitude (x) on a plane surface. The pressure gradient ∇P can be computed and geostrophic velocity V_G can be calculated since the Coriolis parameter (f) is known and density (ρ) for dry air can be estimated from station temperatures (Kozo et al. 1987).

Station errors of 1 °C in temperature can cause errors of 0.34% in velocity magnitude since they affect ρ estimates. Errors of 0.25 mb can cause maximum speed errors of 1.5 m/s and direction errors greater than 15% of full scale for wind speeds below 3 m/s. Therefore, at wind speeds of 3 m/s or below, computed wind directions are not reliable.

Calculation of ice velocities

The conversion of geostrophic wind speed (see above) to 10 m wind speed (V_S) is $0.6V_G = V_S$ (Albright 1980). The sea ice, free drift speed (V_i) used to estimate ice advection at the polynyas edges is $0.03V_S = V_i$. This is an oceanographic "rule of thumb" (Csanady 1984). Predicted polynya lengths given below are the product of V_i and the number of days (in seconds) that the wind blew in a given direction.

RESULTS AND DISCUSSION

St. Lawrence Island

Figure 3 shows a Bering Sea DMSP image from 14 March 1988. The apex of the triangular polynya to the lee of St. Lawrence Island lines up with the 170°W meridian. The prior period (10–13 March 1988) had an average V_G of 18 m/s with a wind direction (θ) from 1°. The predicted V_i (Section 3.3) was 0.32 m/s

with a polynya length of 112 km. The measured polynya orientation and length were 0° and 105 km, respectively.

The resultant St. Lawrence Island polynya (Fig. 4), 19 March 1988, edge drift and orientation (prior five day period 14–18 March 1988) was due to an average V_G of 15.4 m/s and a θ of 68°. The predicted V_i was 0.28 m/s and predicted edge drift was 120 km. The measured polynya orientation was 60° from north, using the southwestern extreme edge. The polynya's western edge drift was 115 km.

Nunivak Island

The 13 March 1988, image (Fig. 5) shows a Nunivak Island lee polynya with evidence of two earlier sequential prevailing winds. The eastern edge of the polynya changes orientation at the 165° meridian. The three day period (10–12 March 1988) had an average V_G of 16.2 m/s from 335°. The drift prediction (see *Calculation of Ice Velocities*) from a V_i of 0.29 m/s was 76 km. The actual drift was approximately 80 km with an orientation angle of 330° at 165°W. The V_G one day before 10 March 1988 was from 45° which ap-

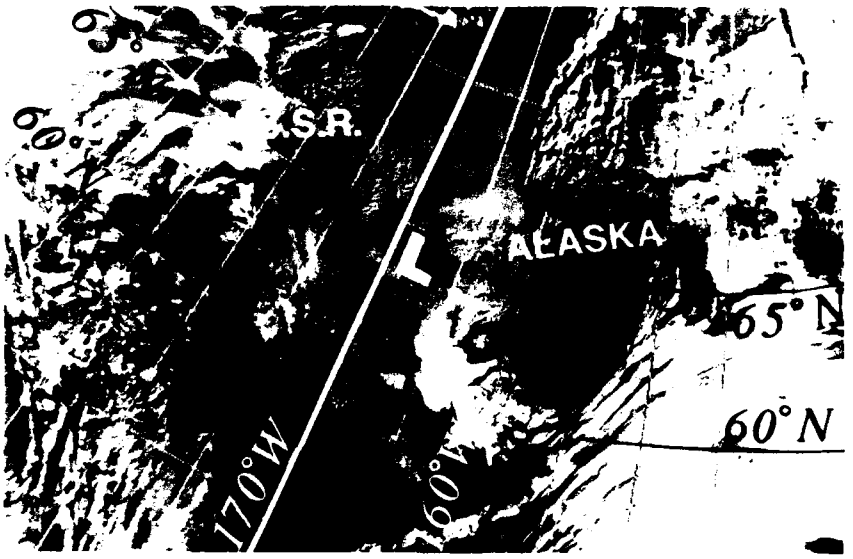

Figure 3. DMSP image taken 14 March 1988. The apex of the polynya south of St. Lawrence Island (L) lines up with the 170° W meridian.

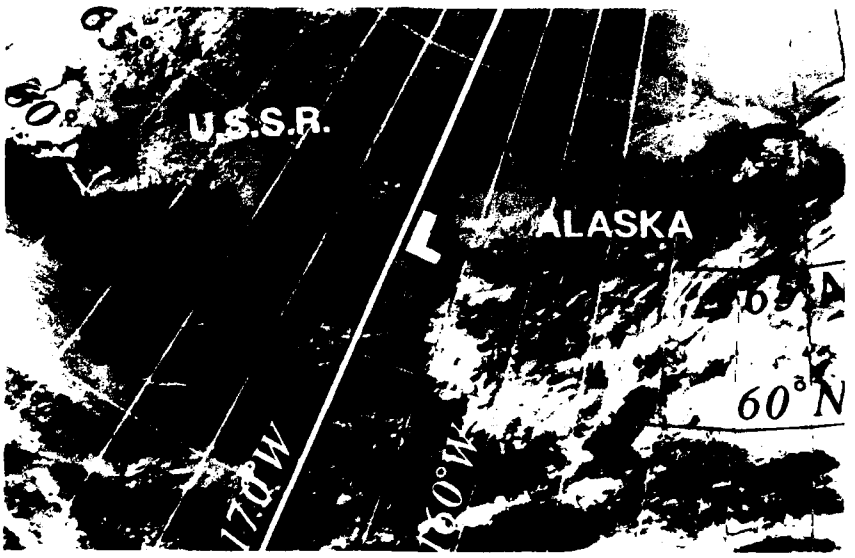

Figure 4. DMSP image taken 19 March 1988. Taking the apex at the southwestern extreme edge, the triangular polynya to the lee of St. Lawrence Island (L) has an orientation of approximately 60°.

Figure 5. DMSP image taken 13 March 1988. The lee polynya for Nunivak Island (N) changes orientation at its intersection with the 165° (bold white line) meridian from 330° to 45°.

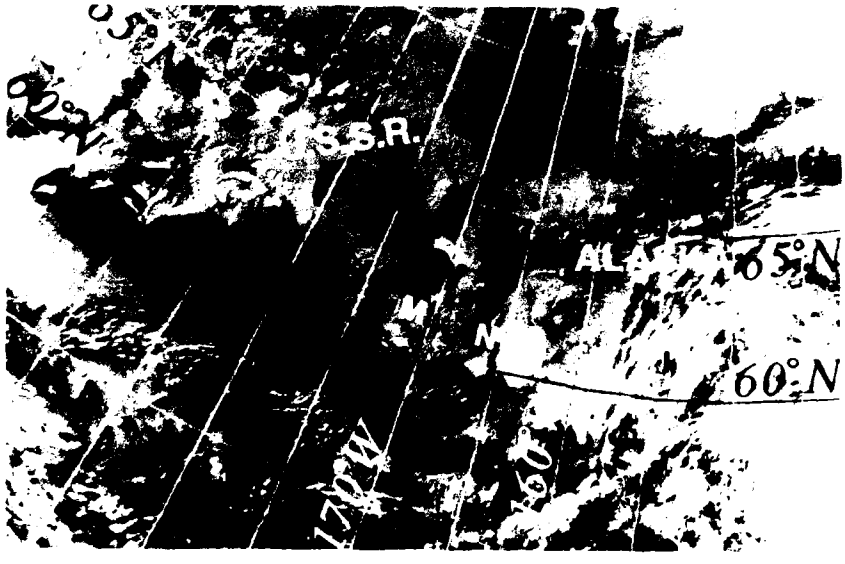

Figure 6. DMSP image from 18 March 1988. The polynya associated with Nunivak Island (N) has a 65° orientation. The polynya associated with St. Matthew Island (M) has a 75° orientation. The analogy with airport windsocks is unmistakable.

proximates the polynya orientation south of its intersection (eastern edge) with 165°W. Prior imagery was poor due to cloud cover.

St. Matthew Island

Figure 6 also shows an example of the St. Matthew Island polynya simulating a windsock. The average V_c for a five-day period (13 [noon] to 18 [noon] March), was 20.3 m/s from 83°. The predicted V_i (see *Calculation of Ice Velocities*) and resultant ice drift were 0.37 m/s and 172 km, respectively. The actual drift was approximately 160 km in a 75° direction.

Three-island summary

The polynya length predictions for all three islands were better than 90% of the measured length and the θ predictions were within 95% of the full scale when compared to measured θ values. The predicted vs actual measurements of polynyas orientation and length are summarized in Table 1.

Table 1. Polynya size and orientation predictions (*P*) vs actual measurements (*M*).

Island	Date Mar 88	V_G (m/s)	V_i (m/s)	Length (km) P	Length (km) M	θ (° from) P	θ (° from) M
St. Lawrence	10–13	18.0	0.32	112	105	1	0
	14–19	15.4	0.28	120	115	68	60
Nunivak	10–13	16.2	0.29	76	80	335	330
	14–18	21.5	0.39	139	130	67	65
St. Matthew	13–18	20.3	0.37	172	160	83	75

SUMMARY AND CONCLUSIONS

In a very short-term, preliminary study during 19 March 1988, DMSP imagery was used to match actual sea ice drift, in polynyas areas, to predicted sea ice drift. The use of mesoscale meteorological networks (instead of synoptic networks) has been proven effective in predicting lee-shore polynya sizes and orientations for three Bering Sea islands. The reductions of V_G to V_S and V_S to V_i (see *Calculation of Ice Velocities*) are relatively standard techniques. The deployment of a meteorological buoy south of the maximum Bering Sea ice edge and an automated land station on St. Matthew Island has "created the geometry" for new polynya-surrounding meso-networks in conjunction with existing land stations.

There is an apparent time lag of 24 hours between the onset of a geostrophic wind and the windsock type tracking of the polynyas. At present, imagery has been obtained only on a daily basis. The polynyas (at this time of year) receive some solar radiation, and do not appear to close. Instead, they seem to "record" the previously prevailing wind. Data were not obtained on polynya creation thresholds since the ice canopy is in a perpetual "unhealed" state with polynyas failing to reach equilibrium size within a typical synoptic period of 5 days (Pease 1987).

ACKNOWLEDGMENTS

The primary funding for this study was obtained from the Naval Ocean Research and Development Activity through the U.S. Navy ASEE Summer Faculty Research Program. This paper was prepared while the first author was the Naval Oceanography Command and the Office of Naval Research Professor in Polar Oceanography at the U.S. Naval Academy, Annapolis, Maryland (contracts N0006589 WR00009 and N0001489 WR24021, respectively). The authors thank L. J. Torgerson of the University of Alaska and employees of the National Weather Service, Fairbanks Forecast Office.

REFERENCES

Albright, M. (1980) Geostrophic wind calculations for AIDJEX. In *Proceedings of the Symposium on Sea Ice Processes and Models* (R.S. Pritchard, Ed.). Seattle: University of Washington Press, p. 402–409.

Cavalieri, D.J., S. Martin and P. Gloersen (1983) Nimbus 7 SMMR observations of the Bering Sea ice cover during March 1979. *Journal of Geophysical Research*, **88**: 2743–2754.

Csanady, G.T. (1984) *Circulation in the Coastal Ocean*. Hingham, Massachusetts: D. Reidel.

Kinder, T.H. and J.D. Schumacher (1981) Circulation over the continental shelf of the southeastern Bering Sea. In *The Eastern Bering Sea Shelf: Oceanography and Resources* (D.W. Hood and J.A. Calder,Ed.). Seattle: University of Washington Press, vol. 1, p. 53–75.

Kozo, T.L. (1983) Initial model results for Arctic mixed layer circulation under a refreezing lead. *Journal of Geophysical Research*, **88**: 2926–2934.

Kozo, T.L. (1984) Mesoscale wind phenomena along the Alaskan Beaufort Sea coast. In *The Alaska Beaufort Sea: Ecosystems and Environment* (P.W. Barnes, D.M. Schell, and E. Reimnitz, Ed.). Orlando: Academic Press, Inc., p. 23–45.

Kozo, T.L., W.J. Stringer and L.J. Torgerson (1987) Nowcasting of sea ice movement through the Bering Strait with a description of major driving forces. *Monthly Weather Review*, **115**: 193–207.

Paluszkiewicz, T. and H.J. Niebauer (1984) Satellite observations of circulation in the eastern Bering Sea. *Journal of Geophysical Research*, **89**: 3663–3678.

Pease, C.H. (1987) The size of wind-driven coastal polynyas. *Journal of Geophysical Research*, **92**: 7049–7059.

Pease, C.H., S.A. Schoenberg, and J.E. Overland (1982) A climatology of the Bering Sea and its relation to sea ice extent. U.S. Department of Commerce, Pacific Marine Environmental Lab, Seattle, Washington, NOAA Technical Report ERL 419-PMEL 36.

Reynolds, M., C.H. Pease and J.E. Overland (1985) Ice drift and regional meteorology in the southern Bering Sea: Results from MIZEX West. *Journal of Geophysical Research*, **90**: 11,967–11,981.

Schumacher, J.D., K. Aagaard, C.H. Pease and R.B. Tripp (1983) Effects of a shelf polynya on flow and water properties in the Northern Bering Sea. *Journal of Geophysical Research*, **88**: 2723–2732.

Shapiro, L.H. and J.J. Burns (1975) Major late-winter features of ice in northern Bering and Chukchi Seas as determined from satellite imagery. University of Alaska, Geophysical Institute Report No. UAG R-236, Sea Grant Report no. 75-8. p. 1–6.
Shapiro, L.H., K. Ahlnas and C. Olmsted (1988) A rapid method for mapping sea ice distribution and motions from NOAA satellite imagery. In *Proceedings of 9th International Conference on Port and Ocean Engineering under Arctic Conditions (POAC '87)*. Fairbanks, Alaska: University of Alaska, vol 1, p. 137–147.
Smith, S.D. (1988) Review of oceanography and meteorology of arctic leads and polynyas. In *Office of Naval Research Arctic Leads Workshop, University of Washington, December 12–14, 1988*. Seattle, Washington: Office of Naval Research, Applied Physics Laboratory, p. 1–21.

Recent Measurements of Sea Ice Topography in the Eastern Arctic

W.B. KRABILL
NASA Goddard Flight Center
Wallops Flight Facility
Wallops Island, Virginia, U.S.A.

R.N. SWIFT
EG&G Washington Analytical Services, Inc.
Pocomoke, Maryland, U.S.A.

W.B. TUCKER III
U. S. Army Cold Regions Research and
Engineering Laboratory
Hanover, New Hampshire, U.S.A.

ABSTRACT

During a multinational remote sensing experiment in May 1987, the NASA Airborne Oceanographic Lidar (AOL) was used to collect profiles of the sea ice surface topography in the eastern Arctic. A Global Positioning System (GPS) receiver was used to provide aircraft positioning to an accuracy of about 50 m. The AOL is a pulsed laser that provides a profile free of phase shift discontinuities common to continuous wave lasers. Similar to other laser data, however, the aircraft altitude variation requires removal from the profile prior to calculation of the ice surface roughness statistics. As with previous data, there remains an uncertainty as to the freeboard level of the ice after the aircraft motion has been removed; thus small-scale roughness statistics are considered unreliable. However, statistics of pressure ridges can be generated with confidence. The statistical results of ridges from this data set, consisting mainly of ridge height and frequency distributions, compare well with previous results obtained from this area of the Arctic. Consistent with previous findings, the AOL data indicate that while the regional mean ridge heights from the area north of Greenland are similar to those reported for other parts of the Arctic, the average kilometer contains substantially more ridges than have been observed in other Arctic locations.

INTRODUCTION

During May 1987, the U. S., Canada and Great Britain participated in a joint remote sensing experiment in the eastern Arctic. A NASA P-3A aircraft, as part of the total mission complement, contained several passive microwave radiometers, a PRT-5 and the AOL system. In addition, this aircraft collected aerial photography with a 9-in. format camera as well as with a 35-mm Flight Research camera. Of primary interest to this study were the lidar and the aerial photography. A GPS receiver was operated whenever a sufficient number of satellites were within view. The GPS receiver provided positioning accuracy to about 50 m.

The AOL was operated on low-altitude (220-m) tracks at a sampling rate of 200 pulses/second. At the nominal cruising speed of the aircraft of about 120 m/s, this translates to a sample spacing of about 0.6 m. The footprint size of the laser on the ice surface from a nominal altitude of 200 m is about 0.6 m. The sampling rate of the aerial photography was not sufficient to provide continuous coverage of the ice beneath the aircraft; instead there were gaps of several hundred meters between successive photographs. The AOL trackline passed approximately through the center of each photograph; thus it was a simple matter to correlate the visible features (ridges, leads etc.) with their corresponding elevation profiles.

The AOL is an aircraft-mounted facility utilized for testing various potential applications for airborne laser systems. During the May 1987 experiment the AOL was equipped with a pulsed nitrogen gas laser with an output wavelength of 337 nm. A more complete description of the AOL system as configured in

the terrain/ice topographic mode can be found in Krabill et al. (1984). The use of a pulsed laser permits the collection of ice that is relatively noise-free and not subject to the phase shift discontinuities that are common for continuous wave lasers. The unprocessed profile does, however, contain the record of aircraft altitude variation upon which is superimposed the ice terrain profile. The aircraft motion must be removed prior to examination of the terrain statistics. Methods have been developed that employ low pass filtering of straight line segments connecting "low points" in the profile and subsequently subtracting this from the original profile to remove the aircraft motion (Hibler 1972, Holyer et al. 1973). In this study we followed the same tack, only we manually constructed and digitized the smooth line through the minima points. These points were carefully selected to be either very thin ice or open water areas that were identified from the aerial photographs. Although this procedure results in removal of the large majority of the aircraft motion, some error still remains in the profile, probably on the order of about 20 cm. For this reason, the profiles are not useful for small-scale roughness statistics such as the identification of ice floe freeboard elevations. They are, however, extremely useful for generating the statistics of sea ice ridges.

High-quality AOL data were obtained on 20 May 1987. On this day two low-altitude tracklines of 120 and 160 km were flown north of Greenland (Fig. 1). Aircraft motion was removed from both tracklines as described above. The statistics of ridges identified on these tracklines were compiled and subsequently compared to previous ridge data from this same area of the Arctic.

RESULTS

Histograms of the elevation data for the 120- and 160-km sections are shown in Figure 2. Substantial differences in the distributions of ice elevations between the two sections are not apparent. Note that the height distributions extend only to 2.5 m; in fact heights of ridges extend considerably higher than this value. They occur so infrequently, however, that they would not appear at the present scale of the figure.

Ridges were identified by a computer algorithm employing the Rayleigh criterion which has been applied previously to laser profiles (Wadhams 1976).

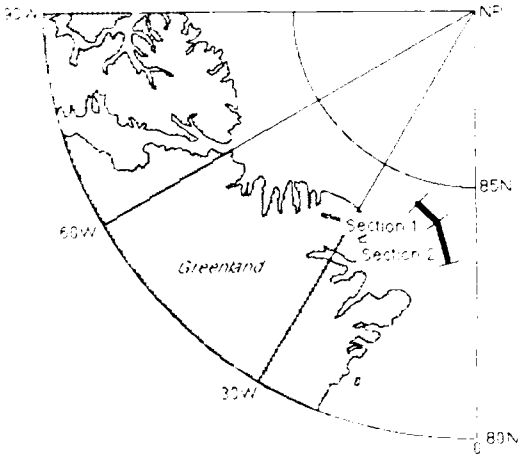

Figure 1. Location of the AOL data tracks on 20 May 1987. Section 1 encompassed 120 km and Section 2 was 160 km in length.

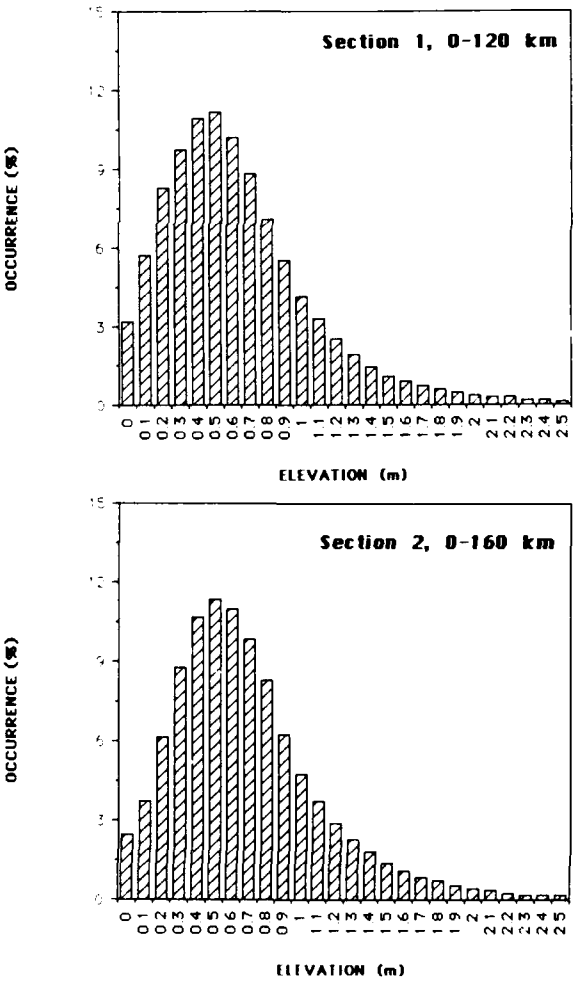

Figure 2. AOL ice elevation distributions for the 120- and 160-km long tracklines.

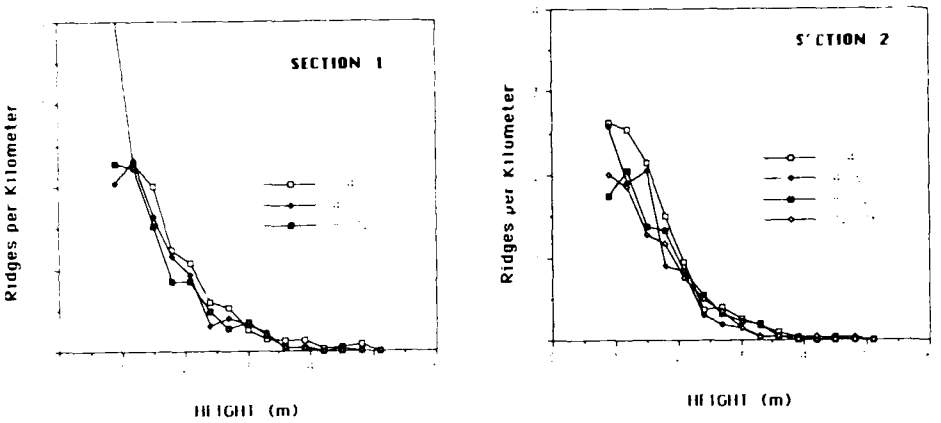

Figure 3. Ridge height frequency distributions for 40-km subsections of AOL Sections 1 and 2.

Basically this technique identifies a value as a ridge peak if 1) it is above a selected minimum value and 2) the elevation of the peak is at least twice as high as the elevation of the valleys to either side.

After some trial and error, we chose 0.8 m as the minimum height criterion. Ridge height distributions for a given trackline were calculated by counting the ridges in 0.3-m-height bins. The 120- and 160-km tracklines were further subdivided into 40-km sections and the ridges were counted for each section.

In Figure 3, the ridge height frequency distributions for each 40-km subsection of the 120- and 160-km sections of track are shown. Except for ridges less than 2.0 m in height, the height distributions for all subsections appear very similar. This indicates that the data are from a reasonably "homogeneous" region, in that ridge statistics within the region are much the same. It is not surprising that considerable variation exists between sections and subsections in the lower ridge height categories; here we are undoubtedly counting occasional sastrugi and miscellaneous upturned blocks from poorly developed ridges. The shape of the distributions appears to be negative exponential in nature, typical of that found for ridge height distributions in other investigations (Tucker et al. 1979, Wadhams 1976, 1980).

In past studies, correlations have been observed between the mean ridge height and the number of ridges (Wadhams 1976, 1980). Other investigations have sought this relationship but have failed to find it (Tucker et al. 1979). However, it is useful to plot data in this fashion for comparison with other data sets. We have plotted the mean ridge height vs the number of ridges per kilometer for each 40-km subsection of the AOL 120- and 160-km sections in Figure 4. In the same figure we have also plotted data from this same general area reported by Wadhams (1980),

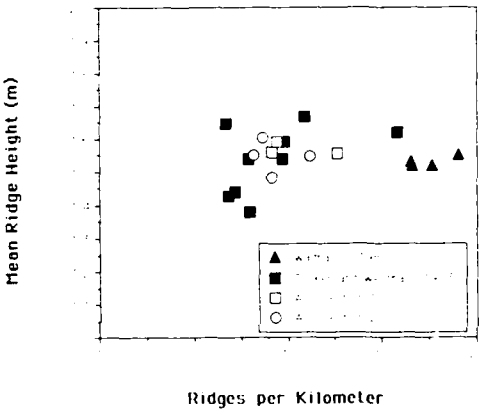

Figure 4. Mean ridge height vs the number of ridges per kilometer for the 40-km subsections of AOL Sections 1 and 2 along with data from the same area of Tucker and Westhall (1973) and Wadhams (1980).

which was collected in October 1976. Likewise, data from the same arctic location reported by Tucker and Westhall (1973) that encompass the fall and winter months are also included on the figure. The Wadhams data were calculated for 100-km sections using a 0.98-m minimum ridge height while the Tucker and Westhall data, like the AOL data, were calculated for 40-km sections with a 0.9-m minimum height cutoff.

While none of the data sets appear to show correlation between mean ridge height and the number of ridges, they appear to agree well with each other. Considering that the data were taken during different seasons over a period spanning nearly two decades, there seems to be reasonable consistency amongst the data. It is especially encouraging that the AOL data lie neatly in the midst of the other data. The exception to the above statements is that the Wadhams

Table 1. Ridge parameters from other arctic areas (from Weeks et al. 1989) compared to the AOL data from northern Greenland.

Location	*Ridges/km*	*Mean ridge ht (m)*
Central Beaufort Sea	2.6	1.47
Beaufort/Chukchi Shear Zone	4.4	1.51
West Eurasian Basin	4.7	1.50
Kaktovic (20 km section)	13.3	1.40
AOL Section 1	9.3	1.56
AOL Section 2	10.4	1.55

data show more ridges than either of the other two data sets. This is somewhat surprising in that the Wadhams ridge identification criteria required ridges to be at least 0.98 m in height, and therefore many small ridges should have been eliminated. It appears that ridging conditions were somewhat more severe during the period in which Wadhams collected his data.

It is worthwhile to compare the ridging intensity values extracted from the AOL data to values obtained from other parts of the Arctic. Values are reported in many varied sources, but Weeks et al. (1989) conveniently extracted a few ridging intensity values from various arctic locations for comparison to ridging observed in the Ross Sea of Antarctica. In Table 1 we compare the number of ridges per kilometer and the mean ridge height obtained from the AOL data to that shown by Weeks et al. (1989) from other arctic locations. All data have presumably had minimum ridge height cutoff values set between 0.8 and 1.0 m and thus should be reasonably comparable. Additionally, all data were collected during the late winter or spring seasons.

The mean ridge heights from the different locations are not significantly different. This again points out that we do not see a significant correlation between mean ridge height and the numbers of ridges. Differences between the numbers of ridges observed from the various locations are significant, however. All areas except Kaktovic (Barter Island, Alaska) have less than half as many ridges as that north of Greenland at the AOL sampling site. The Kaktovic site was the roughest area found in a repeated survey of Alaskan coastal locations (Tucker et al. 1979), resulting from severe shearing of the moving pack ice against stabilized grounded ice adjacent to the shore at that location. The AOL data and the other data shown in Figure 4 clearly point out that the area north of Greenland is one of the most severely ridged areas in the high Arctic. This area marks the entrance to the Fram Strait, the major outflow area for ice exiting the arctic basin; thus it is an area of general ice convergence. It is not particularly surprising then that the deformation is increased here relative to other locations that are far from shore.

CONCLUSIONS

The AOL has been shown to be a very capable instrument for profiling the ice surface. It appears to be somewhat superior to continuous wave lasers in that the profile is free of phase shift discontinuities. Aircraft motion still must be removed from the profile, however. For two segments of track off of northern Greenland, statistics of ridge height distributions compare very well with data collected from previous profiling flights in this area over the past two decades. The ridging statistics clearly point out that the area offshore of northern Greenland contains more ridges than many other areas of the Arctic. This extensive deformation is apparently caused by ice convergence as it approaches the Fram Strait.

ACKNOWLEDGMENTS

The authors gratefully acknowledge the support of the NASA Polar Oceans Program. WBT was supported under contract numbers 3150-OP-529 and 3468-OP-619.

REFERENCES

Hibler, W. D. III (1972) Removal of aircraft altitude variation from laser profiles of the arctic pack ice. *Journal of Geophysical Research*, **77**(36): 7190–7195.

Holyer, I. J. J., P. Wadhams and R. T. Lowry (1977) Laser ice profile analysis using interactive graphics. Scott Polar Research Institute, Cambridge, England, Technical Report 77-1, p. 1-26.

Krabill, W. B., J. C. Collins, L. E. Link and M. L. Butler (1984) Airborne laser topographic mapping results from joint NASA/U. S. Army Corps of Engineers experiments. *Photogrammetric Engineering and Remote Sensing*, **50**(6): 685–694.

Tucker, W. B. III and V. H. Westhall (1973) Arctic sea ice ridge frequency distributions derived from laser profiles. University of Washington, Seattle, Washington, AIDJEX Bulletin, no. 21, p. 1–52.

Tucker, W.B. III, W.F. Weeks and M. Frank (1979) Sea ice ridging over the Alaskan continental shelf. *Journal of Geophysical Research*, **84**(C8): 4885–4897.

Wadhams, P. (1976) Sea ice topography in the Beaufort Sea and its effects on oil containment. University of Washington, Seattle, Washington, AIDJEX Bulletin no. 33, p. 1–52.
Wadhams, P. (1980) A comparison of sonar and laser profiles along corresponding tracks in the Arctic Ocean. In *Sea Ice Processes and Models* (R. S. Pritchard, Ed.) Seattle: University of Washington Press, p. 283–312.
Weeks, W. F., S. F. Ackley and J. Govoni (1989) Sea ice ridging in the Ross Sea, Antarctica, as compared with sites in the Arctic. *Journal of Geophysical Research*, **94**(C4): 4984–4988.

Processes Determining the Bottom Topography of Multiyear Arctic Sea Ice

P. WADHAMS
Scott Polar Research Institute
University of Cambridge, England

S. MARTIN
Department of Oceanography
University of Washington
Seattle, Washington, U.S.A.

ABSTRACT/INTRODUCTION

In May 1987 the first systematic imaging was carried out of the bottom surface of the arctic ice cover, using sidescan sonar from a submarine (Wadhams 1988). The results show that undeformed first-year ice has a smooth bottom topography broken up by occasional long cracks, whereas undeformed multiyear ice is covered with dome-like features (e.g., Fig. 1). These have horizontal scales of 10–50 m and vertical scales of 0.5–1 m. They are scattered apparently at random over the ice bottom, and there appear to be no corresponding hollows; thus the topography resembles an inverted version of the lunar surface, with domes instead of craters.

Similar observations of roughness have been observed by coring from above. Cox and Weeks (1974) give the only known temperature-salinity section across a hummock-depression-hummock sequence in a multiyear floe. They found a wavelength of 12 m between successive hummocks or domes, with a relief of about 1 m in a floe of mean thickness 3 m. These observations support the sonar observations, but do not validate the fact that the hollows appear to be missing.

The purpose of this paper is to address the question of how these under-ice structures form. A number of possible mechanisms suggest themselves.

ORIGIN OF THE TOPOGRAPHIC FEATURES

Possible explanations for the under-ice features fall into two groups.

1. They are related to the summer melt cycle which multiyear ice has undergone. In support of this idea is the observation that the scale of the domes, and the more or less random distribution of them over the floe underside, resemble the scale and distribution of upper surface melt ponds during the arctic summer. Figure 2 shows a typical aerial photograph of such ponds.

2. They represent the almost-vanished relics of worn-down pressure ridges created years earlier in the life of the floe. Against this idea is the observation that there is no linearity to the distribution of the domes, and also the fact that in over 1000 km of sidescan record (representing 103 km^2 of ice surface) there is no intermediate case of a ridge worn down to almost the point where it looks like a sequence of domes. In every area of multiyear ice there is a clear distinction between the undeformed ice bottom, with its gently sloping topography of bulges, and ridges which exhibit a clear linearity and have a local angularity associated with the ice blocks.

We therefore tentatively reject the second explanation, and explore mechanisms related to the melt-freeze cycle.

THE MELT–FREEZE CYCLE

When a first-year ice sheet experiences its first summer melt period, some 30 cm of ablation occurs from the upper surface in the form of snow and ice melt (Untersteiner 1967). This meltwater gathers in melt ponds and pools on the upper surface of the floe, then drains to the underlying ocean. Possible pathways for drainage are *a*) through holes melted in the bottom of the pools, *b*) by channels cut to nearby cracks and leads, *c*) by slow percolation through the ice sheet via grain boundaries, and *d*) through wide brine drainage channels which run throughout the ice.

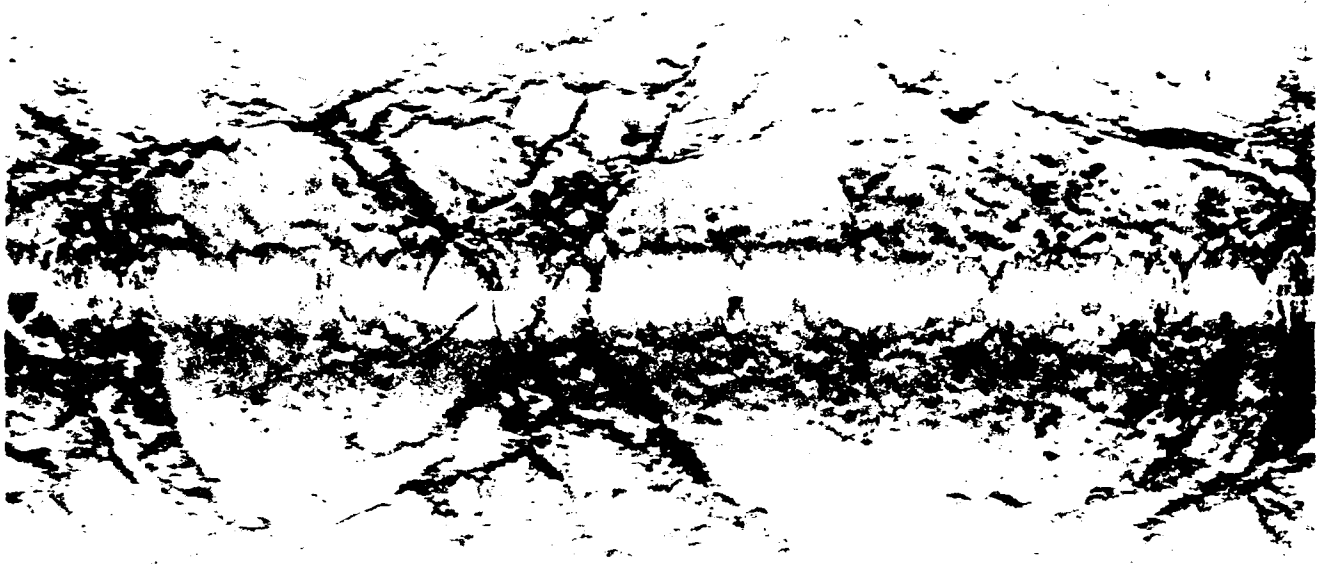

Figure 1. A section of sidescan sonar profile from the Arctic Ocean showing two multiyear floes. Transducer depth is 75 m.

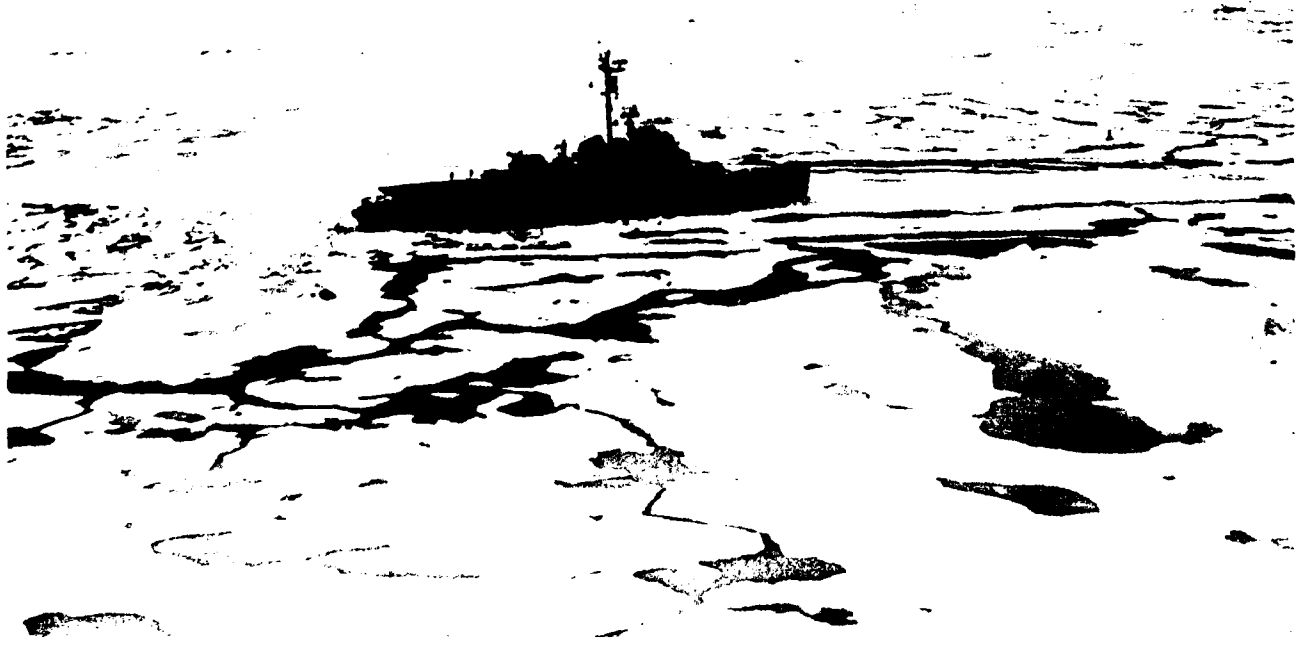

Figure 2. Surface melt pools in August in multiyear ice (near field), and first-year ice (far field). (Photograph courtesy A.R. Milne.)

The extent, or even the existence, of mechanism (c) is unknown, although it can be assumed that surface meltwater plays a role in the mechanism of flushing by which first-year ice desalinates over the summer. Note that because the water is fresh it cannot flow into the underlying ocean through narrow brine drainage channels, in that because the ice temperature generally lies below 0°C, the water would freeze solid and block these small channels. Wider brine drainage channels do, however, provide a pathway. It has been observed in connection with research on the behavior of oil deposited under first-year ice (Martin 1979) that 4-mm-diameter brine drainage channels open up between the top and bottom of the ice in spring, possibly because the sides of the channel act as a waveguide, concentrating solar radiation within the channel. In the case of oil spilled under the ice, they provide an upward pathway, and in the case of meltwater a possible downward pathway; alternatively the channel may simply provide a start point for the growth of a larger thaw hole, which would permit macroscopic drainage.

When a surface melt pool first forms, it is very shallow and positions itself in a random minor depression in the almost perfectly flat surface of the first-year floe. Once a pool of any thickness, however small, has been created, however, its low albedo causes preferential absorption of solar radiation and consequent warming of the water in the pool. It will thus melt its way down into the floe by eroding its own bottom. The difference in elevation between the bottoms of melt pools and bare ice therefore increases as summer progresses (but before drainage empties the pools) until it is several cm or even tens of cm. Some observations from Fiennes (1984) of the water depth of a single melt pool over a period of 23 days may be appropriate here: he found a depth increasing from 35 cm on 10 July, to a maximum of 44 cm in mid-July, then falling to 13 cm by 1 August as drainage proceeded.

Because of the change in surface albedo, some of the energy absorbed by a warm water pool at the top of the ice sheet will be transmitted through the ice, thus causing the bottom of the sheet to melt more rapidly beneath the melt pond than away from the pond. A series of under-ice depressions should therefore be created, with lateral dimensions similar to those of the overlying surface melt pools. The existence of such under-ice cavities has been noted in the work of Hanson (1965) and others (see Martin and Kauffman (1974) for a discussion and literature survey of the problem), although there is scarcely any experimental data on sizes, aspect ratios or distributions of the observed cavities. During the summer we therefore expect a first-year floe to begin to develop an underside topography of depressions, reflecting the surface melt pool topography.

How does a topography of depressions translate into the topography of bulges seen in winter multiyear floes? We believe that the answer lies in the fate of the meltwater that has passed into the ocean via one of the mechanisms (*a*) to (*d*) listed above, which then gathers in the depressions to form under-ice melt pools.

FORMATION AND FATE OF UNDER-ICE MELT POOLS

Fresh water which has run off from the ice surface, or which is generated by melting of the ice underside, will collect preferentially under portions of the ice bottom surface with lower draft. Thus sub-ice depressions tend to form into what Hanson (1965) defined as "under-ice melt ponds." The effect has been described extensively (e.g., Nansen 1897, Zubov 1945, Untersteiner and Badgley 1958), and the subsequent evolution of the ponds has been studied and investigated in laboratory experiments by Martin and Kauffman (1974). Briefly, what happens is as follows (see Fig. 3).

The trapped fresh or brackish water is at its freezing point, i.e., at or near 0°C, while the underlying polar surface water is at its own freezing point of −1.6°C or lower.

Therefore, freezing of the fresh water takes place at the interface (even in summer), creating a thin skim of ice on the inverted surface of the melt pond (Fig. 3). Observations show that the sheet thus formed reaches a thickness of 2–10 cm. The space between the sheet and the lower surface of the floe becomes filled with a mass of loosely packed ice crystals, with a preponderance of thin vertical crystals running from the bottom of the ice floe to the top of the new ice sheet. This effect was explained by Martin and Kauffman (1974) in terms of a density inversion created in the fresh water layer by the rapid diffusion of heat relative to salt, causing high Rayleigh number convection whereby supercooled water rises to the floe bottom to nucleate into thin vertical interlocking ice crystals.

As summer proceeds, the horizontal ice sheet forming the bottom of the melt pond grows thicker and migrates slowly upwards. This occurs because freezing at the top of the sheet releases heat which flows through the ice to the lower surface, where it warms the lower interface to slightly above the freezing curve, causing melting. This upward migration of the

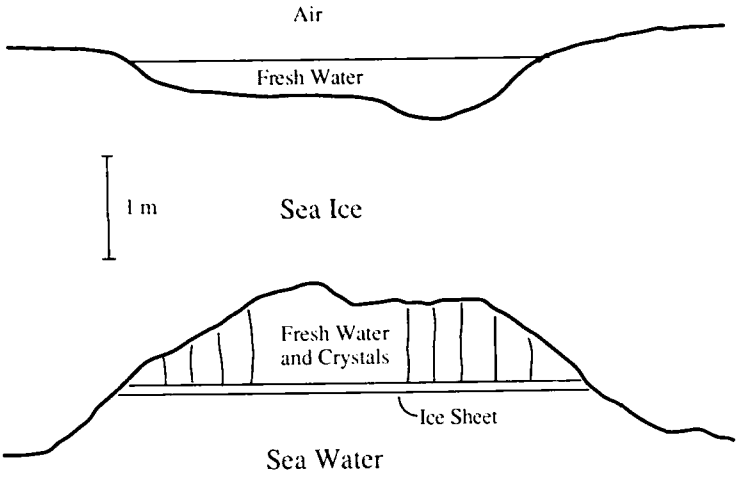

Figure 3. A schematic diagram of an under-ice melt pond during summer, lying beneath a surface melt pond. See text for further description.

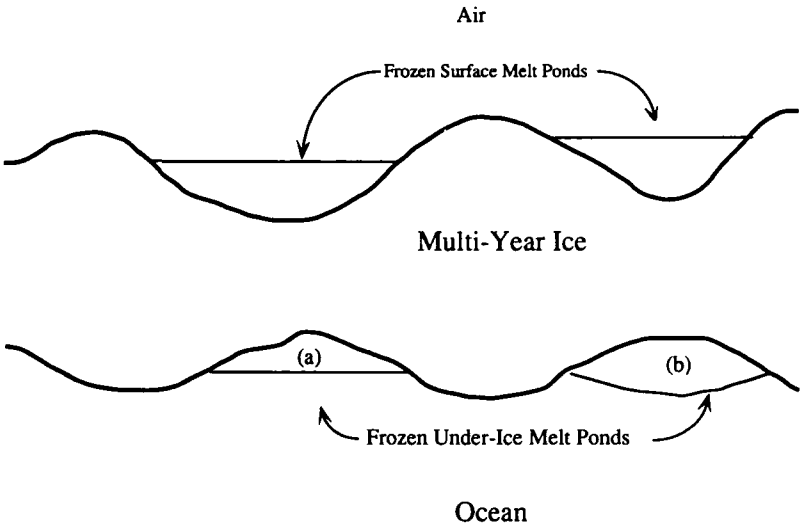

Figure 4. A schematic diagram of the possible winter topography caused by refrozen melt pools. a—Case where the under-ice pond freezes without bulging. b—Case with bulging.

ice sheet at the bottom of the pond means that the pond is shrinking upwards into its own depression and ends up not quite filling that depression. Martin and Kauffman showed that the processes occurring in under-ice melt ponds represent an efficient, and perhaps the only important, way of growing new ice in summer within the Arctic.

When summer ends, the air temperature lowers and freezing begins. We have little experimental or observational knowledge of what happens at this point. If the melt pond has already filled completely with ice from internal processes (the horizontal interface sheet growing thicker and/or the vertical crystal mesh filling the remainder of the pond), then clearly the bottom of the pond's ice sheet simply provides a start point for the next season's growth of congelation ice. Because the pond lies under a depression in the top surface (from which the water by now has probably drained), the ice is locally thinner and so the growth rate will be somewhat greater than that of the thicker ice around the pond. Nevertheless, we surmise that the differential growth rate is low enough, and the initial differential ice draft great enough, that the difference is never made up.

Thus we have one plausible mechanism for the observed bulges. The matrix of flat ice surrounding the bulges actually comprises the lower surfaces of refrozen under-ice melt ponds, which have rectified the depressions in the ice created during the summer melt, but where the rectified surfaces still lie at a lower draft than the regions of the floe which never harbored ponds on the upper or lower surface. These regions stand proud to form the gentle bulges observed (Fig. 4). We believe that this is the most likely explanation.

Another possibility, however, is the complete opposite. If the under-ice melt ponds still contain fresh water at the end of summer, this will freeze and thus expand. If the process occurs slowly enough, the flat ice cover on the under-ice pond could bulge out

below due to the change in volume. Since this process would be taking place with the ice sheet surrounded by water at its freezing point, the ice may be ductile enough to bulge outward without cracking. It is then the ponds themselves which form the bulges. This process could be verified by laboratory experiments. It seems unlikely, however, that reliefs of the order of 1 m could be produced in this way.

TESTS AND IMPLICATIONS

How do we test this model? An indirect test, which would indicate whether melt ponds are indeed connected with the mechanism of dome generation, would be to measure the spatial frequency of domes and the distribution of dome diameters from all the available sidescan sonar imagery, and compare the results with distributions of melt pond frequencies and pond diameters (and the distribution of dimensions of the regions left between melt ponds) obtained from aerial photography of first-year floes in summer. This study is in progress.

A direct test would be to carry out careful coring studies across second-year ice floes at different stages of the winter. A pattern should emerge whereby the zones of lower draft possess lenses of low salinity ice near the bottom of the ice sheet, whereas the zones of greater draft do not. Further direct tests could be done in summer and autumn, examining the evolution and subsequent freezeup of a few under-ice melt ponds on a first-year floe. Finally, many aspects of the process can be reproduced in laboratory experiments.

If the model proves to be valid, the main implication would be that the formation of under-ice melt ponds in first-year floes in summer must be a universal process, rather than a curiosity. This would have important consequences for the thermodynamic modelling of arctic sea ice, since it implies that significant ice growth must occur under existing ice sheets in summer, so that part of the summer ablation is replaced by accretion at the lower surface.

Finally, whatever mechanism proves to be the explanation for under-ice domes, the existence of this kind of topography under multiyear ice has various implications of its own. Models of acoustic propagation under sea ice usually assume that scattering by pressure ridges is the chief source of transmission loss (e.g., Burke and Twersky 1966, Guoliang and Wadhams 1989), while it is now necessary to include the under-ice bulges as scattering elements. Similarly, models which attempt to infer ice-water drag coefficients from parameters of under-ice roughness must take account of roughness elements possessed by undeformed multiyear floes. Finally, the clear characterization of multiyear ice made possible by its underside topography enables sidescan sonar imagery, when recorded concurrently with other remote sensing imagery, to be used as a validation technique for passive or active microwave, since unequivocal identification of ice type is now possible.

ACKNOWLEDGMENTS

P. Wadhams acknowledges the support of the Office of Naval Research under contract N00014-82-C-0064 to Science Applications International Corporation, Polar Oceans Division; and S. Martin acknowledges the support of the Office of Naval Research under contracts N00014-87 and N0014-89-0014. This work was begun while P. Wadhams held a Walker–Ames Professorship at the University of Washington; we are grateful for this support. Publication 1803 of the School of Oceanography, University of Washington.

REFERENCES

Burke, J. F. and V. Twersky (1966) Scattering and reflection by elliptically striated surfaces. *Journal of the Acoustical Society of America*, **40**: 883–895.

Cox, G. F. N., and W. F. Weeks (1974) Salinity variations in sea ice. *Journal of Glaciology*, **13**: 109–120.

Fiennes, R. (1984) Notes on ice melt. Report on the Scientific Work of the Transglobe Expedition 1979–1982, p. 302.

Guoliang, J. and P. Wadhams (1989) Travel time changes in a tomography array caused by a sea ice cover. *Progress in Oceanography* (in press).

Hanson, A.N. (1965) Studies of the mass budget of arctic pack-ice floes. *Journal of Glaciology*, **5**: 701–709.

Martin, S. (1979) A field study of brine drainage and oil entrainment in first-year sea ice. *Journal of Glaciology*, **2**: 473–502.

Martin, S. and P. Kauffman (1974) The evolution of under-ice melt ponds, or double diffusion at the freezing point. *Journal of Fluid Mechanics*, **64**: 507–527.

Nansen, F. (1987) *Farthest North*. New York: Harper, vol. 1, p. 457–459.

Untersteiner, N. (1967) Natural desalination and equilibrium salinity profiles of old sea ice. In *Physics of Snow and Ice* (H. Oura, Ed.). Institute of Low Temperature Science, Sapporo, Japan , vol. 1, p. 659–577.

Untersteiner, N. and F.I. Badgley (1958) Preliminary results of thermal budget studies on arctic pack ice during summer and autumn. In *Arctic Sea Ice*. Wash-

during summer and autumn. In *Arctic Sea Ice*. Washington, D.C.: National Academy of Sciences, National Research Council Publication No. 598, p. 85–92.
Wadhams, P. (1988) The underside of arctic sea ice imaged by sidescan sonar. *Nature*, **333**: 161–164.
Zubov, N. (1945) *Arctic Ice* (English translation). San Diego, California: U.S. Navy Electronics Laboratory, San Diego.

A Fractal Description of Ice Keel Small-Scale Surface Roughness

G.C. BISHOP AND S.E. CHELLIS
Naval Underwater Systems Center
Newport, Rhode Island, U.S.A.

ABSTRACT

Measured under-ice acoustic profile data and several large-scale geometric parameters of ice keels are used to construct and partition an ensemble of large-scale relief features into two subsets: a subset of keel-like features (e.g., ice keels) and a subset of non-keel-like features. The draft data of each feature are regarded as a realization of a nonstationary random process while the draft increment data are regarded as a realization of a stationary zero mean random process. A maximum likelihood estimator technique (MLE) and a technique based on the variance function are used to calculate fractal dimensions for keel-like and non-keel-like features. It is shown that for the same feature, the MLE technique and the variance function based technique yield similar values for the fractal dimension (D) and that for keel-like features $1.2 < D < 1.7$ while for non-keel-like features $1.2 < D < 1.6$. The use of D in feature classification is also indicated.

INTRODUCTION

The fractal dimension of many rough surfaces has been calculated and used to parameterize surface roughness and fractal sets have been used to model many rough surfaces and textures. In this paper, fractal dimensions of large-scale under-ice relief features (e.g., ice keels) are calculated from measured under-ice acoustic profile data. It is shown that the profile data of many features may be regarded as a fractal set and that their small-scale surface roughness may be parameterized by a fractal dimension. Preliminary calculations indicate that acoustic profiles of some features may be regarded as a realization of discrete fractional Brownian motion (DFBM) (Mandelbrot and Van Ness 1968).

Arctic pack ice is formed from large ice sheets or floes that are deformed and/or fractured by forces produced by ocean currents, winds and thermal gradients. The floes are also subject to erosion, cyclical melting and freezing and other physical processes that change the physical and morphological properties of the ice surface. These processes produce localized regions in which ice blocks and/or ice rubble accumulate above and below the seawater surface. These localized regions of deformed ice may differ in composition and morphology and may be regarded as distinct large-scale relief features. The most important and frequently occuring type of relief feature is the pressure ridge, which is formed by the accumulation of ice blocks whose surfaces are more or less rectangular. The portion of the ridge above the ice surface is called a sail and its manifestation in the under-ice surface is called a keel.

These processes produce an under-ice surface that may be partitioned into three more or less distinct roughness regimes based on a linear dimension of the ice structure producing the surface roughness. Large-scale surface roughness is produced by large-scale relief features, may be parameterized locally by the average of the maximum ice draft of all features within the area of interest, and varies between different areas from several meters to several tens of meters. Small-scale surface roughness is produced by ice blocks and/or rubble whose average linear dimension varies between features from several tens of centimeters to several meters. Micro-scale surface roughness is produced on the upper ice surface by snow and/or erosion; on the vertical surfaces of ice blocks by fracture of the parent ice floe; and on the ice surface at the seawater-ice boundary by ice dendrites formed when seawater freezes. The average amplitude of micro-scale surface roughness depends on the type of micro-scale surface roughness and varies from 500 mm to several centimeters (Weeks and Ackley 1982).

An under-ice acoustic profiler measures ice thickness in a vertical plane defined by the profiler track. At small-scale surface roughness length scales, the acoustic profile of an ice keel may be regarded as a curve formed by projecting the faceted surface of the keel onto a randomly oriented vertical plane and consists of a sequence of discrete steps whose statistics are determined by those of the ice block facets. Since different types of large-scale relief features exhibit different types of small-scale surface roughness, the quantification and/or parameterization of small-scale surface roughness may provide information that can be used to assist the process of identification and/or classification of under-ice relief features from their acoustic profiles as well as provide information necessary to develop models to calculate scattering from such rough surfaces.

In a paper that is fundamental to the subject of fractal dimensions and under-ice surface roughness, Rothrock and Thorndike (1980) confirmed the result of Mellen (1966) who found that the asymptotic spectral exponent for the under-ice surface is –3. Additionally, they showed that the spectral exponent is linearly related to the fractal dimension of Mandelbrot (1983) and the Lipschitz exponent. They showed that since a spectral exponent of –3 corresponds to a fractal dimension of 1; the set of under-ice profile data is not a fractal set. However, these results were based on spectral densities of long tracks of under-ice profile data whose smallest lags were significantly greater than the local variations of the draft data, i.e., greater than small-scale surface roughness length scales. Additionally, they assumed that under-ice profile data are realizations of stationary and ergodic random processes. It is important to note that if the set of under-ice profile data is a fractal set which is self-affine or is self-similar at length scales below some upper cutoff (e.g., below the maximum of the small-scale surface roughness fluctuations of the profile data), then at large length scales the fractal dimension is 1, the spectral exponent is –3 and the surface is not fractal-like. In such cases, a fractal dimension exists and may be calculated only in the limit of small length scales.

Since the set of profile data of an individual relief feature is a realization of a nonstationary random process, it is problematic at best to calculate and to characterize such data in terms of their spectral exponent. Although the set of increment data of an individual relief feature may be calculated from the draft data and shown to be stationary, the spectral exponent of these data is difficult to determine and is at best suspect. At best an acoustic profile of an individual relief feature consists of a few hundred data points. This quantity of data is insufficient to calculate an accurate estimate of the power spectral density using periodogram or correllogram techniques. Although in such cases an autoregressive technique may be used to estimate the power spectral density, the spectral exponent determined from such a power spectral density calculation depends on the order of the autoregressive process used to model the data. Additionally, for a discrete set of measured data there is no unique way to define the asymptotic portion of the spectrum regardless of the technique used to calculate the spectral density. Therefore, this technique permits the spectral exponents of different features to be calculated and compared, but does not provide a quantity that can be used reliably to parameterize small-scale surface roughness. The problems associated with the calculation of the spectral exponent necessitate an alternative parameterization of surface roughness and the fractal dimension is a natural choice.

High resolution, under-ice acoustic profile data which were correlated with relief feature type based on visual observation of the upper ice surface were obtained and provided for use in the work described in this paper by Garrison et al. (1978). The data were obtained at a site in the Chukchi Sea in April 1976 with an acoustic profiler which had a beam width of 2°, a sample frequency of 5.9 Hz, and a speed of 3.0 knots and which was located 21.0 m below the ice surface. These parameters resulted in a spot size of 0.73 m and sample spatial increment of 0.26 m. Draft data for smooth ice had a standard deviation of 0.3 ft. It is evident that the resolution of the acoustic profiler was not sufficient to measure micro-scale surface roughness. However, it is evident that large-scale relief features can be resolved and identified, and more importantly for the purposes of this paper, it is assumed that the small-scale surface roughness of individual relief features is resolved sufficiently to determine their fractal properties.

IDENTIFICATION OF LARGE-SCALE UNDER-ICE RELIEF FEATURES

No universally recognized criteria exist to identify and classify large-scale under-ice relief features in an acoustic profile of the under-ice surface based on the acoustic profile they project onto a randomly oriented vertical plane. Therefore, it is necessary to adopt more or less arbitrary criteria to identify these features and to determine their large-scale geometric parameters from their projected acoustic profiles. The criteria used in this paper have been discussed in

detail (Bishop and Chellis 1985); however, for completeness in this paper, these criteria are summarized very briefly. Feature identification criteria may be parameterized by relief which is defined as any distance measured downward from the average thickness of the parent ice floe. Three criteria are necessary and sufficient to identify a large-scale discrete relief feature:

1. The minimum relief criterion distinguishes relief features from surface irregularities and/or undulations. A relief feature satisfies the minimum relief criterion if its maximum relief is greater than some minimum value which was chosen arbitrarily to be 2.0 m.

2. The Rayleigh criterion resolves or distinguishes between adjacent features. A relief feature satisfies the Rayleigh criterion when its relief decreases to some minimum value which was chosen to be half the feature maximum relief.

3. The end criterion determines the lateral length of the acoustic profile of a feature. A relief feature satisfies the end criterion after the Rayleigh criterion is satisfied and its profile attains a local minimum on both sides of the maximum feature profile.

These criteria partition the under-ice acoustic profile into an ensemble of discrete large-scale relief features.

To partition the ensemble of relief features into a set of keel-like features and a set of non-keel-like features, one side of the acoustic profile of all features is partitioned into two straight line segments whose slope angles are called, respectively, the upper and lower slope angles. A relief feature is a keel-like feature if its average slope angle is greater than some mimimum value which was chosen arbitrarily to be 10°.

CALCULATION OF ICE KEEL FRACTAL DIMENSIONS

A maximum likelihood estimator technique (MLE) and the variance function were used to calculate fractal dimensions from draft increment data. The increment data have zero mean and it is assumed they are strict sense stationary. Lundahl et al. (1986) developed a maximum likelihood estimator technique to estimate the Hurst parameter (H) where $D = 2-H$, an asymptotic Cramer-Rao bound on the variance of the estimate of H, and showed that the technique may be used to quantify texture. Since this technique provides an estimate of H even when there are relatively few data, it is ideally suited to calculate an estimate of H from profile increment data. For completeness in this paper, a very brief summary of the MLE development of Lundahl et al. follows.

It is assumed that all data samples are jointly Gaussian distributed and that the covariance matrix is known. The maximum likelihood estimator is given by the following probability density function,

$$p(x; H) = \frac{1}{\sqrt{(2\pi)^N |R|}} \exp\left\{-\frac{1}{2} x^T R^{-1} x\right\} \qquad (1)$$

where $x = \{x_0, x_1, \ldots x_{(N-1)}\}^T$ is the set of increment data, N is the number of data points, and R is the covariance matrix given by

$$R_{ij} = r[\,|i-j|\,]. \qquad (2)$$

$r[k]$ is the autocorrelation function of the increments and is given by

$$r[k] = \frac{\sigma^2}{2}\left[|k+1|^{2H} - 2|k|^{2H} + |k-1|^{2H}\right] \qquad (3)$$

where σ^2 is the variance of the increment data. Since $p(x; H)$ is a unimodal function of σ^2 and H, the estimate of H is that value of H for which $p(x; H)$ is maximum; $\log[p(x; H)]$ is maximized with respect to σ^2 and H. The value of σ^2 for which $\log[p(x; H)]$ is maximized is given by

$$\sigma^2 = x^T R'^{-1} x/N \qquad (4)$$

where

$$R' = R/\sigma^2. \qquad (5)$$

The value of H for which $\log[p(x; H)]$ is maximized is determined numerically.

The variance function of a fractal set of data is given by

$$\mathrm{var}[x_i - x_j] = V_H\,[\,|i-j|\,]^{2H} \qquad (6)$$

where V_H is a constant (Lundahl et al. 1986). It is evident that H can be estimated by calculating the slope on a plot of $\log\{\mathrm{var}\,[x_i - x_j]\}$ vs $\log\, x_i - x_j$.

To obtain a reliable estimate of the fractal dimension of a feature, its increment data are required to satisfy several criteria·

1. The set of increment data must contain a minimum of 20 points. This criterion is based on the minimum number of points necessary to perform a meaningful Kolmogorov-Smirnov test.

2. The signal to noise ratio (SNR) must be greater than 20 dB where

$$SNR = 20 \log (\sigma_s/\sigma_n) \quad (7)$$

and σ_s and σ_n are, respectively, the standard deviations of the increments and the noise (Lundahl et al. 1986). It is assumed that a reasonable estimate of σ_n is given by that for the smooth ice.

3. To calculate a fractal dimension using the MLE technique, the increment data are required to fit a Gaussian distribution.

It is assumed that increment data are Gaussian distributed if the null hypothesis that they are Gaussian distributed can not be rejected at the 20% level of significance based on a Kolmogorov–Smirnov test. The variance function is used to calculate fractal dimensions when the percentage of the variation explained by a linear regression to the log of the variance data is greater than 99%. It is important to note that a fractal dimension may be calculated from the variance function even when the increment data are not Gaussian distributed and the MLE technique is not used.

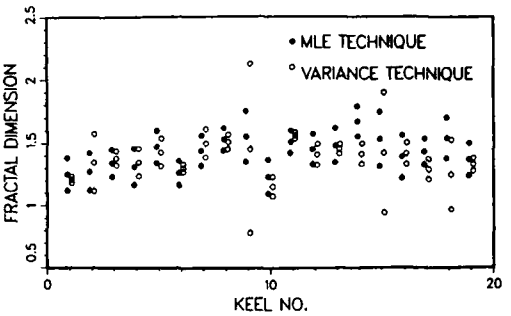

a. Fractal dimensions for keel-like features.

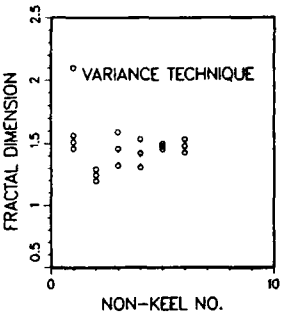

b. Fractal dimensions for non-keel-like features.

Figure 1. Fractal dimensions.

RESULTS AND CONCLUSIONS

Figures 1a and 1b show, respectively, fractal dimensions for 19 keel-like and 6 non-keel-like features. For each feature, the error in the estimate of the fractal dimension is indicated by error bars which represent 99% confidence level intervals. For the MLE technique, the 99% confidence interval is

$$[D-\delta_m, D+\delta_m]$$

where $\delta_m = 2.6\sigma_m$, $\sigma_m = \frac{1}{\sqrt{8N}}$

N = number of points in the data set
D = fractal dimension estimate (Lundahl et al. 1986).

For the variance function technique, the 99% confidence interval is $[D-\delta_v, D+\delta_v]$ where

$$\delta_v = t(N-2, 1-\alpha/2)\sigma_v)\left[\sum (x_i-\bar{x})^2\right]^{1/2}$$

and $\alpha = 0.01$ (Draper and Smith 1966). $t(N-2, 1-\alpha/2)$ is the $(1-\alpha/2)$ percentage point of a t-distribution with $N-2$ degrees of freedom, i.e., the number of points on which the estimate σ_v is based, which is the square root of the mean square. It is important to note that even with these rather conservative error bars, D remains within the fractal region for all features except three.

The number of non-keel-like features for which a fractal dimension can be calculated is significantly less than the number of keel-like features. This result is a consequence of the fact that the increment data of non-keel-like features tend not to be Gaussian distributed and to have a SNR of less than 20 dB. This does not suggest that small-scale surface roughness of these features cannot be described by a fractal dimension, only that it cannot be calculated using the data and techniques described in this paper. However, these results do suggest that if the surface of non-keel-like features is fractal, their fractal properties occur at length scales smaller than those for keel-like features.

The average and standard deviations of fractal dimensions calculated by the MLE technique for keel-like features are, respectively, 1.422 and 0.122, and using the variance function based technique they are, respectively, 1.376 and 0.105. For non-keel-like features, fractal dimensions are calculated by the variance function based technique only and the average and standard deviation of fractal dimensions are respectively 1.430 and 0.964. It is evident that the average and standard deviations of fractal dimensions for keel-like and non-keel-like features do not provide any obvious way to distinguish between these two

groups of features. However, if it is assumed that the surfaces of non-keel-like features are fractal, the limited number of non-keel-like features for which fractal dimensions have been calculated suggests the groups may be distinguished by the length scale at which they exhibit fractal properties, or within context of the work described in this paper, whether or not a fractal dimension can be calculated.

The physical description of the profile of a relief feature begs comparison with a realization of Brownian motion. Preliminary calculations indicate that some profiles may be realizations of fractional Brownian motion as defined by Mandelbrot and Van Ness (1968); however, further calculations are necessary to demonstrate that the data are statistically self-affine.

It may be concluded that portions of under-ice profile data may be regarded as realizations of non-stationary random processes, that many portions whose large-scale geometric parameters are similar to those of ice keels exhibit exhibit small-scale surface roughness that may be parameterized by a fractal dimension, and that preliminary calculations indicate that some feature profiles may be regarded as a realization of fractional Brownian motion.

ACKNOWLEDGMENTS

We would like to express our gratitude to Dr. G.R. Garrison of the Applied Physics Laboratory/University of Washington who very generously supplied us with the high quality under-ice profile data without which this work would not have been possible. This work was supported by the Office of Naval Technology, program manager D.J. Ramsdale (Naval Ocean Research and Development Activity, Code 242); and by the Naval Underwater Systems Center Independent Research Program, program manager K.M. Lima (Naval Underwater Systems Center, Code 10).

REFERENCES

Bishop, G.C. and S.E. Chellis (1985) Sea ice pressure ridges: Development and analysis of an algorithmic approach to their classification, morphology, and statistical aspects. Naval Underwater Systems Center, Newport, Rhode Island, NUSC Technical Report 6410.

Draper, N.R. and H. Smith (1966) *Applied Regression Analysis*. New York: John Wiley & Sons, Inc.

Garrison, G.R., R.E. Francois, E.W. Early and T. Wen (1978) Comprehensive studies of arctic pack ice in April 1976. Applied Physics Laboratory/ University of Washington, Seattle, Washington, APL-UW 7724.

Lundahl, T., W.L. Ohley, S.M. Kay and R. Siffert (1986) Fractional Brownian motion: A maximum likelihood estimator and its application to image texture. *IEEE Transactions on Medical Imaging*, MI-5: 152–161.

Mandelbrot, B.B. and J.W. Van Ness (1968) Fractional Brownian motions, fractional noises and applications. *SIAM Review*, **10**: 422–438.

Mandelbrot, B. B. (1983) *The Fractal Nature of Geometry*. New York: W.H. Freeman Company.

Mellen, R. E. (1966) Underwater acoustic scattering from arctic ice. *Journal of the Acoustical Society of America*, **40**: 1200–1202.

Rothrock, D.A. and A.S. Thorndike (1980) The geometric properties of the underside of sea-ice. *Journal of Geophysical Research*, **85**: 3955–3963.

Weeks, W.F. and S.F. Ackley (1982) The growth, structure and properties of sea ice. USA Cold Regions Research and Engineering Laboratory, CRREL Monograph 82-1.

A Small-Scale Under-Ice Morphology Study in the High Arctic

D.N. CONNORS, E.R. LEVINE AND R.R. SHELL
Naval Underwater Systems Center
Newport, Rhode Island, U.S.A.

ABSTRACT

An ice morphology study, topside and bottomside, was conducted on an arctic floe with first-year and multiyear ridges. Data were obtained in one- and two-dimensional surveys for scales of the order of meters to tens of meters. One-dimensional power spectral density $S(\kappa)$ was estimated as a function of wave number, κ, for 3.1×10^{-2} cpm $< \kappa <$ 3.1×10^{-1} cpm. For homogeneous profiles of first- and multiyear heavily ridged ice, the spectral slope s, where $S(\kappa) = A\,\kappa^{s}$, was estimated to be -2.3 ± 0.05, and -1.8 ± 0.05, respectively. These values correspond to Lipschitz coefficients of 0.6 and 0.4, indicating that the under-ice surface was fractal in nature. For a multiyear ridge, the keel profile was asymmetric, the mean axial draft was 9.2 m, the mean keel/sail ratio

of 4.8, and the mean displacement of the sail to keel axis was 9.6 m. Two-dimensional power spectral density estimates for one realization of a multiyear keel topography suggest anisotropy with increased spectral variance in the cross-ridge direction.

INTRODUCTION

A combination of acoustic imaging and optical surveying techniques has been utilized to characterize the morphology of first-year and multiyear ice on a floe in the Arctic. Objectives of this study included 1) topside/bottomside intercomparison of features, including the relationship between the ridge sail and keel, 2) statistical characterization of first-year and multiyear ridges on small scales, and 3) development of techniques for looking at the two-dimensional spectra of ridge bottom roughness. Acoustic instruments were used to study the under-ice topography, while optical surveying instruments were used to study topside features.

FIELD PROGRAM

Data were obtained during April 1986, on a pack ice floe in the Lincoln Sea, north of 85°N. The one-dimensional (1-D) survey of the under-ice canopy (Fig. 1) consisted of 17 parallel tracks (10–100 m spacing) run under multiyear and first-year ice over a 1.2- × 3.0-km box. The data set was obtained with the DIPS (Digital Ice Profiling System) submarine-mounted upward-looking sonar, which for a 2° beam

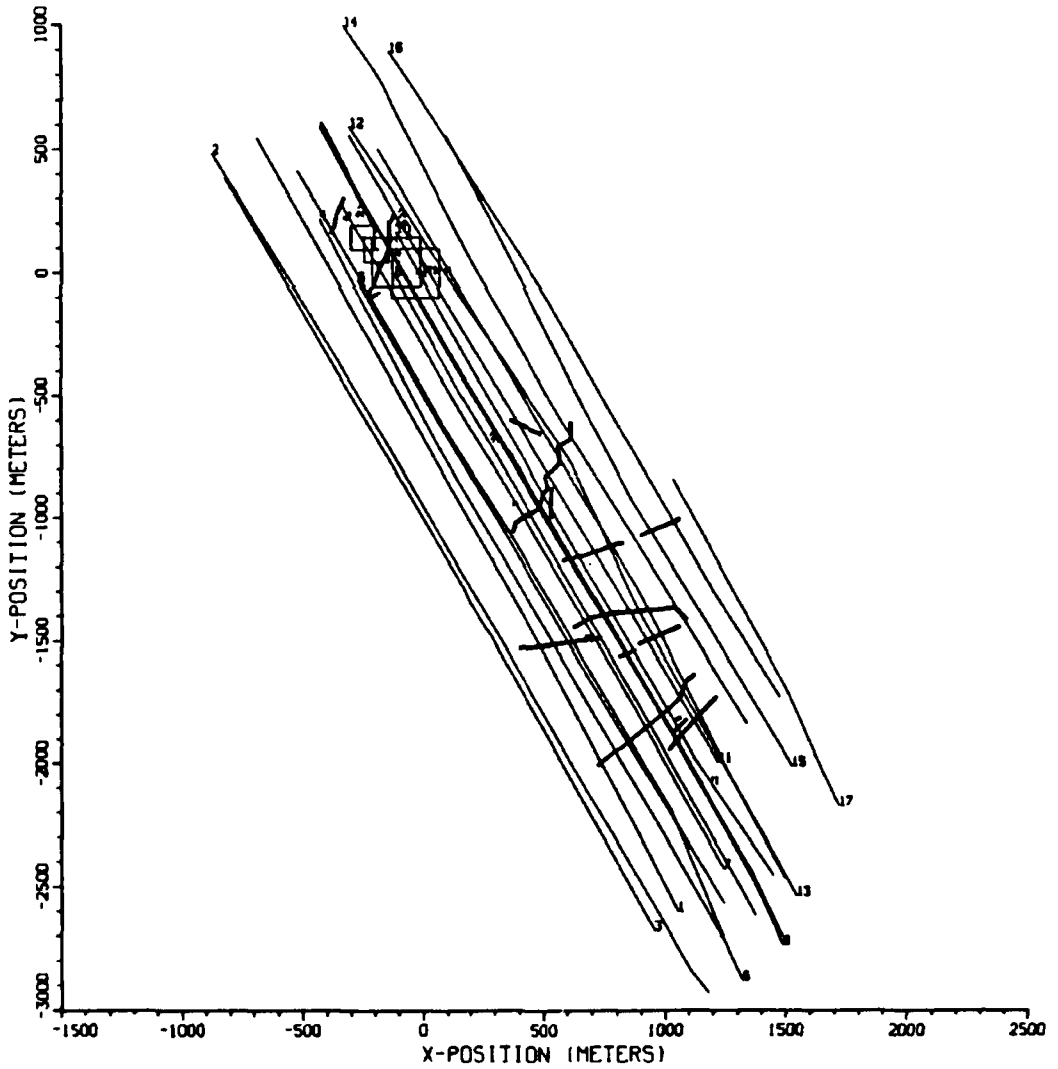

Figure 1. Under-ice surveys including DIPS tracks (thin lines) and Mesotech areas (boxes) superimposed on locations of topside sail axes (thick lines). Track 9 is located near the center of the DIPS survey.

width and a sampling rate of 5.9 Hz, results in data every 0.5 m and a 2-m footprint. The acoustic tracking range consisted of seven tracking hydrophones that were periodically checked with a surveyed sound source, resulting in typical range closing errors of order 0.25 m. Sound velocity measurements were made daily to determine acoustic paths and travel times.

The two-dimensional (2-D) survey was directed to a region with multiyear ridges and hummocks 1–2 m high. Under-ice topography (3–12 m) was mapped for four overlapping sites (Fig. 1) using an Offshore Survey and Positioning Services Acoustic Profiling System based on the Mesotech model 971 profiling sonar system (Lyall and Lanziner 1986). The sensor on this system employs a 330-kHz transducer with a 2.1°beam, and has stepping angles of 4.5° in the horizontal and 0.225° in the vertical. The insonified footprint ranged from 1.5 to 2.4 m for shallow (*s*) sites with a 40-m depth source , and 3.0 to 4.0 for deep (*d*) sites with an 80-m depth source.

Topside positions were surveyed with a theodolite (Leitz/Sokkisha TMG, model TM 20H) and range finder (Sokkisha EDM model RED 2A) from a centrally located 7-m high tower. In the DIPS region, major sail features are shown in Figure 1. For these data, topside and bottomside relative position was known to within 2–3 m. For the 2-D survey of the multiyear ridge, range, bearing, height, snow depth, and width of surface features were obtained along the axis of the sail. Sail height was corrected for snow cover and freeboard to sea level, and sail width was determined to the break in slope at "flat" ice. For these data, topside and bottomside relative position was known to less than 1 m.

RESULTS AND DISCUSSION

A 1-D profile of DIPS data for track 9, near the center of the topside survey, is shown in Figure 2. The keel features indicated in the figure had substantial surface expression with long, generally continuous sails. Most of the other keel-like features were coincident with topside observations of scattered hummocks (1–2 m high) in multiyear ice, and rubble (slabs 4–5 m long , ~1 m thick) in the first-year ice, and exhibit little track to track continuity. On average, the orientation of track 9 to the cross-sail direction is 16° for the first-year ridges, and 39° for the multiyear ridges.

Homogeneous segments of generic ice types in the DIPS data, 256 m in length, were selected for the 1-D power spectral analysis, with guidance from the topside survey. Analysis was performed for 10-track sections of deformed first-year ice (ridges and rubble fields) and 10 of deformed multiyear ice (ridges and hummocks). These data were detrended, high-pass filtered with a recursive filter with a half-power point at 0.31 cpm, windowed, and individual spectra were computed using an FFT. Ensemble averaged power spectral density estimates for deformed first-year and multiyear ice, respectively, are presented in Figure 3, along with error bars for the 95% confidence level.

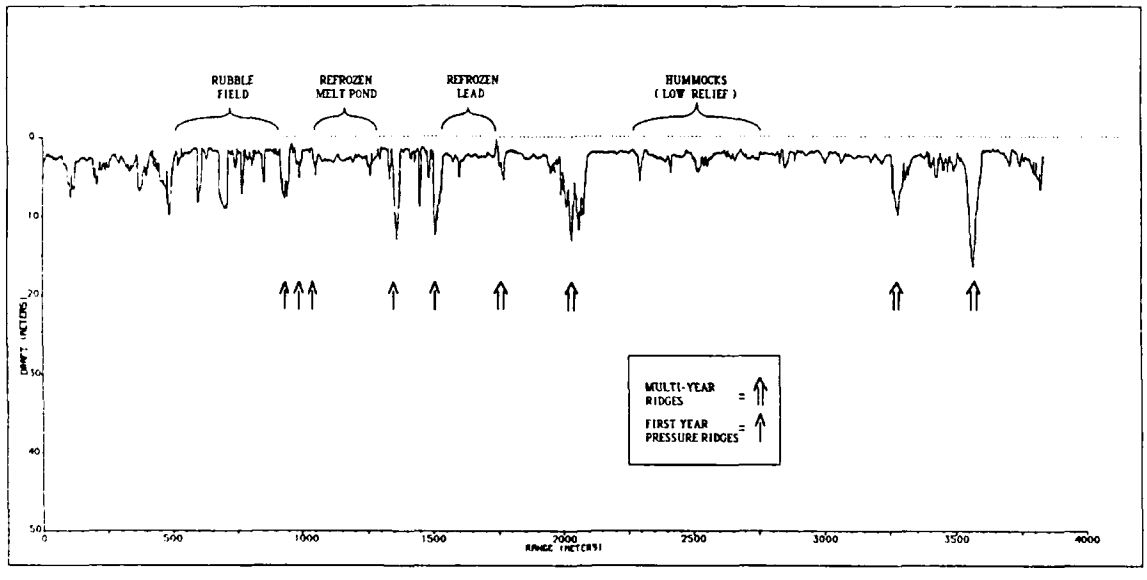

Figure 2. Topside and bottomside ice profile data along track 9.

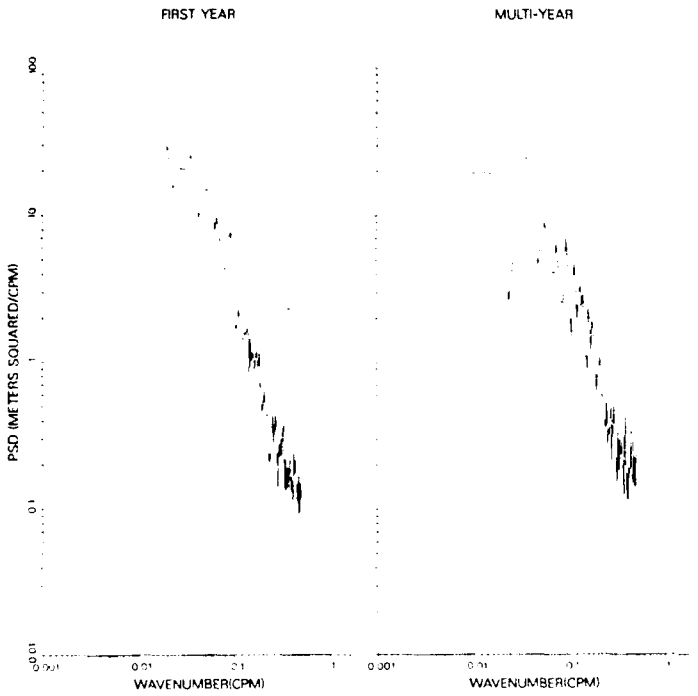

Figure 3. Ensemble averaged 1-D spectra of deformed first-year ice, and deformed multiyear ice. Error bars are for 20 degrees of freedom at the 95% confidence level.

The noise level of the data, based on the manufacturers specification of 0.20-m resolution, and input of a random signal with corresponding variance to the spectral algorithm, was found to be approximately 2.5×10^{-1} m^2/cycles per meter, which occurs at a wave number of approximately 3.1×10^{-2} cpm.

The slope of the averaged power spectral estimate vs wave number, s, on a log-log plot, where

$$S(\kappa) = A\,\kappa^{s}, \tag{1}$$

was determined, by a technique which minimizes X^2 (Press et al. 1986). Parameter estimates were computed for each generic ice type on the decade of scales from 3.1×10^{-2} cpm to 3.1×10^{-1} cpm, from the half-power point of the filter to the cutoff wave number for noise (Fig. 3). Results indicate that for the first-year ice, $s = -2.3 \pm 0.05$, while for the multiyear ice $s = -1.8 \pm 0.05$. These slopes can be compared to previous estimates of spectral slope in a similar wave number band by Kelly et al. (1985), who found for an average of three sites with mixed first- and multiyear ice, and no topside survey, an average $s = -2.3$. The s values obtained by Rothrock and Thorndike (1980) typically show $s = -3.0$ with some values as low as $s = -2.4$, but their "high" wave number band is sampled only to wavelengths greater than 12 m and are not directly comparable with our results.

The fractal dimension, D, and the Lipschitz coefficient, α, can be related to the spectral slope, s, for a stationary and ergodic process, using

$$D = s/2 + 2.5 \tag{2}$$

$$\alpha = -s/2 - 0.5 \tag{3}$$

from Rothrock and Thorndike (1980). According to eq 2 and 3, these values of s correspond to $D = 1.4$, $\alpha = 0.6$ for the first-year case, and $D = 1.6$, $\alpha = 0.4$ for the multiyear case, respectively. These values are well within the range of fractal values, $0 < \alpha < 1$, and describe the degree of roughness of the surface.

Two-dimensional data from sites 2s, 2d and at site 3s were used to create a 200- × 200-m subset of data for further study. These data have been mapped to a 169 × 169 grid using inverse square weighting, and contoured in 1-m increments (Fig. 4). Data spacing varied considerably for both geometric reasons and the horizontal and vertical incremental scanning step angles, with better coverage on the site 3 side (upper left) than the site 2 side (lower right). The 140 m of keel shown was asymmetric, steeper on the site 3 side (average slope ~ 27°) than on the site 2 side (average slope ~19°). The mean axial draft of the keel is 9.2 m and ranges from 12.9 to 5.5 m, while the width was 43 m to the 3-m contour line (the e-folding value is 3.4 m), with a range from 16–55 m. The steeper, left side, had a simpler topography while the right side of the keel displayed a more rugged topography with three spurs projecting into the "flat" ice. The uppermost of these spurs, a major feature of the keel, had a draft of 7 m.

In order to compare under-ice and topside topog-

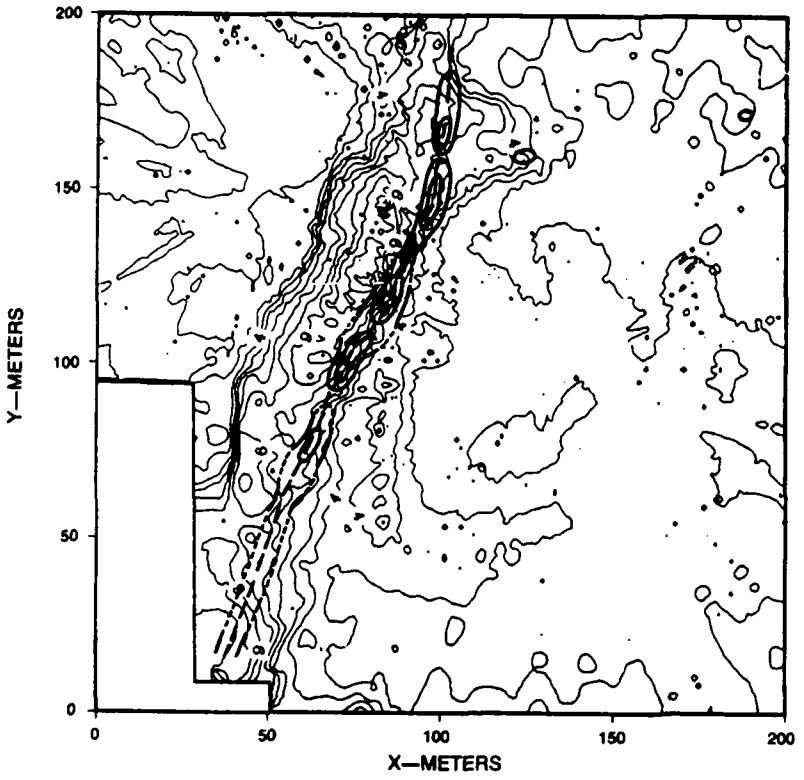

Figure 4. Contours of ice draft (1 m) from sites 2d, 2s, 3s. Data coverage was too sparse for contouring the lower left corner. Sail centerline and height contours (thick lines, 1-m interval) are superimposed upon contours of ice draft.

raphy, 1-m contours of the ridge sail in the range from 1–3 m (darker contour lines) and the sail axis are superimposed on the 1-m contours of the keel topography (Fig. 4). In general, the sail was block-like in nature, which may suggest compressional rather than shear formation mechanisms. Its weathered appearance and granular ice texture were typical of a multiyear sail. In addition to the overall sail/keel structures, two hummocks were observed in the Mesotech subarea which corresponded to under-ice features (Fig. 4). For the 140-m section of the ridge, the mean sail width is 11.9 m to the 1-m surface contour, with a mean keel/sail width ratio of 3.6, and a mean axial sail height of 1.9 m. The ratio of mean keel draft to mean sail height, often used to infer keel draft, was obtained at the topside survey points relative to the closest axial keel draft along the ridge axis, and found to be 4.8, with a range from 3–9. These results are within the range of reported values, e.g., those of Garrison et al. (1978), who obtained a mean ratio of 4.1 from nine laser transects and under-ice acoustic profiles. Results from Parmerter and Coon's (1972) one-dimensional kinematic pressure ridge formation model show that considerable variation in the keel/sail ratio can occur. The most important factor is the termination point in the ridge building cycle, and a secondary factor is the thickness of the parent ice sheets. Early termination of the ridge building cycle would favor low ratios, while proceeding full cycle would tend to produce higher ratios.

A mean offset of 9.6 m between the sail and keel axes was observed. Parmerter and Coon (1972) also examined examples of sail and keel offset, and applied their ridge formation model. For reasonable values of mechanical properties of sea ice, they were able to generate asymmetric sail/keel alignment, dependent on factors such as parent ice thickness, and when and where failure occurs in the cycle. Within the context of their model, a plausible explanation of the ridge profile under discussion would be early termination in the ridge building cycle that had been preceded by bending failure in the thinner ice on the site 3 side of the ridge.

The Mesotech data enable the estimation of several individual realizations of two-dimensional power spectra in the region of the multiyear ridge, although not enough for statistical confidence. Since ice topography is essentially a two-dimensional process, this approach can provide information on horizontal isotropy in regions where there are "special directions" (Czarnecki and Bergin 1986) in the surface under study. Raw data from sites 2s and 3s, and 2d, in a 61- × 61-m box centered on the high point of the ridge, were mapped to a 1-m grid (Fig. 5), with the y axis along the ridge, and the x axis across the ridge. This example was chosen because the data coverage was

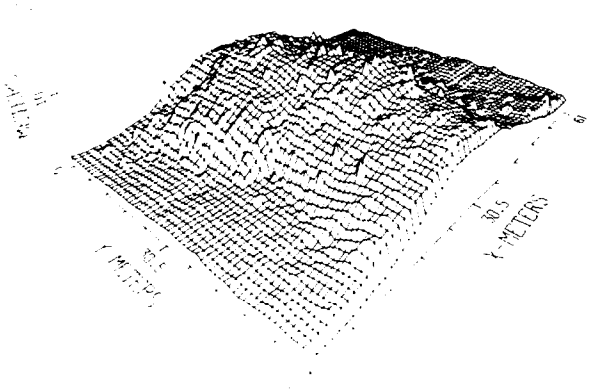

Figure 5. Two-dimensional gridded topography (61 ×61 m), x is across ridge and y is along ridge

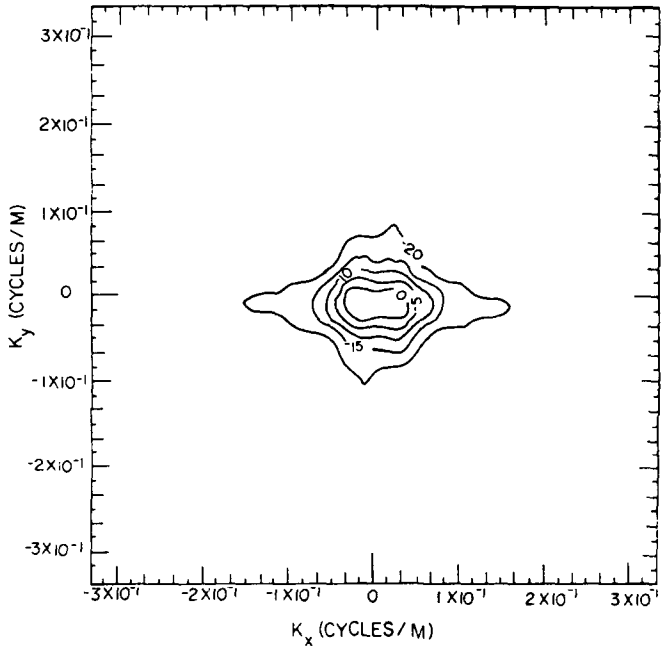

Figure 6. Example of normalized 2D-PSD (SL) estimate from ice ridge topography shown in Figure 5. Contours are in nondimensional units of 10 log (spectral amplitude/ 1 m^2/cpm^2), and x is across ridge and y along ridge.

superior in this region and it symmetrically straddles the ridge structure from the crest (~9 to 12 m) down to the 2- to 3-m contour. The mean and variance of these data are 5.34 m and 8.97 m^2, respectively.

The two dimensional analysis routine computes 2-D power spectral density estimates (2D-PSD) using a correlation method (Dudgeon and Mersereau 1984). The mean and trends are removed from the data by least squares methods, and then the auto-covariance is computed and windowed. The two-dimensional power spectral density estimates are calculated by Fourier transforming this auto-covariance matrix. For this study the spectra represent the distribution of variance over wavelengths from 2–30 m.

In Figure 6, results are shown in wave number space for κ_x and κ_y the cross-ridge and along-ridge wave numbers respectively. Using the convention of Czarnecki and Bergin (1986), the parameter plotted is the 5-dB contour of the normalized log magnitude of the 2D-PSD, or power spectrum level (*SL*) given by

$$SL(\kappa_x, \kappa_y) = 10 \log$$

$$[\text{2D–PSD}(\kappa_x, \kappa_y)/\text{2D–PSD}_{ref}]\ \text{dB} \qquad (4)$$

where $\text{2-D–PSD}_{ref} = 1\ m^2/cpm$ is a normalizing factor, making *SL* dimensionless.

Results, presented in Figure 6, show contours of *SL* in the range from 0 to –20 dB plotted as a function of wave length in the *x*, *y* directions. Since the noise level of the Mesotech data due to quantization in the vertical stepping of the transducer, 0.16 m, corresponds to a spectral noise level of approximately –10 dB, interpretation of contours beyond this value is

not warranted. For the contours in the 0 to –10 range, the results show anisotropy in the x direction, corresponding to increased spectral variance in the cross-ridge direction for the larger wavelengths for which contours are drawn, corresponding to wavelengths greater than 6.7 m. In order to show statistical confidence in this result, many such examples would have to be averaged to reduce the error of the spectral estimate to a reasonable level. For comparison, an individual realization of an *SL* estimate of a wave-like structure on a seamount showed enhanced spectral variance in the direction perpendicular to the wave crest (Czarnecki and Bergin 1986), and 2D–PSD estimates for ice topside topography (Hibler 1972) show indications of low frequency ridge structures with lineation, as well as high frequency snow dune lineation.

CONCLUSIONS

1. For profiles of under-ice topography, estimates of the slope of power spectral density, for 3.1×10^{-2} cpm $< \kappa < 3.1 \times 10^{-1}$ cpm, for heavily ridged first-year and multiyear ice are $s = -2.3 \pm 0.05$, and $s = -1.8 \pm 0.05$, respectively. These values of s correspond to $\alpha = 0.6$, $D = 1.4$ for the first-year case, and $\alpha = 0.4$, $D = 1.6$ for the multiyear case, respectively, within the range for the under-ice surface to be considered fractal in nature.

2. For a multiyear ridge segment, topography was found to be asymmetric in cross-ridge slope, have a mean keel/sail ratio of 4.8, and have an offset of 9.6 m between sail and keel axes. Based on the model of Parmerter and Coon (1972), these observations suggest early termination of the ridge building cycle, with ice sheet failure and steeper ridge building in the thinner ice.

3. For a multiyear ridge, an estimate of one realization of the two-dimensional power spectral density suggests anisotropy, i.e., enhanced variance in the cross-ridge direction for the larger scales.

REFERENCES

Czarnecki, M.F. and J.M. Bergin (1986) Characteristics of the two-dimensional spectrum of roughness on a seamount. Naval Research Laboratory, Report 9022, p. 1–22.

Dudgeon, D.E. and R.M. Merserau (1984) *Multidimensional Digital Signal Processing*. Englewood Cliffs, New Jersey: Prentis-Hall Signal Processing Series, p. 1–400.

Garrison, G.R., R.E. Francois, E.W. Early and T. Wen (1978) Comprehensive studies of arctic pack ice in April 1976. University of Washington, Seattle, APL-UW 7724.

Hibler, W.D. (1972) Two-dimensional statistical analysis of arctic sea ice ridges. In *Sea Ice* (T. Karlsson, Ed.). National Research Council, Reykjavik, Iceland, p. 261–275.

Kelly, J.G., L.R.Leblanc, D.J. O'Neill and S.E. Chellis (1985) Analysis of the under-ice roughness spectrum. Naval Underwater Systems Center, Newport, Rhode Island (unpublished manuscript).

Lyall, R.G. and H.H. Lanziner (1986) Acoustic profiling techniques. Offshore Survey and Positioning Services Ltd., North Vancouver, British Columbia, Canada, p. 1–16.

Parmerter, R.R. and M.D. Coon (1972) Model of pressure ridge formation in sea ice. *Journal of Geophysical Research*, **77**(33): 6565–6575.

Press, W.H., B.P. Flannery, S.A. Teukolsky and W.T. Vetterling (1986) *Numerical Recipes, the Art of Scientific Computing*. Cambridge, England: Cambridge University Press, p. 1–818.

Rothrock, D.A. and A.S. Thorndike (1980) The geometric properties of the underside of sea-ice. *Journal of Geophysical Research*, **85**: 3955-3963.

Simulation of the Ice Ridging Process

M.A. HOPKINS AND W.D. HIBLER III
Thayer School of Engineering
Dartmouth College
Hanover, New Hampshire, U.S.A.

ABSTRACT

In this work a particle simulation is used to model the ridging process in sea ice. With this model it is possible to explicitly calculate the energy lost through the various dissipative mechanisms. The results show the work required to ridge ice to be significantly greater than previous estimates. These results are consistent with large-scale ice rheologies based on a statistical treatment of the ridging process.

INTRODUCTION

A typical sea ice cover in the polar regions contains a variety of ice thicknesses that evolve in response to both dynamic and thermodynamic forcing. The variable thickness of the ice cover is created by deformation that simultaneously causes formation of thick ice through ridge building and thin ice through lead creation. Since the energy expended in deformation is largely determined by the ridging process, investigating the energetics of pressure ridging becomes critical for the determination of ice strength on a geophysical scale.

A framework for describing the variable thickness character of sea ice was developed by Thorndike et al. (1975). Within this framework, pressure ridging is treated statistically by a distribution process whereby thin ice is transferred to thick ice categories. The amount of energy used for this process can be related to the large-scale strength of the pack ice (Rothrock 1975). The key issue here is how much the total energy dissipated in the ridging process exceeds the increase in potential energy. Most estimates have typically placed the total energy losses at about twice the potential energy increase, (cf., Rothrock 1975), a factor that was largely based on a kinematic ridge model developed by Parmerter and Coon (1972). However, while modeling the kinematics of the ridging process, this ridge model did not explicitly calculate frictional and other non-potential energy losses.

A subsequent difficulty was that this factor of two is not consistent with large-scale simulation results. In a seasonal simulation of the Arctic Basin using a variable thickness sea ice model, Hibler (1980) found that unrealistic ice drift and ice buildup results were obtained for total energy losses scaled by only a factor of two times the potential energy. In a one-year sensitivity study, Hibler (1980) found that total energy losses scaled by a factor of 10 times the potential energy yielded unrealistically small drifts, with the basin motion totally stopping in winter. Therefore these two extreme values probably represent upper and lower bounds on total ridging energy.

Because of the critical nature of the dissipative energy losses in the ridging process, it is clearly of interest to investigate explicitly the relative magnitudes of the energetic mechanisms that are a part of ridge formation. As a first step in this direction a particle simulation is used to model the ridging process. In this way it is possible to model explicitly the individual interactions between blocks of rubble and between rubble and floes. As a consequence, a much more detailed picture of the energetics of the ridging process may be constructed. This, in turn, may lead to a more accurate parameterization of the energy losses in ridging based on the increase in potential energy. In this paper, two-dimensional ridge growth is studied using disk-shaped rubble and rigid floes. While this model is somewhat idealized, it still retains much of the essential physics of the ridging process, and yields a valuable explicit first estimate of the magnitudes of the various dissipative energy losses in the formation of pressure ridges. It also provides a sound basis for future, more detailed experiments.

THE DYNAMIC RIDGE MODEL

This work adopts essentially the same conceptual picture of ridge growth as that of Parmerter and Coon, that is, two floes of uniform thickness converging on a lead uniformly filled with rubble. The floes are modeled as plates on an elastic foundation. However, in place of the arbitrary ridge building mechanisms used by Parmerter and Coon, which consisted of assumed transfer coefficients and angles of repose, a particle simulation is used to rigorously determine the dynamics of each particle in the rubble. Since frictional and inelastic contacts are explicitly a part of this model, it should provide a better picture of the energetics of the ridging process than the lower bound provided by Parmerter and Coon based on potential energy alone.

The simulated ridges begin with the configuration shown in Figure 1 and end when a floe breaks in flexure. The floe on each side of the lead consists of a rigid assembly of hexagonally close-packed disks as shown

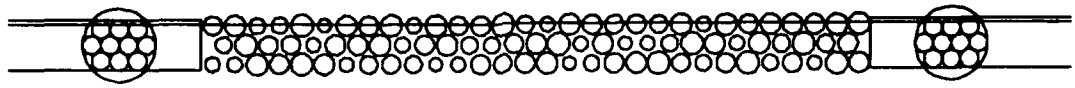

Figure 1. The initial configuration of the simulated ridging experiment.

in Figure 1. The disks making up each floe move as a unit in the horizontal (x) direction at a speed u_{floe}. Although forces are calculated between the disks in the rubble and the disks in the floes with which they are in contact, these forces do not affect the horizontal motion of the floes which remains constant.

Feedback from the rubble to the floes occurs through the analytic equations for the moments caused by unbalanced forces exerted by the rubble on the floes. Only the forces exerted by the rubble due to gravity are considered in this calculation. Periodically in the simulation the moments in the floes are calculated using standard solutions (Hetenyi 1946) in which plate rigidity replaces beam stiffness. When the moment at some point exceeds a critical value, $(h^2/6)\,\sigma_{cr}$, where σ_{cr} is the tensile breaking stress for the material, the floe breaks at that point. Upon breaking, the experiment is concluded.

THE PARTICLE SIMULATION

The particle simulation is a computer program which stores the instantaneous location and velocity of each disk in an array. The interparticle and body forces on each disk are calculated at each time step and the disks are moved to new locations with new velocities according to those forces. The normal component N and the tangential component S of the interparticle force are modeled using linear springs and dashpots as shown in Figure 2 (Walton 1980).

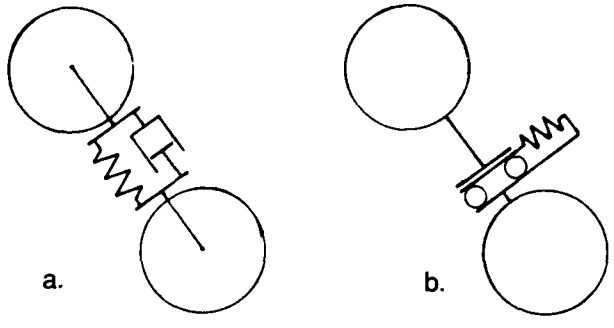

Figure 2. The normal and tangential contact force models.

THE ENERGETICS

The work performed by the pack in building the ridge is transformed into the potential energy of the ridge structure and lost through dissipative mechanisms. The dissipative mechanisms consist of friction between sliding blocks of ice, inelasticity that includes crushing at the point of contact, and breakage, which we ignore in this study. The work performed by the pack may be calculated directly from the forces exerted on the floes by the disks in contact with them. That is

$$\text{work} = u_{floe}\, dt\, \Sigma_i \Sigma_n\, Fx_i^n \qquad (1)$$

where the summations are over the x components of the forces exerted by the disk rubble on the floes at each time step in the experiment. The change in potential energy is given by

$$\Delta PE = g\, dt\, \Sigma_i \Sigma_n\, v_i^n\, (\rho_i A_i - \rho_w A_{is}^n). \qquad (2)$$

The summations are over each disk in the rubble at each time step. A_i is the cross-sectional area, A_{is} the submerged area, ρ_i the ice density, v_i the vertical velocity component of disk i, and ρ_w is the density of seawater. The frictional dissipation ϕ_f is calculated from the work performed by the tangential force S_i between the i^{th} pair of disks using the equation

$$\phi_f = dt\, \Sigma_i\, \Sigma_n\, S_i^n \left(V_{i\,1/2c}^n \cdot t\right). \qquad (3)$$

$V_{1/2c}$ is the relative velocity between the disks at their point of contact. The dissipation ϕ_i by a dashpot in the normal direction, which is equivalent to disk inelasticity, is given by a similar equation

$$\phi_i = dt\, \Sigma_i \Sigma_n N_i^n \left(V_{1/2c}^n \cdot t\right) \qquad (4)$$

where N_i is the normal force between the disks. In both cases the summations are over the pairs of disks in contact at each time step.

SIMULATED RIDGE GROWTH

Simulated ridge growth using this model is shown in Figures 3a–f. The following set of parameters were used in the experiment:

Initial lead width	150 m
Floe thickness	2.0 m
Floe speed	0.25 m/s
Mean disk diam <D>	0.732 m
ρ_i	920.0 kg/m^3

ρ_w	1010.0 kg/m^3
σ_{cr}	350 kPa
C_d	0.25
k_s	2.0 mN/m
μ	1.0.

The nonuniform disk diameters were chosen according to the distribution: $D = \langle D \rangle (1.5 - R\#)^{0.5}$ where $R\#$ is a random number uniformly distributed between 0 and 1. C_d is the fraction of critical damping of the dashpot coefficient κ_d in the normal force model shown in Figure 2a. With $C_d = 0.25$ the rubble will be highly inelastic. In Figures 3a–f the scale is readjusted in each figure. The floe thickness may be used to determine the size of the ridge in each figure.

The simulated ridge growth shown in Figures 3a–f is typical of all of the experiments performed with nonuniform diameter disks. In this sequence of pictures the thickening of the rubble layer is relatively uniform. As the thickness becomes greater than the floes, sloping embankments form beneath each floe. Note that the floes composed of disks (Fig. 1) have a bumpy surface which allows the loose disks to rest in crevices without rolling away. The rubble remains in isostatic equilibrium until the floes begin to approach each other. As the floes approach each other the embankments meet to form a triangular-shaped ridge with a sail to keel ratio of about 1:4. A plot of the energetics vs time for this ridge is shown in Figure 4. Figure 4 illustrates the overall rate of work and its

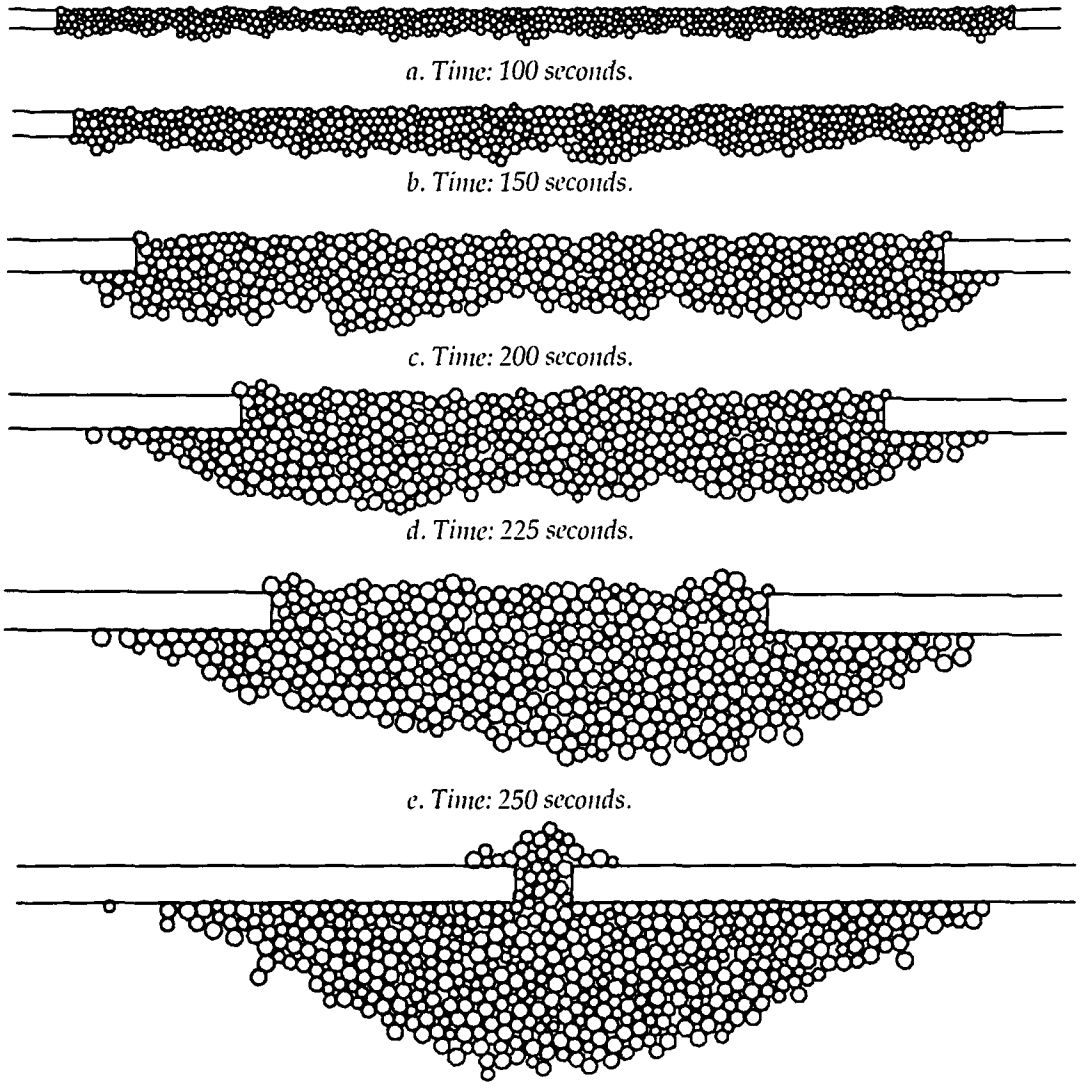

a. Time: 100 seconds.

b. Time: 150 seconds.

c. Time: 200 seconds.

d. Time: 225 seconds.

e. Time: 250 seconds.

f. Time: 295 seconds.

Figure 3. Simulated ridge growth.

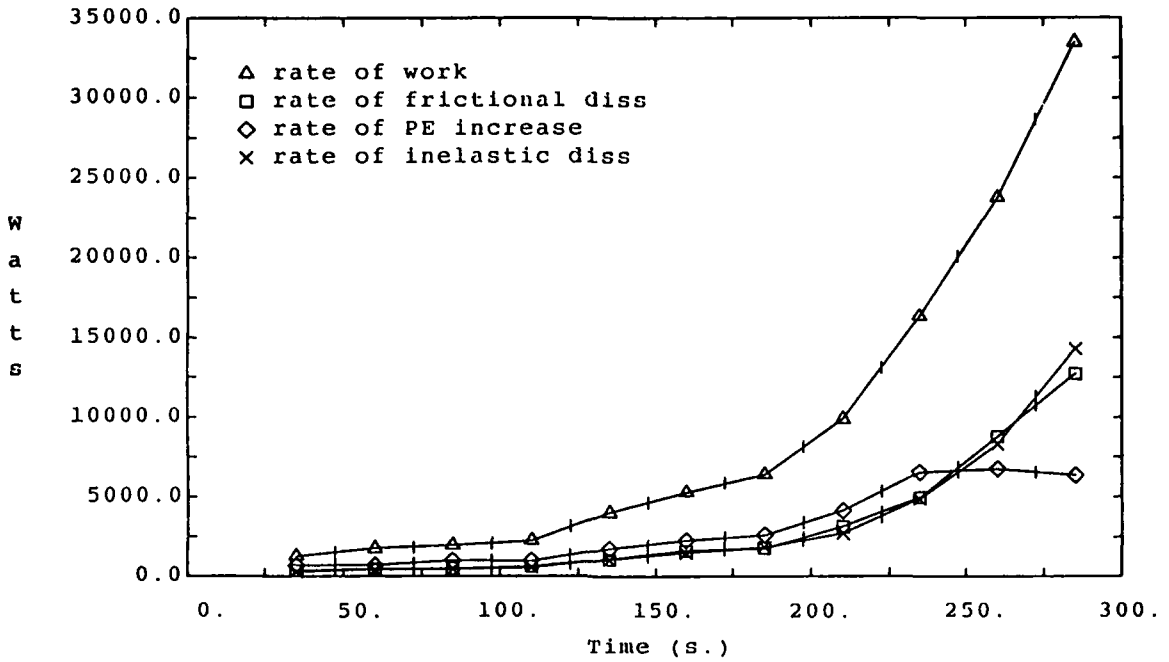

Figure 4. The energetics of the simulated ridge growth.

three constituents for the ridge shown in Figure 3. The method of calculation is discussed above. The smoothness of the increasing rate of work is a consequence of the uniform thickening of the rubble. The rates of the three constituents follow the rate of work except for a decline in the rate of potential energy increase in the final stages of the ridge growth.

CONCLUSIONS

The intent of this work has been to better estimate the energy required to ridge ice. A particle simulation was used to model ridge growth, taking explicit account of frictional and inelastic dissipative mechanisms. At the same time the simulation furnished pictures of the growing ridges that led to a better qualitative understanding of ridging.

The simulation of ridge growth began with a lead filled with pre-existing rubble between two multiyear floes. As the floes converged at a constant speed, the rubble thickened uniformly and the force required to move the floes increased with the square of the thickness. The ratio of work to potential energy increase was slightly greater than two in the early stages of ridge growth and increased somewhat in later stages. Hopkins et al. (in prep.), using a simple analytical ridge model based on classical Rankine theory for cohesionless soils, showed that, in the early stage of rubble ridging, the ratio is equal to the passive pressure coefficient

$$K_p = (1 + \sin\phi)/(1 - \sin\phi).$$

This conclusion was supported by the results of the ridge simulation. In simulated experiments with disk rubble ϕ, the angle of internal resistance, was found to be about 24°. This value of ϕ yields a K_p of 2.33 which is approximately the ratio of work to ΔPE in Figure 4. Keinonen and Nyman (1978), Cheng and Tatinclaux (1977), and others have found ϕ in the range 40° to 50° in experiments with model ice rubble. This range of ϕ yields K_p in the range 4.60–7.55. If the ratio of work to ΔPE is assumed to lie in this range, it would imply that the strength of the ice pack has been significantly underestimated.

The explicit particle simulation is a valuable tool which has already yielded some interesting insight into the formation of pressure ridges (Hopkins et al., in prep.). Future experiments will be conducted that will more realistically simulate the ridging process.

REFERENCES

Cheng, S.T. and J.C. Tatinclaux (1977) Compressive and shear strengths of fragmented ice covers. Iowa Institute of Hydraulic Research, Report No. 206, University of Iowa.

Hetenyi, M. (1946) *Beams on Elastic Foundations*. Ann Arbor, Michigan: University of Michigan Press.

Hibler, W.D. III (1980) Modeling a variable thickness sea ice cover. *Monthly Weather Review*, **108**: 1943–1973.

Hopkins, M.A., G. Flato and W.D. Hibler III (In prep.) The energetics of ice ridging. To be submitted to the *Journal of Geophysical Research.*
Hopkins, M.A. (1987) Granular flow simulations. Civil and Environmental Engineering Research Report 87-7, Clarkson University, Potsdam, New York
Keinonen, A. and T. Nyman (1978) An experimental model-scale study on the compressible frictional and cohesive behaviour of a broken ice mass. In *Proceedings of the IAHR Symposium on Ice Problems, Lulea, Sweden.* Part II, p. 335–353.
Parmerter, R.R. and M.D. Coon (1972) Model of pressure ridge formation in sea ice. *Journal of Geophysical Research,* **77**: 6565–6575.
Rothrock, D.A. (1975) The energetics of the plastic deformation of pack ice by ridging. *Journal of Geophysical Research,* **80**: 4514–4519.
Thorndike, A.S., D.A. Rothrock, G.A. Maykut and R. Colony (1975) The thickness distribution of sea ice. *Journal of Geophysical Research,* **80**: 6565–6575.
Walton, O.R. (1980) Particle-dynamics modeling of geological materials. UCRL-52915, Lawrence Livermore Laboratory, University of California.

Periodicities and Keel Spacings in the Under-ice Draft Distribution

J. KEY AND A.S. MCLAREN
Cooperative Institute for Research in Environmental Sciences
University of Colorado
Boulder, Colorado, U.S.A.

ABSTRACT/INTRODUCTION

During early August 1970, the USS *Queenfish* continuously recorded the under-ice topography across the Canada Basin and North Pole along the 155°W meridian. Observations indicated that under-ice topography in the Canada Basin was quite uniform and moderate in draft (McLaren 1987, 1988, Wadhams 1980), and further analyses revealed a recurring tendency for reversal of the mean clockwise gyre in late summer (McLaren et al. 1987). This provided the impetus to examine further the under-ice profiles recorded by the *Queenfish* to determine what other indications of environmental forcings might be found. This paper presents the results from analyses of periodicities and independent keel spacings in approximately 2000 km of under-ice thickness data.

The *Queenfish* recorded the under-ice topography with a narrow-beam acoustic profiler. Data are interpolated to 145-cm intervals. Gaps occur in the data but account for less than 10% of the study transect; these portions are not used in subsequent analyses.

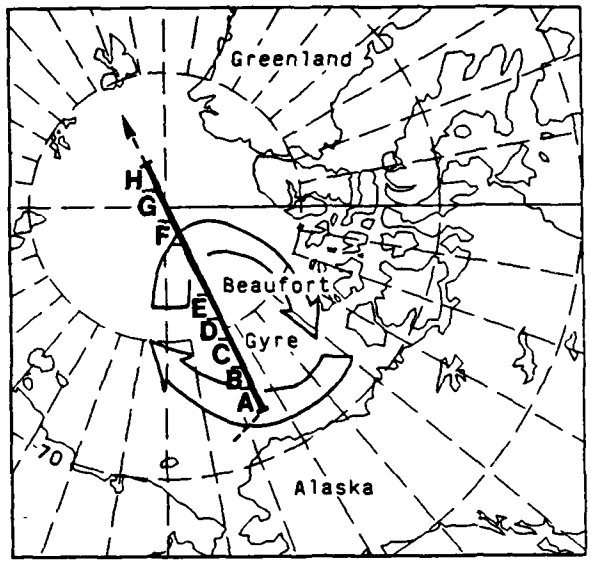

Figure 1. Track of the USS Queenfish *in early August 1970 across the Canada Basin and the North Pole. The study area encompasses approximately 2000 km divided into eight subregions (A–H).*

The track is divided into eight subtracks (Fig. 1) based on similarity of mean draft and variability (Fig. 2), varying in length from 50 to 150 km. The overall track is also divided into 5-km subsections with points averaged over 10 m. This combination of segment length and point spacing was chosen because it sufficiently resolves periodicities in the range of interest (20–1000 m) while providing a relatively high degree of homogeneity within each segment.

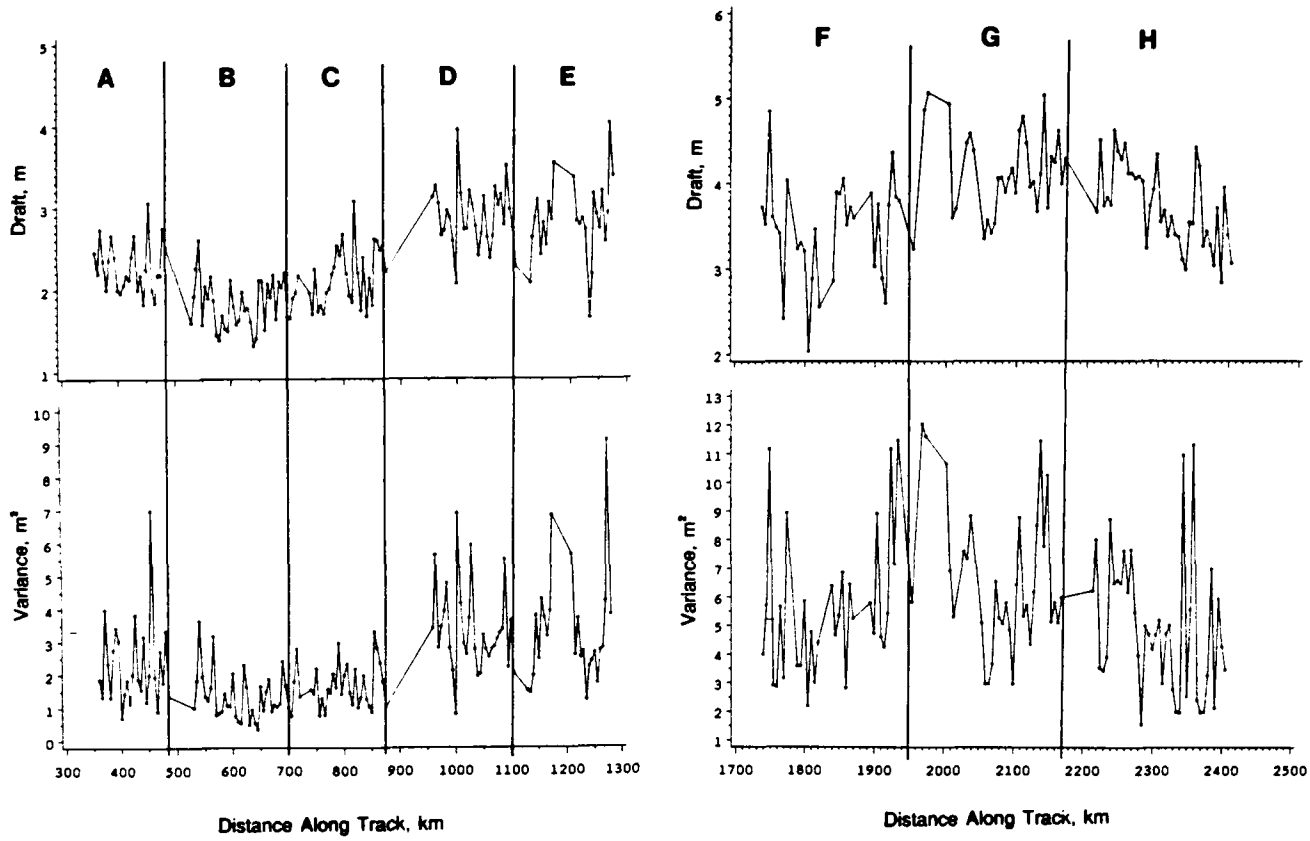

a. Canada Basin. *b. North Pole region.*

Figure 2. Ice draft means and variances for each 5-km section in the study areas.

SPECTRAL ANALYSIS AND INDEPENDENT KEEL SPACINGS

Spectral analysis has previously been applied to the underside of sea ice by Hibler and LeSchack (1972) and Kozo and Tucker (1974). Here, spectral analysis following Mitchell et al. (1966) is applied to each 5-km subsection in the track. To inhibit aliasing in the analysis, frequencies above the Nyquist frequency were removed with a low-pass, 1-2-1 filter. Figure 3 summarizes the periodicities for the entire track, where wavelengths corresponding to significant peaks (90% confidence interval) in the spectra are grouped into 20-m bins and frequencies are tabulated. Periodicities in the range of 30–130 m occur most frequently. The shorter of these may correspond to "blisters" observed by Wadhams (1988) and Wadhams and Martin (1989) in sidescan sonar data, which had wavelengths of 28–63 m. Histograms constructed for each of the eight regions along the track exhibit the same general shape as that for the overall track. Some regional variations exist, for example, an increase in the frequency of wavelengths longer than 1000 m in those areas with greater mean draft and variability, generally beyond kilometer 1000. Similarly, the less variable, thin ice areas show an increase in shorter wavelengths with few greater than 1000 m. Hibler and LeSchack (1972), in a spectral analysis study of the ice surface, also observed that young ice has greater high frequency roughness while multiyear ice is more undulating. This also agrees with Kozo and Tucker (1974), who found an increase in ice thickness variability with increasing distance from the ice edge towards the Greenland coast, and a corresponding increase in the importance of the longer wavelengths (periodicities). The frequency cutoff measure—the number of Fourier components required to account for 95% of the data variance—employed by Kozo and Tucker (1974) was found to average 102 components throughout the track with a range of 90–220. Contrary to the findings of that study, this parameter exhibits only a weak linear correlation with the standard deviation in ice draft.

Spacing distributions of keels are also examined, without assuming a periodic nature, and the results compared to those of spectral analysis. The method of defining independent keels follows Wadhams and Horne (1980). Two models of spacing distributions are examined: the negative exponential model of Hibler et al. (1972), and the three-parameter (mean,

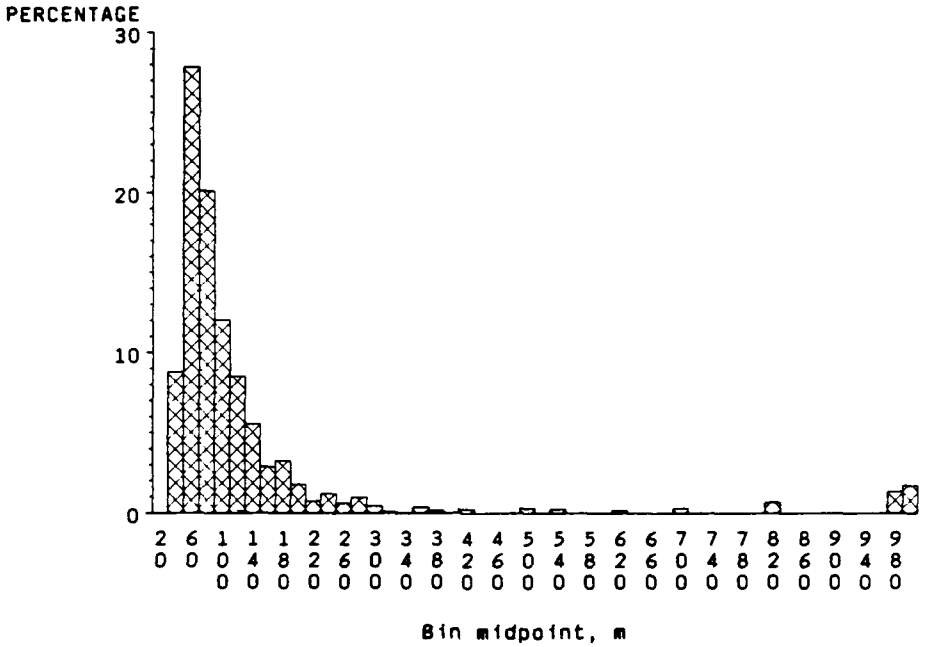

Figure 3. Summary of the relative frequency of significant (90%) peaks in the power spectra for each 5-km section in the study area. Periodicities are grouped in 20-m bins, represented on the horizontal axis by their midpoint.

variance, and a beamwidth-related parameter) log-normal model presented by Wadhams and Davy (1986). The observed spacing distributions are examined for each of the eight regions and for keel draft cutoffs of 3.5, 5.0, and 9.0 m. The original data based on point spacings of 1.45 m are used in these analyses. An example for region G (North Pole) is given in Figure 4, and region B (Canada Basin) is shown in Figure 5, where keel spacings are grouped into 20-m bins for keels at each draft cutoff. A chi-square goodness-of-fit test indicates that in all cases the observed frequencies are significantly different (0.05 level) from the negative exponential distribution.

The threshold, θ, in the three-parameter log-normal distribution is varied from 0- to 18-in.-increments of 3. The chi-square test is applied for each θ and the linear correlation between the logarithm of each spacing and the logarithm of the cumulative probability up to that spacing is calculated. The correlation steadily increases up to $\theta = 15$ (from approximately 0.85 to 0.90) and decreases thereafter. Calculated chi-square values decrease—implying less difference between observed and model distributions—to a minimum at $\theta = 9$ for most regions.

At all keel-draft cutoffs in the North Pole regions, the data are found to be not significantly different from the log-normal distribution. In the Canada Basin, this is true only for spacing distributions that include smaller keels (> 3.5 and < 5 m). This is assumed to be a function of the relatively mild ice conditions found by the *Queenfish* (McLaren 1986). Based on this data set, keel spacing distributions cannot be modeled by either probability density function when ice is thin, such as that found in the Canada Basin, and the threshold value for keel depth is large, e.g., 5 or 9 m. Previous work (e.g., Wadhams and Davy 1986) has been done in areas of greater ice thickness and variability, where the mean number of deep-draft keels per unit length was larger than that found here for the Canada Basin. In these cases, the corresponding spacing distributions follow the model log-normal distribution very closely.

Relationships between simple descriptive ice draft statistics and both the keel spacing results and the spectral analysis are also examined. Significant linear correlations (>0.9, 0.05 level) exist between the mean ice draft and its variance, the mean number of keels per unit length, and the mean keel draft (Fig. 6). Relationships between ice draft and the amount of power in the longer wavelengths from the power spectra are also found (not shown), indicating the importance of larger keel spacings in areas of thicker ice.

CONCLUSIONS

Even though spectral analysis and keel spacing distributions do not describe the under-ice draft dis-

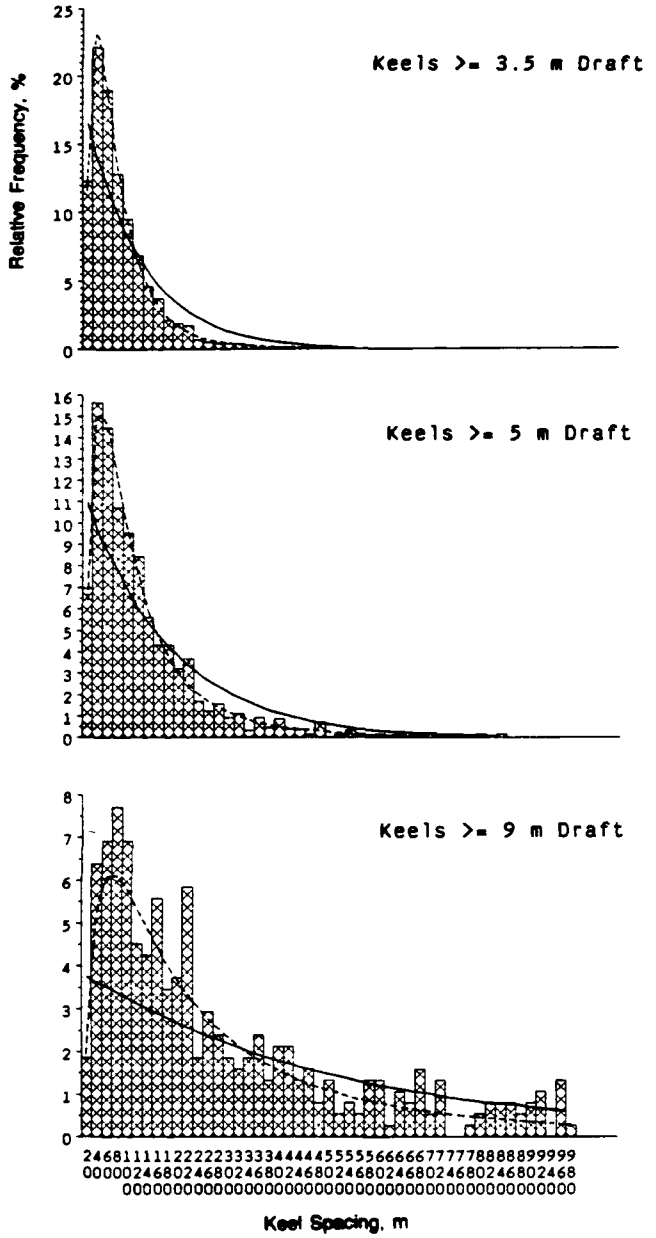

Figure 4. The frequency distribution of independent keels of at least 3.5-m, 5-m, and 9-m draft in the North Pole region. The model negative exponential (solid line) and log-normal curves (dashed line) are also shown. For the log-normal distributions, θ = 9.

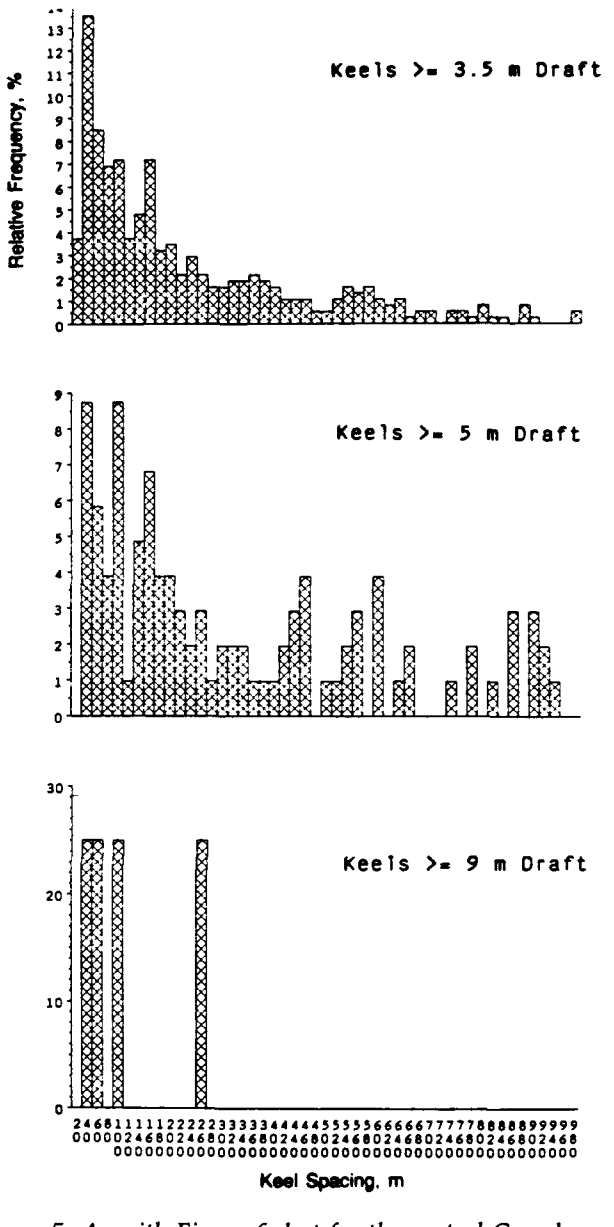

Figure 5. As with Figure 6, but for the central Canada Basin. Model distributions not shown.

tribution in the same manner, general agreement between them was found. In particular, both methods detected a high frequency of periodicities/spacings in the range of 40–130 m. The distribution of periodicities is also in general agreement with spacing distributions of ridges and independent keels described in Hibler and LeShack (1972), Wadhams and Horne (1980), Wadhams (1981), and others, where the highest frequency of spacings occurs at approximately 100–150 m. Power spectra across the Canada Basin, and the North Pole area were similar, although some regional variations exist. Spacing distributions of independent deep-draft (>5m) keels were found to be significantly different between these two regions. These results imply that analyses of periodicities and independent keels may be useful for discrimination between ice regimes, which in turn will aid in the investigation of environmental forcings.

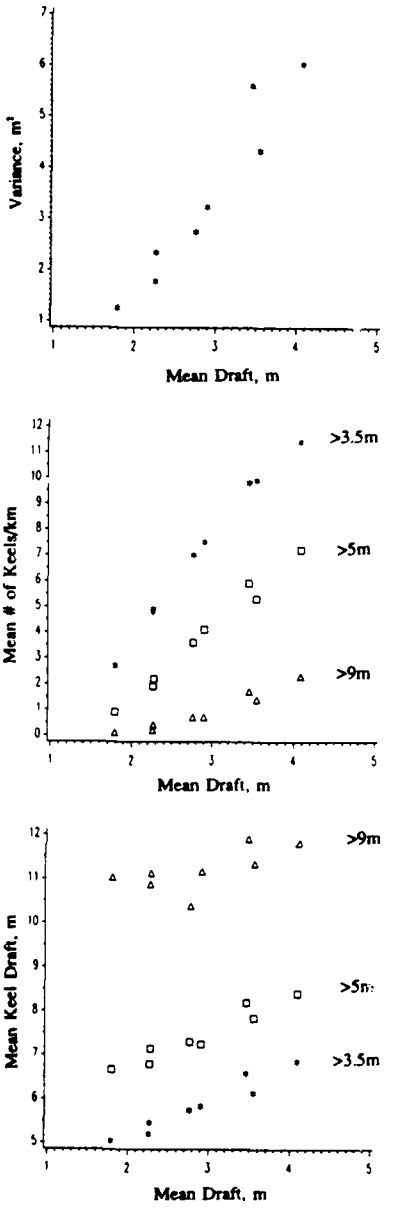

Figure 6. Relationship between mean ice draft and standard deviation in ice draft (top), mean number of keels per kilometer (middle), and mean keel draft (bottom). For keel-related features, each of three draft cutoffs is shown. Data are taken from all study areas.

ACKNOWLEDGMENTS

This work was supported by the Office of Naval Research University Research Initiative Program, contract N00014-86-K-0695.

REFERENCES

Hibler, W.D. III and L.A. LeSchack (1972) Power spectrum analysis of undersea and surface sea-ice profiles. *Journal of Glaciology*, **11**: 345–456.

Kozo, T.L. and W.B. Tucker (1974) Sea ice bottom-side features in the Denmark Strait. *Journal of Geophysical Research*, **79**(30): 4505–4511.

McLaren, A.S. (1988) Analysis of the under-ice topography in the Arctic Basin as recorded by the USS *Nautilis*, August 1958. *Arctic*, **41**: 117–126.

McLaren, A.S., M.C. Serreze and R.G. Barry (1987) Seasonal variations of sea ice motion in the Canada Basin and their implications. *Geophysical Research Letters*, **14**(11): 1123–1126.

Mitchell, J.M. Jr., B. Dzerdzeevskii, H. Flohn, W.L. Hofmeyr, H.H. Lamb, K.N. Rao and C.C. Wallen (1966) Climatic change. World Meteorological Organization, Technical Note No. 79, WMO-No. 95. TP. 100.

Wadhams, P. (1988) The underside of arctic sea ice imaged by sidescan sonar. *Nature*, **333**: 161–164.

Wadhams, P. (1981) Sea-ice topography of the Arctic Ocean in the region 70°W to 25°E. *Philosophical Transactions, Royal Society, London*, **302**(1464): 45–85.

Wadhams, P. and T. Davy (1986) On the spacing and draft distributions for pressure ridge keels. *Journal of Geophysical Research*, **91**(C9): 10,697–10,708.

Wadhams, P. and R.J. Horne (1980) An analysis of ice profiles obtained by submarine sonar in the Beaufort Sea. *Journal of Glaciology*, **25**(93): 401–424.

Wadhams, P. and S. Martin (1989) Processes determining the bottom topography of multiyear sea ice. This volume.

Section III:

Large-Scale Variations in Drift, Extent, Snow Melt and Concentration of Sea Ice

Mountain Barrier Effects on Ice Island Drift in a Coastal Ice Zone

M. LU AND W.M. SACKINGER
Geophysical Institute
University of Alaska
Fairbanks, Alaska, U. S. A.

ABSTRACT

A comparison was made between observed surface winds and geostrophic winds calculated from surface pressure maps, for the Arctic Ocean region near Axel Heiberg Island, during the May–September 1986 interval. For five distinct episodes, during which the geostrophic wind was directed from the west toward the mountain range, the surface wind, measured on Hobson's drifting ice island, 60 km west of the mountain barrier, was from the south. This is interpreted as additional experimental confirmation of the mountain barrier effect on surface winds. The effects on ice island motion near the coast of the Canadian Arctic are discussed.

INTRODUCTION

Albright (1980) and also Thorndike and Colony (1982) stated that the geostrophic winds are related to the observed surface winds and pack ice motion in the central Arctic. Values obtained by Albright (1980) for the ratio in the central Arctic may not be applicable within 150 km of a mountain barrier, if the geostrophic winds are directed either towards or away from the barrier. The effect of mountains is to modify the direction and speed of the surface winds as compared with the geostrophic winds (Kozo 1980, 1988, Parish 1983). A mountain barrier perpendicular to the geostrophic wind creates a surface wind component on the incoming side which is to the left (in the northern hemisphere) blowing parallel to the mountain chain, and extending up to 150 km away from it (Parish 1983).

In our study, the observed surface wind data measured on Hobson's drifting ice island was compared with the geostrophic winds calculated from surface pressure maps. The ice island was located 60 km west of Axel Heiberg Island during the period of the study, May–September 1986. Data showed that when the geostrophic wind was directed from the west toward the mountain range, the surface wind was from the south, parallel to the mountain chain.

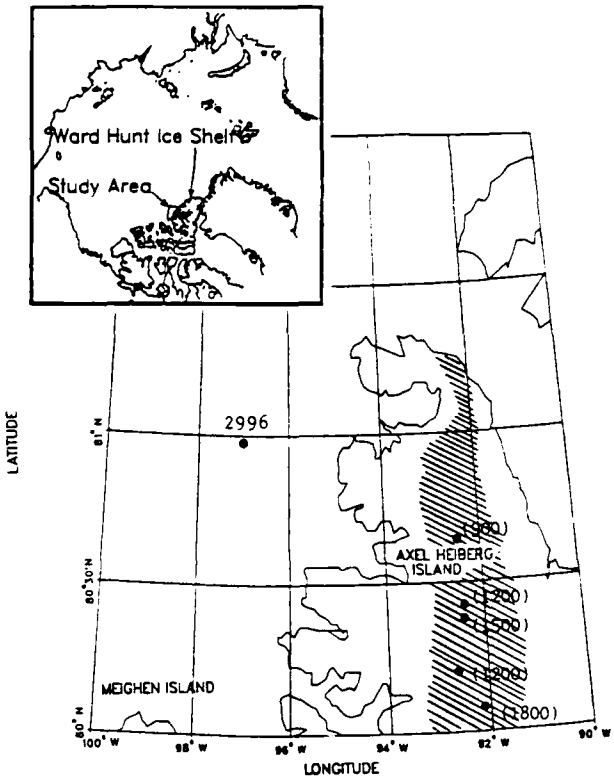

Figure 1. The location of Hobson's ice island with buoy 2996 and its vicinity. The study area and Ward Hunt Ice Shelf are shown in the small map above. Crossed area on Axel Heiberg Island corresponds to surface elevation above 400 m, and with peaks at 900, 1200, 1500 and 1800.

OBSERVED DATA—HOBSON'S ICE ISLAND

Surface winds were measured at a height of 2 m with Argos buoy 2996 deployed on Hobson's ice island. The velocity of the ice island movement was obtained from Transit Satellite Geodetic Doppler Positioning System (Schmidt et al. 1987) and the geostrophic wind was calculated from the synoptic chart (Canadian Meteorological Center, Edmonton, Alberta, CMC). The mountain barrier on Axel Heiberg has an average width of 30 km, with the heights of the ridge crests at 900, 1200, 1500 and 1800 m, respectively, along a 110 km length, as shown in Figure 1.

Hobson's ice island is the largest tabular iceberg that broke off the Ward Hunt Ice Shelf in 1982–83, with a length of about 8.7 km, a width of about 5.7 km and a mean thickness of 42.5 m (Jeffries et al. 1988).

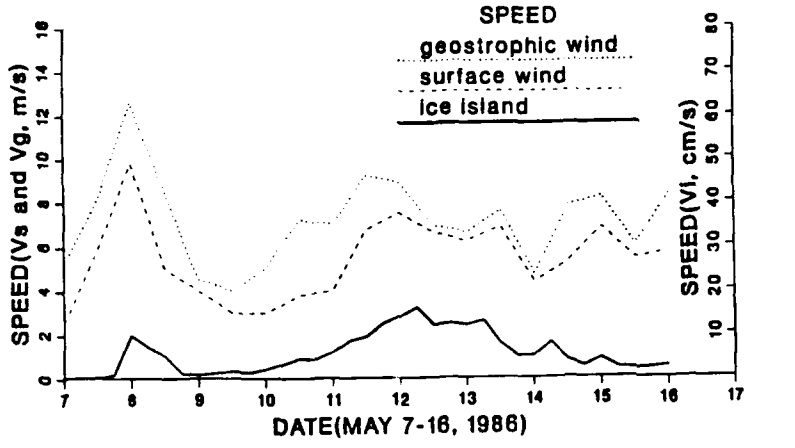

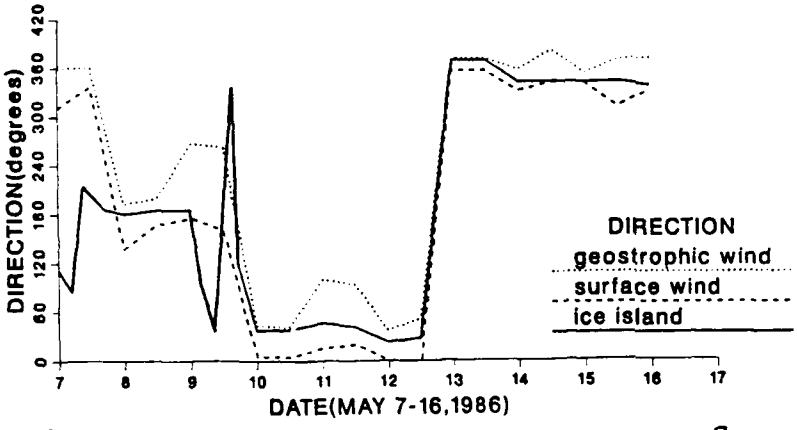

Figure 2. Direction and speed of surface wind V_s, geostrophic wind V_g, and ice island movement, V_i, in the period 7–16 May 1986.

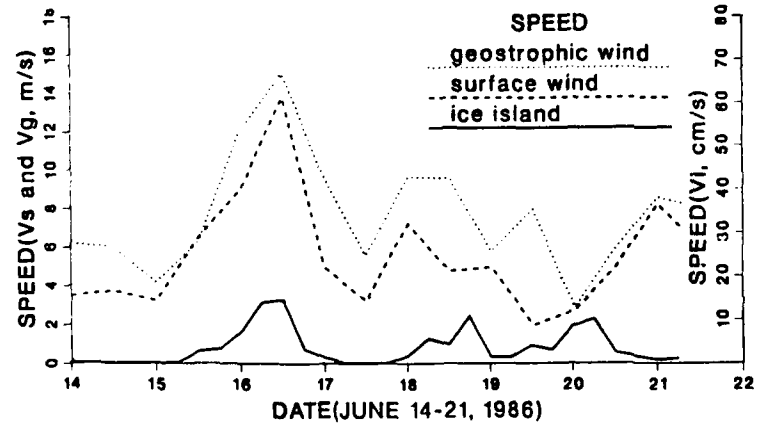

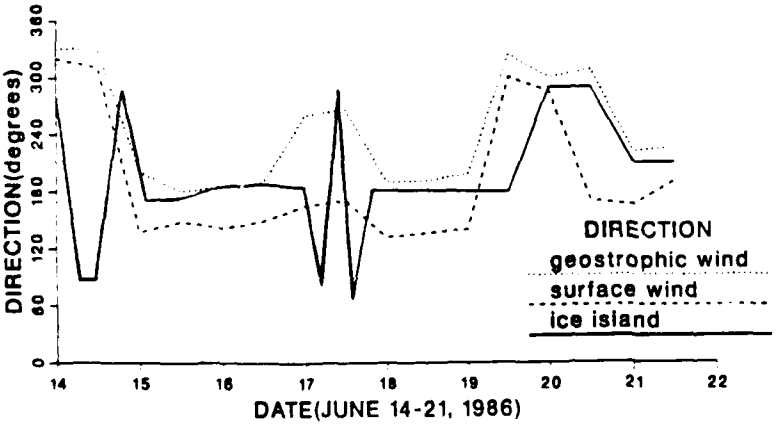

Figure 3. Direction and speed of surface wind, geostrophic wind and ice island movement in the period 14–21 June 1986.

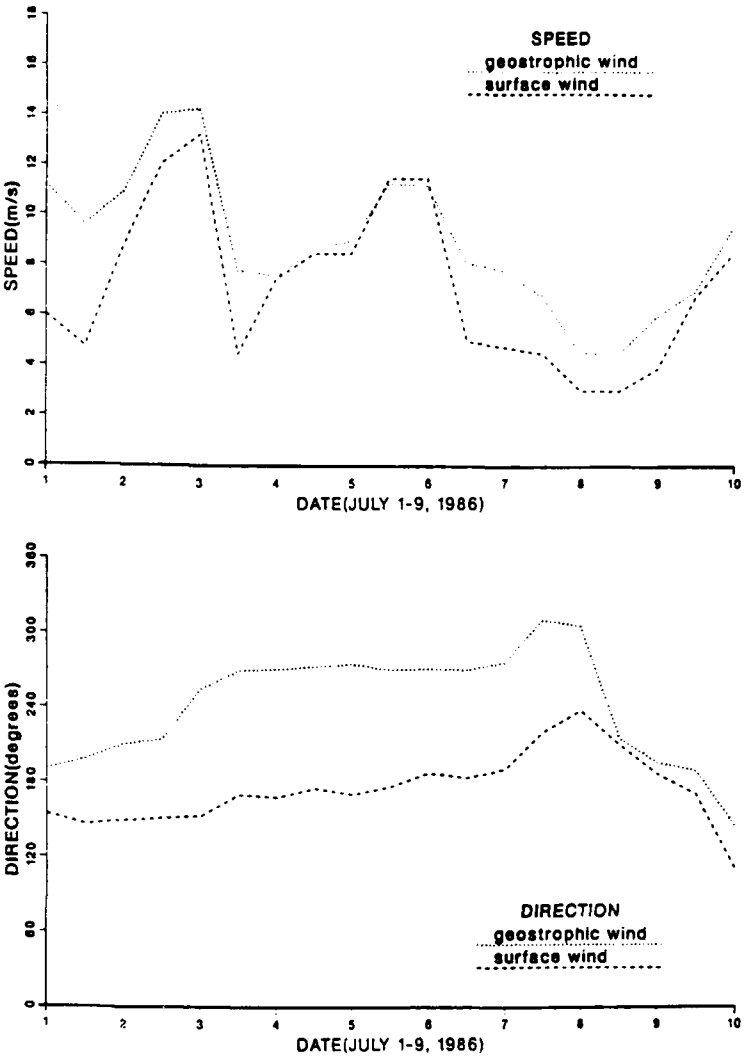

Figure 4. Direction and speed of surface wind and geostrophic wind in the period 1–9 July 1986.

MOUNTAIN BARRIER EFFECT

Data sets for surface wind, for the periods 7–16 May and 14–21 June 1986, are presented in Figures 2 and 3, and are compared with the velocity of the ice island movement and with the geostrophic wind. It can be seen that the ice island movement increased and decreased with the wind speed. The angle of the surface wind direction is smaller than the angle of the geostrophic wind direction, which indicates that the surface wind is turned to the left of the geostrophic wind due to the effect of surface friction. The ice island motion direction was to the left of the geostrophic wind, and to the right of the surface wind, as seen in both Figures 2 and 3, for those times when large daily motions of the ice island took place. Because of the lower wind speed on 7 May and 9 May (Fig. 2), the movement of the ice island was also small at those times and the direction of the movement changed significantly, probably due to tidal effects. The same phenomenon occurred also on 14 June and 17 June (Fig. 3).

The significant data on 9 May and 17 June show a turning angle from the surface wind to the geostrophic wind of greater than 90 degrees. This is probably due to the mountain barrier effect, because the geostrophic wind was directed towards the mountain barrier from the west. Using the results of the model of Parish (1983), it is reasonable to attribute the observed relationship between surface wind and geostrophic wind to the mountain barrier effect. However, since the speeds of the geostrophic wind and the surface wind were small on these two days, the ice island motion was not dominated by wind.

A more significant example occurred during the interval 1–9 July as shown in Figure 4. On the first day of this episode, the geostrophic wind blew from the south parallel to the mountain barrier. The surface wind was also from the south on 1 July with a turning angle of about 30 degrees. The magnitude of the geo-

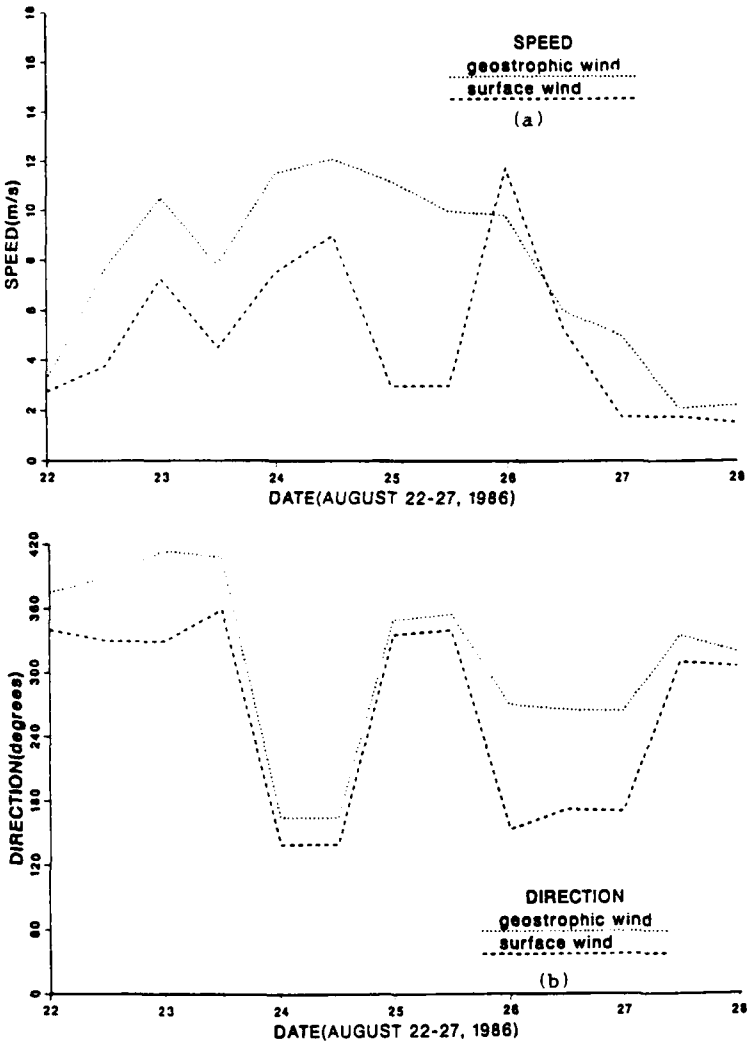

Figure 5. The direction and speed of surface wind and geostrophic wind in the period 22–27 August 1986.

strophic wind was about 11.2 m/s, much larger than the surface wind, which was about 6 m/s. After the second day, on 3–7 July, the geostrophic wind changed direction to southwest, blowing towards the mountain barrier, but the surface wind maintained its direction still parallel to the mountain barrier, from the south. The magnitude of the geostrophic wind approached that of the surface wind, especially on the day of 5 July, when the surface wind was slightly larger than the geostrophic wind. This is likely evidence of the mountain barrier effect.

Evidence of the mountain barrier effects were also observed for 22–27 August, and 11–17 September 1986 (Fig. 5 and 6). The mountain barrier effect occurred on 26 August, when the speed of the geostrophic wind was slightly lower than that of the surface wind during the onset of the mountain barrier effect.

In the September episode, a geostrophic wind from the west produced a surface wind parallel to the mountain barrier, and small changes in geostrophic wind direction did not affect surface wind direction, but did affect the ratio of surface wind intensity to geostrophic wind intensity, as predicted by Parish (1983). The intensity of the surface wind was in the range 6–8 m/s on 11–12 September, and in fact on 14–15 September, in another intense wind event, the wind speed ranged from 6 to 10 m/s, causing more rapid ice island motion.

Relationships between surface wind direction and geostrophic wind direction, for the time segments considered, are plotted in Figure 7. Data points within the smaller square show the influence of the mountain barrier effect, for which the geostrophic wind is in the 270 degree direction (from the west towards the mountains) and the surface wind direction is about 180 degrees (parallel to the mountains). The turning angle between them is about 90 degrees in this case. More details can be found in Lu and Sackinger (1989).

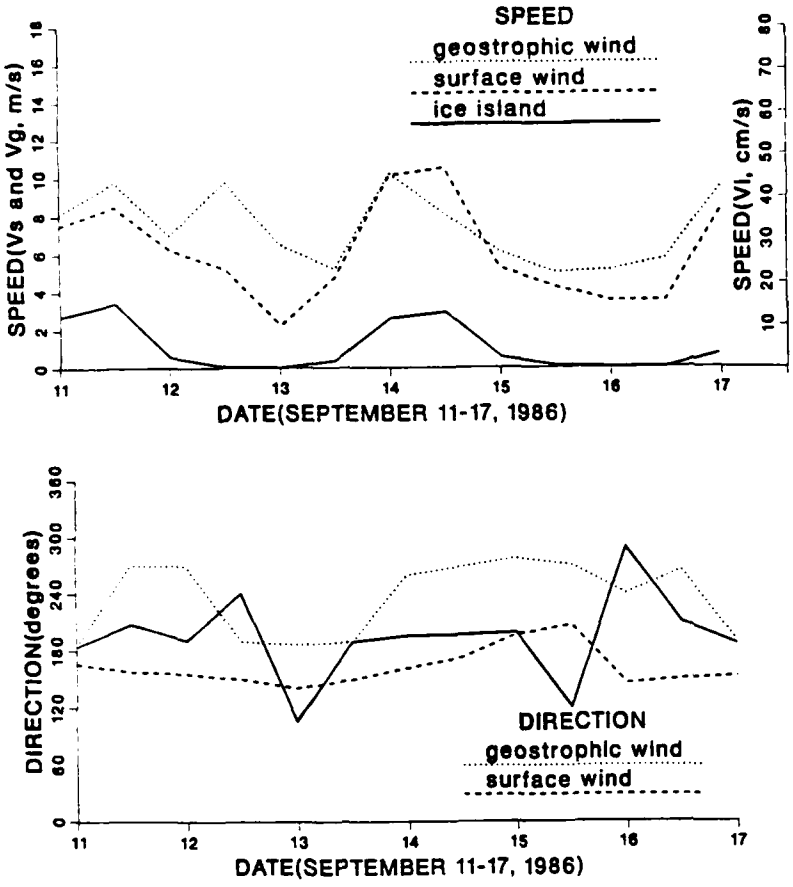

Figure 6. The direction and speed of surface wind, geostrophic wind and ice island movement in the period 11–17 September 1986.

CONCLUSIONS

The mountain barrier effect, in which a surface wind directed to the left was produced by a geostrophic wind blowing towards a mountain barrier, was found. Ice island movement resulted, but only at higher wind speeds. This movement implies that the mountain barrier effect should be taken into account when predicting ice island movement near a mountainous coastline, extending up to 150 km away from it.

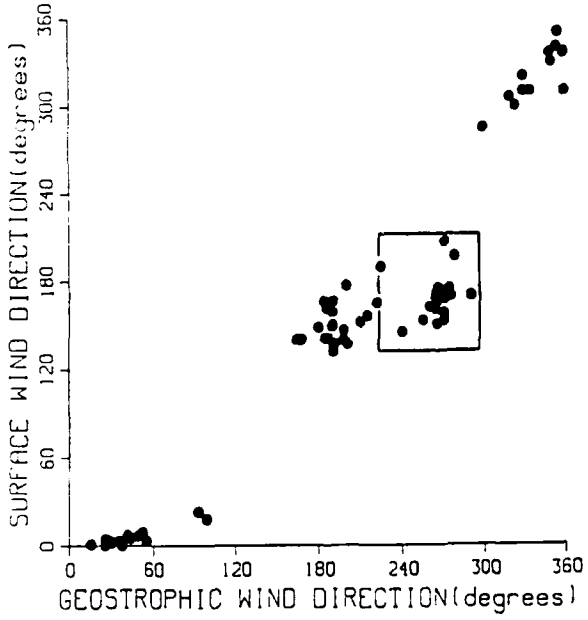

Figure 7. The geostrophic wind direction vs surface wind direction for time segments 7–16 May, 14–21 June, 1–9 July, 22–27 August and 22–17 September 1986. Boxed area shows evidence of mountain barrier effect for north/south mountain chain on Axel Heiberg Island.

ACKNOWLEDGMENTS

Support for the research described was by the U.S. Department of Energy, and by the Geophysical Institute, University of Alaska, Fairbanks, and is gratefully appreciated. Valuable discussions with M.O. Jeffries, Li Fucheng, K. Morris, G. Wendler, and T. Kozo are also appreciated.

REFERENCES

Albright, M. (1980) Geostrophic wind calculations For AIDJEX. In *Sea Ice Processes and Models* (R.S. Pritchard, Ed.). Seattle: University of Washington Press, p. 402–409.

Jeffries, M.O., W.M. Sackinger and H. Shoemaker (1988) Geometry and physical properties of ice islands. In *Port and Ocean Engineering under Arctic Conditions* (W.M. Sackinger and M. O. Jeffries, Ed.). Fairbanks: Geophysical Institute, University of Alaska, vol. I, p. 69–83.

Kozo, T. L. (1980) Mountain barrier baroclinicity effects on surface winds along the Alaska arctic coast. *Geophysical Research Letters*, 7(5): 377–380.

Kozo, T.L. (1988) Mountain barrier effects on sea ice drift in the Beaufort Sea coastal zone. In *Port and Ocean Engineering under Arctic Conditions* (W.M. Sackinger and M.O. Jeffries, Ed.). Fairbanks: Geophysical Institute, University of Alaska, vol. III.

Lu, M. and W.M. Sackinger (1989) *Journal of Coastal Research* (in prep.).

Parish, T.R. (1983) The influence of the Antarctic Peninsula on the wind field over the western Weddell Sea. *Journal of Geophysical Research*, **88**(C4): 2684–2692.

Schmidt, M., J. Popelar and J. Kouba (1987) Ice island 1985–86 navigation and geodetic positioning. Geological Survey of Canada, Polar Continental Shelf Project, Ice Island Contribution No. 6.

Thorndike, A.S. and R. Colony (1982) Sea ice motion in response to geostrophic winds. *Journal of Geophysical Research*, **87**(C8): 5845–5852.

Analysis of Sea Ice Drift in a Coastal Zone

P.A. SMITH
Oceanography Department
U.S. Naval Academy
Annapolis, Maryland, U.S.A.

ABSTRACT

From March to July 1982, a satellite transmitting weather station was deployed in the coastal ice zone (CIZ) 150 km north of Alaska. Sea ice in this area may be influenced by synoptic scale winds, mesoscale w ds (created by Brooks Range mountain barrier effects), ocean currents, and coastal shearing and compaction transmitted through internal ice stresses. These influences complicate ice movement predictions in the CIZ; however, the use of mesoscale-network-computed winds, rather than synoptic scale winds, accounts for many of the influences and simplifies the prediction process. Data were collected to compute mesoscale pressure network winds, surface (3-m) winds, and ice velocity. Speed ratios and turning angles between computed network geostrophic winds, surface winds, and ice drift were compared. A plotting algorithm was implemented to superimpose mesoscale wind vectors on the buoy's track. Also, in late April, a large lead developed along the Canadian Archipelago that resulted in an apparent rotation of the entire ice sheet in the Beaufort Sea and an increase in ice velocity in the study area.

INTRODUCTION

According to Zubov's law, sea ice should travel in the same direction and at 1% of the speed of the geostrophic wind. This estimate is for free ice drift, such that the internal ice stresses are negligible. Also, the effects of currents are ignored. On a short time scale (less than a month), in an open ocean, over 70% of the variance in ice motion can be explained by the geostrophic wind (Thorndike and Colony 1982). Ice motion in the vicinity of a land mass cannot be explained by rules for free ocean ice drift. Thorndike and Colony (1982) defined the region within 400 km of shore where internal ice stress plays an important role as the coastal ice zone (CIZ). In addition to internal stress in the CIZ along the northern Alaskan coast, small atmospheric-scale phenomena, such as mountain barrier baroclinity, corner effects, and sea breezes are often missed by synoptic scale analyses. It has been shown that mesoscale geostrophic wind estimates are more accurate for ice drift predictions in the CIZ (Lipoma 1988). The turning angles and speed ratios between the mesoscale wind vectors and ice velocity vectors in the CIZ are not known. Also, it has not been determined how significant other influences, such as internal ice stresses and coastal ice shearing and compaction, are in CIZ ice drift predictions.

STUDY AREA

The buoy traveled westward in the Beaufort Sea from the 142°W to the 157°W meridian, roughly along the 72°N parallel, in water 2 km deep (see Fig.

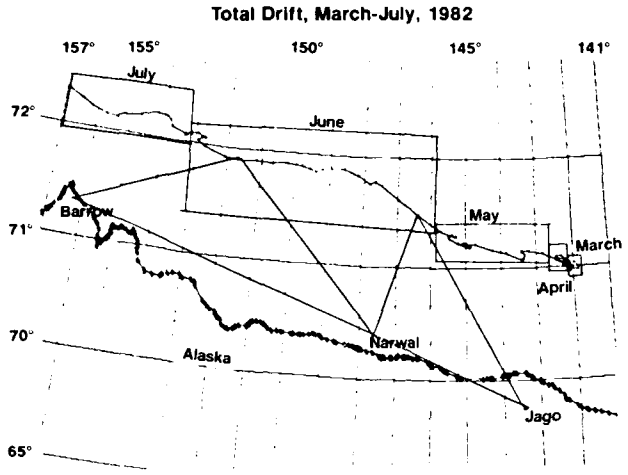

Figure 1. Total buoy drift and mesonet triangles.

1). The Beaufort Sea circulation is dominated by the Beaufort gyre, a clockwise system. McLaren et al. (1987) estimated that the ocean gyre accounts for up to 50% of the long term ice movement in the Canadian Basin, specifically 5 to 6 km of ice drift every day. About 110 km from the northern Alaskan shore, seaward of the 50-m isobath, the Beaufort Sea undercurrent has a mean eastward flow toward 100 T at an average of 0.015 m/s (Aagaard 1984). Lipoma (1988) showed evidence that this undercurrent reaches the surface.

The winds are the most significant influence on the ice drift. Winds, initially driven by atmospheric pressure gradients, are modified by thermal and orographic effects, such as sea breezes (Kozo 1982) and mountain barrier baroclinity (Schwerdtfeger 1974, Kozo 1984).

The local movement of the ice is affected by the general motion of the entire basin ice sheet, to an extent determined by the consolidation of the ice. In the northern hemisphere, along the northern edge of an east-west oriented coastline, a westerly surface wind will cause a net southward transport and a consolidation of the ice against the land mass. This consolidation will restrict the response of the ice to the ensuing wind stress. The fractures and leads in the Beaufort ice pack allow a net northward movement of the ice without compaction or a restriction in movement. An easterly wind will cause a net northward transport of the ice and a loosening of the ice floes near the coast. This loosening will allow the nearshore ice to move more freely in response to the next easterly wind stress.

An additional influence on the local ice drifts unique to the time and location of this study was the opening of a large lead in the arctic pack just west of the Canadian Archipelago. The fracture was either the result of a storm surge (Kozo 1988) or the shearing stress of the Beaufort gyre. The fracture was first noted on 4 April 1982. The lead began opening on 27 April 1982 and stabilized by 15 May 1982, at a length of approximately 1000 km and a width of 80 km.

DATA AND METHODS

To gather data, an automated weather station using an ARGOS Data Collection Platform system was linked to a TIROS-N/NOAA series satellite. The station has 12 fixes per day computed by Service ARGOS, with an accuracy of 3 km (Reynolds et al. 1985). The station collected surface wind velocity, surface pressure and temperature, position, and magnetic heading data from 1 March 1982 to 11 July 1982. The surface wind velocity data were unreliable after 22 June 1982.

Synoptic scale winds were computed twice daily from NWS surface maps. Mesoscale winds were calculated from the two mesonet triangles (see Fig. 1). In each mesonet triangle, the pressures at the automated weather station and two land stations were measured and adjusted to sea level values using the hypsometric equation:

$$p_0 = p_1 \exp\left(\frac{g \cdot \Delta z}{287 \cdot T}\right) \qquad (1)$$

where p_0 = sea level pressure
p_1 = measured atmospheric pressure
g = acceleration due to gravity
Δz = height above sea level
T = absolute temperature.

Cramer's rule was used to determine the pressure gradient at the center of the triangle. The air density (ρ) was estimated using the ideal gas law for the average measured temperatures (T) at the three stations and U.S. Standard Atmospheric pressure (p = 1013.3 mb):

$$\rho = \frac{p}{287 \cdot T}. \qquad (2)$$

The Coriolis parameter (f) was calculated based on the average latitude of the three points:

$$f = 2\,\Omega \sin\theta \qquad (3)$$

where Ω is the angular velocity of the earth and θ is the latitude.

Because the wind flow in the area typically had a radius of curvature greater than 300 km, geostrophic balance was assumed (Kozo 1982) and the wind velocity vectors (v) were calculated using the geostrophic wind equation:

$$\frac{1}{\rho}\frac{dp}{dn} = fv \qquad (4)$$

where ρ is the air density, dp/dn is the atmospheric pressure gradient, and fv is the Coriolis force.

From 1 March to 9 June, the mesonet triangle had base vertices at Jago and Narwhal Island. The third vertex was the automated weather station which drifted from 141.9°W to 148.2°W. From 9 June to 11 July, the base vertices were Narwhal Island and Point Barrow. Again the third vertex was the automated weather station that drifted from 148.2°W to 157.0°W (see Fig. 1). The wind vectors were calculated every 3 hours. The wind stress ($\vec{\tau}$) was also calculated:

$$\vec{\tau} = \rho C_d v^2 \qquad (5)$$

where ρ was the air density and v was the wind speed. The drag coefficient (C_d) was estimated to be 0.0026 in the CIZ of the Beaufort Sea (Overland 1985).

The ice drift velocity was calculated daily based on the rhumb line distance between the daily change in buoy positions. The speed ratios between the geostrophic wind (V_g) and the ice drift (V_i) and between the surface wind (V_s) and the ice drift (V_i) were calculated for each day. The results were divided according to westerly and easterly winds and averaged for each month. The turning angles (α) between the geostrophic wind (V_g) and the ice drift (V_i) and between the surface wind (V_s) and ice drift (V_i) were also calculated for each day. Each month's data were plotted in a scattergram.

The magnetic heading data from the buoy compared to a reference mark were an indication of the orientation of the on-ice buoy. The changing orientation of the buoy was plotted over time and showed the rotation of the ice floe. Data on the occurrence, duration, and extent of the lead west of the Canadian Archipelago was obtained from satellite imagery (Kozo and Torgerson 1988).

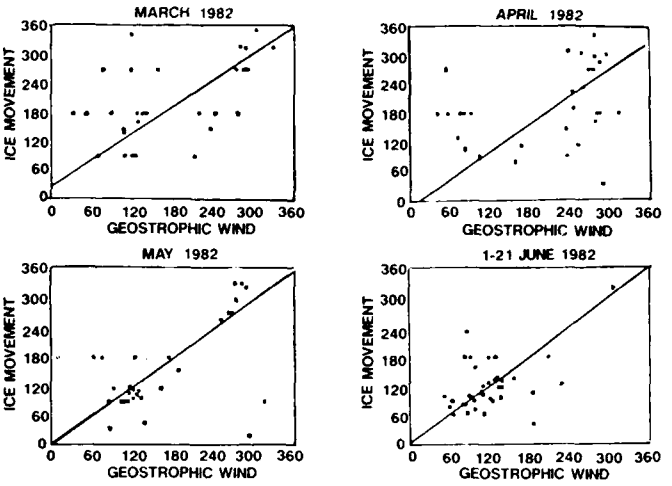

Figure 2. Geostrophic wind-to-ice velocity turning angle scattergrams.

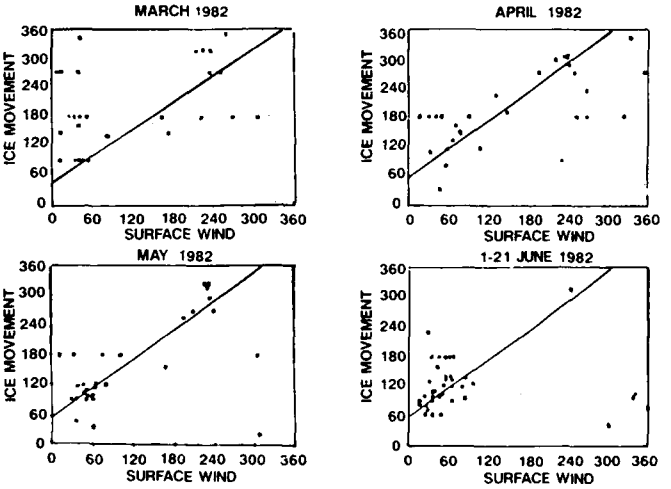

Figure 3. Surface wind-to-ice velocity turning angle scattergrams.

RESULTS AND DISCUSSION

Ideally, the surface winds should be 45° to the left of the geostrophic wind, having a decreased velocity due to the surface friction, and, thus, a decreased Coriolis force. However, the ice should move 45° to the right of the surface wind, turning in response to Coriolis. So, the cumulative effect should be a 0° turning angle between the geostrophic wind and ice drift. On the scattergrams (see Fig. 2), the March and April turning angles average around 0°, but are not consistent. For May and June, when the ice has melted and decoupled from the coast, so as to more closely resemble a free drift situation, the 0° turning angle is more consistent. According to Zubov's law, the ice should move at 1% of the geostrophic wind. The first row of figures in Table 1 shows the monthly average of speed ratios divided into easterly and westerly wind components. The total average is 0.009, slightly less than Zubov's estimate for free drift, probably because this ice was more consolidated, coastal ice. During this transition period from spring to summer, the ice loosens and $|V_i/V_g|$ increases. Also note that the ratio is always higher for the easterly winds as opposed to the westerly winds. The westerly winds cause a compaction of ice against the coast and a re-

striction of motion. The easterly winds cause the ice to turn away from the coast and into the pack ice. Satellite imagery reveals that the pack ice contained many fractures and leads during the study period; thus, the pack ice was not a rigid boundary to inhibit the northward flow of ice.

As stated above, in the ideal situation, ice moves 45° to the right of the surface wind. Reynolds (1985) showed that the ice drifts 30° to the right of the surface wind in the Marginal Ice Zone (MIZ) of the Southern Bering Sea. The MIZ is the zone between pack ice and open ice water, the transition zone between 0% and 100% ice cover. Observing the scattergrams (see Fig. 3), the ice moved 40° to 60° to the right of the surface wind. Some of this exaggerated turning can be explained by the coastline orientation of the northern Alaskan shore (along 115°T). For the predominantly easterly wind, the ice could not maintain a head bearing to the left of 295°T. Reynolds (1985) observed that the ice in the MIZ moved at 0.04 of the surface winds. In the CIZ, during the spring to summer transition period, the ice moved on an average of 0.014 of the surface wind. The CIZ should have a lower wind to ice speed ratio because the ice is more consolidated than the ice in the Bering Sea MIZ. Observing the second row of figures in Table 1, the values increase as they approach the summer months, because the ice is becoming less consolidated. Also, the values for the easterly winds are consistently higher than the values for westerly winds, again due to the westerly wind ice compaction against the coast.

Table 1. Wind/ice drift speed ratios.

March		*April*		*May*		*June*
E	*W*	*E*	*W*	*E*	*W*	*E*
0.007	0.005	0.012	0.004	0.012	0.006	0.014
0.008	0.001	0.015	0.007	0.024	0.012	0.030

The ice drift characteristics changed gradually from the spring to summer season. The melting and disconnection of individual floes allowed the ice to move with the wind at a great speed with less variance. The nature of the ice drift was also changed by the development of an ice lead along the Canadian Archipelago. The magnetic heading data from the buoy show that the ice floe rotated an average of 0.03°/day counterclockwise prior to the fracture. This cyclonic vorticity could be the result of the opposing shearing stress from the land fast ice on the westward drifting floe. From 4 to 10 April, during which period the fracture first appeared on satellite imagery, the ice rotated 5.7°/day clockwise. The

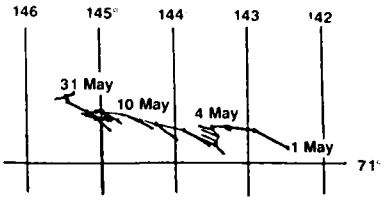

a. 1–31 May.

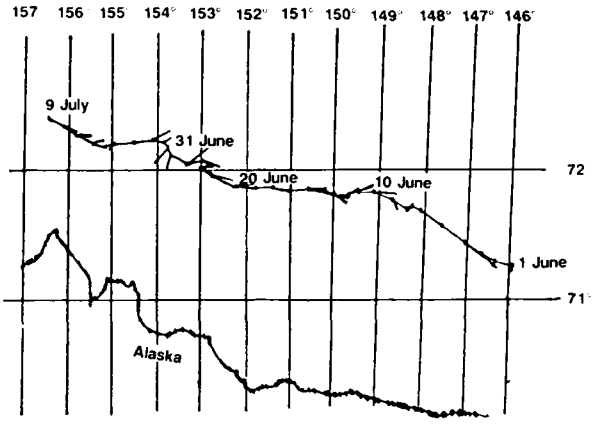

b. 1 June–9 July.

Figure 4. Ice drift and mesoscale wind vectors.

entire ice sheet containing this floe, now freed from the shore, was moving in response to the Beaufort gyre. After the initial fracture of the ice, the floe regained its counterclockwise rotation, possibly because the smaller scale shearing stress was no longer masked by the total ice sheet velocity. Although the ice fractured early in April, the lead did not begin opening to its maximum width of 80 km until a strong easterly wind came during the period of 27 April to 3 May (Kozo and Torgerson 1988). Before this opening of the lead, the ice moved at about 0.015° of the surface wind; immediately after the opening of the lead, the ice began moving at about 0.025° of the surface wind.

The daily mesoscale wind vectors were superimposed on the buoy ice track for May and June data (see Fig. 4). In May, the ice floe traveled at an angle to the right of the wind vector. The turning angles decreased as the wind blew from the same direction for a longer period of time. Note the two reversals in May. The synoptic scale winds shown on weather maps were easterly during these two periods, but the mesoscale network winds were westerly, because of a mountain barrier effect from the Brooks Range (Kozo 1988, Lipoma 1988). The ice drift reflected the mesoscale wind direction. In June, the wind vectors were even closer to the ice track, an indication that ice drift predictions in the CIZ should be simpler in the warmer months as the motion more and more resembles free drift.

CONCLUSIONS

This study is a preliminary step toward a coastal ice flow model. The ice drift in the CIZ is influenced by many forces and conditions. The goal of this study was to determine the significant parameters and begin to quantify the correlations between the parameters and the ice drift. The following is a summary of the findings:

1. In the CIZ during the spring to summer transition, the ice drifts at a higher percentage of the wind speed and at a more consistent turning angle as the summer season approached.

2. In the CIZ during this transition period, the average ice drift speed was 0.009 of the geostrophic wind speed with a 0° turning angle.

3. In the CIZ during this transition period, the average ice drift speed was 0.014 of the surface wind speed with a 50° right turning angle.

4. The lead that opened along the Canadian Archipelago in late April 1982 resulted in an initial clockwise rotation of the ice sheet and a sustained increase of ice to wind speed ratio.

5. The mesoscale geostrophic wind is a better starting point for ice drift predictions than the synoptic scale wind or the difficult to obtain, highly variable surface wind.

6. In addition to the mesoscale wind velocity, the following must be taken into account when predicting the ice drift in a CIZ: coastline orientation, wind direction in relation to the coastline, wind fetch, time of the year, and physical characteristics of the entire ice sheet (fractures and leads).

ACKNOWLEDGMENTS

The experimental data used in this study were partly obtained through the National Science Foundation, Division of Polar Programs funding, and from Mineral Management Services, U.S. Department of Interior as a part of the Outer Continental Shelf Environmental Assessment Program.

I wish to express my thanks to Professors Thomas Kozo and Peter Guth of the Oceanography Department, U.S. Naval Academy, for their assistance.

REFERENCES

Aagaard, K. (1984) The Beaufort Undercurrent. In *The Alaska Beaufort Sea: Ecosystems and Environment* (P.W. Barns, D.M. Schell, and E. Reimnitz, Ed.). Orlando: Academic Press, Inc., p. 47–71.

Kozo, T.L. (1982) An observational study of sea breezes along the Alaskan Beaufort Sea Coast: Part 1. *Journal of Applied Meteorology*, **21**: 891–905.

Kozo, T.L. (1984) Mesoscale wind phenomena along the Alaskan Beaufort Sea. In *The Alaska Beaufort Sea: Ecosystems and Environment* (P.W. Barns, D.M. Schell, and E. Reimnitz, Ed.). Orlando: Academic Press, Inc., p. 23–45.

Kozo, T.L. and L.J. Torgerson (1988) The role of alternating cyclones and anticyclones in triggering sea ice fracture in the Canadian Arctic Basin. In *Proceedings of the Ninth International Symposium on Ice, Sapporo, Japan, 23–27 August 1988* (H. Saeki, Ed.). International Association for Hydraulic Research Committee on Ice Problems, Hokkaido University, p. 633–642.

Kozo, T.L. (1988) Mesoscale effects on wind velocities, ocean currents, and sea ice drift in the Beaufort Sea coastal zone. In *Proceedings of the Ninth International Conference, POAC '87* (Sackinger and Jeffries, Ed.). Univ. of Alaska, Fairbanks (in press).

Lipoma, P.A. (1988) Automated weather station drift in the Alaskan Beaufort Sea coastal ice zone. In *Proceedings of the Ninth International Conference, POAC '87* (Sackinger and Jeffries, Ed.). Univ. of Alaska, Fairbanks (in press).

McLaren, A.S., M.C. Serreze and R.G. Barry (1987) Seasonal variations of the sea ice motion in the Canadian Basin and their implications. *Geophysical Research Letters*, **14**: 1123–1126.

Overland, J.E. (1985) Atmospheric boundary layer structure and drag coefficient over sea ice. *Journal of Geophysical Research*, **90**: 9029–9049.

Reynolds, M., C.H. Pease and J.E. Overland (1985) Ice drift and regional meteorology in the southern Bering Sea; Results from MIZEX West. *Journal of Geophysical Research*, **90**: 11967–11981.

Thorndike, A.S. and R. Colony (1982) Sea ice motion in response to geostrophic winds. *Journal of Geophysical Research*, **87**: 5845–5852.

Thorndike, A.S., R. Colony and E.A. Munoz (1983) Arctic Ocean Buoy Program. Data Report 01 Jan 1982–31 Dec 1982, Polar Science Center, University of Washington–Seattle, 72-8.

Schwerdtfeger, W. (1974) Mountain barrier effect on the flow of stable air north of the Brooks Range. In *Proceedings, 24th Alaskan Science Conference*. Geophysical Institute, University of Alaska–Fairbanks, p. 204–208.

Variations in Antarctic Sea Ice

E. BREITENBERGER AND G. WENDLER
Geophysical Institute
University of Alaska
Fairbanks, Alaska, U.S.A.

ABSTRACT

Antarctic sea ice data from the Navy–NOAA (National Oceanic and Atmospheric Administration) Joint Ice Center for the period 1973–1984 were analyzed. Temporal and spatial variations in the ice edge position and areal coverage of the ice pack were examined. The results show significant interannual variation in these parameters. In general, the ice pack receded dramatically from 1973–1977. From 1978 on this trend was reversed. For the 1973–1984 period, small negative trends in ice extent and area were found. These trends were not statistically significant. Short-term variations in the ice cover provide insights into the mechanisms of ice dynamics. By examining the anomalies in areal coverage and ice edge position, advective processes are seen to greatly affect the evolution of the ice pack. Anomalies in ice area seem to display interannual persistence in some sectors.

INTRODUCTION

It has long been accepted that sea ice may be a sensitive indicator of climatic change (Fletcher 1969). Since the advent of high resolution satellite imagery in 1973, many studies have been made of sea ice variability and its interrelations with the atmosphere (e.g., Streten and Pike 1980, Chiu 1983). Many of these early studies found large decreases in the amount of sea ice in the Antarctic. Subsequent studies showed that this trend reversed itself by 1980 (Lemke et al. 1980, Ropelewski 1983).

Analysis of the data to 1984 shows that ice coverage in the Antarctic has nearly returned to the levels of the mid-1970s. Trend analysis for these data is inconclusive. Small negative trends in ice area and extent are found, but are not judged to be significant. It appears that the satellite data record is not yet of sufficient length for climatic change to be detected.

Statistical analysis of the spatial and temporal variations of the sea ice yields interesting information concerning the physical mechanisms affecting the evolution and decay of the ice. Cross-correlations and auto-correlations between various sectors indicate that the movement of anomalies is dominated by eastward advection. Some interannual persistence of anomalies is apparent. This may relate to the "preconditioning" of the upper ocean by such anomalies (Martinson et al. 1981).

DATA

Digitized Navy–NOAA Joint Ice Center (JIC) weekly charts for the period 1973–1984 were obtained on magnetic tape from WDC–A. These 625 charts, which provide information about ice coverage and concentration, have a resolution of better than 25 km. They are based on subjective interpretations of satellite data, combined with reports from shipping and aircraft. The charts are digitized according to the SIGRID format (Thompson 1981).

To facilitate the handling of this large data set, averaging was performed over 30 degree sectors (Fig. 1). Two sea ice indices were computed: the latitude of the ice edge as determined by 20% concentration, and the area covered by sea ice of more than 20% concentration. The mean annual cycles for the 12 sectors were then computed. The annual cycle was then removed from the data to yield anomaly series.

DISCUSSION

Antarctic sea ice undergoes substantial annual variation (Fig. 2 and 3). The area covered by ice ranges from 3×10^6 km^2 to 20×10^6 km^2. The annual minimum extent usually occurs in the last week of February, with the maximum in mid-September. The date of minimum ice extent exhibits little variation, while the date of maximum ice extent is less predictable.

To determine if any changes in the total antarctic sea ice cover have occurred, the anomaly series for the ice edge and area were examined for linear trends. Regressions utilizing both least-squares and resistant methods were performed. The results show a 0.05×10^6 km^2/yr decrease in both ice area and ice extent over the study period. Non-resistant methods yield 20% greater rates of decrease. Given the variance of the anomaly series, however, these results are not significant.

These results may be compared to those of Gloerson and Campbell (1988), who examined trends in ice cover for the period 1978–1987 using a different data

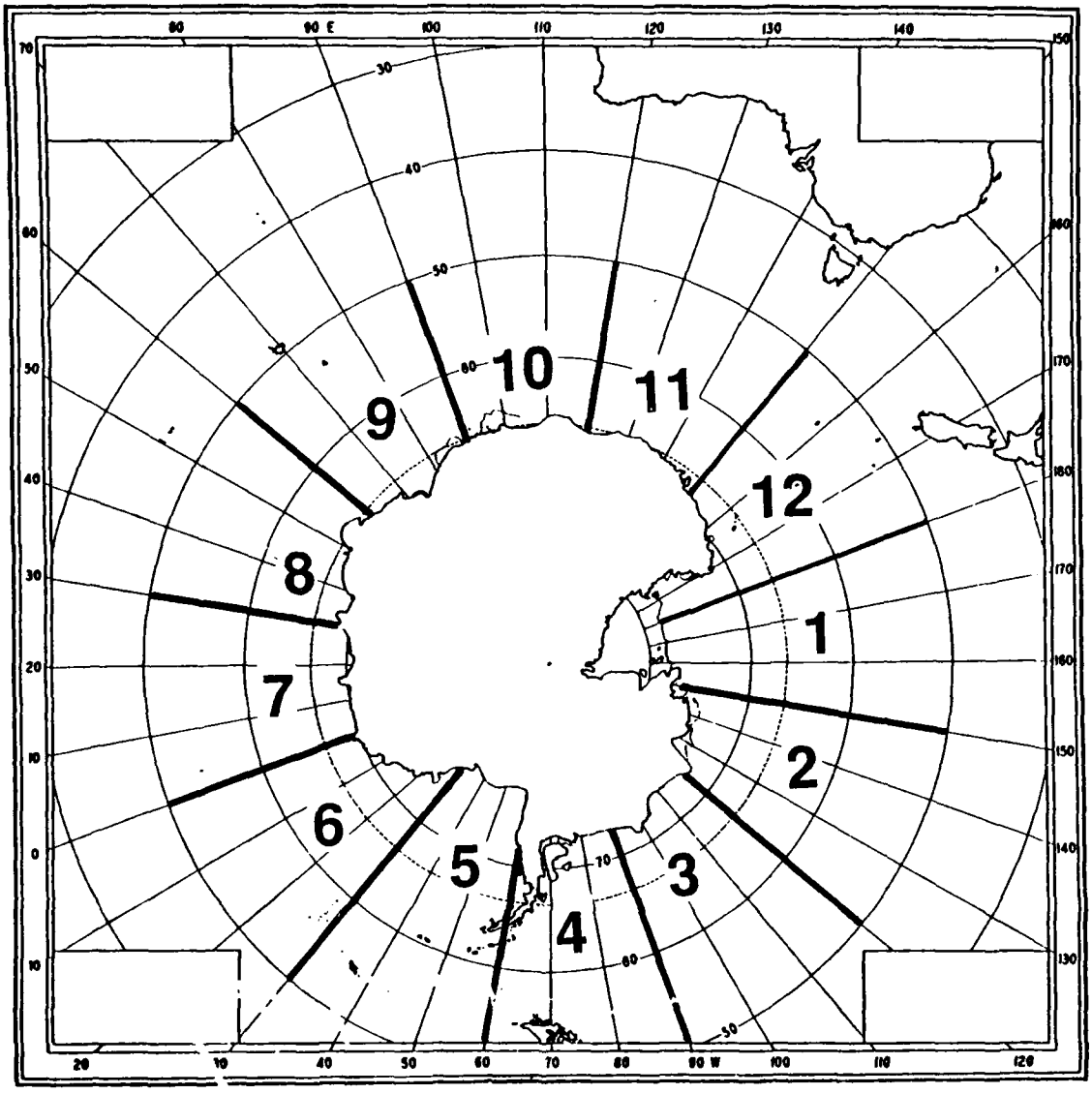

Figure 1. Antarctica and the Southern Ocean. Numbers 1–12 indicate the 30° sectors used in the study.

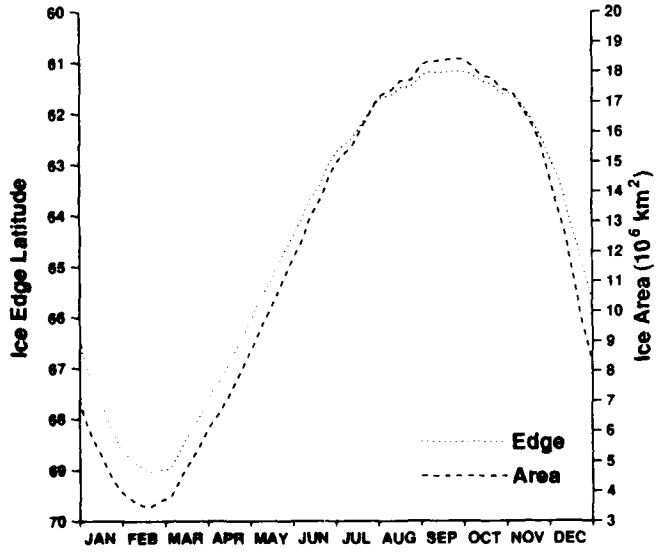

Figure 2. Mean annual cycle of ice in the Antarctic for the years 1973–1984.

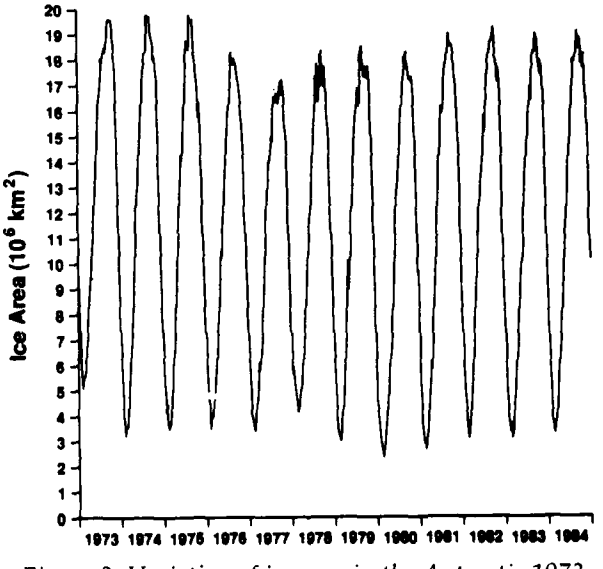

Figure 3. Variation of ice area in the Antarctic 1973–1984.

set. They used the Nimbus-7 SMMR observations, which form a part of the Navy–NOAA JIC grids that we used. The two data sets have a five-year overlap, from November 1978 to December 1983.

Gloerson and Campbell found significant negative trends in the global ice extent maxima. For the Antarctic, they found decreases in ice extent maxima of 0.06×10^6 km^2/yr, and decreases in ice area maxima of 0.03×10^6 km^2/yr. Neither of those results was deemed significant.

It should be noted that Gloerson and Campbell's results apply only to the maxima of the annual cycle. Our results apply to the entire cycle. Considering the differences in the data sets and methodology, it seems interesting that such similar results were found.

The variation in advance and decay characteristics between sectors is substantial. In general, the sectors of the Weddell Sea show both the farthest retreat and the greatest advance (Fig. 4 and 5). This area is responsible for most of the ice production in the Antarctic. It is notable that the ice area in the Ross Sea reaches a maximum in August, well before the September hemispheric maximum. The Weddell Sea sectors are characterized by their rapid ice advance and decay.

Upon examination of Figures 6 and 7, it is evident that substantial differences exist in the auto- and cross-correlations. The Ross Sea sectors (12, 1, and 2) exhibit unusual persistence of anomalies, in contrast to the Bellingshausen Sea sectors (3 and 4). The barrier of the Antarctic Peninsula is evident in the low correlation between sectors 4 and 5. The Weddell Sea sectors (5, 6, and 7) exhibit some unusual properties that are probably related to the complete circulation in this area. Almost all the cross-correlations are greater for positive lags than for negative lags, showing the importance of eastward advection. Some of the correlations show secondary maxima at lags ap-

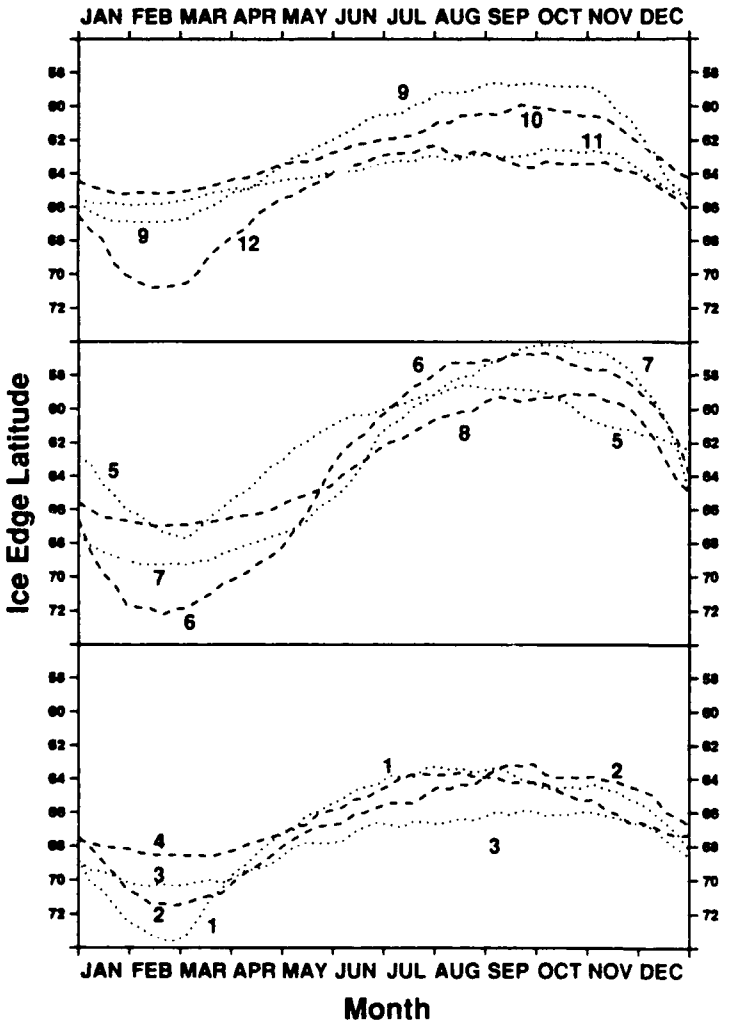

Figure 4. Mean annual cycle of the ice edge for sectors 1–12.

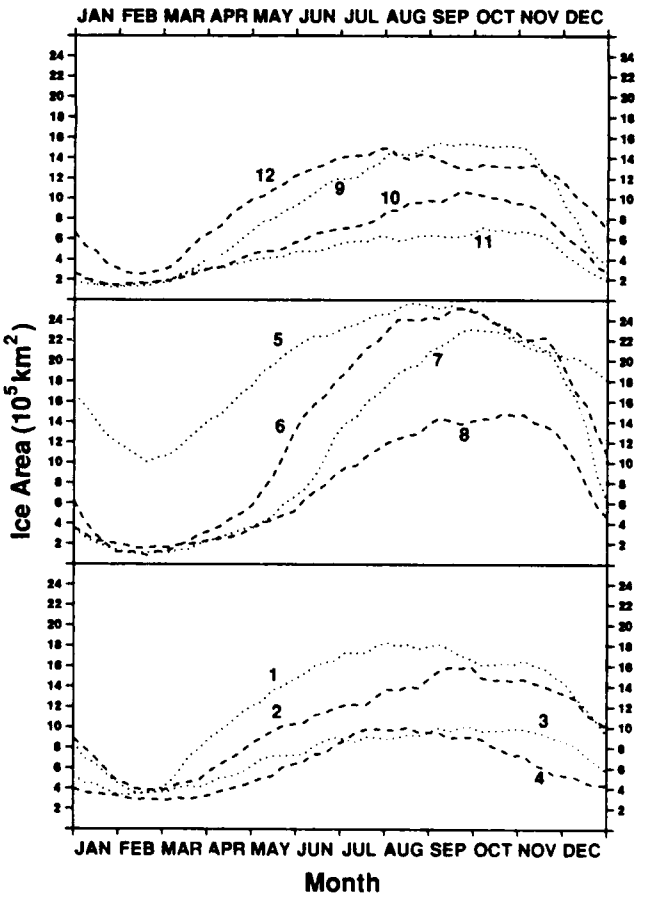

Figure 5. Mean annual cycle of the ice area for sectors 1–12.

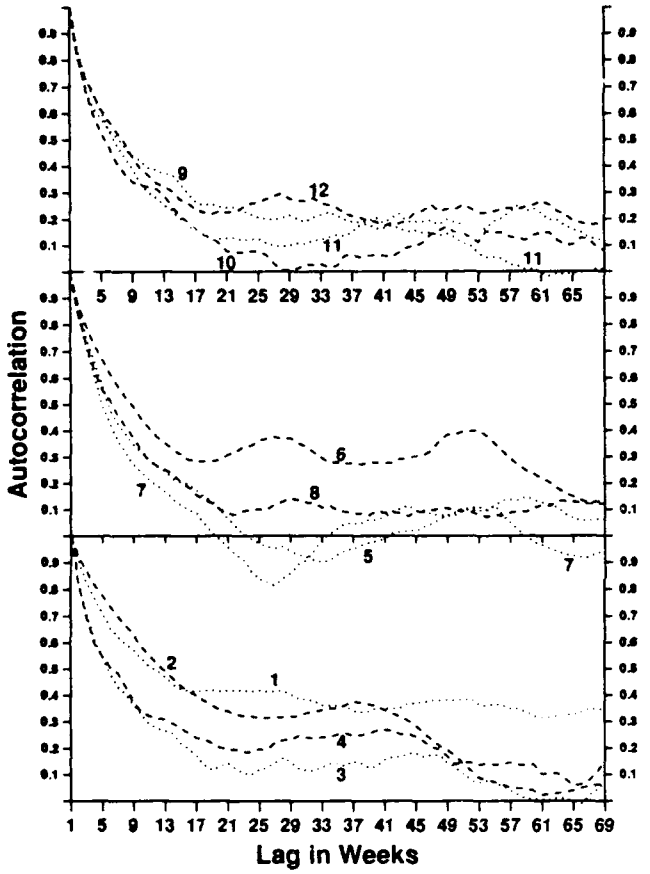

Figure 6. Autocorrelation functions of ice area for sectors 1–12.

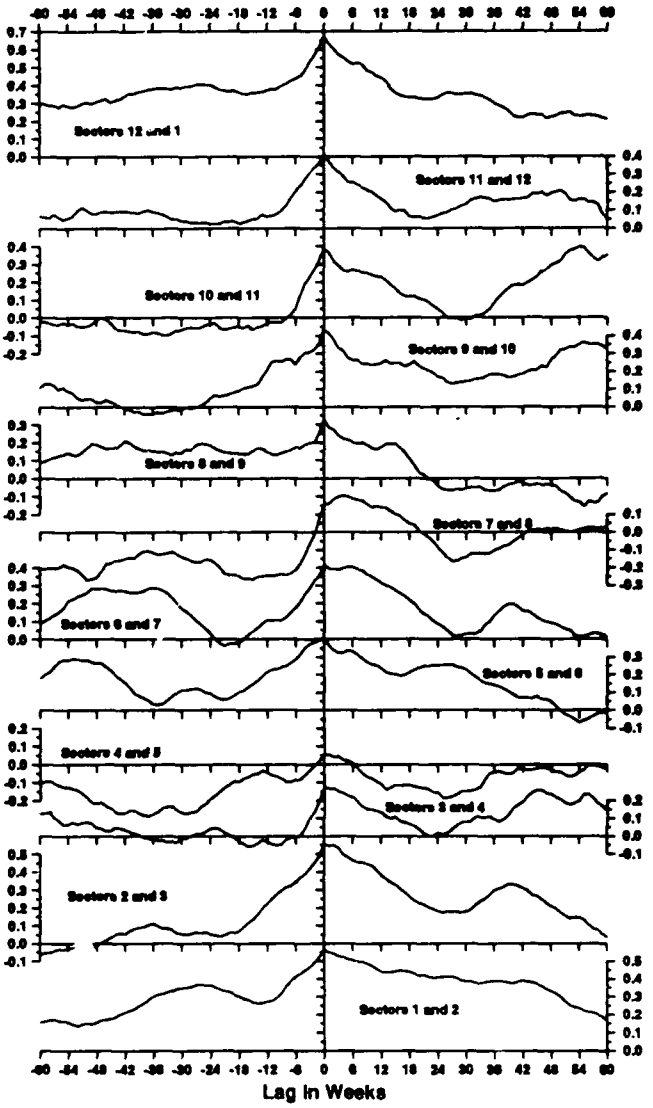

Figure 7. Cross-correlation functions of ice area between adjacent sectors. "Sectors 1 and 2" means that Sector 1 leads Sector 2 for positive lags.

proaching one year, indicating that anomalies in these sectors may return from one year to the next; i.e., an anomaly will "precondition" the area where it occurs such that an anomaly is likely to recur in that place the following year. Such a preconditioned area may move with time; thus this effect is seen both in the auto-correlations and in the cross-correlations. It should be noted that such preconditioning, if very strong, becomes a part of the annual cycle, which is not included in the anomaly series. Thus these features of the auto- and cross-correlations can be identified with sporadic ice anomalies that can appear repeatedly and then disappear.

This may be related to the sea surface conditioning mechanism discussed in Martinson et al. (1981) and Comiso and Gordon (1987). By this mechanism, for example, an open ocean polynya may be established and maintained by the formation of convection cells in the ocean. The ordinarily fresh surface water is replaced by warm, saline water convected from below. When summer comes, there is no ice in the polynya to melt and reestablish a stably stratified surface layer, and the convection may persist until the following winter, when the anomaly (polynya) may reappear. If, at some time during the winter, enough ice is advected into the polynya, the melting ice may release

enough fresh water to stably stratify the surface layer and cut off convection.

CONCLUSIONS

Analysis of the data shows negative trends in both ice area and extent. These trends are not statistically significant. The antarctic ice cover exhibits strong variation over a 5–15 year period (Fletcher 1969, Chiu 1983), so a longer record may be needed to identify any long-term trends.

Examination of the anomaly series provides some insights into the dynamic behavior of the ice pack. It appears that some anomalies may persist from year to year. This is possibly related to oceanic convection.

Eastward advection is found to be the principal form of anomaly motion. This agrees with the general nature of the oceanic and atmospheric circulation in the sea ice zone.

REFERENCES

Chiu, L.S. (1983) Antarctic sea ice variations 1973–1980. In *Variations in the Global Water Budget* (A. Street-Perrott, M. Beran and R. Ratcliffe and D. Reidel, Ed.). Dordrecht: Reidel.

Comiso, J.C. and A.L. Gordon (1987) Recurring polynyas over the Cosmonaut Sea and the Maud Rise. *Journal of Geophysical Research*, **92**(C3): 2819–2833.

Fletcher, J.O. (1969) Ice extent on the Southern Ocean and its relation to world climate. The Rand Corp., Santa Monica, California, Memorandum RM-5793-NS.

Gloerson, P. and W.J. Campbell (1988) Variations in the arctic, antarctic, and global sea ice covers during 1978–1987 as observed with the Nimbus 7 scanning multichannel microwave radiometer. *Journal of Geophysical Research*, **93**(C9): 10,666–10,674.

Lemke, P., E.W. Trinkl and K. Hasselmann (1980) Stochastic dynamic analysis of polar sea ice variability. *Journal of Physical Oceanography*, **10**: 2100–2120.

Martinson, D.G., P.D. Kilworth and A.L. Gordon (1981) A convective model for the Weddell polynya. *Journal of Physical Oceanography*, **11**: 466–488.

Ropelewski, C.F. (1983) Spatial and temporal variations in antarctic sea ice (1973–1982). *Journal of Climatology and Applied Meteorology*, **22**: 470–473.

Streten, N.A. and D.J. Pike (1980) Characteristics of the broadscale antarctic sea ice extent and the associated atmospheric circulation 1972–1977. *Archiv für Meteorolgie, Geophysik und Bioklimatologie*, Ser. A, 29, p. 279–299.

Thompson, T. (1981) Proposed format for gridded sea ice information (SIGRID). World Climate Program, World Meteorological Organization.

A Time-Lapse Motion Study of the "Odden" During 1978–1987 as Observed with the Nimbus-7 Scanning Multichannel Microwave Radiometer

P. GLOERSEN
Laboratory for Oceans
NASA Goddard Space Flight Center
Greenbelt, Maryland, U.S.A.

ABSTRACT/INTRODUCTION

The majority of the poster display at the Weeks Symposium consisted of a video time-lapse study of a sea ice feature occurring in the Greenland Sea known by generations of Scandinavian fishermen as the "Odden." This video was produced from radiance data obtained from the Nimbus-7 Scanning Multichannel Microwave Radiometer (SMMR) for the time period October 1978 to March 1986. The Odden is a prominent sea ice feature that periodically extends far eastward into the Greenland Sea, sometimes to the east of the Greenwich Meridian. Under the appropriate atmospheric conditions, the Odden appears in the cold waters transported away from Greenland in an oceanic feature known as the Jan Mayen Gyre. Work in progress includes a detailed comparison of SAR imagery of the Odden (L. Southerland and R. Shuchman, pers. comm. 1989) obtained during the Marginal Ice Zone Experiment in March/April 1987 (MIZEX '87) and nearly simultaneous observations of the Odden by the SMMR. In this brief paper, the major features appearing in the video are described and a nine-year time-series plot of areal coverage of the Greenland Sea by sea ice (integrated sea ice concentration) is discussed.

THE TIME-LAPSE VIDEO

At the time that the secondary data source (a video laser disk) for time-lapse motion studies of sea ice was produced, there existed an eight-year digital record of global sea ice concentrations on intervals of two days. These digital records were estimates produced from the multispectral microwave radiances from SMMR by means of an algorithm described elsewhere (Gloersen and Cavalieri 1986). The digital maps were displayed on an image processing system in color, and transcribed as individual frames onto a laser video disk (the secondary data source) with a video camera. The video tape was then prepared by sequencing the images on the laser disk at selectable rates by microprocessor control during the second transcription process.

The Odden appeared in all of the eight years shown in the video except for 1984—the year of MIZEX '84. Its absence in 1984 is probably a result of unusually warm local weather conditions during that year, but this conjecture remains to be substantiated by closer scrutiny of the weather records for the eight-year period, a task in progress. Otherwise, its first appearance varied from winter to winter, sometimes occurring as early as November, sometimes as late as March. During a given winter, rapid oscillations in its extent as well as its areal coverage by sea ice are evident from the video. Sometimes the Odden separated from the main Greenland Sea ice pack and persisted for a week or so in the open sea as an "island" of pack ice. At other times, it formed as a disconnected area, later to grow into the main pack. The detailed shape of the Odden varied from year to year, but it generally formed in the east-to-northward-flowing portion of the Jan Mayen Gyre.

A NINE-YEAR RECORD OF SEA ICE AREA

Another means for studying the history of sea ice events in the Greenland Sea is to examine the ice area there, following techniques developed earlier (Gloersen and Campbell 1988). The area covered by sea ice in the Greenland Sea region (as defined by Parkinson et al. 1987) for the nearly nine-year operation period of the SMMR is shown in Figure 1. (Note that the areal coverage by sea ice is obtained by summing the product of ice concentration in a pixel by the area of that pixel over the defined region.) There are over 1600 points in the curve, representing observations obtained, for the most part, every other day from the end of October 1978 to mid-August 1987, when SMMR operations were terminated.

There are a number of noteworthy features in the oscillatory record of the sea ice in Figure 1. The amplitude of the annual cycle varies by as much as 60% during the nine-year period, with the smallest peak occurring in 1984, the only year in which the Odden

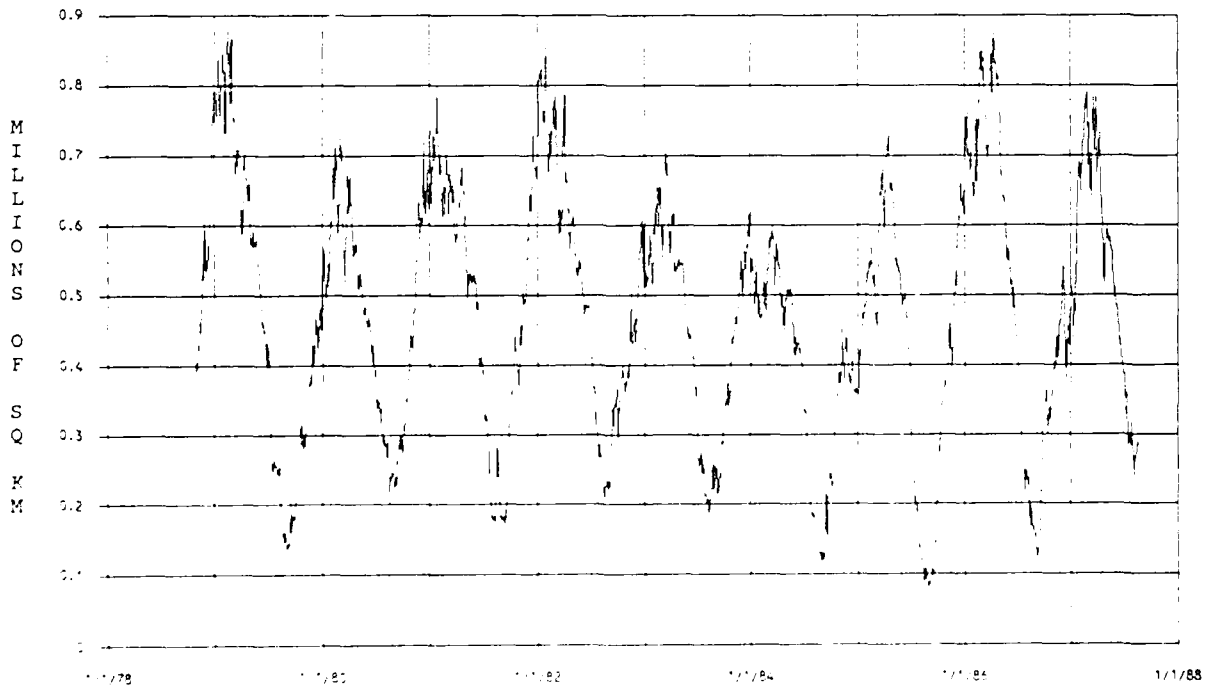

Figure 1. Sea ice area in the Greenland Sea.

was absent. There appears to be a slow oscillation in the amplitude of the peaks, with a period of about four years. On a shorter time scale, there appears to be an oscillation with a period of about 2 to 3 months superimposed on the annual cycle. This phenomenon is currently under investigation, but it may correspond to an alias frequency between the observation interval (48.533 hours) and the M2 (principal lunar) tide. On still shorter time scales, the spikes are not instrument noise, but are attributed to sudden changes in the ice distribution related to the passage of weather systems. Ice concentration changes on this short time scale are clearly evident in the time-lapse video.

Finally, although it is unrelated to the theme of this paper, it is noteworthy that during the most extreme summertime minimum ice area which occurred in 1985 (Fig. 1), the entire northern coastline of Greenland was ice-free, an event that occurred only once in the lifetime of the SMMR.

REFERENCES

Gloersen, P. and D.J. Cavalieri (1986) Reduction of weather effects in the calculation of sea ice concentration from microwave radiances. *Journal of Geophysical Research*, **91**: 868-872.

Gloersen, P. and W.J. Campbell (1988) Variations in the Arctic, Antarctic, and global sea ice covers during 1978–1987 as observed with the Nimbus-7 Scanning Multichannel Microwave Radiometer. *Journal of Geophysical Research*, **93**: 10,666–10,674.

Parkinson, C.L., J.C. Comiso, H.J. Zwally, D.J. Cavalieri, P. Gloersen and W.J. Campbell (1987) Arctic sea ice 1973–1976: Satellite passive-microwave observation. National Aeronautics and Space Administration, Washington, D.C., NASA SP-489.

SMMR Observations of the Sea Ice Regime in the Ross Sea, 1979–1985

S. JACOBS
Lamont Observatory
Columbia University
Palisades, New York, U.S.A.

J.C. COMISO
Ocean Laboratory
NASA/Goddard Flight Center
Greenbelt, Maryland, U.S.A.

ABSTRACT/INTRODUCTION

Sea ice concentrations derived from the Nimbus-7 Scanning Multichannel Microwave Radiometer (SMMR) can be related to atmospheric forcing and to sea floor topography via the ocean circulation. In the Ross Sea, ice concentrations are lower year-round over the continental shelf than above the adjacent deep ocean. The lowest concentrations appear on the west-central shelf, where persistent SSW winds move sea ice away from the coastline. The increased rate of ice formation in the greater expanse of open water in this sector results in the highest-salinity shelf water to be found in the Antarctic. There is little monthly or interannual variability in the average 86% ice concentration over the shelf during the 7- to 8-month winter period when that region is south of the marginal ice zone. There is considerable variability during the remainder of the year, with early opening of the large Ross Polynya followed by insolation and heating of the ocean surface layer and later ice formation in autumn. In terms of ice cover, this ocean heat storage resulted in a spring-summer-autumn cycle about six weeks longer in 1979–80 than in 1984–85 (Fig. 1).

RESULTS

Regions of lower ice concentration occur intermittently within the winter ice cover at locations remote from continental boundaries. These stationary features can be attributed to quasi-permanent upwelling and divergence along portions of the continental shelf break and near topographic highs on the shelf. One of the offshore regions of lower ice concentration, which we refer to as the Pennell Polynya, is associated with the northeast end of the ~250-m Pennell Bank, near 75°S, 180°. Closer to the coastline in the northwest Ross Sea is another area of generally lower ice concentration which we call the Admiralty Polynya. Possibly driven in part by barrier winds, this polynya is characterized by open water in early spring and late autumn and an ice cover as low as 70% during winter. A temperature section through this region indicates that the vertical ocean circulation helps maintain the Admiralty Polynya by means of the warmer deep water that upwells into the surface layer above the upper continental slope (Fig. 2).

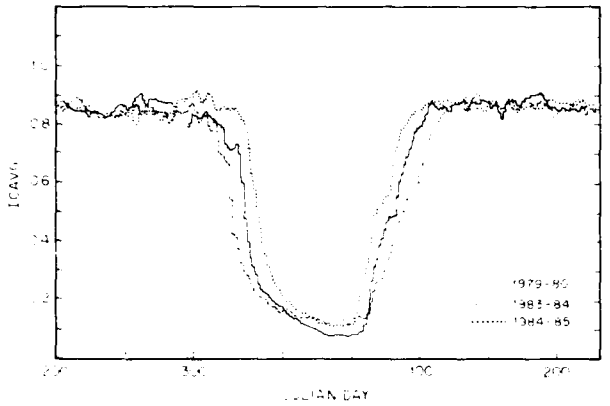

Figure 1. Average ice concentration (ICAVG) on the Ross Sea continental shelf (<1000-m depths) during long, normal and short spring/summer/fall seasons, 1979–85. ICAVG exceeds 80% (0.8) during winter.

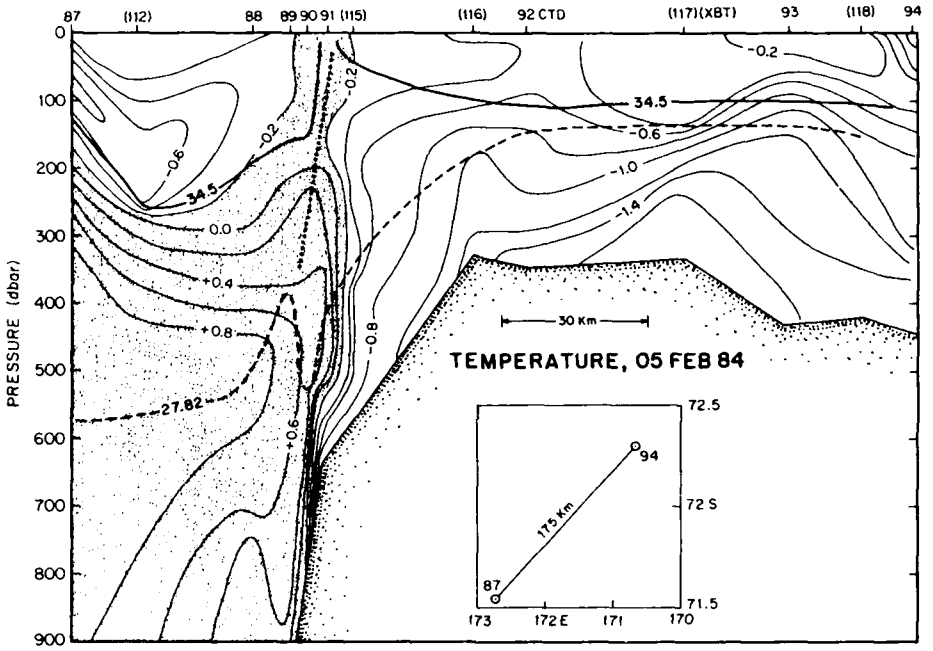

Figure 2. A temperature section across the outer continental shelf and slope in the northwest Ross Sea (see inset), from conductivity–temperature–depth (CTD) and expendable bathythermograph (XBT) data. Circumpolar Deep Water (CDW) is characterized here by temperatures >0.5 °C and shelf water by temperatures <–1 °C. CDW salinities are approximately 34.7 and contribute to the surface salinity >34.5 above the slope front. The dashed 27.82 isopycnal shoals from > 500 dbar (~ 500 m) to <200 dbar near the shelf break.

A sea ice field survives most summers northeast of the Ross Sea continental shelf, and expands rapidly when ice growth begins along the ice shelf front. During winter, migratory cyclones from the circumpolar ocean produce regionally lower ice concentrations for periods of several days, and result in increased current velocities at depth on the shelf. However, the potential for enhanced ice formation due to the greater ocean exposure generated by these storms is countered by the accompanying rise in air temperatures, so that there may be little or no increase in net ice production. On longer time scales, variable areas of low ice concentration can be identified moving with or through the sea ice field and can be tracked for periods of up to several months on the SMMR two-day average images. These features may result from storm-induced divergences in the ice cover that have "healed" with a slightly altered microwave signature, from the presence of icebergs, or from mesoscale features in the underlying ocean.

The relatively low resolution of gridded SMMR data can lead to significant errors in the estimation of

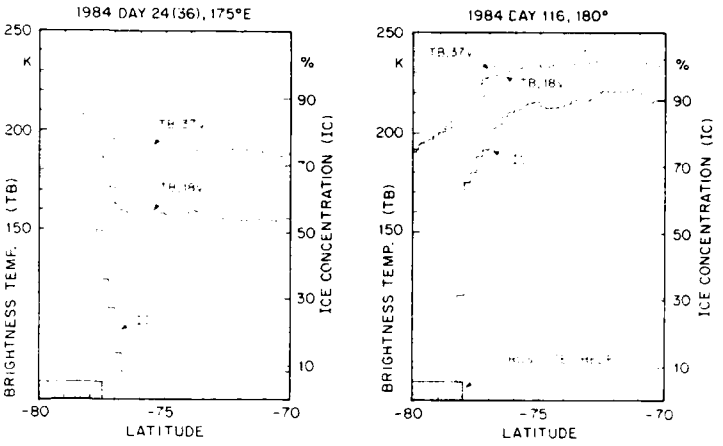

Figure 3. Brightness temperatures and derived ice concentrations along the 175°E meridian in summer (left) and the 180° meridian in winter (right). Julian days 24, 36, and 116 correspond to 24 January, 5 February and 25 April 1984. In these examples, the wide SMMR footprint and 1 pixel offset in the continental mask result in erroneously high (left) and low (right) sea ice concentrations 100 km seaward of the coastline.

sea ice concentration in very small study areas or near coastal boundaries (Fig. 3). In addition, ice shelves advance and recede along half of the Antarctic coastline, which will thus differ in position at any given time from most available maps. This complicates the use of SMMR data to investigate narrow coastal polynyas, which can experience the highest rates of ice production and shelf water modification. Ocean temperatures to depths of several hundred meters are cooled to the surface freezing temperature in these coastal polynyas, but intrusions of warmer water often appear throughout the winter. Obtained from year-long current meter moorings, the ocean temperature records demonstrate a potential sensible heat source for shelf polynyas during winter. The seasonal change of averaged subsurface ocean temperature along the ice shelf front lags the air temperature cycle by 1–2 months, and has an amplitude of about 0.3°C. That is 10% of the potential range of Antarctic Shelf water temperature, between the freezing point (approx. –2°C) and the temperature of the large Circumpolar Deep Water Reservoir (approx. +1°C). Sea ice extent in the Ross sector lags by 1–2 months the air temperature cycles recorded by automatic weather stations in the southern Ross Sea.

ACKNOWLEDGMENTS

This work is supported by the Oceanic Processes Program at NASA (NAGW 1344) and by the National Science Foundation (DPP 85-12540).

Variability of Sea Ice Concentration in the Canada Basin and Associated Atmospheric Forcings: 1979–1984

J.A. MASLANIK AND R.G. BARRY
Cooperative Institute for
Research in Environmental Sciences
and Department of Geography
University of Colorado
Boulder, Colorado, U.S.A.

ABSTRACT/INTRODUCTION

Given the important role of sea ice in the exchange of energy between the surface and the atmosphere, a need exists to characterize more precisely the spatial and temporal distributions of changes in open water areas within the ice pack, and to investigate the mechanisms by which such changes occur. The observations of ice conditions and mean pressure patterns by McLaren et al. (1987) and Serreze et al. (1989) suggest the Canada Basin as a region warranting such study. The objectives of this research are to 1) describe the modes of variability of ice concentration and extent in the Canada Basin and neighboring areas, and 2) define the role of synoptic-scale atmospheric forcings in terms of significant changes in regional ice conditions. Case-study comparisons are made between daily atmospheric data, alternate-day Scanning Multichannel Microwave Radiometer (SMMR)-derived concentrations, and daily ice conditions (concentration, albedo, lead patterns, and floe structure) identified in visible-wavelength satellite imagery to determine the physical validity of the linkages between dominant modes of ice concentration and atmospheric forcings.

DATA

The meteorological data sets used include gridded pressure and temperature fields from the Arctic Ocean Buoy Program and temperatures from the European Centre for Medium Range Weather Forecasts (ECMWF). Daily pressure and buoy interior temperatures for 12 GMT were extracted from the buoy data for the period from 1 January 1979–30 November 1984. ECMWF 1000-mb temperatures at 12 GMT were retrieved for 1 January 1980–31 December 1983. These data are described in more detail in Maslanik and Barry (1987).

SMMR data were extracted from the National Snow and Ice Data Center archive, and had previously been converted from orbital format to a polar stereographic grid true at 70°N, with a grid cell size of 25×25 km and effective resolution of ice concentration data (calculated using the operational NASA Team algorithm) of 50×50 km. Prints and transparencies of imagery acquired by NOAA Advanced Very High Resolution Radiometers (AVHRR) and Defense Meteorological Satellite Program (DMSP) polar orbiters were used to evaluate the SMMR data.

Comparisons with other observations indicate that except when melt ponds are present, SMMR-derived concentrations remain accurate to within a few percent during summer (Steffen and Maslanik 1988, Gloersen and Campbell 1988). Further investigations of time-series of SMMR data and DMSP visible-wavelength imagery in the Canada Basin and in the Kara and Barents Seas (Maslanik 1988) and reconsiderations of ESMR interpretations (Barry and Maslanik 1989) support these conclusions. When melt ponds exist, a characteristic pattern of rapid spatial and temporal variability in the SMMR-derived concentrations and brightness temperatures is observed that is not typical of true reductions in concentration, and is consistent with the formation and subsequent drainage of melt ponds. Comparison of SMMR data and other imagery for the Canada Basin region (Barry and Maslanik 1988) demonstrate these patterns, but also confirms that actual reductions in ice concentration of at least 40% occur in the Canada Basin, and that these reductions are faithfully recorded by the SMMR data. This comparison supports earlier interpretations of reduced concentration areas shown in ESMR imagery (Gloersen et al. 1978).

SYNOPTIC-SCALE ATMOSPHERE–ICE INTERACTIONS

The study region includes the area within approximately 71°N, 162°W; 79°N, 168°E; 83°N, 88°W; and 72°N, 116°W. This entire area will be referred to as the Canada Basin in the following discussion. The region covered by the atmospheric analysis is bounded by 62°N, 177°E; 67°N, 111°E; 75°N, 7°W, and 68°N, 104°W. Key results of analysis for this region are summarized below.

During June through July, the SMMR-derived concentrations reveal the effects of melt. In early June, polarization decreases and brightness temperatures increase as melt commences. Following this initial melt signal, the spatial and temporal variability in the SMMR data is used to indicate areas affected by surface melt. SMMR-derived concentration changes of 20–30% are observed between alternate days, with little spatial persistence to the patterns. Comparison with other imagery for these periods shows that concentrations are in fact high, with reflectivities and surface appearance characteristic of melt and ponding. However, cases are observed where real areas of reduced concentration exist within the perennial ice pack. As expected, these regions are more persistent in location and over time in the SMMR data. Following the period of peak melt in June–early August, brightness temperatures increase due to drainage of melt ponds or refreezing of the surface as suggested by increasing reflectivity in the visible-band imagery.

During the latter part of August and into September, when temperatures have typically fallen below freezing, changes in SMMR-derived concentrations continue to be observed. Observations and statistical analyses (Maslanik 1988) show that two primary pressure patterns are associated with the dynamic reductions in concentration. Concentrations decrease preferentially in the vicinity of the Northwind Ridge in years when low pressure systems are well-established in the Canada Basin. Figure 1 shows mean pressure, wind speed, wind direction, and change in ice concentration from 16 August through 24 August 1980; a period when low pressure dominated in the study area. The second pressure pattern most closely associated with changes in concentration consists of paired high and low pressure cells. The most common arrangement is a high (or low) in the Bering Strait or Chukchi Sea and a low (or high) over the Canadian Archipelego. An example of the second pattern is shown in Figure 2. Ice concentrations decrease from 65% to 40% from 28 August to 2 September 1981, with a 15% drop from 29 August to 31 August. The pattern of concentration change is consistent with advection from the central Canada Basin to locations to the south, west, and east. Similar examples of paired systems and persistent lows are observed in the other years studied.

Following the initial formation of the reduced concentration areas, concentrations tend to increase gradually under weak pressure systems, although the spatial pattern of these areas of lower concentration

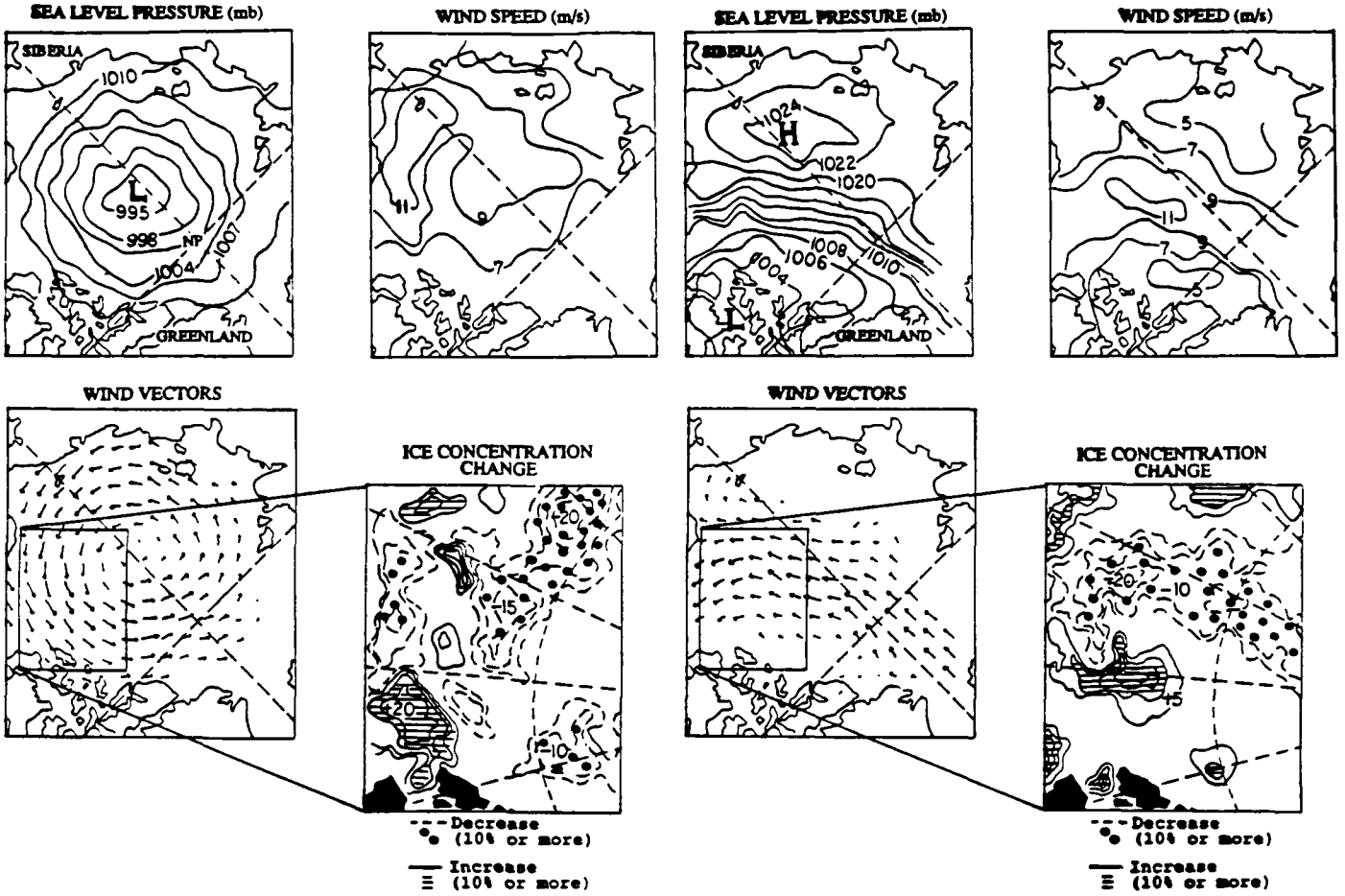

Figure 1. Mean meteorological conditions and change in ice concentration for 16–24 August 1980.

Figure 2. Mean meteorological conditions and change in ice concentration for 28 August–2 September 1981.

may persist for several weeks after the forcing regime has changed. The trend toward increasing concentrations is interrupted on occasion by strong synoptic events that re-establish the original pattern.

Evidence of reduced concentrations can persist into late autumn. For example, SMMR-derived concentrations of less than 75% appear in October 1980 at 73°N, 140°W in association with paired high and low pressure systems. Another decrease in concentration occurs during the first week of December, with concentrations dropping to less than 80% north of the marginal ice zone at 72°N, 150°W. The deep low (< 984 mb) associated with this change is considered by Zwally and Walsh (1987), who describe a decrease in SMMR-derived multiyear ice percentage similar to the changes in total concentration discussed here.

EFFECTS ON ICE GROWTH AND BRINE PRODUCTION

To provide a rough estimate of the possible effects of these reduced-concentration areas on heat flux, ice growth, and brine production, the approach used by Cavalieri and Martin (1985) for ice growth in open water areas was adapted. The bulk transfer method used here includes a calculation of sensible heat flux, a parameterization of total heat flux based on a ratio of latent to sensible heat, and an estimate of ice production based on a frazil-ice growth model. Inputs are air temperature (approximated by the ECMWF 1000-mb temperatures), water temperature (set to –1.8 C), and 10-m wind speed (estimated as 60% of the geostrophic wind speed calculated from drifting buoy pressures). A transfer coefficient for sensible heat of 1.3×10^{-3} is used as a conservative estimate and is not adjusted for stability or fetch. The ratio of latent to sensible heat is set at 0.1 and radiative transfer terms are neglected. Heat flux and ice production are estimated for an approximately 40,000-km^2 box centered at 82°N, 150°W, at two-day intervals from 1 January 1980–31 December 1983. Frazil ice production is calculated by multiplying the estimated rate of ice growth by the total open water area in the box, as defined by one minus the SMMR-derived ice con-

Table 1. Number of days with ice growth, ice production rate, and volume of ice generated within open water areas for individual freeze-up periods within the 40,000-km^2 box.

Calendar year	No. of days with positive growth	Mean ice prod. rate (mm/hr)	Ice vol. (km^3)
1980	262	1.48	7.17
1981	276	1.72	9.51
1982	264	1.80	32.12
1983	256	1.68	27.80

centration. Ice growth rates and cumulative ice thickness for ice generated in open water areas during periods of ice growth are listed in Table 1.

As an example of effects on salinity, the salt input from the new ice growth in 1982 with a 60% brine rejection rate increases the salinity of a 10-m water layer (salinity of 31.5) by about 5%. The large differences between years are caused by relatively small differences in the individual parameters contributing to the ice production calculations. Greater mean temperature contrast and the larger estimated fraction of open water in 1982 and 1983 account for the jump in ice production in these years. The greatest amounts of ice are produced typically in autumn through early winter, suggesting that the persistence of reduced concentrations from late summer into autumn has a potentially greater effect on heat flux and ice production than do smaller fluctuations in ice concentration through winter and spring.

CONCLUSIONS

Time-series analysis of SMMR data, visible-wavelength imagery, and drifting buoy data for 1979–1984 show that significant and rapid reductions in ice concentration occur in the Canada Basin in summer and autumn under the influence of two main pressure regimes. Combinations of different meteorological conditions and open water area in individual years lead to large interannual differences in the potential for new ice growth in leads. While the heat flux and ice growth calculations used here are simplistic and include a variety of assumptions, we feel that the estimates provide some insight into the magnitude of potential effects of open water areas within the perennial ice pack.

ACKNOWLEDGMENTS

This work was supported under NSF Grant DPP 85-20883, and a NASA post-doctoral appointment. SMMR, AVHRR, and DMSP imagery were made available by NSIDC. ECMWF data were provided by the National Center for Atmospheric Research.

REFERENCES

Barry, R.G. and J.A. Maslanik (1988) Arctic sea ice characteristics and associated atmosphere–ice interactions. *GeoJournal*, **18**(1): 35–44.

Cavalieri, D.J. and S. Martin (1985) A passive microwave study of polynyas along the Antarctic Wilkes Land coast. In *Oceanology of the Antarctic Continental Shelf. Antarctic Research Series*, **43**: 227–252.

Gloersen, P, H., J. Zwally, A.T.C. Chang and D.K. Hall (1978) Time-dependence of sea-ice concentration and multiyear ice fraction in the Arctic Basin. *Boundary Layer Meteorology*, **13**: 339–359.

Gloersen, P. and W. J. Campbell (1988) Satellite and aircraft passive microwave observations during the Marginal Ice Zone Experiment in 1984. *Journal of Geophysical Research*, **93**(C8): 6837–6846.

Maslanik, J.A. (1988) Variability of sea ice concentration and extent in the Canada Basin and associated synoptic-scale atmosphere-ice interactions: 1979–1984. Ph.D. thesis (unpublished), Department of Geography, University of Colorado.

Maslanik, J.A. and R.G. Barry (1987) Short-term interactions between atmospheric synoptic conditions and sea ice extent and concentration in the Canada Basin. *Annals of Glaciology*, **9**.

McLaren, A.S., M.C. Serreze and R.G. Barry (1987) Seasonal variations of sea ice motion in the Canada Basin and their implications. *Geophysical Research Letters*, **14**(11): 1123–1126.

Serreze, M.C., R.G. Barry and A.S. McLaren (1989) Seasonal variations in sea ice motion and effects on sea ice concentration in the Canada Basin. *Journal of Geophysical Research* (in press).

Steffen, K. and J.A. Maslanik (1988) Comparison of geophysical sea ice parameters derived from passive microwave data and Landsat imagery. *Journal of Geophysical Research*, **93**(C9): 10,769–10,779.

Zwally, H.J. and Walsh, J.E. (1987) Comparison of observed and modeled ice motion in the Arctic Ocean. *Annals of Glaciology*, **9**: 136–144.

Reversals of the Beaufort Gyre Sea Ice Circulation and Effects on Ice Concentration in the Canada Basin

M.C. SERREZE, R.G. BARRY AND A.S. McLAREN
Cooperative Institute for
Research in Environmental Sciences
and Department of Geography,
University of Colorado
Boulder, Colorado U.S.A.

ABSTRACT/INTRODUCTION

The long-term mean motion of sea ice and upper ocean within the Canada Basin is characterized by the clockwise Beaufort Gyre (Fig. 1). Although the long-term ice drift reflects roughly equal contributions by winds and ocean currents, day-to-day fluctuations are mostly wind-driven (Thorndike and Colony 1982). In recent papers (McLaren et al. 1987, Serreze et al. 1989) we show that in response to synoptic-scale wind forcings the clockwise sea ice circulation commonly breaks down in late summer to early autumn, and can become net anticlockwise for at least 30 days. These "reversals" of ice motion in the Beaufort Gyre can be associated with mean ice divergences exceeding 0.5% per day. The open water areas produced may have some important climatic and oceanographic implications. This paper summarizes our major findings. Readers are referred to McLaren et al. (1987), Serreze and Barry (1988) and Serreze et al. (1989) for details.

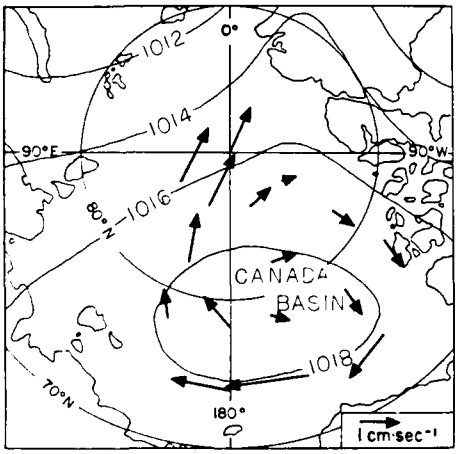

Figure 1. Seven-year (1979–85) mean annual surface pressure and ice drift vectors over the Arctic Ocean based on Arctic Ocean Buoy Program Data. Ice velocity vectors were obtained from optimally interpolated fields (see text) (from Serreze et al. 1989).

DATA

Since 1979, a network of drifting buoys has been maintained in the Arctic Ocean by the University of Washington's Polar Science Center. Started as part of the United States contribution to the First Global Atmospheric Research Program (GARP) Global Experiment (FGGE), the primary aims of the Arctic Ocean Buoy Program are to define the large-scale motion of sea ice and provide temperature and pressure measurements in the data-sparse Arctic Ocean (Thorndike and Colony 1980). Data are currently available for 1979-85.

We use three FGGE data sets: 1) optimally interpolated daily gridded surface pressure analyses with estimates of first and second pressure derivatives, representing a blend of buoy pressure observations, station data and National Meteorological Center (NMC) analyses, 2) daily gridded fields of estimated ice velocity and first derivatives, also processed via optimal interpolation and 3) Lagrangian time series of ice velocity from individual buoys, obtained from satellite-determined buoy positions, merged with optimally interpolated estimates of geostrophic winds at the changing buoy locations. Details are discussed by Thorndike and Colony (1982) and Thorndike et al. (1983). Ice conditions are examined using Advanced Very High Resolution Radiometer (AVHRR) and Defense Meteorological Satellite Program (DMSP) visible-band satellite imagery. Comparisons are made with SMMR (Scanning Multichannel Microwave Radiometer) ice concentration estimates and weekly Navy/NOAA ice charts.

RESULTS

Figures 2 and 3 show the distribution of winter and summer cyclone days for the Arctic Basin above 70°N, based on the FGGE analyses. The number of days with low pressure centers within squares of about 200,000 km^2 were summed and the results contoured. Details of the charting procedure and further results are provided elsewhere (Serreze and Barry 1988, Serreze et al. 1989). Winter cyclones (Fig. 2) are largely restricted to the eastern Arctic, with little

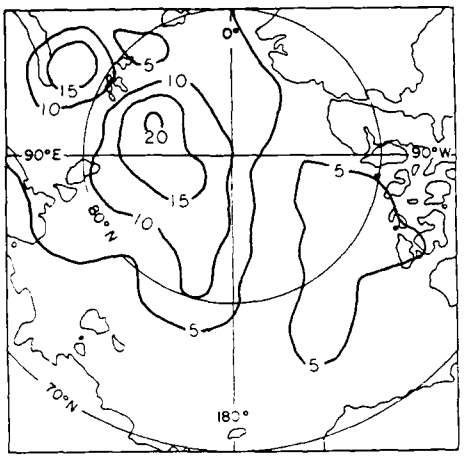

Figure 2. Winter (January–March) cyclone days in squares of approximately 200,000 km² for 1979–85, based on FGGE pressure analyses. Only systems lasting two days or longer and attaining a minimum pressure <1012 mb are considered (from Serreze et al. 1989).

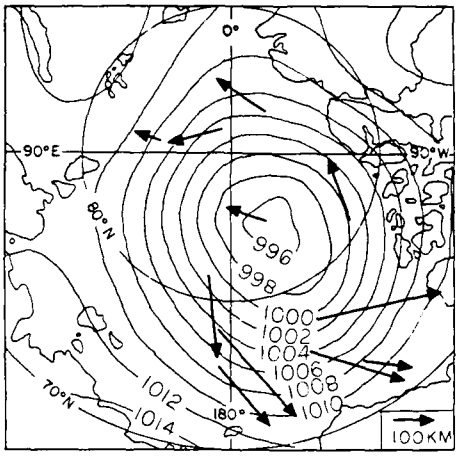

Figure 4. Mean surface pressure and ice drift vectors for the 30-day period in 1980 (13 August–11 September) corresponding to maximum atmospheric cyclonic activity. Drift vectors are based on the first and last buoy positions during the 30-day period rather than from the optimally interpolated fields as used for Figure 1 (from Serreze et al. 1989).

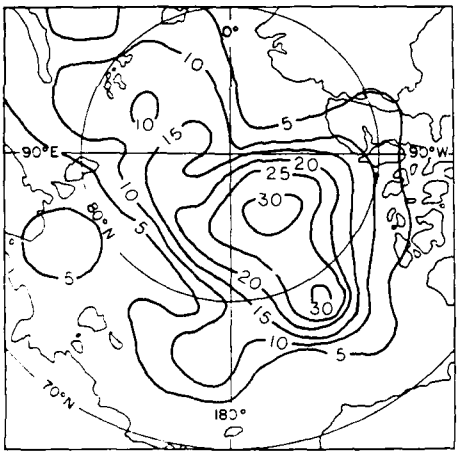

Figure 3. Same as Figure 2, but for summer cyclones (July–September) (from Serreze et al. 1989).

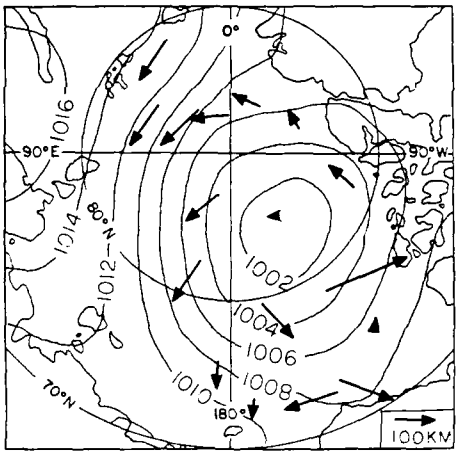

Figure 5. Same as Figure 4, but for July 28–August 26, 1981 (from Serreze et al. 1989).

cyclonic activity in the Canada Basin which is dominated by anticyclones at this time (not shown). In the annual mean, anticyclones are the dominant circulation feature, as is indicated by the mean pressure distribution in Figure 1. In sharp contrast, cyclones are common in the Canada Basin in summer (Fig. 3). Most systems migrate into the Canada Basin from the Eurasian Coast and subsequently stagnate and fill. This results in an area of persistent low pressure, analogous to the Icelandic Low (Reed and Kunkel 1960). Peak cyclonic activity is typically in August, but with an interannual variability of about a month. The pattern was best developed in 1980 and 1981.

Figures 4 and 5 show the mean surface atmospheric pressure and net buoy drift vectors, for the 30-day periods in 1980 and 1981 when cyclonic activity peaked. The pattern for both years is in sharp contrast to the seven-year annual mean pattern shown in Figure 1. Both Figures 4 and 5 show an area of deep low pressure in the Canada Basin and a complete reversal of the ice drift. Similar cyclonic patterns for the atmosphere and sea ice occur in all years examined, partic-

ularly 1979 and 1983. The pattern was relatively weak in 1984 and 1985.

Statistical relationships between ice motion and geostrophic winds were examined using the Thorndike and Colony (1982) linear model. This has the form

$$\mathbf{U} = \mathbf{AG} + \langle c \rangle + \mathbf{E}$$

where **U** is ice velocity, **G** is geostrophic wind, $\langle c \rangle$, in the absence of large internal ice stresses, approximately the mean geostrophic ocean current and **E**, the unexplained residual, are vectors. The term $\mathbf{A} = |A|(\cos\theta - i\sin\theta)$ is a complex multiplier with a scaling factor $|A|$, relating the ice speed to the geostrophic wind speed, and a drift angle of the ice, θ, measured clockwise positive from **G** to **U**. Application of the model to the Lagrangian time series of buoy velocities and geostrophic winds for 1979–85 within the Canada Basin in summer (July–September) yields buoy-averaged values of $|A| = 0.011$ and $\theta = 19°$, meaning that the ice moves at a little over 1% of the geostrophic wind and 19° to its right. The model typically explains 60-80% of the variance of the daily ice motion. These results contrast sharply with winter (January–March), when $|A| = 0.007$ and $\theta = 3°$, meaning a smaller proportional response of the ice to winds and a nearly geostrophic (nondivergent) drift.

Following Thorndike and Colony (1982), we expand the model to relate derivatives of the ice velocity to derivatives of the geostrophic wind, using the average summer results to set spatially-invariant sea ice boundary conditions (Serreze et al. 1989). This allows estimates of the wind-driven component of the ice pack divergence at fixed points where pressure data are provided. Divergences are also computed using the optimally interpolated ice velocity gradients (Thorndike et al. 1983). Results from both techniques for the 30-day period of peak atmospheric cyclonic activity in 1980 are given in Figure 6 as contoured grid point means.

Both techniques (Fig. 6) show a large area where mean divergences exceed 0.5% per day. The wind-driven estimate appears too large. This may be due to ocean current effects not accounted for in the expanded model (Serreze et al. 1989). Peak values for the wind-driven predictions are also located to the east compared to the optimally-interpolated estimates. This again is an artifact of the simplistic model, which predicts maximum ice divergence under the atmospheric relative vorticity maximum (Serreze et al. 1989). Nevertheless, the agreement between the two relatively independently-derived divergence estimates is quite good. Application of both techniques

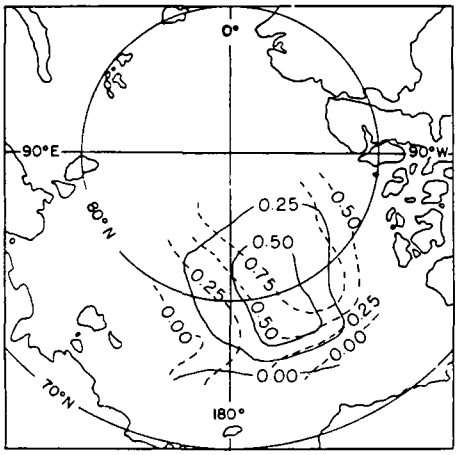

Figure 6. Mean ice divergence (% per day) estimated from optimally interpolated fields (solid) and linear model (dashed) with $|A| = 0.011$ and $\theta = 19°$, 13 August–11 September 1980 (from Serreze et al. 1989).

to the 30-day period of peak cyclonic activity for 1981 (Fig. 5) gave similar results.

The Navy/NOAA ice concentration chart for 26 August 1980, shows a large area where average concentrations are 70–80%, corresponding closely to the region where the buoy data indicate divergence (Fig. 6). AVHRR satellite data show this feature clearly, as well as a similar feature for 1981. SMMR data also show low ice concentration (Barry and Maslanik 1989). Nevertheless, the concentration changes indicated by the satellite imagery, both visible band and SMMR, are larger than can be accounted for by a mean divergence rate of 0.5% per day for 30 days (15%), suggesting that additional mechanisms are at work opening the ice pack.

1980 and 1981 are not the only years in which substantial reductions in ice concentration are noted in the Canada Basin. Although of poor quality, visible imagery for 1969 shows a large area of reduced ice concentration, comparable to that observed in 1980 and 1981. A smaller feature is noted in DMSP imagery 1982. Most recently, large concentration reductions are observed in DMSP imagery during September 1988. Available pressure data indicate a well-developed summer cyclone pattern in that year. Hibler's (1979) dynamic-thermodynamic sea ice model, forced by 8-day averaged geostrophic winds for May 1962–June 1963, predicted a large area of low compactness in the northern Canada Basin. This feature was confirmed by submarine observations (Dunbar and Wittman 1963). Published pressure data show persistent cyclonic activity in the Canada Basin in July 1962.

Concentration reductions observed in some years, e.g., 1982, cannot be related to strong atmospheric cyclonic activity, suggesting other processes are responsible for their development. This is also true of early August of 1958 and 1970, when relatively open ice conditions in the Canada Basin are indicated from submarine sonar data (McLaren 1989). Further studies of these features and their forcing mechanisms are underway.

IMPLICATIONS

Our results indicate that the Canada Basin may be a previously unrecognized region for new ice and brine production. Application of a frazil ice growth model (Cavalieri and Martin 1985) to meteorological data and SMMR-derived ice concentrations in the Canada Basin (Maslanik 1988) indicates that in some years, these open water areas could contribute to as much as half of the 1.9-m additional ice growth necessary in the central Arctic to attribute the observed salinity in the Beaufort Sea to ice production alone (Melling and Lewis 1982). Large sensible and latent heat fluxes through these areas of open water or thin ice could represent an important source of atmospheric heat in autumn and early winter. Since similar climatic conditions could have occurred during interglacial episodes during the Pleistocene, postulated episodes with a seasonally ice-free or more open Arctic Ocean might be attributable to increased storm activity, rather than a warmer climatic regime. Finally, although the Hibler (1979) sea ice model can reproduce the concentration changes examined here, there have been few detailed investigations of the adequacy with which coupled GCM's represent synoptic-scale forcings on the sea ice. The demonstrated sensitivity of the ice pack to current-day synoptic forcings suggests that the representativeness of GCM simulations of greenhouse warming effects in the Arctic may depend on the accuracy with which atmospheric forcings on ice motion can be modeled.

REFERENCES

Barry, R.G. and J.A. Maslanik (1989) Arctic sea ice characteristics and associated atmosphere-sea ice interactions. *Geojournal*, **18**(1): 35–44.

Dunbar, M and W. Wittman (1963) Some features of ice movement in the Arctic Basin. In *Proceedings of the Arctic Basin Symposium, Hershey, Pennsylvania, October 1962.*

Cavalieri, D.J. and S. Martin (1985) A passive microwave study of polynyas along Antarctic Wilkes Land coast. In *Oceanology of the Antarctic Continental Shelf.* Antarctic Research Series 43, p. 227–252.

Hibler, W.D. III (1979) A dynamic thermodynamic sea ice model. *Journal of Physical Oceanography*, **9**: 815–846.

Maslanik, J.A. (1988) Variability of sea ice concentration and extent in the Canada Basin and associated synoptic-scale atmosphere–sea ice interactions. PhD Dissertation, Department of Geography, University of Colorado, Boulder, Colorado.

McLaren, A.S. (1989) The under-ice thickness distribution of the Arctic Basin as recorded by USS *Nautilis* in 1958 and USS *Queenfish* in 1970. *Journal of Geophysical Research*, **94**(C4), 4971-4983.

McLaren, A.S., M.C. Serreze and R.G. Barry (1987) Seasonal variation of sea ice motion in the Canada Basin and their implications. *Geophysical Research Letters*, **114**: 1123–1126.

Melling, H. and E.L. Lewis (1982) Shelf drainage flows in the Beaufort Sea and their effect on the Arctic pycnocline. *Deep-Sea Research*, **29**(8A): 967–985.

Reed, R.J. and B.A. Kunkel (1960) The Arctic circulation in summer. *Journal of Meteorology*, **17**: 489–506.

Serreze, M.C. and R.G. Barry (1988) Synoptic activity in the Arctic Basin 1979–85. *Journal of Climate*, 1(12): 1276–1295.

Serreze, M.C., R.G. Barry and A.S. McLaren (1989) Seasonal variations in sea ice motion and effects on sea ice concentration in the Canada Basin. *Journal of Geophysical Research* (in press).

Thorndike, A.S. and R. Colony (1980) Arctic Ocean Buoy Program Data Report, 1 January 1979–31 December 1979. Polar Science Center, University of Washington, Seattle.

Thorndike, A.S. and R. Colony (1982) Sea ice motion in response to geostrophic winds. *Journal of Geophysical Research*, **87**: 5845–5852.

Thorndike, A.S., Colony, R. and E. Munoz (1983) Arctic Ocean Buoy Program Data Report, 1 January 1982–31 December 1982. Polar Science Center, University of Washington, Seattle, 132pp.

Interannual Variability of Ice Melt in the Kara/Barents Sea

R.C. CRANE
Department of Geography and the
Earth System Science Center
The Pennsylvania State University
University Park, Pennsylvania, U.S.A.

ABSTRACT

Interannual variability in the distribution and timing of ice melt is examined for the Kara/Barents Sea region using five years of Nimbus-7 SMMR data. The early stages of snow and ice melt result in changes in surface emissivity, which are revealed in the gradient ratio between the 18-GHz and 37-GHz vertically polarized brightness temperatures. The variance in the gradient ratio is examined spatially and through time in order to isolate individual melt episodes, and these episodes are then related to the state of the atmospheric circulation. As the melt season progresses the reduction of ice concentration is calculated using the 18-GHz horizontal and vertical brightness temperatures. Interannual variations in the timing and pattern of ice melt are again explained in terms of changes in the synoptic atmospheric circulation over the region.

Arctic Ice Motion from Sequential AVHRR Imagery

J. HAWKINS
Naval Oceanographic and
Atmospheric Research Laboratory
NSTL Station, Mississippi, U.S.A.

W.J. EMERY AND C. FOWLER
CCAR, University of Colorado
Boulder, Colorado, U.S.A.

ABSTRACT

Using filtered cross correlations between relatively cloud-free sequential AVHRR images, we examined temporal changes in the patterns of sea ice motion for the Barents Sea and Greenland Sea regions. Improvements are made in the computational procedure that allows the computation of motion vectors adjacent to land boundaries and improves the spatial resolution of the vector motion through the use of overlapping windows. Automated techniques are also implemented to discern and edit out cloud-covered portions of the images using both multispectral techniques and the coherence of the computed motion. Since clouds move more quickly and less coherently than does the pack ice, ice field requirements that motion vectors be consistent with their neighbors allow one to identify and remove cloud movements from the ice motions. The resulting motion fields are used to compute sea ice divergence and convergence, which are then related to the overlying wind field. Weekly to 10-day sequences of AVHRR images produce time series depictions of the ice velocity fields for comparison with the wind fields as the dominant driving force. Comparisons are also made with similar ice motion simulated with a numerical model driven by the same wind fields.

Quasi-quinquennial Oscillations in the Arctic Sea Ice Cover

V.R. NERALLA
Atmospheric Environment Service
Downsview, Ontario, Canada

ABSTRACT

A natural cycle of severity in sea ice conditions over the Beaufort Sea is examined by searching for significant periodicities using the Maximum Entropy Spectral Technique (MEST). MEST has been shown to have extremely high resolution with accurate frequency and power estimates even for short data samples. The study clearly showed a significant four- to five-year cycle in the sea ice cover.

Observations of Sea Ice Momentum Budget North of Svalbard and the Fram Strait

H.C. HOEBER
Meteorological Institute
Hamburg University
Hamburg, Federal Republic of Germany

ABSTRACT

Two drifting ice buoys were deployed during a cruise of R/V *Polarstern* in pack ice north of Spitsbergen in July–August 1987. While one buoy was lost in October 1987, the second traveled through the Fram Strait and drifted south in the East Greenland

Current for a total of 8.5 months. Reporting through the ARGOS system, the stations provided wind direction and strength, current, pressure, temperature, and position (i.e., ice drift) data. Using bulk formulation for wind and water stresses, the components of the momentum budget were derived, and the internal ice stress was computed as residuum. The time and space variability of all quantities is discussed, and the importance of a good time resolution (better than one hour per position data) is demonstrated. Comparison with antarctic data is presented.

AEDB
Ice-, Water-Surface Drifting Buoy Mooring Experiment Through the Southern Transpolar Drift

S. HONJO
Woods Hole Oceanographic Institute
Woods Hole, Massachusetts, U.S.A.

ABSTRACT

An Arctic Environmental Drifting Buoy (AEDB) was deployed on 4 August 1987 at 86°17'N, 22°13'E by R/V *Polarstern* on a large ice floe about 3.7 m thick. The AEDB consisted of two major components: a 5-ft diameter amphibian surface float housing ARGOS transmitters and a memory stack for ice-profiling thermistors; and 2) a 122-m-long mooring line attached to the sphere and fed through a 1-m ice hole. Along the mooring were deployed two fluorometers, thermistor chains, an acoustic Doppler current meter, and a time-series sediment trap/micropump unit (unit was lost). The AEDB proceeded southwesterly with the Transpolar Drift at an average speed of 15.3 km/day, with a maximum speed of 3.7 km/hour. On 2 January 1988, the AEDB dropped into the water while passing through the Fram Strait and for the remaining drift period was either free floating on the water surface or underneath sea ice of various thickness. Throughout this period the transmitters onboard successfully transmitted position, temperature, and strain caused by ice on the sphere. The AEDB was recovered by the Icelandic ship R/V *Fridriksson* 15 April 1988 at 65°02'N, 31°14'W, off southeastern Greenland, completing 3900 km of drift in 255 days.

The Drift-Ice Route of the Arctic Environmental Drifting Buoy Experiment (AEDB), 4 Aug 1987 to 15 April 1988

R. KRISHFIELD AND S. HONJO
Woods Hole Oceanographic Institute
Woods Hole, Massachusetts, U.S.A.

P. WADHAMS
Scott Polar Research Institute
Cambridge University, United Kingdom

ABSTRACT

The ARGOS platform transmitting terminals on the AEDB sphere provided positions and other parameters throughout the 255-day journey spanning 3900 km along the Transpolar Drift from the deployment point at 86°17'N, 22°13'E, until recovery at 65°02'N, 31°14'W. During the first seven weeks after deployment, the AEDB traveled in a southwesterly direction consistent with historical data. During late September and October it turned to the southeast by approximately 2°, reaching as far east as 82°97'N, 23°18'E, north of Svalbard. The AEDB resumed a SW direction, considerably reducing drift speed to about 0.5 km/hr until it passed 81 latitude. During the drift north of the Fram Strait, the AEDB completed about 12 complete loops, each with a diameter of several kilometers; however, the ice floe rotated only slightly during this time except when it spun over 120° counterclockwise at 82°N. The drift speed increased dramatically to over 3.5 km/hr at 75°N, then reduced speed to less than 0.5 km and often stalled for hours in approximately the same position. The AEDB made a number of semi-loops west of the Vesteris Bank, stopped again for a week west of Jan Mayan, and accelerated to over 2 km/hr through the Denmark Strait until it was recovered on 15 April 1988.

A Diagnostic Examination of the Synoptic Controls on the Annual Reversal of the Beaufort Sea Gyre

E. LEDREW AND D. JOHNSON
Department of Geography
University of Waterloo
Waterloo, Ontario, Canada

M.C. SERREZE
Cooperative Institute for
Research in Environmental Sciences
University of Colorado
Boulder, Colorado, U.S.A.

ABSTRACT

Examination of FGGE ice motion data and submarine sonar data have revealed an annual reversal of the Beaufort Sea gyre in August or September. This has been shown to be related to the replacement of the dominant anticyclone by a low pressure cell over the region (McLaren, Serreze and Barry 1987, *Geophysical Research Letters*, **114**: 1123–1126).

A diagnostic model has been applied to NMC and FGGE data for August of 1980 in an effort to understand the physical controls on the setup and maintenance of this anomalous low pressure cell. The model includes an index of ageostrophic advection (the Q-vector) and parameterization of the surface diabatic and frictional processes.

The daily patterns of the Q-vectors and the 850-mb vertical velocity attributable to the ageostrophic advection and surface effects are analyzed to identify the major synoptic controls of the system and to isolate the contributions by advective vs surface mechanisms.

Model- and Satellite-Derived Variations of Multiyear Sea Ice Coverage in the Arctic

J.E. WALSH
Department of Atmospheric Sciences
University of Illinois
Urbana, Illinois, U.S.A.

H.J. ZWALLY
Laboratory for Oceans
NASA Goddard Space Flight Center
Greenbelt, Maryland, U.S.A.

ABSTRACT

Sea ice deformation is a strong function of ice strength which, in the central Arctic, depends on the relative fractions of multiyear (thick) and first-year (thin) ice coverage. The two-level dynamic-thermodynamic sea ice model of Hibler (1979, *Journal of Physical Oceanography*, **9**: 815–846) has been configured to include both multiyear and first-year ice. The model has been run for a seven-year period 1978–1985, for which the SMMR satellite microwave record of multiyear sea ice coverage is available. The satellite-derived concentrations of multiyear ice are somewhat lower than the simulated concentrations, although the total coverage of simulated multiyear ice agrees very well with the satellite-derived coverage. Both the simulated and satellite-derived multiyear ice coverages undergo large interannual variations that are generally consistent with year-to-year changes in the wind forcing, although the satellite-derived changes in response to extreme synoptic events appear to be considerably larger. On a year-to-year basis, the agreement between the two time series of multiyear ice coverage is best in the Beaufort sector of the Arctic.

Seasonal and Interannual Variations in Arctic Multiyear Sea Ice Distribution

H.J. ZWALLY
Laboratory for Oceans
NASA Goddard Space Flight Center
Greenbelt, Maryland, U.S.A.

J.E. WALSH
Department of Atmospheric Sciences
University of Illinois
Urbana, Illinois, U.S.A.

ABSTRACT

Variations in the areal distribution of multiyear sea ice in the Arctic Ocean are described using Nimbus 7 passive microwave data. The total area of multiyear ice is approximately conserved during winter, but significant changes occur over approximately 1000- × 1000-km regions. Short-term decreases in multiyear concentration during winter are indicative of divergence of the ice pack and the area of new ice formed, and increases are indicative of convergence and ice ridging. Rates of divergence derived from the microwave data are greater than rates inferred from buoy data, possibly due to their sensitivities to different scales of deformation. Some of the observed regional-scale changes during winter are due to large-scale advection of the multiyear ice pack into or out of the regions, and some are due to net convergence or divergence of the ice pack within the regions. Estimates are made of the net wintertime changes, caused by advection and convergence/divergence, respectively, in several regions for the 1979 to 1985 period.

Arctic Ice and Concentrations from SSMI and AVHRR

M. McELROY AND W.J. EMERY
CCAR, University of Colorado
Boulder, Colorado, U.S.A.

ABSTRACT

Relatively cloud-free images of arctic sea ice from the Beaufort Sea, Baffin Bay and the Greenland Sea are used to map the ice edge during brief portions of 1987. The resulting maps of ice edge and extent, based on the 1-km visible and near-infrared AVHRR imagery, are compared with similar maps computed from the microwave brightness from SSMI using the NASA algorithm. SSMI geolocation errors are corrected using a formula derived at the National Snow and Ice Data Center, and the AVHRR-derived ice edge is smoothed with a 5-km running mean for comparison with the 30-km spatial resolution of the SSMI. A classification scheme is developed to compute AVHRR ice concentration maps. In addition, an algorithm is explored using visual and near-IR AVHRR data to compute ice concentration for comparison with coincident concentrations computed from SSMI data for these same two regions. Again data from various times in 1987 are used to explore changes in both data sources due to seasonal variability. The higher spatial resolution of the AVHRR demonstrates the sensing capabilities of the SSMI, which can then be used to sense sea ice edge and extent under cloud-covered conditions.

Snow Melt on Arctic Basin Sea Ice

G. R. SCHARFEN
Cooperative Institute for
Research in Environmental Sciences
University of Colorado
Boulder, Colorado, U.S.A.

D. A. ROBINSON
Department of Geography
Rutgers University
New Brunswick, New Jersey, U.S.A.

R. G. BARRY AND M. C. SERREZE
Cooperative Institute for
Research in Environmental Sciences
University of Colorado
Boulder, Colorado, U.S.A.

ABSTRACT

The timing of snow dissipation in the Arctic Basin is critical to the surface energy balance and to sea ice dynamics due to the effects of snow cover on the radiative environment and the transfer of heat between the atmosphere and the ice/ocean system. The interannual variability in timing of the loss of snow cover on the sea ice is several weeks. Results are based on data derived from visual analyses of 0.6- and 2.7-km resolution Defense Meteorological Satellite Program shortwave (0.4- to 1.1-μm) imagery for eight summer seasons. Charts of snow cover categories were constructed for three-day intervals between 1 May and 16 August. Snow cover was detected from surface brightness signatures and textural patterns on the imagery once it was determined that clouds were not present.

In general, melt begins in late May–early June in the southern portions of the Beaufort and Chukchi seas in the western basin and in the Kara and southern Barents seas in the east. It progresses along the coastal regions of Alaska and northwestern Canada, along the Soviet arctic coast and northward into the basin so that by early July most of the region south of 80°N is snow free. To the north, snow disappears by the end of the third week of July in most years; however, patchy snow occasionally persists on the ice for all of the summer or disappears for only a week or so.

Relationships Between Atmospheric Conditions and Passive Microwave-Derived Melt/Freeze Periods for Hudson Bay During Spring

M.R. ANDERSON AND J.A. SCHUMACHER
Department of Geography
University of Nebraska
Lincoln, Nebraska, U.S.A.

ABSTRACT

The transition from winter to summer sea ice conditions represents a critical period during which ocean-atmospheric conditions undergo rapid fluctuations. Several sea ice melt/freeze periods are determined for Hudson Bay using passive microwave Nimbus 7 Scanning Multichannel Microwave Radiometer (SMMR) data during this period. The gradient ratio, derived from the 18-GHz and 37-GHz vertically polarized brightness temperatures, produces strong signatures during the melt/freeze periods. The variations that are observed between years will be examined. In addition, the atmospheric conditions during the melt/freeze periods obtained from the three radiosonde stations, Churchill, Coral Harbour and Inoucdjouac, surrounding Hudson Bay will also be presented. Understanding the conditions that take place during the melt/freeze periods will give better insight into the processes that are occurring between the sea ice surface and the atmosphere.

Section IV:

Airborne and Satellite Remote Sensing

NASA Sea Ice Validation Program for the DMSP SSM/I

D.J. CAVALIERI
Laboratory for Oceans
NASA Goddard Space Flight Center
Greenbelt, Maryland, U.S.A.

J. CRAWFORD AND B. HOLT
Jet Propulsion Laboratory
Pasadena, California, U.S.A.

D. EPPLER AND L.D. FARMER
Naval Oceanic and Atmospheric
Research Laboratory
Polar Oceanography Branch Office
Hanover, New Hampshire, U.S.A.

K. STEFFEN
Department of Geography
Swiss Federal Institute of Technology
Zurich, Switzerland

C.T. SWIFT
Department of Electrical and
Computer Engineering
University of Massachusetts
Amherst, Massachusetts, U.S.A.

ABSTRACT/INTRODUCTION

On 20 June 1987, a new generation passive microwave imager called the Special Sensor Microwave Imager (SSM/I) was launched as part of the Defense Meteorological Satellite Program (DMSP). The SSM/I operates at four frequencies (19.4, 22.2, 37.0 and 85.5 GHz) with orthogonal (horizontal and vertical) polarizations measured at each frequency except 22 GHz, which has only a vertical polarization channel. Its spatial resolution is frequency dependent and ranges from about 50 km at 19 GHz to better than 15 km at 85 GHz. With a swath width of almost 1400 km, the SSM/I provides near-global coverage every day. A detailed description of the sensor and its radiometric performance is given by Hollinger et al. (1987). The SSM/I will provide the polar research community with microwave radiances for continuing the record of polar sea ice observations that began with the Nimbus 5 ESMR in 1972 and continued until August 1987 with the Nimbus 7 SMMR.

In recognition of the importance of SSM/I data to the research community, NASA established a program to acquire, process, validate and archive both the calibrated SSM/I microwave radiances and the derived sea ice parameters (Cavalieri and Swift 1987). The NASA Ocean Data System at the Jet Propulsion Laboratory in Pasadena, California, was assigned the task of developing software to process and map the geophysical parameters, while the National Snow and Ice Data Center in Boulder, Colorado, will assume the long-term responsibilities of processing and archiving these data. Because the determination of the accuracy of the ice parameters is critical to the development of a scientifically useful data set, a key component of NASA's program is the validation of the derived ice parameters.

This paper briefly outlines the program to validate the sea ice parameters derived from an algorithm described by Cavalieri et al. (1984) and Gloersen and Cavalieri (1986) and presents some of the early results of the validation effort. NASA's progress in processing and archiving the SSM/I data is discussed by Charles Morris elsewhere in this volume. In the next section, the specific validation objectives are given and the general approach is discussed. Some preliminary results from satellite intercomparisons and from aircraft underflights are given in the third section, and finally, a tentative assessment is presented in the last section.

VALIDATION OBJECTIVES AND APPROACH

The prime objective of the validation program is to establish quantitative relationships between the sea ice parameters derived from the SSM/I and those same parameters derived from other data sets covering as many geographical areas as possible for different seasons. These other data sets include visible and infrared satellite imagery, and aerial photographic and high-resolution microwave imagery from aircraft underflights. The sea ice parameters derived from the SSM/I radiances include the position of the sea ice boundary and the total sea ice concentration for both northern and southern polar regions (Fig. 1) and the multiyear sea ice concentration for the northern polar region only. Other objectives include a determination of the accuracy to which the 85.5-GHz channels can locate the ice edge, the accuracy of the parameters in different regions and in different seasons, the accuracy of the parameters under various weather conditions and the effectiveness of the algorithm's weather filter.

The overall approach for meeting these objectives is one of compiling and analyzing spatially and temporally coincident data sets for comparison with the SSM/I ice parameters. Thus, coincident observations were obtained from sensors on the same or different satellites, and from well coordinated field experiments with aircraft flying mosaic patterns to cover

a. Northern hemisphere (17 January 1988).

Figure 1. Winter sea ice concentration derived from the DMSP SSM/I.

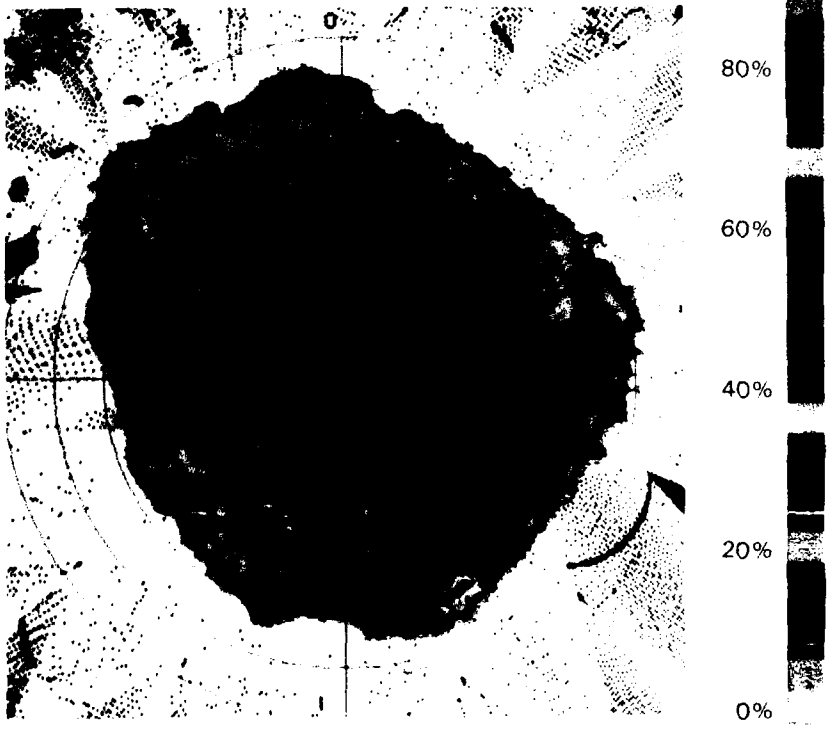

b. Southern hemisphere (9 July 1987)

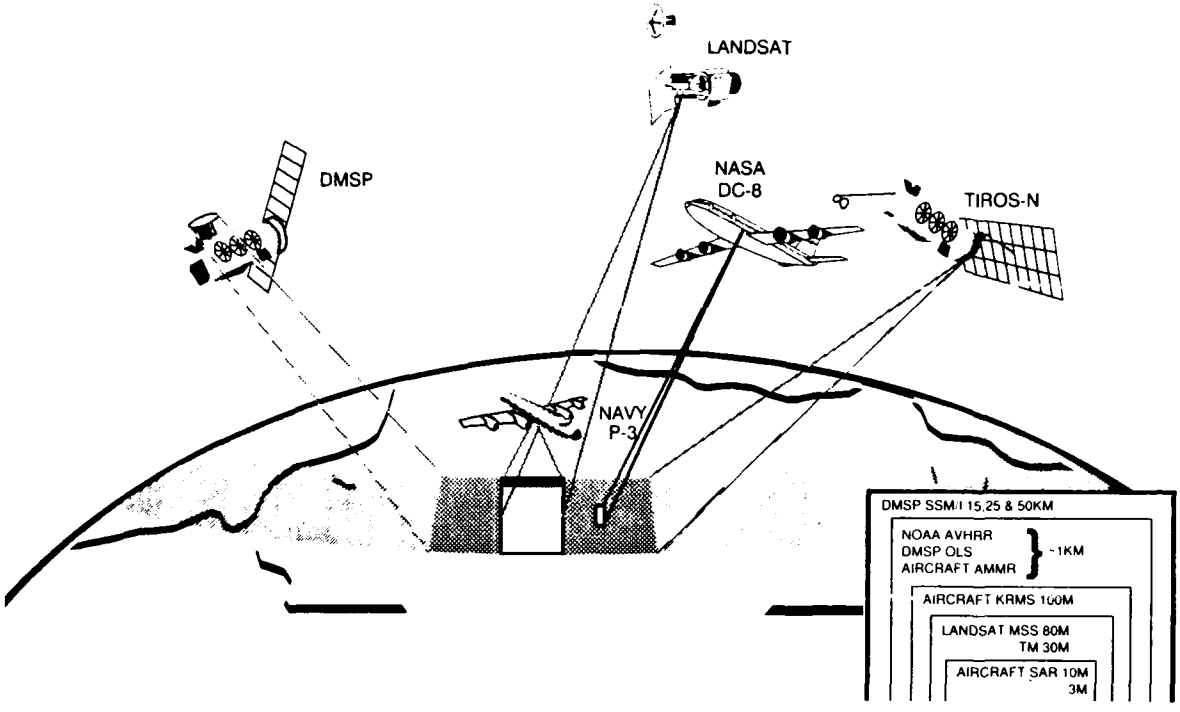

Figure 2. Schematic of the multispatial, multisensor sea ice validation approach using airborne and spaceborne sensors.

several SSM/I footprints. This multisensor/multispatial approach is illustrated schematically in Figure 2. Data sets acquired to date include imagery from Landsat and TIROS N and high-resolution active and passive microwave data from coordinated NASA and Navy aircraft underflights. The highest resolution data will come from aircraft SAR data and will provide sea ice parameters at resolutions of 3 and 10 m. Data providing the next highest resolution include Landsat data at 30 and 80 m, and aircraft passive microwave imagery at 100 m. AVHRR, OLS and fixed-beam passive microwave aircraft data will provide data at a resolution of about 1 km. The SSM/I has spatial resolutions that are wavelength-dependent, ranging from 15 to 50 km. Derived ice concentrations from each of these coincident data sets will be intercompared at progressively larger spatial scales and finally over SSM/I footprints.

MULTISPATIAL/MULTISENSOR COMPARISONS

SSM/I-Landsat comparisons

An important component of the validation effort is the comparison of SSM/I total ice concentration maps with nearly coincident Landsat MSS coverage for different regions and seasons. Landsat MSS imagery is used to calculate ice concentrations as described below at a resolution of 80 m. Eleven case studies or "windows" were defined for these comparisons covering several regions in the Arctic and Antarctic and all four seasons. In addition, a total of 13 MSS scenes were collected in the Beaufort, Bering, and Chukchi Sea regions during the NASA/Navy underflights in March 1988.

Landsat MSS imagery were acquired in two formats: digital and photographic transparencies. The 80-m resolution digital data, obtained from EOSAT Corporation, are mapped to match the SSM/I grid. The MSS channel 7 (0.8–11.1 μm) is the most suitable channel for the determination of ice concentration, since reflectance differences between thin ice types and open water are greatest in the near infrared, while channels 4–6 are frequently saturated due to the high reflectance of the ice. Because digital data for parts of the Bering Sea during the SSM/I underflights were unavailable, real-time photographic transparencies were obtained from the Geophysical Institute, University of Alaska at Fairbanks. Since the geolocation information of this imagery is unreliable due to the lack of accurate ephemeris and satellite attitude information, the imagery were collected in swaths so that at least one frame within each swath contained identifiable landmarks from which a geolocation correction could be calculated for the entire swath.

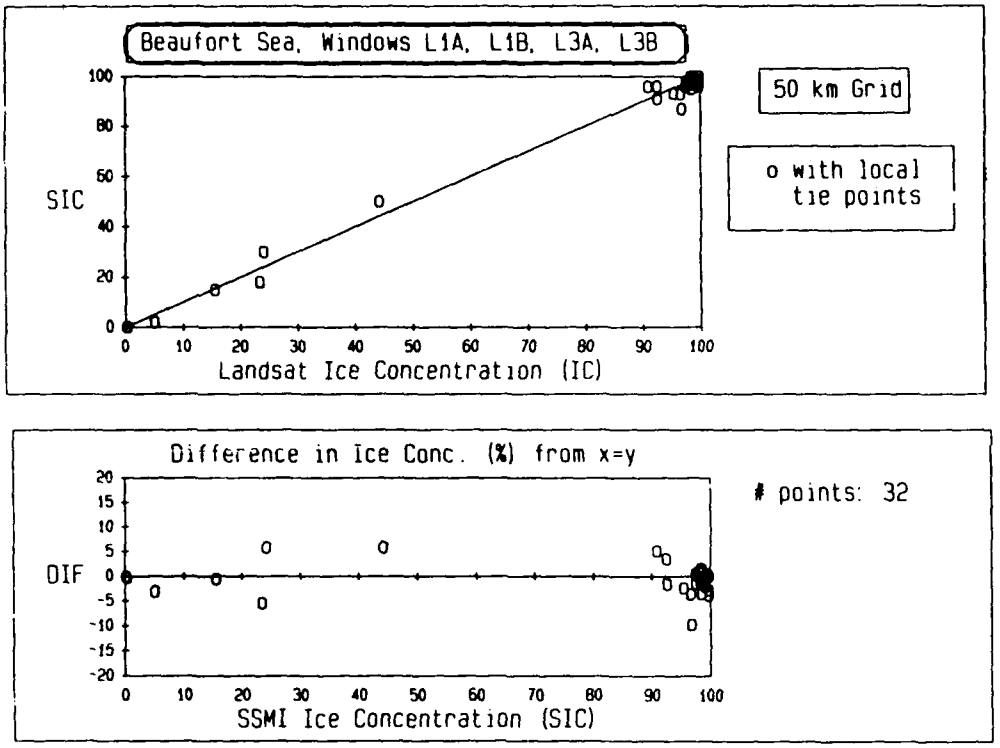

Figure 3. Beaufort Sea ice concentration comparison between Landsat and SSM/I-derived values for three days: 17 September 1987, 10 November 1987, and 12 March 1988. The data were averaged over 50-km cells before comparison (from Steffen et al. 1989).

This method provided imagery with a geolocation accuracy of 1.5 km. Once geocorrected, the photographic images were digitized and projected onto the 50-km SSM/I grid for analysis.

Two methods of ice classification were employed for calculating sea ice types and concentrations. First, a threshold technique provided brightness temperature ranges for different ice types and open water. Second, a tie-point algorithm provided ice concentrations from a linear relationship between two classes of brightnesses: open water and white ice. The latter method implicitly assumes that intermediate brightnesses represent subresolution mixtures of water and white ice. Intercomparison of the two classification techniques shows the tie-point algorithm method to produce more realistic ice concentration distributions (Steffen et al. 1988).

A total of 15 Landsat-SSM/I intercomparisons have been completed covering areas in the Beaufort, Bering and Chukchi seas in the Northern Hemisphere and the Weddell Sea in the Southern Hemisphere. Intercomparisons were made both for 25-km and 50-km grids. Since the archived ice product will be on a 50-km grid, only those results are discussed here. The SSM/I sea ice algorithm was run using both locally and globally defined tie-points. For the Beaufort Sea, four case studies provided an intercomparison of ice concentrations ranging from 0% to 100% and are presented in Figure 3. These results were obtained using locally defined tie-points. The mean ice concentration difference for all four cases is 2.3% and the mean standard deviation is 1.9%. Results of the other case studies and a more detailed discussion of the techniques employed in the Landsat-SSM/I comparisons are given in Steffen et al. (1988 and 1989). A key result of these 15 intercomparisons is that seasonally and regionally adjusted algorithm tie-points improve the agreement between the Landsat and SSM/I concentrations for the arctic regions studied. Global tie-points result in mean differences of up to 10%; the use of local tie-points reduces the mean difference to 3%. Interestingly, the difference is much less for the

Antarctic. For the Weddell Sea comparisons, the use of local tie-points reduces the mean difference from 4% for global values to 2% for local values.

Active/passive microwave comparisons: Aircraft underflights

While the Landsat analysis provides the best available measure of total ice cover for comparison with the SSM/I, no satellite data currently available can provide an accurate measure of multiyear ice concentration with which to validate the SSM/I product. The only sources of multiyear ice concentrations are the high-resolution microwave aircraft sensors flown during the NASA/Navy SSM/I aircraft underflights which were completed in March 1988. The overall goal of these flights was to acquire coincident aircraft and satellite data in different regions of the Arctic for the purpose of assessing the accuracy of the SSM/I-derived ice-edge position, total ice concentration and multiyear ice type concentrations. A secondary objective of the mission was to acquire the requisite data to determine the potential of the new 85-GHz SSM/I channels for polar research.

A total of 15 flights were made with both NASA and Navy aircraft covering portions of the Bering, Beaufort, and Chukchi seas. The NASA DC-8 carried both active and passive microwave sensors, a non-imaging infrared radiometer, aerial cameras, and a capability for utilizing the Global Positioning System. The complement of fixed-beam, dual-polarized radiometers supplied by Goddard Space Flight Center has frequencies and polarizations closely matching those of the SSM/I. The active sensors supplied by Jet Propulsion Laboratory included polarimetric C-, L-, and P-band synthetic aperture radars. The DC-8 flights were coordinated with two Navy research aircraft also supporting NASA's validation program. A Naval Research Laboratory P-3 provided high-resolution (100-meter) passive microwave imagery with the NORDA K_a-band Radiometer Mapping System (KRMS) operating at 33.6 GHz and an NADC P-3 provided wide-swath SAR coverage at C- and X-bands. Both aircraft provided mosaics measuring approximately 100 km by 200 km in area. These mosaics covered several SSM/I footprints and will be used to provide a direct check on the spacecraft algorithm and an estimate of the accuracy of the SSM/I-derived sea ice parameters. Although most of the flights were at night to obtain coincident observations with the SSM/I, some of the flights were made during daylight coincident with NOAA-9 and -10 and Landsat-4 and -5 overpasses. In addition to the aircraft/satellite comparisons, intercomparison of data from the three aircraft sensor suites are expected to provide additional checks on the algorithm and to identify potential algorithm improvements.

Preliminary results from these SSM/I underflights indicate that passive microwave imagery obtained with the KRMS, which can discriminate between open water, old ice, and a range of first-season ice types, provide an excellent check on the NASA DC-8 Aircraft Multichannel Microwave Radiometer (AMMR) profiles and SAR images. An intercomparison of coincident KRMS, SAR cross-polarized C-, L- and P-band, and AMMR data is presented in Figure 4. Dark areas in both the KRMS and C-band SAR imagery correspond to first-year ice whereas light areas correspond to multiyear ice types. These early results suggest that C-band provides good discrimination between multiyear and first-year sea ice types, while the longer wavelength P-and L-bands highlight ridges, but not ice types. The AMMR trace (18 GHz, H-pol.) is observed to delineate the transition from first-year ice off the Alaskan coast to multiyear ice in the central Arctic. Comparison of the AMMR data with the coincident SSM/I multiyear ice concentration map shows that the first-year, mixed, and multiyear ice regions are coincident with similar regions in the SSM/I data as well. The KRMS and SAR imagery shown in Figure 4 correspond to only a small portion of the AMMR trace (approx. 2 minutes of DC-8 flight time), but serve to establish the validity of the transition region as one of mixed ice types.

PRELIMINARY ASSESSMENT

From the several Landsat-SSM/I intercomparisons completed to date, the results show that the use of locally derived tie-points will provide more accurate ice concentrations from the SSM/I. Regionally and seasonally defined tie-points reduce the mean differences to 3% for the Arctic and 2% for the Weddell Sea. Global tie-points result in somewhat lower absolute accuracy because of the regional variability of the microwave signatures of sea ice, but do provide a coherent picture of the global ice cover and its temporal variability needed for monitoring climate change.

The aircraft analysis indicates that the SSM/I multiyear ice concentration maps provide good definition of the position of the edge of the multiyear ice pack if the 25% ice concentration contour is used as the indicator. There is, however, low level (<20%) multiyear ice concentration "noise" over much of the Arctic in general. The accuracy of this product at higher multiyear ice concentrations still remains to be determined. From the Beaufort Sea transect, we

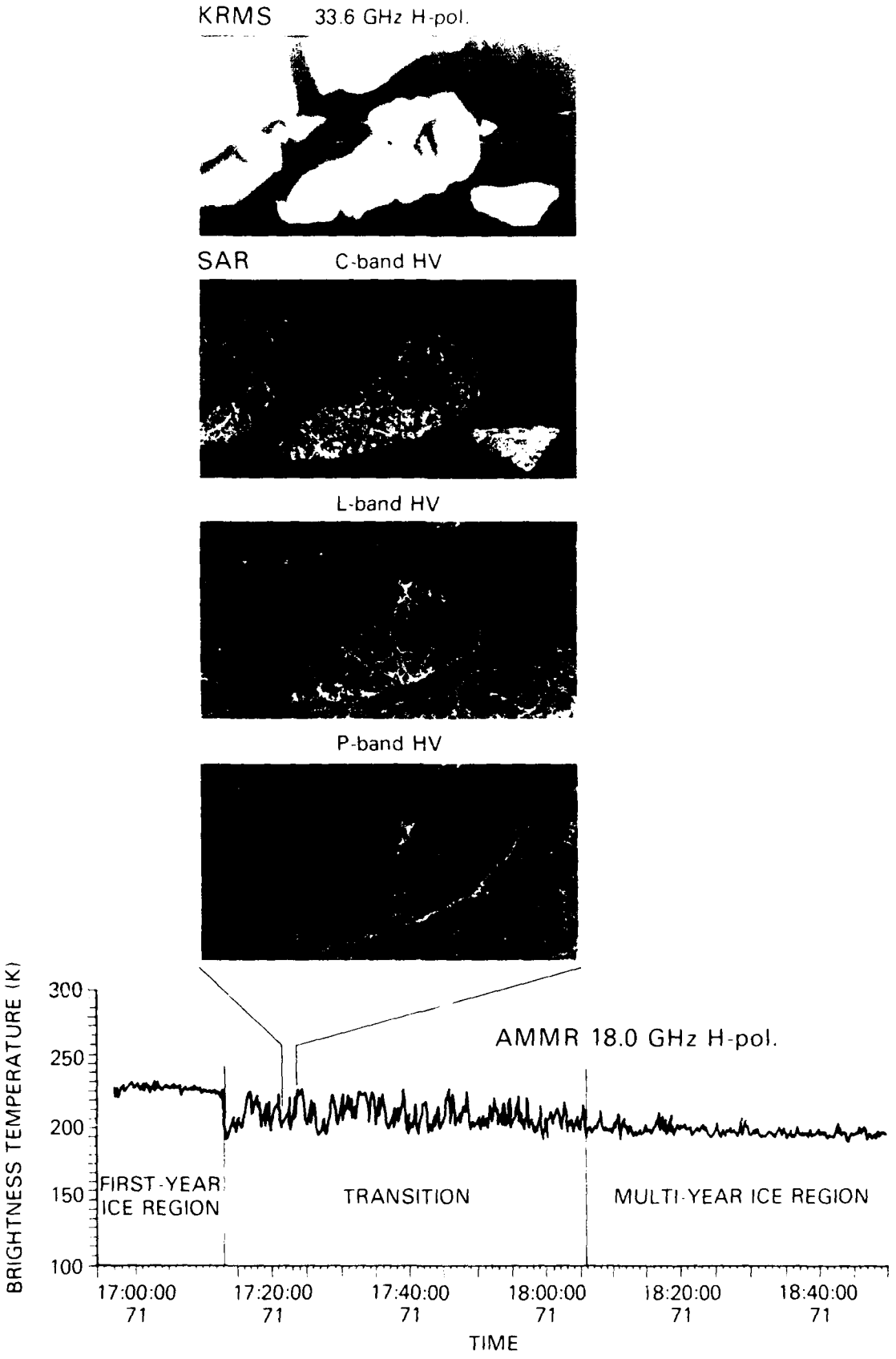

Figure 4. Comparison of KRMS (top), SAR (middle: C-, L-, and P-bands) and AMMR (bottom: 18 GHz H-pol.) data obtained with NASA and Navy aircraft over a portion of the Beaufort Sea.

find that the SSM/I multiyear ice map correctly delineates the first-year ice zone (multiyear ice concentrations≤20%), the transition zone of mixed multiyear and first-year ice, and the zone of predominantly multiyear ice. The SSM/I multiyear concentration map shows a curious drop in concentration just north of Ellesmere Island. Whether this is an actual drop in the fraction of multiyear ice in this region or whether it is due to a change in the multiyear ice signature is currently under study. Finally, a preliminary analysis of KRMS imagery shows variations in the microwave signatures of multiyear ice between the Beaufort and Chukchi seas suggesting once again that regional tie-points may be needed to obtain an optimum measure of multiyear concentration from SSMI.

REFERENCES

Cavalieri, D.J. and C.T. Swift (1987) NASA sea ice and snow validation plan for the Defense Meteorological Satellite Program Special Sensor Microwave/Imager. National Aeronautics and Space Administration, Washington, D.C., NASA Technical Memorandum No. 100683.

Cavalieri, D.J., P. Gloersen and W.J. Campbell (1984) Determination of sea ice parameters with the Nimbus 7 SMMR. *Journal of Geophysical Research*, **89**: 5355–5369.

Gloersen P. and D.J. Cavalieri (1986) Reduction of weather effects in the calculation of sea ice concentration from microwave radiances, *Journal of Geophysical Research*, **91**: 3913–3919.

Hollinger, J., R. Lo, G. Poe, R. Savage and J. Peirce (1987) Special Sensor Microwave/Imager User's Guide. Naval Research Laboratory, Washington, D.C.

Steffen, K., A.J. Schweiger, R.G. Barry and R.L. Weaver (1988) DMSP-SSM/I NASA algorithm validation using primarily Landsat and secondarily DMSP and/or AVHRR visible and thermal infrared satellite imagery. Annual Progress Report to NASA Goddard Space Flight Center, Greenbelt, Maryland.

Steffen, K., A.J. Schweiger, R.G. Barry and R.L. Weaver (1989) DMSP-SSM/I NASA algorithm validation using primarily Landsat and secondarily DMSP and/or AVHRR visible and thermal infrared satellite imagery. Semi-Annual Progress Report to NASA Goddard Space Flight Center, Greenbelt, Maryland, January 1989.

NASA SSM/I Data Processing and Archiving of Sea Ice Products

C.S. MORRIS
Jet Propulsion Laboratory
California Institute of Technology
Pasadena, California, U.S.A.

ABSTRACT/INTRODUCTION

More than a year after launch of the first Special Sensor Microwave/Imager (SSM/I), a passive microwave radiometer carried onboard the Defense Meteorological Satellite Program (DMSP) F-8 satellite, the NASA data processing activities for snow and ice research are in full swing. The processing and archiving of NASA SSM/I polar data were undertaken as a cooperative effort between the NASA Ocean Data System (NODS) and the National Snow and Ice Data Center (NSIDC) in Boulder, Colorado.

The NSIDC has the long-term responsibility for archiving the data, while NODS was tasked with developing the software system. Principal archived products from this effort include global swath brightness temperatures, daily average polar brightness temperatures, three-day average polar sea ice concentrations (first-year, multiyear, total), and daily ice edge location. As part of the archiving task, both NODS and NSIDC are supporting the efforts of the NASA SSM/I Validation Team, which is charged with evaluating the antenna/brightness temperatures measured by the instrument and calibrating/validating the NASA sea ice concentration algorithm(s) used by NODS/NSIDC.

SSM/I INSTRUMENT AND DATA

The SSM/I instrument is a passive microwave radiometer developed by Hughes Aircraft Corporation. It has seven channels spanning four frequencies (19.3, 22.2, 37.0, and 85.5 GHz) with horizontally and vertically polarized channels for each frequency except the 22.2 GHz. The 22.2 GHz frequency has only a vertically polarized channel. SSM/I sweeps out a swath behind the spacecraft of about 1400-km width every 1.9 seconds. For each pair of scans made, the two 85.5-GHz channels are measured 256 times, while the other five channels are measured 64 times during only one of the two scans. Additional information on

the SSM/I instrument can be found in the *Special Sensor Microwave/Imager User's Guide* (Hollinger et al. 1987).

The DMSP F-8 satellite was launched on 20 June 1987 (GMT) into a polar orbit. After the initial instrument checkout, the first sensor data from SSM/I were taken on 9 July 1987. The first several months of data were impounded by the Navy so that their CAL/VAL Team could review the performance of the SSM/I instrument. On 17 November 1987, the Navy officially released the SSM/I swath antenna and brightness temperatures.

NODS began receiving SSM/I swath antenna temperatures via the Satellite Data Services Division (SDSD) of NOAA/NESDIS in mid-March 1988, nine months after launch. The data used by NODS and NSIDC are produced by the Fleet Numerical Oceanography Center (FNOC). Direct data receipt from FNOC was not possible because of the Shared Processing Agreement on data distribution between SDSD, the Navy and the Air Force.

DATA PROBLEMS

It was anticipated that the initial two months of data processing at NODS would be spent testing out the software system. However, even before NODS had received any data, problems in the data, which would require modifications to the software system, became apparent to various researchers. These included an error in the geolocation of the data, a satellite recorder anomaly and apparent data transmission glitches. The latter two introduced spurious data into the data files.

The first system modification involved correcting the latitude and longitude values included with each observation. These values pinpoint the location on the Earth of the center of the observation footprint. By comparing the location of the coastline in the SSM/I data, which is denoted by a steep gradient in the brightness temperatures, it was discovered by several investigators that the latitude/longitude values given in the data were in error by approximately 25 km. Considering that the spatial resolution of the brightness temperature observation is of the same order or greater, depending on the channel, as the location error, this posed a significant obstacle to producing high-resolution products. The problem for gridded products is compounded in that the error will result in a 50-km smear because the spacecraft passes over the grid cell from different directions.

NODS has adopted, at the recommendation of the NASA SSM/I Validation Team, a technique proposed by Mark Goodberlet and Calvin Swift at the University of Massachusetts and Konrad Steffen at CIRES, University of Colorado, to correct the retrospective data. This technique assumes that the shift in the location values is due to a pointing error that can be compensated for by adjusting the roll, pitch and yaw angles of the spacecraft. Islands are used as targets and a regression analysis is used to determine the yaw, pitch and roll values that provide the best agreement between the islands and their antenna temperature images. These yaw, pitch and roll values are then used to correct the latitude and longitude of each swath scene station. This correction is expected to improve the geolocation accuracy to better than 10 km.

Because of the empirical nature of geolocation correction, it has been decided that the NODS/NSIDC swath data archive will not include the corrected locations. The routine to perform the correction will be made available to researchers who wish to use the swath data. The corrections will be applied to the swath data prior to producing the gridded products so that the 50-km smear will be minimized.

It should be noted that the Navy also has been investigating the geolocation problem. Corrections should be implemented in the processing performed at FNOC in the near future. Thus, the need for applying a geolocation correction to the FNOC data may eventually be eliminated.

The second system change was required to detect and manage data anomalies created as a result of a problem with the spacecraft recorder. On an average, more than one swath data file per day (each file is about one orbit) would have spurious data appended to the beginning of the file. This would often show up as a few scans of bad data followed by a time gap or regression after which the "valid" data would be given. The situation was further complicated because the bogus data could masquerade as valid data and the date tag on the valid data might have been changed by a day when the spurious data were added. Fortunately, this problem was corrected by the Navy by the beginning of February 1988.

Losing more than 10% of the available data during 1987 and early 1988 is not acceptable. Thus, software and operational procedures have been developed to detect potential problem files and edit them so that the good data can be retained while maintaining the appropriate quality control. This software has been implemented.

The last major problem was discovered in data beginning in January 1988. Apparently, more than 10% of the FNOC data files suffer from a transmission problem that causes antenna/brightness temperature

values in the lower five channels to alternate between reasonable values and values that are either extremely high (by hundreds of kelvins) or unrealistically low. This effect usually begins at the start of an FNOC data file and can last for a few scans or a complete orbit. Although a significant percentage of FNOC files have this problem, only a small fraction of the data is actually questionable. The software developed by NODS to deal with the data recorder problem was modified to detect and remove the corrupted data resulting from the suspected transmission problem.

Although NODS and NSIDC are taking steps to eliminate periods of bogus data, users of these data should be aware that such problems exist and might show up in the data set. (Other distributors of SSM/I data are either noting problem time periods or leaving it up to the user to find the problems.) Despite these data problems, which corrupt only a very small percentage of the data record, the SSM/I data are of high quality and will prove useful to researchers for many years to come.

CURRENT AND FUTURE DATA ARCHIVING ACTIVITIES

When NODS received the first SSM/I data shipment, several weeks of data were loaded into the computer-based archive in order to test the software system. After data from early 1988 became available, the focus of NODS archiving was diverted, at the request of the NASA SSM/I Validation Team, to the January through March 1988 time period. These data are important to the NASA Validation Team because they covered the time period before and during research aircraft underflights of the SSM/I sensor. NODS has processed, archived, and distributed these SSM/I swath brightness temperatures to the Validation Team. During this initial period, only selected periods of gridded polar brightness temperatures and sea ice concentrations were produced, owing to the geolocation error in the swath data.

The long-term repository for NASA polar SSM/I data is NSIDC. NODS has delivered to NSIDC development versions of the processing and archiving system, so that their personnel could be trained in the operational procedures. Recently, the operational system has been delivered and NSIDC has begun operational processing of SSM/I data.

NODS and NSIDC are currently in a transition period, expected to last until October 1989, during which both groups will be processing and archiving SSM/I data. During the transition period, NSIDC will handle the more current SSM/I data. Gridded products will be produced after correcting the data locations with the geolocation correction scheme. During this period, NODS will have the responsibility to clean up, process, and archive the SSM/I data from July 1987 to May 1988. After the transition, the NASA polar SSM/I data-archiving responsibility will be wholly with NSIDC.

Rapidly improving technology has made it cost effective to provide data to users in ways that were not originally envisioned when the computer-based NSIDC Cryospheric Data Management System (CDMS) was originally designed some four years ago (see Weaver et al. 1987). The emphasis has shifted from an on-line data archive to mass distribution of data to researchers at their home institutions. For NASA polar SSM/I data distribution, the gridded polar one-day average brightness temperature and three-day average ice concentration grids will be available on CD-ROM. As planned, the CD-ROM's will contain about three months of data and will be issued four times a year. The first CD-ROM containing SSM/I gridded polar data should be available by the end of 1989.

ACKNOWLEDGMENTS

This work was carried out at the Jet Propulsion Laboratory, California Institute of Technology, under contract with the National Aeronautics and Space Administration.

REFERENCES

Hollinger, J., R. Lo, G. Poe, R. Savage and J. Peirce (1987) Special Sensor Microwave/Imager User's Guide. Naval Research Laboratory, Washington, D.C.

Weaver, R., C. Morris and R.G. Barry (1987) Passive microwave data for snow and ice research: Planned products from the DMSP SSM/I system. *Eos*, p. 776.

Validation of the SSM/I and AES/YORK Algorithms for Sea Ice Parameters

C.A. BJERKELUND
Norland Science and Engineering Ltd.
Ottawa, Ontario, Canada

R.O. RAMSEIER AND I.G. RUBINSTEIN
Atmospheric Environment Service
Institute for Space and Terrestrial Science
York University, North York, Ontario, Canada

ABSTRACT/INTRODUCTION

The Special Sensor Microwave Imager (SSM/I) is the latest and most versatile of the spaceborne radiometers launched since the early 1970s. Global monitoring of atmospheric and surface geophysical features has been achieved by developing algorithms to convert radiometric brightness temperatures to the required physical parameters. In recognition of the importance of SSM/I to the operational community, the Naval Research Laboratory (NRL) established a working group to validate and calibrate SSM/I radiances and operational algorithms. The validation of SSM/I for sea-ice parameters was carried out by the Atmospheric Environment Service (AES), Environment Canada, from June 1987 to September 1988, and involved the statistical analysis of SSM/I data with almost coincident radar imagery. The validation also included the operational demonstration of the AES/YORK algorithm for ice reconnaissance and forecasting, and was carried out at the AES Ice Branch in Ottawa and at the U.S. Navy/National Oceanic and Atmospheric Administration Joint Ice Center in Washington, D.C. A final validation report by the sea-ice group was produced for NRL in December 1988 (Ramseier et al. 1988a).

The validation objective was to assess the accuracy of the SSM/I and AES/YORK algorithm products using the best corroborative information available. The performance of the algorithms was assessed for total ice concentration, ice fraction concentration, and ice edge location for different seasons and ice regimes. One of the main requirements imposed on the algorithms was for them to be operationally useful under all weather conditions.

ALGORITHMS

The algorithm used by the U.S. Navy for the SSM/I was developed during the 1970s by Environmental Research and Technology Inc. under a subcontract from Hughes Aircraft Corporation, and was tested during the NIMBUS satellite series with the scanning microwave radiometers (SMMR). The SSM/I algorithm was tested extensively from 1982 to 1987 by the Ice Research and Development Division of AES's Ice Branch for both research and operational purposes.

To improve the retrieval of ice information in all weather conditions and to optimize the use of SMMR channels, and subsequently SSM/I, another algorithm was developed known as the AES/YORK version. It also underwent research and operational testing from 1984 to 1987 and was updated in 1987 before the SSM/I launch by AES and the Microwave Group at the Institute of Space and Terrestrial Science (ISTS), York University. The AES/YORK algorithm incorporates weather and sea state corrections to aid in the retrieval of ice parameters for operational ice reconnaissance (Ramseier et al. 1988b). The validation criteria for both the SSM/I and AES/ YORK algorithms are listed in Table 1.

METHODOLOGY

The validation procedure involved the geographical registration of the radar imagery to algorithm maps provided at an equivalent scale to that of the radar imagery. The imagery was analyzed at each footprint for total ice concentration and/or ice fraction, and along the AES/ YORK 10% ice concentration contour and SSM/I 30% ice concentration contour for ice edge location. Inaccuracy, which could be introduced by interpreter bias in estimating ice concentration, was reduced by the use of a sampling template.

Errors because of orbit shift were minimized by implementing a constant 25-km backward shift along the track. However, this did not eliminate systematic errors such as the interpretation of open water or thin ice, rough first-year ice, or old ice. The higher resolution of the radar imagery (which can vary from 30 to 400 m in azimuth as a function of range for the SLAR, and 18 m across all the range of the SAR) caused interpretation difficulties for convoluted ice edges when compared to the SSM/I grid spacing of 25 × 25 km, which results in a relatively smooth ice edge. Radar data were available only during weather conditions suitable for flying, which eliminated validation of SSM/I under severe storm conditions. Altogether over 1.6 million square kilometers was validated for ice concentration and more than 6000 km was validated for ice edge positi ..

Table 1. Ice and wind parameter requirements for SSM/I validation.

Parameter	*Geometric resolution required (km)*	*Range of values*	*Quantization levels*	*Validation criteria*
SSM/I algorithm				
Ice				
Concentration	25	0 to 100%	5%	12%
Age	50	First-year	1 yr	None
		Multiyear	> 2 yr	None
Edge location	25	Present/absent	N/A	12.5 km
Ocean				
Surface wind speed	25	3 to 25 m/s	1	2 m/s
AES/YORK algorithm				
Ice				
Concentration	25	0 to 100%	7%	10%
Age	25	fractions of		
		0–100% first-year	1 yr	10%
		Old ice	> 2 yr	10%
Edge location	25	Present/absent	N/A	12.5 km
Ocean				
Surface wind speed	25	3–40 m/s	1	2 m/s

RESULTS

Table 2 summarizes the validation results and indicates the the AES/YORK algorithm performed better than the SSM/I algorithm for geographic area, season, and time class for total ice concentration. The AES/YORK algorithm met the acceptance criteria for ice edge location more frequently than the SSM/I algorithm. The results from the ice fraction validation are still preliminary and require additional validation work. The old ice concentration was generally less than 20% of the total concentration, and the data set was not considered an adequate validation of the algorithm performance.

There are additional shortcomings with the SSM/I algorithm that are not apparent in the statistical results concerning adverse weather conditions and the appropriateness of the ice edge contour. In particular storms, e.g., in the Gulf of Alaska or Labrador Sea, there were areas occasionally shown by the algorithm as ice-covered where no ice should be present. The problem could be eliminated by a suitable weather filter algorithm, as is incorporated in the AES/YORK algorithm.

The appropriateness of the 30% SSM/I ice edge contour is questioned because of the high ice concentration observed along it; the ice edge (or 0% ice concentration contour) as observed on the radar imagery corresponded to a SSM/I algorithm ice concentration of between 25 and 50%, with an average of 35% ice concentration, depending on ice type. The 30% SSM/I algorithm ice contour (used as effective ice edge) was observed to correspond to an average ice concentration of 56%. In comparison, the AES/YORK algorithm at the 0% radar ice concentration contour corresponded to an ice concentration of between 0 and 25%, with an average ice concentration of 16%, depending on ice type, and the 10% AES/ YORK algorithm ice edge corresponded to an average ice concentration of 25%.

The SSM/I algorithm was designed to flag the presence of old ice only when the old ice concentration reached about 35% or more of the total ice concentration. Because it only flags, but does not determine, the ice fraction concentration, this reduces its usefulness for operational purposes. The AES/YORK algorithm is designed to provide open water, first-year, and old-ice fractions. It also allows retrieval of the ocean surface wind speeds, cloud cover, precipitation, and water vapor for ice-free areas (Ramseier et al. 1988b).

RECOMMENDATIONS

1. Based on the validation results (Table 2) the AES/YORK ice algorithm is recommended over the SSM/I ice algorithm for operational use.

2. Validation of the AES/YORK algorithm should continue for another year to fine-tune the algorithm

Table 2. Final conclusions on the SSM/I and AES/YORK algorithm performance.

Major group	Ice concentration			Ice edge displacement		
	Accuracy (%)	95% C.I.	Meets criteria	Accuracy (km)	95% C.I.	Meets criteria
SSM/I algorithm						
Combined area						
Pooled, less than 3 h*	−17.2	1.6	No	−10.3	2.3	Marginal
Season						
Ice formation	−19.5	1.4	No	−9.8	2.8	Marginal
Winter	−18.4	1.7	No	+4.2	9.0	No
Initial ice melt	−6.6	1.9	Yes	−12.6	3.9	No
Ice melt	−20.7	1.7	No	−11.8	5.0	No
Arctic						
Pooled, less than 3 h	−13.6	1.7	No	−10.5	2.5	Marginal
Ice fraction						
First-year	+6.5	5.4	Yes			
Old ice	−10.8	5.4	No			
Gulf of St. Lawrence						
Pooled, less than 3 h	−27.9	3.2	No	−9.7	3.8	Marginal
AES/YORK algorithm						
Combined area						
Pooled, less than 3 h	−6.3	1.3	Yes	−0.2	1.9	Yes
Season						
Ice formation	−9.1	1.3	Marginal	−0.7	2.6	Yes
Winter	−5.5	1.0	Yes	+21.1	9.6	No
Initial ice melt	−5.1	2.7	Yes	−4.0	9.5	Marginal
Ice melt	−11.5	1.7	No	−4.3	3.6	Yes
Arctic						
Pooled, less than 3 h	−5.8	1.6	Yes	−3.1	2.1	Yes
Ice fraction						
First-year	−8.0	2.7	Marginal			
Old ice	+6.5	2.6	Yes			
Gulf of St. Lawrence						
Pooled, less than 3 h	−7.8	2.2	Yes	−7.4	4.2	Yes

* Pooled, less than three hours of data collection.

using the best combination of observations available (from AIMR, SAR, infrared, etc.).

3. To achieve recommendation 2 and to test possible improvements with the introduction of higher frequency channels, the airborne imaging microwave radiometer (AIMR), operating at 37 and 90 GHz with dual polarization, will be the primary sensor.

4. Detailed analysis of major experimental data from 1) the NRL P-3 Gulf of St. Lawrence experiment (January 1988), 2) the BEPERS experiment in the Gulf of Bothnia (March 1988), 3) LIMEX experiment in the Labrador Sea (March 1989), 4) the *Polarstern* experiment (April–July 1989) in the Arctic Ocean and East Greenland Sea, and 5) the *Polarstern* experiment in the Weddell Sea (August–October 1989) should provide a more global evaluation of the ice algorithm.

REFERENCES

Ramseier, R.O., C. Bjerkelund and I.G. Rubinstein (1988a) Final report on the validation of the SSM/I and AES/YORK algorithms for sea ice parameters. Prepared for the U.S. Naval Research Laboratory SSM/I Validation Team.

Ramseier, R.O., I.G. Rubinstein and A.F. Davies (1988b) Operational evaluation of special sensor microwave/imager by the Atmospheric Environment Service. Centre for Research in Experimental Space Science, York University, North York, Ontario, Canada.

Remote Sensing of Ocean Surface Winds with the Special Sensor Microwave/Imager (SSM/I)

M.A. GOODBERLET AND C.T. SWIFT
University of Massachusetts
Amherst, Massachusetts, U.S.A.

ABSTRACT/INTRODUCTION

The Defense Meteorological Space Program (DMSP) Special Sensor Microwave/Imager (SSM/I) wind speed retrieval algorithm developed by Environmental Research and Technology Inc. (ERT) under contract from Hughes Aircraft is called the *D*-matrix algorithm and has the following form (Lo 1983):

$$SW = C0(j)+C1(j)T_B(19H) + C2(j)T_B(22V) + C3(j)T_B(37V)+C4(j)T_B(37H). \quad (1)$$

Equation 1 is valid only over the open ocean where the wind speed, SW, is in m/s and referenced to a height of 19.5 m above the surface. Equation 1 also contains the terms $T_B(x)$ which represent the SSM/I measured brightness temperature of frequency/polarization combination x and the *D*-matrix coefficients, $Ci(j)$, where j is the climate code index and varies from one to nine. Each of the nine distinct climate codes represents a particular season and latitude band (Lo 1983).

The amount of microwave energy being emitted from the ocean surface is dependent on the wave structure and foam coverage (Ulaby et al. 1986a). Therefore, by measuring the ocean surface microwave emission, the SSM/I is able to predict ocean surface wind speed. Microwave emission at the SSM/I frequencies coming from the ocean surface is effectively masked by the emission and attenuation characteristics of rain and large amounts of water vapor in the earth's atmosphere. Realizing this, ERT suggested the use of the rain-flags, 0, 1, and 2, which identify the conditions of no rain, possible rain, and heavy rain, respectively. These flags are set on the basis of predetermined thresholds for $T_B(19H)$ and the difference between $T_B(37V)$ and $T_B(37H)$ (Lo 1983).

The DMSP accuracy specification for wind speed retrievals under rain-free conditions (i.e., rain-flag = 0) is 2 m/s (standard deviation) over the range 3 m/s to 25 m/s. Accuracy was not specified for wind retrievals from cells flagged either 1 or 2. In fact, the original *D*-matrix algorithm did not attempt to retrieve winds under rain-flag 2 conditions.

NOAA BUOY SYSTEM AND CRITERIA FOR COMPARISON

Validation of the SSM/I wind speed retrievals was done using the anemometer-measured winds of open ocean buoys maintained by the National Oceanic and Atmospheric Administration (NOAA). These buoys make an 8.5-minute average of the wind once every hour with an accuracy of 0.5 m/s for winds of less than 10 m/s and 5% for winds greater than 10 m/s (Gilhousen 1986).

To avoid land contamination of ocean brightness temperatures and to ensure that the land did not restrict the wind speed fetch distance necessary for creating fully developed seas (Ulaby et al. 1986b), only buoys further than 100 km from land were chosen for the validation. Nineteen of the NOAA buoys were used for the validation and their wind speed observations, taken at heights of either 5 or 10 m above the surface, were converted to equivalent winds at 19.5 m above the surface (Liu and Blanc 1984) so that they could be compared directly to the 19.5-m referenced *D*-matrix winds. Converted buoy winds and D-matrix winds were paired only when the SSM/I retrieval was located within 25 km of the buoy position and the SSM/I overpass time was within 30 minutes of the buoy wind speed measurement. Based on the work of Monaldo (1988) the error introduced by the average values of these spatial and temporal differences between SSM/I and buoy measured wind speeds is less than 10% of the total standard deviation of 2 m/s.

REQUIRED NUMBER OF COMPARISONS

In determining the required number of buoys for the validation, one must consider how often each buoy lies within the swath of an SSM/I overpass. The number of SSM/I overpasses depends on the latitude, LAT, of the buoy and can be approximately calculated using eq 2, which is reasonably accurate up through 60° latitude, above which the error exceeds 15%:

$$\text{SSM/I overpasses in 30 days} = 30/\cos(\text{LAT}). \quad (2)$$

The accuracy specification of 2 m/s for D-matrix wind speed retrievals is interpreted as the standard deviation of the comparison between *D*-matrix winds and buoy winds in any subinterval of the 3- to 25-m/s wind speed range. Shown in Table 1 is the number of comparisons out of 1,000 for which the buoy wind

TABLE 1. Expected number of *D*-matrix/buoy wind speed comparisons per 1000 which fall into selected subintervals of the 3-m/s to 25-m/s wind speed range.

ID	*Range (m/s)*	*Comparisons per 1000*
1	3–6	260
2	6–10	395
3	10–14	215
4	14–18	50
5	18–22	25
6	22–25	1

speed falls within each of six selected subintervals of the 3- to 25-m/s range. These comparison counts are based on the global distribution of winds given by Schroeder and Sweet (1986).

It is preferable to have a sample size of 30 or more when doing statistical analysis (Book 1977) of the data. For wind speed subintervals 1, 2, and 3, it appears that this sample size can be obtained by collecting approximately 140 comparisons. Approximately 15% of the data are rain flagged and, since the comparisons are made only with data which is not rain flagged, the sample size required for each climate code must be increased 15% from 140 to 161. Other factors affecting the total required buoy count include lost data due to periodic buoy maintenance and the likelihood of encountering wind speeds distributed according to Schroeder and Sweet (1986). These factors were determined from actual climatic summaries for the individual data buoys which are available from the National Data Buoy Center (Gilhousen et al. 1986b). The climatic summaries established that the 19 buoys selected could more than satisfy the low wind speed validation requirements.

However, the low probability of observing winds greater than 15 m/s makes it difficult to evaluate the overall performance of the D-matrix algorithm in the range from 15 to 25 m/s.

VALIDATION RESULTS

Performance of the climate code 5 (25–50° latitude, spring and fall) version of the original *D*-matrix algorithm is shown by the scatter-plot in Figure 1. Given in the legend of Figure 1 is the *y*-intercept (*bias*) and slope of the regression line, which has been chosen to minimize the sum of the squares of the horizontal distances from each point to the regression line.

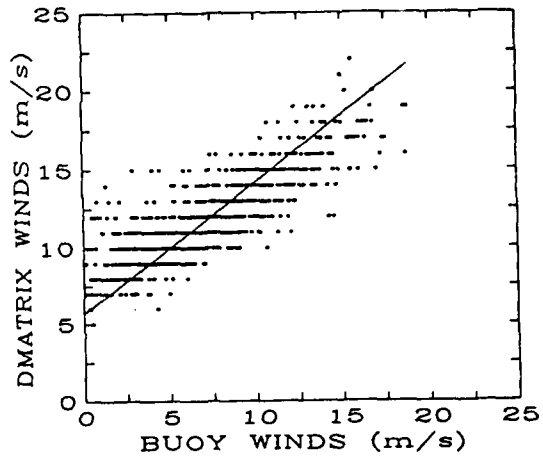

Figure 1. Performance of the original D-*matrix algorithm for climate code 5. Bias = 5.7 m/s, slope = 0.85, SD = 5.1 m/s, corr (R) = 0.82, #OBS = 998.*

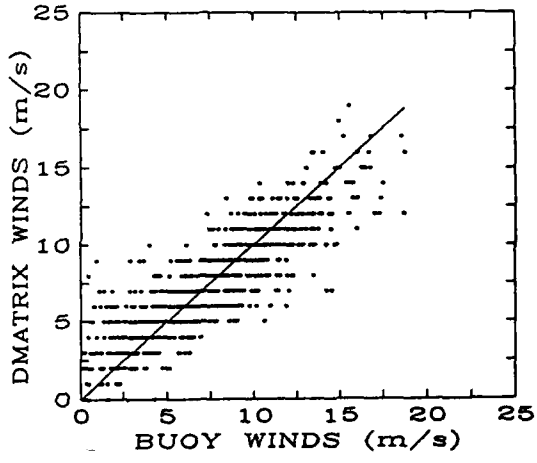

Figure 2. Performance of the revised D-*matrix algorithm for climate code 5. Bias = 0.0 m/s, slope = 1.0 m/s, SD = 1.9 m/s, corr (R) = 0.85, #OBS = 998.*

The SD is the standard deviation of the quantity (*D*-matrix winds minus buoy winds). The term "Corr(R)" is the correlation coefficient (Book 1977) between buoy winds and *D*-matrix winds and the term "#OBS" represents the number of observations or data points in the scatterplot. The poor performance of the climate code 5 algorithm is typical of all nine versions of the original *D*-matrix algorithm. To correct this problem new coefficients were generated using standard linear regression of the buoy wind speed on the coincident SSM/I brightness temperature measurements, $T_B(19H)$, $T_B(22V)$, $T_B(37V)$, and $T_B(37H)$, and the rain-flag criteria were revised. Performance of the new climate code 5 *D*-matrix algorithm is shown in Figure 2. Performance of all nine versions of the revised *D*-

Table 2. Performance of the nine climate code *D*-matrix algorithm.

Climate code	*SD (m/s)*	*Percentage rain flagged*	*Number of comparisons*
1	1.5	17	376
2	1.4	10	63
3	1.5	8	109
4	1.5	9	43
5	1.8	13	1296
6	1.5	12	643
7	1.9	18	516
8	1.8	19	279
9	1.6	9	277

matrix algorithm is summarized in Table 2 and the new coefficients for the algorithm are given in the SSM/I Cal/Val final report (Hollinger 1989). Despite the apparent good performance of the new algorithms, additional improvements are necessary.

In Figure 3, the *D*-matrix wind speed residual is plotted as a function of buoy measured wind speed using data from climate code 5. Dividing the region of Figure 3 into a number of vertical bins and calculating the SD and bias (i.e., average) of the points falling within each bin results in the "interpreted" residual plot shown in Figure 4, which indicates that the accuracy of the *D*-matrix retrievals is best near the global average wind speed of 7 m/s and becomes worse for predictions away from 7 m/s.

Discontinuity of the retrieved winds across climate code boundaries is another problem with the nine-version *D*-matrix algorithm. The average discontinuity across each latitude band boundary was calculated using actual SSM/I data and was found to be as high as 2.0 m/s but was typically 1.0 m/s.

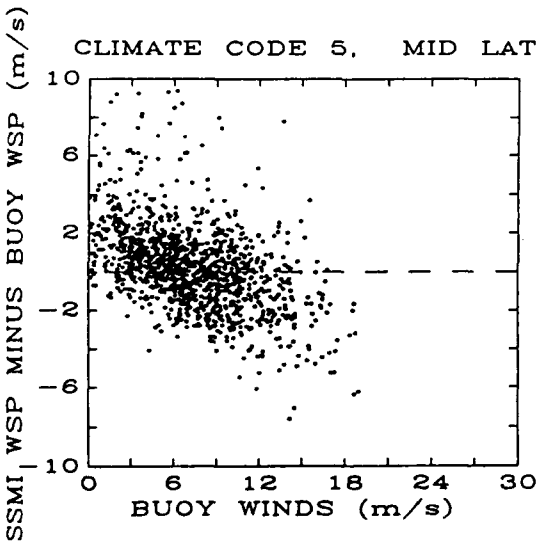

Figure 3. D-matrix residual plotted as a function of the coincident buoy winds for climate code 5.

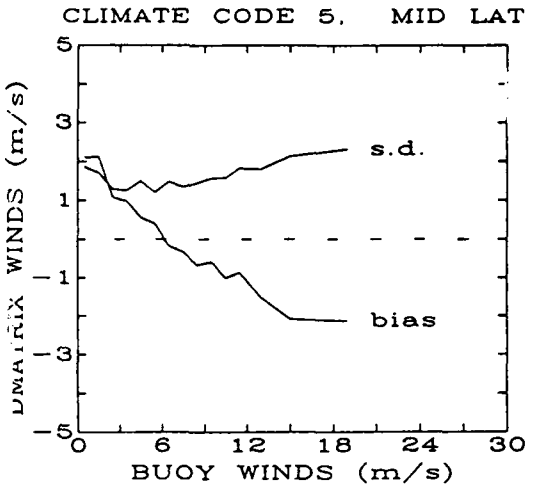

Figure 4. Standard deviation and bias of the D-matrix retrieved winds plotted as a function of buoy wind speed for climate code 5.

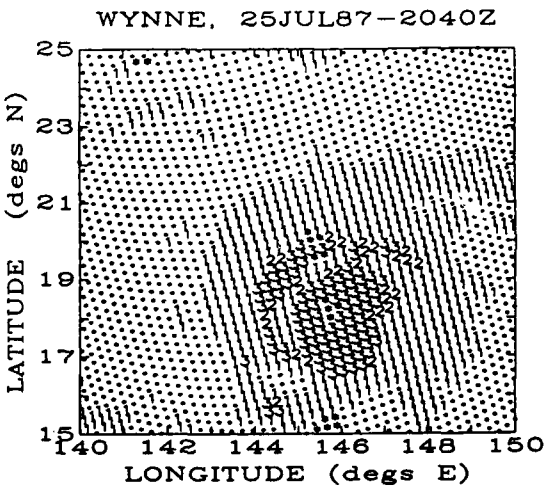

Figure 5. Rain-flagged areas of typhoon Wynne on 25 July 1987. The dots and asterisks indicate rain-flag zero areas and land (Mariana Isles) respectively. The numbers 1, 2, and 3, correspond to rain-flags 1, 2 and 3.

The fact that the accuracy of the SSM/I wind speed retrievals deteriorates rapidly in areas where rain and heavy cloud cover are found severely limits the ability of this instrument to map the wind field in and around typhoons, hurricanes and tropical storms. Figure 5 shows the rain-flagged areas of typhoon Wynne as it appeared on 25 July 1987 at approximately 2040 hours GMT. According to aircraft reconnaissance data collected by the Air Force/Navy Joint

Typhoon Warning Center, the rain-flag 3 area outline corresponds roughly to the 25-m/s wind speed radius of this storm which had visually observed winds as high as 60 m/s near its center.

ALTERNATE WIND SPEED ALGORITHM

A single *D*-matrix algorithm, valid at all latitudes and during all seasons, was developed and found to meet the 2 m/s accuracy specification under rain-free conditions. Details of the global algorithm are given in Table 3. Note the use of the four rain-flags and their interpretation which differs considerably from the rain-flag criteria of the original ERT algorithm. It is recommended that wind speeds be calculated under all conditons and that the associated rain-flag be the user's guide to the accuracy of the retrieval.

Table 3. Specifications of the global *D*-matrix algorithm.

$$SW = 147.90 + 1.0969\,T_B(19V) - 0.4555\,T_B(22V) + -1.7600\,T_B(37V) + 0.7860\,T_B(37H)$$

Rain flag	*Criteria*	*Accuracy (m/s)*
0	$T_B(37V) - T_B(37H) > 50$ $T_B(19H) < 165$	<2
1	$T_B(37V) - T_B(37H) < 50$ $T_B(19H) < 165$	2–5
2	$T_B(37V) - T_B(37H) < 37$	5–10
3	$T_B(37V) - T_B(37H) < 30$	>10

Wind speed cutoff at 25 m/s.

The global wind speed algorithm was developed using 100 randomly selected SSM/I buoy matchups from each of the nine climate codes. Out of this 900-point data set, only the 708 rain-flagged either 0 or 1 were retained and used to develop the new algorithm. In this way, the global algorithm was based on data from types of weather systems where accurate wind speed retrievals were likely, while at the same time being made somewhat tolerant of rain.

Coefficients for the algorithm were generated using a weighted linear regression (Draper and Smith 1981) of the buoy wind speeds on the coincident SSM/I brightness temperatures of $T_B(19V)$, $T_B(22V)$, $T_B(37V)$, and $T_B(37H)$. Note that the new algorithm uses $T_B(19V)$ since it resulted in slightly more accurate retrievals than if the ERT suggested $T_B(19H)$ was used. The weights used in the regression were set equal to one over the square root of the wind speed density function (Schroeder and Sweet 1986), evaluated at the particular buoy wind speed. This type of weighting has the effect of making all wind speed ranges equally important in the creation of the new algorithm. In contrast, the unweighted regression used previously tends to emphasize those wind speed ranges with a lot of data and de-emphasize the ranges with few data. This is precisely why the original *D*-matrix performed well near the global average wind speed of 7 m/s and performed poorly (both in terms of SD and bias) in the high (>15 m/s) range.

True performance of the alternative global wind speed algorithm under rain-free conditions is indicated by the "interpreted" residual plot shown in Figure 6.

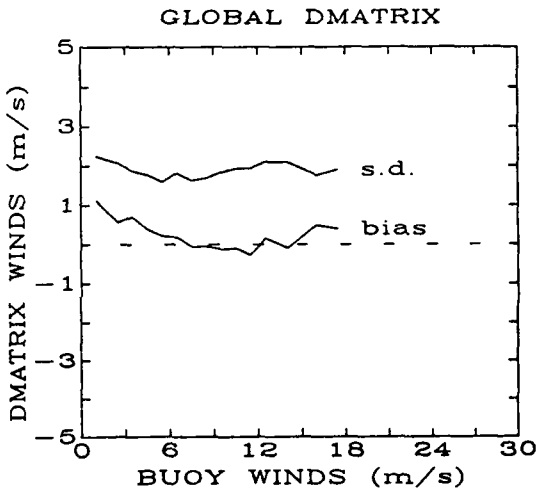

Figure 6. Standard deviation and bias of the global D*-matrix retrieved winds plotted as a function of buoy wind speed.*

Comparison of Figure 6 with Figure 4 shows that much of the high wind speed bias associated with the original *D*-matrix retrievals has been removed by the weighted regression technique. The average retrieval SD of the new algorithm is found to be 2.0 m/s which meets the ±2 m/s DMSP accuracy specification.

CONCLUSIONS

Although wind speed retrievals from the ERT nine-version *D*-matrix algorithm did not meet the DMSP accuracy specification of 2 m/s, regeneration of the *D*-matrix coefficients using standard linear regression resulted in a set of algorithms whose retrievals did meet specifications.

An alternative global *D*-matrix algorithm with a single set of coefficients has been developed that meets retrieval accuracy specifications and does not have the zonal discontinuity and high wind speed bias problems found in the original ERT algorithm.

The rain-flag criteria were revised to be more restrictive and the global algorithm now uses the four rain-flags, 0, 1, 2, and 3, which indicate retrieval accuracy SD of <2 m/s, 2–5 m/s, 5–10 m/s and >10 m/s, respectively. During any particular day, approximately 85% of the *D*-matrix retrieved ocean surface winds will have an accuracy of ±2 m/s. The remaining 15% of the time, the scene will be rain flagged and retrieval accuracies will be worse than ±2 m/s. Since a majority of the scene in and around typhoons and hurricanes is rain flagged, the SSM/I appears to have limited use for studying the wind field of these weather systems. Additionally, the spatial resolutions of the 19-, 22- and 37-GHz channels (55, 49 and 32 km) are incapable of resolving accurately any wind speeds in areas where high wind speed gradients exist.

REFERENCES

Book, S.A. (1977) *Statistics*. New York: McGraw-Hill, New York, p. 221.

Draper, N.R. and H. Smith (1981) *Applied Regression Analysis*. New York: John Wiley and Sons, 2nd edition, p. 108.

Gilhousen, D.B. (1986) An accuracy statement for meteorological measurements obtained from NDBC moored buoys. In *Proceedings, MDS '86 Marine Data Systems International Symposium*. Marine Technological Society, New Orleans, Louisiana.

Gilhousen, D.B., M.J. Changery, R.G. Baldwin, T.R. Karl and M.G. Burgin (1986) Climatic summaries for NDBC data buoys. National Data Buoy Center publication, NSTL.

Hollinger J.P. (1989) DMSP Special sensor microwave/imager calibration/validation. Naval Research Laboratories, Washington D.C.

Liu, W.T. and T.V. Blanc (1984) The Liu, Katsaros and Businger (1979) Bulk atmospheric flux computational iteration program in FORTRAN and BASIC. Naval Research Laboratories Memo. Report 5291, Washington D.C.

Lo, R.C. (1983) A comprehensive description of the mission sensor microwave imager (SSM/I) environmental parameter extraction algorithm. Naval Research Laboratories Memo. Report 5199, Washington D.C.

Monaldo, F.M. (1988) Expected differences between buoy and radar altimeter estimates of wind speed and significant wave height and their implications on buoy–altimeter comparisons, *Journal of Geophysical Research*, **93**: 2285–2302.

Schroeder, L.C. and J.L. Sweet (1986) Merge and archival of SEASAT-A satellite data and in situ at selected illuminated sites over the ocean. NASA Langley Technical Memo., Hampton, Virginia.

Ulaby, F.T., R.K. Moore and A.K. Fung (1986) Microwave Remote Sensing, Active and Passive. Norwood, Massachusetts: Artech House, vol. 3, p. 1440–1467.

Global Snow Variations Derived from SMMR
Preliminary Results

A.T. C. CHANG
Goddard Space Flight Center
National Aeronautics and Space Administration
Greenbelt Maryland, U.S.A.

L.S. CHIU
Applied Research Corporation
Landover, Maryland, U.S.A.

ABSTRACT

Monthly means of snow-covered area and snow volume in Eurasia and North America (excluding Greenland) have been estimated from microwave measurements taken by the Scanning Multichannel Microwave Radiometer (SMMR) on board NIMBUS 7 from November 1978 to 1987. The seasonal cycle is computed and compared to that compiled by Matson et al. (1986) from subjective analyses of visible and infrared satellite imagery for the period 1966 to 1981. While the snow areas in winter in Eurasia are comparable, the snow area in June computed from SMMR is significantly smaller than that derived from VIS/IR by a factor of about two. The interannual variations of monthly means are also smaller by a factor of 1.5 to 5 for the SMMR-derived snow cover. The snow volumes showed higher persistence than the snow area: autocorrelations at one month lag are 0.52 and 0.53 for snow volume and 0.31 and 0.48 for snow area in Eurasia and North America, respectively. Correlation analysis showed higher persistence in winter than in summer. No significant lag relations between snow area and snow volume and between snow variations in Eurasia and North America were found.

INTRODUCTION

Variation of snow and ice play an important role in the variations of climate. In the shortwave portion of the solar spectrum, the reflectivity of snow is about 0.6–0.8, compared to about 0.05–0.2 for bare soil (Robock 1980). Hence, increases in snow and ice cover are associated with less absorption of solar energy, which in turn leads to lower temperatures of the Earth. This decrease, consequently, implies more snow/ice. This so-called temperature albedo feedback has been shown to significantly affect the global climate system (see Schneider and Dickinson 1974). In addition, there is a zonal asymmetry introduced by the snow in Eurasia and North America. The presence of such zonal asymmetry has been shown to enhance the sensitivity of the climate system (North et al. 1983).

Weekly global maps of snow cover have been routinely produced from subjective analyses of visible and infrared satellite imagery by the National Environmental Satellite Data and Information Service of the National Oceanic and Atmospheric Administration (NOAA/NESDIS) (Matson et al. 1986). A different set of weekly maps are produced by the US Air Force Global Weather Center (USAFGWC) whose analysis is based on interpolation of station snow measurements. Because of the radiative properties of snow in the microwave portion of the spectrum, microwave remote sensors can provide information about snow properties such as snow depth and snow water equivalent. The Scanning Multichannel Microwave Radiometer (SMMR) on board NIMBUS 7 contained microwave channels that are sensitive to snow parameters. Algorithms to retrieve snow parameters from SMMR have been developed and monthly maps of global snow data have been compiled (Chang 1986). A preliminary comparison was made between the monthly snow cover area derived from the NOAA/NESDIS and USAFGWC analyses with that derived from SMMR (Chang et al. 1987).

We report here the SMMR-derived snow parameters for the period November 1978 to March 1987. The seasonal cycles of snow cover are compared to those produced by NOAA/NESDIS. Statistics of the time series of the snow parameters are presented.

ESTIMATION OF SNOW PARAMETERS

The retrieval of snow depth at each pixel is based on the algorithm developed by Chang et al. (1987):

$$\text{snow depth} = 1.59\,(T_{18H} - T_{37H})\ \text{cm}$$

where T_{18H} and T_{37H} are brightness temperatures at 18- and 37-GHz horizontal polarization. This algorithm is derived from radiative calculations, with an assumed mean snow crystal radius of 0.3 mm, and could be applied to areas where the snow is less than 1 m deep. Snow parameters are calculated from the algorithm at 0.5 × 0.5 degrees of latitude and longitude. From the monthly mean maps, snow-covered areas for Eurasia and North America (excluding Greenland) are calculated by summing the areas of pixels with snow depth greater than 2.5 cm. Similarly, the snow volumes are sums of the areas weighted by the snow depth with a constant snow density of 0.3 g cm^{-3}.

TEMPORAL VARIATIONS

Seasonal variations

The seasonal cycles of snow area (upper) and volume (lower) computed for the period 1978 to 1987 for Eurasia (left) and North America (right) are shown in Figure 1. The upper and lower curves show, respectively, the ±1 standard deviation (SD) of interannual variability. The largest contiguous area of snow lies in Eurasia, with seasonal amplitude of about 30 million km^2, with a maximum in February and a minimum in July. The seasonal variations in North America is in phase with that in Eurasia, with an amplitude of about 10 million km^2. The total seasonal amplitude for the Northern Hemisphere is thus about 40 million km^2. The snow volume in Eurasia shows a maximum of 2.5×10^{18} g in February and a minimum of less than 10^{16} g in July/August, compared to a seasonal amplitude of about 0.7×10^{17} g for North America. The minima in snow volumes are reached a little earlier than those for the snow area, suggesting a rapid decrease in the average snow depth during the melt season.

The seasonal cycle of snow area in Eurasia presented by NOAA/NESDIS for the period 1966–81 (Matson et al. 1986) is also shown in Figure 1 (bottom) for comparison. The snow area derived from the NOAA/NESDIS analysis and from SMMR are comparable for the winter months. Major differences exist for the months of small snow extent. A Student *t* test showed that for the month of June, the SMMR-derived snow cover for Eurasia is significantly lower than that produced by NOAA/NESDIS (Table 1). The difference may be attributed to the following factors. First, the high threshold (2.5 cm) used in defining the snow area in the SMMR retrieval probably misses light snow areas that may be picked up by the NOAA/NESDIS analysis. Second, the snow melt during the early summer gives a higher brightness

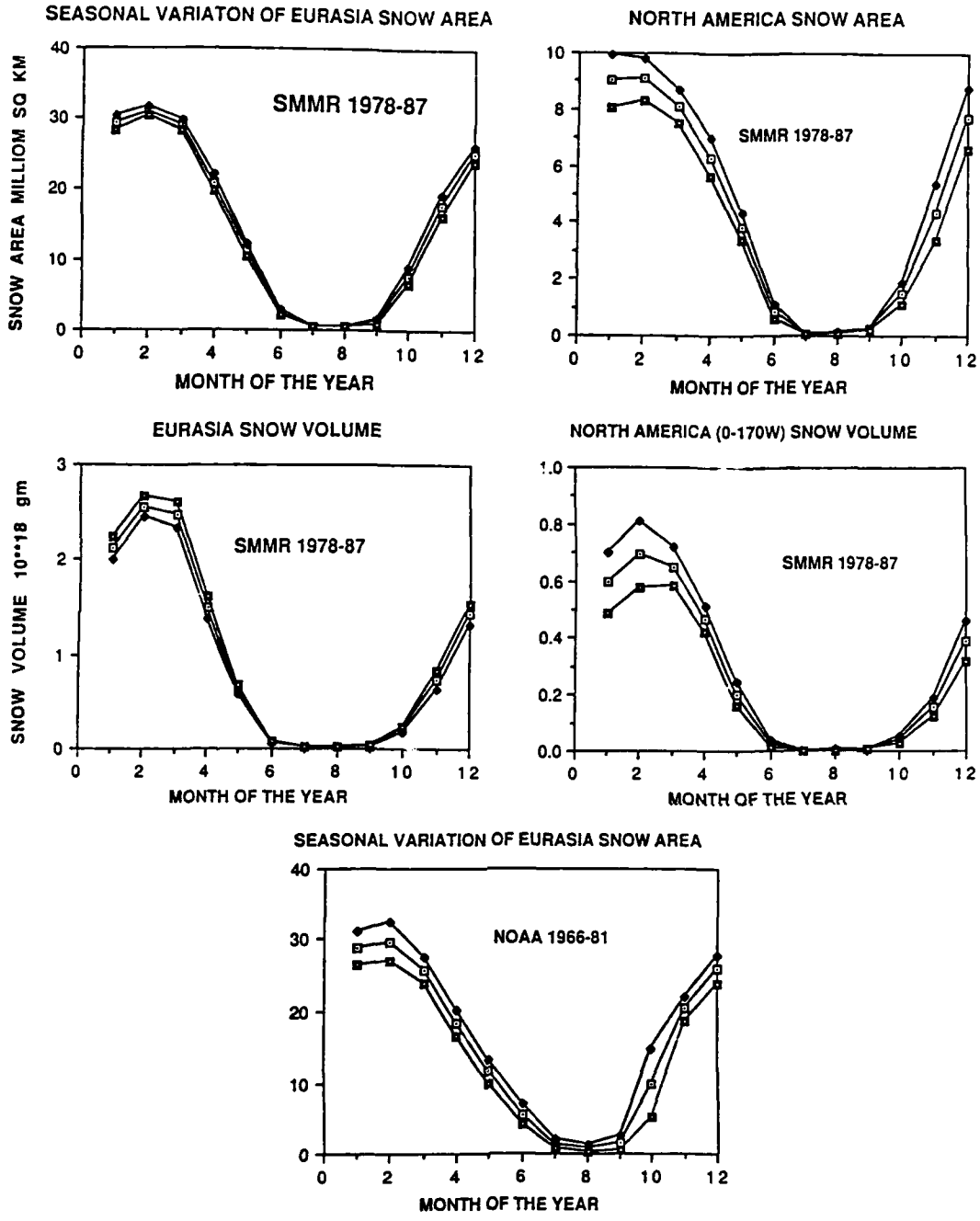

Figure 1. Seasonal variations of snow area (upper) and volume (lower) for Eurasia (left) and North America (right). The upper and lower curves indicate the + and –1 SD of interannual variations. The bottom curve shows the seasonal variation derived from NOAA/NESDIS analyses.

temperature at 37 GHz, thus giving rise to the non-identification of snow area. Another feature to note in Figure 1 is the large interannual variability in SDs in snow areas derived from NOAA/NESDIS analyses. Can this difference in SDs between NOAA/NESDIS and SMMR be attributed to the inclusion of light snow areas in the NOAA analyses?

Long-term trends

The nonseasonal variations of snow area and volume for Eurasia and North America are calculated as the departure from the seasonal cycle. Linear regression analyses show positive trends in the time series, but they are not significant statistically. Similar analyses have been performed on the monthly values (i.e., for all Januaries, Februaries, etc.). Again no signifi-

Table 1. Comparison of monthly mean snow area derived from SMMR and Visible/IR.

	J	F	M	A	M	J	J	A	S	O	N	D
						Eurasia (SMMR) 1978–87						
Mean	29.35	30.94	29.03	20.90	11.39	2.43	0.54	0.52	1.17	7.62	17.70	25.12
Std. dev.	0.94	0.68	0.75	1.17	0.91	0.33	0.09	0.10	0.30	1.19	1.48	1.12
						Eurasia (VIS/IR) 1966–81						
Mean	28.90	29.70	25.70	18.40	11.60	5.50	1.40	0.80	1.60	10.00	20.40	25.90
Std. dev.	2.30	2.70	1.80	1.90	1.60	1.40	0.60	0.50	1.00	4.70	1.70	2.00
t-Stat	0.18	0.45	1.71	1.12	0.11	2.13*	1.42	0.55	0.41	0.49	1.20	0.34

Note: Units: 10^5 km^2; *t*-values are defined as:

$$t = |m_1 - m_2| / \sqrt{s_1^2 + s_2^2}$$

* Denotes significance at the 95% level for a *t* test with 18 degrees of freedom.

cant trends are found. Longer records and other refinements are required for further detection of trends.

Persistence and correlation

The autocorrelation and cross correlation functions between the time series are computed and presented in Table 2. It can be seen that the time series of the snow volumes have slightly higher persistence than the snow area: autocorrelation at a lag of 1 month are 0.305 and 0.408 for Eurasia and North America snow areas, compared to 0.520 and 0.533 for the respective snow volumes.

The correlation coefficients between the time series have been computed. For autocorrelated time series of size N, the number of independent samples n^* can be estimated following an approach adopted by Angell (1981):

$$n^* = N/f$$

where

$$f = 1 + 2\left\{\sum_{i=1}^{\infty} p_i q_i\right\}$$

and p_i and q_i are autocorrelation coefficients at a lag of i months. The f values corresponding to the time series have been estimated. To get a conservative estimate, the summation of the series in the brackets are terminated when either p_i or q_i becomes negative. From Table 2, it can be seen that the only significant correlations are those between snow area and volume in Eurasia (0.854) and in North America (0.818), with no apparent lag relation between snow area and volume.

Table 2. Maximum correlations between snow area and volume in Eurasia and North America.

	Eurasia area	*Volume*	*North America area*	*Volume*
ρ(1)	*0.305*	*0.520*	*0.408*	*0.533*
*n**	*34*	*13*	*18*	*11*
Eurasia area	1.000	0.818*	0.331(1)	0.344(1)
		[25]	[27]	[24]
Eurasia volume		1.000	0.346(1)	0.336(1)
			[15]	[12]
North America area			1.000	0.854*
				[14]
North America volume				1.000

The number in parentheses following the correlation coefficients are lags in months with the variable on the upper row leading the variable on the left-hand side. The number of independent samples appears in square bracket underneath the coefficients.

* Denotes significance at the 95% level

DISCUSSION

Comparison between SMMR-derived and NOAA/NESDIS analyses showed general agreement; however, large differences in snow area in June in the seasonal cycle and in interannual variabilities are also found. We plan to obtain monthly snow maps from the NOAA/NESDIS analyses and examine in detail the difference between the two data sets. The added feature of snow volume obtained from the SMMR retrieval holds great potential for water management and stream flow prediction. This potential needs to be exploited.

REFERENCES

Angell, J.K. (1981) Comparison of variations in atmospheric quantities with sea surface temperature variations in the equatorial eastern Pacific. *Monthly Weather Review*, **109**: 230–243.

Chang, A.T.C. (1986) Nimbus 7 SMMR snow cover data. *Glaciological Data*, Report GD-18, 181-187.

Chang, A.T.C., J.L. Foster and D.K. Hall (1987) Nimbus 7 SMMR-derived global snow cover parameters. *Annals of Glaciology*, **9**: 39-44.

Matson, M., C.F. Ropelewski and M.S. Varnadore (1986) Atlas of satellite-derived northern hemisphere snow cover frequency. U.S. Department of Commerce, NOAA, NESDIS/NWS.

North, G.R., J.G. Mengel and D.A. Short (1983) Simple energy balance model resolving the seasons and the continents: application to the astronomical theory of the ice ages. *Journal of Geophysical Research*, **88**(C11): 6576–6586.

Robock, A. (1980) The seasonal cycle of snow cover, sea ice and surface albedo. *Monthly Weather Review*, **108**: 267–285.

Schneider, S.H. and R.E.Dickinson (1974) Climate modeling. *Reviews of Geophysics and Space Physics*, **12**: 447–493.

Antarctic Ice Sheet Brightness Temperature Variations

K.C. JEZEK
U.S. Army Cold Regions Research and Engineering Laboratory
Hanover, New Hampshire, U.S.A.

D. J. CAVALIERI
Goddard Space Flight Center
Greenbelt, Maryland, U.S.A.

A. HOGAN
U.S. Army Cold Regions Research and Engineering Laboratory
Hanover, New Hampshire, U.S.A.

ABSTRACT

In this paper we explore the possibility of extracting geophysical information about the great ice sheets from passive microwave data. This work was stimulated by calculations done by Zwally (1977) who showed that typical snow grain sizes at the surface of the ice sheet measurably influence the microwave emissivity of the near surface. This result led to speculation that ice-sheet-wide accumulation rates could be estimated by using empirical relations between grain size and accumulation rate, but little quantitative progress has been made towards that goal using single channel radiometer data alone. Data from the Scanning Multichannnel Microwave Radiometer are now in a convenient format for analysis, prompting us to perform a qualitative analysis of the 18- and 37-GHz vertically and horizontally polarized data in the context of Zwally's earlier work. An additional premise of our investigation is that this analysis can be simplified by hypothesizing that large-scale glaciologic regimes have characteristic surfaces controlled by local environmental conditions. In turn, characteristic surface properties contribute to unique microwave signatures. To test whether a segmentation of the SMMR data set into particular glacial regimes could be used to identify differences between the physical properties of each regime, we examined mean monthly brightness temperatures at 18- and 37-GHz for both horizontal and vertical polarizations over five areas. We find measurable differences between brightness temperature trends for the different areas that we attribute, in part, to fluctuations in the large-scale surface temperature field of the ice sheet.

INTRODUCTION

Satellite-borne microwave radiometers have provided images of the Antarctic Ice Sheet since 1973

when the Electrically Scanning Microwave Radiometer (ESMR) was launched aboard the NIMBUS 5 spacecraft (Zwally et al. 1983). This instrument operated at a single frequency (18 GHz or a 1.55-cm wavelength) and a single polarization (horizontal). Yet as pointed out by Zwally and Gloersen (1977), the instrument revealed complex patterns in brightness temperature (T_b) contours that suggested correlations to important glaciological variables such as surface accumulation rate and surface melting events. Zwally (1977) quantified several of these suggestions by calculating the emitted radiation as a function of measured temperature and grain size depth-profiles for the ice sheet. Comparisons between calculated emissivities and measured emissivities determined by taking the ratio of measured brightness temperature to surface-station-derived mean annual temperatures were very good. That result supported Zwally's additional calculations that estimate the effect of changing accumulation rate and changing mean annual temperature on bulk emissivities and brightness temperatures. Comiso et al. (1982) pursued this calculation further by expanding the radiative transfer model used in the calculation and producing comparisons between seasonal brightness temperature variations and predicted brightness temperature variations based on measured temperature and grain size profiles.

Previous analysis of brightness temperature data over large ice sheets has concentrated on understanding the electrical properties of polar firn in relation to the mechanical and thermodynamic properties of the firn. As such, most of the work has focused on brightness temperature data acquired over the very limited number of surface stations where in situ data are available. While some research into the regional distribution and timing of surface melt events on the marginal ice shelves has occurred, there has been little analysis of brightness temperature data on an ice-sheet-wide scale. Given the physical understanding mentioned above, we feel it is reasonable to extend analysis away from the isolated points where surface station data are available to larger regions more commensurate with the capabilities of the satellite. Essentially, the satellite provides resolution of a few tens of kilometers of events occurring over the entirety of the ice sheet, potentially offering for the first time an integrated picture of how the ice sheet as a whole responds to changing glaciologic and meteorologic forcings.

Preliminary examination of brightness temperature maps over the ice sheet quickly reveals that changes in the T_b field are occurring at most time scales and that those changes are complicated. To simplify our problem while maintaining a view toward understanding the T_b field over the ice sheet as a whole, we have adopted the following hypothesis: specific glacial regimes exhibit characteristic microwave signatures. If this hypothesis is true, then microwave data can be, on one hand, more easily interpreted given existing knowledge about the physical structure of polar firn in particular regimes and on the other hand. used to map changes in glacial regimes over time. Already, Zwally and Gloersen (1977) have shown strong qualitative correlations between brightness temperature patterns and the locations of outlet glaciers, ice streams, drainage basins and ice divides. Therefore our initial approach has been to segment large portions of Antarctica by rough glacial regimes, such as ice shelf, ice stream, polar plateau, etc., to see if known variations in accumulation rate or surface temperature can be uniquely separated from the T_b signal based on known glaciologic attributes. Moreover, this concept can now be meaningfully extended over time because of the 8-year record of observations compiled from the Scanning Multichannel Microwave Radiometer (SMMR) launched on the Nimbus 7 satellite in 1977. Images of Antarctica compiled from data acquired with the SMMR are generally similar to the ESMR data, an encouraging result as we expect no major changes in ice sheet properties over the 15-year period from the start of the ESMR mission to the termination of the SMMR mission. But along with establishing a several year time series of data, SMMR also collected data at several frequencies and polarizations including 18- and 37-GHz vertical (V) and horizontal (H) channels that have been found useful in other ice-related applications.

Before proceeding to a discussion of our particular analysis approach, we point out that a new series of global microwave measurements has been initiated with the June 1987 launch of the Special Sensor Microwave Imager (SSM/I) (Hollinger and Lo 1983). This currently operational instrument includes two channels operating at 94 GHz that provide roughly 12-km resolution. That scale of spatial observation should be sufficient to study details of glaciologically significant features such as ice streams. The fact that the SSM/I instrument now in orbit is but the first in a planned series of such instruments presages the capability to monitor the ice sheets on a decadal time scale, which is about the time scale of many glacial processes.

APPROACH

The goal of this work is to separate the geophysical signals of changing physical temperature and changing electrical properties of polar firn from observed

brightness temperatures. Our approach is to look for techniques that simplify the data set, highlighting spatial and temporal fluctuations. Hence our method is to identify specific glaciologic regimes within which we do not expect radical variations in glacial processes. Implicit in this method is the assumption that surface properties are correlated within a glacial regime and that by spatially averaging data over the regime we can reduce a large data set to a few parameters. Averaging in time is also possible, as SMMR imaged the ice sheet almost completely once every two days (no data were collected at latitudes above 85°). Given the two-day period as the lower limit of repeat observations and annual observations as the upper limit for our study, we focused on mean monthly variations. We opted for mean monthly observations rather than mean annual observations because processes that determine accumulation rate are likely to have a seasonal variation. Similarly, trying to average on a seasonal scale was difficult, given uncertainties about the definition of each season. In that regard, there are even problems associated with monthly averages. For example, breakup of the Antarctic Circumpolar Vortex markedly changes surface temperature fields, but as the event generally occurs between late October and early November, monthly mean values can easily be biased relative to previous years pending the exact date of breakup.

We have identified five spatial regimes as shown in Figure 1. The West Antarctic Ice Streams (WAS) are unique both glaciologically and meteorologically because of the enormous drainage systems that feed the Ross Ice Shelf. The meteorologic regime is forced primarily by weather systems in the Amundsen and Weddell Seas (Rubin and Giovinetto 1962) and is also characterized by strong katabatic flow down the ice streams. The Ross Ice Shelf (RIS) was selected as characteristic of the floating ice sheets that bound parts of the interior ice sheet and because of the coupling of moist air arriving from the Ross Sea and associated with air masses advecting down from West Antarctica and through East Antarctic outlet glaciers. Finally, three sectors tied to the South Pole were chosen. The Queen Maud Land (QML) sector lies on the flank of the polar plateau. The last two, East Antarctic Plateau (P) and Ice Domes (ID), cover regions of the highest topography and the lowest accumulation rates in Antarctica (Bromwich 1988).

The areas selected are geographically large and, not unexpectedly, there are variations in mean annual brightness temperature up to 10% across each area. These variations are in part associated with topographic influence on surface wind field dynamics across the region (Parish and Bromwich 1987) wherein adiabatic warming of air masses moving down the topographic gradients controls the broad scale patterns of surface temperature across the interior ice sheet. The relationship between topography and the mean annual surface temperature is demonstrated when climatic data from Schwerdtfeger (1984) are plotted against elevation (Radok 1973) (Fig. 2).

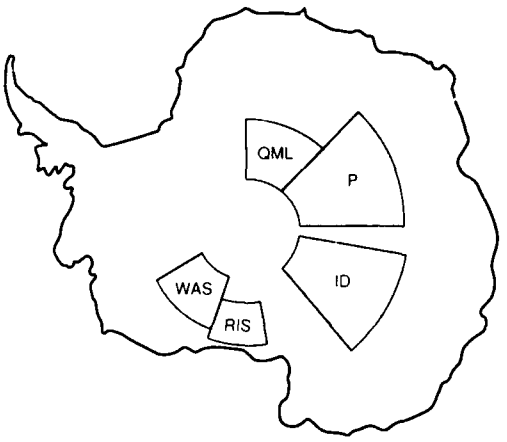

Figure 1. Five sectors used to bound spatial averages of SMMR brightness temperature data. Our sectors only roughly correspond to geographical areas with the same names. (WAS—West Antarctic Ice Streams; RIS—Ross Ice Shelf; ID—Ice Domes; P—Plateau; QML—Queen Maud Land.)

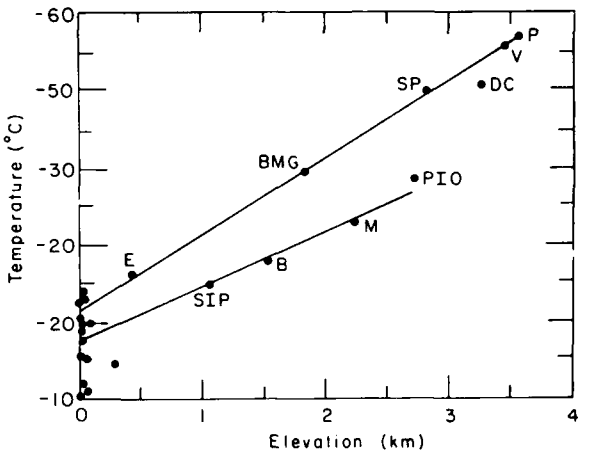

Figure 2. Mean annual temperature vs elevation for Antarctic surface stations. Data appear to fall along two lapse rate curves. Data from Plateau Station (P), Vostok (V), South Pole (SP), Eights (E), Pioneerskaya (PIO), Byrd (B), Siple (SIP) and various coastal stations clustered near the origin are from Schwerdtfeger (1984). Beardmore Glacier (BMG) datum was measured at a 10-m depth (A. Hogan, unpublished).

This linear relationship in turn is manifested as a pronounced correlation between surface elevation and mean annual brightness temperature.

Given these general properties of the ice sheet, it is useful to examine in detail our procedure for reducing the SMMR data set over each glaciological regime. Essentially we perform two averages of the brightness temperature field, one over space at the resolution of the instrument and one over time at monthly intervals. The brightness temperature (T_b) recorded in a SMMR pixel is:

$$T_b = e \langle T \rangle + r \langle T_s \rangle$$

where $\langle T \rangle$ is the weighted average physical temperature over depth (Zwally 1977) and e is the bulk emissivity, r is the Fresnel reflection coefficient of the surface and $\langle T_s \rangle$ is the mean value of the sky temperature. Obviously both terms on the right-hand side of the equation for T_b are influenced by gradients in physical properties that affect the temperature or emissivity profiles. The terms are also dependent on frequency, as observation at lower frequencies will detect energy upwelling from greater depths in the ice sheet. In this paper, we will assume that e does not vary significantly over any individual glaciological regime and that spatially averaging data produce a stationary, average value of e for each frequency. In fact, e is not necessarily constant if surface conditions are changing. Our sole justification for this assumption is that no strong long-term trends are observed in the SMMR data, at least to the level of detail of our analysis.

As pointed out above, $\langle T \rangle$ varies with location because of the variation of surface temperature with elevation and it also varies with time as seasonal temperature waves propagate into the ice sheet. Because of the finite time required for a change in surface temperature to propagate to some depth into the ice sheet, there is a phase lag between the surface temperature and $\langle T \rangle$. At 18 GHz, Zwally estimates about a 30-day lag and there is a suggestion that summer peak brightness temperatures recorded at 37 GHz lead the peaks recorded at 18 GHz (Fig. 3–7). We expect less at 37 GHz because of diminished penetration depth, but our time average precludes any firm conclusion about its magnitude.

The physical temperature at the surface of the ice sheet is controlled both by topography, which is largely fixed in time, and by meteorological transport of heat, which can vary on several time scales. So we consider $\langle T \rangle$ at any point and time to be the sum of a constant term and a varying term

$$\langle T \rangle = aE + \langle T(t) \rangle$$

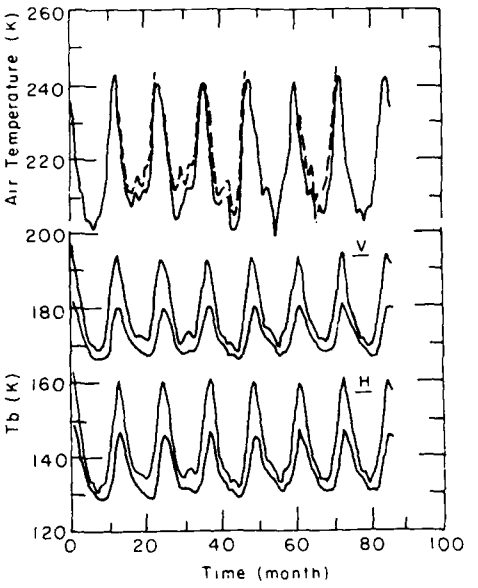

Figure 3. Mean monthly surface air temperature data from Dome C (upper dashed curve) and Vostok (upper solid curve). Vertical channel mean monthly brightness temperatures, middle curves; H channel mean monthly brightness temperatures, lower curves. 37-GHz data are warmer than 18-GHz data for both polarizations. Month 1 corresponds to January 1979.

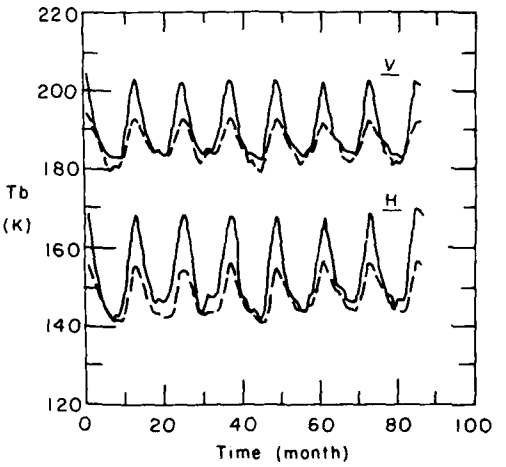

Figure 4. Mean monthly brightness temperature data for the Plateau Sector. Vertical channel mean monthly brightness temperatures, middle curves; H channel mean monthly brightness temperatures, lower curves. 37-GHz data (solid curves) are warmer than 18-GHz data (dashed curves) for both polarizations. Month 1 corresponds to January 1979.

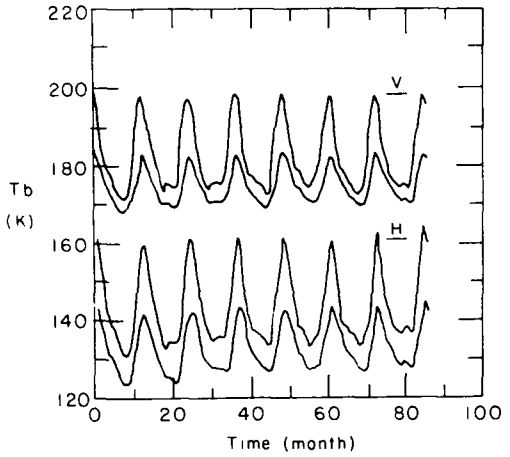

Figure 5. Mean monthly brightness temperature data for the Queen Maud Land Sector. Vertical channel mean monthly brightness temperatures, middle curves; H channel mean monthly brightness temperatures, lower curves. 37-GHz data are warmer than 18-GHz data for both polarizations. Month 1 corresponds to January 1979.

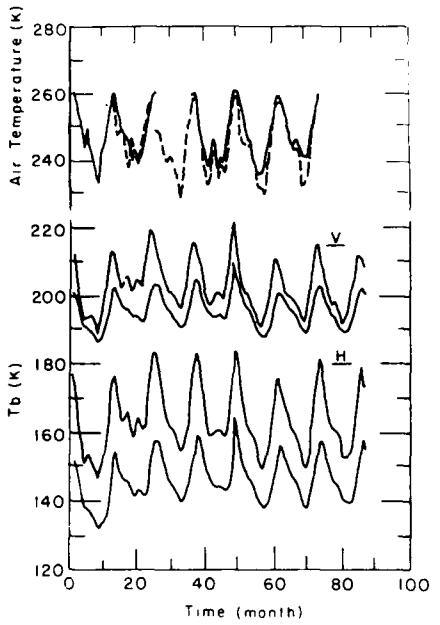

Figure 6. Mean monthly surface air temperature data from Byrd (upper dashed curve) and Siple Stations (upper solid curve) and mean monthly brightness temperature data for West Antarctic Ice Streams Sector. Vertical channel mean monthly brightness temperatures, middle curves; H channel mean monthly brightness temperatures, lower curves. 37-GHz data are warmer than 18-GHz data for both polarizations. Month 1 corresponds to January 1979.

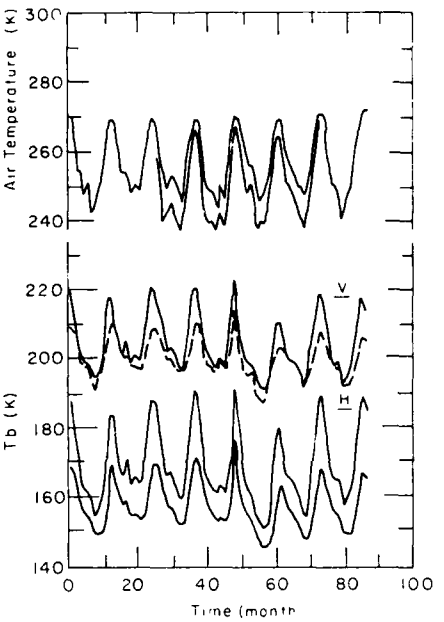

Figure 7. Mean monthly surface air temperature data from McMurdo Station and Manning Automatic Weather Station (upper curves with McMurdo showing the warmer temperatures) and mean monthly brightness temperature data for Ross Ice Shelf Sector. Vertical channel mean monthly brightness temperatures, middle curves; H channel mean monthly brightness temperatures, lower curves. 37-GHz data are warmer than 18-GHz data for both polarizations. Month 1 corresponds to January 1979.

where E is the elevation and a is a constant of proportionality and where we assume that over each glacial regime, the weather-related effects are largely the same.

To reduce the T_b data we perform the following average by temporarily ignoring the sky component

$$T_b = \frac{1}{\tau}\sum_{t=0}^{\tau}\frac{1}{N}\sum_{n=0}^{N} e\langle T\rangle_{t,n}$$

where e is the average emissivity, τ is the one-month time period over which the average is taken and N is the number of spatial points in the average. Then substituting the expression for $\langle T\rangle$

$$T_b = \frac{1}{\tau}\frac{1}{N}\sum_{t=0}^{\tau}\sum_{n=0}^{N} e\,(a\,E_n + \langle T\rangle_{t,n})\,.$$

As the elevation term is assumed stationary

$$T_b = C + \frac{1}{\tau}\frac{1}{N}\sum_{t=0}^{\tau}\sum_{n=0}^{N} e\ \langle T\rangle_{t,n}$$

where C is a constant brightness temperature associated with mean annual physical temperatures (associated with stationary surface topography) and average emissivities over the region. This facilitates our analysis because it means the elevation term simply biases the variations in brightness temperature by an offset associated with the mean elevation of the region. Variations in e between regions will modify the peak to peak swing of the T_b data. This suggests, that for T_b time series collected over different glacial regimes, similar frequency and phase variations in T_b (but possibly different amplitudes) imply a similar external forcing causing the T_b variations over each region.

RESULTS

The above analysis was applied to SMMR, TCT-calibration data (Gloersen 1987). The results of our analysis are shown in Figures 3 to 7, which include available surface air temperatures compiled from the journal, *Climate Monitor*, or measured by Automatic Weather Stations (Antarctic Automatic Weather Station Project, University of Wisconsin). Figure 3 shows the 18 and 37 V and H channels for our Ice Dome region as well as AWS surface air temperature data collected at Dome C and air temperatures measured at Vostok Station. The T_b data are driven by seasonal air temperature fluctuations and reflect the characteristic peaked summer and coreless winter of the Antarctic Plateau. The amplitude swing of the 37-GHz channels exceeds that of the 18-GHz channels reflecting the increased thermal mass associated with the more deeply penetrating 18-GHz channel. Shifts in mean values between like polarization channels reflect differences in bulk emissivities again attributable to changing penetration depths. Differences between H and V channels are associated with differences in Fresnel reflection coefficients for each polarization.

Notice that the difference between brightness temperatures at different frequencies but like polarizations is maximum in the summer and minimum in the winter. This is likely due to the asymmetric seasonal forcing. In the winter, temperatures stay uniformly cold for several months causing the temperature profile to equilibrate partially; hence there is less of a difference in $\langle T\rangle$ between data collected at different frequencies. In the summer, temperatures remain warm only briefly; hence the deeply penetrating signal is more affected by the underlying cold temperatures than the shallow penetrating signal, which is biased by the brief, near-surface warming event. Plateau data (Fig. 4) and ice domes most strongly exhibit this behavior. Queen Maud Land, West Antarctic Ice Streams and Ross Ice Shelf all show variations from this in varying degrees (Fig. 5, 6, 7).

Also note that except for the interior East Antarctic Plateau, the difference in brightness temperature between like polarizations is greater for the H channels than for the V channels. This is most obvious when winter temperature data are compared. RIS, for example, shows almost no difference in winter temperatures between the V channels but considerable difference for the horizontal channels. That the H channels are more sensitive to surface geometric and dielectric roughness suggests the possibility that this observation may be used to compare surface properties between different glacial regimes.

Finally, the peak to peak seasonal swing is greatest for the H channel, particularly at 37 GHz. This is contrary to our expectation as the emissivity for the H channels should be less than the emissivity for the V channels. However, the Fresnel reflection coefficient at the ice surface is larger for the H channel than for the V channel; hence the H channel will receive a greater amount of radiation emitted by the atmosphere and reflected from the ice surface. Since the 37 H channel suffers the least phase lag between $\langle T\rangle$ and air temperature, the contribution from the atmosphere would be nearly in phase with the surface temperature swing. Hence, 37 H may be the best channel for monitoring changes in near surface physical temperature. The 18 H channel, on the other hand, lags the air temperature by at least one month and hence the contribution of the air would be smeared over that period.

Examining the T_b data for the West Antarctic Ice Streams in detail, we find that fluctuations in T_b correspond well with fluctuations in air temperature recorded at Byrd Station. Although there is a suggestion of increasing trends in T_b, it is likely that such trends are instrumental rather than geophysical. There is some evidence that there was an instrument-related upward shift of about 1 to 2 K in 18H SMMR data during 1983 (unpublished data). This shift is apparent in the T_b curves for the Ice Dome and Plateau regions (Fig. 3 and 4, respectively). It is not apparent in the other regions because of their larger natural variability. This apparent instrumental effect is opposite the shift observed in the brightness temperature curves associated with changes in surface air temperature discussed in the next paragraph, during 1983 for the Ice Stream region.

Significant changes do seem to be occurring in the

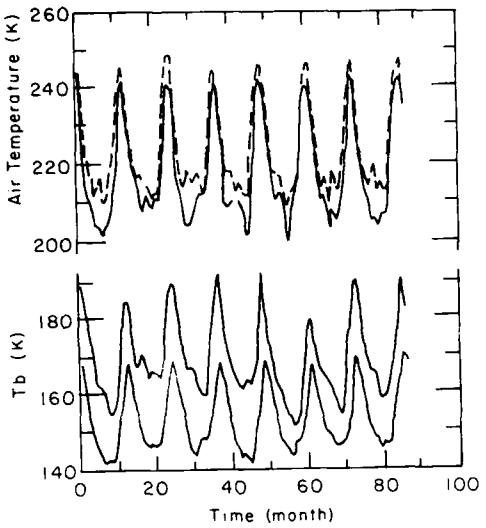

Figure 8. Mean monthly surface air temperatures from South Pole (upper dashed curve) and Vostok Stations (upper solid curve). Mean monthly brightness temperature data from the 37-GHz channel for the Ross Ice Shelf (middle curve) and Plateau (lower curve) sectors.

minimum winter temperatures observed at all frequencies and for all regimes. Referring to the Ice Dome data, we see that the minimum winter brightness temperature in 1982 is measurably less than that in the years preceding or succeeding it. Curiously, it was the winter of 1983 in West Antarctica that is cold relative to preceding and succeeding years. More direct comparison is shown in Figure 8, which includes air temperature data from South Pole and Vostok Stations along with T_b data from our Plateau and Ross Ice Shelf sectors. These data clearly show a cold winter during 1983 in West Antarctica preceded by a cold winter in 1982 in East Antarctica.

Savage et al. (1988) noted the decrease in 1983 minimum winter air temperatures at South Pole Station and associated it with the El Niño of 1982. The one year phase lag between El Niño events and minimum winter temperatures at South Pole was reported by Savage et al. to correlate over most of the 30-year South Pole temperature record. They comment that the lag occurs because of enhanced drainage flow of cold air from the interior of the continent. Our results support this hypothesis by showing that snow surface temperatures inferred from the SMMR data during the El Niño year are unusually cold over the interior East Antarctic Plateau. Subsequent release of the inferred cold air mass built up over East Antarctica starting in 1982 may be partly responsible for the cooling observed in other sectors of Antarctica in 1983.

CONCLUSIONS

Our analysis suggests that T_b data can be used to study classes of meteorological variation over sectors of the Antarctic Ice Sheet. When tied to surface station data, spatially averaged satellite data can be used to distinguish trends in the temperature field that may not be readily discernible in the isolated surface station data. Moreover the satellite data can be used to study continent-wide, long-term trends so far unachievable by any other technique.

REFERENCES

Bromwich, D.H. (1988) Snowfall in high southern latitudes. *Reviews of Geophysics*, **26**(1): 149–168.

Comiso, J.C., H.J. Zwally and J.L. Saba (1982) Radiative transfer modeling of microwave emission and dependence on firn properties. *Annals of Glaciology*, **3**: 54–58.

Gloersen, P. (1987) In-orbit calibration adjustment of the Nimbus 7 SMMR. National Aeronautics and Space Administration, Washington, D.C., NASA Technical Memorandum No. 100678.

Parish, T.R. and D.H. Bromwich (1987) The surface wind field over the Antarctic ice sheets. *Nature*, **327** (6125): 51–54.

Radok, U. (1973) Energy fluxes over polar surfaces. In *Proceedings of I MAP, IAPSO, SCAR, WMO Symposium, Moscow 1971*. World Meteorological Organization, WMO Technical Note 129.

Rubin, M.J. and M.B. Giovinetto (1962) Snow accumulation in central West Antarctica as related to atmospheric and topographic factors. *Journal of Geophysical Research*, **67**(13): 5163–5170.

Savage, M.L., C.R. Stearns and G.A. Weidner (1988) The southern oscillation signal in Antarctica. In *Proceedings of the Second Conference on Polar Meteorology and Oceanography, March.* Boston; Madison, Wisconsin: American Meteorological Society, p. 141–144.

Schwerdtfeger, W. (1984) *Weather and climate of the Antarctic.* Amsterdam, the Netherlands: Elsevier Science Publishers.

Zwally, H.J. (1977) Microwave emissivity and accumulation rate of polar firn. *Journal of Glaciology*, **18**(79): 195–215

Zwally, H.J. and P. Gloersen (1977) Passive microwave images of the polar regions and research applications. *Polar Record*, **18**(116): 431–450.

Zwally, H.J., J.C. Comiso, C.L. Parkinson, W.J. Campbell, F.D. Carsey and P. Gloersen (1983) Antarctic sea ice 1973-1976. Satellite passive microwave observations. National Aeronautics and Space Administration, Washington, D.C., NASA Sp-459.

Polar Ice Research Using Passive Microwave Observations

H. J. ZWALLY
Laboratory for Oceans
NASA Goddard Space Flight Center
Greenbelt, Maryland

Since the first passive microwave images of the Earth were acquired by the Nimbus 5 ESMR in December 1972, passive microwave imagery has proven to be uniquely useful for a variety of polar ice research applications. The physical basis for measurement of ice parameters is the strong dependence of the thermal emission at microwave frequencies on the composition and structure of the emitting material. The near-transparency of the atmosphere, the large emissivity and polarization contrasts between sea ice and open water, the wavelength-dependent contrast between first-year and multiyear sea ice, the variations of snow emissivity with grain size, and the strong contrast between wet and dry firn are principal physical properties of microwave emission that enable quantitative measurements of ice parameters. Although the typical resolution (instrument field-of-view) is large compared to the size of different surface components (e.g., open water, first-year sea ice, and multiyear sea ice) the linear combination of emitted radiation enables inversion of multi-wavelength and polarized measurements to extract the relative areal coverage of each component. Principal results include discovery of the Weddell polynya and numerous transient coastal polynyas in the Antarctic, studies of the interannual variability of sea ice extent, measurement of the area of open water within the ice pack, studies of the large-scale advection and convergence/divergence of the arctic ice pack, determination of the extent and duration of surface melt, and inference of ice sheet accumulation rates.

Characteristics of Sea Ice During the Arctic Winter Using Multifrequency Aircraft Radar Imagery

B. HOLT, J. CRAWFORD AND F. CARSEY
Jet Propulsion Laboratory
California Institute of Technology
Pasadena, California, U.S.A.

ABSTRACT

During March 1988, in support of the SSMI Validation Aircraft Experiment, extensive synthetic aperture radar imagery was obtained of arctic sea ice using the NASA JPL polarimetric radar system. This system operated at three frequencies (440 MHz, 1.28 GHz, and 5.3 GHz) and four polarizations to provide a 12-channel data set. From the seven flights, imagery was collected in the Beaufort, Chukchi, and Bering seas. There was strong discrimination between multiyear and first-year ice types in the 5.3-GHz (C-band) imagery, with the multiyear ice appearing bright due to reduced salinity and larger surface scattering and the first-year ice appearing darker. As the frequency decreased, ridges became quite pronounced, particularly at the 440-MHz channel (P-band), which is most likely due to increased radar penetration into the ice and therefore increased volume scattering, especially in the larger air spaces contained within ridges. Also collected during the flight program was passive microwave data from both imaging and profiling instruments, additional wide swath radar imagery at 5 and 9 GHz, as well as Landsat and SMM/I data. Both video and voice observations were made simultaneously to data collection. Intercomparisons with the more verified capabilities of the other sensors tend to confirm the ability of the C-band SAR to discriminate the two major ice types. The polarimetric data are useful for determining the principal types of scattering from surfaces. Preliminary results from polarimetric analysis likewise confirm the difference in scattering with frequency and ice type and feature. The C-band frequency has been selected as the single frequency for both the ERS-1 and Radarsat SARs and will also be included on the Eos and SIR-C SAR packages. The preliminary results from this aircraft data indicate that C-band will be quite valuable for discriminating ice types.

This work was performed under contract with the National Aeronautics and Space Administration.

Airborne Sea Ice Thickness Sounding*

A. KOVACS
U.S. Army Cold Regions Research and Engineering Laboratory
Hanover, New Hampshire, U.S.A.

J. S. HOLLADAY
Geophysics Laboratory
University of Toronto
Toronto, Ontario, Canada

ABSTRACT

Results from the use of airborne electromagnetic induction technology for profiling sea ice thickness are presented. The airborne sea ice thickness soundings indicated that the thickness could be estimated but the resolution decreased as the ice became rough. However, it was found that the average ice thickness estimated by airborne electromagnetic sounding for a given flight track was in reasonable agreement with the average ice thickness determined by direct drill hole measurement. Examples of the ice thickness profiles obtained by airborne sounding and direct drill hole sounding are presented and compared. Future development of the airborne system is discussed.

INTRODUCTION

Airborne remote measurement of sea ice thickness has been an elusive goal. Many sensing systems have been tried and evaluated for measuring ice thickness (Canadian Defence Research Establishment 1971), including on-surface and airborne impulse radar sounding (Rossiter and Bazeley 1980, and Kovacs and Morey 1980, 1986 and 1987). All these systems were found to have limited capabilities at best. Fixed-frequency airborne electromagnetic (AEM) induction systems have been used for several decades in mineral exploration. System technology has now advanced to where more demanding sounding applications can be considered. Sea ice thickness and bathymetric sounding are two areas where AEM technology can, in principle, now be used successfully. In this method, a tubular sensor platform (bird) is towed by a cable suspended from a helicopter. Fixed frequency transmit coils are located at one end of the bird and related receiver coils at the opposite end. When operated over sea ice, the transmit coils produce a primary electromagnetic field which induces eddy currents in the conductive seawater. These currents, in turn, produce a secondary electromagnetic field which is sensed by the receiving coil. The voltage amplitude and phase of the secondary field relative to the primary field at the receiver coil are functions of the bird height above and the conductivity of the seawater. A laser profilometer mounted in the bird measures the distance between the platform and the ice surface. Subtracting the AEM distance from the laser distance gives an estimate of the relative ice (or snow and ice) thickness.

Previously we reported on the use of a four-frequency (AEM) system for measuring sea ice thickness (Kovacs et al. 1987, Kovacs and Valleau 1987). This field program, undertaken in May 1985, verified the feasibility of using AEM sounding for the measurement of sea ice thickness and under-ice bathymetry using a relatively standard geophysical survey system with a 7-m-long, ½-m-diameter bird. Shipping this long, ~220-kg bird to the Arctic proved very expensive and it was cumbersome to handle.

To reduce the size and weight problem, a bird only 3½ m long and 0.35 m in diameter and about 150 kg in weight was designed and fabricated by Geotech, Ltd. Mounted in the bird was a high resolution, 0.01-m accuracy laser profilometer. A global satellite positioning system was used to monitor flight line location and record the position of the sounding data.

FIELD ACTIVITIES

The new AEM sounding system was tested in May 1987 off the coast of the Beaufort Sea coast of Alaska. Extensive ground truth information (snow and ice [S–I] thickness, water depth, temperature and conductivity, and satellite position data) was collected at numerous sites over which AEM soundings would be made. The sites included both first-year and multiyear sea ice. The data collected at several of the sites are presented in this paper.

Linear system drift can be dealt with when analyzing the AEM sounding data. Nonlinear drift cannot be satisfactorily accounted for. Nonlinear drift effects can be seen in the AEM S–I thickness data obtained at stations H through O located along an 18-km-long line laid out on first-year sea ice. Table 1 lists the aver-

* An expanded version of this paper to appear in the 1989 International Conference on Port and Ocean Engineering under Arctic Conditions, Lulua, Sweden and as a Cold Regions Research and Engineering Laboratory report.

Table 1. Drill-hole-measured vs AEM determined snow-ice thickness for stations H through O.

	Snow-ice thickness (m)	
Station	*Drill hole*	*AEM sounding*
H	1.90	1.15
I	1.91	1.75
J	1.88	0.37
K	1.84	2.50
L	1.93	2.24
M	1.95	2.45
N	1.03	0.79

age of four drill-hole-measured S–I thickness measurements at each station vs the AEM-determined value. The AEM S–I thicknesses at the beginning of the flight line, at station H, were lower than the measured value. As the 10-minute flight progressed, the AEM S–I thicknesses gradually increased to where they exceeded the measured ones and then decreased. The variation in the AEM-determined S–I thicknesses vs the measured values must be eliminated before AEM sounding of sea ice thickness can be considered a viable measurement technology.

On a multiyear ice floe, a 50-m-wide × 450-m-long grid was laid out. The snow and ice thickness and the freeboard were determined by drill hole measurement at 5-m-intervals over the entire grid area. The purpose of the grid, and related drill hole measurements, was to ascertain whether the AEM-determined S–I thicknesses agreed with the measured values. In our previous study (Kovacs et al. 1987), we determined that the AEM footprint, or the area over which the integrated S–I thickness is estimated, ranges from one to two times the bird altitude. If the bird is flown 25 m above the surface, then the footprint is, as a first approximation, at least 25 m in diameter. Therefore, the average drill hole measured S–I thicknesses within an area of ice about the diameter of the AEM footprint would be required to assess the validity of the AEM S–I thickness determination.

The objective at the grid site was to fly down its center (Fig. 1), sounding the S–I thickness and referring these measurements to the location of station markers placed on the surface. Common fiducial numbers recorded on the AEM data and the flight path video allowed for location-data cross correlation.

The average snow thickness, ice freeboard and keel draft along the length of the grid are given in Figure 2. The thinnest average S–I ice area was about 3 m thick, while the thickest areas were about 6 m thick.

Snow-ice thickness profiles for four flights flown

Figure 1. The grid area on multiyear sea ice floe 1. The snow trampled during drilling produced the outline shown. A dyed centerline can also be seen.

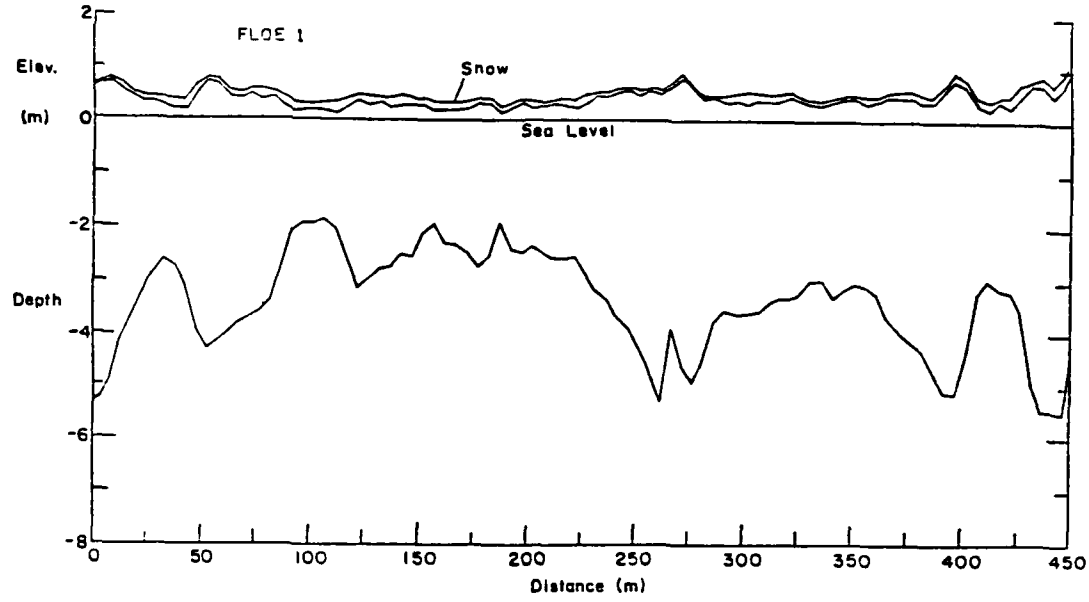

Figure 2. Cross section of the grid site on floe 1 as constructed from the averaged drill hole measurements.

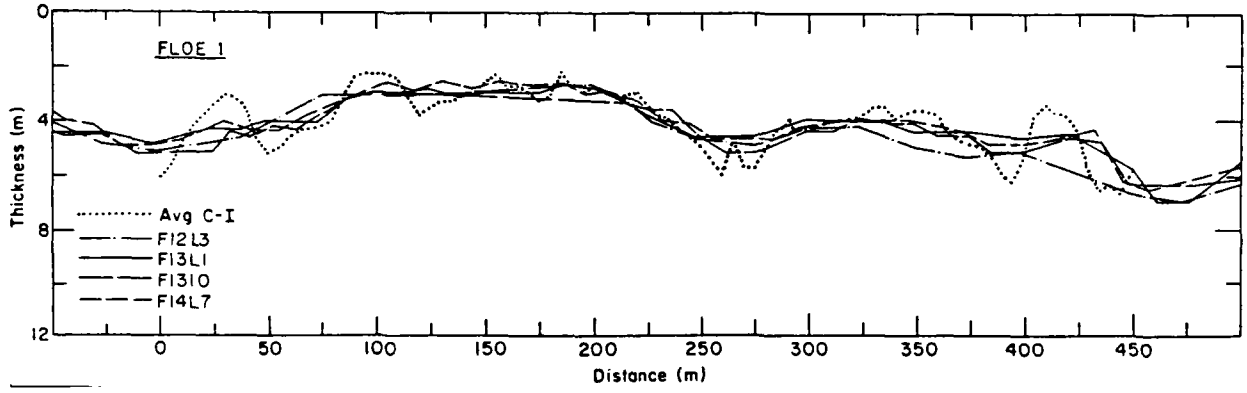

Figure 3. Average measured vs four AEM-determined snow and ice thickness profiles along the grid on multiyear floe 1.

down the grid are shown in Figure 3, along with the average drill hole measured S–I thickness. It is apparent that the AEM profiles follow the long period variation of the measured snow-ice thickness profile but not the short period undulations. As previously discussed, this is due to the averaging associated with the footprint area over which the ice thickness is being integrated as well as the use of a one-dimensional analytical model to characterize three-dimensional relief. It appears that short-period thickness variations, which occur over distances of less than about two times the bird height, will not be well defined, if defined at all, in the AEM sounding profiles.

The mean drill hole measured S–I thickness for the floe was 3.96 m with a standard deviation of ±1.31 m. Similar values for flights F1213, F13L1, F1310 and F14L7 are 4.27 m (±1.09 m), 4.18 m (0.89 m), 4.09 m (±0.92 m) and 4.11 m (±0.88 m), respectively. All AEM mean S–I thickness flight line values are biased to the high side but are well within 10% of the drill hole determination. This suggests that a properly designed and developed AEM system can provide useful information on the mean ice thickness of ice floes with relatively mild relief.

The AEM thickness profiles obtained along a 50-m-wide × 220-m-long grid established on first-year sea ice, which included a 20-m-thick first-year pressure ridge (Fig. 4), are shown in Figure 5. The most striking aspect of the AEM profiles is that they do not adequately define the thick ice of the ridge. As previously stated, because of the footprint size and the model constraints as well as the relatively steep-sided relief of the ridge keel, it is currently not possible to properly define such ice features with widths of about two times the bird height. As the thick ice area is less than 60 m wide and the bird was flown at about 23 m above the undeformed surface relief, the results shown in Figure 5 are not unexpected. The

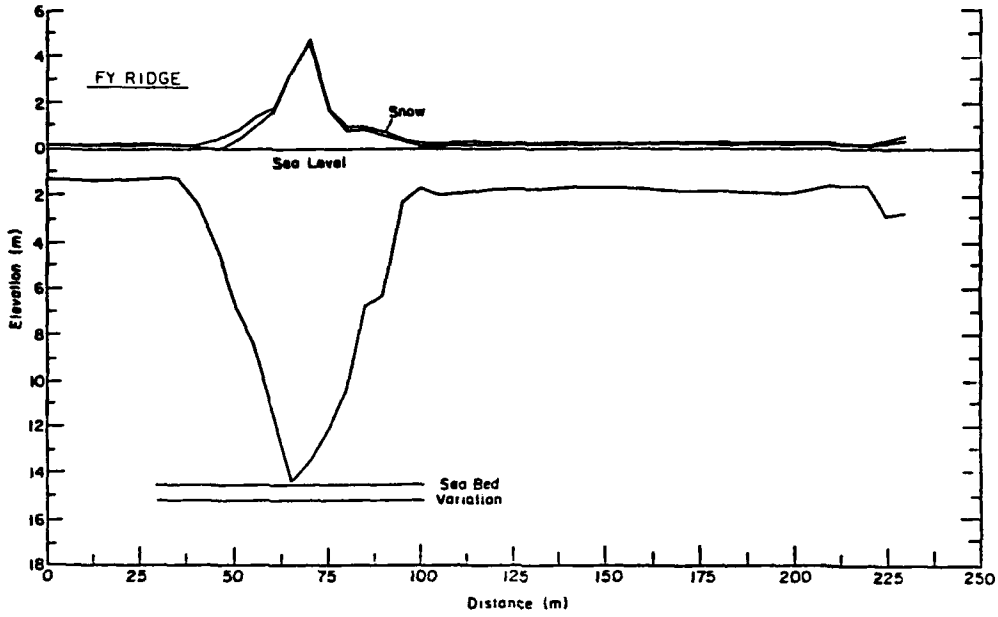

Figure 4. Cross section of first-year pressure ridge grid site as constructed from the averaged drill hole measurements.

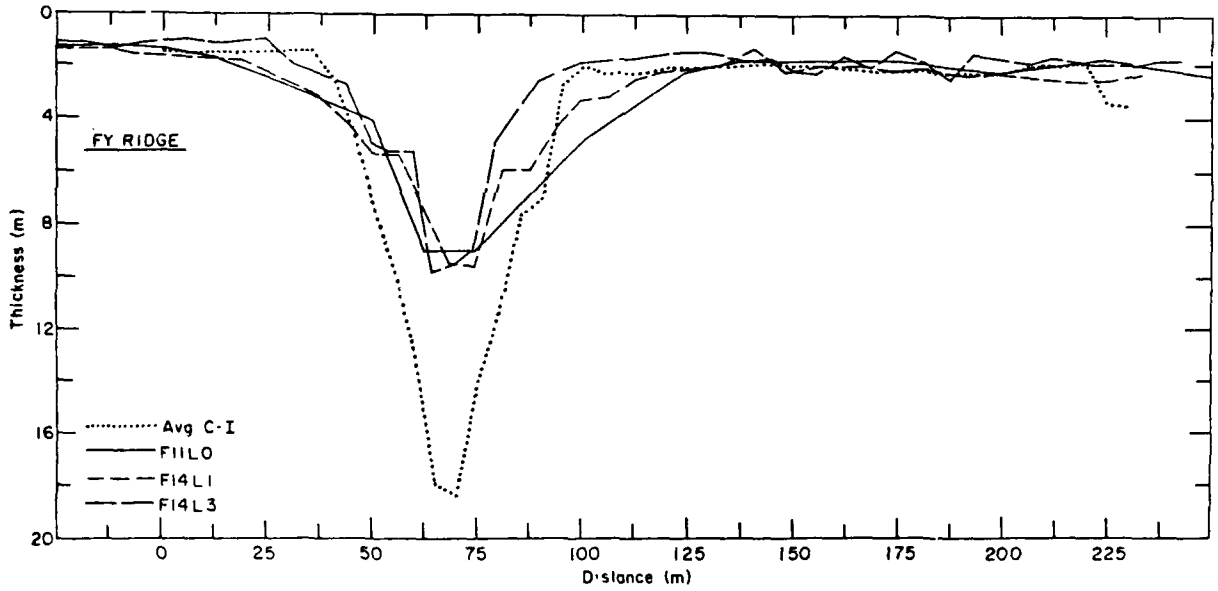

Figure 5. Average measured vs three AEM-determined snow and ice thickness profiles along the grid at the first-year pressure ridge.

AEM S–I thicknesses do agree reasonably well with the measured thicknesses on either side of the ridge and do indicate the location of the thicker ridge ice. Smoothing of the relief in the area of the ridge is again associated with footprint size, ridge geometry and model constraints.

DISCUSSION

During the 1987 field study, major linear and non-linear drift (as well as noise) problems were experienced during sounding flights, especially long ones, which adversely affected the quality of the AEM data and made their interpretation difficult. As a result, it is appropriate to conclude that the new Geotech AEM ice measurement system used in this study does not represent a sufficiently mature technology for use in obtaining accurate measurements of sea ice thickness. This would especially be true in determining ice cover thickness distribution over large areas for use in modeling ice pack dynamics or in assessing heat transfer from an ice-covered sea to the atmosphere.

Nevertheless, the results of this and the 1985 field study (Kovacs et al. 1987, Kovacs and Valleau 1987) indicate that the AEM sounding system could be used to find areas of thick and thin sea ice and to give an indication of the thickness. Such information may be useful in ship routing through ice-covered waters. However, the cost, complexity and lack of real-time analysis and display of the data appear to make the current technology not very attractive for this use.

The above discussion is an expression of caution on the usefulness of AEM sea ice thickness sounding at this stage of its technological development. On the optimistic side, we have reason to believe that AEM sounding of sea ice will evolve into a mature, user-friendly technology capable of providing accurate sea ice thickness data useful for many scientific and applied uses. In the near term, we envision a lighter-weight system with very stable electronics, high sampling rates, real-time calibration, faster data processing and real-time display of ice thickness. Indeed, we are currently addressing these areas in our development of a single-transmitter, wideband, time-domain, helicopter-deployed electromagnetic sea ice thickness sounding system, which should be flying in 1990.

REFERENCES

Canadian Defence Research Establishment (1971) *Proceedings of a Seminar on Thickness Measurement of Floating ice by Remote Sensing*. Canadian Defence Research Establishment, Ottawa, DREO Technical Note Mp/71-14.

Kovacs, A. and N.C. Valleau (1987) Airborne measurement of sea ice thickness and subice bathymetry. In *Proceedings, 9th International Conference on Port and Ocean Engineering under Arctic Conditions (POAC '87)* (W.M. Sackinger and M.O. Jeffries, Ed.). University of Alaska–Fairbanks, vol 1, p. 111–120.

Kovacs, A. and R.M. Morey (1980) Investigation of sea ice anisotropy, electromagnetic properties, strength, and under-ice current orientation. USA Cold Regions Research and Engineering Laboratory, CRREL Report 80-20.

Kovacs, A. and R.M. Morey (1986) Electromagnetic measurements of multiyear sea ice using impulse radar. *Cold Regions Science and Technology*, **12**: 67–93.

Kovacs, A. and R.M. Morey (1987) Estimating sea ice thickness from radar sounding time-of-flight data. In *Proceedings, 9th International Conference on Port and Ocean Engineering under Arctic Conditions (POAC '87)* (W.M. Sackinger and M.O. Jeffries, Ed.). University of Alaska–Fairbanks, vol. 1: 121–136.

Kovacs, A., N.C. Valleau and J.S. Holladay (1987) Airborne electromagnetic sounding of sea ice thickness and subice bathymetry. *Cold Regions Science and Technology*, **14**: 289–311.

Rossiter, J.R. and D.P. Bazeley (Ed.) (1980) *Proceedings of the International Workshop on the Remote Estimations of Sea Ice Thickness*. Center for Cold Ocean Resources Engineering, Memorial University, St. Johns, Newfoundland, C-CORE Publications no. 80-5.

On the Relationship Between Ice Thickness and 33.6-GHz Brightness Temperature Observed for First-Season Sea Ice

D. EPPLER, L.D. FARMER,
AND A.W. LOHANICK
Naval Oceanic and Atmospheric
Research Laboratory
Polar Oceanography Branch Office
Hanover, New Hampshire, U.S.A.

ABSTRACT/INTRODUCTION

Passive microwave images of seasonal sea ice were obtained with the Navy's 33.6-GHz K_a-band Radiometric Mapping System (KRMS) during field experiments in March 1983 (NORDA experiment), 1987 (NORDA GEOSAT Validation Experiment), and 1988 (Navy-NASA SSM/I Validation Experiment). Imagery obtained during these flights in the Bering, Chuckchi, Beaufort, and East Greenland seas show that a range of radiometric brightness temperatures are associated with first-season sea ice (new ice, nilas, young ice, and first-year ice). In areas where a new ice cover is forming from water exposed in polynyas or leads, temperatures typical of the ice sheet range from very low (approximately 140 K for ice-free open water) to very warm (approximately 230 K for newly consolidated ice) (Fig. 1). Once the ice sheet consolidates, thickens, and its surface ages, KRMS images suggest that its radiometric temperature declines by as much as 18 K. Images of regions where a thick first-season ice sheet is already established typically show a matrix of radiometrically warm to very warm ice that surrounds slightly cooler first-season floes that are older and persumably thicker (Fig. 2). Physical changes in ice and overlying snow that result in this observed radiometric cooling are not well understood.

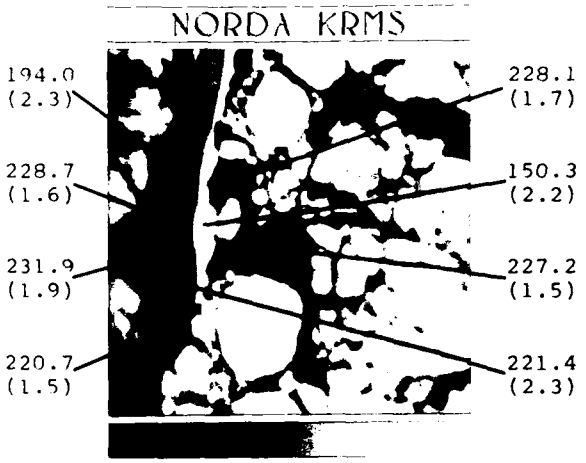

Figure 1. Passive microwave image (33.6-GHz) of ice forming in a lead. Radiometrically cool floes of old ice are light-toned. Scene widith is 14.5 km.

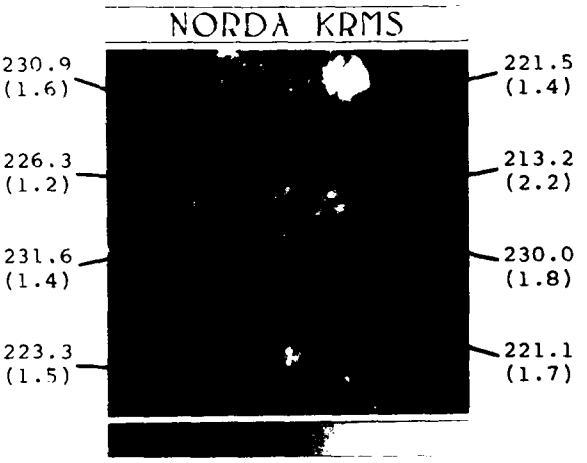

Figure 2. Passive microwave image (33.6-GHz) showing variation in radiometric temperature of consolidated first-season ice. Mean brightness temperatures for indicated areas are in kelvins and were computed from digital radiances using methods of Farmer et al. (1989). Standard deviation, also in kelvins, is in parenthesis. Scene width is 14.5 km.

FORMATION OF NEW ICE

A radiative model supported by laboratory experiments and field observations suggests that observed variation in radiometric brightness temperatures of freezing water and accumulating sea ice can be explained by considering the changing physical characteristics of a surface composed of ice and water. Calm seawater and saline first-year ice are characterized by contrasting emissivities (approximately 0.50 and 0.95) and so display very different brightness temperatures. The 33.6-GHz temperature of open water typically is between 135 K and 155 K (depending on roughness), and that of newly formed first-year ice typically is near black body temperature (230 K to 260 K, depending on physical temperature) (Farmer et al. 1989). Brightness temperatures observed over actively freezing open leads and polynyas typically fall between these values (Eppler et al. 1986) (Fig. 1, 3, 4, and 5).

Where the water surface is not covered by a continuous sheet of slush or ice, brightness temperature is a function of the concentration of ice crystals at the ocean surface and represents the integrated radiance of materials falling within the radiometer beamspot. As accumulating slush and frazil consolidate and interstitial water freezes, freeboard increases and the ice surface rises above sea level. Liquid water and

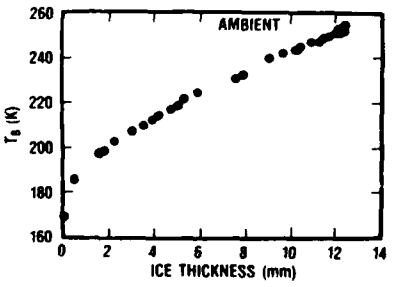

Figure 3. Radiometric temperature (33.6-GHz) of sea ice as a function of ice thickness for ice in a freezing arctic lead.

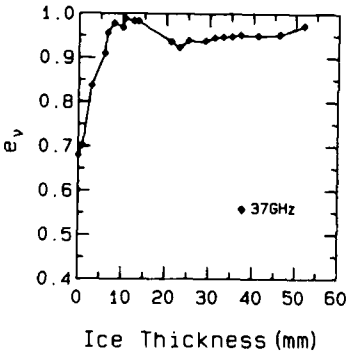

Figure 4. Emissivity of saline ice (37-GHz) as a function of ice thickness for ice growing in an outdoor tank at CRREL (from Grenfell et al. 1988).

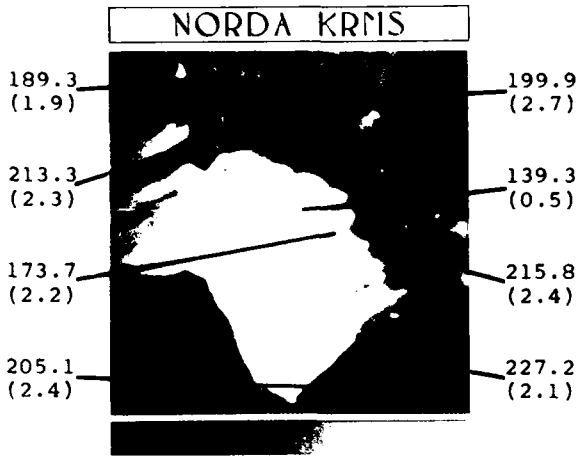

Figure 5. Passive microwave image (33.6 GHz) of ice forming in an arctic polynya. Scene width is 33.6 km.

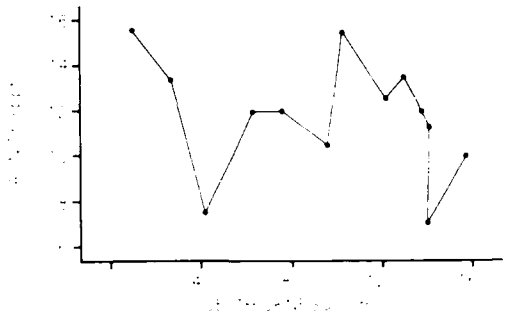

Figure 7. Surface salinity of a first-season ice sheet in the high Arctic as a function of ice thickness (from Nakawo and Sinha 1981).

brine drain through the still-permeable sheet, causing the ice surface to become less reflective and highly emissive. This results in a radiometric temperature for the newly consolidated ice sheet that approaches the black body temperature.

AGING OF A CONSOLIDATED ICE SHEET

Mechanisms that explain the apparent change in radiometric temperature observed for thicker and older first-year ice (Fig. 2) are less clear. Figure 6 portrays undeformed first-year ice in schematic form as a three-layer system, each component of which changes with time and has potential effect on radiometric temperature. Cooler temperatures could arise, for example, from a significant decrease in the salinity of the first-year ice itself. Field and laboratory experiments suggest, however, that the decline in surface salinity is insufficient and too erratic to produce uniform cooling of the magnitude observed over entire floes (Nakawa and Sinha 1981) (Fig. 7 and 8).

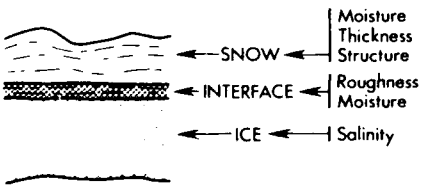

Figure 6. Factors that have potential effect on apparent brightness temperature sensed for a consolidated first-season ice sheet.

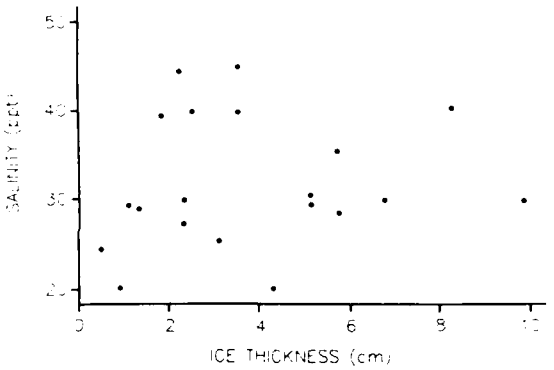

Figure 8. Surface salinity of saline ice grown in an outdoor tank at CRREL as a function of ice thickness.

Changes in moisture and roughness at the interface between snow and ice also could affect apparent temperature; laboratory results suggest that both factors can cause radiometric cooling. In one experiment, the emissivity of laboratory-grown sea ice declined when the ice surface was roughened with a single layer of 25-mm crescent-shaped ice pieces (Grenfell et al. 1988) (Fig. 9). In another experiment, falling snow that turned to slush on contact with bare, unroughened ice produced a significant drop in brightness temperature (Fig. 10). However, these data also show an increase in temperature as the ice continues to thicken and the slush ages. Return to a radiometrically warm surface after initial cooling is supported by another experiment in which the base of an existing snow cover was flooded when a somewhat thicker ice sheet became depressed below water level.

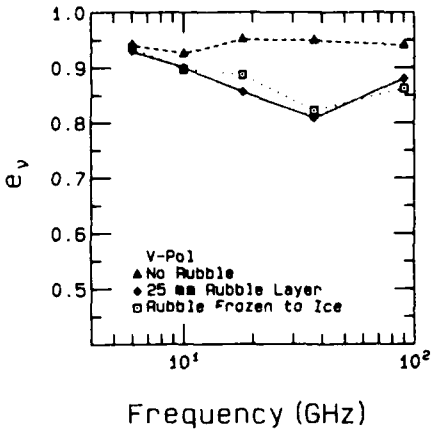

Figure 9. Effect of surface rubble on emissivity of a saline ice sheet (from Grenfell et al. 1988).

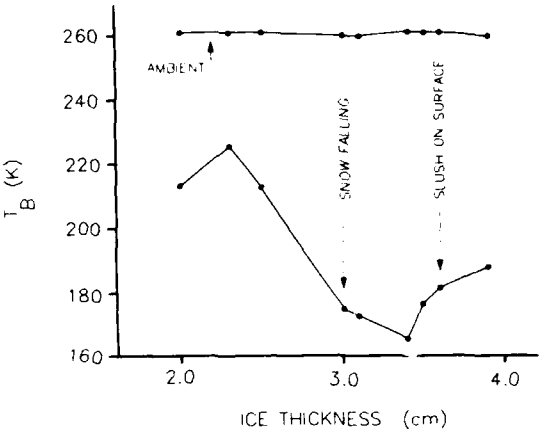

Figure 10. Effect of a slush layer of 37-GHz brightness temperature of a saline ice sheet grown in an outdoor tank at CRREL.

CONCLUSIONS

Changing radiometric characteristics of actively freezing leads and polynyas are reasonably well understood and are derived primarily from the relative proportions of liquid and solid that comprise the imaged surface. Physical changes in the ice or overlying snow that reduce radiometric temperature once the ice sheet has consolidated are understood less well. Experimental results (Nakawo and Sinha 1981; CRRELEX) suggest that, 1) changes in salinity at the snow/ice interface are insufficient to produce radiometric cooling, and 2) that although increased moisture at the snow/ice interface initially promotes cooling, the long-term effect is radiometric warming. Observed cooling (Fig. 2) probably is related to development of enhanced scattering, either through formation of roughness elements at the snow/ice interface or through metamorphism of overlying snow.

REFERENCES

Eppler, D. T., L.D. Farmer, A.W. Lohanick and M. Hoover (1986) Classification of sea ice types with single-band (33.6 GHz) airborne passive microwave imagery. *Journal of Geophysical Research*, **91**(C9): 10661–10695.

Farmer, L. D., D.T. Eppler and A.W. Lohanick (1989) Converting digital passive microwave data to kelvin units of brightness temperature. NORDA Technical Note 427.

Grenfell, T. C., D.L. Bell, A.W. Lohanick, C.T. Swift and K. St. Germain (1988) Multifrequency passive microwave observations of saline ice grown in a tank. In *Proceedings, International Geoscience and Remote Sensing Society (IGARSS) '88 Symposium, Edinburgh*, p. 1687–1690.

Nakawo, M. and N.K. Sinha (1981) Growth rate and salinity profile of first-year ice in the high Arctic. *Journal of Glaciology*, **27**(96): 315–330.

Airborne Passive Microwave Observations of Arctic Sea Ice

J.C. COMISO, R. KUTZ AND T. DOD
Laboratory for Oceans
NASA Goddard Space Flight Center
Greenbelt, Maryland

J. CRAWFORD
Jet Propulsion Laboratory
California Institute of Technology

ABSTRACT

Multispectral passive microwave measurements from a NASA P-3 aircraft on 19–23 May 1987 reveal winter ice conditions and a very active but highly consolidated sea ice cover in the central Arctic. The aircraft was equipped with a 19-GHz electrically scanning microwave radiometer (ESMR), a dual polarized advance multispectral microwave radiometer (AMMR) operating at 19 GHz, 21 GHz, and 37 GHz, and an advanced oceanographic lidar (AOL) for surface topography measurements. The mission was conducted in conjunction with near-simultaneous coverages by an X-band SAR on board a Cessna aircraft and submarine sonar sensors.

RESULTS/DISCUSSION

The regions studied include the Canadian side of the Central Arctic Basin including the North Pole, Baffin Bay, Fram Strait and Greenland Sea. The P-3 aircraft was flown at altitudes of 6000 and 245 m, providing along-track resolutions of 750 and 31 m for the AMMR and 370 m and 15 m for the ESMR, respectively. Changes in the multispectral signature of sea ice were apparent as the aircraft flew over various surfaces from multiyear ice, through first-year ice and new ice in lead areas, and open water. A sample set of observations in the Lincoln Sea from ESMR at 6000-m altitude, AMMR at 245 m altitude and SAR is shown in Figure 1. The white horizontal lines on the SAR image correspond to the P-3 aircraft track that went east (labeled A) and then west (B) at 6000 m altitude before going down to 245-m altitude (see red line labeled C) going east on the way to Svalbard. The ESMR images show the same basic features which can be identified in the SAR image. They confirm current interpretation of high brightness temperature for first-year ice, intermediate values for multiyear ice and low brightness temperatures for open water and some types of new ice. Figure 1 also shows that the active (SAR) and passive (ESMR) sensors provide complementary information about the sea ice cover since the active system shows strong contrast between open water and multiyear ice, while the passive shows strong contrast between open water and first-year ice. If an ice type cannot be unambiguously identified by one sensor, the other sensor would most likely remove the ambiguity.

The lower part of Figure 1 shows color-coded plots of AMMR data taken at the 245-m altitude and hence at a resolution of 31 m along the track. The fine resolution enables observation of variations in brightness temperatures over the same multiyear ice floes. Data that have been identified in the SAR image as leads are labeled 1, 2, and 4 while some of those exhibiting first-year ice signatures are labeled 3 and 5. These two different surfaces show unique separation of the different AMMR channels, i.e., large multispectral separation in brightness temperatures for leads and much smaller separation for first-year ice. The small separation for first-year ice is consistent with the expected opacity of the ice surface, which in turn minimizes frequency dependence. The signatures for multiyear ice appears intermediate between those of first-year ice and open water. The multiyear ice brightness temperature also show considerable variations spatially, partly because of small tiny refrozen leads imbedded within large multiyear ice floes. However, it is obvious that the variability is caused by more than just the introduction of first-year ice within the field of view of the sensor. For example, the multiyear ice region immediately to the right of the first-year ice cover, which is labeled 3, shows brightness temperatures significantly lower than those of the other ice surfaces shown in the image. Variations within floes apparently not contaminated by first-year ice can also be observed. The observation of such variations is possible only because of the small footprint of the AMMR.

Variations in brightness temperatures of multiyear ice over much larger spatial scale are shown in scatter plots of 18 vs 37 GHz at horizontal polarization (Fig. 2). The scatter plots are for the 31-m resolution data taken (at 245-m altitude) near or over (50°W, 87°N), (30°W, 85°N), and (8°W, 83°N) on 19 May, 20 May, and 21 May, respectively. In all three cases, most of the multiyear ice floes were large enough to fit several AMMR footprints inside the boundaries. Thus, the minimum values (as marked) in each of the scatter plots should represent brightness temperatures from some of these consolidated multiyear ice covers. The lowest values are 140 K, 153 K, and 163 K, for the 19 May, 20 May, and 21 May data. During this

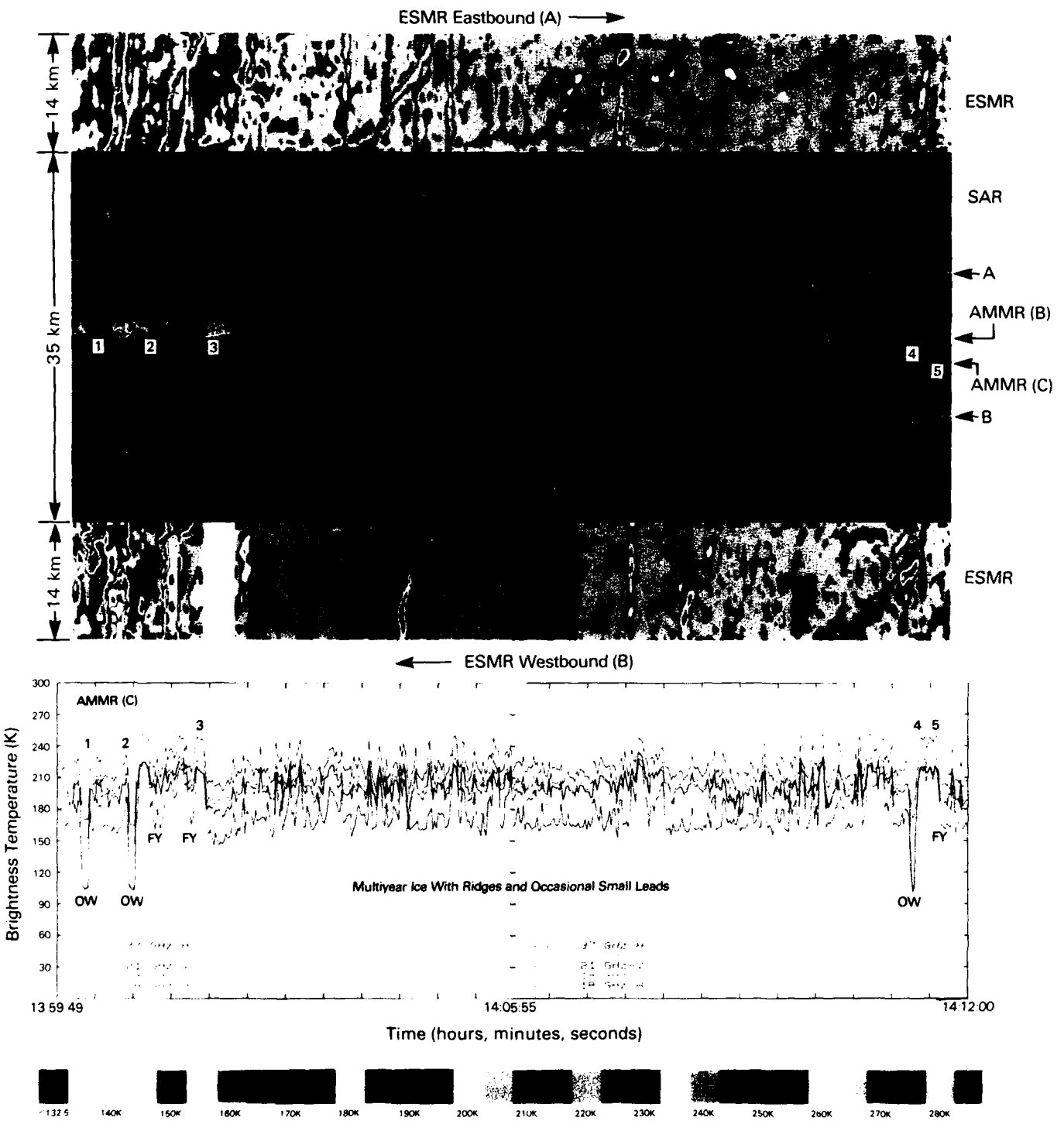

Figure 1. Sea ice conditions in Lincoln Sea as observed by ESMR at 6000-m altitude, SAR, and AMMR at 245-m altitude. The white horizontal lines on the SAR correspond to P-3 aircraft tracks during its eastbound (A) and westbound (B) legs, respectively. The red line in the middle (labeled C) corresponds to the low altitude eastbound leg. The color-coded line plots represent multispectral AMMR observations along track C at about 31-m resolution.

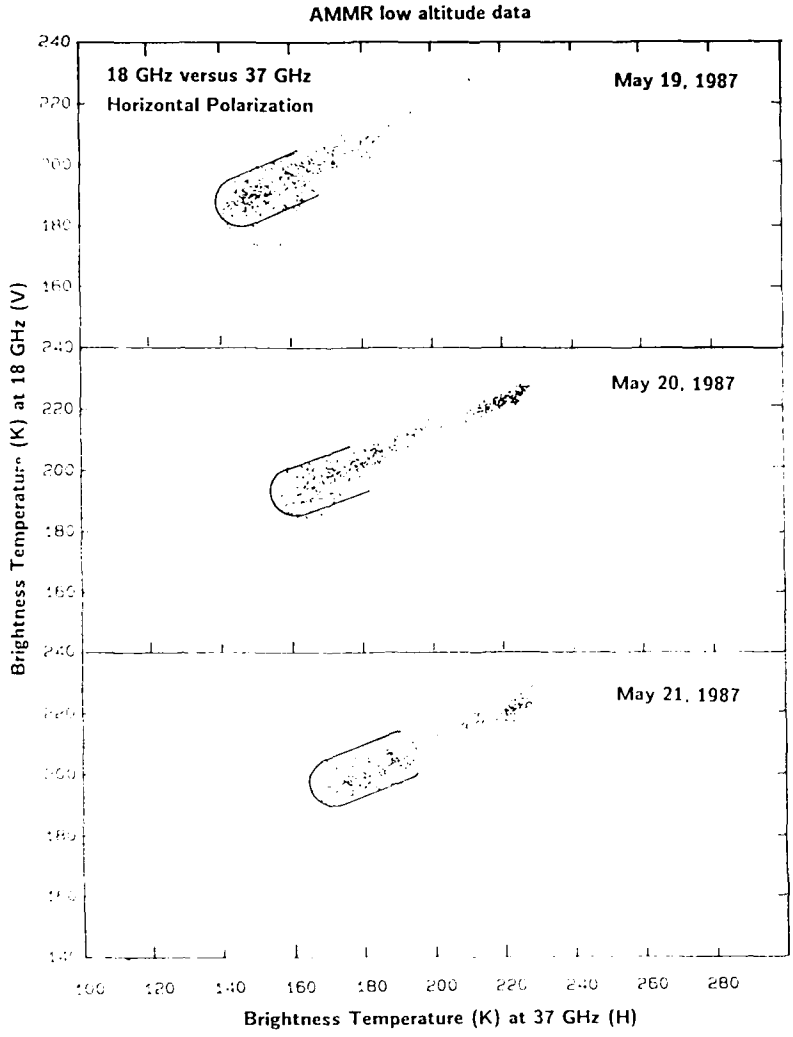

Figure 2. Scatter plots of 18- vs 37-GHz multispectral data over predominantly multiyear region near or over 50°W, 87°N, 30°W, 85°N, and 8°W, 83°N on 19 May, 20 May and 21 May, respectively.

time period, the surface temperature over ice as measured by the PRT-5 sensor was almost constant. Thus, the different values are likely associated with different emissivities for multiyear ice.

Significant variations in emissivities of multiyear ice in the Arctic region have been observed on a small scale and also on a global scale. Lower emissivities are observed deeper in the ice pack than near the marginal sea ice region. This is consistent with spatial variations observed in satellite data (Comiso 1986)* and indicate that such variations are not just due to variations of the fraction of first-year ice. The data also show that a combination of active and passive systems provide a more powerful tool for studying the characteristics of Arctic sea ice cover than just one of the two systems.

*Comiso, J.C. (1986) Characteristics of Arctic winter sea ice from satellite passive microwave observations. *Journal of Geophysical Research*, **91**(C1): 975–994.

Section V:

Sea Ice and Ice–Ocean Modeling

A Cavitating Fluid Sea Ice Model

G.M. FLATO AND W.D. HIBLER III
Thayer School of Engineering
Dartmouth College
Hanover, New Hampshire, U.S.A.

ABSTRACT/INTRODUCTION

The influence of the polar oceans on global climate is determined to a large degree by the movement, extent and makeup of their ice cover. An ice cover provides an effective insulating blanket, impeding the exchange of heat between the atmosphere and ocean, and a relatively reflective surface, reducing the incoming shortwave radiation. The insulating effectiveness of an ice cover is strongly dependent on its thickness, or more precisely, since pack ice is composed of a variety of thicknesses, on the areal fraction of each thickness. Of particular importance is the fraction of open water (ice of zero thickness) through which a large portion of the heat exchange takes place.

A feature of the large-scale behavior of sea ice is the observation that it is strongly resistant to convergence and yet relatively free to diverge. This can be understood by noting the similarity of pack ice to a granular medium—a collection of discrete particles (ice floes) separated by cracks and leads. Although this granular analogue more accurately describes the ice pack at small scales, at large scales it is more convenient to describe the aggregate behavior in terms of a continuous rheology. It is this rheology that relates the change in structure of an ice cover to the forces applied by winds and currents and is therefore a key to modeling ice dynamics.

The motivation for the present work is the development of a sea ice rheology parameterization that retains most of the essential physics of large-scale drift, yet is conceptually simple and computationally fast enough to be useful for long-term climate studies. The approach is to reformulate the velocity correction method of Nikiforov et al. (1967) and Parkinson and Washington (1979) and obtain the so-called cavitating fluid rheology. The rationale is that pack ice can be viewed as a two-phase medium (in two dimensions), one phase being ice and the other open water. The open water phase is considered to have no strength and so convergence will reduce the area of open water. The ice phase has some strength and so convergence is restricted if no open water is present. Divergence, on the other hand, is unhindered and causes open water to be created. In the model discussed here, the ice pack is assumed to have no shear strength which, although counterintuitive, has certain advantages: first, the model is much simpler, and second, a more robust (and realistic) circulation of the ice is maintained for wind fields averaged over periods of days or weeks.

By incorporating the cavitating fluid rheology into a complete dynamic–thermodynamic sea ice model and performing several three year simulations of the arctic sea ice cover, the effect of various parameters and time step lengths can be evaluated. Comparison with the more complete viscous-plastic model of Hibler (1979), which includes shear strength, yields insight into the effects of this simplified parameterization.

NUMERICAL SCHEME

While the concept is similar, the essential features of the numerical scheme to implement the cavitating fluid rheology differ from previous work. The basic idea is to start with free drift, i.e., the ice velocity field calculated by ignoring ice interaction, and then correct these velocities in a manner that reflects the compressive strength of the pack ice. Nikiforov et al. (1967) used a similar scheme in their model of nearshore ice flow in the East Siberian and Chukchi seas. Their correction scheme was simply to remove the onshore component of velocity when the compactness reached 100%. This scheme was extended by Parkinson and Washington (1979) to include the case of convergent flow away from a coast. In their scheme, the inward velocity components at any computational grid cell were reduced in an iterative fashion so that the compactness remained at or below a specified amount. Hibler (1979) pointed out that this method does not conserve momentum and in certain cases seems to stop almost all motion. The numerical scheme presented below preserves the spirit of these *ad hoc* schemes in that it is a correction to free drift. However, the correction is consistent with what an internal ice pressure would do to the velocity field and hence conserves momentum. An important aspect of the present numerical scheme is that the internal ice pressure is explicitly calculated. In the present case, this is made particularly simple by assuming linear wind and water drag formulations.

Aside from providing a rationale for the velocity correction, the pressure calculation can be used, in conjunction with an assigned failure strength, to allow some convergence and so provide a mechanism for dynamic increase of ice thickness. In our model's simplest form, the "incompressible cavi-

tating fluid," divergence is allowed to occur unhindered while convergence is not allowed. In other words, the pack is assumed to have no tensile or shear strength and infinite compressive strength. The scheme is easily extended to allow convergence (and the concomitant increase in thickness) if the strength of the ice, taken to be a linear function of thickness, is exceeded. This modification is found to be particularly important in long-term integrations.

A FEW RESULTS

Preliminary testing of the model was conducted using a 160-km square grid covering the Arctic Ocean and part of the Greenland Sea. Climatological thermodynamic and current forcing were used along with daily wind fields from 1979, which were averaged and gave a monthly mean wind twice that of existing climatology. Space limitations prevent discussion of all the results and so only a few selected results are presented.

The incompressible cavitating fluid model is of interest because the internal ice pressure required to halt convergence is obtained directly. During the first month of a simulation, with daily varying winds, no

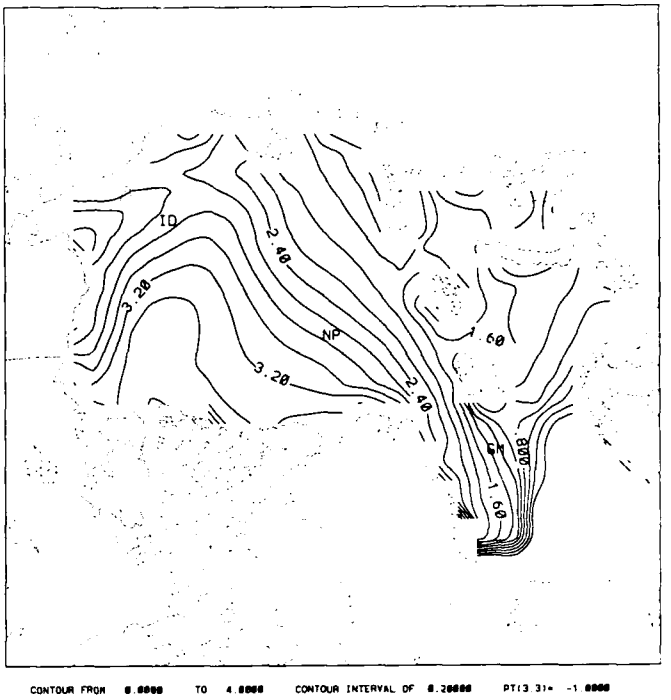

Figure 1. Contours of ice thickness (m) at the end of January, year three, for the cavitating fluid model with one-day time steps (contour interval of 0.2 m).

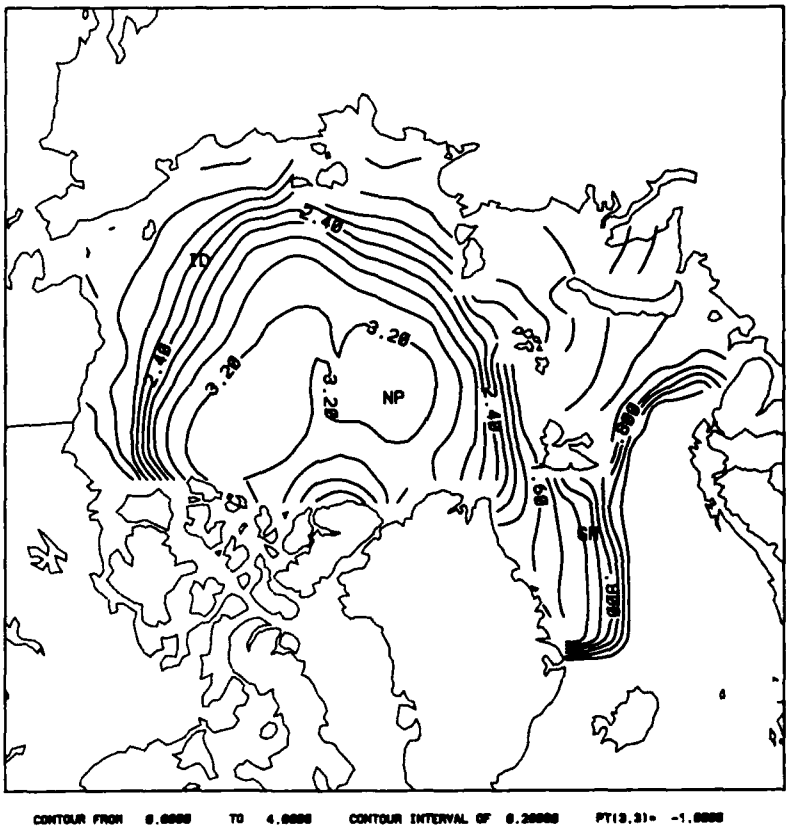

Figure 2. Contours of ice thickness (m) at the end of January, year three, for the cavitating fluid model with 30-day time steps (contour interval of 0.2 m).

thermodynamic growth and the ice maintained at a uniform 2-m thickness, the maximum two-dimensional pressure was about 100 kN/m. These high pressures were most prevalent off the North Slope of Alaska and the Canadian Archipelago.

Dynamic buildup of thickness can be simulated by allowing a certain amount of convergence if the pressure required to halt convergence is larger than some specified strength—in this case a linear function of thickness. The amount of convergence is chosen as some fraction of the free drift convergence such that the thickness, after the advection step, is just sufficient to prevent the remaining convergence. The slope of the linear thickness-strength relationship was chosen after some experimentation to give a thickness buildup and ice export from the basin comparable to the more complete Hibler (1979) model; the result was a strength of 10 kN/m per meter of ice thickness. Figure 1 shows thickness contours at the end of January, year three of the model, of a full dynamic–thermodynamic simulation using this strength relationship and one-day time steps. The pattern of thickness buildup compares favorably with that of the Hibler (1979) model. To demonstrate the ability of the cavitating fluid model to tolerate long time steps, a similar run was made using 30-day time steps. In this case the advection had to be performed in several steps to satisfy the Courant-Freidrichs-Levy criterion. As shown in Figure 2, the thickness buildup is about the same; however, the pattern is somewhat different (the thicker ice being concentrated near the pole rather than the Canadian Archipelago) reflecting the less robust forcing of 30-day averaged wind fields. The pressure field, although not shown, confirms this interpretation.

The presence of shear resistance in Hibler's (1979) model, while obviously more realistic, causes the circulation to decrease dramatically when daily wind forcing is replaced by monthly averaged forcing. Although this same change in forcing caused a noticeable change in the thickness characteristics, the circulation, as shown by Figures 3 and 4, changed very little. In fact, the average velocity magnitude for the 30-day time step case (0.166 m/s) is about 4%

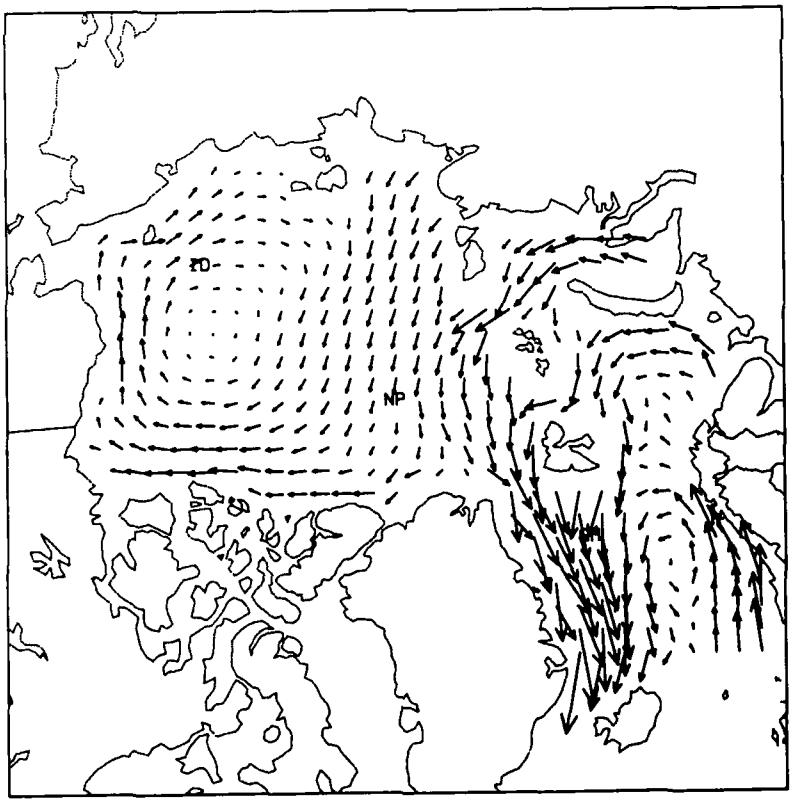

Figure 3. Velocity field for January, year three, for the cavitating fluid model with one-day time steps (a vector one grid cell long is about 0.1 m/s).

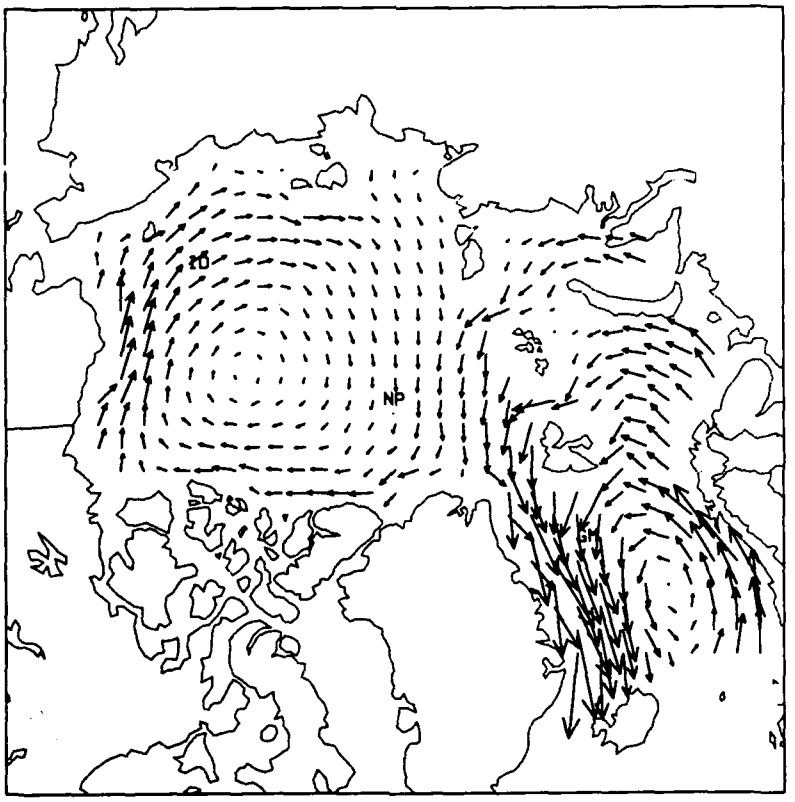

Figure 4. Average velocity field for January, year three, for the cavitating fluid model with 30-day time steps (a vector one grid cell long is about 0.1 m/s).

larger than the average magnitude in the one-day time step case (0.159 m/s). The average velocity in the one-day time step case is lower due to the nonlinear effect of ice interaction on fluctuating velocities.

CONCLUSIONS

The cavitating fluid rheology shows considerable promise as a simple parameterization for modeling sea ice dynamics. Its advantages are simplicity, speed and tolerance of long time steps, which particularly suit it to long-term climate studies. Its disadvantage, for short time steps, is the unrealistic lack of shear strength; however, at longer time steps this actually offsets the excessive smoothing of the wind field and produces a more realistic ice circulation. When the ice strength parameters have been appropriately "tuned," the cavitating fluid model produces velocity and ice thickness distributions similar to those of the more complete viscous-plastic model of Hibler (1979).

ACKNOWLEDGMENT

This work was supported by the Office of Naval Research under contract no. N00014-85-K-0695.

REFERENCES

Hibler, W. D. III (1979) A dynamic–thermodynamic sea ice model. *Journal of Physical Oceanography*, **9**: 815–846.

Nikiforov, Y.G., Z.M. Gudkovich, Y.I. Yefimov and M.A. Romanov (1970) Principles of a method for calculating the ice redistribution under the influence of wind during the navigation period in arctic seas (in Russian, 1967). English translation in *AIDJEX Bulletin*, no. 3, p. 40–64.

Parkinson, C.L. and W.M. Washington (1979) A large-scale numerical model of sea ice. *Journal of Geophysical Research*, **4**: 311–337.

The Importance of an Interactive Ocean on the Simulation of the Annual Cycle and Interannual Variations of Ice Cover in the Arctic

G.H. FLEMING
Naval Postgraduate School
Monterey, California, U.S.A.

ABSTRACT/INTRODUCTION

A coupled ice–ocean numerical model is used to simulate the annual cycle and interannual variations in ice cover that occur in the Arctic. The coupled model is a further development of the work by Semtner (1987). It incorporates the best features of several previous modeling efforts by numerous authors (Parkinson and Washington 1979, Hibler and Bryan 1987, Walsh et al. 1985). The ocean portion is a full primitive equation model with 13 vertical levels and 110-km horizontal resolution. Bottom topography, islands and coastlines are represented to the limits of the resolution. The ice portion of the model accounts for both dynamic and thermodynamic forcing. The ice dynamics are handled using a "viscous-plastic" rheology similar to that of Hibler (1979), although the ice dynamics code was modified to use monthly mean forcing instead of daily forcing to reduce the computational requirements. The ice thermodynamics were represented by the Semtner (1976) "3-layer" thermodynamic ice model. The ice and ocean models were linked through a common 30-m mixed layer with appropriate salt, heat and momentum fluxes at each grid point. The linked ice–ocean model was forced by monthly averaged fields of observed atmospheric variables as provided by J. Walsh (pers. comm., 1988) with specified river inflow and mass flux at the open boundaries.

J. Walsh also provided "observed" monthly ice concentration fields on an equivalent grid for direct comparison with the simulation results. The decade 1971–1980 was chosen for examination, as the inclusion of microwave data into the "observed" ice fields in this time period significantly improved their accuracy. It was shown in Fleming (1987) and Garcia (1989) that correlations between ice concentration and forcing variables such as sea surface temperature, air temperature, winds, atmospheric pressure and ice history vary considerably from region to region in the Arctic. In order to gain some appreciation of this feature but still maintain the amount of data manipulation within reasonable limits, the complete grid space was divided into four regions (see Fig. 1). The divisions were selected based on the ease

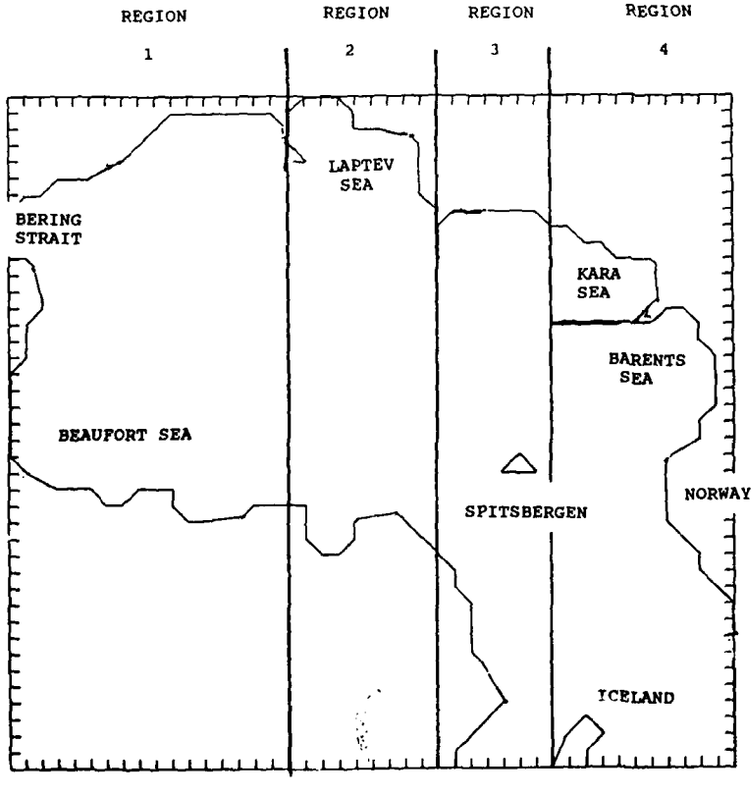

Figure 1. Grid space geography and regional boundaries.

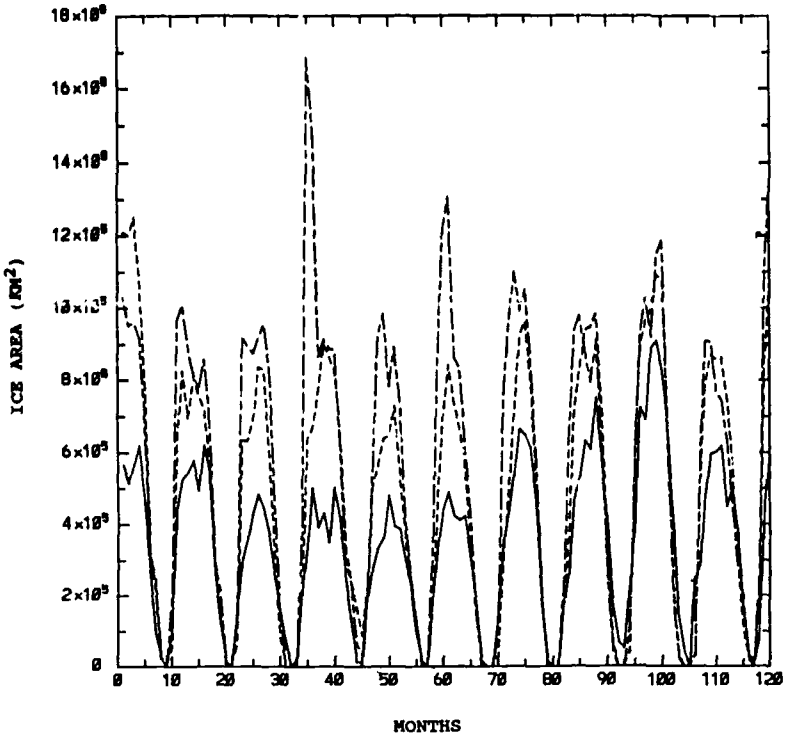

Figure 2. Total ice area time series in region 4. Solid line is observed data; dotted line is output from interactive ocean model; dash-dot line is output from prescribed annual ocean cycle model.

of boundary definition and the general ocean current regime. The four regimes represented were the following:

Region 1. Beaufort Gyre.

Region 2. Transpolar Drift, Ellesmere Island and Greenland ice convergence zone.

Region 3. Transpolar Drift, East Greenland Current (EGC).

Region 4. Norwegian Current.

THE EXPERIMENT

This work involved two primary model runs. The first run used the complete linked model with forcing and boundary conditions as described above. All oceanic variables were saved at each time step. The stored data were then averaged over each month for 10 years to produce a mean annual cycle ocean. The second run was identical to the first except the mean annual cycle ocean was substituted for the interactive ocean model. The ice concentration output fields from the two runs were then compared to the "observed" fields using statistical correlation to assess the skill of each ice concentration simulation. The differences between the two simulations were a measure of the importance of including an interactive ocean in ice simulation models.

The average time for a single year in the mean annual cycle ocean case, where the ocean condition was predetermined, was 275 seconds using a Cray XMP. Inclusion of the interactive ocean, approximately doubles the computation requirements; however, the computation load remains very manageable.

ANALYSIS AND OBSERVATIONS

A qualitative comparison between the two simulation cases, and with the observed data, was achieved by plotting the contours of ice concentration, ice thickness, two ocean layer velocities and oceanic heat flux into the mixed layer for all simulated months.

Quantitative analysis of the results was confined to the ice concentration fields as these were the only data that had reasonably "true" values for direct statistical comparison. The total ice area for each region for each month for each data set was calculated by multiplying the ice concentration at each grid point by the grid box area (e.g., Fig. 2). For ease of description, the observed data were designated A, the interactive ocean output B, and the mean annual cycle ocean output C. The mean annual cycles of ice concentration for A, B and C were determined and subtracted from their respective ice concentration time series. This produced time series of ice concentration anomalies or differences from monthly means (Fig. 3 and 4).

The following general observations were made:

1. The region of transition from 10/10 to 0/10 concentration (the MIZ) is narrower for both B and C than for A.

2. Both B and C overpredict the ice coverage in winter, especially in the Barents Sea and EGC; however, B is usually closer to the observed coverage than C.

3. Both B and C underpredict the coverage in summer, especially in the western Arctic Ocean and Kara Sea. B is again usually closer to the observed cover-

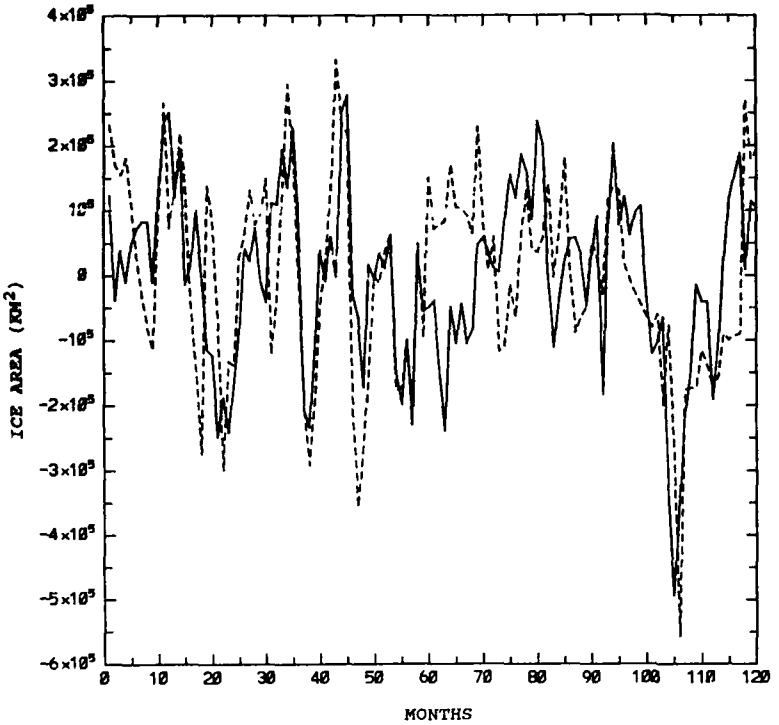

Figure 3. Anomaly ice area time series in region 3. Solid line is observed data; dotted line is data from the interactive ocean model.

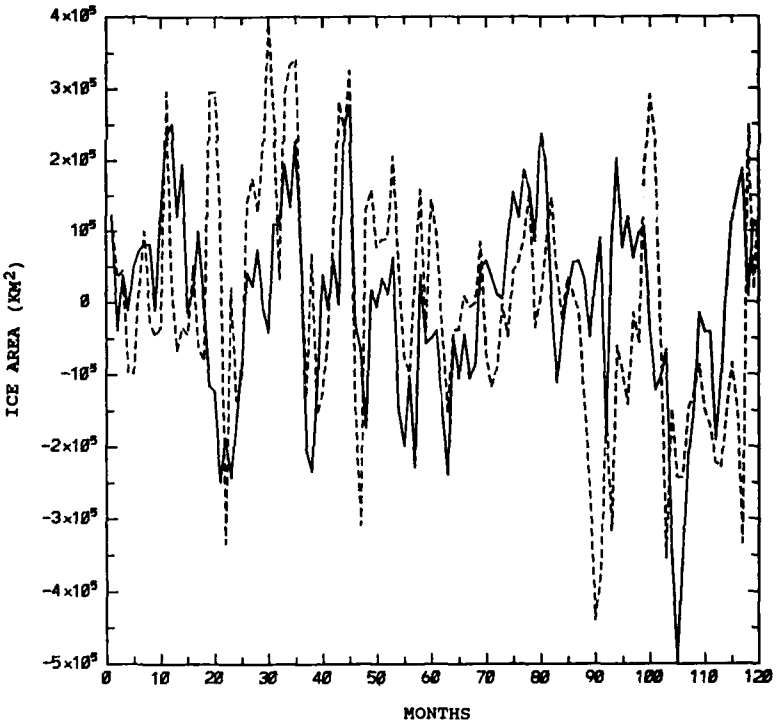

Figure 4. Anomaly ice area time series in region 3. Solid line is observed data; dotted line is data from the prescribed annual ocean cycle model.

age than C in the eastern Arctic but the improvement in the central and western Arctic is minimal.

4. The general shape of the ice edge is reasonably well simulated by both B and C. The Kara and Barents seas are notable exceptions.

5. The simulated pack ice thicknesses in the central Arctic Basin are 1–2 m or 50–100% less than average observed values. Thicknesses produced in the B case tend to be larger than those in C. The simulated thickness data indicate that both models are compacting ice along the north coast of Greenland and Ellesmere Island as expected; however, thickness values in this region were too low by a factor of three or more. Bourke and Garret (1987) was the source of ice thickness data for comparison.

6. The geographic boundaries of the four regions

Table 1. Statistical comparisons of observations and models by region.

	Standard deviation			*Correlation coefficient*	
	A	*B*	*C*	*A–B*	*A–C*
Ice area time series					
Region 1	0.3169E+06	0.7776E+06	0.8246E+06	0.9126	0.8852
Region 2	0.1434E+06	0.3729E+06	0.3996E+06	0.9271	0.8807
Region 3	0.4283E+06	0.6755E+06	0.6910E+06	0.9461	0.9106
Region 4	0.2292E+06	0.3667E+06	0.4220E+06	0.9186	0.8332
Anomaly time series					
Region 1	0.1146E+06	0.2220E+06	0.2701E+06	0.4936	0.3963
Region 2	0.5898E+06	0.1660E+06	0.1821E+06	0.7761	0.5981
Region 3	0.1376E+06	0.1518E+06	0.1677E+06	0.5375	0.3039
Region 4	0.9937E+06	0.1311E+06	0.1418E+06	0.6172	0.3332

limit the seasonal variability of the total ice area; however, a large amount of variability from year to year is still evident. Variations of total regional ice area between years in the observed data vary from approximately 15% of the mean in regions 1 and 2, to 40% in region 3, to 100% in region 4. The simulated data have a larger variance in interannual ice area differences, ranging from approximately 40% of the mean in regions 1 and 3, to 60% in region 2, to 100% in region 4.

7. The mean annual cycles of ice area for A, B and C show that the melt–freeze cycle in the modeled cases is in phase with the observed annual cycle but of higher amplitude. C generally has the largest amplitude, A the least.

8. The time series of ice area anomalies (difference from annual cycle) for both observed and simulated data vary significantly from region to region. Some similarities can be found in adjacent regions; however if not adjacent, the regional independence is quite apparent.

9. The degree of monthly variability or "noisiness" in the anomaly series increases markedly in regions 3 and 4 as compared to regions 1 and 2.

10. The anomaly time series show periods when both B and C are significantly different from A and both differ with the same sign. There are also times when the simulated anomalies differ significantly from the A anomalies but with opposite signs.

11. Over the 120-month period, model runs using the interactive ocean (B) produced ice concentration fields that correlated higher with the observed data than the average ocean case (C) in all regions. This was true for both the total ice area time series and the anomaly (interannual variability) time series (see Table 1).

CONCLUSIONS

Inclusion of the interactive ocean produced an improved accuracy of simulation of the total ice area, particularly in region 4. The degree of improvement is somewhat masked in the first half of Table 1, as the very high correlations are primarily a reflection of the strong annual cycle. However, the absolute sum of the differences between the simulated and observed fields was also calculated and confirmed the improvement. The fully linked ice–ocean model represents the monthly variable ocean forcing (heat and momentum) much better than the average annual cycle ocean model. This suggests that monthly variable ocean forcing is very important to the evolution of ice area in the eastern Arctic. By contrast, in regions 1 and 2, the interactive ocean run did not improve the representation of total ice area as much. In these regions, it is probably the atmospheric forcing or the ice rheology, the parameters of which were not changed between experiments, that control the evolution of total ice area.

Inclusion of the interactive model also produced notable improvements in simulating the interannually varying ice concentration field in all regions of the Arctic. This indicates that the interannual changes in the ocean forcing are a major influence on the interannual variability of the ice field over the entire Arctic Basin. The importance of including an interactive ocean in seasonal ice prediction models is therefore demonstrated.

Simulated ice thickness has not been improved substantially. Again, as for total ice area in the western Arctic, modifications to the way atmospheric forcing is handled (albedo, drag coefficients) or to the ice rheology will probably be required to improve this parameter.

BIBLIOGRAPHY

Bourke, R.H. and R.P. Garret (1987) Sea ice thickness distribution in the Arctic Ocean. *Cold Regions Science and Technology*, **13**: 2107–2117.

Fleming, G.H. (1987) Predictability of ice concentration in the high-latitude North Atlantic from statistical analysis of SST and ice concentration data. M.Sc. Thesis, Naval Postgraduate School, Monterey, California.

Garcia, K.S. (1989) Predictability of ice concentration anomalies in the high latitudes of the North Atlantic using a statistical approach. M.Sc. Thesis, Naval Postgraduate School, Monterey, California.

Hibler, W.D. III (1979) A dynamic thermodynamic sea ice model. *Journal of Physical Oceanography*, **9**: 815-846.

Hibler, W.D. III and K. Bryan (1987) A diagnostic ice–ocean model. *Journal of Physical Oceanography*, **17**: 987–1015.

Parkinson, C.L. and W.M. Washington (1979) A large-scale numerical model of sea ice. *Journal of Geophysical Research*, **84**: 311–337.

Semtner, A.J. (1976) A model for the thermodynamic growth of sea ice in numerical investigations of climate. *Journal of Physical Oceanography*, **6**: 379–389.

Semtner, A.J. (1987) A numerical study of sea ice and ocean circulation in the Arctic. *Journal of Physical Oceanography*, **17**: 1077–1099.

Walsh, J.E., W.D. Hibler III and B. Ross (1985) Numerical simulation of Northern Hemisphere sea ice variability 1951-1980. *Journal of Geophysical Research*, **90**: 4847–4865.

On Modeling the Baroclinic Adjustment of the Arctic Ocean

W. D. HIBLER III
Thayer School of Engineering
Dartmouth College
Hanover, New Hampshire, U.S.A.

ABSTRACT

Over the deep portions of the Arctic Basin the currents are largely geostrophic with relatively small barotropic components. To examine the character of the process that leads to these currents, a geostrophic ocean circulation model is developed and used to examine the wind-driven baroclinic adjustment of the Arctic Ocean.

INTRODUCTION

Since ocean currents play an important role in driving ice drift, it is necessary to understand the main characteristics of the Arctic Ocean circulation in order to understand ice drift. A critical feature of the Arctic Ocean circulation is the rather complete baroclinic adjustment and the role played by the bottom torque term in the mean circulation. An essential difference between the Arctic Ocean and midlatitude seas is the absence of any beta effect leading to a western intensification of the currents. Instead, in the Arctic the barotropic flow is largely dictated by the bottom depth contours. If the currents were only barotropic, this would lead to extremely small surface currents. However, the baroclinic adjustment is rather complete, so that a strong surface current can occur. This density adjustment also couples with the bottom topography to yield a bottom torque term on the integrated flow that is very significant. In order to better understand this adjustment process a geostrophic ocean model has been constructed and used to examine the character of the wind-driven baroclinic adjustment of the Arctic Ocean.

MODEL DESCRIPTION

The governing momentum equations of the ocean circulation are given by:

$$0 = -\frac{\partial p}{\partial x} + A_H \nabla^2 u + fv + \tau_x \delta(z)$$

$$0 = -\frac{\partial p}{\partial y} + A_H \nabla^2 v + fu + \tau_y \delta(z)$$

where p = pressure in the ocean at a given depth
u and v = x and y components of ocean currents
A_H = horizontal eddy viscosity
z = depth
τ_x and τ_y = x and y components of the surface wind stress on the ocean.

These momentum equations are coupled to conservation equations for temperature and salinity and a simple convective adjustment process. The momen-

tum equations are integrated to a steady velocity solution with a fixed wind forcing at 5.3 day time steps. These velocity fields are then used in the conservation equations which are also integrated at 5.3-day time steps. The topography, geometry and number of layers in the ocean model are effectively the same as used by Hibler and Bryan (1987).

Two different types of initial conditions are employed: spatially constant but vertically varying temperature and salinity profiles, and observed temperature and salinity fields from Levitus (1982). The spatially constant fields are obtained by spatially averaging the observed data. These two experiments will be referred to as the "spatially constant" and "diagnostic" initializations, respectively. In the standard runs a lateral kinematic eddy viscosity of 2×10^{9} $cm^{2}s^{-1}$ is utilized. The wind stress is taken to be constant and is derived from 30-year mean geostrophic winds. Both these models are integrated for a number of years to yield some insights into the time scales and character of the baroclinic adjustment.

SIMULATION RESULTS

Some of the results of these simulations in terms of the vertically integrated stream function are shown in Figures 1 and 2. Also in Figure 3 are shown some surface pressure patterns and pressure differences which effectively represent streamlines for the highly geostrophic surface flow patterns.

As can be seen, the time scale is on the order of several years for the wind-driven baroclinic adjustment, with both the run initialized with observed data and the spatially constant run yielding quite similar stream functions at 10 years. Figure 2, for the prognostic run initialized with spatially constant fields, also demonstrates the very low currents that the purely barotropic flow yields. Specifically, due to the spatially constant temperature and salinity fields, the stream function at the end of year 1 is close to the barotropic field. As the system spins up, almost all the flow is due to the bottom torque term induced by the wind stress depressing the density fields in the middle of the basin. The basic idea here is that the circulation patterns induced by the wind stress curl do not well match the bottom topography so that very little flow occurs at depth, even though such flow is a solution of the equations of motion in the absence of forcing and lateral viscosity. Viewed from a different perspective the bending of the density fields by the wind curl induces significant currents in the upper part of the ocean which contribute to the stream function when the vertically integrated flow is calculated.

That the flow is concentrated in the upper layers is

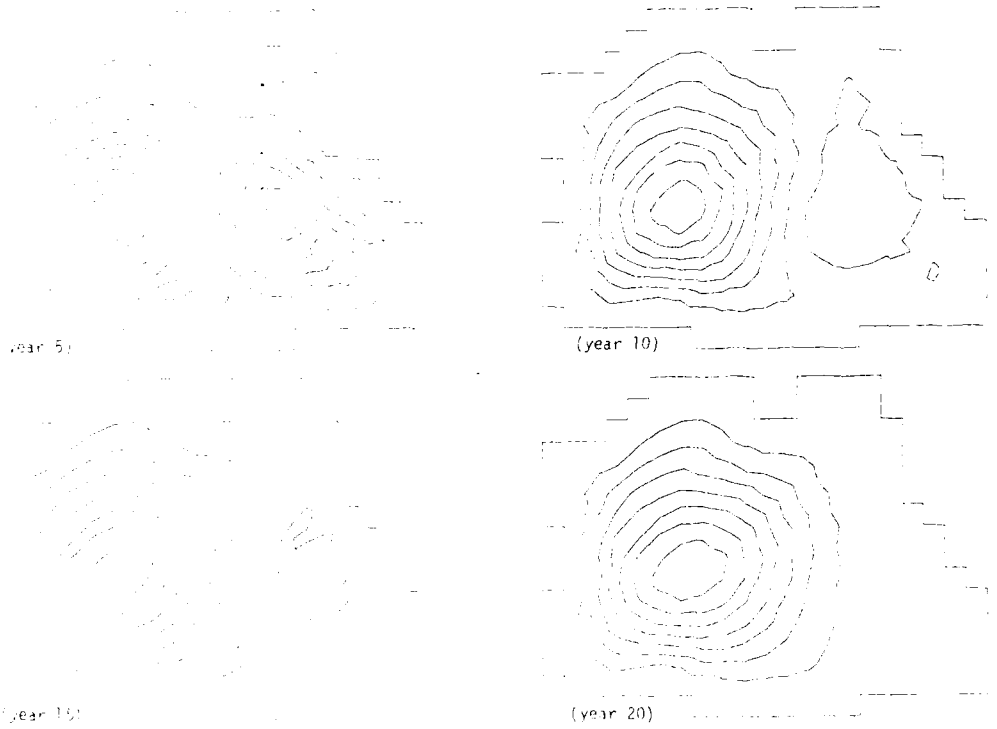

Figure 1. Vertically integrated stream function (0.4 sv contours) for numerical simulation initialized with diagnostic initial conditions. (Eddy viscosity of 2×10^{9} cm^{2} s^{-1}.)

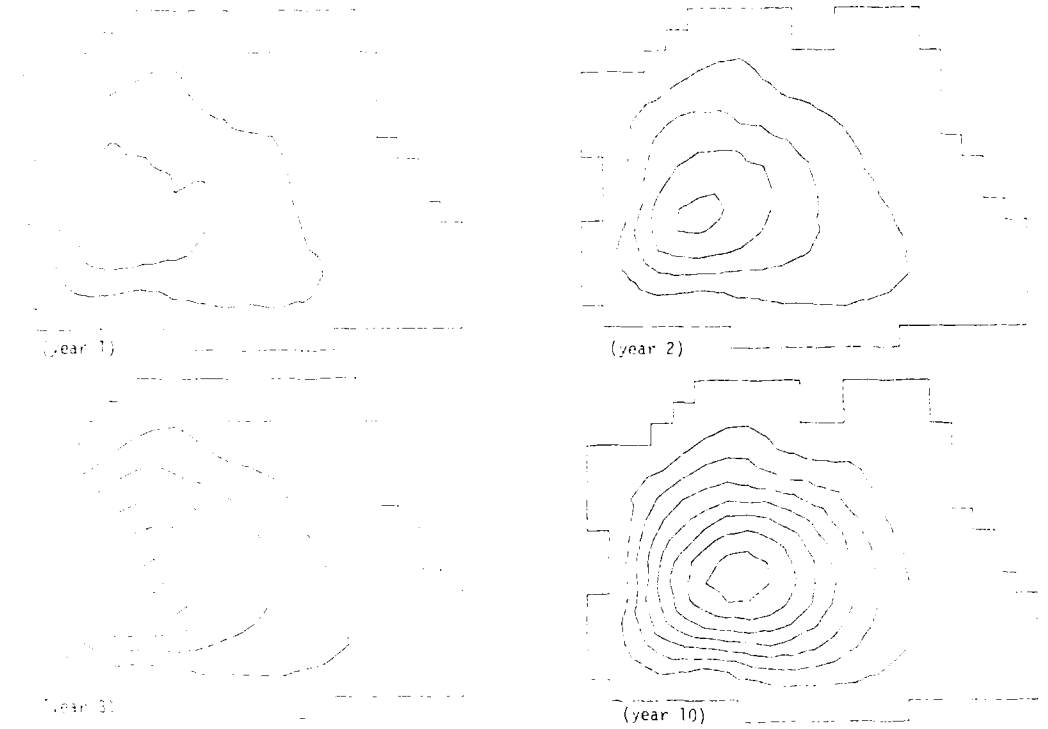

Figure 2. Vertically integrated stream function (0.4 sv contours)l for five spatially constant initial temperatures and salinity fields. (Eddy viscosity of 2×10^{9} cm^{2} s^{-1}.)

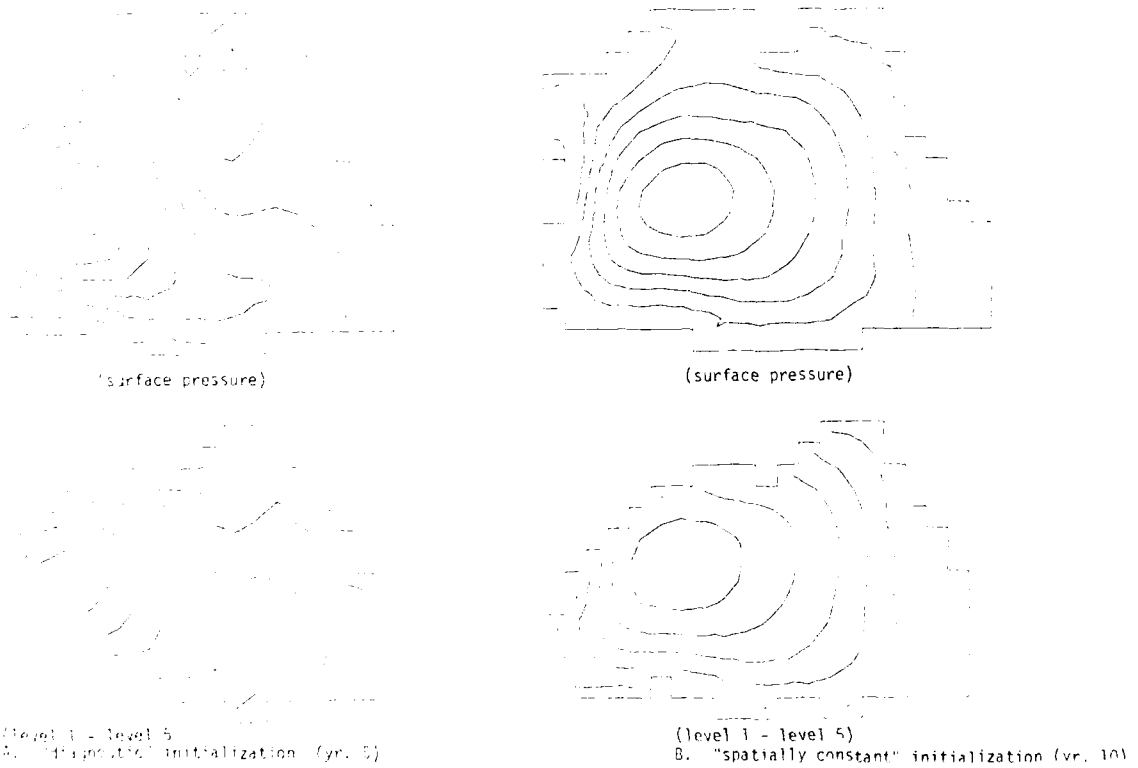

a. Year 5 of the diagnostic initialized run. b. Year 10 of the spatially constant initialized run.

Figure 3. Surface pressure and pressure difference between level 1 and level 5 (contour intervals of 5-cm dynamic height).

illustrated by examining the pressure differences between the top layer of the ocean and different levels, as shown in Figure 3 for year 5 of the "diagnostic" model and year 10 of the "spatially constant" simulation. (These pressure contours come close to being a stream function for the highly geostrophic flow.) As can be seen most of the flow occurs between levels 1 and 5 (level 5 is about 300 m in depth) as the variations in surface pressure and the pressure difference between levels 1 and 5 are very similar. However, while the pressure changes are small in the deeper layers, these depths also are substantially thicker so that the integrated flow can be significant. In particular, from the integrated stream function for the "diagnostic" run, we see that there is a flow reversal at depth, which would agree with limited existing observations of the Atlantic water flow, at least in the Eurasian Basin.

Note, however, that this flow reversal has largely disappeared at year 10 and never develops in the prognostic simulation. This phenomenon is currently being investigated in more detail, utilizing a full primitive equation model with higher resolution.

This significant flow reversal also induces some slight, but important, changes to the surface pressure fields, as can be seen by comparing Figures 3a and 3b. For the "spatially constant" initialized model, the surface pressures at year 10 are similar to those of the "diagnostically" initialized run, although the "diagnostic" run has the center of the pressure contours shifted slightly toward the Canadian coast of the Beaufort Sea by the presence of the second gyre, in better agreement with observations (see Coachman and Aagaard's [1974] results plotted in Hibler and Bryan [1987], for example.)

CONCLUSIONS

Overall, the results discussed in this note show that the initial conditions dissipate after about 10 years, and that the "spatially constant" initialized simulation, while quite similar to the "diagnostic" initialized simulation after 10 years, is significantly different earlier in the model runs. Consequently, while the time scale of the baroclinic adjustment takes several years, there is a potential here for considerable interannual variability in the wind-driven forcing as the average winds change on decadal or shorter time scales.

The similarity of the model results after 10 years also demonstrates the utility of a geostrophic model for modeling many features of large scale ice ocean circulation. However, inadequacies in the results, due partially to the large eddy viscosities, emphasize the need for higher resolution studies to fully investigate details of the Arctic Ocean circulation. To investigate time varying wave effects, primitive equation models will also be required. Such investigations are currently underway in the Dartmouth Ice Ocean Group.

REFERENCES

Coachman, L.K. and K. Aagaard (1974) Physical oceanography of arctic and subarctic seas. In *Marine Geology and Oceanography of Arctic Seas* (Y. Herman, Ed.). New York: Springer Verlag, p. 1–72.

Hibler, W.D. III and K. Bryan (1987) A diagnostic ice ocean model. *Journal of Physical Oceanography*, **7**: 987–1015.

Levitus, S. (1982) Climatological atlas of one world ocean. National Oceanic and Atmospheric Administration, NOAA Publication 13, Department of Commerce, Washington D.C.

Sensitivity Studies With a Coupled Ice–Ocean Model

M. N. HOUSSAIS
L.O.D.Y.C.
Université de Paris VI
Paris, France

W.D. HIBLER III
Thayer School of Engineering
Dartmouth College
Hanover, New Hampshire, U.S.A.

ABSTRACT

A two-dimensional ice–ocean model on a zonal slab is presented. The basic version of the model is a dynamic-thermodynamic sea ice model. Including a viscous plastic rheology, which is coupled with a two-dimensional ocean primitive equation model. Vertical mixing in the upper layer of the ocean is parameterized by an embedded mixed layer.

The model is applied to the central gyre of the Greenland Sea, which is known to be an active winter convection area. Meridional advection, which controls the preconditioning of the area with respect to deep convection, cannot be predicted within a two-dimensional framework. A damping term is therefore added in the ocean conservation equations. In order to parameterize the meridional heat flux associated with the Atlantic water circulation, the model is run with prescribed atmospheric forcing until a seasonal equilibrium is reached. Various studies are then carried out in order to test the sensitivity to changes in different components of the system.

In the first sensitivity experiment the ocean is at rest and only turbulent entrainment and mixing are considered. The influence of Ekman pumping and of zonal advection on the ocean stratification and on the related ice distribution is estimated. Secondly, the efficiency of turbulent mixing in convection conditions is tested by comparing the basic version of the model with a fixed-depth mixed layer version. The time-space distributions of the oceanic heat flux to the ice are compared when different parameterizations of this flux are applied. Regarding ice these dynamic effects are estimated by comparison with a thermodynamic-only version of the ice model. Zonal ice advection effects are also compared with meridional ice advection effects as prescribed from a climatological seasonal cycle. Various wind stresses representative of typical MIZ conditions are used. The ice drift field and the momentum transfer through the ice are highly dependent upon the wind stress distribution and the mechanical behavior of the ice.

Full Sea Ice Model Forced With GCM Atmosphere
Alleviation of a Systematic Thickness Bias through a Modified Strength Parameterization

P. LOEWE
Max Planck Institut für Meteorologie
Hamburg, Federal Republic of Germany

ABSTRACT/INTRODUCTION

The climatic impact of increasing CO_2 as projected by global GCM-type models is critically affected by the response of sea ice (Manabe and Stouffer 1980, Dickinson et al. 1987, Washington and Meehl, in press). Typically this response is based on a simple thermodynamic model disregarding ice dynamics. As an evolutionary step in the direction of a more realistic coupled model Hibler's (1979) full dynamic-thermodynamic sea ice model is integrated over a period of five years repeatedly employing a single year of modeled, daily varying atmospheric forcing fields. The forcing is specified from an atmospheric simulation with the European Centre's spectral T21 GCM being further developed in Hamburg for climate research.

RESULTS/DISCUSSION

Figure 1 (left panel) illustrates the seasonal extremes of the equilibrium thickness cycle as obtained for the fifth year of the control simulation. An outstanding feature of this figure is the excessive mechanical buildup in the East Siberian Sea, which is observed to become relatively ice-free in summer. As may be inferred from the seasonal drift characteristics depicted in Figure 2 (left panel), biased wind-forcing is largely responsible for this misplaced heavy ice in winter (Loewe 1989). It is interesting to note that the same ice model has produced a similar "unrealistically large buildup against the Siberian shore" when driven with "atypical" FGGE-winds (Hibler and

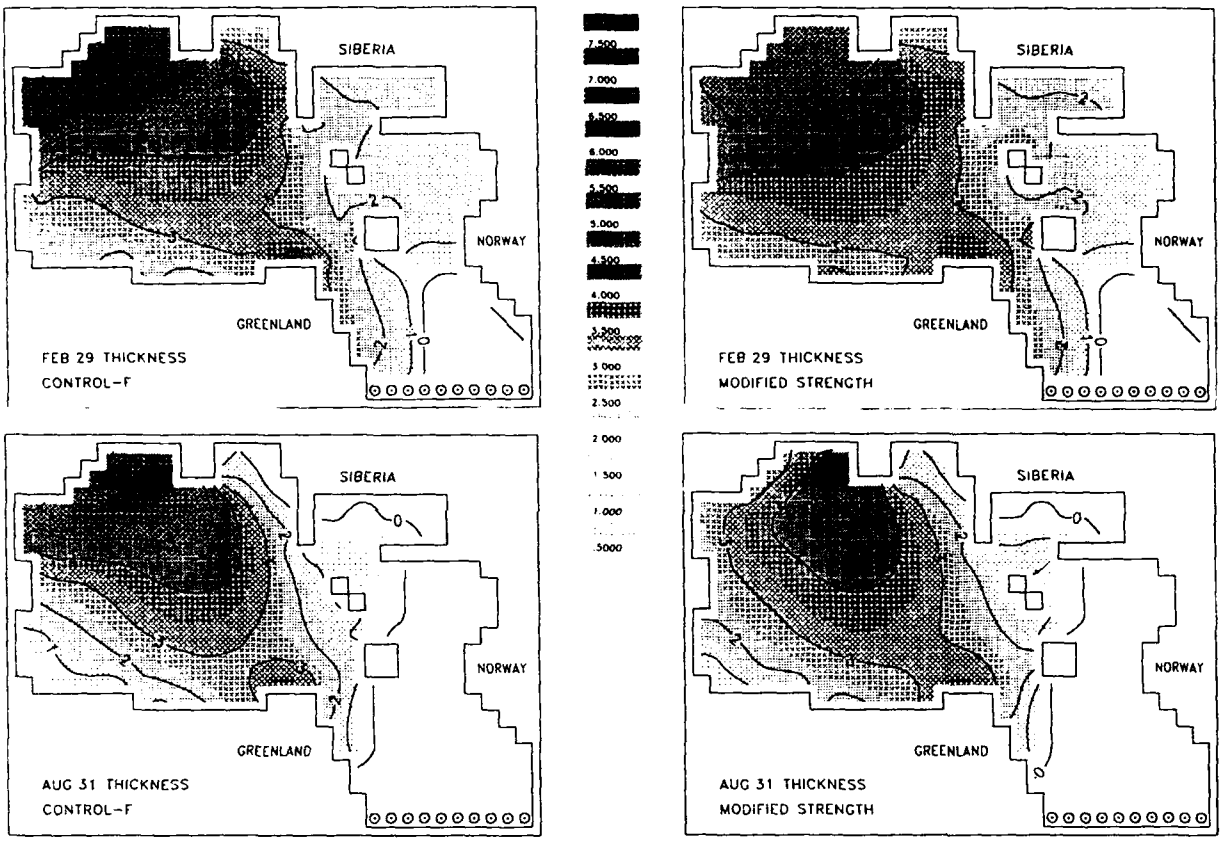

Figure 1. Close to maximum and minimum ice thickness fields for the control simulation and the modified strength simulation, employing eq 1) and eq 6, respectively.

Bryan 1987, Fig. 10). Although generated by an anomalous or biased wind stress, the excessive buildup might also reflect exceedingly sensitive behavior of internal sea ice dynamics. Evidence (not proof) in support of this hypothesis has been previously advanced together with a modified strength parameterization (Loewe 1988). In the following, the background for this parameterization is presented in greater detail along with results from a sensitivity simulation, demonstrating its effect.

From the point of view of climate modeling, the limitation of mechanical pileup appears to be the chief function of an ice rheology. The thickness response heavily depends on how the strength of the ice (as a measure of its ability to resist compression) is related to its changing physical state. In the framework of his viscous-plastic rheology Hibler (1979) parameterized the yield strength P in terms of the two-level thickness characteristics as

$$P = P^* h\, e^{-c(1-A)} \qquad (1)$$

where $P^* = 2.75 \times 10^4$ N/m^2, $c = 20$, and A and h denote compactness and grid-square mean thickness, respectively. Hardening (or weakening as $\partial P/\partial t < 0$), associated with an expanding (contracting) elliptical yield curve, occurs in response to the ice becoming thicker (thinner) or more (less) compact. The significance of strength is not only due to $-P$ defining the maximum supportable compressive stress and thus the size of the yield curve in principal stress space; as the literally central point (of the yield ellipse) $-P/2$ represents negative *hydrostatic pressure* or, equivalently, the stress state in case of no motion (or rigid motion). The force due to internal ice stress ($div\sigma$) in this case is due only to an inhomogeneous pressure field: $div\sigma = -\text{grad}\, P/2$.

As is apparent from Figure 2, in spring all motion nearly stops in the East Siberian Sea. Moreover, Figure 3 confirms that $div\sigma$ is dominated by the pressure gradient that finally is sufficiently strong to prohibit further ice buildup by essentially balancing the wind stress. To gain further insight into the heavy ice problem and its alleviation it should be noted that eq 1 is a particular form of

$$P = f[h(x,y,t)]\, g[A(x,y,t)]. \qquad (2)$$

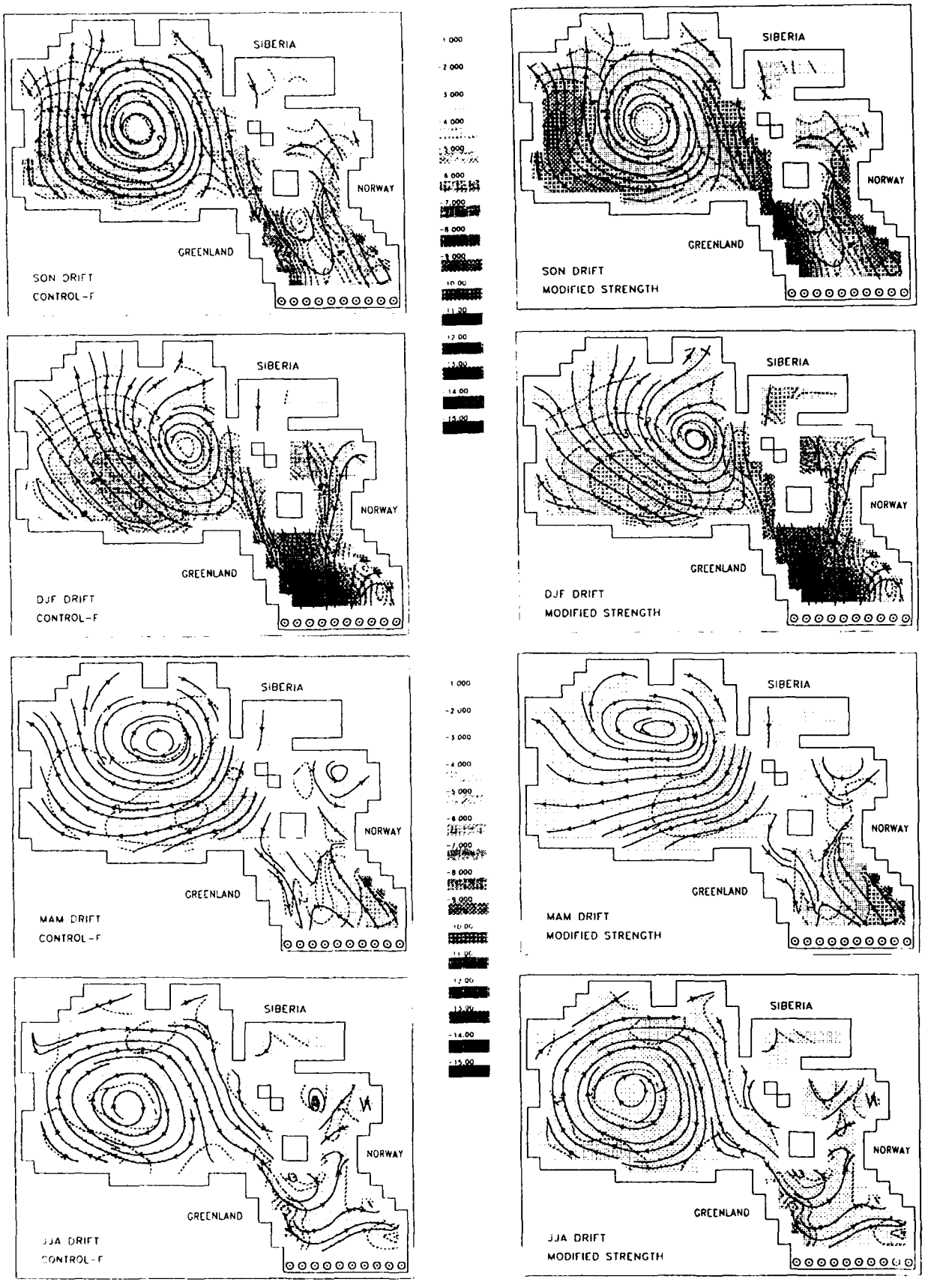

Figure 2. Seasonal drift characteristics (SON = Sep–Oct–Nov, etc.) for the control simulation (left panel) and the modified strength simulation. Streamlines and drift rates (m/s) represent direction and velocity of seasonal vector means.

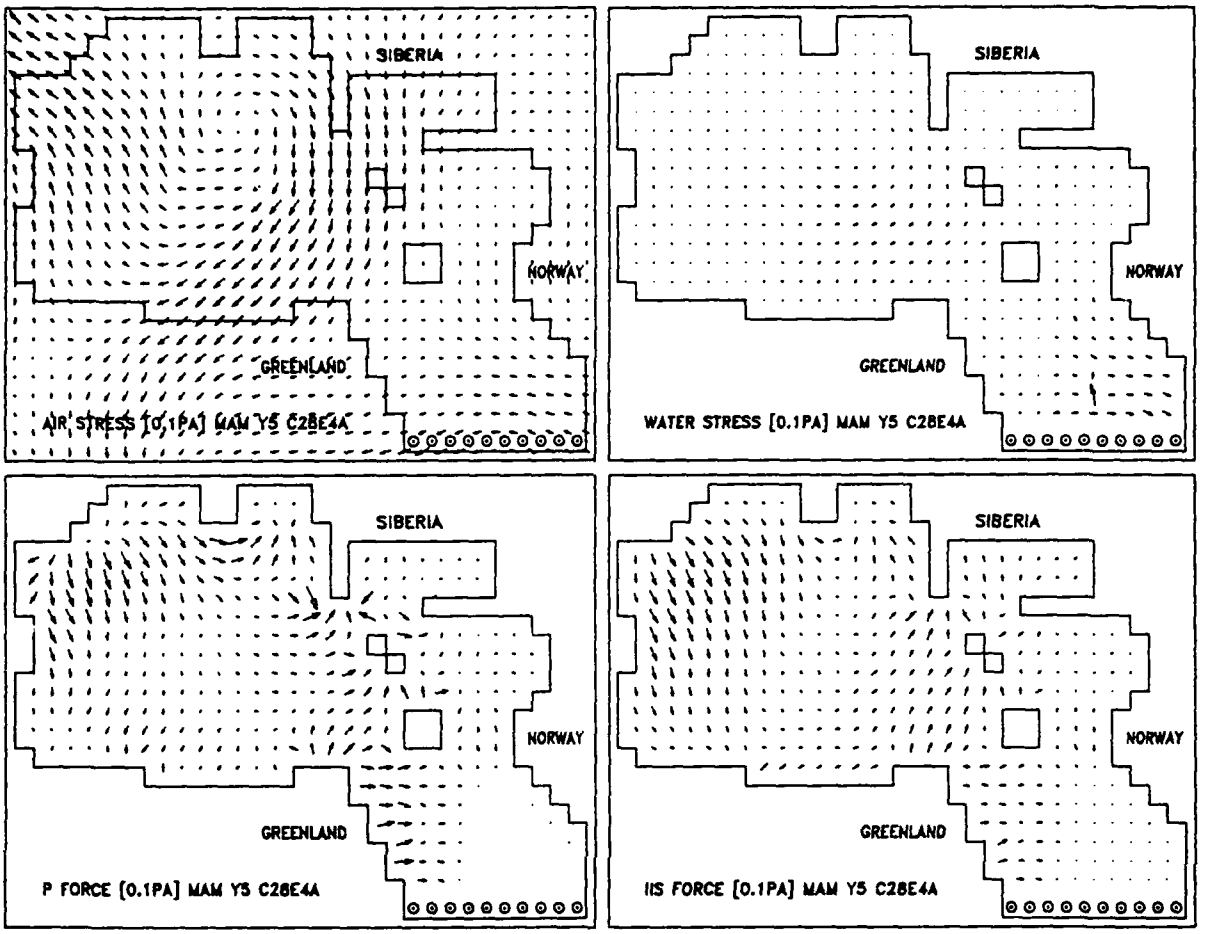

Figure 3. Selected components of the momentum balance in spring (MAM) as of the fifth year of the control run. A vector 1 grid space long represents a force of 0.1 Pa. Wind stress (top left) is the prime external force, while the internal pressure force (–grad P/2, bottom left) dominates the total internal ice stress divergence (bottom right).

Applying the gradient operator and the chain rule yields

$$\nabla P = f'g\,\nabla h + fg'\nabla A \tag{3}$$

with the prime denoting differentiation with respect to h and A. Using $f(h)$ and $g(A)$ from eq 1 gives $f' = 1$ and $g' = cg$. In this case eq 3 becomes

$$\nabla P = g\,[f'\,\nabla h + cf\,\nabla A] = P^*\,e^{-c(1-A)}\,[\nabla h + ch\,\nabla A]. \tag{4}$$

Simulated heavy ice in the East Siberian Sea is characterized by strong thickness gradients on the order of 1 m per grid length (160 km). The compactness field, on the other hand, is virtually homogeneous with $\Delta A/\Delta x < 1$ per mil per grid length. Employing these estimates and specifying $ch = 20 \times 5$, the ratio of the two additive terms of eq 4 is found to be ∇h: $ch\ \nabla A > 10$. Furthermore, $e^{-c(1-A)} \cong 1$ (and $g \cong P^*$), because the ice cover closed up tightly, that is $A \cong 1$. In consequence, the internal pressure force in the limit of heavy ice may be written as

$$-\nabla P/2 = -P^*\,\nabla h/2. \tag{5}$$

Ice buildup in the East Siberian Sea, created by persistent onshore winds, is mainly limited by the gradient of ice thickness (see eq 5), with 1 m/Δx creating a counteracting force of 0.086 N/m^{-2}. A higher strength constant P^* evidently would limit the buildup to more desirable, lower thickness levels. While probably advantageous in the critical domain, excessive tuning of this parameter can easily decrease the ice motion to levels well below those observed in other regions.

A more appealing approach derives from the notion that resistance to compression may not only depend on ∇h but also on the thickness level itself. In other words, thick ice should offer stronger resis-

tance than thin ice for identical gradients. For the force (in the limit of eq 5) to depend on h directly it is sufficient to specify $f(h)$ nonlinearly in h such that $f' = f'(h)$. Taking $f(h) = h^2/3$ as a suitable function the *modified strength* equation reads

$$P = P^* h^2/3 \, e^{-c(1-A)}. \quad (6)$$

Note that all ice thicker (thinner) than 3 m is stronger (weaker) than ice of the same thickness characterized by eq 1. As the terms involving compactness may still be neglected, the force corresponding to eq 5 simply follows as

$$\nabla P/2 = -P^* h \nabla h/3. \quad (7)$$

For equal gradients eq 7 predicts $f'(h) = 2h/3$ times stronger a force than determined from eq 5.

Figures 1 and 2 give a direct comparison of thickness and drift characteristics as obtained for the standard and modified strength parameterization (as given by eq 1 and 6, respectively). Modified strength shows virtually no effect on ice drift in summer and fall when a less consolidated ice state allows only weak ice interaction. While the drift pattern still remains unchanged in winter and spring, drift rates are somewhat reduced in the Pacific section of the Arctic Basin. This desired regionally limited effect is complemented by changes in the thickness field that are confined to the region enclosed by the 4-m-contour (Fig. 1). Specifically, the maximum thickness of 8 m (control run) is reduced to 5 m (mod. strength), yielding the same strength as the high value ($5 \times 5/3 \cong 8$). The pressure force of eq 7 had to be 3 times ($2 \times 5/3$) that of eq 5 if not concurrent (to a reduction in thickness) and ∇h had to be adjusted to appreciably lower values.

The modified strength formulation, above all, reduces the sensitivity of the thickness field to extremely anomalous or biased wind-forcing. The rapid increase of strength with h^2 efficiently prevents excessive buildup without causing noticeable side effects outside the critical region. While based on a physically reasonable notion, this parameterization or any other is difficult to validate because of insufficient data. Specifically, the seasonal evolution of the thickness field is not well known. However, some theoretical support for a quadratic thickness–strength coupling is provided by Rothrock's (1975) analysis of the energetics of the ridging process in the environment of a multilevel thickness distribution. He finds that both the production of gravitational potential energy during the ridge formation and frictional losses through pushing a plate into a rubble pile are proportional to h^{*2}. However, h^* stands for the cutoff thickness of the thinnest fraction of the ice cover, while h (in the context of the two-level model utilized here) is the mean ice thickness in a grid box. Further evidence for the usefulness of a quadratic thickness–strength coupling has been produced by Overland and Pease (1988), who have also developed such an approach in the face of similar buildup problems in modeling sea ice on a 1-km scale.

ACKNOWLEDGMENTS

Thanks are due to Dr. Peter Lemke and Dr. Benjamin Santer for their comments on a draft of this paper.

REFERENCES

Dickinson, R.E, G.A. Meehl and W.M. Washington (1987) Ice-albedo feedback in a CO_2 doubling simulation. *Climatic Change*, **10**: 241–248.

Hibler, W.D. III (1979) A dynamic–thermodynamic sea ice model. *Journal of Physical Oceanography*, **9**: 815–846.

Hibler, W.D. III and K. Bryan (1987) A diagnostic ice–ocean model. *Journal of Physical Oceanography*, **17**: 987–1015.

Loewe, P. (1988) Full sea ice model exposed to GCM atmosphere in the Arctic. In *Research Activities in Atmospheric and Oceanic Modelling* (G.J. Boer, Ed.). World Meteorological Organization, Report No.11, WMO/TD-No.263, p. 8.17–8.21.

Manabe, S. and R.J. Stouffer (1980) Sensitivity of a global climate model to an increase in CO_2 concentration in the atmosphere. *Journal of Geophysical Research*, **85**: 5529–5554.

Overland, J.E. and C.H. Pease (1988) Modeling ice dynamics of coastal seas. *Journal of Geophysical Research*, **93**: 15619–15637.

Rothrock, D.A. (1975) The energetics of the plastic deformation of pack ice by ridging. *Journal of Geophysical Research*, **80**: 4514–4519.

Washington, W.M. and G.A. Meehl (In press) Climate sensitivity due to increased CO_2: Experiments with a coupled atmosphere and ocean general circulation model. *Climatic Change*.

The Warming Effect of Meridional Sea Ice Transport on Climate

T.S. LEDLEY
Department of Space Physics and Astronomy and
the Earth Systems Institute
Rice University
Houston, Texas, U.S.A.

ABSTRACT

Sea ice is an important factor in controlling the exchange of energy between the ocean and atmosphere in the polar regions and has an important impact on climate. A coupled energy balance climate–sea ice model is used here to examine the effect of sea ice transport on the ocean–atmosphere energy exchange and atmospheric temperature. The model results show that the transport of sea ice thins the pack ice in the central Arctic and around Antarctica. This thinning produces a larger lead fraction within the ice pack and a longer period of ice-free conditions, which results in warmer conditions near the poles.

INTRODUCTION

The exchange of energy between the ocean and atmosphere is a major factor in determining atmospheric temperature. This exchange is altered by the existence of sea ice on the ocean surface, because sea ice insulates the relatively warm ocean from the cold winter atmosphere and has a significantly higher surface albedo than open ocean. The net impact of sea ice on surface energy exchange depends both on its latitudinal extent and characteristics such as thickness, snow cover, impurities, and the area of open ocean within the ice pack (leads). The effect of some of these characteristics of sea ice has been examined in previous studies using climate models. That work has shown that the impact of sea ice on the surface energy fluxes is not simply a matter of whether or not sea ice exists, but also depends on the fraction of the ice pack that is made up of leads. In this report the effect of sea ice transport on the energy exchange between the atmosphere and ocean, and thus on climate, is examined using a coupled energy balance climate–thermodynamic sea ice model (the CCSI model).

The CCSI Model

The energy balance climate model used in this study encompasses four parts of the climate system, the atmosphere over land, the atmosphere over sea, a mixed layer ocean, and a ground layer. The zonally averaged vertical energy fluxes over land and over ocean are computed at the boundaries of the layers of the system. The horizontal energy fluxes between land and sea within a zone and between latitude zones over land and sea are computed, and the horizontal fluxes between zones in the ocean are specified. The vertical energy fluxes included are the sensible heat flux, latent heat flux, shortwave radiation, and long wave radiation. The temperatures of the atmospheric and surface layers are adjusted in response to the gain or loss of energy as determined by the sum of these energy fluxes, the net energy exchange, at these boundaries. The model simulates seasonal cycles, a necessary feature for the study of the impact of sea ice variations on climate.

The energy balance climate model is coupled to a three-layer thermodynamic sea ice model (Maykut and Untersteiner 1971, Semtner 1976, Ledley 1985). The sea ice model includes conduction within the ice, penetration of solar radiation into the ice layers, surface energy balances, leads, and sea ice transport.

The CCSI model does not explicitly compute the dynamic processes involved in lead formation. Therefore, it is necessary to specify the minimum lead fraction (MLF, representing the minimum fraction of open ocean within the ice pack that is formed due to dynamic processes during the winter when leads are filling with ice) of the total ice/ocean area to be occupied by leads, and to parameterize the transport of sea ice to equatorward zones.

A more detailed description of the CCSI model appears in Ledley (1988).

Sea Ice Transport Parameterization

The sea ice transport parameterization has four main parameters. These control, when ice can be transported, the response of the ocean temperature to the transported ice, and also include the MLF and the fraction of the ice displaced by the opening of leads that is ridged or transported. In the results presented here, if more than 10% of a zone is covered by ice, then transport is permitted to occur. The mixed layer ocean may be above the freezing point when ice is transported into the zone. The transported ice will not be melted if the ocean temperature is below a value determined as a linear function of the lead fraction. In this study the limiting temperature ranges from the freezing point, if the zone is ice-covered, to 10 K above the freezing point, if the zone is ice free. The MLF is a function of latitude, increasing from 0.03% at the poles in the base case (see Table 1 for additional cases). The partitioning of the displaced

ice is also a function of latitude in this study, ranging from 80% ridging and 20% transport at the poles, to 40% ridging and 60% transport at 45 N.

EXPERIMENTS

Climate simulations were made with the CCSI model to determine the impact of sea ice transport and variations in the MLF on climate. This was done through two series of experiments, one in which sea ice transport was included and the other in which it was neglected. Within each series the minimum lead fraction was varied (see Table 1).

RESULTS

Figure 1 shows that, while changes in the MLF have a large impact on the sea ice thickness, the effect of the transport of sea ice is much larger. When transport is neglected the forced opening of leads during the winter results in a large ice growth rate and thus thick ice in the poleward-most zones. This new ice production increases as the MLF increases. Since the ice is constrained to remain in the latitude zone in which it is formed, the mean annual ice thickness in the poleward-most zones increases as the MLF increases, ranging from 5.8 to 17.7 m at 85°N for cases A to D (see Table 1). When transport is included, Figure 1 shows that the mean annual ice thickness is

Table 1. MLF scenarios.

	MLF (% per day)			
Latitude	Case A	Case B	Case C	Case D
85	0.3	0.5	1.1	4.3
75	0.5	1.1	1.1	4.3
65	1.1	2.2	1.1	4.3
55	2.2	3.3	1.1	4.3
45	3.3	4.3	1.1	4.3

much smaller in the poleward-most zones and extends equatorward to 55°N and 55°S. In addition, the mean annual sea ice thickness decreases for increasing MLF, ranging from 2.9 m to 1.0 m at 85°N for cases A to D.

The reason for the overall decrease in the ice thickness when transport is included is that a lot of the new ice formed in the leads is transported equatorward, where it is subjected to higher temperatures and eventually melted away. The reason for the decrease in ice thickness as the MLF is increased when transport is included relates to the effect of the MLF on the mean annual surface air temperature.

Figure 2 shows how the mean annual surface air temperature is affected both by changes in the MLF and the addition of transport. The thinning of the ice in the poleward regions when transport is included is reflected in the increased temperatures at all latitudes. The main reason for this increase is that the thinner ice resulting from transport is easier to melt

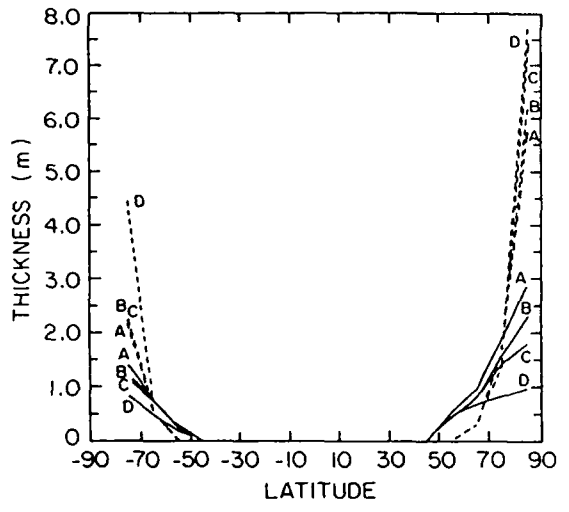

Figure 1. The mean annual sea ice thickness as a function of latitude when sea ice transport is included (solid lines) and neglected (dashed lines) for the various MLF scenarios, cases A, B, C, and D (see Table 1 for the definition of the different cases).

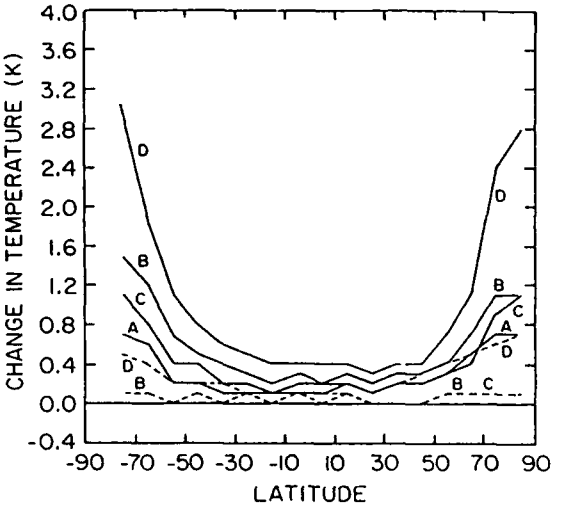

Figure 2. The change in the mean annual surface air temperature as a function of latitude for each of the experiments depicted in Figure 1 from case A with no transport. Transport cases are depicted with solid lines and no transport cases are depicted with dashed lines.

away during the summer season, producing a larger maximum lead fraction and longer periods of ice-free conditions. This results in a greater heat transport from the ocean to the atmosphere and thus warmer air temperatures.

When transport is neglected, the increase in the surface air temperature between case A and case D is 0.7 K. This is not enough to overcome the large ice growth rates during the winter and the resulting large mean ice thickness. When transport is included, the increase in the surface air temperature between case A and case D is 2.1 K. This increased warming is large enough, along with the transport of some of the new ice equatorward, to overcome the high ice growth rates near the poles to produce thinner ice in case D than in case A in that region.

The increase in the surface air temperatures when transport is added (Fig. 2) is mainly the result of the increase in the sensible heat flux from the ocean to the atmosphere when the summer lead fraction and the period of ice-free conditions increase. However, the increase in the sensible heat flux is confined to the polar regions. In the regions into which the transported ice extends, the sensible heat flux from the ocean to the atmosphere decreases. This is because of the insulating effect of the transported sea ice on the ocean surface. This decrease in the ocean-to-atmosphere sensible heat flux would indicate a cooling; however, Figure 2 shows a warming at all latitudes. The reason for the overall warming is the horizontal energy transport in the atmosphere. Increases in temperature in the poleward-most zones produce a decrease in the meridional energy convergence in those regions and an increase in the meridional energy convergence equatorward. In the equatorward-most zones that contain the transported ice, this increase in the energy convergence is greater than the decrease in the sensible heat flux from the ocean to the atmosphere, resulting in a net warming.

SUMMARY

The results presented here show that meridional sea ice transport and the rate of lead formation during the winter can have a significant effect on climate. The transport of sea ice produces a thinning of the ice in the poleward-most zones and an extension of the ice edge equatorward. The thinning of the poleward-most ice increases the maximum lead fraction and the period of ice-free conditions. This results in an increase in the sensible heat flux from the ocean to the atmosphere in the poleward-most zones, which produces an increase in atmospheric temperatures. The sensible heat flux from the ocean to the atmosphere is decreased in the zones that contain the ice edge, due to the increased ice coverage. However, the warming in the poleward-most zones results in an increased meridional energy convergence at the ice edge that offsets the decrease in the sensible heat flux to the atmosphere, resulting in a net warming at all latitudes.

REFERENCES

Ledley, T.S. (1985) Sensitivity of a thermodynamic sea ice model with leads to time step size. *Journal of Geophysical Research*, **90**: 2251–2260.

Ledley, T.S. (1988) A coupled energy balance climate–sea ice model: Impact of sea ice and leads on climate. *Journal of Geophysical Research*, **93**: 15,919–15,932.

Maykut, G.A. and N. Untersteiner (1971) Some results from a time dependent thermodynamic model of sea ice. *Journal of Geophysical Research*, **76**: 1550–1575.

Semtner, A.J. (1976) A model for the thermodynamic growth of sea ice in numerical investigations of climate. *Journal of Physical Oceanography*, **6**: 379–389.

Preliminary Testing of a Sea Ice Model for the Greenland Sea

R.H. PRELLER
Naval Oceanographic and
Atmospheric Research Laboratory
Stennis Space Center, Mississippi, U.S.A.

A. CHENG
Sverdrup Technology, Inc.
Stennis Space Center, Mississippi, U.S.A.

P.G. POSEY
Berkeley Research Associates
Springfield, Virginia, U.S.A.

ABSTRACT

The Hibler dynamic–thermodynamic sea ice model (Hibler 1980) has been adapted to the Greenland Sea. The goal of this study is to design an accurate model for the ocean region adjacent to the Greenland coast that may be used as a sea ice forecasting model. The model is driven by atmospheric fields from the Naval Operational Global Atmospheric Prediction System (NOGAPS) model run at the Fleet Numerical Oceanography Center (FNOC). These fields consist of surface pressures used to calculate geostrophic winds, surface air temperature, total heat flux, solar radiation and vapor pressures. In addition, the model is driven by monthly mean geostrophic ocean currents and deep oceanic heat fluxes from the Hibler–Bryan (1987) ice–ocean model. The model domain contains the Greenland Sea and the region adjacent to the southeastern coast of Greenland. The model uses a grid resolution of 20 km and a 6-hour time step. The model's southern boundary is an ice "outflow" boundary. The northern boundary, at the Fram Strait, is both an ice inflow and outflow boundary with inflow information derived from a coarser resolution Arctic Basin model.

The Greenland Sea model has shown some promising results as well as some problem areas. The model predicts thicker ice in winter than in summer, with the thickest ice found adjacent to the Greenland coast. At present, however, the model underpredicts ice in the southern half of the basin in summer. It also predicts ice drift weaker than that observed. Tests made to improve the ocean currents have not completely corrected this problem. Improvements to the existing ice rheology will be implemented as a correction to this problem in the future.

INTRODUCTION

The Naval Ocean Research and Development Activity (NORDA) is designing a sea ice forecasting model that will cover the Greenland Sea, the Denmark Strait and the ice-covered ocean adjacent to the southeastern coast of Greenland. The Hibler dynamic–thermodynamic sea ice model (Hibler 1979, 1980) has been adapted to this region using a high resolution, 20-km grid. The model is driven by atmospheric forcing from the Naval Operational Global Atmospheric Prediction System (NOGAPS) (Rosmond 1981) and initially, by monthly mean ocean currents and deep ocean heat fluxes from the Hibler and Bryan (1984, 1987) coupled ice–ocean model. Inflowing ice thickness values at the Fram Strait are obtained from the Polar Ice Prediction System (PIPS) (Preller and Posey 1989). The southern boundary is an ice outflow boundary after Hibler (1979).

The Greenland Sea has been characterized as a region of robust circulation in the ice, ocean and in the atmosphere. In addition to new ice formed locally, a large part of the ice in the Greenland Sea has old (multiyear) ice that has been advected through the Fram Strait. For this reason, a significant amount of ice exists in the Greenland Sea throughout the summer. Climatology from the Naval Polar Oceanography Center (NPOC) indicates that the minimum southward extent of ice along the Greenland coast occurs in September (Fig. 1a). Ice starts advancing southward in October and reaches maximum coverage during April (Fig. 1b). Once ice leaves the central Arctic and enters the Greenland Sea, the free or open eastern boundary allows for increased mobility of the ice. Ice drift has been measured in recent years by a number of automatic data buoys deployed on sea ice (Colony and Munoz 1985). These measurements show that ice drift in the Greenland Sea can often be 5–10 times as large as drift observed in the central Arctic.

Along with semipermanent atmospheric features such as the Icelandic low and the Greenland high, the Norwegian and Greenland seas are affected by a series of cyclonic systems that originate along the coast of North America and track through the region. These storms seem to be stronger in winter than in summer, maintaining maximum wind speed in winter (Gathman 1986). These cyclonic systems result in the dominance of northerly winds in the Norwegian and Greenland seas. The region is also often affected by small but very intensive cyclonic systems called polar lows which form near the ice–ocean transition region.

The surface circulation of the Greenland Sea is dominated by the East Greenland Current (EGC).

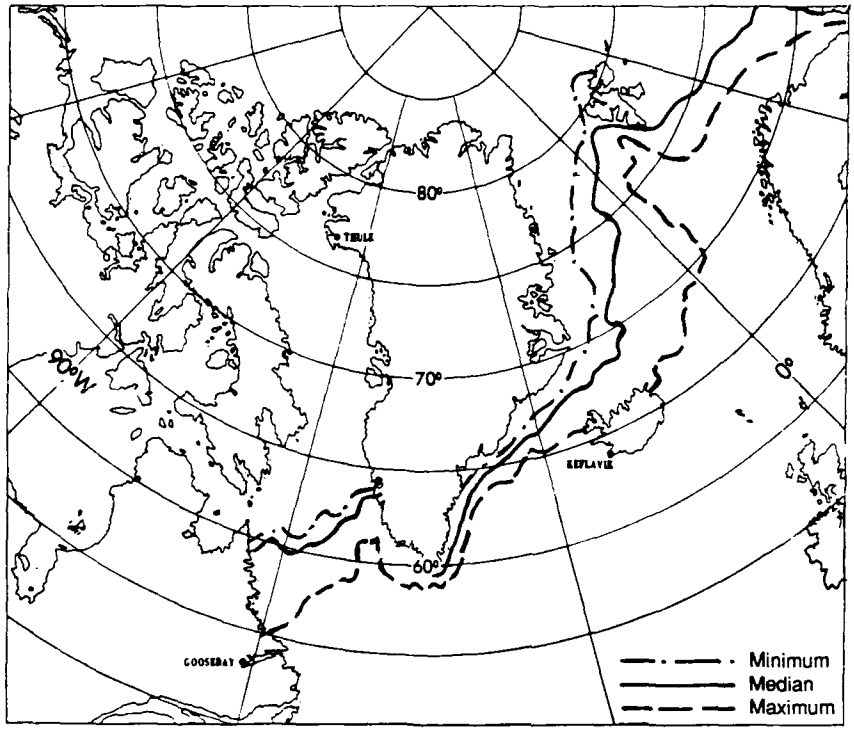

a. 15 September.

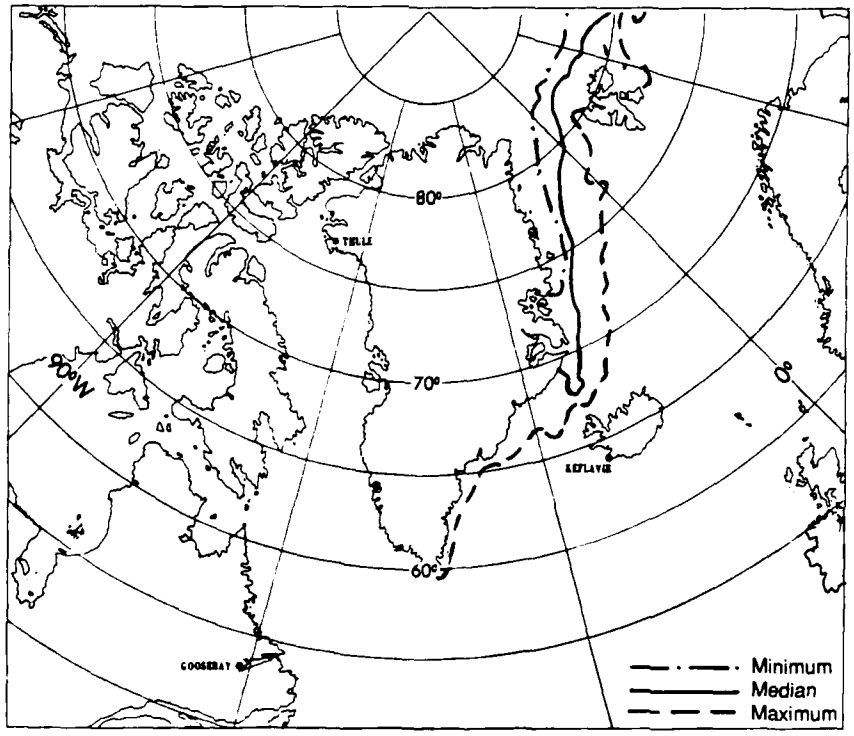

b. 15 April.

Figure 1. Ice edge climatology from the Navy–NOAA Joint Ice Center.

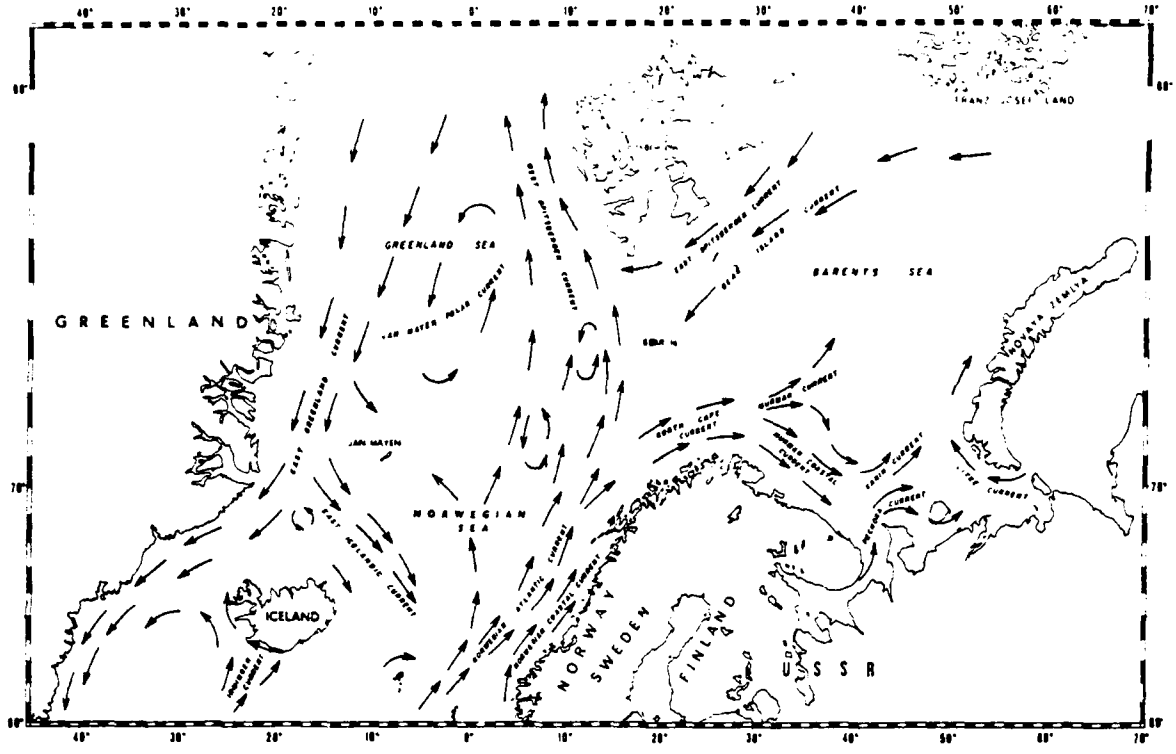

a. Greenland Sea and Norwegian Sea (from Trangeled 1974).

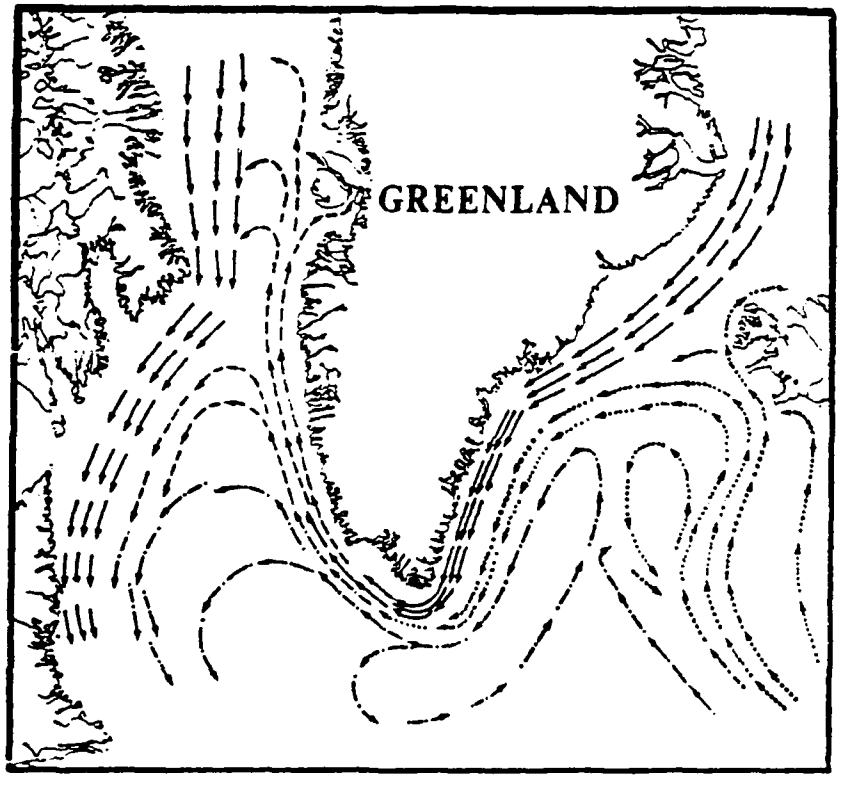

b. The region south of and including the Denmark Strait (from Vibe 1967). Solid lines represent Arctic water, dotted lines represent Atlantic water, dashed lines represent the West Greenland Current and dashed lines with dots represent sub-arctic mixed water.

Figure 2. Surface ocean currents.

This current carries polar water from the central Arctic south through the Fram Strait into the Greenland Sea. The magnitude of the EGC is high when compared with that of other Arctic surface currents. Over the shelf velocities are approximately 5–10 cm/s. Near the shelf break velocities have been observed to be of the order of 20–40 cm/s (Aagaard and Coachman 1968a, Bourke et al. 1987, Foldvik et al. 1988). The EGC has large current shears. These characteristics cause the ice entering the Greenland Sea to break up into a field of floes much smaller than those observed in the central Arctic.

In addition to the EGC, an extension of the Norwegian Atlantic Current flows into the Greenland Sea. The Norwegian Atlantic Current, carrying warm water from the south, curves to the west, away from the Norwegian coast. Part of the current enters the Barents Sea while the rest of the current moves westward. One branch carries warm water along the west coast of Spitzbergen while the other branch curves farther west and underlies the polar water of the EGC (Fig. 2a).

North of Iceland an eastward-moving current, called the East Icelandic Current, is found. Between Iceland and Greenland, in the narrow Denmark Strait, the currents form a complicated pattern. The EGC continues southward through the Denmark Strait, hugging the Greenland coast. A slow northward flow, an extension of the Irminger Current, is found just west of Iceland along the Icelandic shelf. In the region just south of the Denmark Strait, the remainder of the Irminger Current curves back toward the south (Fig. 2b).

Such a highly dynamic region may prove a difficult one to model, no less to forecast. Accurate atmospheric and oceanic forcing will play a major role in making an accurate forecast of sea ice conditions in the Greenland Sea. The fact that the Greenland Sea has an open eastern boundary while the central Arctic is basically a closed region changes the appearance and possibly the internal ice dynamics of the ice from the central Arctic as it enters the Greenland Sea.

The Hibler ice model was originally tested on the Greenland Sea by Tucker (1982). Tucker used a version of the Hibler model identical to that used in this study but applied different atmospheric and oceanic forcing. He also specified a constant profile of ice thickness to serve as the boundary condition in the Fram Strait. The model grid resolution was half that used in this study (40 vs 20 km). Tucker made a number of observations based on sensitivity studies. He found that inflow from the Fram Strait was necessary to predict the correct ice thickness and concentration. He found that the ice drift in the Greenland Sea was mainly controlled by the wind. He also suggested that since his modeled ice drift was too weak, geostrophic ocean currents were not an accurate representation of the oceanic forcing. In addition, Tucker also concluded that his model showed excessive ice growth.

In this paper, we will look at some of the results of the NORDA version of the Greenland Sea ice model. It is not the purpose of this study to reproduce the sensitivity studies made by Tucker. Instead, we will use what Tucker learned from his study and expand upon it in order to develop an accurate sea ice model for the Greenland Sea. The design of the model, some preliminary results and future planned work will be discussed.

MODEL DESCRIPTION

The regional Greenland Sea model uses the Hibler dynamic–thermodynamic sea ice model as its basis. The ice model is defined by five major components: a momentum balance, ice rheology, ice thickness distribution, ice strength and an air/ice/ocean heat balance.

The momentum balance used to determine ice drift is given by

$$m\frac{D\vec{u}}{Dt} = -mf\hat{k}\times\vec{u} + \vec{\tau}_a + \vec{\tau}_w - mg\,\mathrm{grad}\,H + \vec{F}$$

where m = ice mass per unit area
$\vec{u}$ = ice velocity
f = Coriolis parameter
$\vec{\tau}_a$ and $\vec{\tau}_w$ = air and water stresses
g = acceleration of gravity
H = sea surface dynamic height
$\vec{F}$ = force due to variation in the internal ice stress.

Ice is considered to move in a two-dimensional field with forcing applied through simple planetary boundary layer formulations.

The air and water stresses are defined using constant turning angles

$$\tau_a = \rho_a C_a |\vec{U}_g| (\vec{U}_g \cos\phi + \hat{k}\times\vec{U}_g \sin\phi)$$

$$\tau_w = \rho_w C_w |\vec{U}_w - \vec{u}| [(\vec{U}_w - \vec{u})\cos\theta + \hat{k}\times(\vec{U}_w - \vec{u})\sin\theta]$$

where $\vec{u}$ = ice drift velocity
$\vec{U}_g$ = geostrophic wind
$\vec{U}_w$ = geostrophic ocean current
C_a and C_w = air and water drag coefficients

ρ_a and ρ_w = air and water densities
ϕ *and* θ = air and water turning angles.

For a more detailed discussion of model dynamics and the spatial finite differencing code, see Hibler (1979).

The ice rheology, a viscous-plastic constitutive law, relates the ice stress to ice deformation and ice strength in the following manner:

$$\sigma_{ij} = 2\eta(\varepsilon_{ij}, P)\,\varepsilon_{ij} + [\zeta(\varepsilon_{ij}, P) - \eta(\varepsilon_{ij}, P)]\,\varepsilon_{kk}\,\delta_{ij} - P\delta_{ij}/2$$

where σ_{ij} = two-dimensional stress tensor
ε_{ij} = strain tensor
$P/2$ = pressure term
ζ = nonlinear bulk viscosity
η = shear viscosity.

Ice flows plastically for normal strain rates and deforms in a linear viscous manner for small strain rates.

The ice thickness distribution takes into account the ice thickness evolution as a result of dynamic and thermodynamic effects. The regional Greenland Sea model uses a two-level approach (Hibler 1979). This approach specifies that ice is broken up into two categories, thick and thin, with the division between the two being 0.5 m. The compactness, A, is defined as the area within a grid cell covered by thick ice, while $(1-A)$ is the area covered by thin ice.

The equations for thickness and compactness are

$$\frac{\partial h}{\partial t} = -\frac{\partial(uh)}{\partial x} - \frac{\partial(vh)}{\partial y} + S_h + \text{diffusion}$$

$$\frac{\partial A}{\partial t} = -\frac{\partial(uA)}{\partial x} - \frac{\partial(vA)}{\partial y} + S_A + \text{diffusion}$$

where S_h and S_A are thermodynamic terms defined by

$$S_h = f\left(\frac{h}{A}\right)A + (1-A)f(0)$$

$$S_A = \begin{cases} \dfrac{f(0)}{h_0}(1-A) & \text{if } f(0) > 0 \\ 0 & \text{if } f(0) < 0 \end{cases} + \begin{cases} 0 & \text{if } S_h > 0 \\ \left(\dfrac{A}{2h}\right)S_h & \text{if } S_h < 0 \end{cases}$$

with $f(h)$ as the growth rate of ice of thickness h (h_{eff}) and h_0 a fixed demarcation between thick and thin ice. In all model simulations, $h_0 = 0.5$ m. The term S_h is the net growth or melt of ice. S is the change in compactness due to the growth or decay of ice.

Ice strength is treated as a function of the ice thickness distribution and compactness given by the equation

$$P = P^* h \exp[-C(1-A)]$$

where P^* and C are fixed empirical constants, h is the ice thickness and A the compactness. This relationship shows the strength of ice to be strongly dependent on the amount of thin ice $[(1-A)]$. It also allows the ice to strengthen as it becomes thicker.

The thermodynamic portion of the code determines growth and decay rates of ice based on a heat budget balance between the atmosphere, ice and ocean, including the effects of heat absorbed by leads via lateral mixing. Similar to Semtner's (1976) formulation, heat is transferred through the ice by assuming a linear temperature profile along with a constant ice conductivity. When open water is losing heat to the atmosphere, the heat budget growth rates are taken to be vertical growth rates. When open water absorbs heat, the heat mixes underneath the floes to reduce the vertical growth rate. Any remaining heat can either cause lateral melting or raise the temperature of the mixed layer. In the presence of an ice cover, the mixed layer temperature is always set equal to freezing. Thus, excess heat absorbed by leads is used for lateral melting until the ice disappears. During growth conditions, ice is not allowed to form until the mixed layer reaches the freezing temperature of seawater.

Following Bryan et al. (1975) and Manabe et al. (1979), the effects of snow cover are treated such that the ice surface albedo is that of snow (0.75) when the calculated surface temperature is below freezing and that of snow-free ice (0.66) when the surface temperature is at the melting point. Thus, the upward heat flow I_h through ice of thickness h is

$$I_h = (K/h)(T_w - T_0)$$

where K is the ice conductivity, T_w is the water temperature and T_0 is the surface temperature of the ice.

The surface heat budget, after Parkinson and Washington (1979) and Manabe et al. (1979) is given by

$$(1-\alpha)F_S + F_L + D_1\left|\vec{U}_g\right|(T_a - T_0) +$$

$$+ D_2 |\vec{U}_g| [q_a(T_a) - q_s(T_0)] - D_3 T_0^4$$

$$+ (K/H)\,(T_w - T_0) = 0$$

where α = surface albedo
T_0 = surface temperature of ice
T_a = air temperature
T_w = water temperature
$\vec{U}$ = geostrophic wind
q_s = specific humidity of the ice surface
F_s = incoming shortwave radiation
F_L = incoming longwave radiation
D_1 = bulk sensible heat transfer coefficient
D_2 = bulk latent heat transfer coefficient (water or ice)
D_3 = Stefan–Boltzmann constant times the surface emissivity
H = initialization ice thickness.

This surface heat budget defines a surface temperature for the ice that balances the heat budget. This temperature then determines the conduction of heat through the ice and the growth rate. If the derived temperature is above freezing, it is set back to the freezing point. Surface and bottom ablation rates are then determined by the imbalances in the surface heat budget and by conduction of heat into the mixed layer. Heat transfer from the deep, warmer ocean water can either be treated as a constant or as a variable heat flux into the mixed layer. For a detailed discussion of the thermodynamic portion of the model, see Hibler (1980).

THE MODEL DESIGN

The Greenland Sea model grid was designed as a subsection of the FNOC northern hemisphere polar stereographic grid. The model grid covers the Greenland Sea, the Denmark Strait and the ice-covered region along the southeastern coast of Greenland. The model grid resolution is 20 km (Fig. 3).

Model boundaries are solid walls except for the southern boundary, which is an ice outflow boundary, and the Fram Strait boundary. The southern boundary contains two rows of "outflow" grid cells. Ice can be transferred into these grid cells only by advection and once there, flows out of the basin. One row of grid cells at the Fram Strait boundary is used as an inflow/outflow boundary. If ice drift indicates inflowing ice in a particular grid cell, then ice thickness from a larger scale Arctic Basin model, the Polar Ice Prediction System (PIPS) (Preller and Posey 1989)

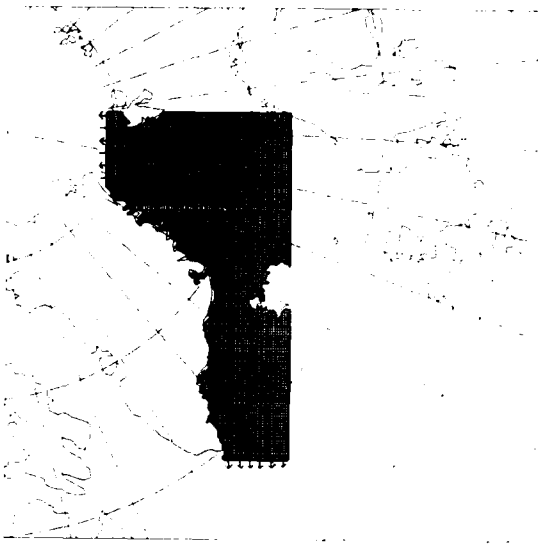

Figure 3. Greenland Sea model grid with outflow and inflow/outflow boundaries indicated by arrows.

is placed into the cell and allowed to advect in. If ice drift indicates outflow, the outflow condition previously described is applied at that cell (Preller et al. 1989).

FORCING

The Greenland Sea model is driven by both atmospheric and oceanic forcing. The atmospheric forcing is obtained from the NOGAPS model. This global atmospheric model provides surface pressure fields (NOGAPS field AOI) that are used to determine geostrophic winds. In addition to surface pressure, the NOGAPS model also provides surface vapor pressure (A12) that is used in conjunction with surface pressure to determine the specific humidity at the ice surface; surface air temperature (A07), incoming solar radiation (shortwave, A11), sensible heat flux (A16) and total heat flux (A18). These last three fields are used to determine longwave radiation. At present, the NOGAPS resolution is approximately 400 km while the ice model's resolution is 20 km. The coarse grid used by the atmospheric model will certainly reduce the ice model's capability to resolve mesoscale features in the ice drift and ice thickness fields. The NOGAPS model will, however, be upgraded to twice the present resolution in the summer of 1989. This should improve the forecast capability of all of the Navy's ice models.

Monthly mean geostrophic ocean currents and deep ocean heat fluxes derived from the Hibler/ Bryan coupled ice–ocean model are used as the ocean forc-

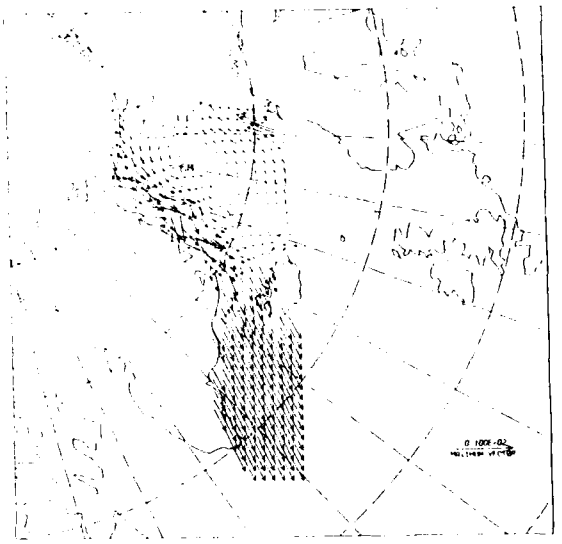

Figure 4. Monthly mean extrapolated ocean currents from the Hibler and Bryan ice–ocean model. Maximum vector length is 10 cm/s.

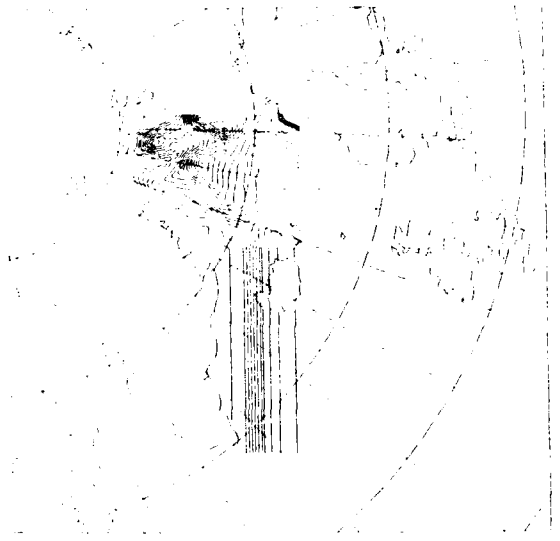

Figure 5. Monthly mean extrapolated deep ocean heat fluxes from the Hibler and Bryan ice–ocean model. Contours are in watts/m² with a contour interval of 20.

ing for the model. The effects of the variability of ocean currents on ice drift has been shown to be of importance over long time scales (Thorndike and Colony 1982). On the time scale of a forecast (five days), the variability of the ocean currents has a much smaller effect on the ice drift than the variability of the wind stress fields. For this reason, monthly mean ocean currents can be used as a reasonable estimate for oceanic forcing.

A problem does exist in using the Hibler and Bryan oceanic forcing for the Greenland Sea model. The southern boundary of the Hibler and Bryan model runs through the Denmark Strait and then continues east from Iceland toward Great Britain. The ice model's southern boundary extends all the way to the southern tip of Greenland. In order to initially test the model, a crude representation of the ocean currents was defined by extending the Hibler and Bryan ocean currents to the south as a constant value derived from the southernmost (non "outflow" boundary) grid cell (Fig. 4). A similar technique was applied to extend the oceanic heat flux to the southern boundary of the ice model (Fig. 5).

Including variable deep ocean heat fluxes has been shown to be very important in determining edge location in the marginal ice zone. Hibler and Bryan (1984, 1987) have shown that this oceanic heat flux can melt large amounts of ice in the marginal ice zone. A drastic improvement in ice edge location was seen in the results of the PIPS model when monthly mean deep oceanic heat fluxes were included (Preller 1985 and Preller and Posey 1989).

INITIAL CONDITIONS

The Greenland Sea model was spun up to a cyclic "equilibrium state" where ice thickness, ice velocity and ice concentration take on similar values on corresponding days of successive years. Initialization for the equilibrium state case requires setting ice drift velocities to zero and ice thickness to a constant value of 3.3 m (3.0×10 kg/m$^2/\rho_i$) and ice concentration to 100% at all grid points. From these initial conditions, it takes approximately two years of model integration to reach a cyclic equilibrium state. One particular year of NOGAPS forcing (1983) is used repeatedly to reach the equilibrium state.

MODEL PARAMETERS

The Greenland Sea model uses a six-hour time step. In the initial testing of the model, atmospheric forcing fields were interpolated from the 63×63 northern hemisphere polar stereographic grid used by FNOC to the Greenland Sea grid. Ocean forcing is updated each month. Turning angles for the geostrophic wind and drag coefficients were based on values derived from the testing of PIPS (Preller and Posey 1989). Additional parameters used by the model are given in Table 1. These parameters are discussed in some detail in Hibler (1979).

Table 1. Parameters used in Greenland Sea model.

Parameter	*Definition*	*Value*
C_a	Drag coefficient of air	0.0008
C_w	Drag coefficient of water	0.0055
C	Empirical constant in the strength equation	20
e	Ratio of the principal axis of the elliptic yield equation	2
f	Coriolis parameter	Latitude dependent variable
h_0	Thickness limit between thick and thin ice	0.5
ρ_i	Density of ice	0.91×10^3 kg m^{-3}
ρ_a	Density of air	1.3 kg m^{-3}
P^*	Pressure constant	2.75×10^4 N m^{-2}
$\Delta x = \Delta y$	Horizontal grid spacing	20 km
Δt	Time step	6 hour
ζ_{max}	Nonlinear bulk viscosity	$(P/4) \times 10^{9}$ kg s^{-1}
η_{max}	Nonlinear shear viscosity	ζ_{max}/e^2
ϕ	Turning angle of air	23°
θ	Turning angle of water	25°
H	Initialization ice thickness	3.3 m

MODEL RESULTS

Model results using 1983 atmospheric forcing and the extrapolated ocean forcing, show fairly realistic ice edge location (Fig. 6a and 6b) in the northern half of the model domain when compared to the NPOC analysis. The only problem area is along the west coast of Spitzbergen where excessive amounts of ice exist. The problem is due to the coarse resolution of the Hibler and Bryan model and its resultant inability to resolve the West Spitzbergen current. Along the southeastern coast of Greenland, model results show slightly too much ice in winter and too little ice in summer.

Figure 7 shows the winter ice thickness field. The thickest ice is located along the Greenland coast north of 70°N and is approximately 2.5–3.0 m. South of 70°N, the ice thins rapidly taking on an average value of 0.5 m with some slightly thicker ice along the coast.

Although the ice edge and ice thickness results from the model look reasonable, a serious problem exists in the model-derived ice drift. Figure 8 shows the path of two buoys in the Greenland Sea during 1983 (Colony and Munoz 1985). A "model" buoy was placed at the same starting location and allowed to drift in time according to the model-derived ice drift. The model buoy in Figure 8b was shifted 3 degrees to the east of the actual buoy's starting point. Without this adjustment, the model drift quickly drives the buoy into the land boundary. Thus, for the sake of comparing the magnitudes of the ice drift, the starting location is moved to the east. When forced to start farther away from land, the model buoy drifts about half as far as the actual buoy. Table 2 shows the mean magnitude as well as the standard deviation and the RMS error of ice drift for the model buoys and the observed buoys.

This inconsistency between the modeled drift and the observed drift was also found by Tucker (1982). He found that reducing his currents to zero had little effect on the ice drift. In another test, Tucker used 60-day averaged ice drift derived by using zero ocean currents as his ocean forcing. These currents were often close to an order of magnitude larger than the geostrophic currents. Tucker found that the effect of these currents was to increase the model ice drift such that it was greater than that observed. Tucker concluded that the appropriate ocean current field must lie somewhere between a geostrophic current and the averaged ice drift field.

Observations of currents in the East Greenland Current system indicate that surface currents are of the order of 5–10 cm/s with currents increasing to 30–40 cm/s near the shelf break (Bourke et al. 1987, Foldvik et al. 1988). The Hibler and Bryan modeled currents (Fig. 4) have a maximum of 5–7 cm/s in the

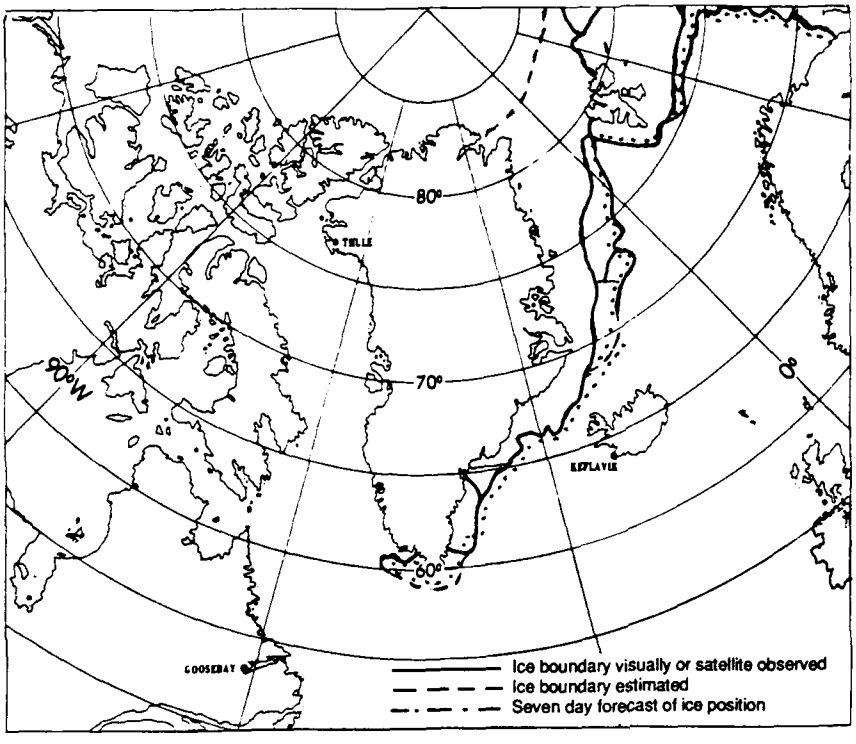

a. NPOC ice concentration from 29 March 1983.

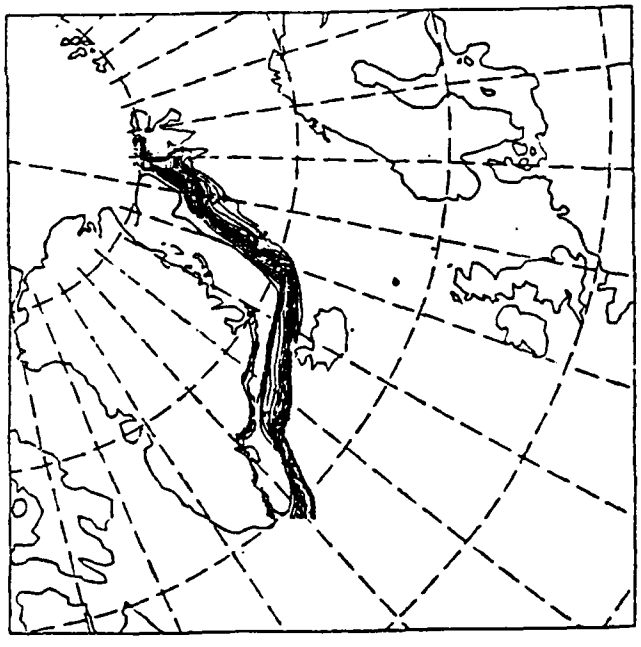

b. March monthly mean ice concentration from the model.

Figure 6. March ice concentrations. (Contours are in 10% intervals.)

EGC. The strong jet of current observed near the shelf break is not resolved by this model. Test cases were run in which the Hibler and Bryan currents were increased, but not beyond these observed values. All other forcing remained the same in these tests. Figure 9a shows the modeled buoy trajectory using currents three times as large as the original currents (15–20 cm/s) and and Figure 9b uses currents 5.5 times as large as the original currents (35–40 cm/s). The results show that increasing the magnitude of the ocean currents does increase the modeled ice drift, but not enough to agree with the observations.

Increasing the magnitude of the currents beyond this point would force the currents to be much larger than observed. Instead, we chose first to improve our ocean forcing by improving the currents in the south-

Figure 7. March monthly mean ice thickness (m) from the Greenland Sea model.

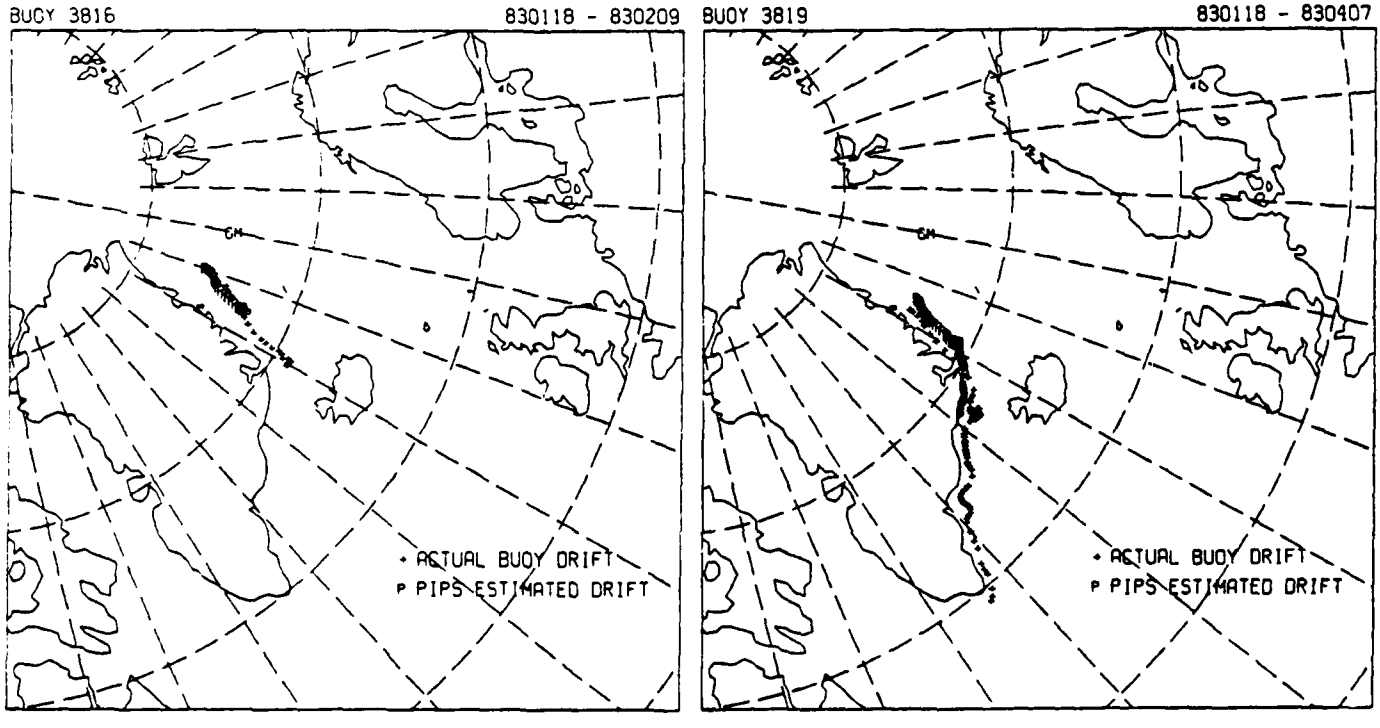

a) Buoy 3816. *b) Buoy 3819.*

Figure 8. Modeled and observed buoy drifts from 1983. Dates in the upper righthand corner indicate the starting and ending dates of the actual buoy observations

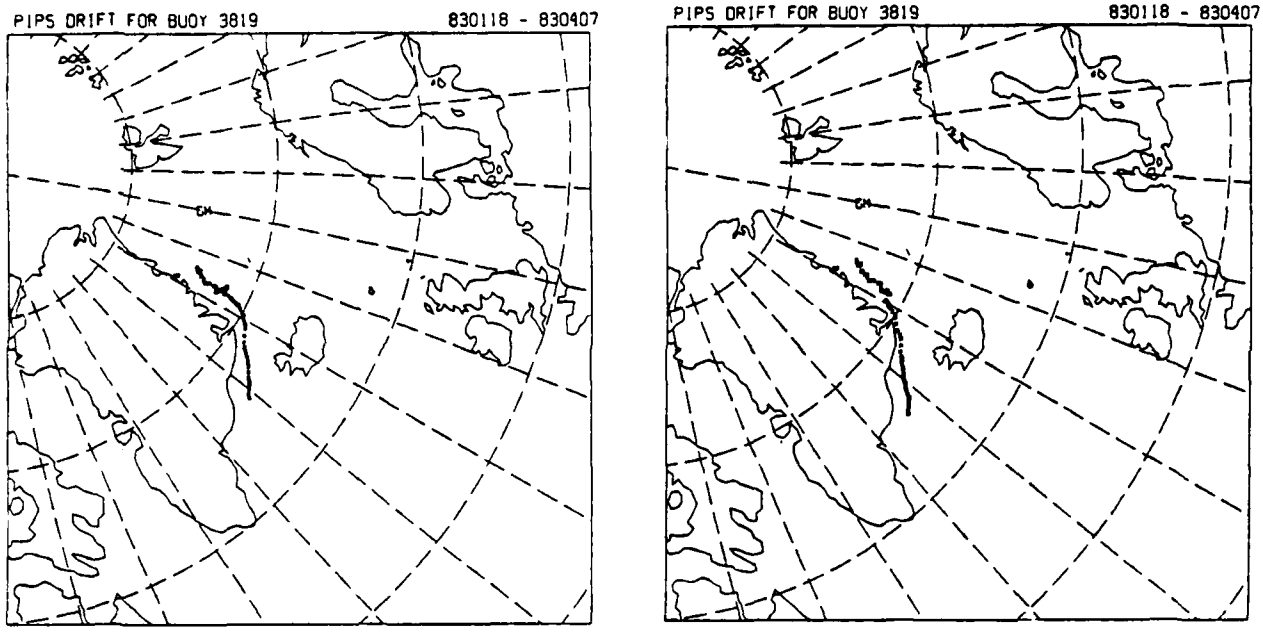

a. Ocean currents increased by a factor of 3.

b. Ocean currents increased by a factor of 5.5.

Figure 9. Model-derived ice drift for Buoy 3819 .

Table 2. Ice drift magnitude.

	Mean	*95% confidence limit*	*Standard deviation*	*95% confidence limit*	*Root mean squared deviation*	*95% confidence limit*
PIPS		0.21		0.09		
	0.17		0.07			
		0.13		0.03		0.34
					0.28	
Buoy 3816		0.56		0.20		0.22
	0.45		0.16			
		0.35		0.09		
PIPS		0.18		0.10		
	0.14		0.08			
		0.10		0.05		0.34
					0.26	
Buoy 3819		0.42		0.24	0.18	
	0.32		0.19			
		0.25		0.11		

ern half of the model domain. Inconsistencies between the NPOC analysis and the model ice edge in the southern half of the domain might also be due to the crude estimate of the ocean forcing used in this region. To improve the oceanic forcing, the Bryan–Cox multilevel, baroclinic ocean model (Bryan 1969, Bryan and Cox 1972) was set up to run on a grid similar to that used by PIPS but extended to cover the entire Greenland coast (Fig. 10). The actual grid resolution used by this model was one third that of PIPS, approximately 40 km. The model's vertical grid and bottom topography are shown in Figures 11 and 12. Bottom topography was derived from the Navy's Digital Bathymetric Data Base 5 (DBDB5) (1987). The model was initialized from seasonal climatological temperature and salinity from Levitus (1982) and driven by monthly means from the NOGAPS model. The location of the ice edge was estimated from the

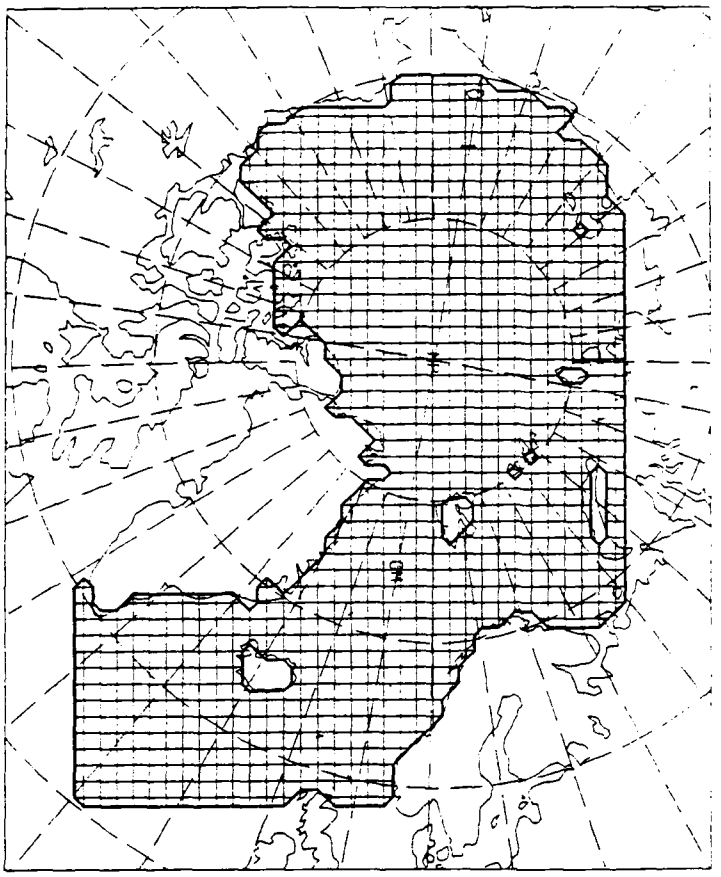

Figure 10. The extended PIPS model grid used for the Bryan and Cox ocean model. Every third grid point is plotted.

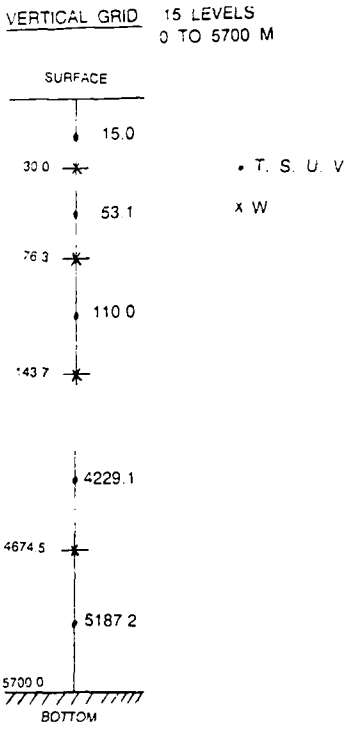

Figure 11. Vertical grid applied to the Bryan and Cox model for the domain described in Figure 10.

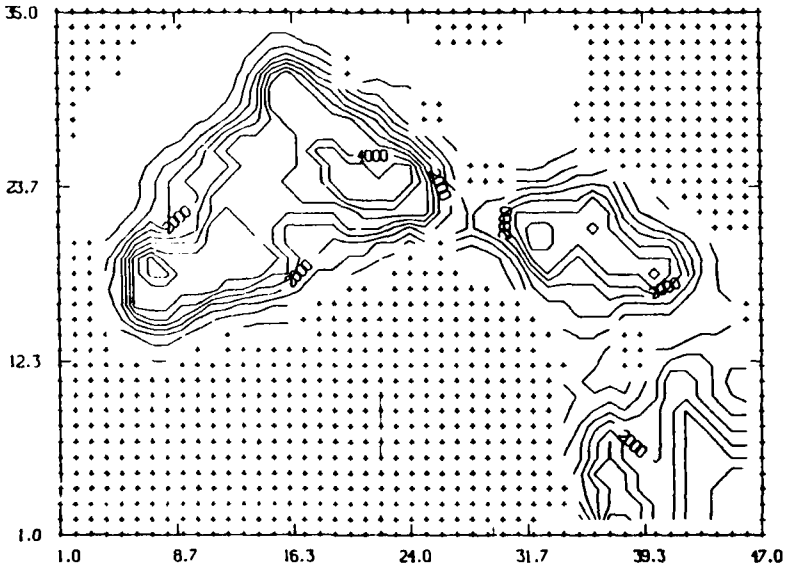

Figure 12. Bottom topography derived from the DBDB5 data base for the domain described in Figure 10. Contour intervals are 500 m.

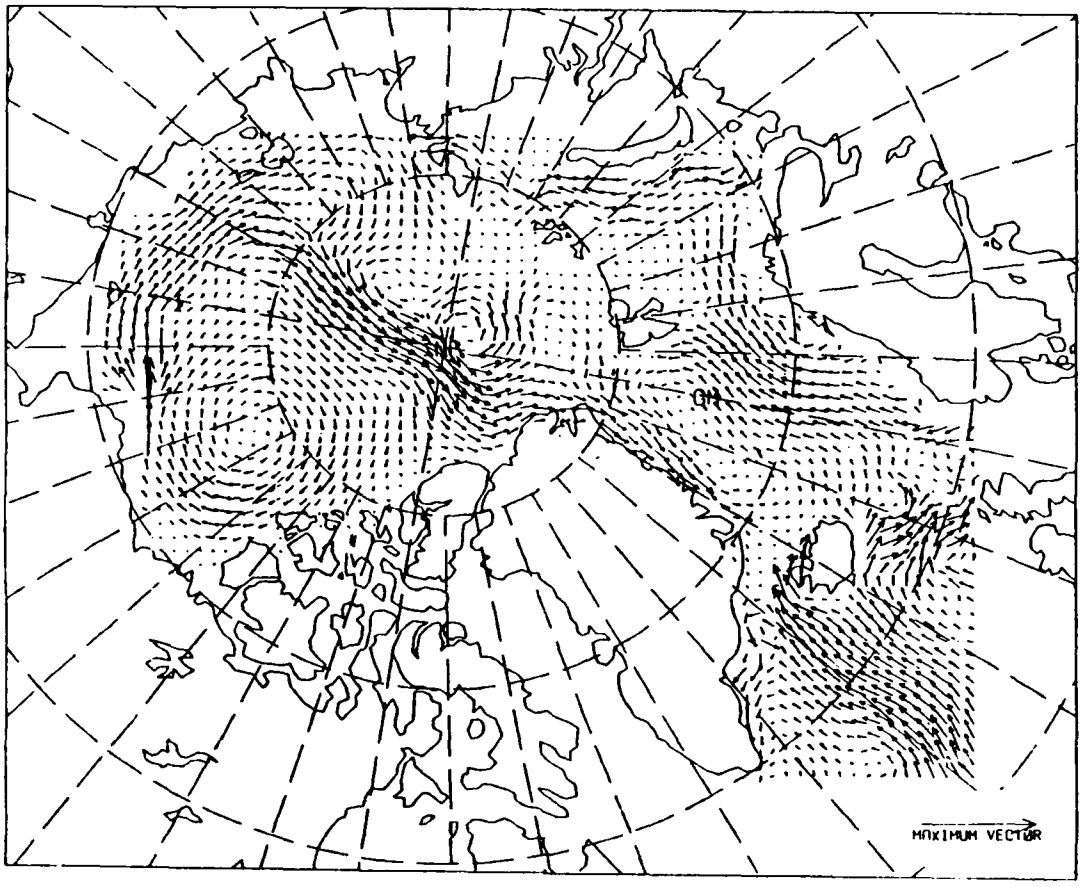

Figure 13. March monthly mean level 2 (53-m) ocean currents derived from the Bryan and Cox ocean model. Maximum vector length is 20 cm/s.

NPOC analysis. The surface stress used in the ice-covered regions was estimated to be one tenth of the actual wind stress. All model boundaries were closed, solid wall boundaries. The model was run to obtain monthly mean ocean currents. The second level of the model was used to estimate the geostrophic ocean currents needed to drive the ice model. Figure 13 shows the resultant March monthly mean second level ocean current. The circulation generated by these currents agrees very closely with the circulation shown in Figure 2. The magnitude of these currents in the northern half of the basin are almost identical to that found in the Hibler and Bryan calculation and generally agree with the observed currents for the EGC. However, the strong current feature observed at the shelf break is not resolved by this model either. This feature is of the order of 30 km in diameter while the Levitus climatology is defined at 1° intervals. Therefore, this strong current region is not resolved by the initialization data and does not appear in the model results.

The currents derived from the Bryan and Cox model were then used to replace the extrapolated currents. Figure 14 shows the March mean ice thickness distribution from this case. Although the differences are not large, the ice is noticeably thicker along the coast both north and south of the Denmark Strait. The effect of the currents from the Bryan and Cox model is to push more ice toward the Greenland coast. A similar trend appears in the ice concentration. The gradient of ice concentration at the ice edge is much tighter in this case than in the previous case. This trend indicates that there is a larger shoreward component in the ice drift increasing the ice concentration gradient near the ice edge.

Figures 15a and 15b show the monthly mean ice drift from February while Figures 16a and 16b show the monthly mean ice drift from March. Changing the ocean currents have a noticeable effect on the monthly mean ice drift, mainly in and south of the Denmark Strait. The largest changes should occur here since it is the region in which the extrapolated currents and the Bryan–Cox modeled currents differ the most. The addition of the Irminger Current west of Iceland is

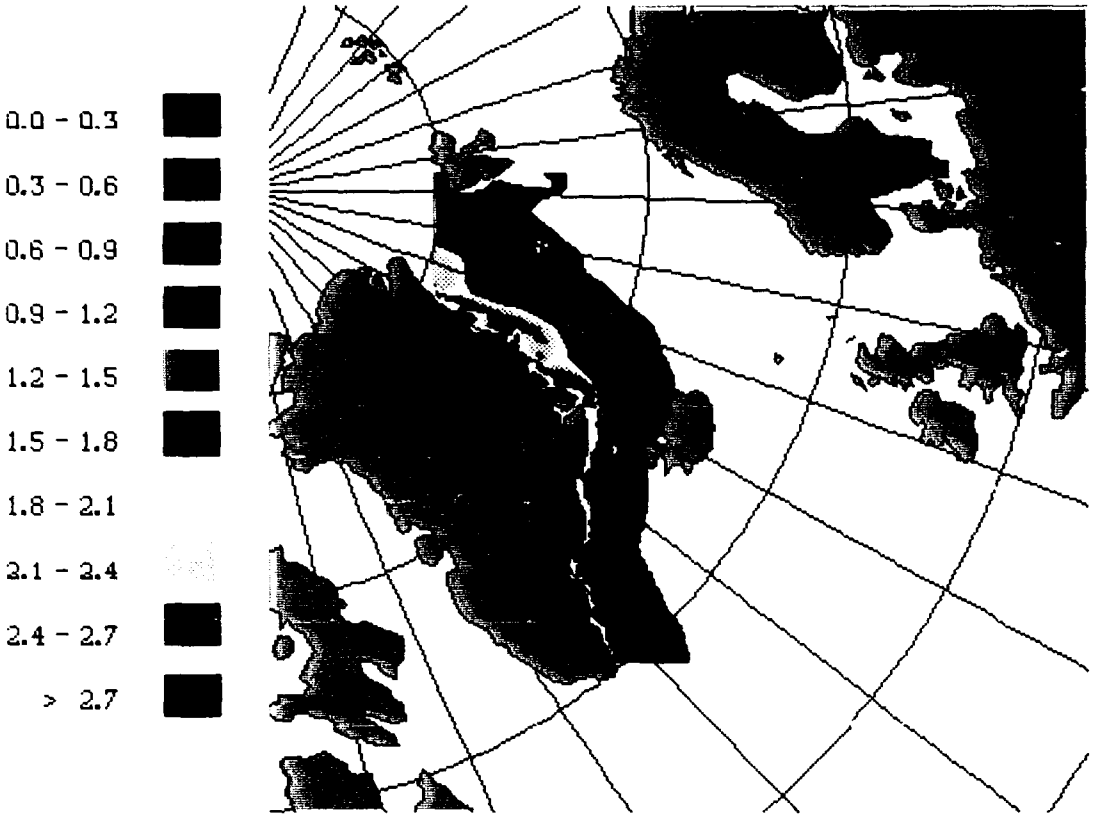

Figure 14. March mean ice thickness (m) from the model driven by the Bryan and Cox ocean currents.

responsible for the most noticeable changes in the results. The extrapolated currents assumed a total southward flow through the strait. The Irminger Current adds a northward component to the drift in the eastern part of the Denmark Strait.

Modeled buoy tracks, similar to those in Figures 8a and 8b, for this second test case showed that there is little difference between drifter tracks when the new currents were used. Figure 17 shows the observed and the modeled buoy tracks, using the Bryan and Cox modeled currents, with the buoy initialized from a position in the Denmark Strait. The modeled track follows the observed very closely, but still at approximately half the speed.

Figures 18a and 18b show the monthly mean ice concentration for August and a corresponding NPOC analysis from the same month. Although results compare well in the northern half of the basin, improving the ocean currents alone does not add ice to the southern coast of Greenland in summer.

SUMMARY AND FUTURE PLANS

The Hibler ice model has been adapted to run in the ice-covered ocean region adjacent to the east Greenland coast. The model, when driven by NOGAPS atmospheric forcing and ocean currents and heat fluxes from the Hibler and Bryan ice–ocean model, provides a fairly accurate representation of the ice edge and ice thickness, but results in ice drift values much weaker than those observed.

The upgrade made to ocean current forcing by using the Bryan–Cox model currents, improved the results, but not as well as anticipated. This improved ocean forcing has made small improvements in the ice thickness and the ice concentration. These currents have also helped to improve the ice drift in the southern half of the model domain, particularly near the Irminger Current. However, these improvements to the ocean forcing have not helped to increase the magnitude of the modeled ice drift.

For the sake of accurate forecasts of ice drift as well as ice edge location, further improvements to the model are necessary. New monthly mean oceanic heat fluxes obtained from the Bryan and Cox ocean model will soon be tested in the Greenland Sea model. These new heat fluxes may improve the model's ability to forecast the ice edge location in the southern half of the model domain in the summer.

If we assume that the ocean forcing and the atmospheric forcing are reasonable, then it may be the

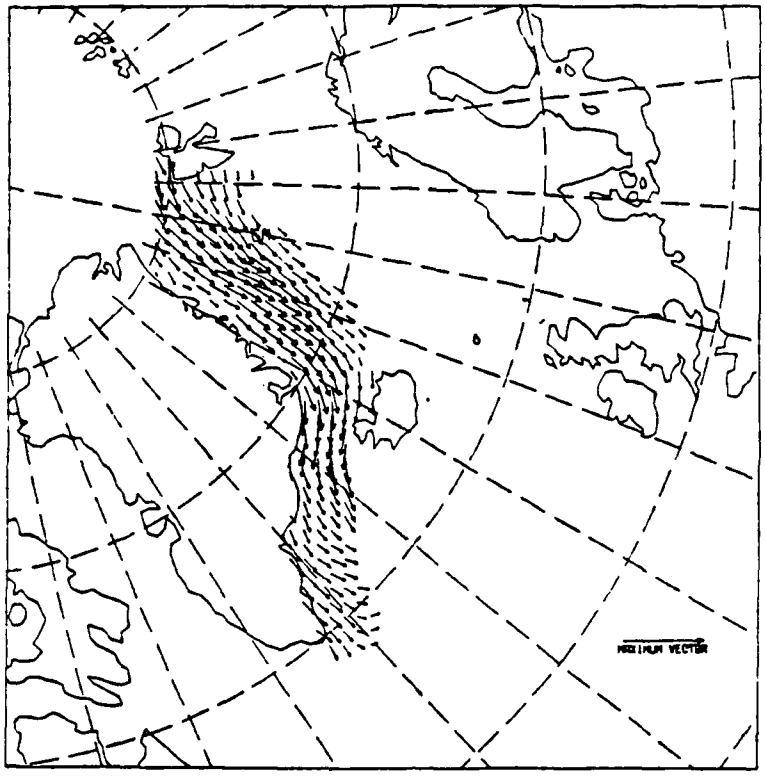

a. Using the extrapolated currents.

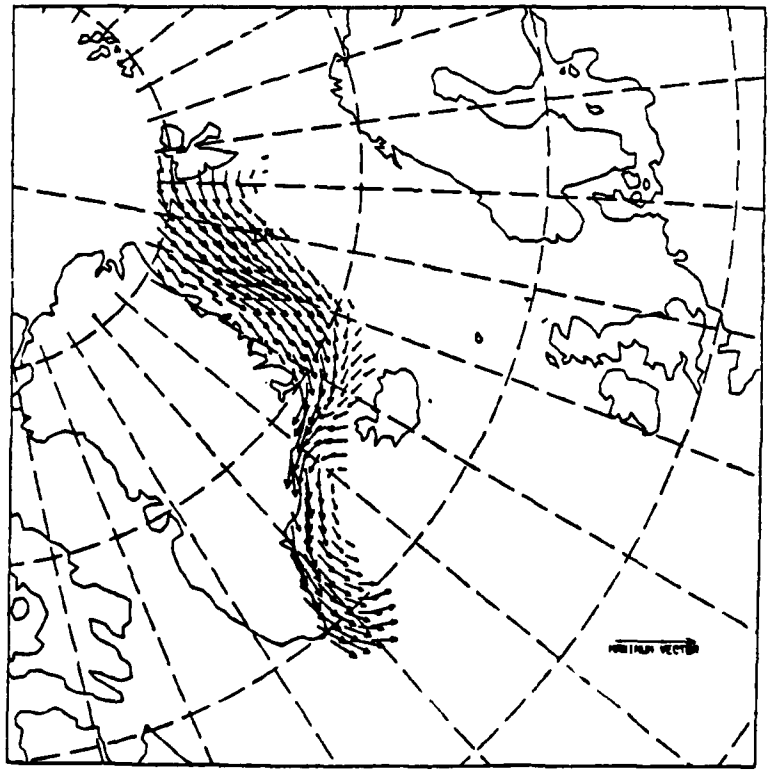

b. Using the Bryan and Cox model currents.

Figure 15. February monthly mean ice drift vectors. Maximum vector length is 30 cm/s.

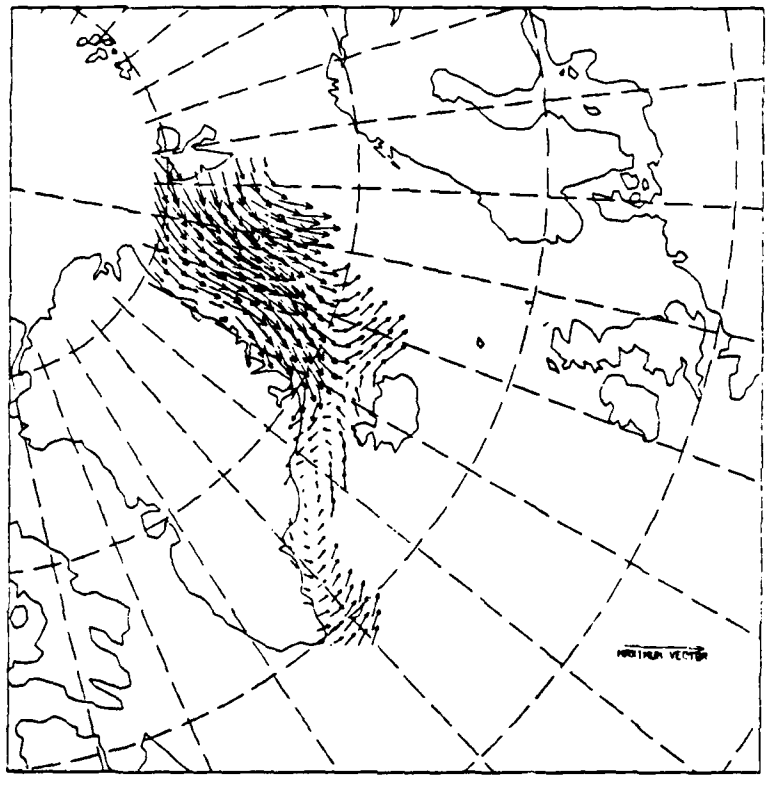

a. Using the extrapolated currents.

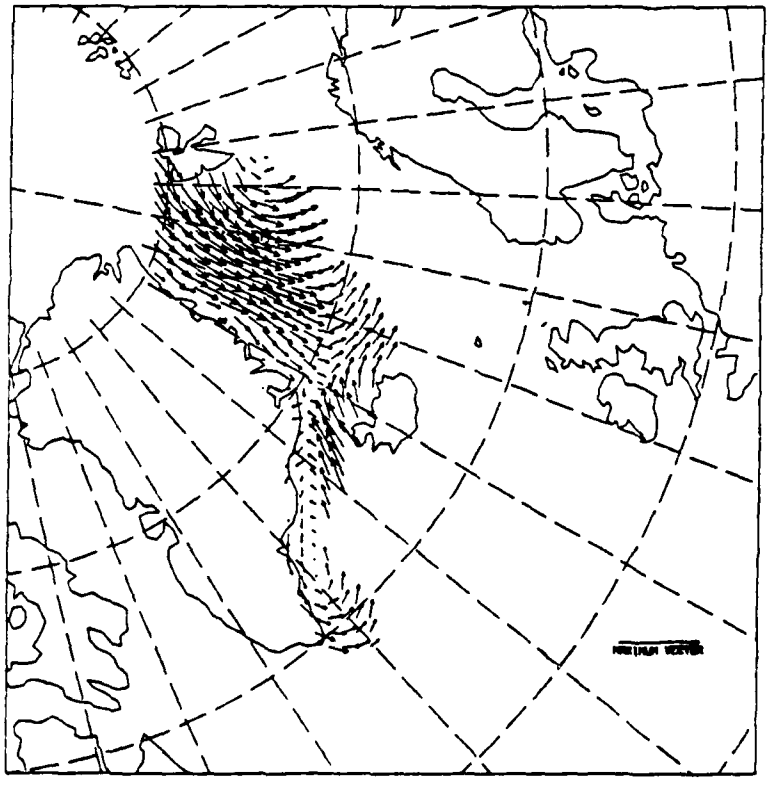

b. Using the Bryan and Cox model currents.

Figure 16. March monthly mean ice drift vectors. Maximum vector length is 30 cm/s.

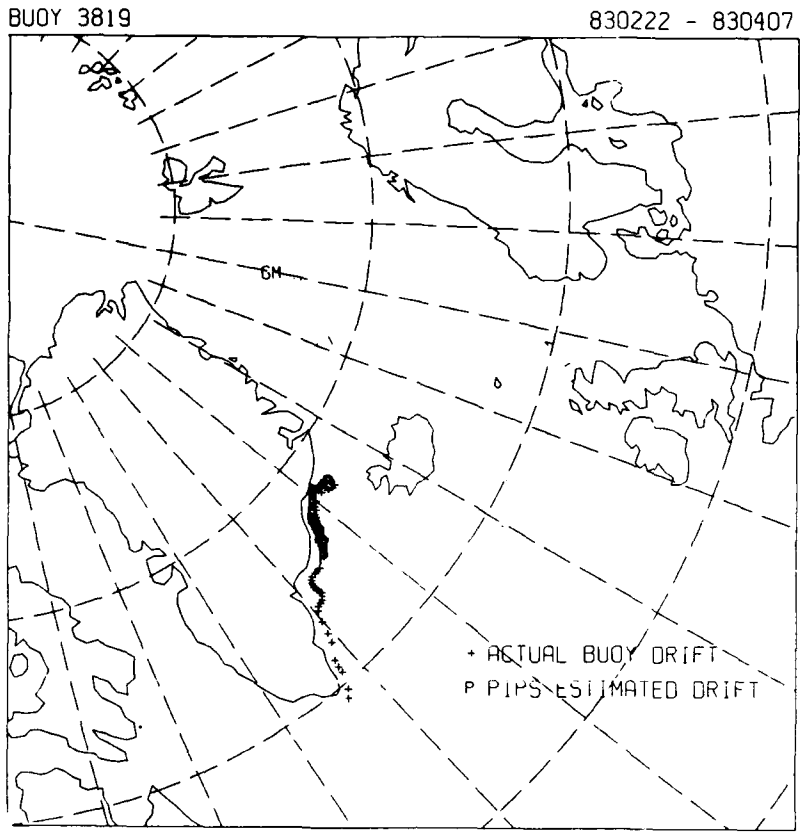

Figure 17. Observed and modeled buoy tracks for Buoy 3819 starting on 22 February from a location in the Denmark Strait.

design of the ice model itself which is responsible for the inaccuracies in the ice drift. The version of the Hibler model used in this study treats ice as a continuum defined by a viscous–plastic ice rheology. Since ice in the Greenland Sea is more representative of a field of floes than a continuum, future plans for this work involve changing the existing ice rheology. The need for such a change has already been suggested by other scientists such as Shen et al. (1987) and Brachte (1984) who have designed and tested methods for treating ice in the marginal ice zone as a floe field. A second possible method for improving the existing ice rheology is to change the shape of the yield curve (Hibler 1979) to one in which the relationship between stress and strain are more representative of the marginal ice zone. Tucker (1982) attempted to improve his model by setting the ice pressure term

$$P = P^* h \exp[-C(1-A)]$$

to zero by setting the constant P^* to zero. This effectively damps out the ice interaction with itself creating a free-drift type situation. He found that this change resulted in an excessive buildup of ice along the Greenland coast. Setting the ice pressure to zero removes the ability of the ice to resistance deformation. The onshore component of the wind piles ice up, unrealistically, along the coast. Changing the dependence of the pressure term on the ice thickness and concentration (as opposed to removing it completely) may be another possible method of improving the model results. Experiments to test these and other improvements to the model are ongoing at NORDA. It is hoped that the model will be improved and ready for operational (forecast) testing within the next year.

ACKNOWLEDGMENTS

This work was funded by the U.S. Navy Space and Naval Warfare Systems Command through the Air Ocean Prediction Program (program element 63207N) under Captain J.J. Jensen. PR 89:040:322 This document has been reviewed and is approved for public release.

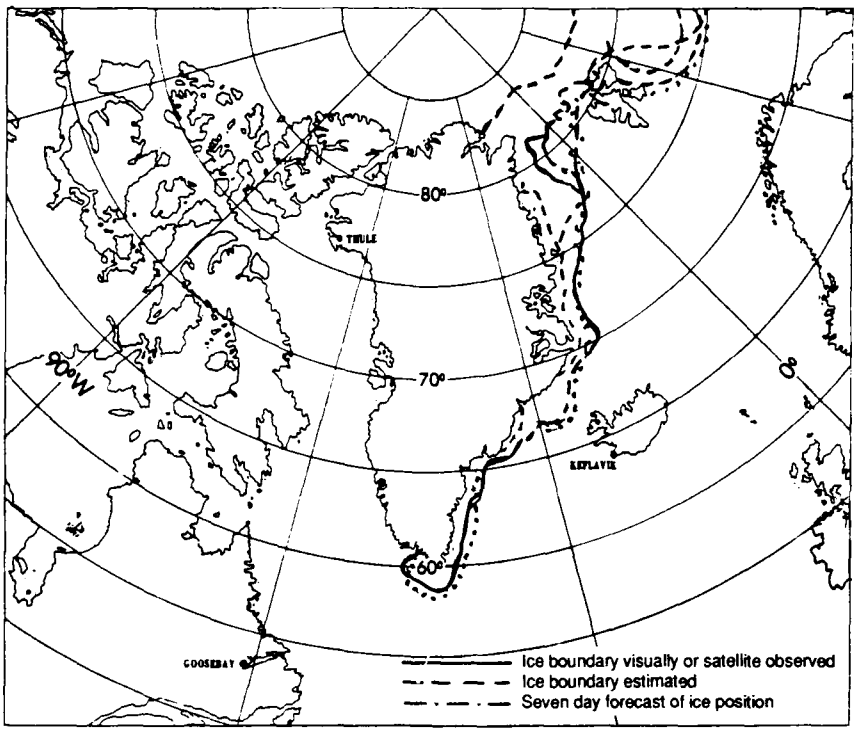

a. NPOC ice concentration from 16 August 1983.

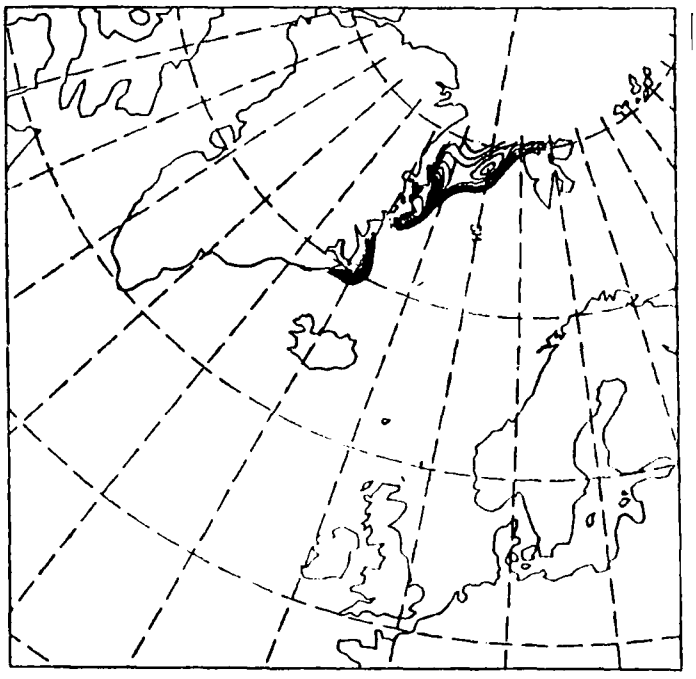

b. August monthly mean ice concentration for the case using the Bryan and Cox ocean currents.

Figure 18. August ice concentration. (Contour interval is in 10%.)

REFERENCES

Aagaard, K. and L.K. Coachman (1968a) The East Greenland Current north of Denmark Strait, Part I. *Arctic*, **21**: 181–200.

Aagaard, K. and L.K. Coachman (1968b) The East Greenland current north of Denmark Strait, Part II. *Arctic*, **21**: 267–290.

Brachte, I. (1984) Rheology of an ice floe field. *Annals of Glaciology*, **5**: 23–28.

Bryan, K. (1969) A numerical method for the study of the circulation of the world oceans. *Journal of Computational Physics*, **4**: 347–376.

Bryan, K. and M.D. Cox (1972) An approximate equation of state for numerical models of ocean circulation. *Journal of Physical Oceanography*, **2**: 510–514.

Bourke, R.H., J.L. Newton, R.G. Paquette and M.D. Tunnicliffe (1987) Circulation and water masses of the East Greenland Shelf. *Journal of Geophysical Research*, **92**: 6729–6740.

Bryan, K., S. Manabe, and R. Pacanowski (1975) A global ocean–atmosphere climate model, Part II. The oceanic circulation. *Journal of Physical Oceanography*, **5**: 30–46.

Colony, R. and E.A. Munoz (1985) Arctic ocean buoy program. Data Report, 1 January 1983–31 December 1983. Polar Science Center, Applied Physics Laboratory, University of Washington, Seattle.

Foldvik, A., K. Aagaard and T. Torresen (1988) On the velocity field of the East Greenland current. *Deep-Sea Research*, **35**: 1335–1354.

Gathman, S.G. (1986) Climatology. In *The Nordic Seas* (B.G. Hurdle, Ed.). New York: Springer-Verlag, p. 1–18.

Hibler, W.D. III (1979) A dynamic–thermodynamic sea ice model. *Journal of Physical Oceanography*, **9**: 815–846.

Hibler, W.D. III (1980) Modeling a variable thickness sea ice cover. *Monthly Weather Review*, **108**: 1944–1973.

Hibler, W.D. III and K. Bryan (1984) Ocean circulation: Its effects on seasonal sea-ice simulations. *Science*, **224**: 489–491.

Hibler, W.D. III and K. Bryan (1987) A diagnostic ice–ocean model. *Journal of Physical Oceanography*, **17**: 987–1015.

Levitus, S. (1982) Climatological atlas of the world ocean. National Oceanic and Atmospheric Administration, Rockville, Maryland, Professional Paper 13.

Manabe, S., K. Bryan and M. Spelman (1979) A global ocean–atmosphere climate model with seasonal variation for future studies of climate sensitivity. *Dynamics of Atmosphere and the Ocean*, **3**: 393-426.

Naval Oceanographic Office (1987) Data base documentation for digital bathymetric data base confidential (DBDBC). Naval Oceanographic Office, NSTL, Mississippi, OAML-DBD-17A.

Parkinson, C.L. and W. Washington (1979) A large-scale numerical model of sea ice. *Journal of Geophysical Research*, **84**: 311–337.

Preller, R.H. (1985) The NORDA/FNOC Polar Ice Prediction System (PIPS)—Technical Description. Naval Ocean Research and Development Activity, SSC, Mississippi, NORDA Technical Report 108.

Preller, R.H. and P.G. Posey (1989) The polar ice prediction system—A sea ice forecasting system. Naval Ocean Research and Development Activity, SSC, Mississippi, NORDA Technical Report 212.

Preller, R.H., S. Riedlinger and P.G. Posey (1989) The regional polar ice prediction system—Barents Sea (RPIPS-B): A technical description. Naval Ocean Research and Development Activity, SSC Mississippi, NORDA Technical Report 182.

Rosmond, T.E. (1981) NOGAPS: Navy Operational Global Atmospheric Prediction System. In *Proceedings, Fifth Conference on Numerical Weather Prediction, Monterey, California*. Boston, Massachusetts: American Meteorological Society, preprint volume, p. 74–79.

Semtner, A.J. (1976) A model for the thermodynamic growth of sea ice in numerical investigations of climate. *Journal of Physical Oceanography*, **6**: 379–389.

Shen, H.H., W.D. Hibler III and M. Leppäranta (1987). The role of floe collisions in sea ice rheology. *Journal of Physical Oceanography*, **92**: 7085–7096.

Trangeled, S. (1973) Oceanography of the Norwegian and Greenland Seas and adjacent areas. Vol. I—Bibliography. Saclant ASW Research Centre Memorandum SM-4, Italy.

Tucker, W.B. (1982) Application of a numerical sea ice model to the East Greenland area. USA Cold Regions Research and Engineering Laboratory, CRREL Report 82-16.

Thorndike, A.S. and R. Colony (1982) Sea ice motion in response to geostrophic winds. *Journal of Geophysical Research*, **87**: 5845–5892.

Vibe, C. (1967) Arctic animals in relation to climate fluctuations. *Meddelelser om Gronland*, 170/5.

Sea Ice Modeling with SMMR and Buoy Data, and a Kalman Filter

D.A. ROTHROCK AND D.R. THOMAS
Applied Physics Laboratory
University of Washington
Seattle, Washington, U.S.A.

It is striking that, to date, there has been little use of the 10 years of multifrequency passive microwave satellite data in sea ice modeling. One reason is undoubtedly the dichotomy between what satellite sensors "see" and what models model. Whereas ice models have described the physically important ice motion, ice thickness distribution, and vertical heat exchange, microwave sensors respond to ice "concentration" (of ice thicker than an uncertain cutoff thickness), ice age, and surface conditions—especially surface wetness.

We are experimenting with a newly formulated sea ice model and applying it to the interpretation of passive microwave observations. The model describes the concentrations of open water, first-year ice, second-year ice, and multiyear ice. These concentrations are governed by simple physical processes: advection, deformation, freezing or melting, and aging. In the absence of these processes, the concentrations are observed. Advection and deformation are determined by kinematic data from the Arctic Buoy Program; the onsets of melting and of freezing are determined from the microwave data, and aging occurs once a year at autumn freeze-up. These processes are contained in the part of the model referred to as the physical model.

There is a complementary portion of the ice model called the measurement model. It contains the "algorithm" relating the modeled variables to the microwave observations. An important function of the measurement model is to take into account the fact that the microwave brightness temperatures of the pure surface types (i.e., their signatures) have an uncertainty of several kelvins in winter and tens of degrees in summer. Accounting explicitly for this uncertainty restrains the model from interpreting small changes in the microwave signal as actual changes in the ice cover.

The interpretation of the microwave satellite data with this model has several advantages. It allows one to, in a sense, extrapolate the observations into the data "hole" around the north pole (north of 84°N for SMMR). It allows one to integrate through the summer—when the microwave observations become quite difficult to interpret—on the strength of the physical model. It allows one to incorporate additional data to resolve how the ice cover is evolving; the use of drifting buoy (and, in the future, SAR) kinematic data helps determine what changes in ice concentrations are physically possible.

The Interaction of an Ocean Eddy with a Marginal Ice Zone Ocean Front

D.C. SMITH IV AND A.A. BIRD
Naval Postgraduate School
Monterey, California, U.S.A.

W.P. BUDGELL
Institute of Ocean Sciences
Sidney, British Columbia, Canada

ABSTRACT

The interaction of an ocean eddy with an ocean front and overlying ice edge is studied using a two-layer ocean model with coupled free-drift ice model. Ocean eddy propagation is shown to be related to eddy–front interaction. The signature of these processes in the ice concentration field is illustrated. The effects of along-ice-edge winds on the above processes are shown.

INTRODUCTION

While a number of hypotheses concerning the formation of ice edge eddies in the East Greenland Current (EGC) marginal ice zone have been suggested, recent observations (Gascard et al. 1988) have indicated that the eddies are most likely manifestations of existing open ocean eddies from the West Spitzbergen Current (WSC). These eddies are advected across the Fram Strait and then interact with the EGC and the marginal ice zone.

MODEL DESCRIPTION

A coupled two-layer ocean / free-drift ice model is used in this study. Model parameter choices and equations are given in Smith et al. (1988). In that study, the interaction of an isolated eddy with a

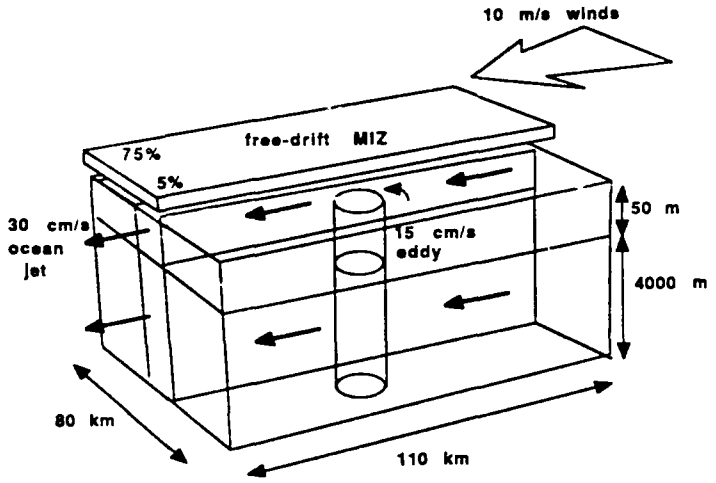

Figure 1. Coupled ice–ocean model and initial conditions in eddy–ice edge front interaction study.

marginal ice zone was considered. In these experiments an along-ice-edge ocean front has been added to the initial conditions. The strength of the ocean jet is initially 30 cm/s and is Gaussian in lateral structure with a width scale of 5 km. Adjacent to the ocean jet is a 15-cm/s Gaussian eddy with the same width scale. Figure 1 shows the model configuration and initial conditions.

EDDY-JET INTERACTIONS

The interaction of an ocean eddy with an adjacent jet in the absence of ice was initially considered by Stern and Flierl (1987). They showed that interactions of the eddy with the jet can produce vortex propagation tendencies on an f-plane. In particular an anticyclone could "capture" cyclonically sheared fluid on one side of the jet, and propagate laterally away from the jet. The propagation is related to the mutual advection of opposite sign vorticities. This process was further examined by Smith and Davis (1989) for mid-latitude eddies and jets of Gulf Stream strength. A goal of this study has been to determine the extent to which this process may occur in high-latitude eddy–jet interactions such as in the East Greenland Current marginal ice zone.

RESULTS

Although numerous experiments have been conducted to examine the sensitivity of model results to initial parameters, only several key experiments are described here. Open ocean eddies interacting with the East Greenland Current would sense the cyclonically sheared edge of the southwestward flowing jet. We will contrast the interaction of open ocean anticyclones and cyclones with the jet and discuss briefly the influence of along-ice-edge winds on the process.

As discussed in the previous section, the interaction of an open ocean anticyclone with the cyclonic sheared edge of a jet can pair with the cyclonically sheared fluid and propagate laterally away from the jet. Figure 2, which shows the evolution of ocean upper layer potential vorticity, demonstrates that this process can occur for flow strength parameters of the East Greenland Current. In the process, ice is advected seaward by the dipolar flow field in a fashion consistent with that suggested by synthethic aperture radar (SAR) during the Marginal Ice Zone Exper-

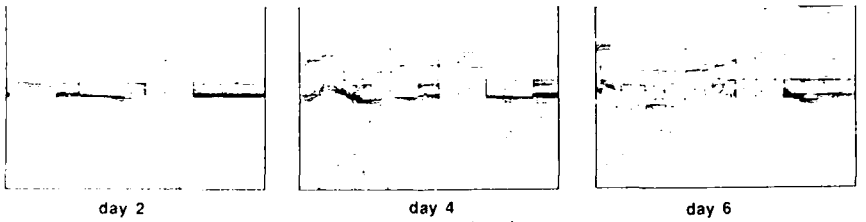

a. Ocean upper layer relative vorticity (10^{-6} s^{-1}). Dashed (solid) contours indicate anticyclonic (cyclonic) relative vorticity.

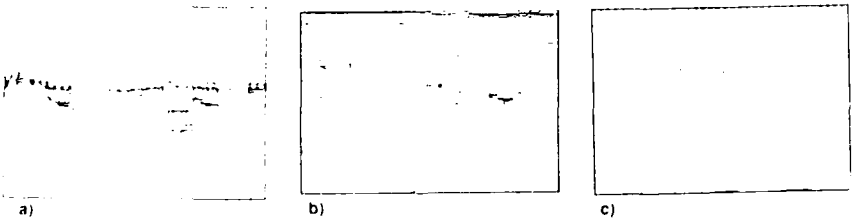

b. Ice concentration.

Figure 2. Anticyclone–jet experiment without wind.

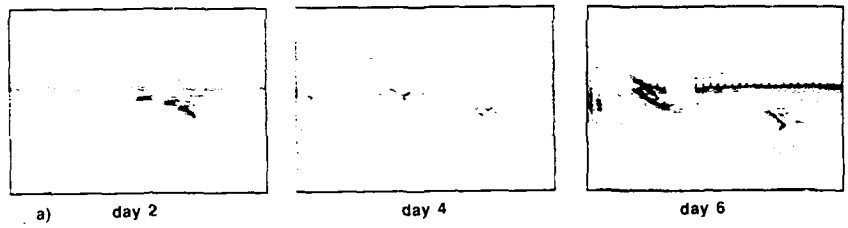

Figure 3. Ice concentration. Cyclone–jet experiment without winds.

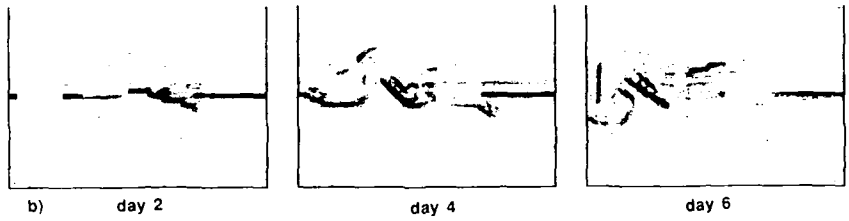

Figure 4. Day 6 for cyclone–jet experiment with along-ice-edge upwelling favorable winds. a) Ocean upper layer relative vorticity. b) Ice concentration. c) Ocean interface height anomaly (in meters, positive contours represent upward distortions).

iment (Shuchman et al. 1988). While this simulation illustrates a mechanism for the formation of eddy pairs and ice advection seaward consistent with observations, the observations of Johannessen et al. (1987) and Gascard et al. (1988) indicate that the majority of eddies in the East Greenland Current marginal ice zone are cyclonic.

Experiments with cyclonic eddies seaward of the cyclonic side of the jet fail to produce a dipolar ocean flow field (see Fig. 3). Cyclone–jet interactions can produce distortions in the ice edge that are then subsequently advected downstream by the jet which itself can be substantially perturbed by the interaction. When the effects of along-ice-edge winds are also included, additional eddies are formed. Figure 4 shows ice concentration and ocean interface height anomaly for this cyclone–jet interaction where upwelling favorable 10-m/s winds have been included. By day 6 of the simulation, a 15-m upwelled eddy can be seen in the interfacial height anomaly field (Fig. 4). Hakkinen (1986) has shown that upwelling winds along a sinuous ice edge leads to alternating upwelled and downwelled flow patterns. This experiment illustrates a mechanism by which a sinuous ice edge can physically occur and one which does not require unstable meandering of the jet.

CONCLUSIONS

The evolution of perturbations in the ice edge observed in numerous SAR images in the East Greenland Current marginal ice zone may be related to the interaction of open ocean eddies with the current. Anticyclone–jet interaction can lead to the evolution of dipolar-like ocean flow fields which advect ice seaward from the ice edge, thereby contributing to the melt rate at the ice edge. Cyclone-jet interactions do not result in dipolar structures but can lead to perturbations on the jet that are reflected by ice edge perturbations. Along-ice-edge winds in this case drive local upwelling centers favoring formation of additional eddies downstream of the initial cyclone–jet interaction.

REFERENCES

Gascard, J.-C., C. Kergomard, P.-F. Jeannin and M. Fily (1988) Diagnostic study of the Fram Strait marginal ice zone during summer from 1983 and 1984 Marginal Ice Zone Experiment Lagrangian observations. *Journal of Geophysical Research*, **93**: 3613-3641.

Hakkinen, S. (1986) Coupled ice–ocean dynamics in the marginal ice zones: Upwelling /downwelling and eddy generation. *Journal of Geophysical Research*, **91**: 819–832.

Johannessen, J.A., O.M. Johannessen, E. Svendsen, R. Shuchman, T. Manley, W.J. Campbell, E.G. Josberger, S. Sandven, J.-C. Gascard, T. Olaussen, K. Davidson and J. Van Leer (1987) Mesoscale eddies in the Fram Strait marginal ice zone during the 1983 and 1984 Marginal Ice Zone Experiments. *Journal of Geophysical Research*, **92**: 6754–6772.

Shuchman, R.A., L.L. Sutherland and B.A. Burns (1988) MIZEX 1987 SAR Data Summary. Informal In-

formation Report, Environmental Research Institute of Michigan.
Smith, D.C. IV, A.A. Bird and W.P. Budgell (1988) A numerical study of mesoscale ocean eddy interaction with a marginal ice zone. *Journal of Geophysical Research*, **93**: 12461–12474.
Smith, D.C. IV and G.P. Davis (1989) A numerical study of ocean eddy interaction with a jet. Accepted by *Journal of Physical Oceanography*.
Stern, M.E. and G.R. Flierl (1987) On the interaction of a vortex with a shear flow. *Journal of Geophysical Research*, **92**: 10733–10744.

Using the Free-Drift Force Balance to Estimate Drag Coefficients and Ice Thickness

M.G. MCPHEE
McPhee Research Company
Naches, Washington, U.S.A.

ABSTRACT

Estimating wind and water drag coefficients, c_a and c_w, and mean ice mass, m, over some regional scale pertinent to sea ice dynamics is one of the most basic (and elusive) tasks of sea ice research. The steady-state, free-drift (no internal ice stress gradient) momentum equation provides a powerful constraint, through the Coriolis term, on the relationship among the drag coefficients and ice mass. If periods of reasonably steady free-drift can be identified, we show that knowledge of one of the three quantities is enough to determine the other two, if we also know the ice speed relative to underlying geostrophic flow (i.e., the wind drift speed), the ratio of drift speed to wind speed, the rightward deflection of drift relative to surface wind, and the planetary-boundary-layer turning angle in the ocean. The free-drift constraints should be carefully considered in the design of unmanned data buoys.

INTRODUCTION

In the context of measurements from remote buoys or drifting ice stations, it is germane to ask what minimum measurements are required to estimate the air-to-ocean momentum flux through pack ice. In this note we manipulate the steady-state, "free-drift" momentum equation to show that measurements of wind velocity, ice velocity with respect to surface geostrophic flow, mean ice mass per unit area, and the angle of turning in the oceanic boundary layer are enough for credible estimates of wind and water drag coefficients, provided drift periods with low internal ice stress gradients can be identified. Alternatively, if one or the other drag coefficients is known, the equations provide an estimate of mean ice mass per unit area over the region for which the local force balance holds.

The method is similar to one developed by Pease et al. (1983), except that where they expressed water stress as proportional to the square of current speed in the surface layer just under the ice, here water stress is expressed as an operator that scales and rotates the relative ice velocity, i.e., the velocity of the ice with respect to the velocity it would have in the absence of wind or water stress.

EQUATIONS

Let $\vec{u}_o$ be the relative ice velocity:

$$\vec{u}_o = \vec{u} - \vec{u}_g \tag{1}$$

where

$$f\vec{k} \times \vec{u}_g = -g\nabla\eta. \tag{2}$$

Here $\vec{u}$ is the actual ice velocity, g is the acceleration of gravity, and η is the sea–surface elevation. In essence, $\vec{u}_o$ is the negative of current velocity measured just below the frictional boundary layer; a typical depth would be 30 m under the ice. In what follows we refer to $\vec{u}_o$ as the ice velocity, since wind-driven drift velocity is typically an order of magnitude greater than geostrophic current in much of the Arctic.

The steady-state, horizontally homogeneous momentum equation in the absence of an internal ice stress gradient is

$$imf\ \hat{u}_o = \hat{\tau}_a - \rho_w u_* \hat{u}_* \tag{3}$$

where the circumflex denotes a complex (two-dimensional) vector; scalar magnitude is indicated by the absence of the circumflex; m denotes ice mass per unit area, f is the Coriolis parameter, and $\hat{\tau}_a$ and $\rho_w u_* \hat{u}_*$ are air and water stress, respectively.

Let the complex ratio of ice velocity to wind velocity, be

$$\hat{u}_o/\hat{W} = re^{i\theta} \tag{4}$$

where θ is the clockwise angle of surface drift with respect to the wind. Let the ratio of ice velocity to oceanic friction velocity be

$$\hat{\Gamma} = \hat{u}_o/\hat{u}_* = \Gamma e^{-i\beta} \tag{5}$$

where $\hat{\Gamma}$ is the nondimensional surface velocity with magnitude equal to the reciprocal square root of the oceanic drag coefficient, c_w. But note that there is no assumption of quadratic or linear drag; in fact, we found from analyzing AIDJEX data that Γ is not constant, but instead varies much as predicted by Rossby-similarity scaling (McPhee 1982).

With air density, ρ_a, and the drag coefficient, c_a, appropriate for wind measured at some level in the surface layer (i.e., so that wind and air stress are colinear) the momentum equation in terms of $\hat{\tau}_a$ is

$$imf\,\hat{u}_o = \rho_a c_a \frac{u_o}{r^2} e^{i\theta}\hat{u}_o - \rho_w \frac{u_o}{\Gamma^2} e^{i\beta}\hat{u}_o. \tag{6}$$

Separating real and imaginary components leads to two scalar equations:

$$c_a\Gamma^2 = r^2\frac{\rho_w \cos\beta}{\rho_a \cos\theta} \tag{7}$$

$$\Gamma^2 = \frac{\rho_w u_o}{mf}(\cos\beta - \tan\theta - \sin\beta) \tag{8}$$

The first expresses the ratio of air and water drag coefficients, while the second determines the magnitude of the water drag from the "known" quantities: m, u_o, θ and β.

Alternatively, with Γ or c_a specified, an expression for ice mass is

$$m = \frac{\rho_w u_o}{\Gamma^2 f}(\cos\beta\ \tan\theta - \sin\beta). \tag{9}$$

This suggests a novel method for calculating regional ice mass: equip a buoy with surface wind anemometer and two current meters, capable of measuring u_o, $re^{-i\theta}$ and u_*. The last is, of course, a difficult measurement, but recent work has shown that a "smart" current meter capable of measuring the variance in horizontal current components within, say, 4 m of the ice/ocean interface, can provide a good estimate of u_* (McPhee 1989). The mass is similarly proportional to the air drag coefficient:

$$m = \frac{c_a u_o \rho_a}{fr^2}(\sin\theta - \tan\beta - \cos\theta). \tag{10}$$

If criteria (e.g., ice divergence) for identifying episodes of free drift can be established, eq 9 or 10 may then be used to estimate the average ice mass. Accuracy in direction measurement is needed, but note that it is the relative angles between vectors that is important, thus maintaining rigid alignment among the three sensors is probably a better strategy then relying on separate magnetic compasses. As ice thickness approaches zero, θ approaches β and the system becomes indeterminate. Note also if ice exists in a true state of steady, free drift, θ cannot equal β.

EXAMPLES

Examples are drawn from two projects: mean drift during the summer months of AIDJEX in 1975, and mean drift during a particular storm in MIZEX 1984. Mean wind and drift data from an 80-day period during summer at four AIDJEX camps in the central Arctic indicated free-drift conditions (McPhee 1980), and can be summarized as: u_o = 13.0 cm/s; r = 0.020; θ = 46.8°. The drift/wind ratio and angle were determined from smoothed data when the wind exceeded 2.5 m/s, with u_o taken as the vector difference of the ice velocity and the geostrophic current from the mean dynamic topography. For the entire project, the average value of β from current meters located 2 and 30 m below the ice was 23.6°. (The current meter records showed intermittent speed errors and thus were not used for the relative surface velocity.) Average ice thickness at the AIDJEX camps is not well known, especially over an area large enough to govern the momentum balance, but was estimated to be between 2.5 m (2300 kg/m) and 3.5 m (3220 kg/m).

Drag coefficients and other derived values corresponding to the average values of u_o, r, θ, and β, are given in Table 1 for three values of ice thickness. The range of drag coefficients is reasonable based on the AIDJEX determinations of air drag. Banke et al. (1980) reported a neutral value of $c_{10} = 1.55 \pm 0.37 \times 10^{-3}$, for ice relatively free of pressure ridges. Leavitt (1980) reported a 10-m drag coefficient of 2×10^{-3} from 25-m tower measurements at AIDJEX, but suggested that the regional value was higher because the camps were situated on relatively smooth floes. By integrating pilot balloon profiles, Carsey (1980) arrived at a 10-m drag coefficient of about 1.9×10^{-3} for the summer period. At any rate, the range of ice thickness

Table 1. Calculation of drag coefficients for summer AIDJEX drift conditions, for three ice thickness values. Parameters are u_0 = 0.13 m/s, r = 0.02, θ = 46.8 , β = 23.6 .

Ice thickness (m)	c_a/c_{aw}	c_a (×1000)	Γ	c_{aw} (×1000)
2.5	0.42	1.77	15.5	4.2
3.0	0.42	2.13	14.1	5.0
3.5	0.42	2.48	13.1	5.9

seems to encompass the range of drag coefficients, especially considering that the AIDJEX measurements were probably lower than the actual regional air stress.

During the 1984 MIZEX project in the Greenland Sea marginal ice zone, our instrumented floe drifted steadily south during a three and a half day storm. Since we were near the ice margin, surrounded by areas of open water, it is safe to assume that internal ice stress was negligible. McPhee et al. (1987) summarized drift, current, and turbulence data (see especially their Fig. 7 and 8). In this case, the relative ice velocity was taken from the average current at 30 m determined by a continuously cycled profiling current meter. Over the course of the wind event, average observed quantities were as follows: u_0 = 0.151 m/s, r = 0.018, θ = 41 , β = 32 . For ice thickness ranging from 1.5 to 2.5 m, the free drift solutions are summarized in Table 2. The average neutral air drag coefficient determined from turbulence measurements on the floe was 2.3 × 10^{-3} (P. Guest, pers. comm.); thus the regional ice thickness based on air stress measurements is about 2 m.

During MIZEX we had independent measurements of turbulent stress in the oceanic boundary layer (this was not the case for AIDJEX, where oceanic drag parameters were generally inferred from the free-drift force balance). From Figure 8 of McPhee et al. (1987), assuming the stress 4 m below the ice is "fully developed" to local topographic roughness features, we can adjust the stress back to its surface value assuming an exponential falloff of stress in the boundary layer (McPhee 1989). Based on the 4-m Reynolds stress, the magnitude of u_* is about 0.0123 m/s, and γ is 12.3. This implies that c_a is 1.9×10^{-3} and the implied regional ice thickness is about 1.6 m.

Table 2. Calculation of drag coefficients for summer MIZEX drift in the Greenland Sea marginal ice zone. Parameters are u_0 = 0.151 m/s, r = 0.018, θ = 41 , β = 32 .

Ice thickness (m)	c_a/c_{aw}	c_a (×1000)	Γ	c_{aw} (×1000)
1.5	0.29	1.73	12.9	6.0
2.0	0.29	2.30	11.2	8.0
2.5	0.29	2.88	10.0	10.0

DISCUSSION

There is a long tradition of using the "free-drift" force balance to constrain values for air and water drag coefficients. Pease et al. (1983) showed that single level measurements of wind and current in the atmospheric and oceanic surface layers were sufficient to define drag coefficients applicable to the measurement levels, provided $\vec{u}_0$ is known. The approach here, to emphasize instead of the "geostrophic" drag, is simpler in the sense that only direction of current in the surface layer is required (to establish β), and the resulting drag coefficient is applied directly to the relative ice velocity. Knowledge of β is implicit in the formulation of Pease et al. (1983), and just as with eq 2, if β approaches θ (i.e., if wind and surface layer current approach colinearity), their system, like the present formulation, becomes indeterminate. Application of either technique thus depends on the Coriolis force in the ice dominating all other forces except the principal balance between air stress and water stress. Because the Coriolis force is often relatively small, the methods should be used only when free-drift conditions are clearly identifiable.

REFERENCES

Banke, E.G., S.D. Smith and R.J. Anderson (1980) Drag coefficients at AIDJEX from sonic anemometer measurements. In *Sea Ice Processes and Models* (R. S. Pritchard, Ed.). Seattle: University of Washington Press, p. 430–442.

Carsey, F.D. (1980) The boundary layer height in air stress measurements. In *Sea Ice Processes and Models* (R. S. Pritchard, Ed.). Seattle: University of Washington Press, p. 443–451.

Leavitt, E. (1980) Surface-based air stress measurements made during AIDJEX. In *Sea Ice Processes and Models* (R. S. Pritchard, Ed.). Seattle: University of Washington Press, p. 419–429.

McPhee, M.G. (1980) An analysis of pack ice drift in summer. In *Sea Ice Processes and Models* (R. S. Pritchard, Ed.). Seattle: University of Washington Press, p. 62–75.

McPhee, M.G. (1982) Sea ice drag laws and simple boundary layer concepts, including application to rapid melting. USA Cold Regions Research and Engineering Laboratory, CRREL Report 82-4.
McPhee, M.G. (1989) Inferring ice/ocean surface roughness from horizontal current measurements. *Journal of Offshore Mechanics and Arctic Engineering*, **111**: 155–159.
McPhee, M.G., G.A. Maykut and J.H. Morison (1987) Dynamics and thermodynamics of the ice/upper ocean system in the marginal ice zone of the Greenland Sea. *Journal of Geophysical Research*, **92**: 7013–7031.
Pease, C.H., S.A. Salo and J.E. Overland (1983) Drag measurements for first-year sea ice over a shallow sea. *Journal of Geophysical Research*, **88**: 2853–2862.

Coupling of Ice–Ocean Flow in Coastal Seas

J.E. OVERLAND AND C.H. PEASE*
NOAA/PMEL
Seattle, Washington, U.S.A.

ABSTRACT

A sea-ice, barotropic-ocean model with a 1-km resolution is used to investigate the coupling of ice motion to wind-driven coastal currents. The model emphasizes the ice thickness/strength relation on downwind coasts, and resolving oceanic boundary layers for finite depth situations through the use of vertical structure functions. An appropriate constitutive law appears to be a hardening plastic based on qualitative observations from Alaskan continental shelves. For first-year ice, strength is taken to be proportional to the square of ice thickness. A north wind example of 10 m/s with the coastline to the set shows the depth-dependence of rotational shear in the sea-ice/ocean boundary layer and sea-surface tilt which contributes an alongshore slope current. There is a slight convergence of sea ice over the shelf, a coastal shear zone of 4 km, and an alongshore ice speed seaward of the shear zone of 6% of the wind seaward of a coastal rubble field, which grows seaward with time. The hardening plastic interpretation of the rubble field has the stress state at a yield limit in contrast with a rigid plastic of high constant strength that yields only at the coast. We conclude that ice thickness/motion feedback is important on scales less than 10 km and that the relation of ice velocity to wind stress in coastal seas is variable because the ocean slope current responds only to the alongshore component of the wind.

*See Overland, J.E. and C.H. Pease (1988) Modeling ice dynamics of coastal seas. *Journal of Geophysical Research*, **93**(C12): 15,619–15,637.

Section VI:
Polar Oceanography
Field observations

An Attempt to Measure Deep Saline Outflow through Barrow Canyon

A.T. ROACH AND K. AAGAARD
NOAA/PMEL
Seattle, Washington, U.S.A.

ABSTRACT

We deployed two densely instrumented, 14-m-long arrays in Barrow Canyon during 1986–87. The measured flow was predominantly down-canyon, with record long mean speeds of 13–18 cm/s. Up-canyon reversals were most frequent in the fall, reaching speeds up to 120 cm/s, and advecting warm, saline Atlantic Intermediate water onto the shelf. Even though we found no hypersaline water, created during the formation of sea ice and which we expected to flow along the bottom of the canyon, salt flux estimates show a net delivery of salt to the Arctic Ocean.

MOTIVATION

The present study was motivated by the earlier measurements of Aagaard et al. (1981, 1985) showing a pronounced northeasterly flow along the coast during winter of very saline water (approaching 36 psu in February 1982) at the freezing point. We had two primary objectives: 1) to quantify the salt flux and thereby determine its importance as a source for both the Arctic Ocean halocline and the deep salinity maximum; and 2) to determine the vertical structure of the dense plumes, and particularly the degree to which they are stratified. The latter issue is probably important to their subsequent mixing history as they flow off the shelf, and therefore to their effectiveness in ventilating the Arctic Ocean (Aagaard et al. 1985). Barrow Canyon has been suggested by a number of investigators (Coachman et al. 1975, Garrison and Becker 1976, Mountain et al. 1976, Garrison and Paquette 1982, Aagaard et al. 1985, D'Asaro 1988) to be a likely avenue of exchange between the shelf and the deep ocean. Nature proved uncooperative, however, and provided no dense plumes. Instead, we were provided extensive demonstrations of the exchange across the shelf edge of less dense waters, and it is this topic that provides the focus of our discussion.

METHODS

We moored two 14-m long arrays in Barrow Canyon from October 1986 to August 1987 (Fig. 1). The array BC1 (71°27.48'N, 156°52.87'W) was near the axis of the canyon at a depth of 145 m, while array BC2 (71°26.16'N, 156°40.10'W) was on the shoreward wall of the canyon at about 90 m. These taut-wire moorings were each instrumented with three Aanderaa RCM-4 current meters, four Sea-Bird SeaCat conductivity-temperature data loggers, and one Aanderaa TG-3A pressure gauge. All instruments, except the top current meter on each array and the pressure gauge on the shallower mooring, recorded data of good quality throughout the deployment period. The pressure gauges monitored the vertical motion of the moorings, so that pressure variations could be accounted for in the salinity calculations (tidal heights are of order 10 cm and can be ignored for these purposes). The salinity errors due to mooring motion were significantly less than the errors due to conductivity uncertainties and the effects of mooring motion are thereby ignored.

Comparison of the pre- and post-deployment calibrations for the SeaCats suggests that the temperatures were stable over the year to within 0.005°C. Unfortunately, the pre-deployment calibration of conductivity was invalidated by a glycol leak into the calibration tank. An accumulation of silt in the conductivity cell apparently degraded the signal further during the course of the deployment. Nonetheless, we were able to calibrate the conductivity cells in situ by comparing the observed temperature-salinity (T-S) correlations during periods of upwelling of warm intermediate waters into the canyon, with a canonical T-S correlation derived from a large number of regional CTD casts. A linear least squares fit to the monthly offset (assuming accurate temperatures) was computed for each instrument over the deployment period to provide a time-dependent salinity correction. We estimate that the final salinities are accurate to within 0.06 psu.

The current data were low-pass filtered using a cosine-squared Lanczos filter with a half-power point of 35 hr. We also calculated four year-long time series of 6-hr surface winds by reducing (36%) and rotating (27° CCW) the geostrophic wind at locations near Nome, Barrow and Barter Island. Finally, a surface pressure difference series was created by subtracting a demeaned, detrended pressure series at Barrow from one at Nome.

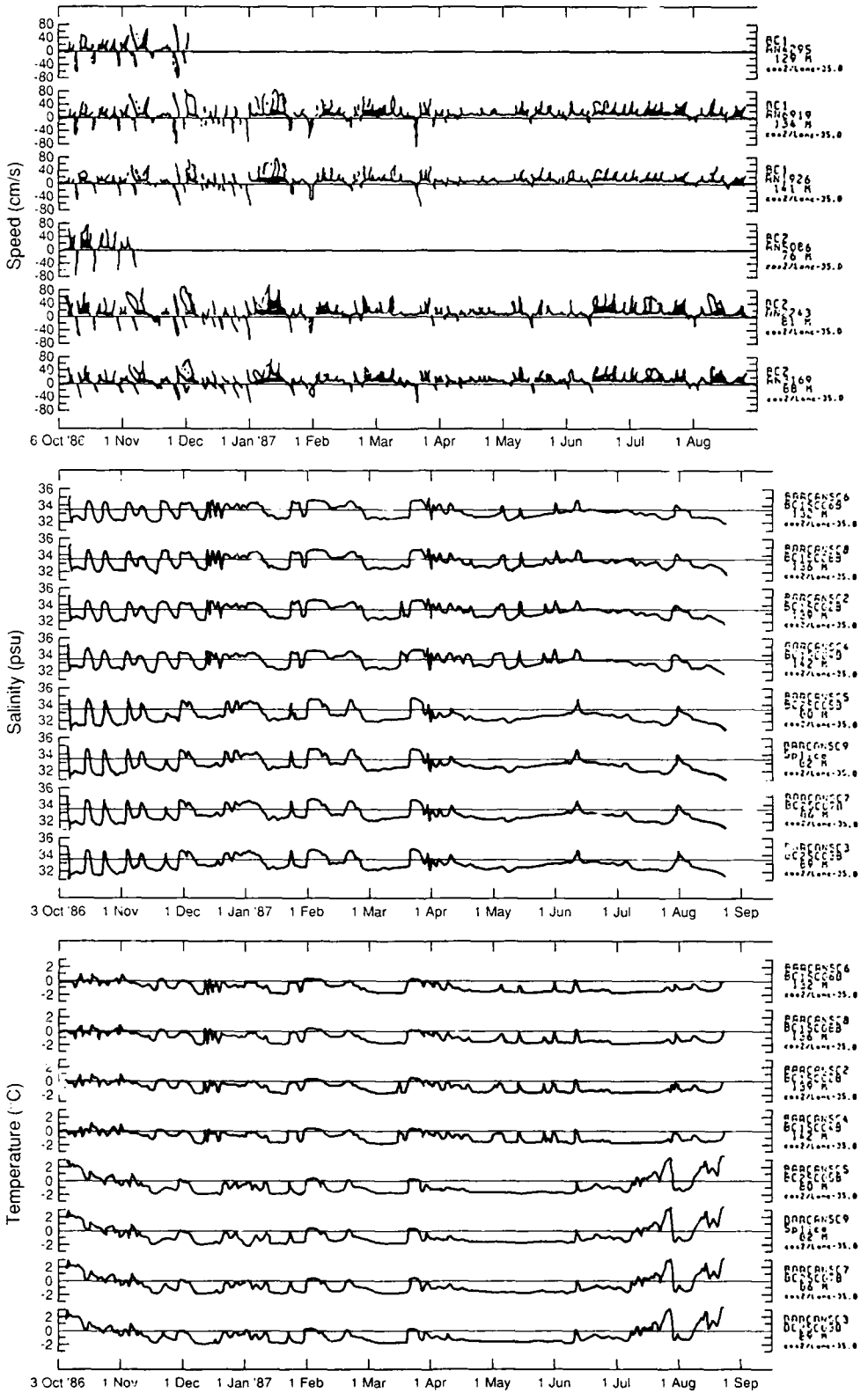

Figure 1. The location of Barrow Canyon and the orientation of the moorings is shown to the right. The time series are presented below. The current vectors are resolved on 50°T and the vertical scale of salinity is from 31.0 to 36.0. All series are filtered with a 35-hour cosine-squared Lanczos filter.

Table 1. Current meter statistics. Instrument designated by mooring and elevation above sea floor (m).

Instrument	Mean velocity (cm/s)	(T)	Principal axis (T)	(% of variance)
BC1 /14.0	14.8	54.4	225	97.5
/9.0	15.9	59.8	226	97.2
/2.0	12.8	59.7	223	97.7
BC2 /14.0	22.7	53.4	229	98.0
/9.0	18.0	45.8	223	94.0
/2.0	16.9	48.0	222	97.8

BARROW CANYON RESULTS

The record-length bulk statistics of the mean flow through Barrow Canyon indicate a transport to the northeast throughout the bottom layer (Table 1). Embedded in this down-canyon flow were reversal events with transport southwest from the Beaufort to the Chukchi seas. While a seasonal signal was not evident in the current speeds, the number and intensity of reversals were greatest in the fall and steadily decreased into the spring (Fig. 1). The relation of current direction to water mass properties during periods of reversed flow shows that warm, saline Arctic Intermediate Water (AIW) was advected into the Chukchi Sea through Barrow Canyon.

Both moorings had flow primarily focused along the major axis of the canyon, with nearly 98% of the current speed variance contained within 45–60°T for all the records, reflecting the strong topographic steering of the canyon. The direction of the axis of greatest variance was slightly more variable on the slope, but that mooring had no significant rotational energy, even surrounding reversal events. At BC1, there was a suggestion of an eastward rotation of the velocity component following a reversal. Mean speeds were 12–15 cm/s at the bottom of the canyon, with a stronger flow of 17–23 cm/s on the shoreward wall of the canyon at BC2. Both moorings had peak outflow speeds in excess of 100 cm/s.

The SeaCat time series show that the water column responded similarly to temperature and salinity fluctuations at both locations. Comparably placed instruments from each mooring were coherent (> 0.85 at 95% confidence) for periods > 3 days. During the four inflow events in October–November 1986, each mooring responded nearly uniformly with the current at each instrument leading the one above it by 2–3 hours. Vertical shear in the up-canyon velocity components was 3–9 cm/s. There was a distinct difference between the moorings, with the range of salinity variations on the wall of the canyon of about 3.3

Table 2. SeaCat statistics.

Mooring	Depth (m)	Mean sal. (psu)	Sal. RMS (psu)	Max. sal. (psu)	Min. sal. (psu)
BC1					
SC 6	32.2	33.199	0.093	34.849	31.839
SC 8	136.4	33.244	0.091	34.848	31.843
SC 2	139.0	33.260	0.093	34.848	31.689
SC 4	142.0	33.300	0.093	34.850	31.649
BC2					
SC 5	79.2	32.754	0.10	34.802	31.161
SC 9	82.4	32.789	0.110	34.831	30.997
SC 7	86.0	32.828	0.110	34.844	31.247
SC 3	89.0	32.869	0.105	34.785	31.357

Mooring	Depth (m)	Mean temp. (C)	Temp. RMS (C)	Max. temp. (C)	Min. temp. (C)
BC1					
SC 6	132.2	–1.012	0.182	1.287	–1.940
SC 8	136.4	–0.985	0.180	1.105	–1.942
SC 2	139.0	–0.952	0.179	1.070	–1.944
SC 4	142.0	–0.920	0.178	1.076	–1.940
BC2					
SC 5	79.2	–0.762	0.230	3.587	–1.904
SC 9	82.4	–0.791	0.203	3.512	–1.915
SC 7	86.0	–0.759	0.237	3.334	–1.919
SC 3	89.0	–0.755	0.237	3.230	–1.91

psu (from about 31.5 to 34.8) while that at BC1 was 2.4 psu (32.2 to 34.6). The temperature and salinity mean values at BC2 were fresher (by 0.5 to 0.6 psu) and colder (by about 0.15°C) than at BC1 (Table 2). In addition, the temperature record at BC2 had a cooling trend until mid-November, after which the temperatures leveled off and the frequency content of the temperature signal became more comparable to that of salinity. Even though BC1 had a high frequency content at the beginning of the record like that of BC2, the mean temperature did not show the same decrease in the autumn, but the salinity maximum encountered decreased by about 0.006 psu day^{-1} until mid-January.

A correlation analysis between major axis currents and salinity yielded a –0.56 correlation, with currents leading by 48 hours, which, with a nominal speed of 40 cm/s, would mean a water mass would travel nearly 70 km. Mooring BC1 led BC2 on inflow, usually by 12 to 13 hours. On outflow, BC2 led by 1–2 hours. Peak speeds of inflow events were about 80 cm/s and they lasted from 2–6 days.

Both moorings were similar in their distribution of water types, with Chukchi water masses (cold and fresh) and those of intermediate temperature and salinity (centered around –0.5°C and 33.8 psu) being

Table 3. Correlations of Barrow Canyon currents to regional winds and surface pressure gradients. 87119–87240, 6-hourly data.

	Barrow	*Barter Island*	*Nome*	*Barrow–Nome Del. P*
BC1-134	0.45 (6)	0.49 (6)	0.52 (18)	–0.53 (24)
BC1-141	0.45 (6)	0.48 (6)	0.52 (24)	–0.51 (24)
BC2-81	0.46 (6)	0.55 (6)	0.50 (24)	–0.55 (24)
BC2-88	0.46 (6)	0.53 (12)	0.50 (24)	–0.57 (24)

( ) lag in hours.
+ lag = column leads.

most common. BC1 showed a broader range of water types than did BC2, whereas the latter had a predominance of Chukchi water. Mooring BC2 (on the sidewall of the canyon) had a tighter distribution of AIW, the absence of a large mass of intermediate water and a broader band of temperatures (from –2.0 to –1.0°C) among the lower salinity waters (32.3–32.6 psu).

The winds are consistently related at about 0.50 (95% level of confidence) and lead the currents by 6 to 12 hours (Table 3). Surprisingly, the Nome wind is also related at that level, albeit with a 24-hour lag, indicating the influence of northerly flow over the Chukchi shelf. We found about the same level of correlation (0.5 with a 24-hour lag) using the surface pressure difference between Barrow and Nome. Thus, about 25% of the current variance can be accounted for by this pressure difference, significantly less than found by Mountain (1976).

Eddy flux calculations for the entire record show a net transport of both heat and salt off the shelf. The sign of the flux estimates indicates that density gradients were positive down canyon and offshore. We also calculated eddy salt and heat flux estimates for mooring locations approximately 100 and 400 km east of our Barrow Canyon moorings (MA2 and MB2). Those calculations show an order of magnitude smaller flux than that in Barrow Canyon, with a positive correlation offshore for the significant (95% level) contributions.

The lack of a strong atmospheric connection leads us to formulate the hypothesis that the mass exchange through Barrow Canyon is driven oceanically, at least in part, with contributions both from the Arctic Ocean Basin to the north and from the regional flow to the south. The implication of a positive flux of salt through the canyon, even in the absence of a brine outflow, is that there may be a recirculation of the upwelled water in the canyon. Thus, inflowing Atlantic water from the deep Canadian Basin may act to resupply the Arctic Ocean halocline.

REFERENCES

Aagaard, K., L.K. Coachman and E.C. Carmack (1981) On the halocline of the Arctic Ocean. *Deep-Sea Research*, **28**: 529–545.

Aagaard, K., J.H. Swift and E.C. Carmack (1985) Thermohaline circulation in the arctic mediterranean seas. *Journal of Geophysical Research*, **90**: 4833–4846.

Coachman, L.K., K. Aagaard and R.B. Tripp (1975) *Bering Strait: The Regional Physical Oceanography*. Seattle: University of Washington Press.

D'Asaro, E.A. (1988) Generation of sub-mesoscale vortices: A new mechanism. *Journal of Geophysical Research*, **93**: 6685–6693.

Garrison, G.R. and P. Becker (1976) The Barrow Submarine Canyon: A drain for the Chukchi Sea. *Journal of Geophysical Research*, **81**: 4445–4453.

Garrison, G.R. and R.G. Paquette (1982) Warm water interactions in the Barrow Canyon in winter. *Journal of Geophysical Research*, **87**: 5853–5859.

Mountain, D.G., L.K. Coachman and K. Aagaard (1976) On the flow through Barrow Canyon. *Journal of Physical Oceanography*, **6**: 461–470.

Oceanic Heat Flux in the Fram Strait Measured by a Drifting Buoy

D. K. PEROVICH AND W. B. TUCKER III
U. S. Army Cold Regions Research and Engineering Laboratory
Hanover, New Hampshire, U.S.A.

R. A. KRISHFIELD
Woods Hole Oceanographic Institute
Woods Hole, Massachusetts, U.S.A.

ABSTRACT

Two thermistor strings were installed through the ice to measure ice temperatures and determine oceanic heat fluxes as the Arctic Environmental Drifting Buoy drifted from the Arctic Basin into the Greenland Sea. Ice temperature data between 14 December 1987 and 2 January 1988 were retrieved. During this period the AEDB progressed from approximately 81°N 4'E to 77°N 5'W. This constituted the most rapid displacement of the entire drift, coinciding with the entry of the floe into the marginal ice zone of Fram Strait. Once in the MIZ, water temperatures increased, most notably at a depth of 16 m, where values changed from −1.8°C to more than 2°C. Bottom ablation rates of 34 mm/day were observed between 21 and 28 December. During this excursion into warmer water, the oceanic heat flux increased by a factor of 18, from 7 W/m^2 to 128 W/m^2.

INTRODUCTION

Both the extent and the thickness of the polar sea ice covers are sensitive to the transfer of heat from the ocean to the underside of the ice. Maykut and Untersteiner (1971) demonstrated that an oceanic heat flux (F_w) of 2 W/m^2 was consistent with observations of ice equilibrium thickness in the Arctic Basin and that an increase to 8 W/m^2 would be sufficient to remove the entire ice cover. Maykut (1982) discussed in detail the impact of the oceanic heat flux on large-scale heat exchange in the Central Arctic. In the Antarctic, Allison (1981), studying sea ice near Mawson, estimated the oceanic heat flux to be in the 10–20 W/m^2 range, while Gordon et al. (1984) report a mean annual F_w of 12 W/m^2 for the Weddell Sea. These large values suggest that the oceanic heat flux may play an even more important role in the annual cycle of antarctic sea ice.

Direct measurements of sensible heat flux in the ocean are quite difficult and are rife with uncertainties. However, an ice cover provides an opportune platform to monitor indirectly the time-integrated oceanic heat flux. The complex task of measuring detailed temperature and salinity profiles in the water and estimating exchange coefficients is replaced by the considerably simpler job of measuring ice temperature, salinity, and mass changes at the ice bottom. The oceanic heat flux is then computed as the residual of the energy balance equation of the lower portion of the ice. This indirect method has been used successfully by McPhee and Untersteiner (1982), who observed values of F_w less than 1 W/m^2 in the Arctic northwest of Spitzbergen. In sharp contrast to the small Central Arctic values of 1–2 W/m^2, observations in the marginal ice zone of the Greenland Sea during summer indicate oceanic heat fluxes of 1600 W/m^2 at the the extreme ice edge (Josberger 1987) and 200 W/m^2 roughly 30 km in from the ice edge (McPhee et al. 1987).

Because of the importance of the oceanic heat flux to sea ice thermodynamics and the potential for large spatial variations, values from diverse regions should be obtained. One approach is to acquire these data through buoy-based measurements. In this paper we present data from one such experiment.

EXPERIMENTAL CONFIGURATION

The Arctic Environmental Drifting Buoy (Honjo 1988) was a sophisticated instrument package consisting of ice thermistor strings, Argos transmitters, fluorometers, an acoustic Doppler current profiler, and a sediment trap. On 4 August 1987 the buoy was deployed on a multiyear ice floe at 86°17'N, 22°13'E. It drifted on the ice until 2 January 1988 (77°36'N, 5°12'W) when the floe broke up while traversing Fram Strait. It floated in the water from 2 January until recovery on 15 April 1988. In total the buoy drifted nearly 4000 km in 255 days.

The ice temperature portion of the AEDB consisted of two thermistor strings in the ice plus a data logger in the buoy. The strings were installed adjacent to the buoy in multiyear ice that was 3.7 m thick with a 0.08 m snow cover. One string was a finely spaced (0.05-m) vertical array centered on the bottom of the ice, with more coarsely spaced (0.10, 0.25, 1.00 m) thermistors extending 0.75 m up into the ice and 1.8 m down into the water column. The other string comprised 13 thermistors spaced at 0.25-m intervals from the surface of the ice to a depth of 3.0 m. Prior to installation the thermistors were calibrated in the labora-

tory at three temperatures to provide an accuracy of 0.01°C. Every 6 hours the data logger interrogated the thermistor strings and recorded the results.

The ice temperature measurements were terminated on 2 January when the ice floe was crushed and the thermistor strings were sheared off from the buoy. Unfortunately, due to a malfunction in the datalogger's storage module, data from the earlier portion of the drift was lost. Because of these two difficulties, the only ice temperature data retrieved were from 14 December (day 348) to 2 January (day 367). Although only 20 days in duration, this period proved to be most intriguing, manifesting large values of ice speed, bottom melt rate, and oceanic heat flux.

RESULTS

From 14 December to 2 January the AEDB progressed from roughly 81°N 4'E to 77°N 5'W, which constituted the most rapid displacement of the entire drift. Figure 1 displays the drift track of the buoy during this period. Ice edge positions obtained from the Naval Polar Oceanography Center weekly ice analyses are also shown in Figure 1. There was a sharp increase in displacement on day 357 as the buoy entered the marginal ice zone of the Fram Strait. Between days 357 and 367, the position of the ice floe varied from within 30 to 100 km of the ice edge.

Buoy speed as a function of time is plotted in Figure 2. Speeds from day 348 to 356 are comparable to mean values for the entire experiment. After day 356 the speed increased sharply, with the buoy moving as fast as 80 km/day. The sharp increase in speed as ice enters Fram Strait from the Arctic Basin has been pointed out by Moritz and Colony (1988), who examined the drift statistics of many buoys in this region.

Temperatures at selected depths within the ice and the water column are also plotted in Figure 2. The 16-m temperatures were obtained from an RD Instruments acoustic Doppler current profiler (ADCP) (A.J. Plueddeman, Woods Hole Oceanographic Institution, pers. comm., 1989). The ADCP uses a YSI thermolinear component that has an accuracy better than 0.1°C. The 16.0-, 5.6-, and 3.0-m thermistors were in the water, while the 2.75-, 2.50-, and 2.25-m probes were initially in the ice. From day 348 to 355 the water column to a depth of 16 m was essentially isothermal at its freezing point. On day 355, associated with the increase in speed, a transition to warmer water occurred. The warmest water temperature (2.25°C) was observed at a depth of 16 m near the end of day 356.

Thermistor data indicate that from day 348 to day 355 the temperature profile in the ice was linear with a gradient of approximately 5°C/m. With this linear profile it was straightforward to determine that the ice temperature was equal to the water temperature at a depth of 2.98 m, thereby delineating the bottom of the ice. At any depth, temporal variations in tem-

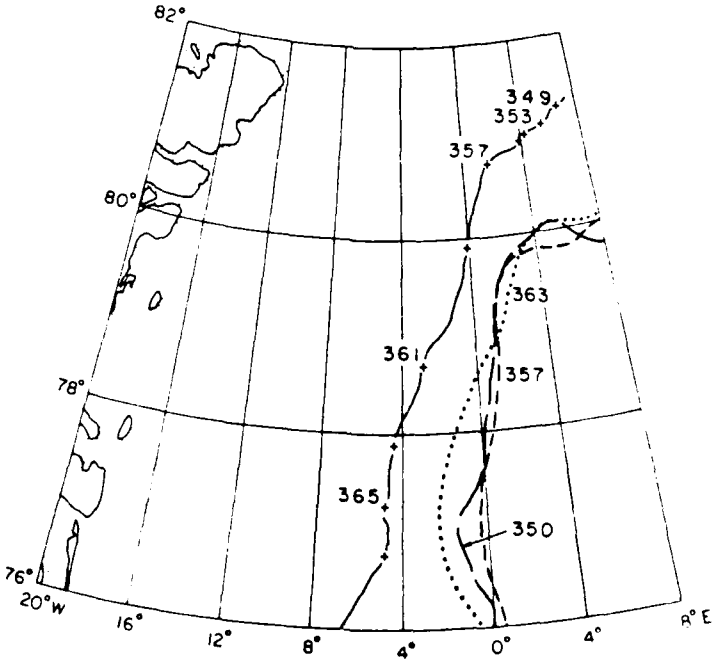

Figure 1. Map of the AEDB track for days 348 to 367. Ice edge positions are plotted for days 350 (– – –), 357 (—), and 363 (···).

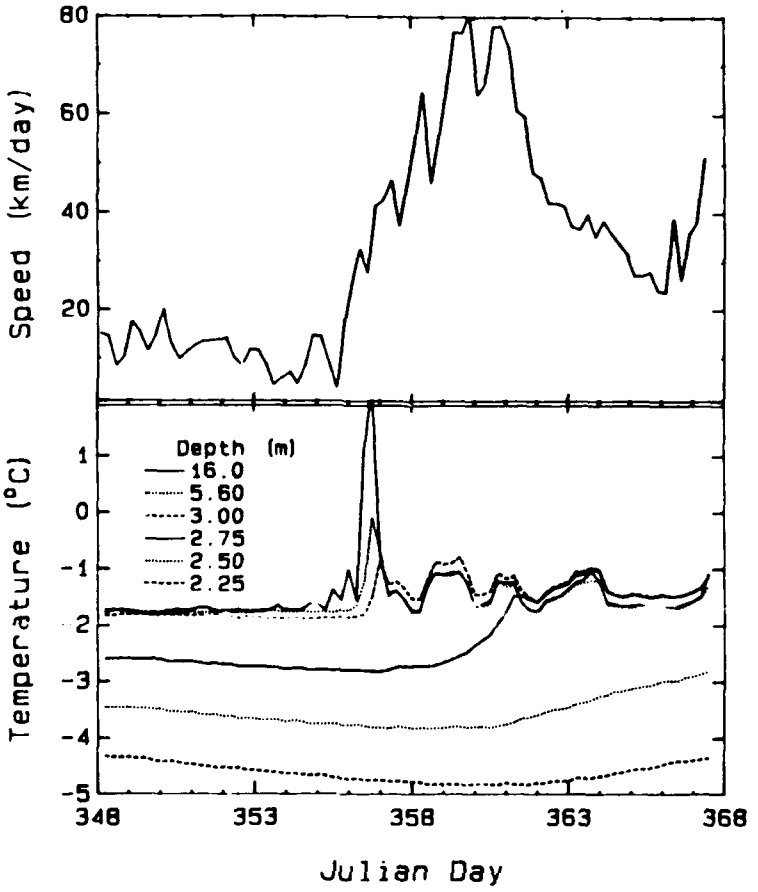

Figure 2. Speed vs time and temperature (at selected depths) vs time. The 16.0-, 5.6-, and 3.0-m depths were in the water and the 2.75-, 2.50- and 2.25-m depths were in the ice. Depths are measured from the surface of the ice. Top: Speed vs time. Bottom: Temperature at selected depths vs time.

perature were small—on the order of a few tenths of a degree per day. There was no appreciable bottom ablation during this period. After the floe entered warmer water on day 356 there was a continual increase in temperature in the bottom meter of the ice. This trend was most pronounced for the 2.75-m probe, which melted free of the ice on day 362. Between days 355.25 and 362.00, the ice bottom moved from 2.98 to 2.75 m, constituting 0.23 m of ablation. While large, this average ablation rate of 34 mm/day is comparable to those reported by Maykut and Perovich (1985), Morison et al. (1987), and Josberger (1987) for the summer MIZ. Our measurements occurred in winter, and that even as the underside of the ice was undergoing this considerable ablation, air temperatures ranged from –15 to –30°C.

McPhee and Untersteiner (1982) describe the method for computing the oceanic heat flux from ice temperature profiles and measurements of ablation/accretion at the ice bottom. The time-averaged oceanic heat flux is the residual of the conductive (Q_f), specific (Q_s), and latent (Q_L) heats,

$$F_w = (1/\Delta t)(Q_f + Q_s + Q_L), \quad (1)$$

where Q represents heat fluxes integrated over time (t). The latent heat associated with ice formation is negative, and with ice ablation, positive.

The conductive heat term describes the heat flow through a reference level within the ice and is expressed as

$$Q_f = \int k_s(\partial T/\partial z)dt, \quad (2)$$

where the thermal conductivity of sea ice (k_s) is defined using Untersteiner's (1961) expression $k_s = k_i + (bs_i/T)$, k_i is the thermal conductivity of fresh ice (2.04 J/m), B is a constant equal to 117.3 J/m s, s_i is ice

salinity (mass of solute per mass of solution), T is ice temperature (°C), and z is depth.

The specific heat contribution refers to the change in heat content of the ice and is

$$Q_s = \rho \int \int c_s dT dz, \quad (3)$$

where ρ is the ice density and c_s is the specific heat of sea ice. Schwerdtfeger (1963) gives the specific heat of sea ice as

$$c_s = -s_i L/(\alpha T^2) + s_i(c_w - c_i)/(\alpha T) + c_i$$

where α is a constant (–0.0182°C^{-1}), L is the latent heat of fusion for pure ice (333.9 kJ/kg), and the specific heat of pure water (c_w) and pure ice (c_i) are 4.23 and 2.01 kJ/°C kg, respectively. The integration over z is performed from the reference level in the ice to the bottom of the ice.

The latent heat expression is

$$Q_L = \rho \int q_m dz \quad (4)$$

where q_m is the heat needed to melt a parcel of ice starting from temperature T_o and is given by Schwerdtfeger (1963) as

$$q_m = (L - c_i T_o)[1 - s_i/(\alpha T_o)] + (1/A)\, s_i(c_w - c_i) \ln[(s_i/(\alpha T_o)].$$

Equation 1 was evaluated by substituting the expressions for Q_i, Q_s, and Q_L from eq 2, 3, and 4. An ice salinity of 3‰ was selected as representative of the lower portion of multiyear ice (Weeks and Ackley 1982). The conductive term was calculated using a selected depth of 2 m as a reference level with $\partial T/\partial z$ evaluated using a central difference scheme. The time integral in eq 2 was evaluated numerically using a trapezoid rule with a 6-hour time step. In eq 3 the integration over temperature was performed analytically, while the integration over depth was done numerically using a 0.05-cm spacing. Similarly, the depth integral in eq 4 was computed using the trapezoid rule with a spacing of 0.01 m.

Computations of oceanic heat flux for two time intervals are presented in Table 1. Determining the position of the ice bottom is the largest source of error in the calculations, resulting in an uncertainty of 2 W/m^2. The first interval (days 348.25 to 355.25) is the period prior to the floe entering warmer water. During this period, water temperatures were at or near the freezing point and there was no discernible bottom melting. The second interval (355.25 to 362.00) begins with the entry into warmer water and ends when the 2.75-m thermistor melted free. Heat flux calculations were not performed for days 362 to 367 because the amount of bottom melting could not be accurately determined. As the ice entered warmer water, F_w changed by a factor of 18, increasing from 7 W/m^2 to 128 W/m^2. As Table 1 indicates, virtually all the additional heat was applied to melting on the underside of the ice. This large ocean-ice transfer of sensible heat in the MIZ is not surprising in light of the warm water and the rapid ice movement.

Let us now speculate about the earlier portion of the drift. While there are no ice temperature data available from the beginning of the drift on 4 August (day 216) through 14 December (day 348), we do know that the ice thinned from 3.70 to 2.98 during this period. Two simple scenarios to account for this ice loss are 1) that it occurred in a few discrete warm-water events or 2) that the ice was ablating continuously throughout the drift. Water temperatures at 16 m from day 216 to 367 are shown in Figure 3 (A.J. Plueddeman, Woods Hole Oceanographic Institution, pers. comm., 1989). The excursion into warm water on day 356 is by far the largest thermal event of the drift. Aside from a slight increase in water temperature near day 325, no other such events are ap-

Table 1. Summary of heat data for periods from 14 to 21 December and from 21 to 28 December. *Q* is the heat per unit area (MJ/m^2), % is the percent of the net *Q*, and *F* is the flux (W/m^2).

	348.25 to 355.25			*355.25 to 362.00*		
	%	*F*	*Q*	%	*F*	*Q*
Conduction	5.7	134	9.3	5.4	7	9.2
Specific heat	–1.4	–34	–2.4	1.4	2	2.5
Latent heat	0.0	0	0.0	68.0	91	116.6
Ocean	4.2	100	7.0	84.4	100	128.3

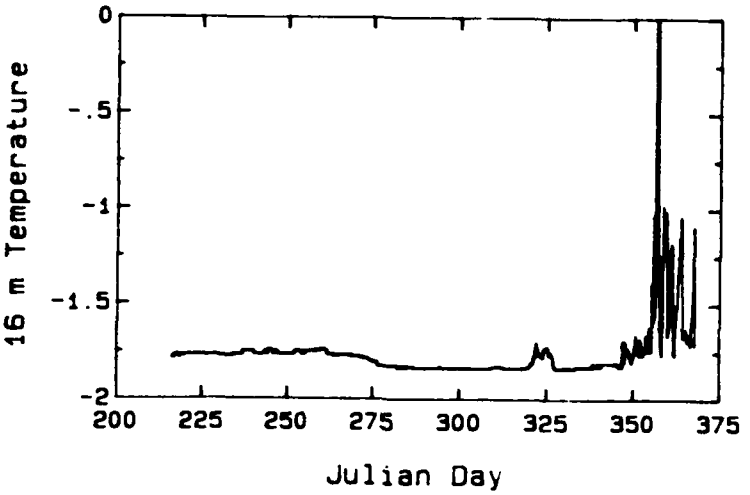

Figure 3. Water temperature 16 m below the ice surface vs time from 4 August 1987 to 2 January 1988.

parent. This argues that, at least in a general sense, the mass loss at the bottom was constant during the entire drift.

Constant ice loss would yield an average melt rate of 5.5 mm per day. Assume, somewhat simplistically, that on 4 August the ice temperature profile was isothermal (–1.0°C) from 2 to 3.4 m, and then decreased linearly to –1.5°C at 3.7 m. Given this initial temperature profile there would have been a latent heat loss of 185 MJ/m² due to melting and a change in heat content of –27 MJ/m² due to cooling. The conductive heat flux is more difficult to estimate. Untersteiner (1961) indicates that temperature gradients in the ice interior are less than half a degree per meter from August through October, then increase gradually to maximum values in early January. We shall assume that at a depth of 2 m the ice is isothermal from August through October, followed by a uniform cooling to the profile observed on 14 December, resulting in a conductive heat loss of 7 MJ/m². Combining these estimated heats in eq 1,

$$F_w = (7-27+185)/(348-216)$$

$$= 1.2 \text{ MJ/m}^2\text{day} = 14 \text{ W/m}^2$$

produces an oceanic heat flux of 14 W/m².

Being an order of magnitude larger than standard estimates of oceanic heat flux in the Central Arctic, our time-averaged value is large enough to engender some further discussion. Certainly with the many assumptions there is considerable potential for error. In fact it is suspicious that the estimated flux of 14 W/m² is twice as large as the value for the period 348–355. It is evident though that the time-averaged oceanic heat flux will be on the order of 10 W/m², rather than 1 W/m². However, it is possible that a disproportionate share of the melting occurred in the August–September time frame. During this period the water column is stratified from the input of fresh meltwater so that temperatures at 16 m may not be representative of water temperatures at the ice bottom. In addition there is a sizable input of shortwave radiation into the water column, which could result in enhanced bottom ablation.

SUMMARY

There was 0.72 m of bottom melting between the deployment of the AEDB on 4 August 1987 at 86°N 22'E and when it entered Fram Strait on 14 December 1987 at 81°N 4'E. Examination of the 16-m ocean temperature leads us to believe that there were no dramatic melting events during this period. By making some simple assumptions regarding the temperature profile in the ice, we determined that the time-averaged oceanic heat flux was 14 W/m². Between 14 December and 2 January we obtained high-resolution temperature data in the ice and upper ocean. The buoy drifted from 81°N 4'E to 77°N 5'W during this time, reaching speeds as great as 80 km/day. At the onset of the high drift rates, warmer water was encountered, resulting in 0.23 m of bottom ablation over a 7-day winter period. During this period of rapid bottom melting the oceanic heat flux was 128 W/m².

Although this experiment was hampered by equipment difficulties, buoy-based systems show promise as an effective means of measuring oceanic heat flux in ice-covered waters. Buoys afford a platform for

far-ranging spatial and long-term temporal measurements of F_w. Increased accuracy in F_w could be obtained by reducing uncertainties in ice bottom mass changes through the addition of an independent ice ablation sensor.

ACKNOWLEDGMENTS

Thanks to Dr. A.J. Plueddeman for graciously providing the 16-m temperature data. We appreciate the helpful discussion with J. Wettlaufer. This article benefited from the reviews provided by Dr. E.L Andreas and S.F. Ackley. Finally, we express our gratitude to Dr. S. Honjo for the opportunity to participate in the AEDB effort. This work was funded under ONR Contracts N0001489AF00001 and N0001487K0007.

REFERENCES

Allison, I. (1981) Antarctic sea ice growth and oceanic heat flux. In *Sea Level, Ice and Climate Change*. International Association Scientific Hydrology, Publication no. 131, p. 161–170.

Gordon, A.L., C.T.A. Chen and W.G. Metcalf (1984) Winter mixed layer entrainment of Weddell deep water. *Journal of Geophysical Research*, **89**: 637–640.

Honjo, S. (1988) AEDB: Ice-, water-surface drifting buoy mooring experiment through the southern transpolar drift. *EOS Transactions, American Geophysical Union*, **69**: 1277.

Josberger, E.G. (1987) Bottom ablation and heat transfer coefficients from the 1983 Marginal Ice Zone Experiment. *Journal of Geophysical Research*, **92**: 7012–7016.

Maykut, G.A. (1982) Large-scale heat exchange and ice production in the central Arctic. *Journal of Geophysical Research*, **87**: 7971–7985.

Maykut, G.A. and D.K. Perovich (1985) MIZEX heat and mass balance data. Applied Physics Laboratory, University of Washington, Report APL-UW 12-85.

Maykut, G.A. and N. Untersteiner (1971) Some results from a time dependent, thermodynamic model of sea ice. *Journal of Geophysical Research*, **76**: 1550–1575.

McPhee, M.G. and N. Untersteiner (1982) Using sea ice to measure vertical heat flux in the ocean. *Journal of Geophysical Research*, **87**: 2071–2074.

McPhee, M.G., G.A. Maykut and J.A. Morison (1987) Dynamics and thermodynamics of the ice/upper ocean system in the Marginal Ice Zone of the Greenland Sea. *Journal of Geophysical Research*, **92**: 7017–7031.

Morison, J.A., M.G. McPhee and G.A. Maykut (1987) Boundary layer, upper ocean, and ice observations in the Greenland Sea Marginal Ice Zone. *Journal of Geophysical Research*, **92**: 6987–7011.

Moritz, R.E. and R. Colony (1988) Statistics of sea ice motion, Fram Strait to North Pole. In *Proceedings of 7th International Conference on Offshore Mechanics and Arctic Engineering*, vol. 4, p. 75–82.

Schwerdtfeger, P. (1961) The thermal properties of sea ice. *Journal of Glaciology*, **4**: 789–807.

Untersteiner, N. (1961) On the mass and heat budget of Arctic sea ice. *Archiv für Meteorologie, Geophysik und Bioklimatologie*, Ser. A, **12**: 151–182.

Weeks, W.F. and S.F. Ackley (1982) The growth, structure, and properties of sea ice. USA Cold Regions Research and Engineering Laboratory, Monograph 82-1.

Mesoscale Ocean Processes in the Marginal Ice Zone

O.M. JOHANNESSEN, S. SANDVEN
AND J.A. JOHANNESSEN
Nansen Remote Sensing Center
Solheimsvik, Norway

ABSTRACT

In the last decade new knowledge about mesoscale physical processes in the Marginal Ice Zone has been obtained. In the Fram Strait and Greenland Sea region where the ice cover encounters open ocean, investigations of eddies, vortex-pairs, jets and chimneys have been possible because of the extensive use of remote sensing techniques, especially microwave instruments such as SAR, combined with in situ measurements. Under moderate wind conditions the ice floes serve as tracers, allowing a detailed study of the upper ocean circulation. In presence of major ocean currents, such as the West Spitzbergen Current and the East Greenland Current, local oceanic jets, typically 10 km wide and 100 m deep, are observed to shoot out from the ice edge, and grow into mushroom-shaped currents with one cyclonic and one anticyclonic eddy. This development is characteristic for the formation of vortex-pairs of horizontal scale 30 km. Open ocean eddies, propagating into the ice, and eddies generated along the ice edge can break up

the ice cover, transport it into warmer water, and thus increase the melt rate. The ice cover is also essential for wind-generated eddies, because the wind stress is generally higher over ice compared to open ocean, causing divergence or convergence. Several upper ocean chimneys, 300–500 m deep and 10–20 km wide, were also documented in which intermediate water masses were lifted to the surface by eddies or upwelling. If these chimneys are cooled at the surface, deep convection and bottom water formation are possible, which is important for the uptake of carbon dioxide and the global climate.

Vertical Mixing in a Highly Stratified Regime under Landfast Sea Ice

R.G. INGRAM and S. LEPAGE
Meteorology Department
McGill University
Montreal, Quebec, Canada

K. SHIRASAWA
Sea Ice Research Laboratory
Hokkaido University, Mombetsu, Japan

ABSTRACT

Vertical mixing in the upper water column under a complete landfast sea ice cover in southeast Hudson Bay is discussed. The effects of varying stratification are studied along a radial from the mouth of the Great Whale River to the offshore limits of the plume. Closely spaced CTD profiles along an offshore transect, moored salinity chains (fine and coarse vertical resolution) and current meters are used to describe the changes in vertical stratification as a function of ice presence or absence, river input, in-situ ice melt (buoyancy), tidal amplitude and low frequency current variability (kinetic energy).

Freshwater budget calculations based on river discharge and local sea ice melt show an almost equal contribution over the period of the spring freshet. The presence of a highly buoyant upper layer attenuates vertical mixing at the time of fragmentation of the landfast ice into individual floes. Local meteorological data are used to estimate the minimum wind energy required to initiate mixing and collapse the large freshwater plume to its much smaller open water extent. Velocity spectra (for frequencies of less than 1/hour) show a major increase of the low frequency (less than 0.08 /hour) and inertial contributions for the open water compared to the ice-covered regime.

The Freeze Experiment
Oceanographic Conditions During Autumn Freezeup in the Western Arctic

C.H. PEASE
PMEL/NOAA
Seattle, Washington, U.S.A.

R.D. MUENCH
SAIC
Bellevue, Washington, U.S.A.

The Freeze Experiment was conducted in the Chukchi Sea and northern Bering Sea between August 1987 and October 1988 to examine the fine-scale processes of freezing in the autumn in the context of the regional conditions just before and during initial freeze-up. The NOAA Ship *Surveyor* was used in August and October 1987 to deploy 10 current meter and pressure gauge moorings for overwintering at key locations, to set out four drifting ARGOS ice buoys for tracing the advancing ice edge, and to map heat and salt budgets for two distinct periods through high density CTD casts. During late November 1987, a 10-day series of cruises were completed on the tugboat *Nanuk III* from Nome, Alaska. A CTD attached to a remotely operated vehicle with a video camera was used to make horizontal CTD "casts" to observe spatial variability of the brine rejection and to photograph frazil. At the same time, a fixed mooring made high-frequency profiles of velocity, salinity, and water temperature. In September and October 1988, the *Surveyor* recovered the overwinter moorings and took an additional set of early autumn CTD observations over the shelves. Preliminary results show that an ice conveyor belt helps cool the upper water column by melting ice over the open Chukchi Shelf in early autumn, that freezing in nearshore areas is driven by radiative cooling during low winds and by turbulent transfer during high winds, beginning before the summer pycnocline is broken down, and that the freezing during turbulent conditions is probably organized by Langmuir cells.

Acoustic Doppler Current Measurements from the Arctic Environmental Drifting Buoy

A. J. PLUEDDEMANN
Department of Physical Oceanography
Woods Hole Oceanographic Institute
Woods Hole, Massachusetts, U.S.A.

T.B. CURTIN
Office of Naval Research
Arlington, Virginia, U.S.A.

ABSTRACT

Current measurements were made from the Arctic Environmental Drifting Buoy (AEDB) using a 150-kHz RD Instruments Acoustic Doppler Current Profiler (ADCP). The ADCP was deployed at a depth of 12 m below the flotation sphere with four acoustic beams separated by 90° in azimuth and pointed downward at 60° from the horizontal. Velocity profiles spanning depths between 40 and 330 m with 16-m resolution were collected at half-hour intervals over a period of 221 days while the buoy drifted from its starting point near 86°N, 23°E to 79°N, 16°W. The instrument was quite stable during the first two-thirds of the experiment, with heading variability of about 10 and typical tilts of 1 to 2°. Low frequency (subinertial) currents relative to the buoy during this period ranged from 1 to 10 cm/s. The later third of the experiment was marked by increasing variability in instrument orientation, with tilts of up to 10° and rapid heading changes of 10 to 90°. Relative, low-frequency currents increased to 10 to 20 cm/s during this period. Velocities in the high-frequency band for the full experimental record were separated into several overlapping pieces and analyzed in terms of the variability of the internal wave spectrum with latitude. Existing observations indicate that significant variability in the shape and level of the internal wave spectrum accompanied the transition from the open ocean to the sub-ice region of the Arctic, but the role of dynamic processes in determining the arctic internal wave spectrum has yet to be established.

Bering Sea Contributions to the Arctic Ocean

S. SALO AND K. AAGAARD
NOAA/PMEL
Seattle, Washington, U.S.A.

ABSTRACT

Many of the features of the Arctic Ocean are maintained by shelf processes. The structure of the upper Arctic Ocean north of Alaska indicates that its waters have two distinct sources in the Bering Sea. The temperature maximum near 75 m has salinity and nutrient concentrations similar to those on the northeastern Bering Sea shelf (and to a small volume of the upper waters farther west). The temperature minimum layer near 150 m, which coincides with the nutrient maximum, probably derives from the highly productive western Bering Sea shelf. Ammonia measurements suggest that the high-nutrient western shelf water, which has transited the Chukchi Sea, is carried eastward along the Arctic Ocean margin by the Beaufort Undercurrent. A nutrient gradient across the Beaufort Gyre indicates that other processes also contribute to the upper Arctic Ocean structure.

AUTHOR INDEX

Aagaard, K.; p. 287, 298
Ackermann, N.L.; p. 100
Ackley, S.F.; p. 16, 28, 79, 86
Anderson, M.R.; p. 193
Andreas, E.L.; p. 119
Barnes, P.W.; p. 106, 109, 114
Barry, R.G.; p. 119, 181, 185, 193
Bird, A.A.; p. 278
Bishop, G.C.; p. 141
Bjerkelund, C.A.; p. 206
Breitenberger, E.; p. 173
Brock, C.A.; p. 119
Buckley, R.G.; p. 49
Budgell, W.P.; p. 278
Carsey, F.; p. 224
Cavalieri, D.J.; p. 197, 217
Chang, A.T.C.; p. 213
Chellis, S.E.; p. 141
Cheng, A.; p. 259
Chiu, L.S.; p. 213
Clayton, J.R.; p. 97, 111
Close, A.R.; p. 35, 92
Comiso, J.C.; p. 179, 233
Connors, D.N., p. 145
Cox, G.F.N.; p. 40
Crane, R.C.; p. 189
Crawford, J.; p. 197, 224
Curtin, T.B.; p. 298
Denner, W.W.; p. 78
Dieckmann, G.; p. 86
Digby-Argus, S.; p. 5
Dod, T.; p. 233
Eicken, H.; p. 28, 86
Emery, W.J.; p. 189, 192
Eppler, D.; p. 197, 229
Farmer, L.D.; p. 126, 197, 229
Flato, G.M.; p. 239
Fleming, G.H.; p. 243
Fowler, C.; p. 189
Garrison, D.L.; p. 35, 92
Garrity, C.; p. 57
Gilbert, G.D.; p. 53
Gloersen, P.; p. 177
Goodberlet, M.A.; p. 209
Gordon , L.I.; p. 35
Gow, A.J.; p. 5, 67
Hawkins, J.; p. 189
Hibler, W.D. III; p . 152, 239, 247, 251
Hoeber, H.C.; p. 189
Hogan, A.; p. 217
Holladay, J.S.; p. 225
Holt, B.; p. 197, 224
Honjo, S.; p. 190, 190
Hopkins, M.A.; p. 152
Houssais, M.N.; p. 251
Hunter, R.E.; p. 109
Ingram, R.G.; p. 297
Jacobs, S.; p. 179
Jezek, K.C.; p. 67, 217
Johannessen, J.A.; p. 296
Johannesen, O.M.; p. 296
Johnson, D.; p. 191
Kempema, E.W.; p. 97, 106, 111, 114
Key, J.; p. 156
Kosloff, P.; p. 5
Kovacs, A.; p. 225
Kozo, T.L.; p. 126
Krabill, W.B.; p. 132
Krishfield, R.; p. 190, 291
Kutz, R.; p. 233
Lange ,M.A.; p.16,22,28,67,79,86,102
Ledley, T.S.; p. 256
LeDrew, E.; p. 191
Lee, A.; p. 109
Lepage, S.; p. 297
Levine, E.R.; p. 145
Lewis, J.K.; p. 78
Loewe, P.; p. 251
Lohanick, A.W.; p. 61, 229
Lu, M.; p. 163
Martin, S.; p. 136
Maslanik, J.A.; p. 181
McCormick, M.P.; p. 119
McElroy, M.; p. 192
McLaren, A.S.; p. 156, 185
McPhee, M.G.; p. 281
Meese, D.A.; p. 32
Miles, M.W.; p. 119
Moore, R.M.; p. 41
Moorell, J.L.; p. 119
Morris, C.S.; p. 203
Muench, R.D.; p. 297
Murrell, S.A.F.; p. 84
Neralla, V.R.; p. 189
Overland, J.E.; p. 284
Payne, J.R.; p. 97, 111
Pease, C.H.; p. 284, 297
Perovich, D.K.; p. 45, 291
Pfirman, S.; p. 102
Plueddemann, A.J.; p. 298
Pomalaza-Raez, C.A.; p. 75
Posey, P.G.; p. 259
Preller, R.H.; p. 259
Radke, L.F.; p. 119
Ramseier, R.O.; p. 206
Reimnitz, E.; p.92,97,106,109,111,114
Richter-Menge, J.A.; p. 79
Roach, A.T.; p. 287
Robinson, D.A.; p. 193
Rothrock, D.A.; p. 278
Rubenstein, I.G.; p. 206
Sackinger, W.M.; p. 163
Salo, S.; p. 298
Sammonds, P.R.; p. 84
Sandven, S.; p. 296
Scharfen, G.R.; p. 193
Schnell, R.C.; p. 119
Schoonmaker, J.S.; p. 53
Schumacher, J.A.; p. 193
Serreze, M.C.; p. 185, 191, 193
Shanan, S.S.; p. 75
Shell, R.R.; p. 145
Shen, H.H.; p. 75
Shen, H.T.; p. 100
Shirasawa, K.; p. 297
Smith, D.C. IV; p. 278
Smith, P.A.; p. 168
Smith, S.D.; p. 123
Spindler, M.; p. 86
Spitzer, W.; p. 41
Stanton, T.K.; p. 67
Steffen, K.; p. 197
Stein, P.J.; p. 78
Swift, C.T.; p. 197, 209
Swift, R.N.; p. 132
Thomas, D.R.; p. 278
Trodahl, H.J.; p. 49
Tucker, W.B. III; p. 132, 291
Voss, K.J.; p. 53
Wadhams, P.; p. 16, 136, 190
Walsh, J.E.; p. 191, 192
Weber, W.S.; p. 97, 109
Weeks, W.F.; p. 5
Welsh, J.P.; p. 126
Wendler, G.; p. 173
Wollenburg, I.; p. 102
Zwally, H.J.; p. 191, 192, 224